NASA CR-176,108

A Reproduced Copy

OF

NASA CR-176,108

JPL No. 9950-1062

ADVANCED BEAMED-ENERGY AND FIELD PROPULSION CONCEPTS

FINAL REPORT

31 May 1983

BDM/W-83-225-TR

PRINCIPAL INVESTIGATOR: L. N. Myrabo, Ph.D. (now Assistant Professor, Department of Mechanical Engineering, Rensselaer Polytechnic Institute, Troy, N.Y.)

Prepared for the California Institute of Technology and Jet Propulsion Laboratory Under NASA Contract NAS7-918, JPL Contract No. 956396.

This Page Intentionally Left Blank

ABSTRACT

The primary objective of this study is to investigate specific phenomena which might lead to major advances in payload, range and terminal velocity of very advanced vehicle propulsion. The effort focuses heavily on advanced propulsion spinoffs enabled by current government-funded investigations in directed-energy technology: i.e., laser, microwave, and relativistic charged particle beams. Futuristic (post-year 2000) beamed-energy propulsion concepts which indicate exceptional promise are identified and analytically investigated. To warrant inclusion in the study, the concepts must be sufficiently developed to permit technical understanding of the physical processes involved, assessment of the enabling technologies, and evaluation of their merits over conventional systems. The study investigates propulsion concepts that can be used for manned and/or unmanned missions for purposes of solar system exploration, planetary landing, suborbital flight, transport to orbit, and escape. Speculations are made on the chronology of milestones in beamed-energy propulsion development, such as in systems applications of defense, satellite orbit-raising, global aerospace transportation, and manned interplanetary carriers.

This Page Intentionally Left Blank

TABLE OF CONTENTS

TABLE OF CONTENTS

TABLE OF CONTENTS

TABLE OF CONTENTS

TABLE OF CONTENTS

This Page Intentionally Left Blank

LIST OF FIGURES

LIST OF FIGURES

LIST OF FIGURES

LIST OF FIGURES

LIST OF FIGURES

LIST OF FIGURES

LIST OF FIGURES

LIST OF FIGURES

LIST OF FIGURES

LIST OF FIGURES

LIST OF FIGURES

This Page Intentionally Left Blank

LIST OF TABLES

CHAPTER I
INTRODUCTION

As man extends his activities deeper and with increasing frequency into space, he will demand more sophisticated and energetic propulsion systems with capabilities greatly surpassing those of conventional chemical propulsion systems. Current chemical rocket engines that were developed for the space program are attaining performance close to the theoretical maximum. The "conventional" advanced propulsion technologies of nuclear-electric and solar-electric propulsion are advancing in their development cycles and will probably see application in space vehicle systems before 1990. However, these technologies are clearly inadequate for emerging more ambitious missions involving ever expanding human activity in space, such as large-scale space industry and the utilization of lunar and asteroidal materials. When human needs create a demand for new solutions to technical problems, history shows that available inefficient solutions will not be tolerated for long. In space, efficient, high-speed propulsion will be of such central importance that this issue deserves detailed consideration now. In fact, it is even more likely that demonstration of the plausibility and feasibility of efficient advanced propulsion methods could provide the critical leverage to engender major space activities, rather than the other way around.

The history of advanced propulsion research has produced large swings in funding levels over the past 30-40 years. NASA and the military services actively pursued advanced propulsion research during the 1960s and early 1970s, thereby giving rise to a substantial body of literature documenting this period. Since the early 1970s, funding for advanced propulsion research has been severely limited. However, significant studies were published by the USAF Rocket Propulsion Laboratory (AFRPL)[1] in 1972, Jet Propulsion Laboratory (JPL)[2] in 1975, and JPL[3] again in 1982. Nevertheless, the fact remains that today, R&D work on very advanced propulsion systems is carried out on a considerably lower level of effort than in

decades past. Understandably, generation of new concepts has been severely retarded by the reduced funding level.

A. ADVANCED PROPULSION STUDIES OF THE PREVIOUS DECADE

The focus and significant conclusions of the 1972 AFRPL study[1] can be summarized in the following paragraphs.

The purpose of the study was to identify and stimulate transitions to concepts beyond chemical rocket propulsion that would bring about substantial improvements in propulsion performance by the turn of the century. Advanced concepts falling under the general headings of Thermal Propulsion, Field Propulsion, and Photon Propulsion were evaluated to define their potential. The study attempted to reestablish the kind of unrestricted free-thinking, inventiveness, and creativity that existed during the late 1950s and early 1960s.

Three major conclusions are emphasized in the AFRPL study. First, the more intensive sources of energy will provide higher performance possibilities (e.g., an improvement of five orders of magnitude exists between chemical and nuclear energy sources). Second, the creativity of propulsion researchers should be strongly directed toward "infinite specific impulse" (Isp) concepts that draw prime energy and/or material freely from the ambient environment (whether through active interactions or through capitalization of natural phenomena), because of the implications for outstanding performance. The study defines the ideal infinite Isp propulsion system as one which takes both its working fluid and its energy from the environment. Third, advances in certain areas of technology could make a number of unconventional concepts suddenly very attractive. Previously, these concepts have been evaluated and quickly discarded. The study suggests that improvements in the energy output of high-power lasers by several orders of magnitude, or perhaps the invention of other competitive concepts for long distance energy transfer - are exemplary advances that have revolutionary potentials for laser propulsion and the infinite Isp ramjet. For the Field Propulsion concepts, the development of higher

current density superconductors, metallic hydrogen, or perhaps room temperature superconductors are promising breakthrough technologies.

The focus, approach and significant conclusions for the 1975 JPL study[2] can be summarized in the following paragraphs.

The primary objective of the study was to generate new advanced propulsion concepts having high potential for the more energetic propulsion applications in the post-1990 era of space exploration. The principal topics investigated included lasers, thermonuclear fusion, matter/antimatter annihilation, electronically excited helium, and energy exchange through the interaction of various fields.

Two distinctively different investigative directions were pursued in parallel. One investigated the possibility of using energy sources of known capability for releasing large amounts of energy (as compared to the chemical propellants used currently). Candidate energy intensive sources included nuclear fission and fusion, lasers, metastable and radical chemical species, and matter/antimatter annihilation. The second investigative direction explored potentials for exploiting energy resources existing in space and in the vicinity of planets: i.e., energy stored in the form of various fields (such as gravitation, magnetic, and electric), or in elementary particle concentrations. The study acknowledges that this direction was more difficult to pursue, largely due to the low-energy density level of such resources.

The JPL study utilized two basic criteria to evaluate the concepts with high potential for advanced propulsion applications: state of readiness, and energy-releasing capabilities (i.e., as it affects specific impulse). The following are a few of the conclusions reached in evaluating laser propulsion and matter/antimatter annihilation concepts. In the case of laser propulsion research, there is only a relatively small body of literature available. Second, there seems to be a strong tendency to oversimplify the problem, and to focus on limited aspects. This may be due to a lack of data in many related critical areas. Third, this shortcoming becomes critical when researchers attempt to evaluate the concepts, and compare their performance with other advanced propulsion concepts. Fourth,

in comparative studies of solar-electric and laser-electric propulsion, it is suggested that laser sources cannot compete with solar sources for interplanetary missions. Existing literature indicates that laser propulsion may be most readily applied to surface-to-orbit, orbit transfer, and planetary escape applications.

The JPL study mentions the two factors which make the use of matter/antimatter annihilation an attractive energy source for propulsion applications: extremely high rates of energy release (i.e., two orders of magnitude greater than that of thermonuclear fusion), and the "clean" products of the involved reactions (i.e., from the view of radioactive contamination). However, in the study, it was emphasized that the severe problems associated with antimatter production and storage put the current state of this technology at the conceptual level, and project the nearest successful propulsive implementation beyond the year 2000 A.D.

The focus and significant conclusions of the 1982 JPL study[3] are related in the following paragraphs.

The primary objective was to identify and evaluate new advanced propulsion concepts that enable or significantly advance the performance of interplanetary missions. A major finding in the study was that the missions to the outer planets and beyond are seriously constrained by state-of-the-art propulsion performance, and hence justifies the enthusiastic search for ultra-high performance propulsion systems. The scope of the 1982 study was limited to a consideration of the propulsion requirements for unmanned planetary orbiter missions and small scientific payloads, with no requirement for return flights.

The conclusion of the study was that the nuclear-electric option is the most attractive propulsion concept for the near-term outer planet orbiter mission. Also identified in the study were a number of new high thrust-to-weight ratio advanced propulsion concepts for outer planet missions which require a soft lander and/or sample return operations.

B. WHY THIS STUDY IS DIFFERENT

Taken as a whole, this study presents a broad challenge to many of the traditionally held viewpoints of what it takes to trek the heavens. The effort utilizes a high-risk/high-payoff approach to identify promising unconventional propulsion concepts with the potential for generating major breakthroughs.

Over the last two decades, a great number of unique thruster ideas have been either published in the open or classified literatures, or collected as informal technical notes into relatively dormant personal files of a few interested propulsion researchers. These propulsion ideas range from clearly low-risk, conventional realms to the unconventional and "radical fringe" groups. Traditionally, the last category has been widely ignored by most reputable researchers.

Recent revolutionary developments in the directed energy technologies (laser, microwave, and particle beam) hold much potential for shedding new light on many lesser-known propulsion concepts. Hence, the work presented here began with a thorough search through numerous privately held libraries for those unique thruster ideas which, although unconventional, may have exceptional compatibility with remote beamed high power, and which (thereby) might gain a significant competitive advantage over the performance of conventional systems.

This study continues where the previous studies of laser propulsion have left off. For example, it expands the focus of "beamed-energy" propulsion to include the serious consideration of microwave/millimeter-wave bands, as well as relativistic charged particle beams. The latter categories might very well enable a whole new dimension in high thrust, action-at-a-distance propulsion utilizing large-scale atmospheric charging techniques and powerful electrostatic fields. (The prospects for this kind of electrostatic propulsion have never been seriously examined.) The study also reflects a positive attitude that "All things (within reason) are possible in time." For instance, it is assumed that sometime beyond the year 2000, short-wavelength high-power lasers will have been scaled to the

gigawatt levels, presently exemplified by today's city-scale power plants. The study then proceeds to ask an intriguing question: "If beam power were unlimited, then what revolutionary new propulsion applications would be feasible?" Likewise, free reign is given to the full availability of any desired laser/microwave frequency and waveform (CW vs. repetitively pulsed power, possibly with variable pulse energy, width, and repetition rate). The study then attempts to uncover the most efficient propulsive methodologies to employ the specialized forms of high-grade power inherent in generic laser, microwave/millimeter, and charged-particle beam classes.

Once a thorough and complete description of promising thruster concepts is presented, this study speculates on the chronology of "milestone" systems for future beamed-energy propulsion applications. These "milestones" are then explored in some detail to discover the additional critical enabling technologies--beyond that of the thrusters themselves. The following briefly describes the speculated "milestone" applications, the chronology by which they might appear in the future, and the organization of the attendant supporting material presented in this final report.

C. EVOLUTION OF BEAMED-ENERGY PROPULSION "MILESTONES"

Chapter II details the projected development of one exemplary power-beaming technology: the free-electron laser (FEL). Sometime before the year 2000, it is anticipated that exceptionally flexible FELs with high-conversion efficiency (e.g., 25 to 50 percent) will be constructed by the military for future use in anti-ballistic missile (ABM) applications. It is known that laser power levels required for ABM roles closely match that of laser propulsion for "near-term" orbit-raising missions (e.g., 20 to 200 MW). The only additional enabling technology required for orbit-raising propulsion of useful payloads (e.g., tens to hundreds of metric tons), outside of the laser device itself, is the development of closed-cycle nuclear (or solar) power supplies - to replace the open-cycle nuclear military systems of the future.

Chapters III-VII assume the future availability of ground-based and/or space-based gigawatt power level FELs, and proceed to explore the range of laser propulsion engine concepts which appear compatible with delta-shaped and radially-symmetric (e.g., the Apollo command/reentry module) shuttle vehicle configurations. Next, Chapters VIII and IX investigate the candidate laser propulsion engines which might be suitable for propelling significantly larger cylindrical-shaped shuttle vehicles, some of which could be neutrally-buoyant in dense planetary atmospheres.

Chapter X analyzes the feasibility of integrating high power laser mirrors with the lower aerodynamic surface of radially-symmetric shuttlecraft configurations. These highly specialized manned or unmanned single-stage-to-orbit (SSTO) vehicles are proposed for two useful functions: (1) laser relay satellites for multi-purpose space power stations, and (2) USAF Space Command light-weight "fighters" for the space-superiority mission - a squadron of which could easily defeat today's most awesome nuclear offensive threat, a massive ballistic missile attack. This work was originally part of a Defense Advanced Research Projects Agency (DARPA) study and is included in this report since the laser relay technology discussed in this chapter is applicable to a variety of uses, including the global aerospace transportation system described in Chapter XI and the interplanetary cruisers described in Chapter XV.

Chapter XI suggests the possibility of a commerical laser-powered global aerospace transportation system, which might appear some time beyond the year 2000, but certainly before 2020. Enabling technologies are the laser-boosted shuttlecraft discussed in Chapters III through IX, and the gigawatt laser power-beaming technology reviewed in Chapter II.

Chapter XII suggests the possibility of laser-boosting large (e.g., 100 to 1000 m long) cylindrical heavy-lift launch vehicles (HHLV) directly into orbit for purposes of space industrialization and colonization. The launch vehicle design is based upon lighter-than-air vehicle structures technology, and innovative variable-cycle laser propulsion engines which are attached to the HLLV vehicle ends as movable power-heads. Once the

flexible outer skin is stripped off, the vehicle center section can function as a standardized building module for rapid assembly of large space structures. For example, they could be used as "vertebrae" in electrically conducting backbones of photovoltaic satellite solar power stations, the primary structure for O'Neill-type space colonies, or hotels in orbit.

Chapter XIII proposes concepts for high-thrust electrostatic propulsion within a planetary atmosphere - by using remote microwave/millimeter-wave and relativistic charged particle beam technology. Although these electrostatic schemes are the most speculative of all beamed-energy propulsion concepts investigated in this study, they may also have the greatest payoff when measured by their potential for efficient momentum exchange with the atmosphere (e.g., propulsive thrust per input beam power).

Chapter XIV examines present and future space nuclear multi-mode reactor technology for application in hypothesized year 2000 space battle cruisers. The space platform, envisioned for use by the USAF Space Command, would be equipped with high-power lasers, particle beams and electromagnetic cannons for strategic defense roles. Three nuclear bi-modal reactors (e.g., 4000 MW each) would be integrated with each vehicle to generate either high-propulsive thrust for orbital transfer (as a direct nuclear-thermal rocket), or high-electric power (e.g., at the gigawatt level) in the open-cycle mode--rejecting heated coolant to space. For near-term experiments, it would be possible for the battle station to "beam-up" its own laser-propelled manned shuttlecraft from the earth's surface (e.g., the Monocle Shuttle discussed in Chapter X), mating with it in orbit. In the far term, next generation battle cruisers would utilize, higher power density gas-core reactors and high-temperature, closed-cycle MHD conversion systems to generate peak electric power in the closed-cycle mode--for either electric propulsion engines or power-beaming. In this era, space battle cruisers could (for the first time) make practical the concept of laser-propelling their own shuttle craft to and from the Earth's surface. Although originally based on a DARPA-funded study, this work is included in this report since these types of vehicles would finally be

sufficiently energetic to enable the serious consideration of large-scale interplanetary missions.

The final chapter of this study hypothesizes a far future era (e.g., post 2020) when mammoth interplanetary cruisers (e.g., perhaps based upon the 10 km long O'Neill Model 3 space colonies) are propelled throughout the solar system with ultra-high performance fusion or matter-antimatter propulsion systems. Upon reaching a destination planet, the interplanetary cruiser would deploy large SSTO shuttlecraft "carriers" designed to float, neutrally-bouyant, in the dense low-altitude atmosphere. Next the carrier, acting as a "mobile field generator," might artificially charge up a portion of the planet's atmosphere, then deploy landing/survey craft to fly on this field (in order that they may conduct their explorations largely from the air). When the decision is made to return to the interplanetary cruiser, the shuttlecraft would be gathered up and the carrier vehicle would be boosted back into orbit on laser power beamed from the interplanetary cruiser. Self-propelled (or laser-propelled) laser-relay satellites would have been deployed in great numbers about the planet, enabling the cruiser to beam laser power to shuttlecraft or carrier vehicles located anywhere around the entire globe.

D. LONG-TERM OBJECTIVE

The long-term objective of this study is to help stimulate creative thinking in the aerospace community, the public, and the government towards the far future of atmospheric and space flight.

This Page Intentionally Left Blank

REFERENCES FOR CHAPTER I

1. Mead, F. B., et al., "Advanced Propulsion Concepts - Project Outgrowth," AFRPL-TR-72-31, June 1972.

2. Papailiou, D. D., "Frontiers in Propulsion Research: Laser, Matter, Anti-Matter, Excited Helium, Energy Exchange, Thermonuclear Fusion," JPL TM 33-722, February 1975.

3. Garrison, P. W., et. al., "Ultra High Performance Propulsion for Planetary Spacecraft, FY81 Final Report," JPL No. 715-151, Jet Propulsion Laboratory, NASA Contract NAS7-100, January 1982.

CHAPTER II
POWER-BEAMING TECHNOLOGY FOR LASER PROPULSION

This chapter addresses some of the basic research and technology issues associated with high-energy laser (HEL) power-beaming stations: specifically, HEL devices, optics, power supplies, atmospheric (and space) beam propagation, basing modes, and laser/relay engagement dynamics.

A. LASER PROPULSION TECHNOLOGY

The concept of beaming power from a remote source directly to a spacecraft propulsion system presents a revolutionary point of departure from conventional chemical and electric rocketry. Since the power source remains independent of the spacecraft, a beamed-energy propulsion system can simultaneously overcome the two classical limitations of specific impulse (e.g., 400-500 sec for chemical rockets), and thrust/mass (e.g., 10^{-2} to 10^{-4} N/kg thrust/mass ratio for nuclear-electric rockets). As a result, beamed-energy thrusters may attain specific impulses (e.g., 1000 to 3000 sec) approaching the regime of electric propulsion, with thrust/mass ratios more typical of chemical rockets.

Beamed-energy thruster design strives for simplicity and high performance--in exchange for placing as much system complexity as is practical at the remote location of an incredibly sophisticated power source. High-grade electromagnetic power is beamed along direct line-of-sight paths to the thruster. Herein lies the most obvious of several basic system limitations: the maximum range of beam transmission is fixed by the laser wavelength, finite size of collectors, and diffraction-limited optics. In addition, linear and nonlinear atmospheric losses must be included for ground-based sources.

The most serious problem is the availability of a suitable high-energy laser (HEL) source and power supply. However, such HEL devices are aggressively being developed by the military for potential use in future anti-ballistic missile (ABM) applications. Laser power levels required for the

ABM role are found to closely match that of laser propulsion for "near-term" USAF and NASA orbit-raising missions (e.g., at least during the next 10 to 20 years). The embryonic field of laser propulsion stands to benefit greatly from the future availability of a high-power ground- or space-based laser source with superior pointing and tracking capabilities that far exceed propulsion needs.

1. Thruster Design

Ideally speaking, the thruster design process would begin with the widest consideration of potential wavelengths from micro- and millimeter bands, through the far- and near-infrared, to the visible and ultraviolet. Each wavelength has its own implications for detailed thruster and spacecraft design. However, wavelength selection (in the broadest sense) is usually driven by the specific mission application. For example, near-term orbit-raising missions with attendant ranges of 10^4 km or more will dictate the use of very short laser wavelengths (e.g., from 0.35 to 2.5 μ). Other useful missions with ranges from several hundred to several thousand km could potentially use the microwave or millimeter bands with sufficiently large transmitting antennas.

A great diversity of continuous (CW) and repetitively pulsed (RP) laser propulsion engine concepts has been suggested in the literature (See Appendix A). However, they can all generally be placed into three distinct generic classes: Laser-thermal, laser-electric, and combined laser-thermal/electric cycles. Most current research is focused on the laser-thermal cycle.

A number of laser-thermal rocket engine concepts is shown in Figure II-1. Laser-thermal rockets absorb beamed radiation into solid, liquid, and gaseous propellants by the mechanisms of: (1) inverse Bremmstrahlung (both laser-supported combustion and detonation regimes), (2) continuum absorption, (3) molecular (line) absorption, (4) particulate absorption, and (5) indirectly, by way of heat exchangers. To trigger inverse Bremmstrahlung, the mechanisms of laser-induced breakdown, electric sparks, seed gases/liquids/particles, and solid igniter-surfaces have been proposed.

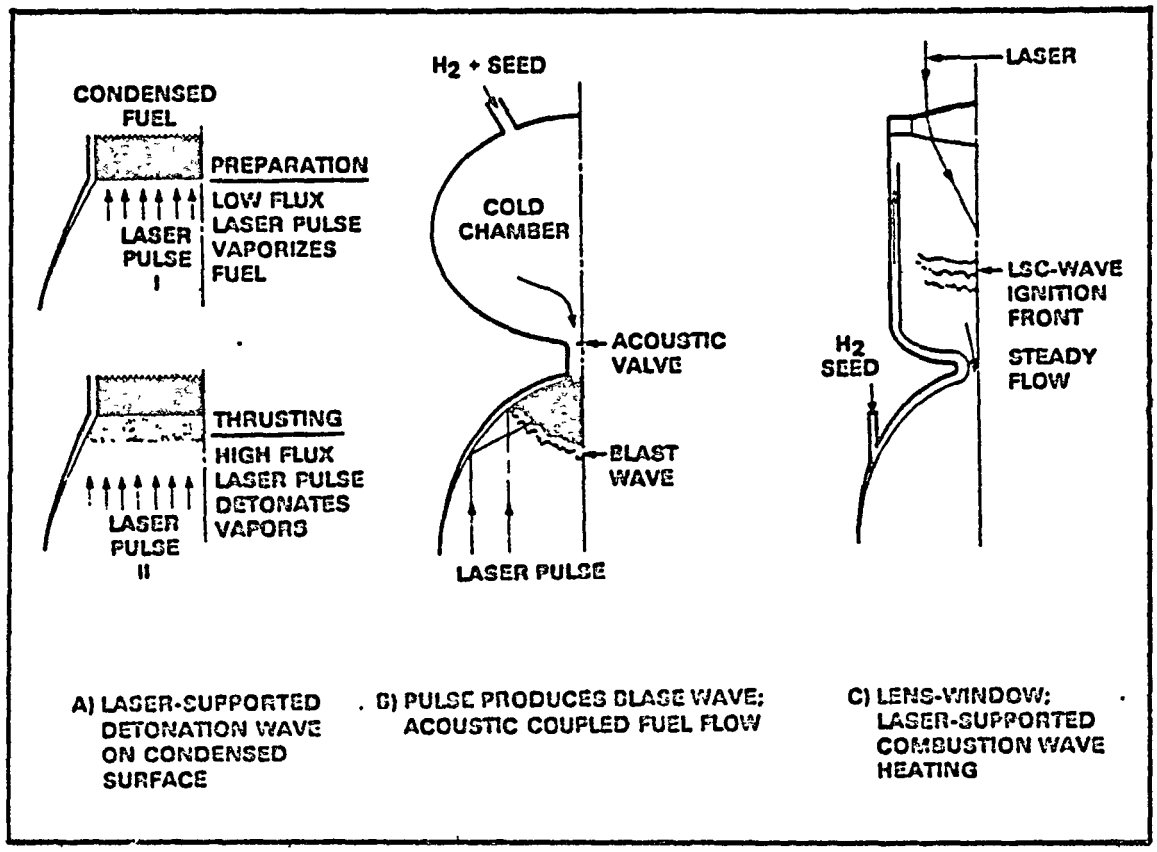

Figure II-1. Laser-Thermal Rocket Engine Concepts

Laser-thermal thrusters use one of two basic window concepts for transmission of laser energy into internal engine chambers: a) material (solid) windows, or b) aerodynamic window alternatives--shown in Figure II-2. For solid windows, current research is centered on developing low absorption, low reactivity materials, and in understanding the mechanisms of optical surface degradation. Aerodynamic windows are, of course, being developed for a number of laser generators themselves. In addition to other research areas, basic mechanisms of gas transport are being modeled to examine the limits on aero-window operation in the space environment. Specific impulses (I_{sp}) attainable by this class of engines fall in the range of 800 to 2000 sec. Peak I_{sp} values are limited by propellant dissociation and ionization losses, and cooling restrictions of thrust chamber walls.

Figure II-3 portrays the second generic class of laser propulsion engines: laser-electric rockets. This category requires the interim conversion of laser-to-electric power, before delivery to conventional electric thrusters. Both continuous and repetitively-pulsed conversion cycles have been proposed for either AC or DC electric power. Candidate laser-to-electric power converters include conventional Brayton or Rankine cycles--utilizing turboalternator, CW or RP MHD generators, reciprocating Sterling engines (with alternators), photo-electric cells, photo-electron chemical cells, thermionic, or photo-emissive approaches. In addition to conventional finned-tube and heat-pipe space radiators, other lightweight radiator concepts have been suggested for very high temperature operation: e.g., flattened-tube refractory, liquid-drop, and "light bulb" radiators. The laser-electric thruster class can theoretically attain specific impulses beyond the 2000 second limit of laser-thermal thrusters, but not without a significant penalty in overall system thrust-to-weight ratio.

Finally, the laser-thermal/electric combined-cycle thrusters represent a merging of elements essential to the first two classes of laser propulsion engines. Direct laser heating of the propellant first brings it to plasma temperatures; then, electrostatic or electromagnetic forces accelerate the plasma to final exhaust velocities. The latter process

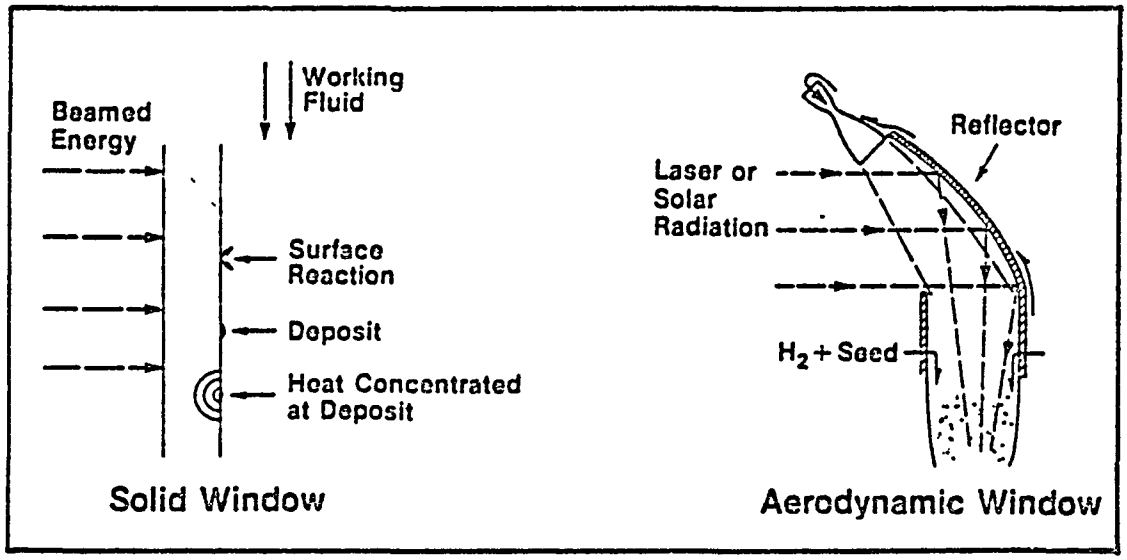

Figure II-2. HEL Window Concepts

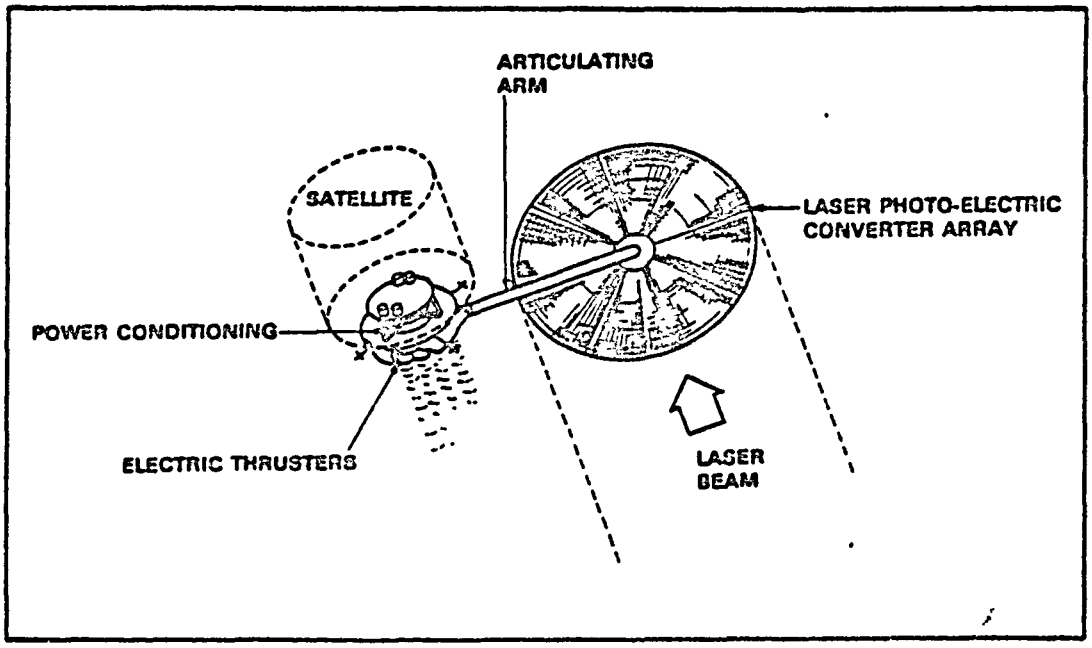

Figure II-3. Laser-Electric Rocket Engine Concept
(From Reference 1)

requires part of the remote laser power to be simultaneously converted to electricity. This high-grade electric power is then directly imparted to the gas as pure translational energy--rather than first being deposited into molecular vibration or rotational energy states. An exemplary schematic diagram for such a thruster is displayed in Figure II-4.

2. Optical Train Design for OTV/Thruster

Mission and engine requirements strongly influence overall optical train design. Earth-based laser transmitters must be equipped with adaptive optics to successfully propagate the beam up through the atmosphere without suffering excessive distortion caused by turbulence and thermal blooming. Clearly, space-based sources will avoid all such requirements on the laser transmitter.

The overall geometry, size, articulation and, therefore, weight of the receiver optics (mounted to the laser-propelled spacecraft) are dictated by the choice of laser wavelength, distance between source and receiver, and basing of the source. Mirror elements in the train can be reflecting or refracting, simple or compound. In most cases, reflecting elements will require high-reflectivity, multi-layer films to reduce cooling loads and thermal-induced optical distortion. High-power windows and refracting mirrors may need anti-reflection coatings to reduce losses.

Depending upon the incident time-average flux, engine mirror elements can either be radiantly-cooled (e.g., large primary receiver mirrors) or actively-cooled by gaseous, liquid or perhaps cryogenic coolants. For certain spacecraft designs, optical elements may be rotated (i.e., spun) to reduce the time-average thermal load by smearing the laser flux over a large surface area. Heavy mirror cooling loads might be met by a new class of advanced "heat-pipe" system with superior heat transfer capabilities. Certain reflecting optical elements may avoid heavy thermal loads by using grazing-incidence optics to spread the laser beam over a much larger footprint--thereby greatly reducing the incident laser flux density. In some cases, transpiration-cooled (rather than regenerative) optics may be the answer, although the application would need to be highly specific.

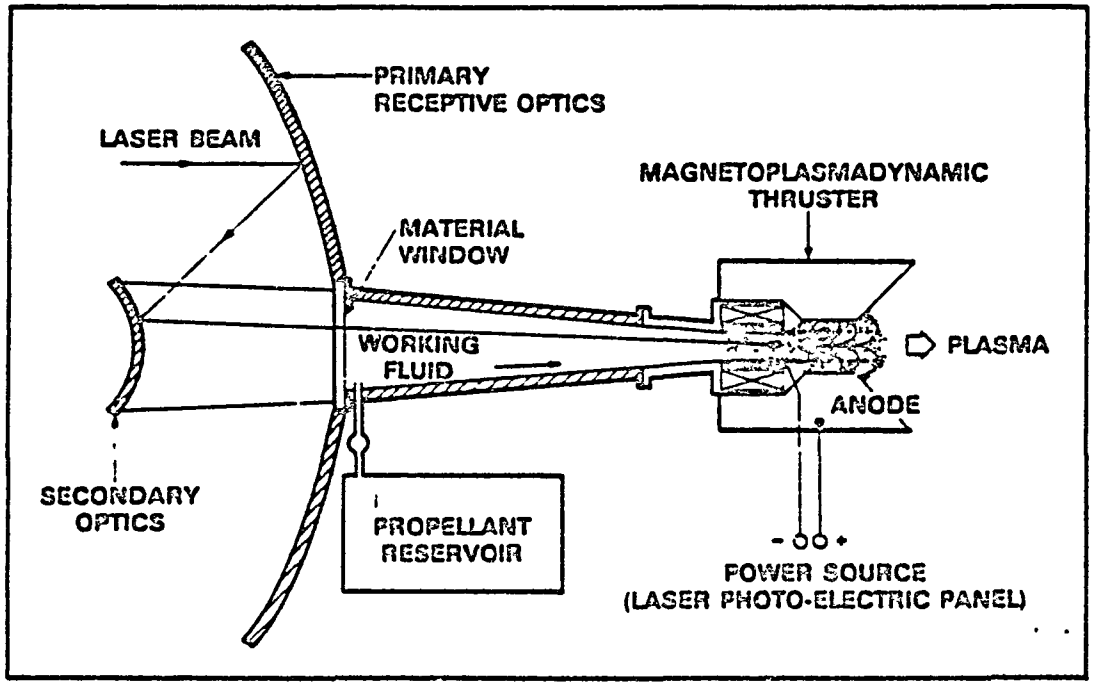

Figure II-4. Laser-Thermal/Electric Combined-Cycle Thruster Concept (After Lee, Reference 2)

In any case, strict control over the incident laser beam pulse energy, fluence, time-average flux, and beam spot location is necessary to avoid exceeding the damage limits of elements in the optical train, as well as cooling limits of internal engine chamber walls. Inaccuracies in pointing would cause the powerful beam to stray across "softer" spacecraft external skins, so fail-safe control systems must be developed to prevent self-inflicted damage.

Finally, for certain laser propulsion engines requiring seeding, careful control must be maintained over: a) injection of solid or liquid alkali "seed" materials into internal engine chambers, and b) subsequent ejection of contaminated high-velocity exhaust plumes--to prevent coating spacecraft optical surfaces with highly absorbent particles. Otherwise, these surfaces might become so seriously degraded in reflectivity as to trigger their own destruction.

B. ASSESSMENT OF LASER POWER-BEAMING STATUS

The principal elements of laser power-beaming systems are the primary energy source, conversion, power-processing, storage, and transmission as indicated in Table II-1. The interrelationship between system elements for an exemplary solar/photovoltaic/electric-laser system is shown in Figure II-5. The following discussion explores these elements in greater detail.

1. Laser Device Technology

As suggested above, the great diversity of candidate energy conversion concepts for laser propulsion engines will collectively demand an unusually high degree of flexibility from any futuristic HEL device technology. Therefore, laser power-beaming stations must have the inherent ability to deliver either CW or RP waveforms (with variable pulse repetition frequency, pulse energy and pulse duration), be throttleable over a significant power range, and generate a wide variety of laser wavelengths with high operational efficiency.

The primary energy sources available for laser power-beaming include chemical, nuclear and solar. Laser device technologies which

TABLE II-1. POWER BEAMING TECHNOLOGIES

1. ENERGY SOURCES
- CHEMICAL
- NUCLEAR
- SOLAR

2. CONVERSION TECHNIQUES
- PHOTOELECTRIC
- THERMOELECTRIC
- THERMIONIC
- ELECTROCHEMICAL
- GASDYNAMIC
- MAGNETOHYDRODYNAMIC

3. POWER PROCESSING
- ELECTRICAL
- MECHANICAL

4. STORAGE
- CHEMICAL
- THERMAL
- MECHANICAL
- ELECTRICAL

5. TRANSMISSION
- LASER
- MICROWAVE
- MILLIMETER-WAVE

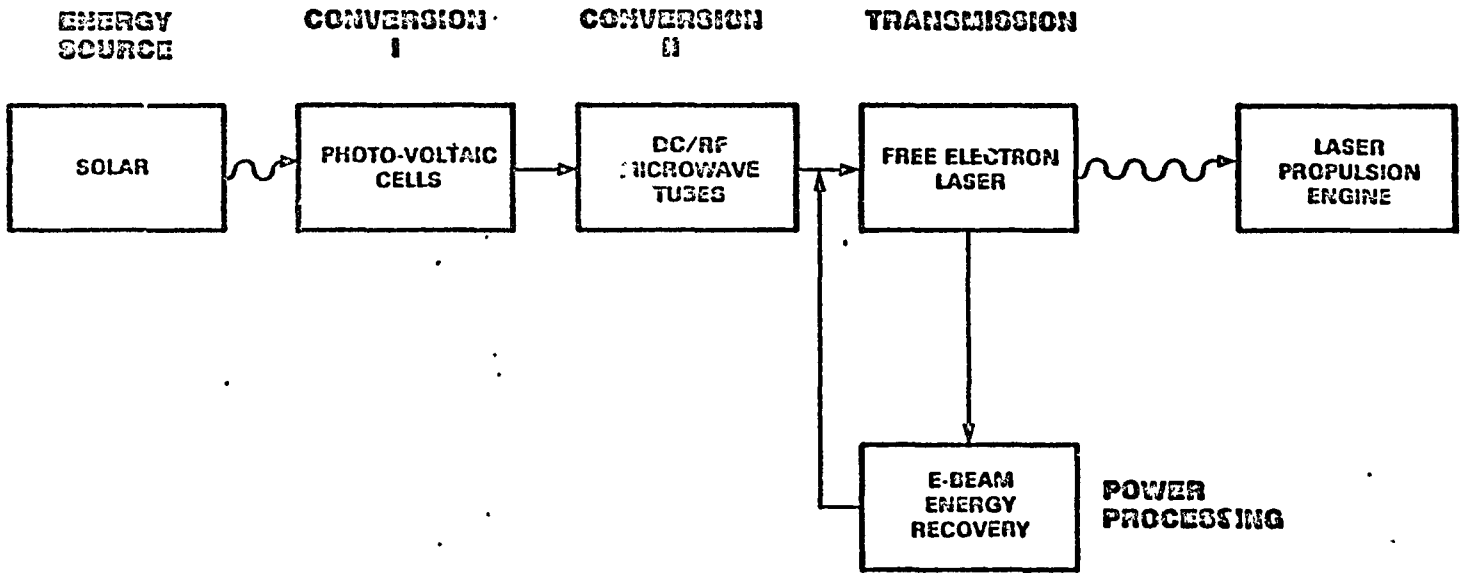

Figure II-5. Elements of Beamed-Energy Propulsion System

depend upon direct-pumping by these sources (regardless of whether the laser working medias are gaseous, liquid-dye, or solid state) can be immediately eliminated from consideration for future widespread use in laser propulsion applications. (They will be used only in limited roles for near-term experiments.) By the very nature of their design, direct chemical-, nuclear-, and solar-pumped lasers impose severe restrictions upon the resulting wavelengths and waveforms which can be generated. Only the combined synergistic application of: a) interim energy conversion to "high-grade" electric power, b) appropriately flexible power-processing, and c) highly versatile laser device technology--can lead (most expediently) to a power-beaming system which has the greatest chance of satisfying stringent requirements for laser propulsion.

The free-electron laser is the only high-energy electric laser technology which holds great promise for such versatility. Coincidentally, the FEL is undergoing extensive development at many laboratories for military defense power-beaming roles--largely because of its excellent prospects for achieving high brightness at short wavelengths (e.g., 0.35 to 1.0 μm) with high "wall-plug" efficiency (e.g., 25 to 50 percent).

The basic principles of the free electron laser concept shown in Figure II-6 seem very straightforward: Electrons accelerated nearly to the speed of light are injected into an alternating magnetic field where the resulting transverse accelerations cause them to emit synchrotron radiation in the direction tangent to their motion. Because of Lorentz contraction, the wiggles in the magnetic field appear to the relativistic electrons to have a very short wavelength, approximating the wavelength of light. Corresponding to any choice of electron energy and magnet periodicity, there will be an appropriate resonant wavelength, where the synchrotron radiation from electrons in one "wiggle" tends to add in phase with the radiation from the electrons in subsequent wiggles. Hence the synchroton light field grows in the mean direction of electron motion.

As the light field becomes stronger, it tends to trap the electrons in a traveling potential "bucket", caused by the interaction of the light field with the electron charge. If the electrons are injected with

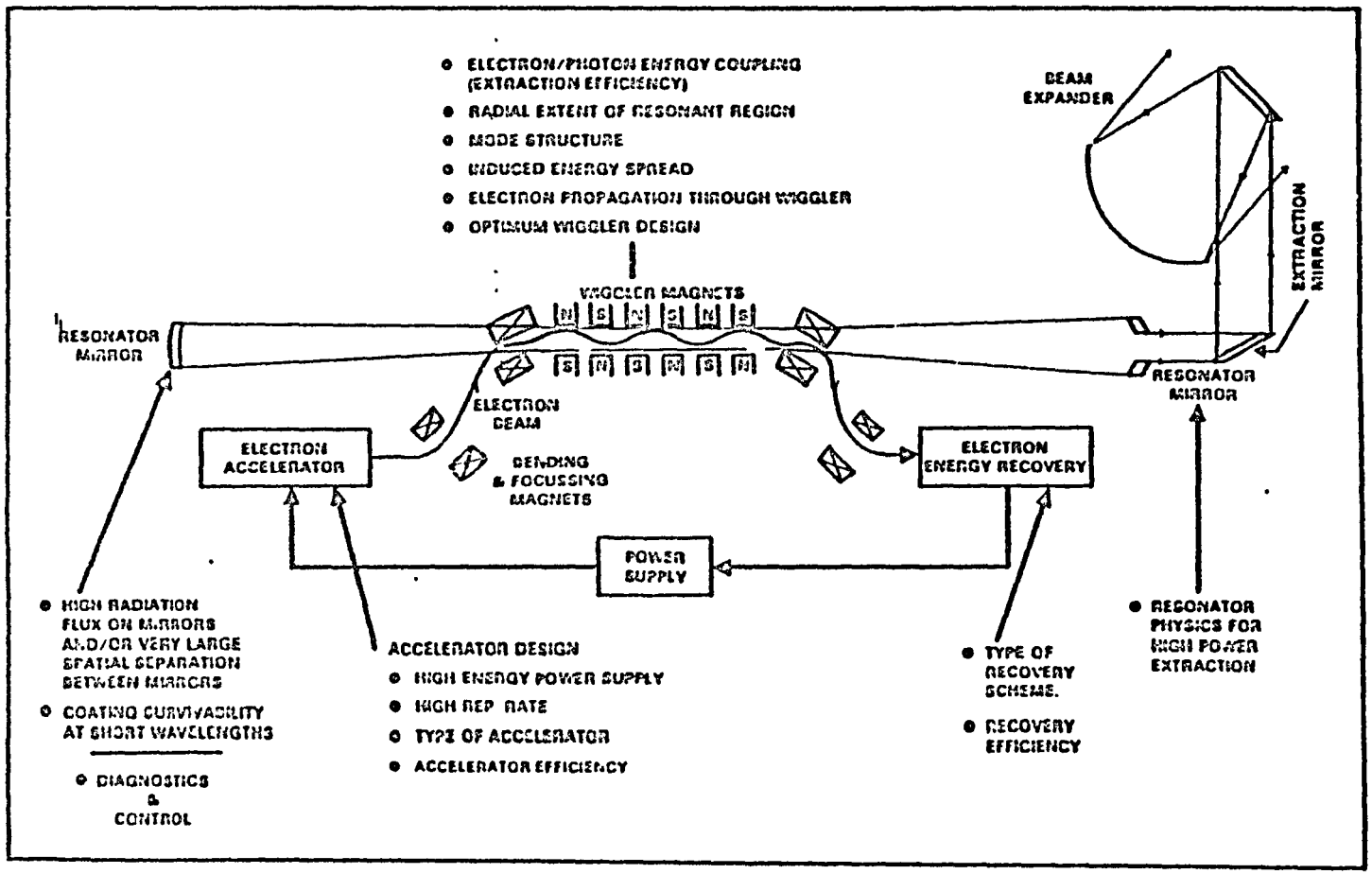

Figure II-6. Technical Bottlenecks: Free Electron Laser (From Reference 7)

slightly more energy than the exact resonant energy, the trapped electrons then oscillate about a mean energy in the bucket and give up energy to the light field as they pass down through the wiggles, so that net gain in the strength of the light field occurs. (The resulting amplifier superficially resembles the traveling wave tubes familiar to microwave engineers.) The FEL is completed by placing mirrors at opposite ends of the device to feed back radiation so that the process continues to the point of saturation--wherein all of the available (i.e., correctly phased) electrons are trapped and give up the maximum available excess energy.

The device can run as an oscillator if the gain is sufficient, and the feedback is arranged so that the electrons and the light cohabit for a long enough time. Alternatively, the device can be run as a master-oscillator/power amplifier (MOPA) if it is designed so that a strong light pulse from another laser is injected to initiate the electron trapping; and a large amount of energy is then extracted in a single pass to yield large amplification.

Even though several benchmark achievements remain to be demonstrated before the feasibility of high-energy FEL devices can be declared certain, there are numerous compelling reasons for believing that there will be no major roadblocks. The principal reason for this claim is that FELs represent a natural outgrowth of many years of experience with well known phenomena in well understood regimes of theoretical and experimental physics. Unlike the disappointing history of, for example, controlled fusion research (where ever-more energetic experiments were pushing ever-more deeply into unknown parameter regimes of plasma physics), the basic single-particle physics of the FEL process is thoroughly understood and fully validated.

The present laboratory experiments have already reached a point where a single pulse demonstration of FEL operation (comparable to the required performance level for a postulated high-energy machine) has been accomplished at 10 microns wavelength. Demonstration of similar success at 1 micron (or shorter) wavelength might be accomplished in one year, barring ulterior impediments such as inadequate research funding. After that

demonstration, building a short wavelength high-energy FEL machine can be characterized as an engineering problem mostly in the realm of accelerator physics, which is an old and mature discipline. People who are deeply involved in detailed accelerator design regard the planning of the required high-average power accelerator as a straightforward engineering challenge.

Because most present accelerators have rather poor emittance, Smith and Madey at Stanford[3] have explored possibilities for matching the full acceptance of a short linear wiggler magnet to the emittance of present accelerators. The short wiggler forgives poor emittance and energy spread but requires a huge current to overcome poor trapping efficiency. This results in systems with good gain and power output over the entire wavelength range from the far infrared to the far ultra-violet. For an optimized system, the gain turns out to be independent of the wiggler length, while the output power scales as the reciprocal of the cube of the length. A typical example for a 20 MW laser operating at 1 micron wavelength with a gain of 0.016 requires a 72 MeV beam operating at 560 amperes.

A second approach undergoing extensive research by Brau et al[4] at Los Alamos National Lab involves the use of a 100 MeV RF Linac delivering an average current of ~ 1 Ampere to a tapered wiggler a few meters long. Scaled-down experiments have already demonstrated 3.5 percent extraction efficiency at 10 microns, proving the physical viability of this approach. Since overall laser efficiency will not exceed a few percent, energy recovery is necessary to get the wallplug efficiency up to 25 percent.

A third method is particularly suitable for the high-current beams being investigated at Lawrence Livermore National Lab by Proznitz, Neil, et al.[5] In this approach, a very long wiggler is intended to achieve both high trapping and high extraction with no need for energy recovery. This method is particularly suitable for a master-oscillator, power amplifier (MOPA) configuration because the very high gain can eliminate the need for feedback mirrors--an important simplification. Computer models point to overall laser efficiencies approaching 40 percent.

Finally, Madey[6] is continuing his investigation of a long gain-expanded wiggler in a storage ring accelerator to achieve high efficiency (~25 percent) in spite of very low extraction efficiency (~10^{-3}). A 10 MW machine for visible wavelengths would require 1 GEV with 3 amps of trapped current.

Each of these four methods has particular merits that need to be investigated in depth to determine the best approach. A good review of the several possible paths to high-efficiency, high-power FELs is given in Reference 7.

Therefore, because of the programs outlined above, chances are good that an efficient FEL which exactly meets the needs of future laser-propulsion orbit-raising missions will exist well before the year 2000.

2. HEL Mirror Technology

The ability of an HEL mirror to handle a given level of laser power depends heavily upon its diameter, total reflectivity and cooling method.

At power levels of interest for FEL power-beaming laser propulsion systems, actively-cooled bare metal mirrors will be unable to maintain the required figure at all interesting wavelengths, due to excessive levels of thermal absorption. One exception is for the case of very large mirrors which dilute the energy fluence to a survivable value. In this instance, aluminum is best at 0.35μm giving 92 percent reflectivity; silver is best at 1.0μm, yielding 99 percent reflectivity.

Mirror coatings to achieve reflectivities better than 99.5 percent appear feasible at all but the shortest visible wavelengths, where atomic dimensions become significant in determining the achievable uniformity of layer thickness. Multi-layer thin films will be necessary to achieve reflectances of 99.5-99.9 percent. For example, at 0.35μm twenty layers are required, maintaining an overall thickness uniformity consistent with ~ $\lambda/40$ total figure. Layer thickness uniformity must be controlled to 0.1nm, which is less than the diameter of an atom. At 1.0μm, fewer layers are required because of better underlying metal reflectivity. Required layer uniformity to ~1.0nm is readily achievable.

Mirror cooling constraints are very severe, but new innovations appear to be providing the needed advances in the state-of-the-art for all but the shortest visible wavelengths. Consistent with $\lambda/40$ optical distortion, 4 J/cm^2 per pulse appears to be a hard upper limit on present state-of-the-art in coated mirrors for pulsed laser systems.* In the CW limit, water-cooled mirrors have been demonstrated successfully at 30 W/cm^2 absorbed sustained flux (heat transfer coefficient = 5 W/cm^{2}K). In the CW limit, liquid-metal-cooled (NaK eutectic) mirrors with 0.30 cm thick tungsten carbide faceplates have successfully withstood 200 W/cm^2 (heat transfer coefficient = 35 W/cm^{2}K). Gaseous or cryogenic cooling appears unpromising due to the low thermal conductivity of the gaseous layer at the mirror surface. Heat-pipe mirrors with wicking grooves theoretically may yield effective heat transfer coefficients of 350 W/cm^{2}K. An excellent comprehensive review of HEL mirror coating and cooling technology can be found in Reference 8.

Shown in Figure II-7 are the limits on total incident laser power imposed by the properties of mirrors using the representative cooling schemes mentioned above: i.e., a) water, b) liquid-metal (NaK eutectic), and c) wick-type heat-pipes. Boundaries are shown on 99 percent and 99.9 percent surface reflectivity. A line is also indicated for 92 percent reflective bare aluminum at 0.35 μm. The 99 percent figures represent bare metal at 1.0μm. As indicated, a 5 meter diameter mirror with 99.9 percent reflective coating and heat pipe cooling system can handle (at near normal incidence) a 50MW laser beam; 10m mirror - 200MW; 20m mirror - 800MW.

3. Basing Considerations

The most expedient route for earliest deployment of an effective FEL power-beaming system for laser propulsion applications would be to base it on the ground, and use light-weight "relay" mirrors (placed in fixed orbits) to reflect the laser beam as shown in Figure II-8. These mirrors would then be precisely aimed to propel OTV spacecraft.

---

* These data are based on a 45 layer MgO/MgF_2 dielectric stack on aluminized molybdenum substrate 0.5mm thick, heat transfer coefficient 5 W/cm^{2}K; 0.35μm wavelength; 1μsec pulse-length at 100 Hz.

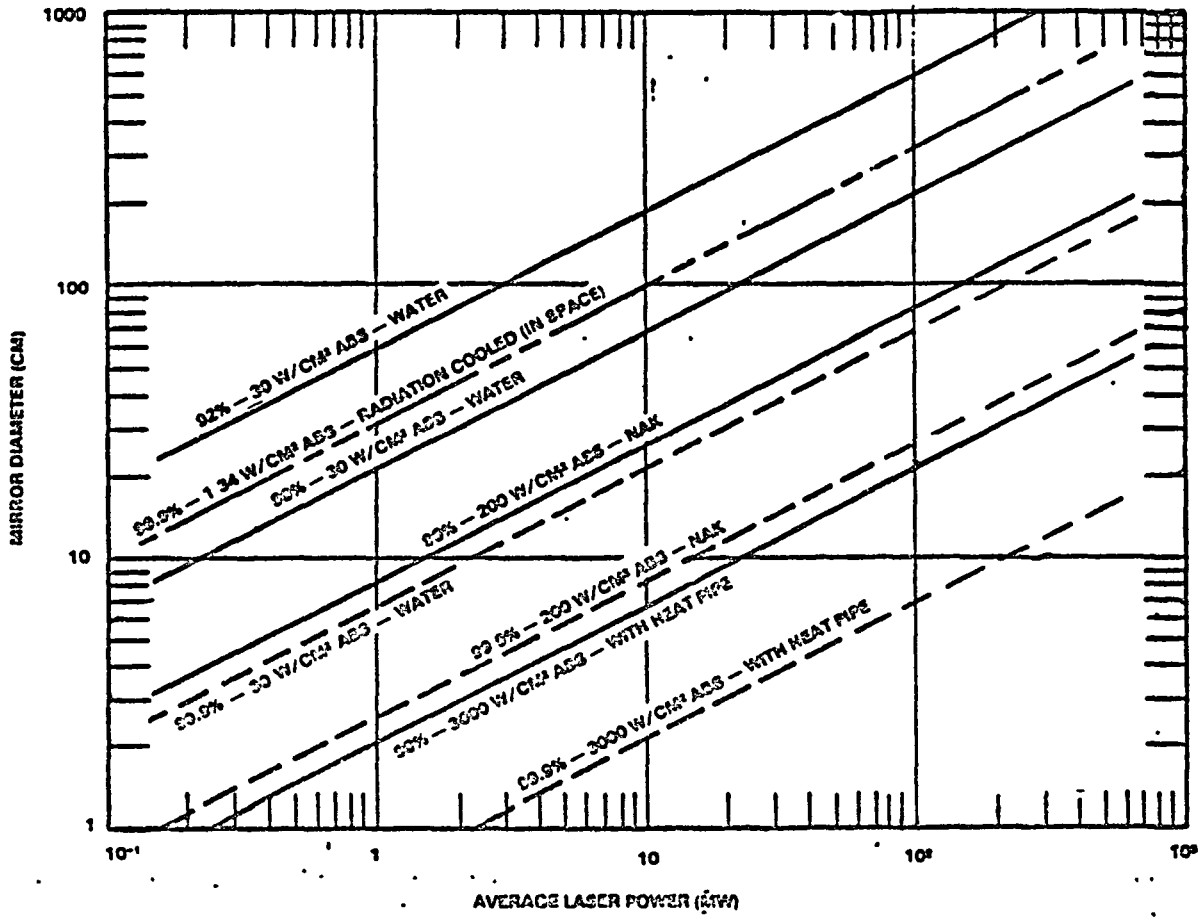

Figure II-7. Power Handling Capabilities of HEL Mirrors (From Reference 7)

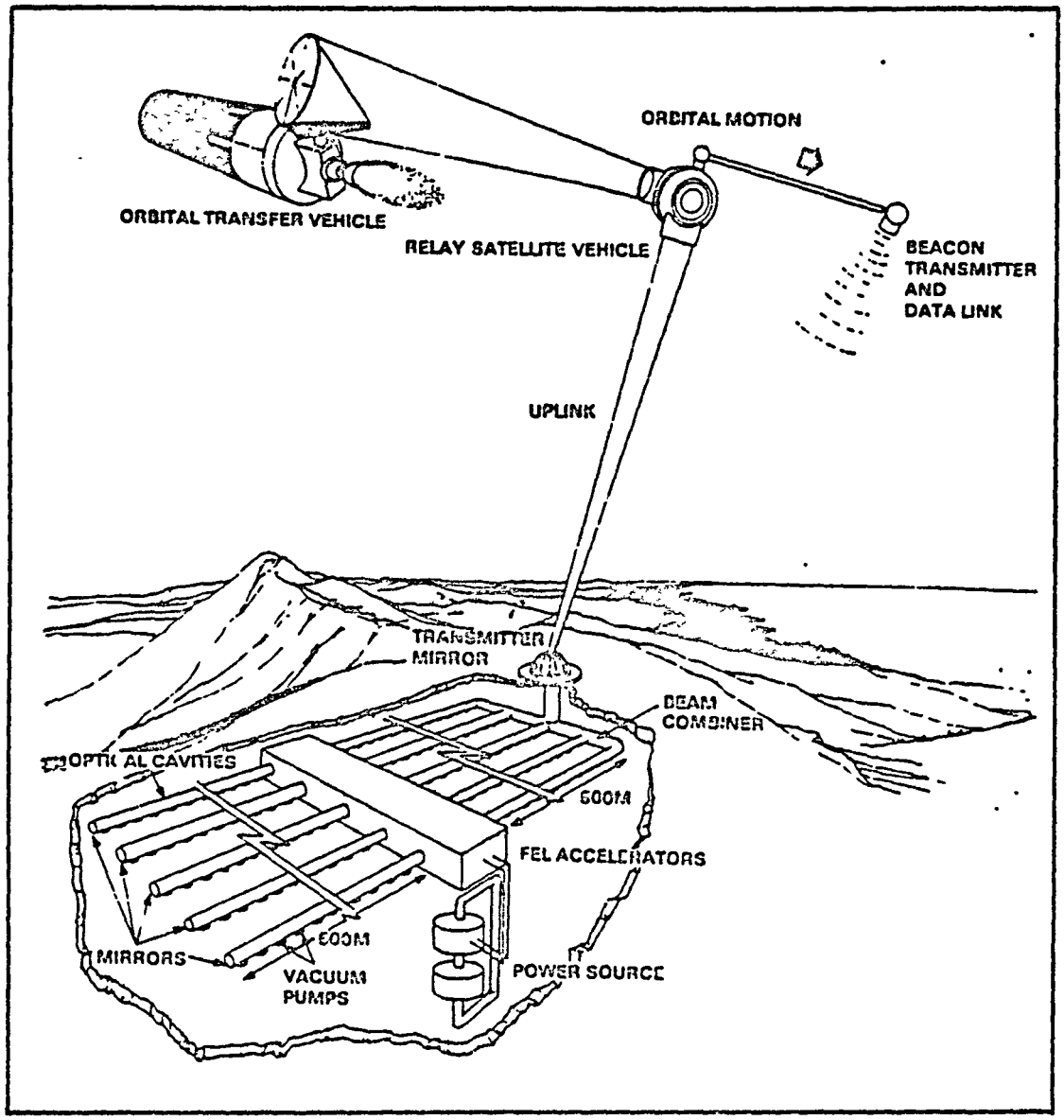

Figure II-8. Free Electron Laser Site with Orbital Relay Mirror and Autonomous Power Source High Elevation Reduces Losses Due to Atmospheric Extinction.

Since the laser installation would be on the ground, the efforts of scientists could be strictly devoted to developing the basic device and optical train, without simultaneously having to worry about such potentially critical issues as the system mass, volume, overall dimensions, and survivability in a high-vibration launch environment. The electric power plant becomes a non-issue, since today's conventional city power plants reliably generate 1000 MWe or more. Also, the laser device and optical train could be engineered for easy maintainability, initially using traditional laboratory practices.

Ground-based laser (GBL) installations would be placed upon mountain tops in order to minimize beam distortion effects of the atmosphere. The use of FEL device technology would permit the laser wavelength to be selected for minimum atmospheric absorptivity; hence, thermal blooming could then be reduced to insignificance (if not entirely eliminated) by the proper choice of beam power and output projector diameter. The beam-spreading effects of atmospheric turbulence can be greatly reduced by using adaptive "uplink" projector optics.

The simplest embodiment of this scheme employs a beacon attached to the space relay platform. The beacon transmits an initially undistorted spherical wavefront from the relay satellite toward the ground transmitter to diagnose the effects of the atmosphere on the beam path. (The transmitter aperture would be shared by a sensing system operating between laser power pulses.) The sensing system would provide feedback correction signals for the adaptive elements to pre-bias outgoing high-power wavefronts so that they would arrive at the relay satellite as a diffraction-limited beam. This concept is further described in Reference 9.

A full-scale power-beaming system for laser propulsion would involve, for example, 6 to 10 mountain top installations with perhaps 2 to 4 GLBs at each site. Installations would be placed in "sunbelt" sites carefully selected from long-term meterological data--such that one site could always count on clear access links to space relays. The number of relay mirrors at moderate (e.g., 3000 to 5000 km) orbits would be selected to maintain "uplink" zenith angles within $\pm 60^{\circ}$ from vertical. OTV

spacecraft coming in low over the horizon would seldom be engaged directly, but by way of the space relay mirror in order to minimize atmospheric attenuation.

Space-based lasers (SBL) have the advantage of inherently avoiding the atmospheric turbulence correction problem, but face the severe restrictions of lightweight design engineering for the laser device, power supply, beam projector and integrating spacecraft structure. Efficient packaging for shuttle boost to orbit, as well as methods of packaging for easy erection (once in space) are additional major considerations. The rejection of waste heat from both power supply and laser device (to space) becomes a problem of paramount importance. Therefore, these requirements may push the deployment of space-based free-electron lasers for OTV power-beaming applications into the "far-term," possibly as late as the 21st century.

Figure II-9 from Reference 10 is a mapping of representative laser parameters into beam brightness, the best measure of overall power-beaming laser system capability. Since this quantity is measured at the final output mirror (or projector)--on a direct line-of-sight path to the OTV vehicle, the chart applies equally well to both space-based and ground-to-space-relay laser systems. The map reveals the interplay of equivalent mirror (aperture) diameter, wavelength, pointing and tracking accuracy ("jitter"), and laser power. An expression for beam brightness (B) is given as:

$$B = (P/2\pi\sigma_T^2)\ L, \text{ (watts/sterradian)} \qquad (1)$$

where P is the laser power in watts, σ_T is the total beam spread in radians, and L is the beam quality.

As indicated in Figure II-9, a 50MW beam of 0.35μm radiation will give a brightness of $5X10^{21}$ watts/sterradian with a 5 meter aperture, a very low value of jitter and perfect beam quality. A 10MW beam appears close to the minimum useful level for "near-term" orbit-raising propulsion applications.

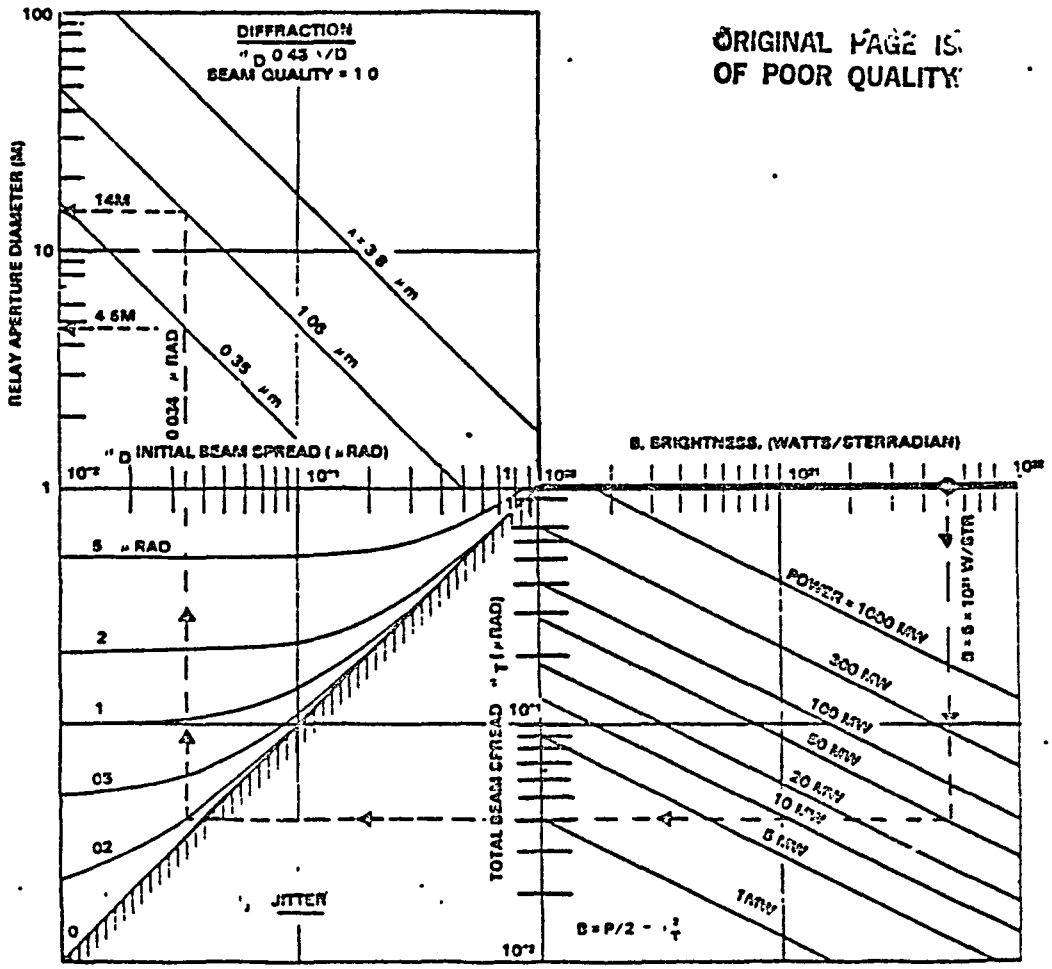

Figure II-9. Mapping of Laser Device/System Parameters
(From Reference 10)

4. Adaptive "Uplink" Optics

Several approaches are being considered to address the "uplink" turbulence correction problem. These include piezo-electrically driven mirrors of both segmented and deformable membrane type, and also electro-optical devices (particularly non-linear phase conjugators) which potentially can generate the needed phase corrections with no moving parts.

Requirements for vigorous "uplink" turbulence correction will require a frequency response of 3 KHz. In the near-term (5-10 years), this requirement will probably dictate a segmented approach (e.g., such as the Rocketdyne multi-hex system shown in Figure II-10) to construction of the phase adaptive mirror, rather than the deformable membrane alternative. The low mass of the hexagonal elements permits high-frequency response together with needed cooling, without prohibitive power requirements for the piezo-electric actuators. This approach should also permit use of inexpensive, optically flat elements instead of expensive, large continuous optical surfaces. Phase conjugation in a non-linear medium remains a "dark-horse" possibility whose time of availability for high-power applications remains unpredictable at present.

At the shortest wavelength (0.35 μm) and large zenith angles (e.g., 60°), the atmospheric coherence scale (r_o) is 2-3 cm under worst conditions. This situation will require the transmitter primary mirror to perform the phase correction function, because thermal loading of thousands of tiny elements in a secondary mirror would pose unsolvable problems.

For laser propulsion applications, uplink projection of a several hundred megawatt beam at 0.35 μm requires roughly a 4 m primary aperture because of linear and non-linear atmospheric propagation limitations. Hence, the primary mirror must be assembled from ~4×10^4 adaptive elements. This will require the use of mass production techniques in the manufacturing of these elements which, as suggested above, probably need only be figured to an optical flat surface. This approach, however, should result in a considerable decrease in the production times and costs associated with figuring large monolithic mirrors.

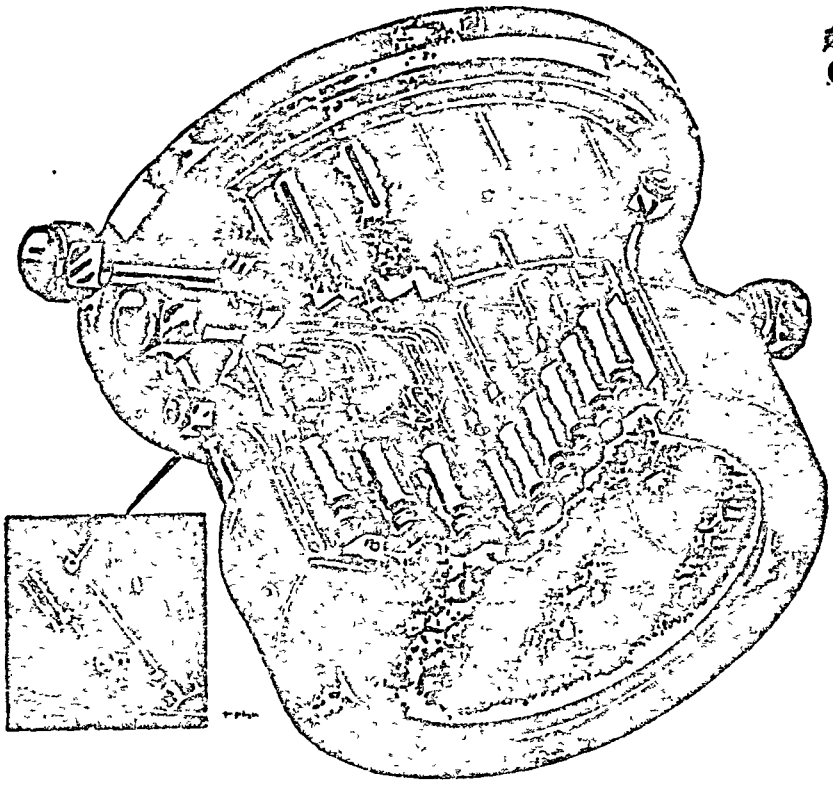

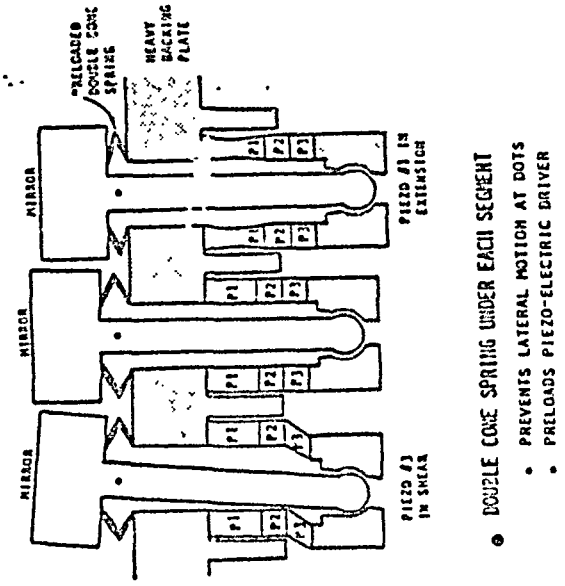

Figure II-10. Rocketdyne Multi-Hex Adaptive Optics (From Reference 9)

High-reflectivity coatings (e.g., at least 99.9 percent reflective) will have to be developed to reduce the absorbed flux loadings on small secondary mirrors within the optical train in order to permit cooling them with water or liquid metal. If these same coatings were applied to the primary mirror adaptive elements, the absorbed flux would be reduced to roughly 10 times solar irradiance (for a 200 MW beam). Therefore, active cooling for the adaptive elements themselves may not be required, although some cooling system may be needed for removing laser energy (e.g., 0.1 percent) falling into the cracks between HEX elements.

As with all other technical issues mentioned above, the problem of parallel computer processor control of 10^4-10^5 adaptive elements falls into the category of an engineering challenge, rather than a technical bottleneck indicative of any fundamental or physical limitations.

5. Atmospheric Propagation Constraints

Any serious consideration of the Ground-Based Laser/Space-Based Relay (GBL/SBR) concept must recognize that up-link propagation of the laser beam through the atmosphere will be a decisive factor in determining feasibility of the system. It appears, on the basis of the current perspective, that turbulence problems are solvable in much of the wavelength range from 0.35 to 2.4 microns, but that the longer wavelengths are preferable because of much lower absorption and scattering losses, provided that other system issues do not dominate the propagation issue.

Atmospheric extinction for short wavelength laser radiation has been studied to a considerable extent and tabulated information is available for laser lines of interest and a number of different atmospheric models.[11-12] Numerical values for absorption and scattering are normally compiled as function of altitude. For a given beam path, then, the atmospheric transmittance may be written as:

$$T_R = \exp\left\{ - \int (K_a + \sigma_a + K_m + \sigma_m)\, dR \right\} \qquad (2)$$

where K_a and σ_a are the aerosol absorption and scattering coefficients, K_m and σ_m are the corresponding values for molecules. The transmittance for a given wavelength is best for clear days, i.e., low aerosol contamination.

Any attempt to propagate a high power laser beam from the ground to space will be heavily influenced by the integrated properties of the atmosphere in the beam path. The height of the ground site above sea level is the principal determinant of the overlying air mass and its molecular composition, which fundamentally affects the transmittance to space through both absorption and scattering processes. The prevailing weather patterns at the site heavily influence the aerosol content (i.e., vapors and dust), which plays a major role in determining the scattering of power out of the beam. The zenith angle (i.e., angle, Z, from the point straight overhead) determines the total distance traversed through the atmosphere, which is proportional to secant Z to a very good approximation. The air turbulence and its effect on the laser beam is strongly dependent upon altitude, wind velocity, temperature, time of day, season of the year, and geographical features of the environment. The relative and absolute importance of all of these factors is, in turn, greatly affected by the wavelength, which is the key system parameter.

For any GBL/SBR system, all of the foregoing factors directly affect the system properties. To deliver a prescribed brightness to the relay, the laser power must increase as a direct function of zenith angle to make up for losses caused by the atmosphere. Since there are practical, as well as physical upper limits to the laser power, the required number of relay satellites also becomes a function of zenith angle, because one or more satellites must always be visible within the reachable cone of zenith angles. Within limits imposed by other mission constraints, the required number of relay satellites can be reduced by placing them in higher orbits where each satellite moves slower and views more of the earth; but this drives up the mirror size, and hence the mass, of each relay device (as well as system inertia and dynamic response complexity).

Other atmospheric factors are involved with the design of the ground-based transmitter optics. The projector aperture must be large

enough to prevent the power density in the beam from exceeding the threshold where non-linear effects (e.g., breakdown) take place. Such effects vary greatly with wavelength. Also, the size of the atmospheric coherence length, r_o, varies with wavelength. The associated disturbances can be corrected with adaptive optics of either the continuous membrane or multi-segmented types, so r_o determines the size, and thus the required number, of the adaptive zones in the mirror surface. The required frequency response of the adaptive elements is determined by the frequency of the turbulence, typically 3 kHz maximum, as mentioned above.

In this section, the entire atmospheric transmission problem is analyzed in sufficient detail to determine a good approximation for all of the required system parameters. The work was first done analytically, and then the results were checked by modifying the Air Force state-of-the-art propagation code, ESP4-SWL, to simulate the GBL/SBR problem for laser propulsion applications. The results by both methods are in excellent agreement.

Figure II-11 displays the typical atmospheric transmittance to space from 3 km mountain peaks as a function of wavelength for several zenith angles of interest: 0^o, 45^o, 60^o and 70.5^o. A zenith of 60^o is equivalent to two vertical atmospheric path-lengths, and 70.5^o is equivalent to three. The overall atmospheric bandpass spectrum is adapted from astronomical data. Atmospheric transmittance to space is clearly a strong function of wavelength and zenith angle.

Superimposed upon the plot are values of transmittance calculated by the ESP4-SWL code for various wavelengths and zenith angles of interest, with the following exemplary assumptions: Mid-latitude summer atmosphere, 10 m/sec crosswind to clear the beam, 3 km altitude ground-based laser site, and beam slew calculated for direct uplink to relay mirrors in orbit at 3000 km. Figure II-12a displays this same ESP4-SWL data, cross-plotted to show more clearly the transmittance versus zenith angle as a function of wavelength.

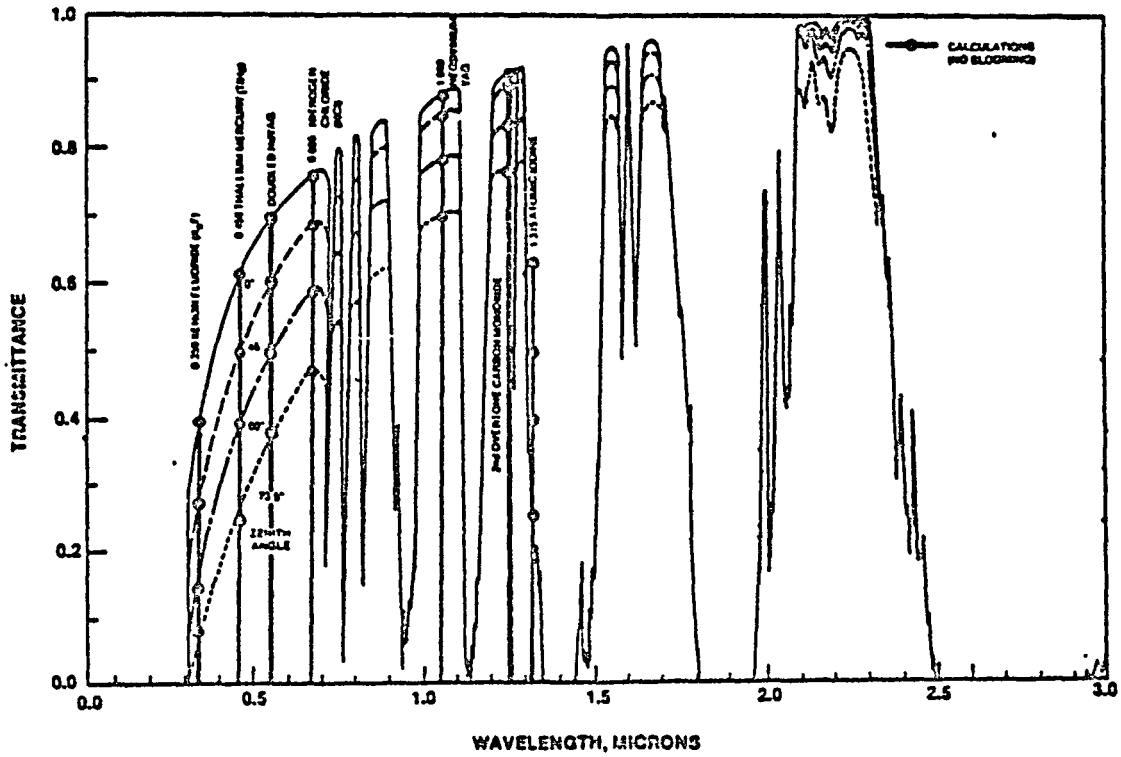

Figure II-11. Typical Atmospheric Transmittance to Space From 3km Mountain Peaks (From Reference 10)

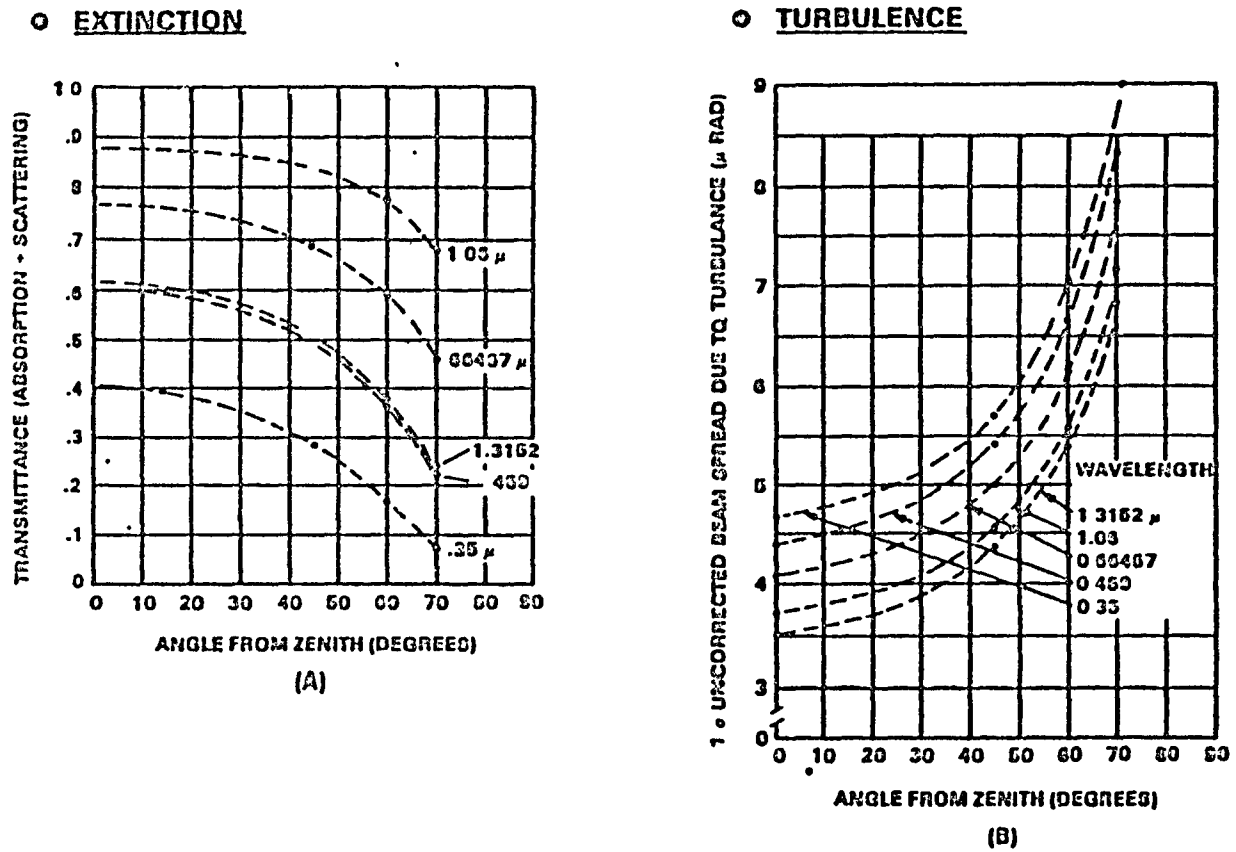

Figure II-12. ESP4-SWL Calculation Results: Extinction and Turbulance

Note that exceptional transmittance occurs at 1.0 μm by Nd:Glass lasers, at 1.25 μm by 2nd overtone CO lasers, at 0.53 μm by frequency-doubled Nd:Glass--or at any of these wavelengths by free electron lasers. The iodine laser family, operating at 1.315 μm, encounters major molecular absorption due to a mixture of molecules naturally occurring in the atmosphere. This not only absorbs a large fraction of the beam power, but also causes a large amount of thermal blooming.

Figure II-12b displays the values for uncorrected turbulence-induced beam spread calculated by the ESP4-SWL code. It is evident that a factor of 30 to 40 reduction in these values must be accomplished by the adaptive transmitter optics in order to prevent the uplink beam from being dominated by turbulence considerations alone.

Presented in Figure II-13 are the values for the thermal blooming parameter, IREL (relative irradiance), calculated by the code. The results for 1.315 μm, the iodine laser, are not included because it bloomed so badly. The best iodine IREL value was 0.015 for a 50 MW beam and vertical propagation. The other results indicate that for wavelengths of 0.35 μm, 0.459 μm, 0.66567 μm, and 1.06 μm, thermal blooming probably can be completely corrected by adaptive optics at zenith angles out to 60° and power levels up to 350-400 MW. It is interesting to note that the transmission to space at 0.35 μm and 0.459 μm is less than 1.315 μm, but the blooming is much less also because the beam attenuation at the short wavelength is due primarily to scattering rather than absorption.

Figure II-14 shows the anticipated values for the coherence length, r_o, as a function of zenith angle and laser wavelength. The calculation was made with Fried's turbulence model assuming a C_n^2 value typical of conditions at a 3 km altitude site (Maui). Using the Miller and Zriske profile for the Maui site, the turbulence coherence length can be expressed as

$$r_o = 0.1847 \left\{ \frac{\lambda^2}{\int_0^\infty dz\, C_N^2(z)} \right\}^{3/5} \qquad (3)$$

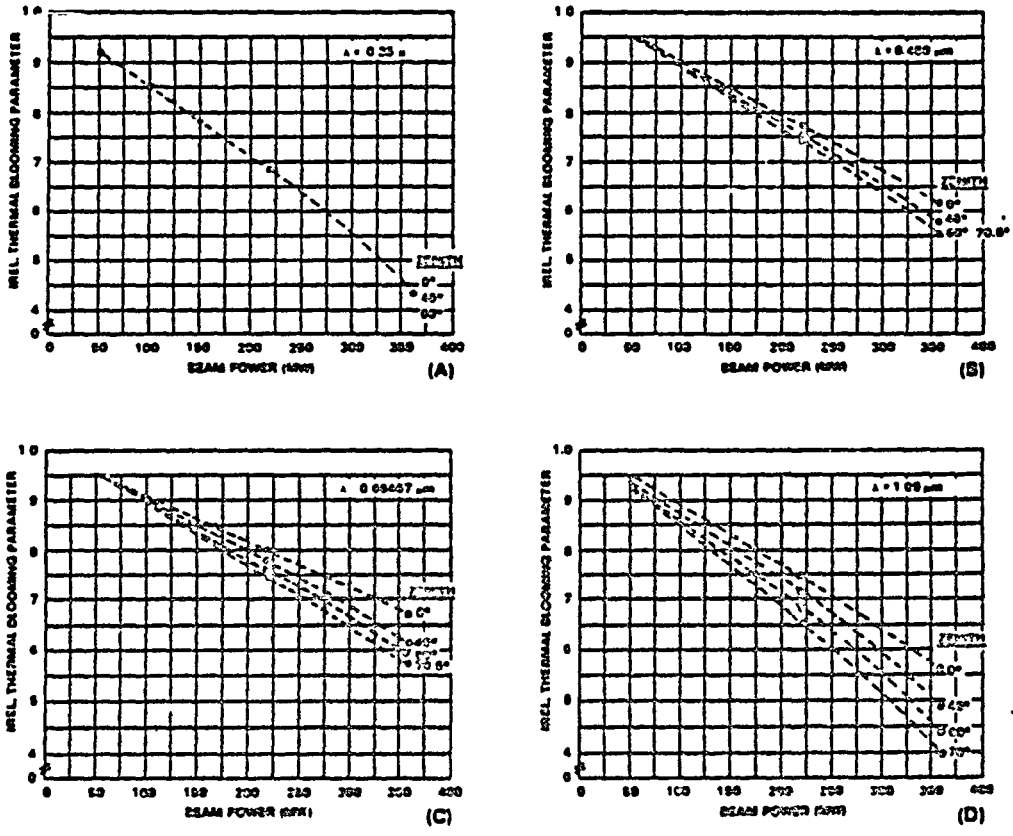

Figure II-13. ESP4-SWL Calculation Results: Thermal Blooming

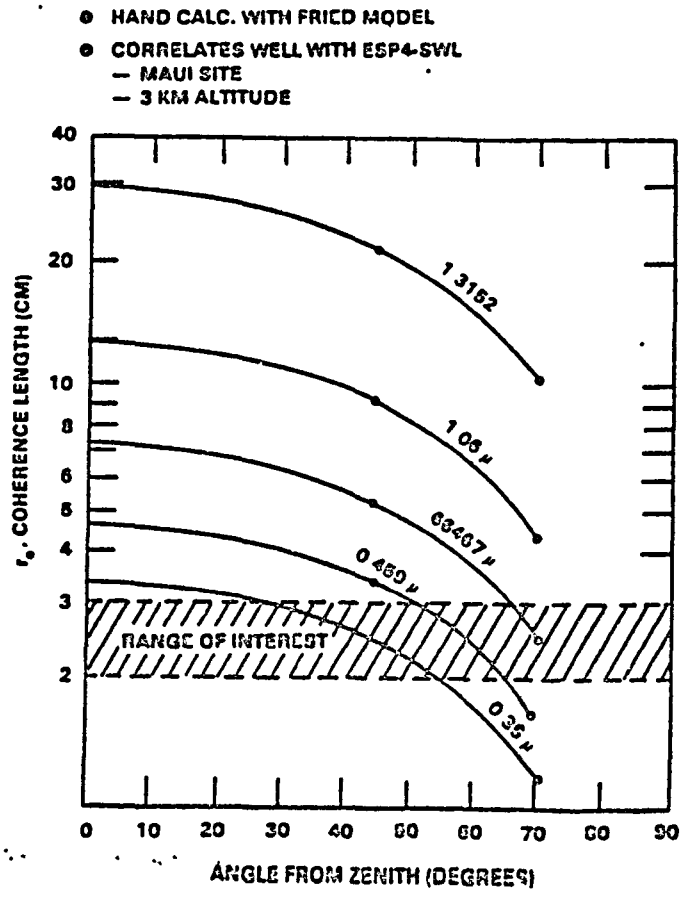

Figure II-14. Turbulence Coherence Length as a Function of Wavelength and Zenith Angle

where

$$\int_0^\infty C_N^2 (z)\, dz = 6.65 \times 10^{-13}, \text{ (Fried, 1980)} \qquad (4)$$

and, therefore, the turbulence-induced, long term beam spread is

$$\sigma_T \text{ (Long Term)} = 0.45\ \lambda/r_o \qquad (5)$$

Fried's formulation generates turbulence-induced beam spread values which agree well with those predicted by the ESP4-SWL computer run (displayed in Figure II-12b).

For mountain-top ground-based lasers with power levels of up to 300-400 MW, a transmitter diameter of 4 m appears adequate for reducing thermal blooming to within limits correctable by adaptive optics (assuming a 10 m/sec cross-wind velocity to clear the beam), even for zenith angles approaching 60°. Simple calculations indicate that electrical air breakdown will not occur at these power levels, pulse repetition frequencies, and pulse durations of interest. No other non-linear atmospheric propagation effects are anticipated. Therefore, the problem reduces to the linear regime where the necessary relay satellite receiver aperture becomes a direct function of transmitter diameter, zenith angle, relay altitude and, of course, laser wavelength.

The "uplink" map in Figure II-15 presents the results of such a calculation. The following initial assumptions are made in the analysis: a) the laser device has a specific beam quality*, b) the "uplink" zenith angle is set at zero degrees (i.e., straight up), c) the ground-based laser is placed at the top of a 3 km altitude mountain (e.g., Maui), d) the use of adaptive optics reduces turbulence-induced beam spread by a factor of 40 from the uncorrected case, and finally, e) the relay receiver aperture is sized to intercept 95 percent of the incident radiation. Assuming a gaussian distribution to represent the received beam intensity, the relay

* Here beam quality refers to the narrow-angle beam spread component, and not the wide angle component associated with distant side-lobes.

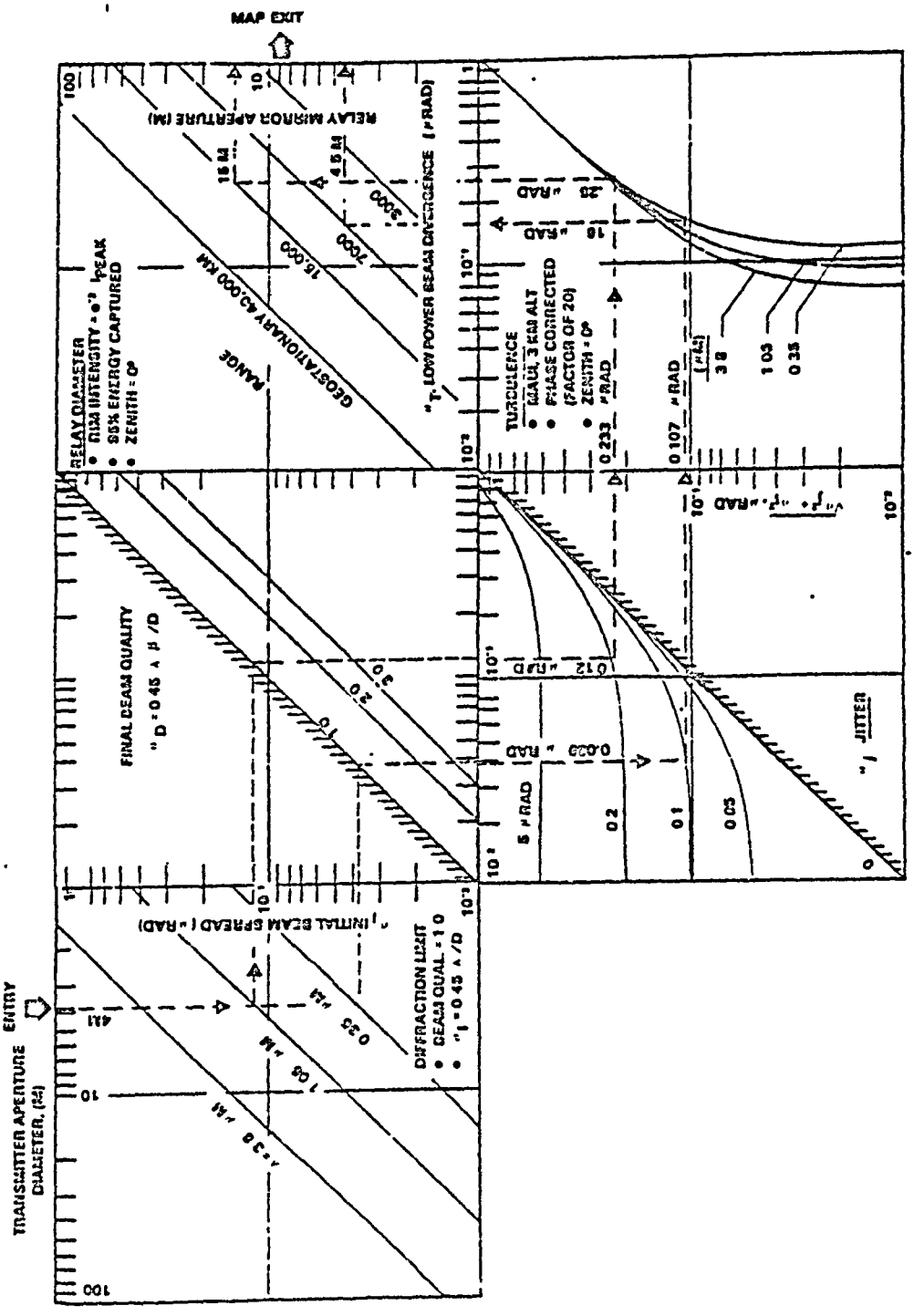

Figure II-15. Mapping of "Uplink" Laser Propagation Parameters

extends only to the e^{-2} intensity level. (Previous ARED space relay studies, e.g., Refs. 13 and 14, have truncated the beam at the e^{-1} intensity level or higher for relays placed in geostationary orbit, thus accepting major beam spillover and consequent power loss in exchange for a small aperture diameter.)

The minimum beam spot size projected by a GBL on the space relay receptive optics is a large function of the beam spreading due to diffraction, atmospheric turbulence, thermal blooming and jitter of the transmitting optics. The total beam spreading may be expressed as

$$\sigma^2 = \sigma_D^2 + \sigma_T^2 + \sigma_J^2 + \sigma_B^2 \qquad (6)$$

where D, T, J, and B denote the contributions due to diffraction, turbulence, jitter and thermal blooming. The beam spread component due to diffraction alone is given by:

$$\sigma_D = 0.45\ \lambda\beta/D \qquad (7)$$

where λ is the laser wavelength, β is the (narrow-angle) beam quality, and D is the diameter of the GBL transmitter aperture. Hence, the peak intensity I_o projected upon the relay mirror is

$$I_o = P\ T_R/2\ \pi\ (\sigma R)^2 \qquad (8)$$

where P is the total transmitted power at the GBL aperture, T_R is the transmissivity of the atmosphere, σ is the one-sigma beam spread angle, and R is the range between the GBL laser and relay satellite.

Several interesting conclusions are reached by examining Figure II-15. First, it is evident that ground-based laser pointing accuracy requirements are an order of magnitude less stringent than those for the relay cross-link to laser-propelled OTVs: 1 sigma jitters in range of 0.1 to 0.2 μrad are entirely adequate. It is also clear that a factor of 30 to 40 improvement in uncorrected turbulence-induced beam spread is

required to bring turbulence-induced beam spread in line with the other components (diffraction and jitter). Finally, it should be noted that for zenith angles near zero and low relay altitudes (e.g., 3000 km), the required relay receiver diameter to intercept 95 percent of the uplink beam power is substantially smaller than the relay projector aperture diameter required for brightness-to-target. Therefore, for the monocle approach, which combines both requirements upon a single mirror, the uplink beam best be de-focused to flood the entire aperture, because the final relay aperture size is determined by what is needed to project the requisite brightness to the laser-propelled OTV.

Additional conclusions become evident when the initial uplink mapping analysis is extended to include zenith angles of 60° and 70°, and poorer beam qualities. Turbulence beam spreading effects for 0.35 μm wavelength finally cause the beam to completely flood a 4.5 m receiver aperture at a zenith angle of 70.5 degrees and a slant range of 4,480 km, although the power required for such a large zenith angle would be prohibitive because of large amounts of atmospheric scattering loss.

Clearly, it is the shortest wavelengths and the largest zenith angles that place the most stringent requirements on uplink adaptive optics--and fix the minimum effective atmospheric coherence length, which in turn sets the maximum dimensions of the GBL adaptive transmitter elements themselves. For 0.35 μm radiation, the elements must be roughly 2-3 cm across to be effective in turbulence correction at zenith angles between 60° and 70°. Regarding the effects of reduced beam quality (narrow angle beam spread only), the results summarized above are not significantly changed for any zenith angles between 0° and 60° if the relay design requires the same aperture diameter for projector and receiver elements. Generally, the beam would have to be expanded anyway to fill the entire receiver aperture.

6. Space-Based Power Supplies

Clearly, the electric power supplies for ground-based FEL power-beaming stations will pose no particular technology problems regardless of

whether they take open-cycle or closed-cycle configurations. By sharp contrast, the total mass of space-based power supplies is of critical concern, since it all must be boosted from the Earth's surface. This section explores the alternatives for SBL power supplies based upon chemical, nuclear and solar primary energy sources.

The most powerful chemical sources suitable for generating tens to hundreds of MWe are rocket-driven turbo-alternators and MHD generators. In addition to liquid hydrogen and liquid oxygen, these gas generators can utilize a great variety of fuels and oxidizers, and must operate in an open-cycle mode. The best chemical rocket generators can exhibit a propellant specific power of 2000 kJe/kg. Although the total mass (i.e., dry mass plus propellants and tankage) of such electrical power sources can be exceedingly small for run times less than several hundred seconds, their overall performance is easily exceeded by bimodal nuclear power plants.

Bimodal nuclear reactors, which are being studied for military space power-beaming roles, generate peak electric power with MHD generators or turbo-alternators operating in the open-cycle mode (i.e., rejecting the heated working fluid to space) then flash back into a closed-cycle mode for producing station-keeping electric power and for removing reactor afterheat. Figure II-16 is an artist's concept of such a system using lightweight liquid droplet radiators for waste heat rejection in the station-keeping mode. Although the dry mass of such power plants significantly exceeds that of open-cycle chemical sources, the propellant specific power can be as high as 10,000 kJe/kg (e.g., with hydrogen)--easily five times better than the best chemical systems. Therefore, nuclear bimodal power plants are favored for military missions requiring run times of from several hundred seconds to 1-2 hours duration.

In order to generate 100 to 1000 MWe, space bimodal power plants will require reactor thermal powers of 500 to 5000 MW(th), respectively, assuming a 20 percent efficient conversion cycle. This thermal power regime is exactly compatible with that demonstrated by solid-core nuclear rocket engines developed in the Nerva program: the Pewee reactor ran at 500 MW(th), Nerva - 1000 MW(th), and Phoebus - 4000 MW(th). Ir the supersonic rocket nozzles are replaced with open-cycle MHD generators (20 to

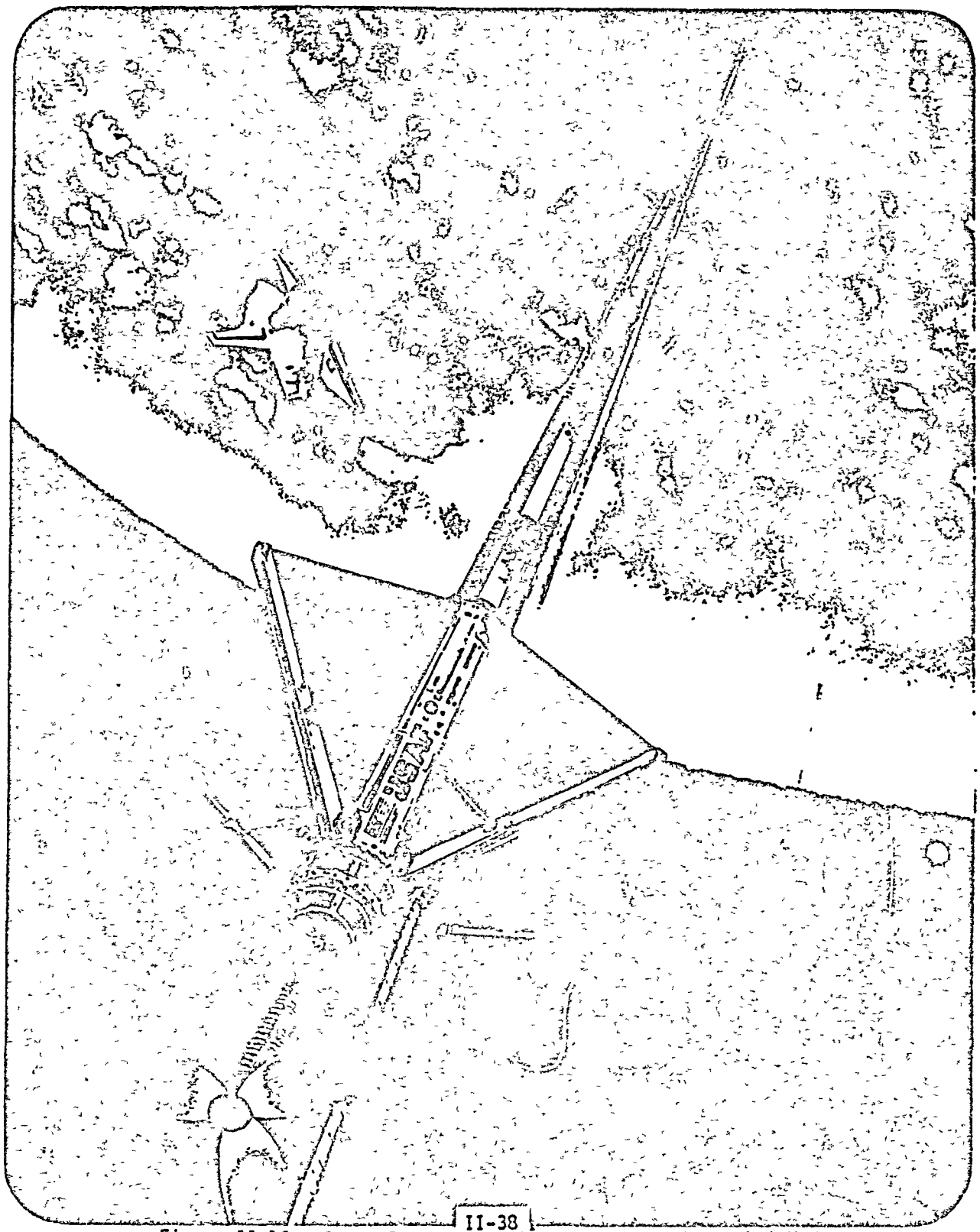

Figure II-16. Space-Based Free-Electron Laser with Multi-Mode Nuclear Power Plant and Liquid Droplet Radiators (Artist: R. Carter)

30 percent efficient) or turboalternators (40 to 50 percent efficient), these powerful nuclear sources could certainly satisfy the FEL power-beaming needs of many military missions. (Other missions demand particle-bed reactors which have far superior response times in rapidly-pulsed power applications.) An in-depth treatment of multi-mode space nuclear power plant technology can be found in Reference 15.

Because of the long run times required for most laser propulsion orbit-raising missions, suitable space-based nuclear-electric power plants must operate in the closed-cycle mode. (For example, a thrusting time of several days would not be uncommon for orbit-transfer of a 10-100 metric ton payload.) Such nuclear-electric power supplies need a compatible working-gas recirculation system: i.e., compressors, turbines, heat exchangers, regenerators, miscellaneous ducting, and large, lightweight space radiators--all designed around the above-mentioned military (open-cycle) nuclear source. The technological risk and cost associated with the development of a brand new reactor generally dwarfs the costs of all other power plant components. Hence, a compatible gas recirculation system could be developed with low technological risk at a small additional cost beyond that of the original military bimodal reactor. This could certainly be accomplished by private industry investment (without governmental funding), but clearly not without government cooperation in the transfer and licensing of reactor technology.

In a future era when commercial multi-purpose space power-beaming stations are built, they will probably employ solar energy sources. Although very soft (in the military sense) and difficult to harden, solar sources have every indication of being less expensive than closed-cycle nuclear systems--and are certain to have much greater public acceptability.

Although multi-purpose solar satellite power stations (SSPS) will apparently be most economical in the 5 to 10 GWe power range, the first operational power satellites may have to be considerably smaller to attract investment capital from the private sector before the year 2000. Therefore, the first publicly funded SSPS is likely to be a 250 to 500 MWe demonstrator, placed in low Earth orbit or possibly in geosynchronous

orbit. Since present SSPS research favors solar cell conversion, the sub-scale demonstrator is likely to incorporate this technology. The mating of this power plant to a 50-100 MW FEL will enable the first civilian orbit-raising propulsion experiments, as well as other space industrialization enterprises (e.g., extractive, refining and manufacturing).

Several variations of the full-scale 5-10 GWe SSPS concept have been proposed. The Marshall Space Flight Center's (MSFC) concept utilizes reflecting concentrators to increase the solar intensity falling upon photo-voltaic (PV) conversion cells above the space ambient value. The Johnson SFC concept uses a planar, non-concentrating PV array. (Marshall's SSPS baseline unit measures 21 km by 3.8 km, whereas the Johnson's is 21 km by 5 km.) Aerospace Corporation has suggested a segmented, cable-connected array stabilized by gravity-gradient forces. Another strong candidate is the closed solar Brayton cycle, based on concentrating reflectors and conventional turbomachinery.

These kilometers' long SSPS structures will roam about in their orbits, and sufficient boundary space must be allowed to prevent collisions. It is estimated that a maximum of one-hundred 10 GWe satellites will fit comfortably along the geostationary orbit. In a future era, possibly by the year 2000, these mammoth SSPSs and advanced laser propulsion engines will enable launch of the space equivalent of high-speed freight trains into low earth orbit--finally giving us efficient, economical, and safe access to space.

C. LASER POWER AND RUN TIME REQUIREMENTS: NEAR-TERM OTV MISSIONS

Long running high-energy FELs will also provide an exciting option for laser propulsion systems to perform useful orbital transfer missions. Significant payloads (e.g., 3×10^4 Kg) can be raised to long-term parking orbits using moderate size laser systems (e.g., 20 MW) with run times of less than a day.

There are many ways to group and plot intersecting system parameters to serve as mission analysis tools. The "first-order" estimate charts in Figures II-17 and II-18 (from Reference 16) show the logical relationships

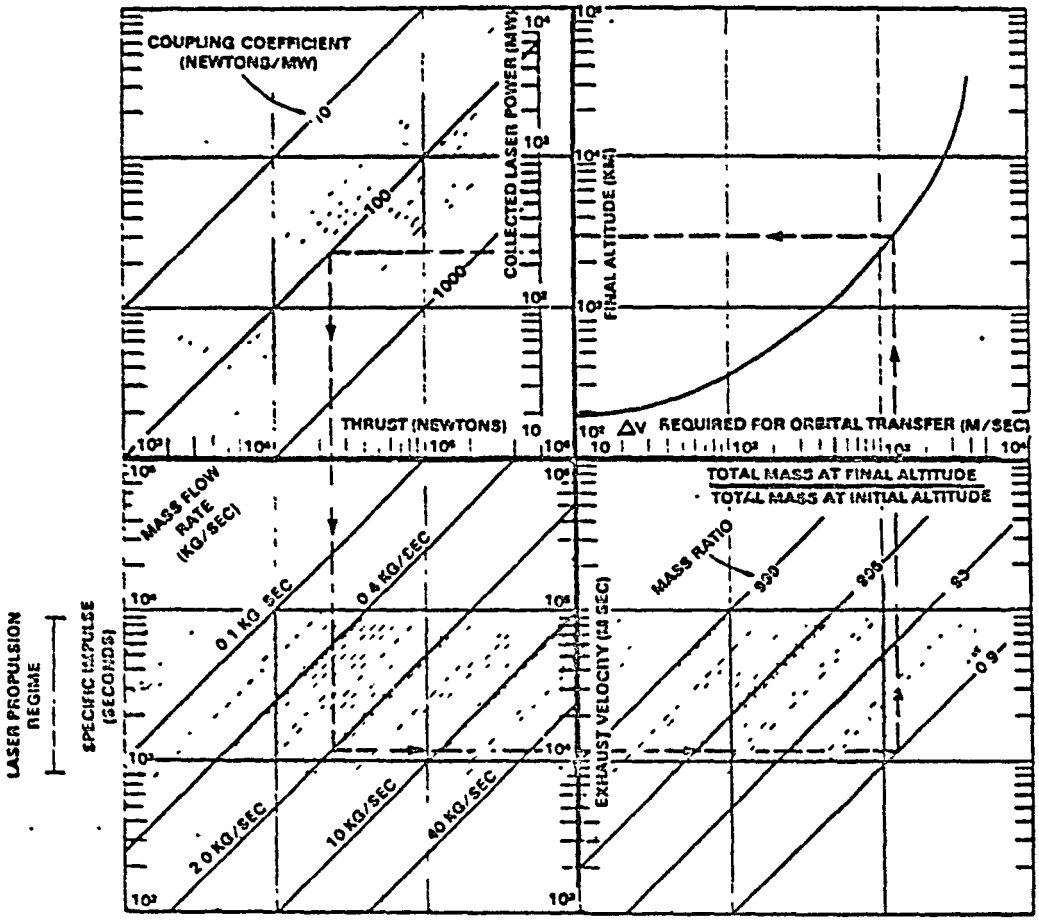

Figure II-17. Mapping of Laser Propulsion Parameters for Orbit-Raising from 185km (From Reference 16)

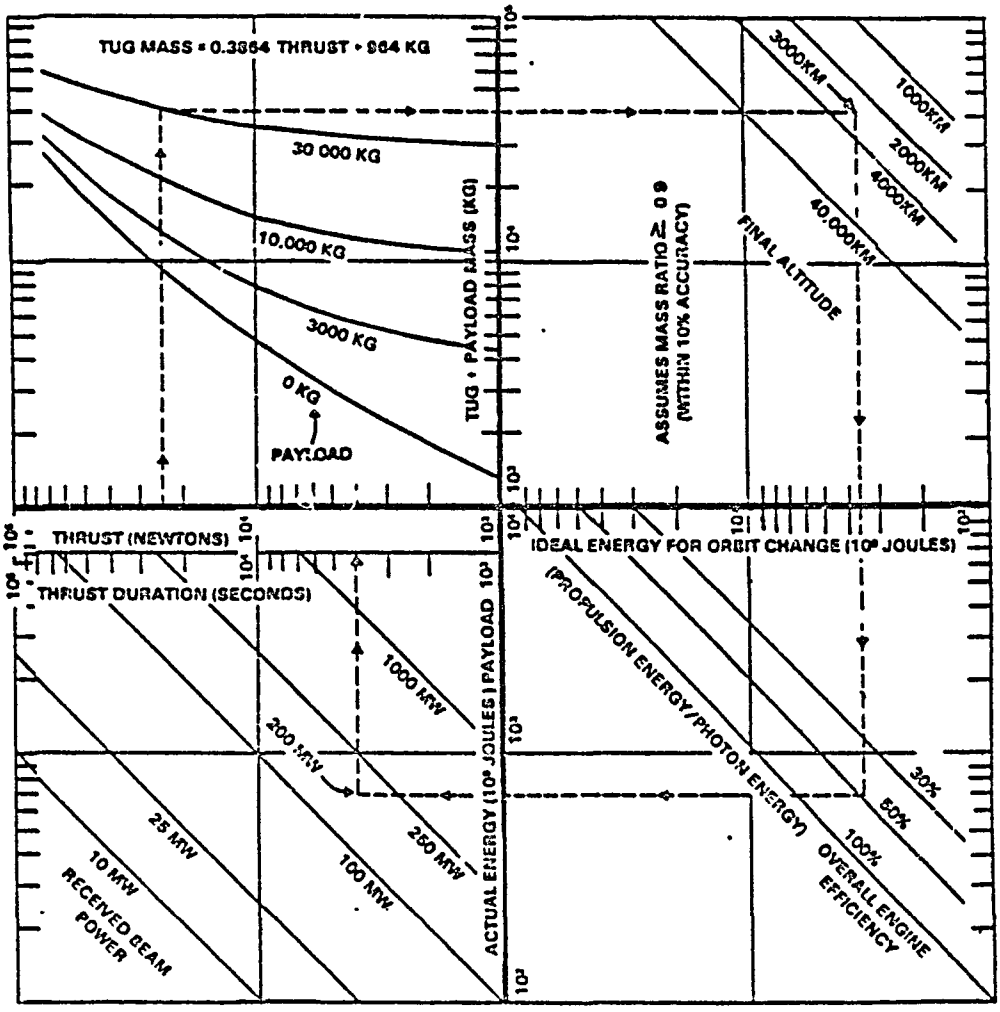

Figure II-18. Mapping of Performance Parameters for TRW Laser-Propelled Orbital Transfer Vehicle (From Reference 16)

among all of the principal parameters of laser propulsion for orbit-raising missions. The first chart (Figure II-17) relates laser power to achievable orbital height for specified performance of the laser propulsion engine. Figure II-18, the second, uses a plausible tug model to find the duration of operation to raise a given payload to a given orbital height using the laser power found from the first chart.

In the upper right hand quadrant of Figure II-17, the facing graphic plots the key mission parameter of a given increase in orbital velocity (total ΔV) required to deliver any payload from a 185 kilometer orbit to any selected orbital altitude. The remaining curves represent parametric assumptions to describe particular propulsion system options that lead to required laser power (upper left hand quadrant of Figure II-17). The significant engine performance parameters are specific impulse, I_{sp}, and the energy coupling coefficient, C, which relates to the conversion efficiency from collected laser power to rocket thrust (e.g., units of dynes/watt). The chosen combination of C and I_{sp} defines the required fuel flow rate. Knowing what altitude is desired then defines the mass fraction (final-total-mass/initial-total-mass) required to get there. Alternatively, for a specified mass fraction, Figure II-17 shows what altitude can be reached.

An example of how to use this plot is shown for the mission of raising a 32 metric ton payload (approximate weight of the expended shuttle main tank) from 185 kilometers to 3000 kilometer orbit using 3.6 metric tons of residual hydrogen and a family of tug-like propulsion systems weighing between 1 and 5 metric tons (i.e., a mass fraction of approximately 0.9). Exhaust velocity for this example is selected as 10,000 meters per second, corresponding to a thrust of 23,000 Newtons, and the coupling coefficient is chosen to be C = 12 dynes per watt. If these assumptions comprise a valid propulsion system, then the total power required is approximately 200 megawatts.

Stippled areas have been added to Figure II-17 to designate areas of validity or plausibilty. The chart may not be accurate to within 10 percent for mass ratios lower than 0.9, because if the fuel mass is sufficiently larger, then it will affect optimum mission parameters (see

Figure II-18). The other boundaries of the stippled areas indicate a plausible regime vis-a-vis achievable physics.

To go further, we must adopt a model of the laser tugboat. The mass of the tug is primarily related to the thrust, both because of the size of the engine and pumps and because of the required stress-bearing components of the system as a whole. (Interestingly, the laser light collectors will have the same diameter regardless of the thrust for a specified laser wavelength and range to the laser source.)

TRW has modeled a laser-propelled tug (pictured in Figure II-19, with the addition of a shuttle external tank for payload), which seems to have plausible and justifiable characteristics.[17] For our purposes here, we have adopted the TRW tug model as expressed by the equation

$$M_T = 0.386\ T + 964,\ (Kg) \qquad (9)$$

where M_T is the total mass of a tug having a laser propulsion engine which develops thrust, T, measured in newtons. We also assume that the fuel mass will, in general, be a small fraction of the tug plus payload mass (<10 percent of the total).

It is important to understand that the chart in Figure II-18 is "slaved" to that in Figure II-17. The same thrust, altitude, and laser power must be used here that were chosen on the previous chart. In addition, the laser engine conversion efficiency is closely related to the coupling coefficient on the previous chart for a given engine design. Fifty percent efficiency is regarded as a reasonable value. With these constraints, we can then find the total thrusting time to perform the OTV mission.

The dashed line in Figure II-18 applies to the mission of raising the Space Shuttle main tank to a 3000 kilometer orbit from 185 kilometers. It can be seen that this mission can be accomplished in ~3500 seconds of thrusting time with 200 megawatts of delivered laser power. Or, retracing all of the steps, we find that the same mission can be performed in ~ 26,000 seconds (7.2 hours) with 20 megawatts of laser power.

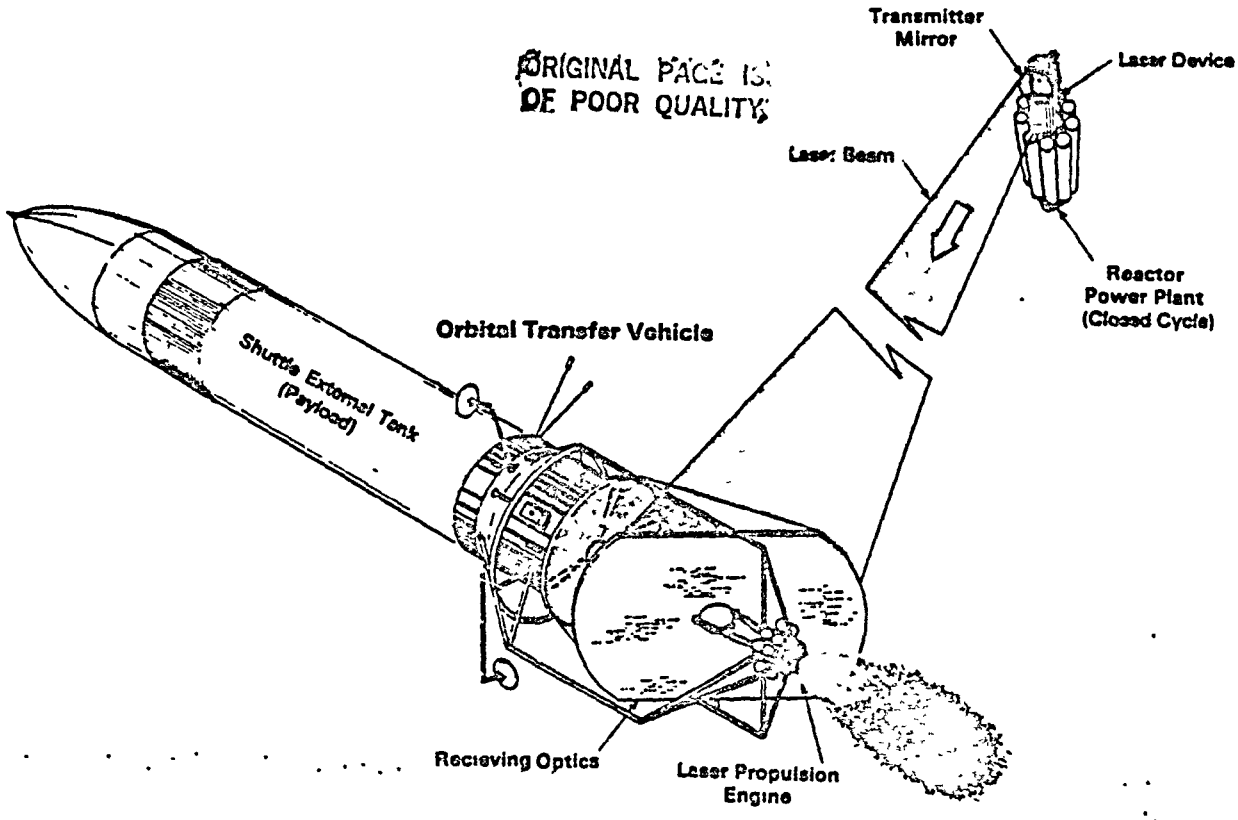

Figure II-19. TRW's Laser-Propelled OTV Tug Concept With Shuttle Main ET Tank for Payload (After Reference 17)

D. SUMMARY AND CONCLUSIONS

The great diversity of continuous and repetitively pulsed laser propulsion engine concepts which has been suggested in the literature uses a variety of laser energy absorption schemes. These include inverse Bremmstrahlung, particulate, molecular, and heat-exchanger mechanisms. Hence, compatible photon sources must run either CW or RP, possibly with variable pulse repetition frequency, pulse energy, and pulse duration. They must also be throttleable over a wide power range, and operate at an assortment of wavelengths, e.g., for engines using molecular absorption. Ideally, since the development of such a power-beaming technology will be expensive, one would want to advocate a high-energy laser technology which holds the greatest promise for high versatility--to serve the widest variety of potential engine concepts and missions.

It is pointless for laser propulsion researchers to: a) constrain their thruster concepts to operate on the narrow range of wavelengths and waveforms available with current laser technology, or b) worry about the future availability of a versatile full-scale, high-power laser to exactly suit the needs of these thrusters--in 10 to 20 years when the technology is finally mature. The principal reason is that an ideal potential source already exists in the embryonic stage: i.e., the free-electron laser. Furthermore, the military is aggressively pursuing FEL technology for potential use in antiballistic missile applications, because of the FEL's exceptional flexibility and promise of short wavelength operation at very high efficiencies.

Projected laser power levels for "robust" ABM roles agree well with that required for laser propulsion engines in near-term orbit-raising missions: e.g., tens to hundreds of megawatts. Also, a parallel intense development in sophisticated acquisition, pointing and tracking (AP&T) systems is being funded by the military. The demands placed upon AP&T systems by laser propulsion applications are significantly less severe than that required for ABM missions.

Beyond the year 2000, multi-purpose space power stations will link gigawatt power-level FELs to powerful closed-cycle nuclear, solar-photovoltaic, or solar thermal-electric sources--to supply large quantities of cheap, plentiful power for widespread proliferation of laser propulsion, as well as other enterprises in space industrialization. For the foreseeable future, however, it is important to note the scaling of laser propulsion engines themselves to high levels of thrust will be limited solely by the available power level of HEL devices.

E. ACKNOWLEDGEMENT

Some of the technical background and illustrations for this chapter have been derived from prior work by the author, and J.D.G. Rather (previously of the BDM Corporation, now with DESE Research and Technology, McLean, VA).

This Page Intentionally Left Blank

REFERENCES FOR CHAPTER II

1. Forward, R. L., "Comparative Study of Solar-Electric Propulsion and Laser-Electric Propulsion," HAC No. D3020, Hughes Research Laboratories, Malibu, CA, June 1975.

2. Lee, J. H. and Jalufka, N. W., "Radiation-Driven MHD Systems for Space Applications," Chapter VI-12, Proceedings of the AFOSR Special Conference on Prime-Power for High Energy Space Systems, Norfolk, VA, 22-25 February 1982.

3. Smith, T. I. and Madey, J. M., "Realizable Free Electron Lasers," Stanford University High Energy Physics Laboratory, Stanford, CA, Publication #HELPL-885, December 1980.

4. Brau, C. A., "Free Electron Lasers," Los Alamos National Laboratory, Report #LA-UR-80-2015, Los Alamos, NM.

5. Neil, V. K. and Prosnitz, D., "Theoretical Investigation of a 10 μM Free Electron Laser Amplifer Using a 50 MeV Multi-kA Electron Beam," Lawrence Livermore National Laboratory, Livermore, CA, Report #UCRL-85653, June 24, 1981.

6. Madey, J. M., "Scaling Relations for the Power Output of Gain Expanded Storage Ring Free Electron Lasers," Stanford University High Energy Physics Laboratory, Publication #HEPL-853, Stanford, CA, June 1979.

7. Rather, J. D. G., Myrabo, L. N., and Henderson, W. D., "Free-Electron Lasers in Space," Report No. BDM/W-1217-82-S, Contract No. DAAH01-80-C-1587, The BDM Corporation, McLean, VA, April 1982.

8. Sparks, M., "Assessment of Materials and Coatings Requirements for UV Laser Optics," BDM/W-81-447-TR, Contract No. MDA903-81-C-0151, The BDM Corporation, McLean, VA, 7 August 1981.

9. Rather, J. D. G. and Myrabo, L. N., "Alternative Laser Initiatives in Space," Report No. BDM/W-2180-82-S, Contract No. DAAH01-80-C-1587, The BDM Corporation, McLean, VA, 9 October 1981.

10. Henderson, W. D., "Space-Based Lasers--Ultimate ABM System?," Astronautics and Aeronautics, Vol. 20, No. 4, May 1982, p. 44ff.

11. Elterman, L., "UV, Visible, and IR Attenuation for Altitudes to 50 km," Environmental Research Papers No. 285, AFCRL-68-0153, Air Force Cambridge Research Laboratories, Bedford, MA, April 1968.

12. Zeiders, G. W., Schaefer, R., and French, F. W., "Short Wavelength Laser Beam Propagation Analysis for BMD Applications," WJSA-STR-78-106, W. J. Schafer Associates, Inc., Wakefield, MA, 28 February 1978.

13. Scherfflins, J. H. and Lush, K. J., "ARIS Aperture Relay," LMSC-L030203, Contract No. DAAK90-76-C-DADE, 30 July 1977.

14. Decker, L., Aspinwall, D., Pohle, D., Dotson, R., and Bartosewcz, M., "Aperture Relay Experimental Definition," LMSC-L048510, Contract No. DASG60-78-C-0100, Lockheed Palo Alto Research Laboratory, Palo Alto, CA, 28 August 1979.

15. Myrabo, L. N., et. al., "Space Prime Power and Propulsion," Report No. BDM/W-83-116-TR, prepared for DARPA under contract 55713-S by The BDM Corporation, McLean, VA, January 1983.

16. Rather, J. D. G., Borgo, P. A., and Myrabo, L. N., "Laser Propulsion Support Program," Report No. BDM/W-80-652-TR, prepared for NASA Marshall SFC by The BDM Corporation, McLean, VA, 1 November 1980.

17. Huberman, M., et. al., "Investigation of Beamed Energy Concepts for Propulsion," AFRPL-TR-76-66, Volume 1, TRW Defense and Space Systems Group, Redondo Beach, CA, October 1976.

CHAPTER III
DESIGN CONSIDERATIONS FOR LASER-PROPELLED SHUTTLECRAFT

It is clear that the minimum buy-in power for manned shuttlecraft propulsion falls in the range of several hundred megawatts to one gigawatt. In today's experience, multi-gigawatt power levels are not unusual. For example, a single Atlas rocket engine develops 2.7 GW; the Rocketdyne F-1 engine, 25 GW. (By comparison, a large jumbo-jet requires 40 MW to maintain high altitude cruise.) It is anticipated that light-weight laser-heated engines can successfully absorb power densities that would destroy conventional turbomachines, but which are commonplace in present chemical-combustion rockets. These simple laser propulsion engines can easily generate overall vehicle thrust/weight ratios greater than one. Hence, engine thrust power need not be a critical or limiting consideration in the design of future laser-propelled shuttlecraft.

This chapter attempts to provide some insight into the conceptual design process for such advanced manned shuttlecraft. The various mechanisms for absorbing beamed power into candidate laser-heated thrusters are reviewed. Both air-breathing and rocket engines are considered. A set of design premises is suggested, which is subsequently used to postulate a methodology for engine/optics/airframe integration into three basic types of shuttlecraft configurations.

A. FUNDAMENTAL CONSIDERATIONS

In order to propel a flight vehicle from a point of origin on the earth's surface to a destination point (in space or on the ground) using strictly beamed power and compatible propulsion convertors, several considerations must be borne in mind:

(1) The availability of powerful bursts of beamed energy (e.g., hundreds to thousands of megawatts) will permit sufficient power for vertical takeoffs and landings, and unconventional flight trajectories.

(2) The boost phase may be divided into two identifiable regimes. First, beamed power is used to lift the shuttle vertically to an altitude of perhaps seventy thousand meters; second, the beamed power must rapidly accelerate the vehicle laterally across the Earth's surface in a direction perpendicular to the beam, up to escape velocities.

(3) Depending upon the overall vehicle/engine configuration, these distinctively different flight regimes will necessitate two sets of specialized thrusters: one for VTOL, another for lateral propulsion.

(4) The basic principles of optics must be utilized in designing an optical train that will capture the incident power beam, manipulate it and finally direct it into the thruster.

(5) A small beacon laser mounted aboard the shuttle and directed back towards the space relay transmitter will provide flight trajectory/position data necessary to close the information loop--thereby providing a "cooperature target" for directing the transmitter optics.

(6) The shuttle must provide an optically stable platform for receiving the orbital beam so that near perfect alignment can be maintained even through severe atmospheric turbulence.

(7) The shuttle must be able to negotiate a lateral turn without performing the conventional banking maneuver that would cause a severe misalignment of receptive optical elements which are firmly affixed to the shuttle airframe.

(8) The shuttle must be able to use aerodynamic braking during re-entry in order to avoid requiring large amounts of beamed power to decelerate (e.g., after "cruising" efficiently in the vacuum of space).

(9) A considerable reduction in thruster complexity is permitted by the use of pulsed electromagnetic power and inverse Bremsstrahlung absorption into simple radiation-heated pulsejet

engines. Such engines do not require heat exchangers and heavy rotating turbo-machinery.

(10) A large degree of optics/airframe/engine integration is necessary due to the many overlapping system requirements for successful utilization of beamed energy in air-breathing and rocket engines. For example, depending on the shuttle configuration, portions of the vehicle external surface will be called upon to serve as optical elements or thruster surfaces, in addition to providing an aerodynamic skin able to withstand high temperatures generated during re-entry. Several of these multi-purpose surfaces are likely to require transpiration or regenerative cooling.

This set of premises will permit entirely new and unconventional flight trajectories. For example, a laser-powered shuttle could boost out of the dense atmosphere into space, negotiate free fall in a ballistic trajectory, then glide into the destination port--requiring just enough maneuvering power and breaking energy to touch down for a gentle landing. Conventional runways can be eliminated in favor of launch "pads." The vehicle would climb out and return through very small operational corridors in tightly controlled airspace. Dozens of laser flight vehicles could land simultaneously in the space occupied by any present airport. The aerodynamic requirements for low-speed flight stability and control become subordinate to that for VTOL thrusters. External laser-heated engines can provide VTOL thrust.

The efficient incorporation of remote laser energy into propulsive engines is predicated on several unique and peculiar requirements quite foreign to conventional engines and chemical fuels. The basic premises for design of suitable air-breathing laser-heated engines are twofold. First, the laser energy must be absorbed directly within the engine gaseous propellant so that working fluid temperatures may exceed the limitations of solid materials. This mechanism permits greater engine efficiencies to be realized than ever before possible. The propulsive energy converters will incorporate direct gas-phase absorption of incident radiation by the process of electrical breakdown and inverse Bremsstrahlung absorption into

the engine working fluid. Secondly, pulsed laser power will permit non-equilibrium heating processes to come into play, so that engine gas temperatures do not have time to reach steady state equilibrium levels. Continuous wave laser heating rapidly drives gas temperatures to 20,000 K and higher. Alternatively, with pulsed laser heating, the engines can process propulsive working fluid to a great range of final temperatures and pressures--simply by varying the incident beam intensity and the degree of beam focusing within the internal engine chamber.

The two basic types of engines addressed in this study are: simple radiation-heated engines, and electrically augmented systems. The first category uses simple optics to cause incident laser energy to be absorbed into the engine working fluid which is then gasdynamically accelerated to produce thrust. The second category requires an intermediate conversion to pulsed electric power. The beam energy is first converted to translational energy of a partially ionized gas stream, then to pulsed electric power by a MHD generator, and finally back to translational energy of the external air stream (e.g., within an annular MHD fanjet). The following section provides a technical description of the physical processes involved in laser absorption physics.

B. LASER ABSORPTION PHYSICS

The basic premises upon which laser energy "absorption chambers" can be designed are two fold: (1) The beamed energy must be absorbed into the engine working fluid in order that elevated gas temperatures can permit higher engine efficiencies, (2) The laser power must be absorbed at high intensities and utilized in repetitively pulsed fashion in order that working fluid temperatures are not allowed enough time to reach their steady state equilibrium value (i.e., when the temperature of the more massive ion particles reach the temperature of quickly heated electrons). At steady state working gas temperatures of 15,000 to 20,000 K which are characteristic of laser-heated engines utilizing continuous wave (CW) power, severe

radiation losses are in evidence. In addition, cooling of engine walls becomes a design problem of massive proportions.

Consequently, this section will address the use of pulsed EM power and direct gas-phase nonlinear absorption of beamed radiation by the process of inverse Bremsstrahlung. By properly adjusting the intensity and degree of focusing of the beam, a laser absorption "wave" can be made to pass through the engine working fluid volume at a precise wave velocity that is tailored to bring the gas state to any desired final temperature and pressure.

1. Laser-Supported "Detonation" LSD

Figure III-1 illustrates the absorption wave structure characteristic of the detonation wave regime. Laser flux is projected from right to left, and the LSD wave is captured at a moment in time when the initial transients due to ignition have died away. Virtually all the incident laser energy is absorbed in a thin zone behind the leading-edge shock wave. The wave is shown propagating towards the right (into the beam) at a detonation wave velocity V_{DW} first calculated by Razier[1] as

$$V_{DW} = [2(\gamma^2 - 1)\ I_o/\rho_o]^{1/3}, \qquad (1)$$

where γ is the ratio of specific heats, ρ_o is the ambient density of the gas ahead of the LSD wave, and I_o is the intensity of the laser radiation. The wave velocity is directly proportional to the cube root of the laser intensity over the ambient gas density ahead of the wave. A region of hot, high-pressure gas occupies the space immediately behind the shock wave. The gas pressure within this region can be expressed by[1]

$$P_{DW} = \rho_o V_{DW}^2/(\gamma + 1), \qquad (2)$$

and is seen to vary with the square of the detonation wave velocity. Viewed from a distance, the external gasdynamic effect of an LSD wave passage through a stationary air mass bears close resemblance to the flight of a supersonic projectile of the same diameter as the beam. Rapidly

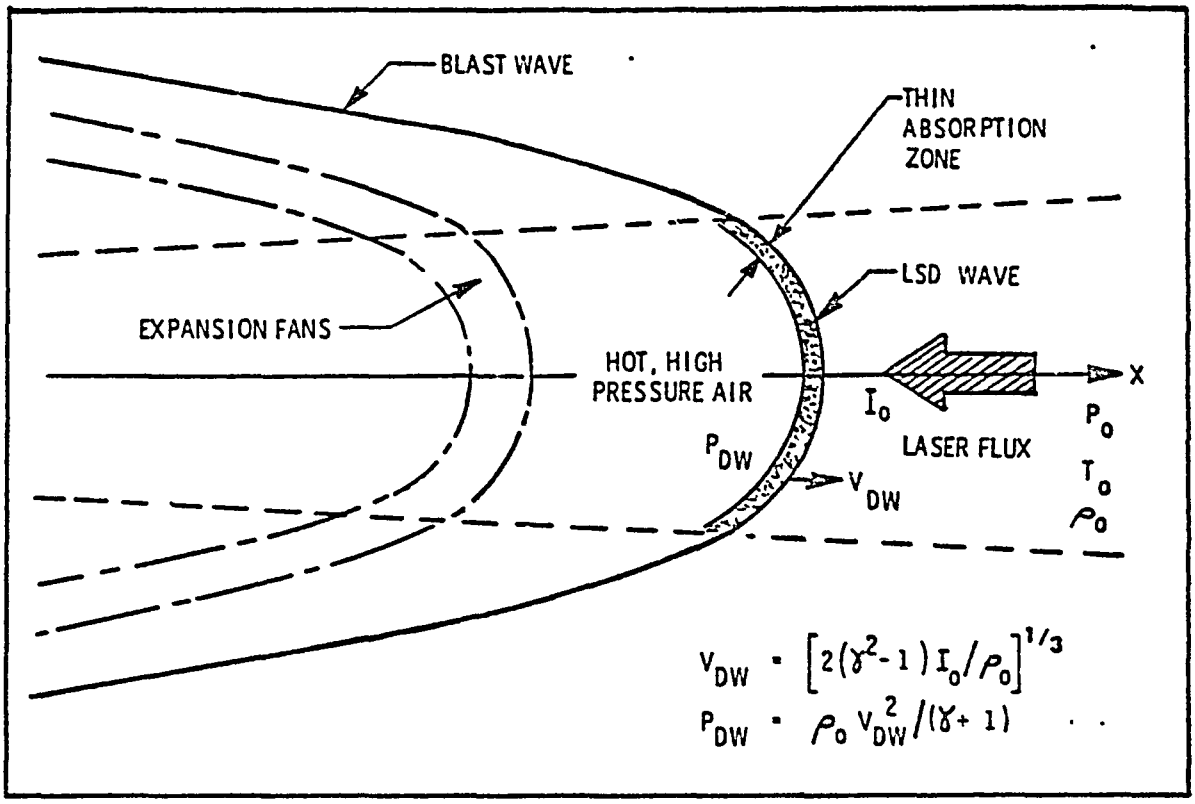

Figure III-1. LSD Wave Plasma, Non-Equilibrium Heating

expanding conical blast waves are generated by passage of the central heating zone, followed by a region of conical expansion fans.

For the case of 10.6 μm wavelength radiation, the LSD/LSC transition region falls at about 5×10^6 W/cm^2. Beam intensities above this value are associated with increasing LSD wave velocities and therefore lower gas temperatures. This effect is a natural consequence of an LSD wave which must process a larger mass flow rate of gas at the higher velocity - which in turn results in less energy deposition per unit volume. Insufficient "heating time" is available for electrons to elevate the temperature of massive ion and neutral particles into steady state equilibrium with the higher electron temperature. Hence, LSD waves are classified as a non-equilibrium heating process.

2. Laser-Supported "Combustion"LSC

As beam intensities are reduced below 5×10^6 W/cm^2 (for 10.6 μm radiation), the laser-supported combustion regime sets in, and an entirely different physical model is required to describe the equilibrium heating process. As shown in Figure III-2, laser flux is projected from right to left, and the absorption wave advances at a relatively slow velocity towards the right into the beam and into ambient gas. Very low density, hot air occupies the region just aft of the absorption wave. "Blow-off" of this low density, hot air (in the directions indicated in Figure III-2) is in part responsible for driving the absorption wave into the beam--through action/reaction forces. Although LSC wave heating is characteristically a constant pressure process, P_1 is slightly larger than the pressure ahead of the wave, P_0. As indicated, the thickness of an LSC wave is typically orders of magnitude greater than that of an LSD wave. LSC wave propagation velocities in air fall in the range of 1000 to 6000 cm/sec. Since the slower wave velocities result in the ingestion of very small mass flows of ambient gas, temperatures skyrocket. Peak temperatures within the absorption wave may reach 15,000 to 20,000 K. Radiation losses in all directions are normally substantial. Radiative transport in the forward direction is an important factor in determining the LSC wave velocity and the mass flow rate of processed gas.

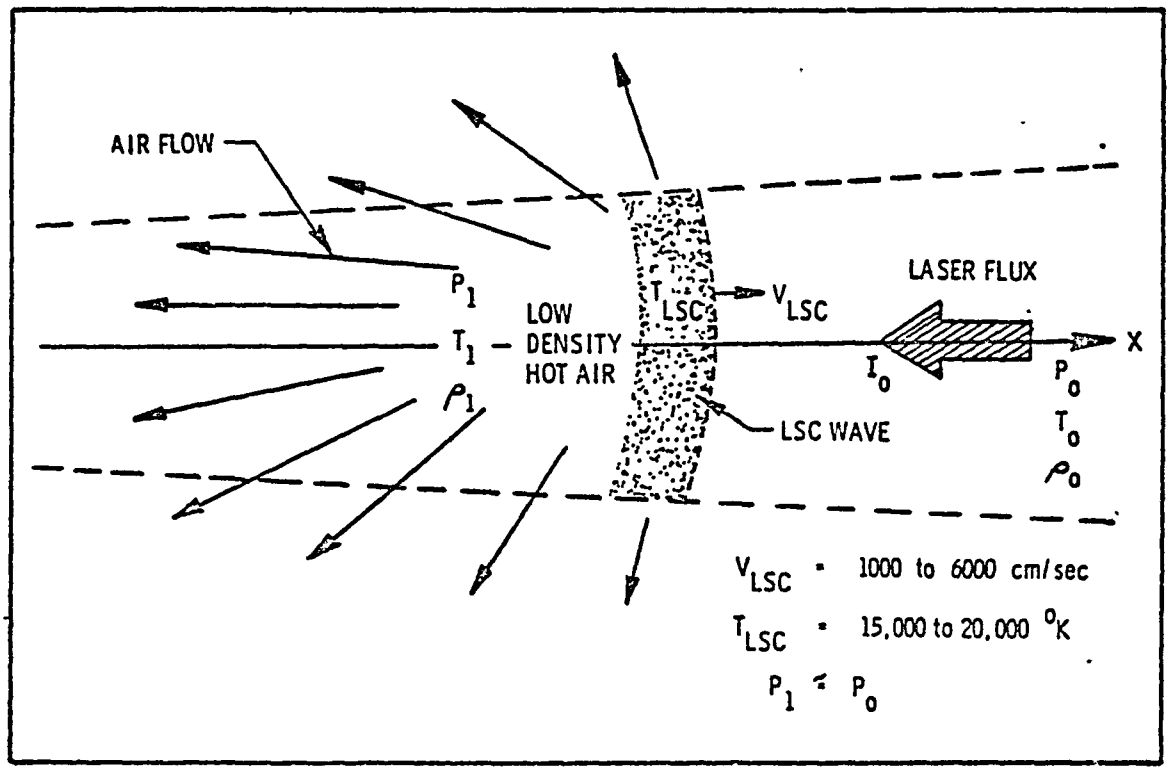

Figure III-2. LSC Wave Plasma, Equilibrium Heating

The interrelationship between the various laser energy absorption mechanisms of interest is displayed in Figure III-3 for the case of 10.6 μm radiation and air at 1 atm. Laser radiation in a sharply focused condition (not shown to scale) is projected from the right towards the focal spot on the left side of the page. The LSC wave regime falls in the vicinity of 10^4 to $10^{[illegible]}$ W/cm^2. Below 10^4W/cm^2, the LSC wave cannot maintain itself; hence, this point is called the "maintenance threshold." Between 10^6 and 10^7W/cm^2, the wave will transition from the LSC to the LSD wave regime. At laser intensities beyond 10^8 to 10^9W/cm^2, some researchers[2] address a "super detonation" regime where wave velocities substantially exceed Mach 10 or 20. The laser-supported super detonation (LSSD) regime is exemplified by radiation intensities up to and including what is called the clear-air breakdown threshold.

Ignition of a laser-supported absorption wave may be prompted by any of several mechanisms including a) laser-induced gas breakdown (as indicated in Figure III-3), b) electric spark discharge, c) molecular or particulate absorption, or d) ignition off a metal "target" especially designed for that purpose. This study will concentrate on laser-driven engine concepts which primarily utilize laser-induced breakdown as the sparking mechanism.

3. Laser-Induced Electrical Breakdown

Much of the experimental data on laser-induced gas breakdown has been gathered with air as the subject gas. Air (as well as most gases for that matter) is seldom free from contamination by a very rich spectrum of particle sizes and number densities. Therefore, the comprehensive treatment of laser-induced air breakdown should also address the effects of particulate contamination.

Laser-induced breakdown is characterized by a highly luminous region which absorbs a large fraction of the incident laser power. Not necessarily indicative of breakdown is the emission of radiation from the region of laser-particle interaction. In some cases the irradiated particles may emit enough vapor to form a hot plasma detectable by a visible spark, but still not absorb a measurable amount of laser radiation.

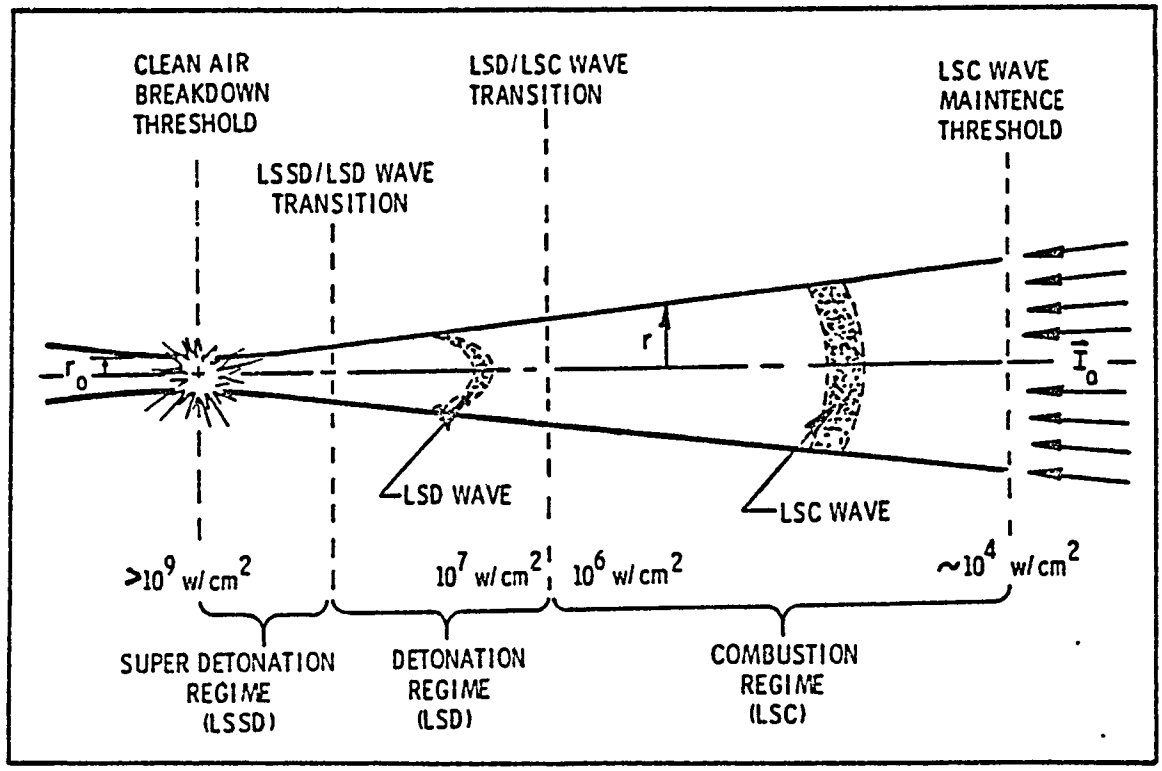

Figure III-3. Laser Radiation Absorption Mechanisms

Breakdown normally occurs at a variable time after onset of radiation. The delay period is largely a function of the contamination particle size and number density, incident laser intensity (Watts/cm^2) and pulse time. Open shutter and time-resolved photography have shown breakdown to be characterized by formation of a pre-breakdown luminous vapor or plasma region. These two phenomena suggest that the contaminated air breakdown mechanism begins first with the rapid vaporization of the external surface of particles and the growth of individual particle vapor "bubbles." If the vapor produced from the hot particles has a lower ionization potential than that of the constituents of air, it is possible that the first free electrons are emitted from the ionized vapor. The particles can also emit electrons thermionically as they are heated. Even though the latter emission process is impaired by electrostatic effects as the particle charge builds up, the few electrons which are produced may be adequate to trigger laser-induced breakdown at the higher intensities.

Presented in Figure III-4 is a summary of the observed breakdown data in air for 10.6 μm laser radiation.[3] Note that the lowest observed threshold is on the order of one megawatt per cm^2 and is associated with the 30 μm particles. With the larger particles and lowest intensities, no breakdown is observed until 10 μsec into the pulse[4]. Breakdown with shorter pulses is accomplished only at considerably greater flux levels.

The physics of air-breakdown in the presence of particulate matter is not well understood. Current modeling efforts are specifically tailored to investigate either the high-intensity non-equilibrium regime or the low-intensity equilibrium regimes of particle-induced breakdown. Triplett and Boni[5] have examined the interaction of high-intensity laser radiation with a single suspended particle. Their analysis assumes that sufficiently large laser intensities are incident upon the particle to rapidly evaporate or explode the particle. Under these conditions, a strong shock wave is driven into the surrounding air; and breakdown occurs by the non-equilibrium cascade process either in the vapor or in shock-heated air. The simple model of Triplett and Boni was unable to predict a reduction in threshold by much more than one order of magnitude below that

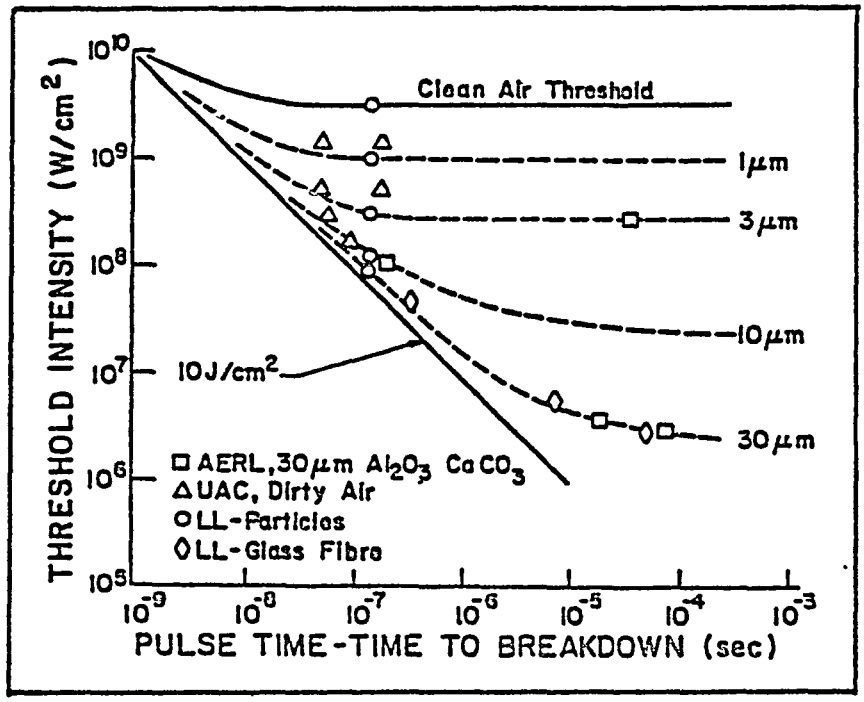

Figure III-4. Measurements of Air Breakdown in the Presence of Particulate Ma.ter (From References 2-4)

of clean air. A reduction in several orders of magnitude for the longer pulses and lower intensities are in evidence from experimental data.

Figure III-5 illustrates particle-induced breakdown at the lower laser intensities. At the beginning of the laser pulse, energy is absorbed by the particles and results in bulk vaporization of the outer surface of larger particles or in complete vaporization of the smaller particles. Subsequently, vapor bubbles are formed whose aggregate effect is the interception of a large fraction of the incident laser energy. Depending upon the vapor absorption coefficient, the temperature of the initially 4000 to 5000 K vapor climbs slowly at first, then rapidly to the order of 10,000 to 12,000 K. Then through the processes of thermal conduction and radiation, energy is transferred from the vapor to heat the air (in local equilibrium). At roughly 10,000 K, an LSC wave is ignited and the inverse Bremsstrahlung absorption coefficient of air climbs rapidly with the increased temperature. Finally, the wave reaches a maximum temperature of 15,000 to 20,000 K and slowly propagates in the direction of the incident radiation, maintaining itself by radiative and conductive heat transfer in the forward direction.

A pictoral representation of particle-induced breakdown at the higher laser intensities is portrayed in Figure III-6. The powerful incident radiation rapidly evaporates or explodes the particles, driving strong shock waves into the surrounding air. The air/vapor is heated and ionized as the shock wave propagates at the local sonic velocity in all directions except for that portion of the wave which propagates directly into the beam. Here a thin zone of non-equilibrium radiative absorption is transported behind a shock front which, in turn, propagates at the LSD wave velocity. Again, the detonation wave velocity is proportional to the cube root of the ratio of the incident intensity over the ambient density of the unprocessed air. The subsequent cascade process occurs very rapidly, and shortly triggers the complete breakdown absorption of the incident radiation.

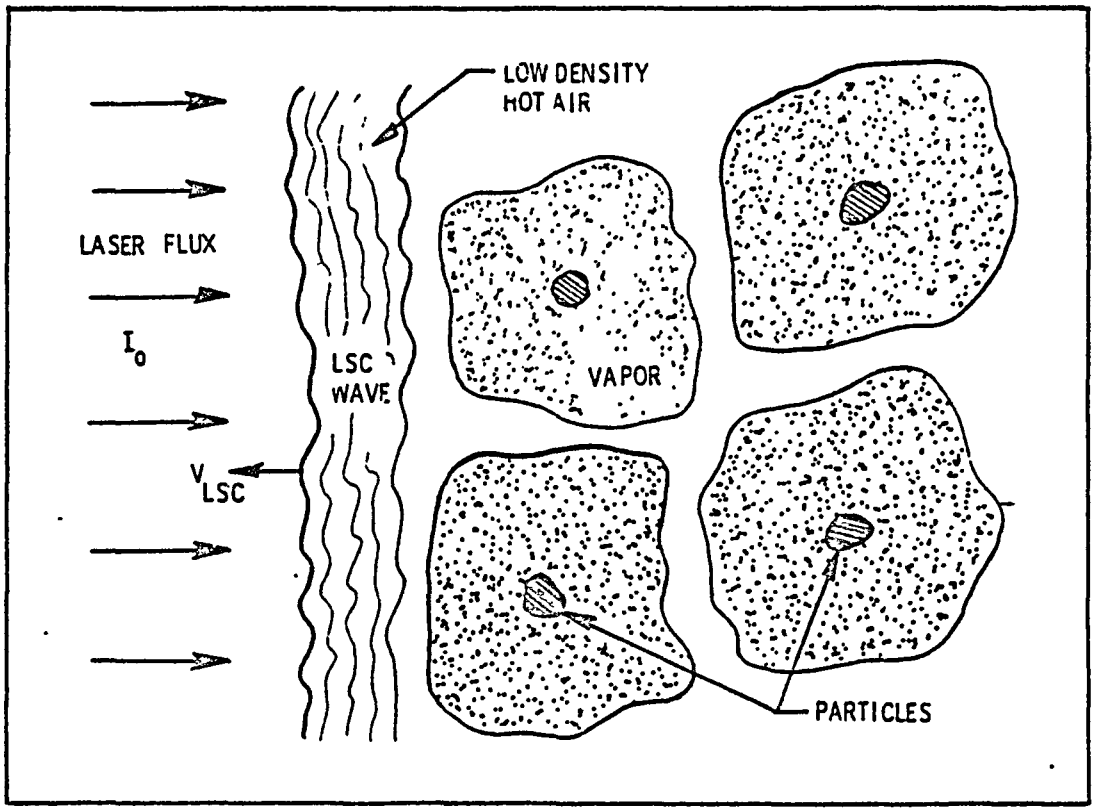

Figure III-5. Particulate-Induced Breakdown: Low Intensity Radiation

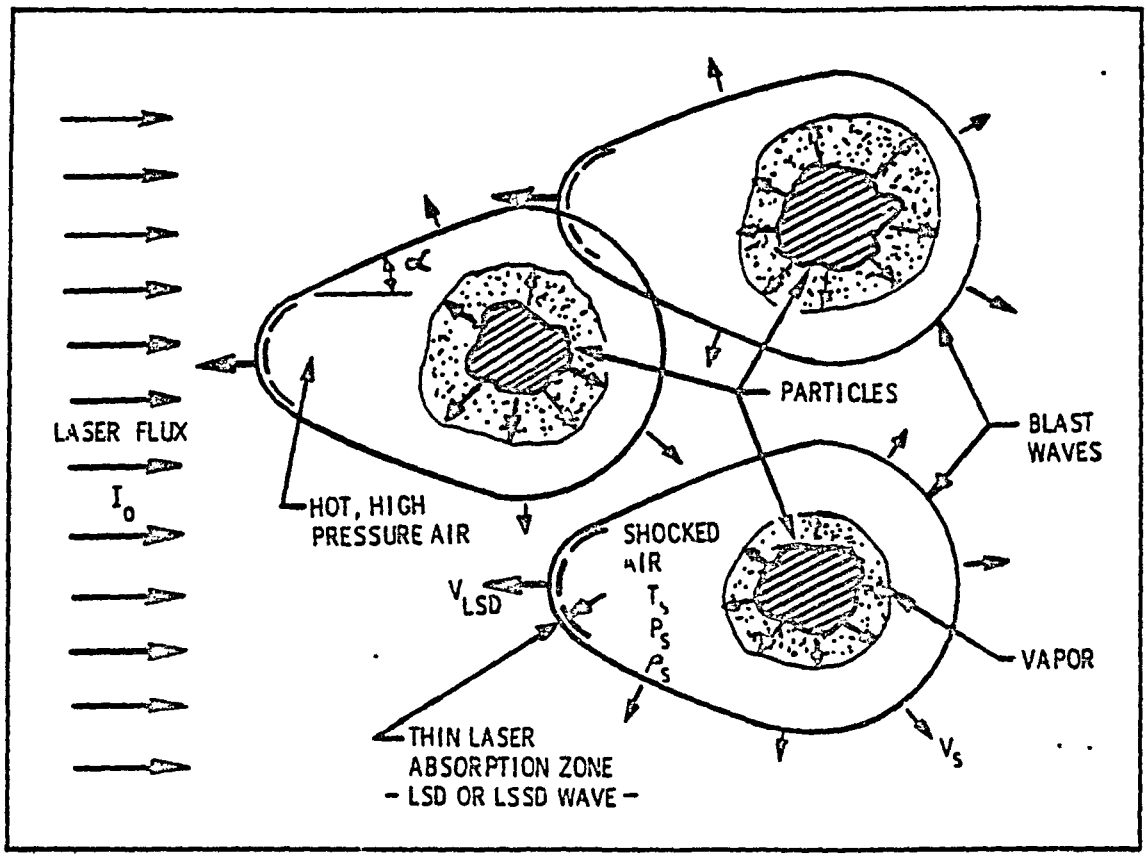

Figure III-6. Particulate-Induced Breakdown: High Intensity Radiation

C. BRIEF HISTORY OF LASER-HEATED PULSEJET RESEARCH

Kantrowitz was first to postulate the use of unconventional rocket engines and remotely stationed high-power lasers to propel a shuttlecraft to low Earth orbit.[6,7] Since this time, much experimental and theoretical research has been conducted on both air-breathing and rocket varieties of laser-heated pulsejet engines.

1. Air-Breathing Pulsejet Engines

Pirri, et. al.,[8,9] have addressed two basic types of laser-powered pulsejets where air is utilized as the working fluid. The first propulsion scheme, illustrated in Figure III-7, develops impulse by direct irradiation of the lower thruster surface by a high-power laser pulse. For clarity, it is appropriate to identify this laser-heated thruster by the physical environment in which the laser energy is added to the working fluid: i.e., an "External" Radiation-Heated (ERH) pulsejet engine. The high intensity incident beam ignites a laser-supported detonation wave in the air above the surface. Upon formation of the wave, all the laser radiation is absorbed in a thin zone of shocked air behind the detonation. Since this air is shocked to a high pressure, Pirri suggests that it may be possible to propel a vehicle by repetitively pulsing the laser and utilizing the strong detonation waves (initiated with each pulse) to provide thrust. Higher laser intensities (up to the limit of clean air electrical breakdown) permit larger impulse couplings to the surface and, therefore, associated increases in propulsive efficiency.

Experiments have been performed with ERH thrusters which are a close kin to the variety suitable for use in VTOL propulsion of shuttlecraft. The beam/surface interaction geometry for these experiments is shown in Figure III-8, and the results are displayed in Figure III-9. Experimental and theoretical evidence[10] suggest that such propulsion engines can be optimized to produce coupling coefficients as high as 50-100 dynes/Watt. Optimum conditions are realized when a very high-intensity laser pulse is shortened to the nanosecond regime, and when the

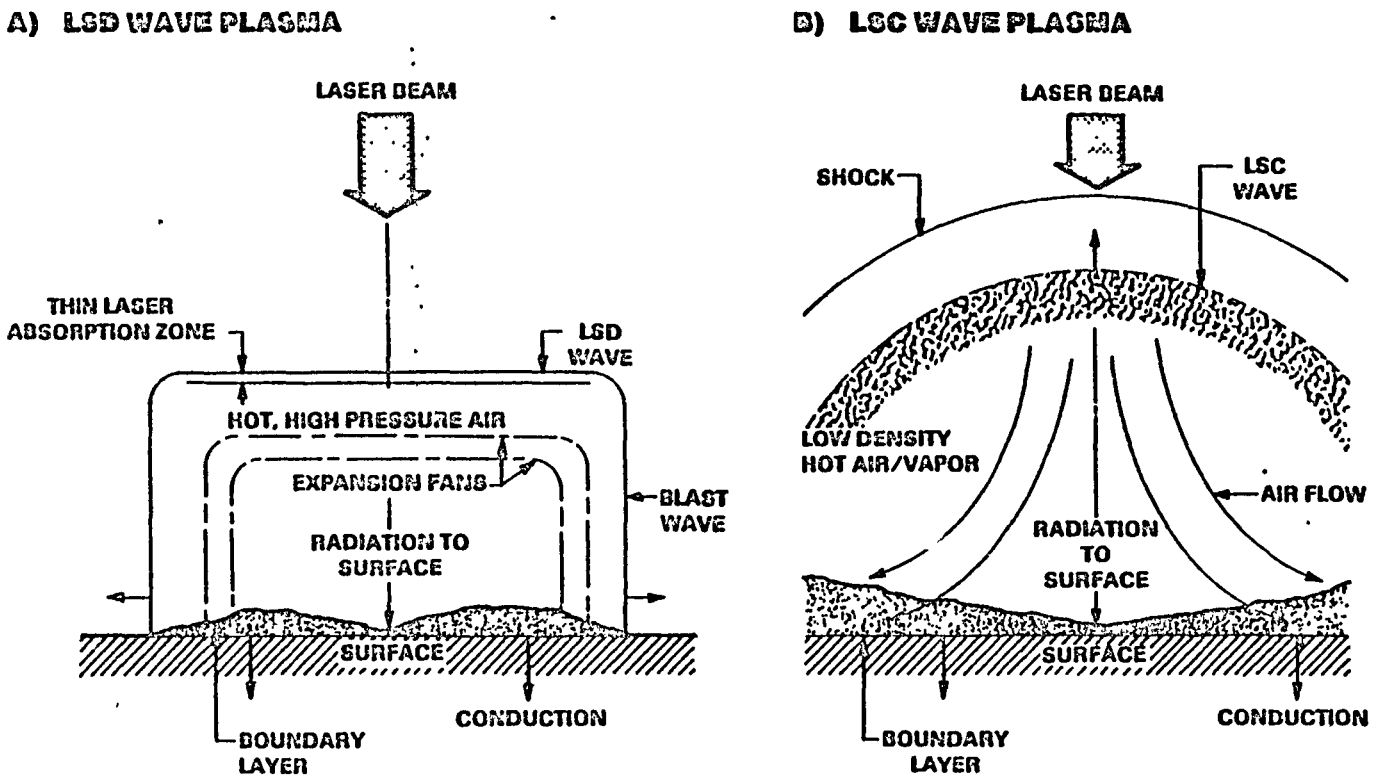

Figure III-7. Impulse Coupling to a Surface by High Power Laser Irradiation (LSD and LSC Wave Plasma Dynamics) --After Pirri, Root, and Kemp.

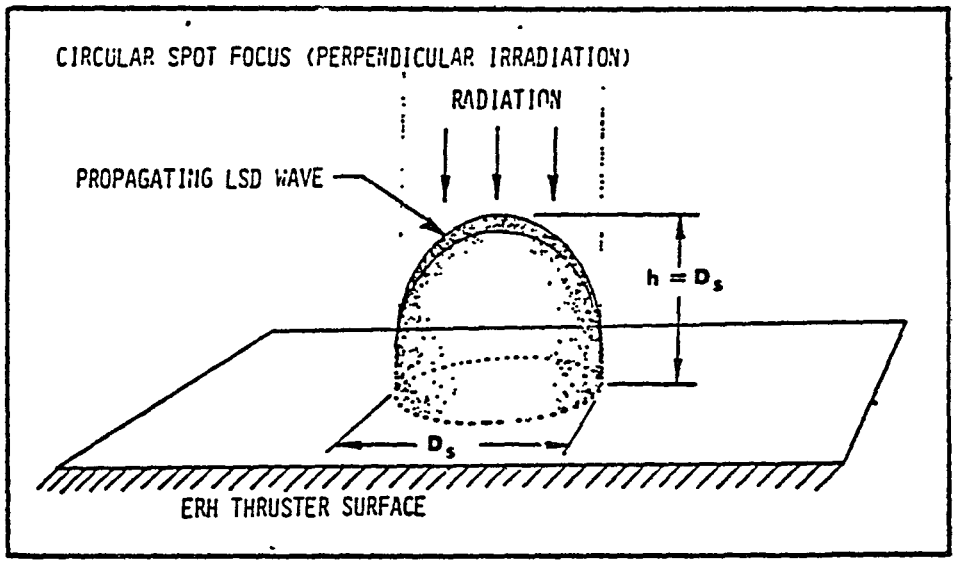

Figure III-8. Beam/Surface Interaction Geometry for Impulse-Generation Experiments

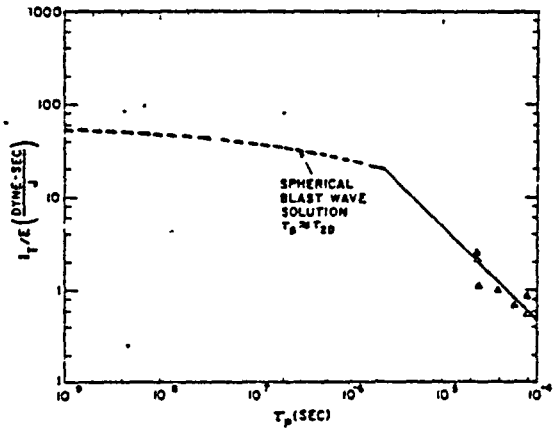

Figure III-9. Theoretical Results for Coupling Coefficient vs. Pulse Time (After Pirri, Reference 10)

target surface area is infinite in diameter compared to that of the laser-irradiated spot. This situation permits sufficient time for all the impulse to couple to the target surface without "spilling" shock wave energy off the edges of the target. Since the incident laser radiation must greatly exceed the LSC/LSD wave transition intensity in order to assure good propulsive coupling, some difficulty may be encountered in successfully propagating such a high-intensity laser beam directly through a highly absorbing plasma exhaust. This exhaust stream may occasionally intercept a significant fraction of the incident laser power, resulting in a severe loss of thrust.

The second type of air-breathing pulsejet engine addressed by Pirri, et. al.[8-9], is pictured in Figure III-10. In this thruster scheme, the laser energy is absorbed within a volume that is enclosed by physical engine walls; therefore it falls within the class of "Internal" Radiation-Heated (IRH) thrusters. The engine utilizes a highly reflecting parabolic nozzle (which doubles as the primary optics) to focus an incident laser pulse of low intensity to the high intensity required for nonlinear absorption. Air breakdown occurs at the focus of the parabola; and the hot, high pressure air expands aft as directed by the nozzle skirt. If some means is found to refill the nozzle with fresh air between laser pulses, the engine should operate successfully as a laser-powered pulsejet. Since the incident laser intensity is below the LSC wave threshold, the beam may be propagated through the exhaust gases with little, if any, attenuation.

Figure III-11 displays the results of small-scale experiments with the air-breathing pulsejet configuration shown in Figure III-10. The tests, which were conducted at one atmosphere, generally produced peak thrust-to-laser power couplings of 20 to 25 dynes/Watt. As shown in Figure II-11, theory suggests that 40-50 dynes/Watt may be attainable, and Soviet researchers claim to have demonstrated such performance in recent single pulse tests.

Two papers by Bunkin, Prokhorov, et. al. (Refs 10 and 12) review this recent USSR-funded theoretical and experimental research on a Laser Air-Jet Engine (LAJE) which propels itself by an "explosive mechanism

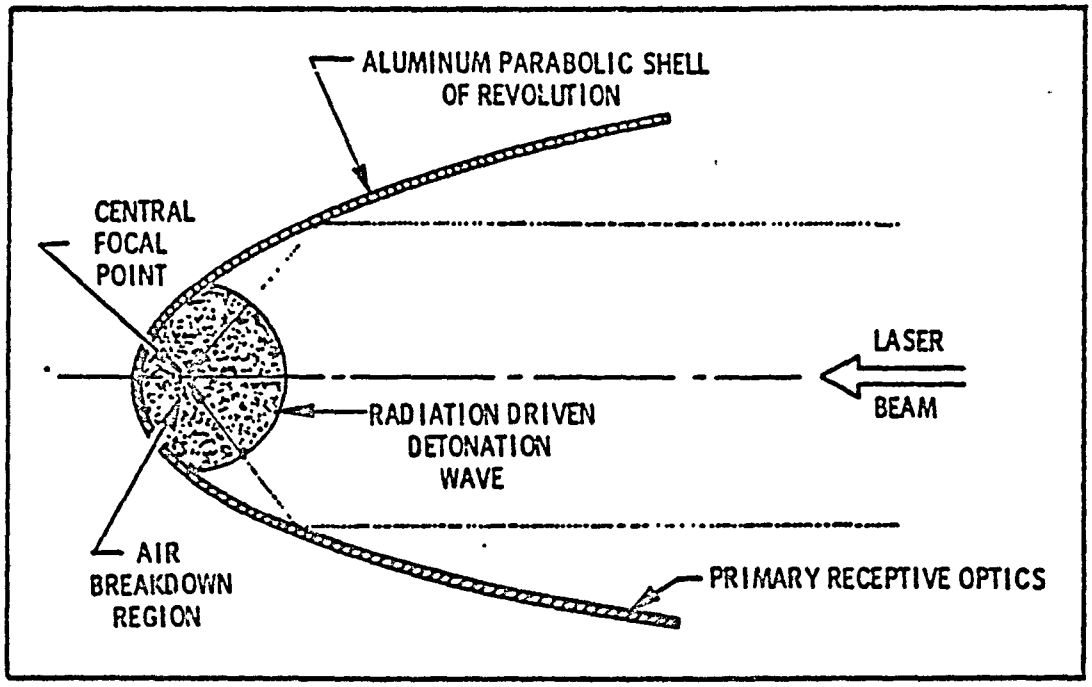

Figure III-10. AERL Laser-Powered Internal Expansion Pulsejet Experiment (From Reference 8)

C-2

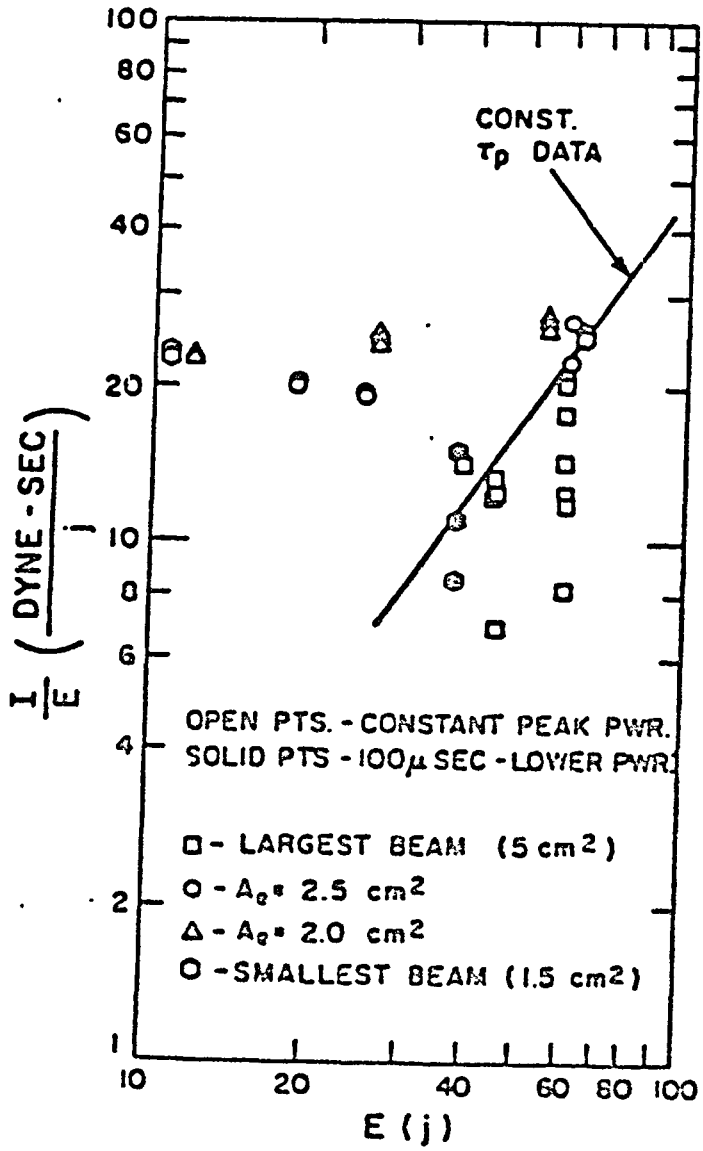

Figure III-11. Coupling Coefficient Results for Air-Breathing Pulsejet Engines (From Reference 9)

due to laser-induced breakdown and the excitation of a shock wave." The engine is envisioned to operate in a pulse-periodic (pulsating) mode, whereby the working volume is completely refreshed (with cold air) prior to receiving a new laser pulse. In order to initiate nonlinear absorption of laser energy at the vehicle site, the authors indicate the necessity of a focusing system, since the beam cannot propagate through the atmosphere to the craft at intensities above the breakdown level. They suggest that a parabolic reflecting surface (doubling in function as the thruster nozzle) be located "in the tail part of the flying craft and firmly affixed to it." For certain flight vehicle geometries, the authors propose that refracting-type lenses might also be used to provide the focusing function.

The attainment of high repetitively-pulsed coupling coefficients by the engine concept pictured in Figure III-11 will no doubt be impaired by three inherent thruster design flaws: First, the laser energy must be added to the supersonic diverging portion of the nozzle; whereas, for maximum efficiency the heating should take place in an upstream subsonic high-pressure reservoir. Secondly, the exact engine diverging nozzle contour is dictated by optical requirements for good focusing, and not by gasdynamic requirements for efficient expansion of the flow. Subsequently, the overall propulsion system performance attainable with this engine configuration will be inferior to that of a hypothetical engine for which the precise optical and gasdynamic requirements are met with relatively minor compromise. The third flaw relates to the problem that no means of quickly refilling the engine with fresh air has been provided--although it may be possible to incorporate a reed-type valve (i.e., similar to the German V1 "Buzz-Bomb").

2. Rocket Pulsejet Engines

Other experiments have been performed with pulsed laser-heated rockets and hydrogen propellant, at very reduced (e.g., a few Torr) ambient atmospheric pressures. Figure III-12 is a schematic diagram of the laser-heated rocket pulsejet model used by Physical Sciences, Inc. to generate the performance data shown in Figure III-13. The rocket incorporated an

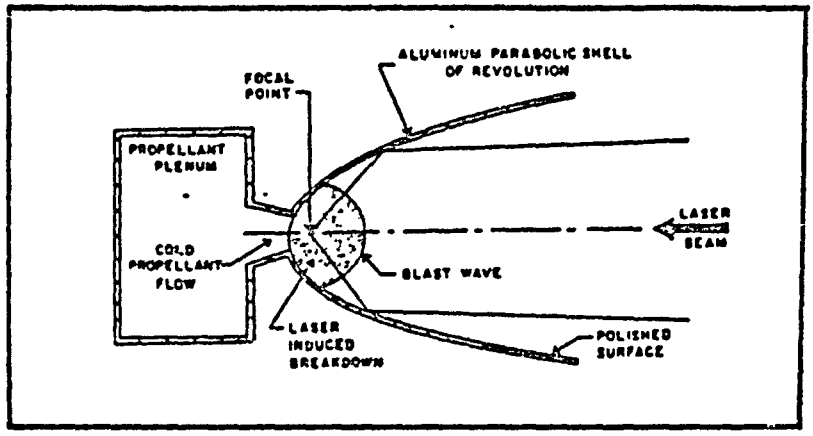

Figure III-12. Schematic Diagram of PSI's Laser-Heated Rocket Pulsejet Which Uses an Acoustic Valve to Meter the Cold H_2 Propellant Flow (From Reference 13)

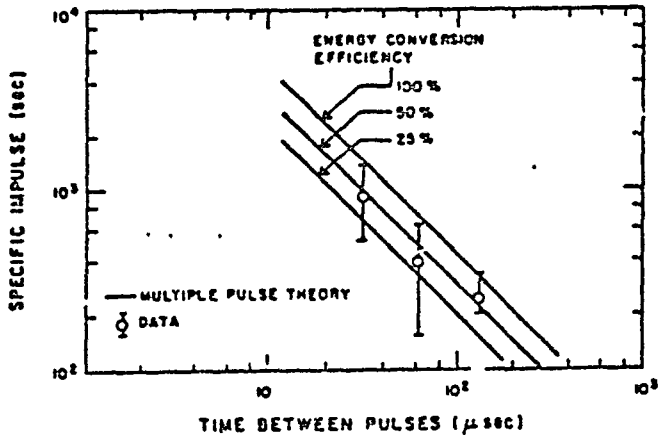

Figure III-13. IRH Rocket Pulsejet Performance Data (PSI Experiment With H_2 Propellant) --From Reference 24

acoustic valve to meter cold H_2 propellant into the nozzle. The experiments typically demonstrated optimum conversion efficiencies (i.e., thrust-power-to-laser-power) of 50 percent, coupling coefficients of 12.5 dynes/Watt, and a specific impulse of 1000 seconds.[13]

D. HIGH ENERGY LASER WINDOW CONCEPTS

There are a number of additional possibilities for high-power laser windows enabled by the atmospheric environment which can be utilized by certain air-breathing propulsive engine concepts. The two major HEL window categories mentioned in Chapter II, material windows and aero-windows, are suitable for laser-heated engines in both atmospheric and space environments. Material windows can be used by both CW and RP engines, but aero-windows will probably work for only steady-state CW engines.

Figure III-14A is a schematic diagram of the gasdynamics of conventional aero-windows. On-board high-pressure gas is expanded to supersonic velocities to create a strong shock wave. This shock contains the higher pressure internal-engine gas against the lower pressure ambient atmospheric environment--while permitting the HEL beam to pass freely through.

A second aero-window candidate suitable for CW engines is shown in Figure III-14B. Here centrifugal forces are used to first accelerate the ambient atmosphere to a high velocity (possibly supersonic--without producing Mach waves) adding energy to the flow. Next a vaneless diffuser would decelerate the air to low subsonic mach numbers, compressing it perhaps to 4-5 atmospheres in a single stage. A high-speed centrifugal compressor would accomplish this function, and its upper surface contour (between the impeller vanes) would serve as a primary mirror. This mirror would collect the incident laser beam and re-project it radially outward between the impeller blades. From here the beam would be focussed directly into the heating chamber.

Another candidate aero-window is exemplified by the RP engine concept in Figure III-14C. For this scheme, a primary receptive optic (not shown) focuses the incident low-intensity laser beam upon a secondary optic which

A) SUPERSONIC EXPANSION AND COMPRESSION (STEADY STATE)

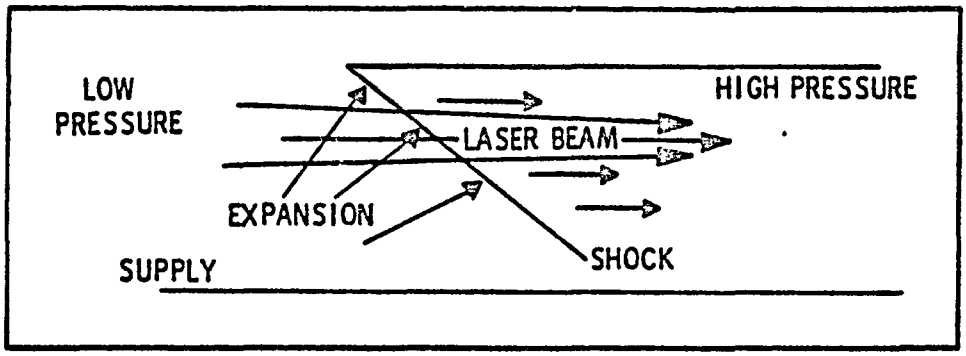

B) CENTRIFUGAL COMPRESSION (STEADY STATE)

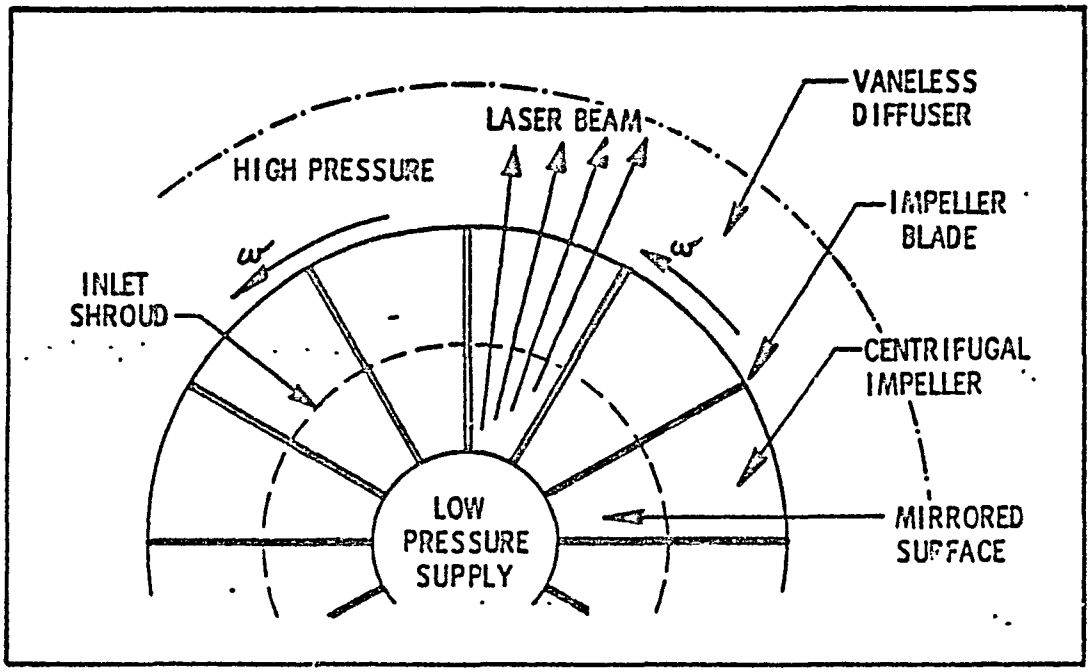

Figure III-14. Three Approaches for Aerodynamic Windows

C) SHOCK COMPRESSION BY PROPAGATING LSD WAVE (TRANSIENT)

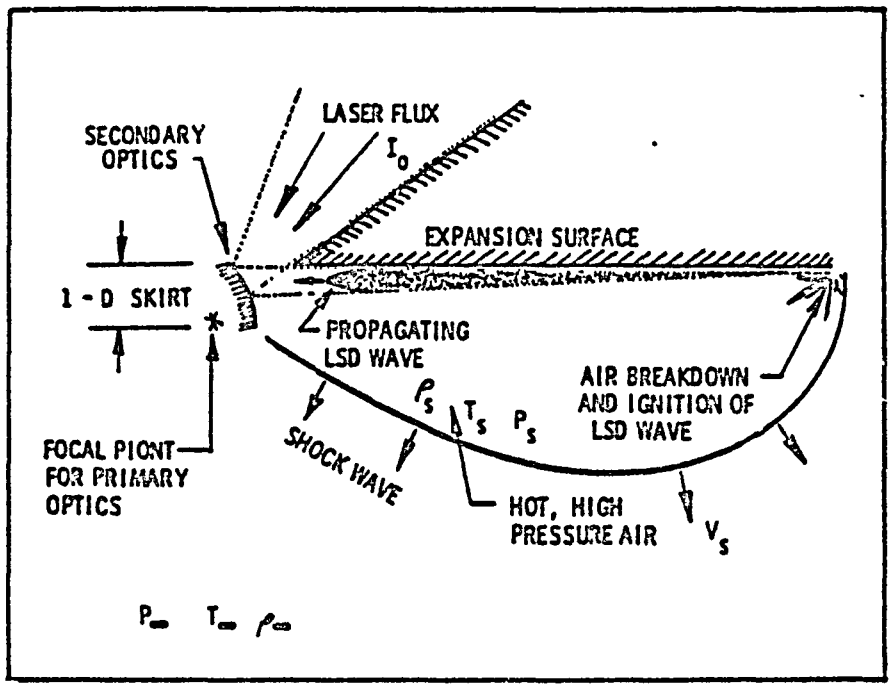

Figure III-14. Three Approaches for Aerodynamic Windows (Continued)

re-projects the beam (now concentrated to a high intensity) across the lower vehicle surface. There is no pressure differential across this aero-window. The engine accomplishes transient shock compression of the air working fluid simply by propagating an LSD wave across the lower vehicle surface--to which the reaction propulsion forces are momentarily communicated. Pressure ratios of several hundred atmospheres can be produced.

Other aero-window schemes analogous to that shown in Figure III-12C, and suitable for CW engines can be envisioned. The optical train, and air-breathing engine inlet geometries can be configured to balance LSC or LSD waves in subsonic or supersonic duct flows--at the appropriate engine "combustor" locations. These CW engines would rely upon supersonic compression of engine inlet air, and would produce useful levels of thrust only in transonic, supersonic, or hypersonic regimes--becoming, in effect, ramjet engines.

E. SUMMARY OF ENGINE-RELATED ISSUES

The following general statements can be made regarding the design of laser-heated engines suitable for propelling advanced manned shuttlecraft:

(1) To successfully propagate beamed energy through the atmosphere to a remote shuttlecraft, laser intensities must be held below the LSC-wave threshold. Laser intensities above this value could accidentally produce catastrophic attenuation of the beam, triggered by shock waves off the craft, plasma exhaust plumes, or atmospheric "dust" contamination.

(2) Molecular absorption mechanisms do not look promising because of the need to inject "seed" materials into the engine working fluid. This seed can contaminate the shuttlecraft optics and produce highly attenuating exhaust plumes.

(3) The most viable laser propulsion concepts will probably incorporate direct gas phase heating of engine working fluid using inverse Bremsstrahlung absorption of laser energy--which requires no seed.

(4) In order to initiate inverse Bremsstrahlung absorption in the laser propulsion engine, a focusing system (optical train) firmly affixed to the vehicle is required.

(5) Lower intensity CW radiation (suitable for LSC wave heating) produces excessively high working gas temperatures and large radiation losses, which can easily cause internal engine walls to melt--unless protected by exotic wall-cooling schemes. Alternately, the use of unconventional CW engine geometries which require only partial confinement of the LSC plasma "torch," can greatly reduce cooling loads.

(6) In sharp contrast, LSD waves (high-intensity laser radiation regime) are able to process a working gas to almost any desired final temperature and pressure, simply by adjusting the intensity of the beam and the ambient density of the engine gas.

(7) The most promising laser propulsion engines will probably operate in a pulse-periodic (pulsating) mode, whereby the thruster working fluid is completely refreshed with unprocessed gas before the next laser pulse arrives.

(8) The complicated turbomachinery usually required in today's high-performance air breathing propulsive engines to produce high, continuous engine pressures can be eliminated in favor of much simpler laser-heated engines. Here, elevated pressures are provided not by heavy mechanical compressors, but by transient shock compression caused by propagating laser supported detonation (LSD) waves.

(9) The use of pulsed power and LSD waves can permit the construction of incredibly simple, reliable air-breathing and laser-heated rocket propulsion systems for advanced manned shuttle-craft.

F. OPTICS/AIRFRAME/ENGINE INTEGRATION

A large degree of optics/airframe/engine integration is necessary due to the many overlapping system requirements for successful utilization of

beamed energy in air-breathing propulsive engines. For example, depending on the shuttle configuration, portions of the vehicle external surface will be called upon to serve as optical elements or thruster surfaces. In addition, they will provide an aerodynamic skin able to withstand high temperatures generated during re-entry. Some of these multi-purpose surfaces may require regenerative (or perhaps transpiration) cooling.

In the interest of clarity, it is useful to classify the various elements in an optical train according to the order in which the beam strikes them. For example, a "primary" lens is the first optical surface to receive the beam; a "secondary" lens is next; the tertiary lens follows, etc. Depending on the specific optics/airframe/engine configuration, lenses may be of either the reflecting or refracting type and may have a variety of dimensional topographies. The candidate topographies can be describes as follows: One-dimensional optics are those which have planar optical surfaces, e.g., flat mirrors or windows. Two-dimensional optics are able to expand or condense light in only one plane, e.g., "cylindrical" lenses and refracting prisms. Finally, three-dimensional lenses are those with compound curvature which can expand or condense light in a radially symmetric fashion, e.g., conventional hand-held magnifying lenses.

Another variation in lens classification is embodied in the choice of conventional versus Fresnel optics. With the Fresnel lens approach, the entire optical surface is divided into minute refracting or reflecting facets. Refractive optics permit the construction of lightweight, large diameter lenses with short focal lengths. A potential problem with using refracting Fresnel lenses with beamed high-energy radiation is the thickness non-uniformity of the lens material. When the lens is heated by passage of the beam, significant stresses may be generated by non-uniform heating and expansion, and cracks may appear along the thin portion of refractive facets.

It appears that both reflecting and refracting Fresnel lenses can be successfully integrated into the shuttlecraft upper surface airframe--to collect the lower intensity incident radiation. Thereafter, only

regeneratively cooled reflecting lenses may be used to direct the high-intensity beam into propulsive engines.

G. ORGANIZATION OF SUBSEQUENT CHAPTERS

Table III-1 gives the organization of the following five chapters. The technical material is assembled by the basic categories of air-breathing laser propulsion engines and shuttlecraft airframe configurations. The basic engine categories are laser-thermal and laser-electric; the airframe configurations are delta, radial, and cylindrical. Laser-electric propulsion is generally envisioned for high supersonic and hypersonic regimes.

The "delta" airframe configuration is exemplified by the current space shuttle orbiter; the "radial," by the Apollo command/reentry vehicle; the "cylindrical," by a conventional rocket launch venicle. Both heavier-than-air and lighter-than-air varieties of "cylindrical" shuttlecraft are examined.

TABLE III-1. AIR-BREATHING LASER PROPULSION CATEGORIES

THRUSTER TYPE / AIRFRAME	LASER-THERMAL	LASER-ELECTRIC
DELTA	CHAPTER IV	-
RADIAL	CHAPTER V	CHAPTER VI
CYLINDRICAL	CHAPTER VIII	CHAPTER IX

This Page Intentionally Left Blank

REFERENCES FOR CHAPTER III

1. Razier, Y. P., "Heating of a Gas by a Powerful Light Pulse," J. Exptl. Theoret. Phys., Vol. 48, May 1965, pp. 1508-1518; also, Sov. Phys.-JETP, Vol. 21, 1965, pp. 1009 ff.

2. Schlier, R. E., Pirri, A. M., and Reilly, D. J., "Air Breakdown Studies," Technical Report No. AFWL-TR-72-74, Avco Everett Research Laboratory, Everett, MA, February 1973.

3. Lencioni, D. E., "Real Air Breakdown," presented at HELREG Propagation Subpanel Meeting, MITRE Corp., Bedford, MA, November 1975.

4. Lencioni, D. E. et al., "The Effect of Dust on 10.6 μm Laser-Induced Air Breakdown," LPT-20, MIT Lincoln Laboratory, Lexington, MA, April 1973.

5. Triplett, J. R. and Boni, A. A., "The Interaction of Suspended Atmospheric Particles with Laser Radiation," SSS-R-71-1167, Systems, Science and Software, La Jolla, CA, June 1972.

6. Kantrowitz, A., "The Relevance of Space," Astronautics and Aeronautics, Vol. 9, No. 3, March 1971, pp. 34-35.

7. Kantrowitz, A., "Propulsion to Orbit by Ground-Based Lasers," Astronautics and Aeronautics, Vol. 10, No. 5, May 1972, pp. 74-76.

8. Pirri, A. N., and Weiss, R. F., "Laser Propulsion," AIAA Paper No. 72-719, AIAA 5th Fluid and Plasma Dynamics Conference, Boston, MA, 26-28 June 1972.

9. Pirri, A. N., Monsler, M. J. and Nebolsine, P. E., "Propulsion by Absorption of Laser Radiation," AIAA Journal, Vol. 12, No. 9, September 1974, pp. 1254-1261.

10. Pirri, A. N., "Theory for Momentum Transfer to a Surface with a High-Power Laser," The Physics of Fluids, Vol. 16, No. 9, September 1973, pp. 1435-1440.

11. Barchukov, A. I., Bunkin, F. V., Konov, V. I. and Prokhorov, A. M., "Laser Air-Jet Engine", JETP Lett., Vol. 23, No. 5, 5 March 1976, pp. 213-215.

12. Bunkin, F. V. and Prokhorov, A. M., "Use of a Laser Energy Source in Producing a Reactive Thrust", Sov. Phys. Usp., Vol. 19, No. 7, July 1976, pp. 561-573.

13. Nebolsine, P. E., Pirri, A. N., Goela, J. S., and Simons, G. A., "Pulsed Laser Propulsion," Proceedings of 1978 JANNAF Conference, Incline Village, Nevada, 14 February 1978.

CHAPTER IV
LASER-THERMAL AIR-BREATHING PROPULSION: DELTA CONFIGURATIONS

Lasers are capable of providing working gas temperatures significantly beyond that attainable with chemical combustion, and consequently can enable the conceptualization of new, high-temperature thermodynamic cycles. Hand in hand with these higher "combustor" working fluid temperatures comes the potential for increased flight speed and performance from future high Mach number air-breathing engines.

Presently, air-breathing aircraft are limited by aerodynamic heating and deteriorating turbojet engine performance to speeds of about Mach 3 or 4. Beyond this velocity, a mechanical compressor becomes an undesirable commodity, and the existence of a turbine at all tends largely to restrict the maximum combustion gas temperatures. Because of these limitations on turbine engines, high-supersonic and hypersonic propulsion research has concentrated on ramjet engines, of both internal-burning and external-burning varieties. (However, note that these engines are only able to generate thrust at flight speeds above Mach 1, so other engines must be used in the subsonic flight regime.) By necessity, much of the research has centered on "supersonic" combustion of chemical fuels. Here, beamed-energy propulsion can really excel; LSD absorption waves can be made to propagate at speeds up to, and substantially beyond Earth orbital velocity.

This chapter explores the prospects for air-breathing propulsion of "delta" - configuration shuttlecraft integrated with internal and external radiation-heated thrusters (IRH and ERH, respectively). Table IV-1 indicates the design concept classes for delta airframes. The shuttlecraft described below are generally capable of VTOL, subsonic, supersonic and hypersonic flight within the atmosphere. In addition, they are able to fly along, as well as perpendicular to the propulsive laser beam.

Let us begin this examination of various potential optics/airframe/engine concepts by concentrating first upon the genre which incorporate two-dimensional lenses within traditional, highly swept delta airframes.

TABLE IV-1. DESIGN CONCEPT CLASSES FOR DELTA AIRFRAME CONFIGURATIONS

THRUSTER TYPE	FLIGHT MODE	
INTERNAL RADIATION-HEATED (IRH)	-	TRANSLATION+
EXTERNAL RADIATION-HEATED (ERH)	VTOL*	TRANSLATION+

* FLIGHT ALONG LASER BEAM

+ FLIGHT PERPENDICULAR TO LASER BEAM

Generally in these configurations, the airframe forebody precompresses the inlet air, while the airframe afterbody acts as a hypersonic nozzle.

A. DELTA/ERH FOR GROUND-BASED LASER

The first of such configurations was invented by A. Kantrowitz and R. Rosa.[1] This concept, illustrated in Figure IV-1, was proposed as a hypersonic flight research vehicle powered by a ground-based laser power station. As shown in Figure IV-1, the continuous high-power beam (denoted as callout No. 2) is projected directly upon the aft portion of the vehicle lower surface (callout No. 18), which is a highly polished cylindrical reflecting lens that also doubles as an expansion-deflection exhaust nozzle (No. 16). This two-dimensional primary lens concentrates the incident beam to a very high intensity and projects it directly into the throat (No. 13) of the ramjet engine.

Propulsive thrust is obtained from the ramjet as follows. Air enters the ramjet engine at the intake (No. 8), is adiabatically compressed (by supersonic internal diffusion) to a high pressure and density. At this time, a "seed" material is added to the duct flow at a station near the throat (which serves as a "combustion" section) where most of the laser radiation is absorbed into the flow. This high-pressure, high-temperature duct flow then expands out the exhaust nozzle, generating thrust.

There are several potential problems with the concept, however. Conflicting requirements in the specification of mirrored-exhaust-nozzle contours for (a) efficient gasdynamic flow expansion and (b) adequate optical beam focusing, must be resolved if optimum performance of the overall system is to be realized. In addition, the exhaust flow may continue to absorb incident laser radiation aft of the throat section. If the gas is still supersonic here, the flow will be driven towards subsonic flow. This would significantly degrade available propulsive thrust. Furthermore, conventional ramjets cannot develop static thrust below sonic flight velocities and therefore cannot operate from conventional airports without an auxiliary propulsion system. Finally, the configuration shown in

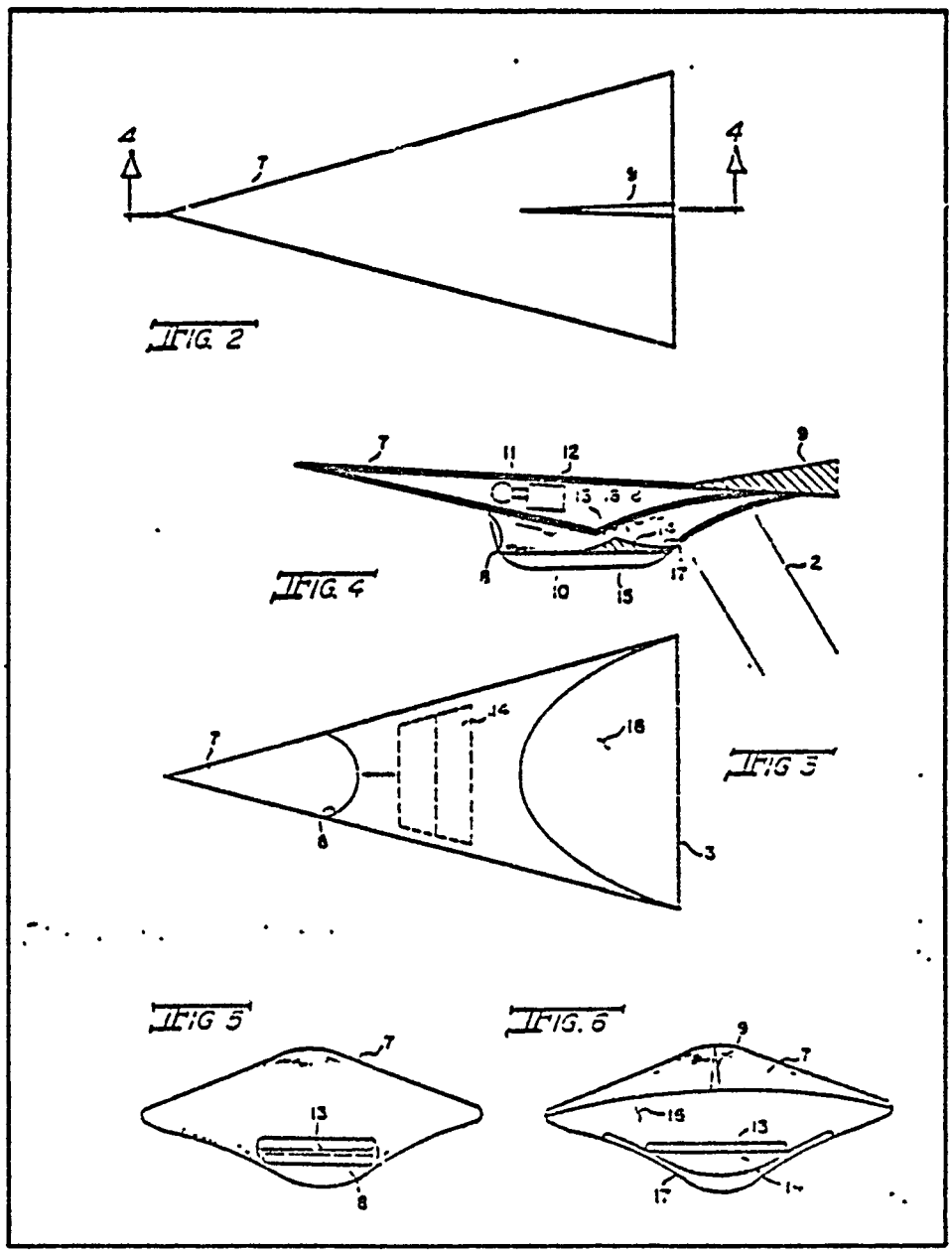

Figure IV-1. DELTA/IRH for Ground-Based Laser
(No VTOL or Subsonic Propulsion Capability)
--From Reference 1

Figure IV-1 is unable to receive an aerial propulsive power beam, although this could (in principle) be accomplished by inverting the entire airframe aft of the engine throat.

B. DELTA/IRH CONFIGURATION WITH TRANSVERSE 2-D FRESNEL LENS

Figure IV-2 illustrates another version of an airframe-integrated external-expansion hypersonic ramjet. Just like the previous concept, the aircraft forebody precompresses the inlet air and thus provides part of the inlet function. Similarly, the vehicle afterbody serves as an external expansion nozzle. Instead of the reflecting primary optics used in Figure IV-1, the vehicle incorporates a 2-D Fresnel-type lens to concentrate the incident beam into a line focus within the "combustion" chamber. Continuous radiation can be used to heat the engine gases if a "seed" material is injected into the flow; repetitively pulsed radiation can be used with a LSD-wave heating (i.e., following electrical breakdown and subsequent inverse Bremsstrahlung absorption).

Vertical takeoff and landing (VTOL) may be accomplished by rotating a secondary reflecting cylindrical lens into a position near the line focus (within the ramjet internal duct chambers), and thereby projecting a high-intensity beam forward out the ramjet inlet--finally coming to a focal point near the nose. At this point, the air would be caused to break down, and an LSD wave would traverse the entire vehicle undersurface. This would create a hot, high-pressure plasma sheet, which would subsequently expand downward, generating vertical thrust. In short, the aircraft undersurface could double as an external radiation-heated (ERH) thruster when operated in a repetitively pulsed fashion. Upon reaching an altitude of several thousand feet, transition to horizontal flight would be accomplished in helicopter fashion.

Roll stabilizing forces during VTOL flight could be provided by projecting two smaller beams (each containing half the required laser power) upon the primary optics. As a result, the vehicle would be balanced on two "rails" of high pressure air as it is lifted vertically. Pitch

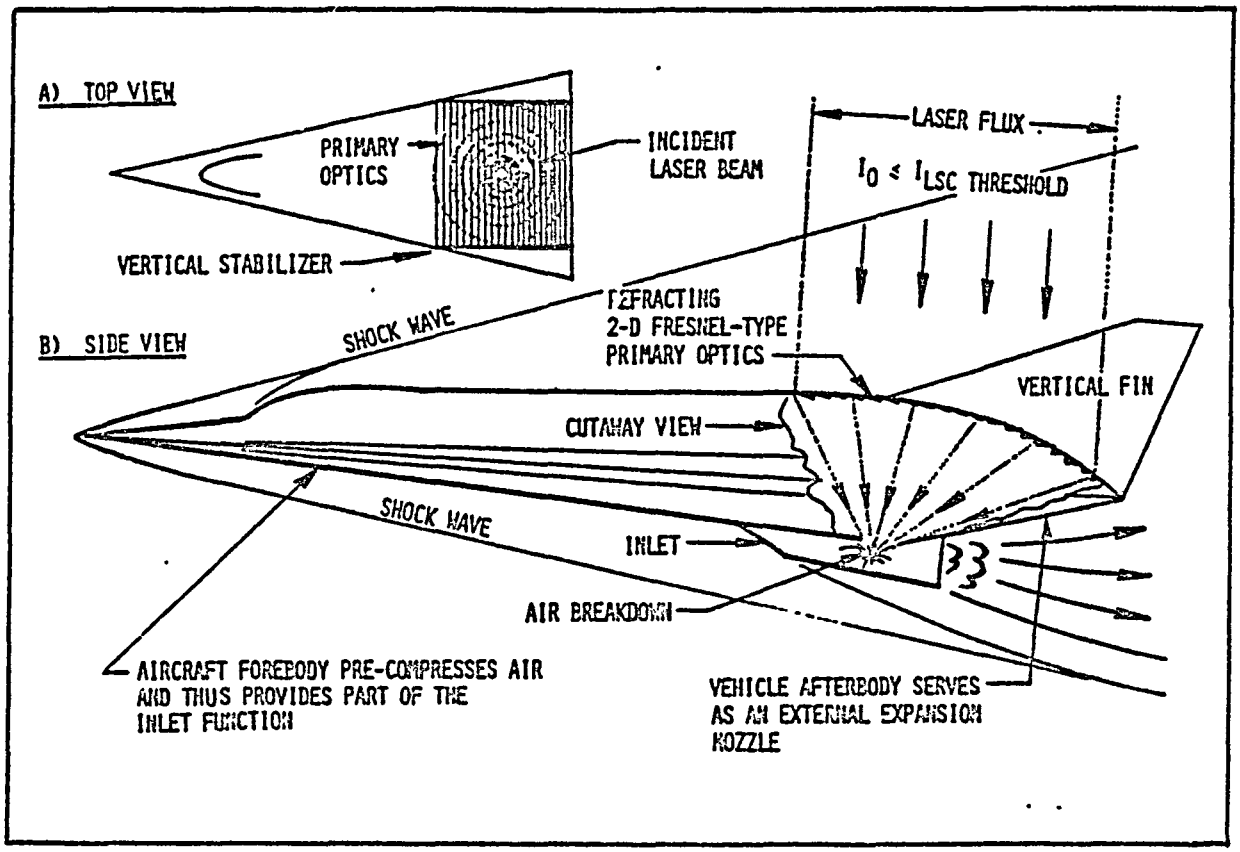

Figure IV-2. DELTA/IRH With Transverse 2-D Fresnel Lens (Subsonic and VTOL Capability)

stabilization could be controlled by varying the ignition point of absorption waves and the duration of the laser pulse--in order to alter the longitudinal distribution of vertical thrust generated across the vehicle lower surface.

Obvious problems with the concept are as follows. As with the previous concept in Figure IV-1, the vehicle cannot be expected to provide an exceptionally stable optical platform for reception of the orbital beam. Furthermore, difficulties may be encountered in bringing the beam through the internal engine duct housing--without the aid of a material or aerodynamic window. A material window may experience excessive beam heating at the high-focal intensities; alternately, the aerodynamic window may require auxiliary on-board power and the associated consumption of liquid fuels. Finally, the vehicle cannot accelerate rapidly from subsonic to supersonic flight speeds since the ERH thruster is configured to generate a vertical thrust vector. However, lateral acceleration may be accomplished by a) tilting the vector in the direction of intended flight (i.e., helicopter fashion), or b) by first boosting vertically to a substantial altitude, then using a combination of aerodynamic lift, gravity, and a forward tilting of thrust vector while performing a diving maneuver. Once supersonic, the vehicle will continue to accelerate since the ramjet engine will be operative at that time.

C. DELTA ERH/IRH CONFIGURATIONS WITH LONGITUDINAL 2-D FRESNEL LENSES

Several additional variations-on-a-theme of the delta airframe and 2-D Fresnel refracting primary lenses are evident. For example, Figure IV-3 shows two configurations having Fresnel lens facets aligned with the longitudinal flight axis. Note that the vehicle afterbodies are removed for clarity, and that the Fresnel facets are linearly tapered towards the nose of the vehicle. It would seem that the twin-beam approach can permit a more efficient usage of a centrally located cargo bay compartment.

The vehicle configurations presented in Figure IV-3 incorporate both IRH and ERH engines, rather than just the IRH engine portrayed in

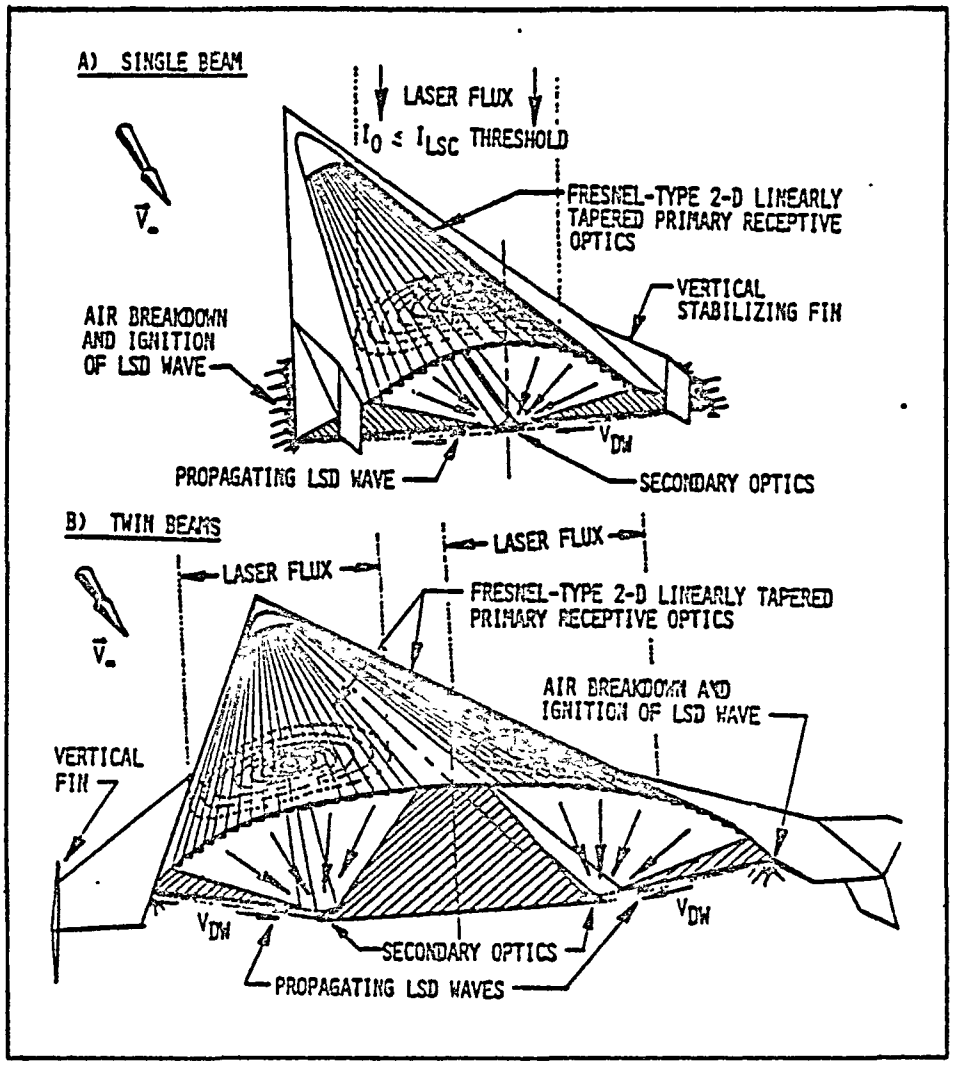

Figure IV-3. DELTA ERH/IRH Configuration With Longitudinal 2-D Fresnel Lens (Subsonic and VTOL Capability)

Figures IV-1 and IV-2. These hypersonic propulsion concepts eliminate the internal engine flow duct (and associated drag) in favor of completely external energy addition. As before, the vehicle forebody serves to precompress the air prior to entering the "combustor" heating region. Unlike the previous concepts, this hypersonic engine requires the use of two reflecting secondary lenses to direct the beam into the heating regions.

The hypersonic engines portrayed in Figure IV-3 are designed to operate in repetitively pulsed fashion as follows. The incoming beam is concentrated towards two line focii lying just beyond the secondary optics. In turn, these optics intercept and project the beam out towards the wingtips, just below the vehicle lower surface.

Shortly after pulse initiation, electrical air breakdown occurs at the wingtips, and laser-supported detonation (LSD) waves are ignited. These LSD waves then "burn" across the thruster surface; just before the LSD waves contact the secondary optics, the beam is shut off (thereby avoiding the possibility of damage to the secondary optics). In the process, the air is heated to a high temperature and pressure; as it expands away from the vehicle lower surface, propulsive thrust is generated.

The same heating cycle can be used to accomplish a vertical takeoff or landing. In addition, the beam(s) can be moved forward or aft to cause the vehicle to pitch up or down, respectively. Similarly, the vehicle can be made to roll right or left by depositing more beamed energy (and hence thrust) under the left or right wing tip, respectively. For the vehicle concept in Figure IV-3A, this is accomplished by moving the beam left or right, respectively; for the Figure IV-3B vehicle, the left beam is pulsed more often than the right beam.

Acceleration from a standstill to high forward speeds can be accomplished in helicopter fashion (as described earlier), or by the following mechanism. Let us assume that a retractable subsonic valved inlet (e.g., a vibrating reed-type valve) is able to provide a pulsed air supply to the interior volume enclosed beneath the Fresnel lens. In addition, assume that the secondary lenses are rotated to close and seal the slit(s) in the vehicle undersurface, and in turn cause the beam to come to a line focus

within the enclosed internal thruster volume. Finally, envision an auxiliary exhaust nozzle to vent air (from this volume) out the vehicle afterbody. This enclosed volume of air, when heated with pulsed radiation, could operate in a repetitively pulsed fashion analogous to the old German V1 "Buzz-Bomb" propulsion system.

D. DELTA/ERH CONFIGURATIONS WITH REFLECTING PRIMARY LENSES

Quite unlike the previous vehicle configurations, the concepts presented in Figures IV-4 and IV-5 attempt to integrate 2-D linearly tapered reflecting lenses with the vertical stabilizing fin of the aircraft. Low-intensity, indicent radition is collected to a high level of brightness upon the 2-D secondary lenses which are wrapped about the vehicle perimeter. (Note the constant intensity contours of the incident beam falling upon the primary receptive optics, i.e., the vertical fin.) These secondary lenses reflect the beam back towards the vehicle center undersurface, and electrical air breakdown occurs along the centerline. Note that the vehicle afterbody has radial symmetry and serves as a 3-D parabolic primary lens (over the upper surface). The lower afterbody surface serves as an external expansion nozzle during hypersonic operation. As before, the aircraft forebody (in the hypersonic flight mode) serves to precompress "inlet" air before it receives LSD-wave heating.

VTOL operation can be accomplished in maneuver similar to that described for the previous concept in Figure IV-3. Acceleration to supersonic speeds will be aided by a forward vectoring of ERH thrust, which is accomplished by irradiating the radially symmetric primary lens of the vehicle afterbody. Note in Figure IV-5 that a normal vector to the afterbody ERH thruster surface has a significant forward component. (The thrust vector acting on an ERH thruster surface is generally perpendicular to that surface at subsonic speeds.)

As for the previous vehicle concept, pitch and roll control maneuvers can be accomplished by proper placement of the incident beam upon the primary receptive optics.

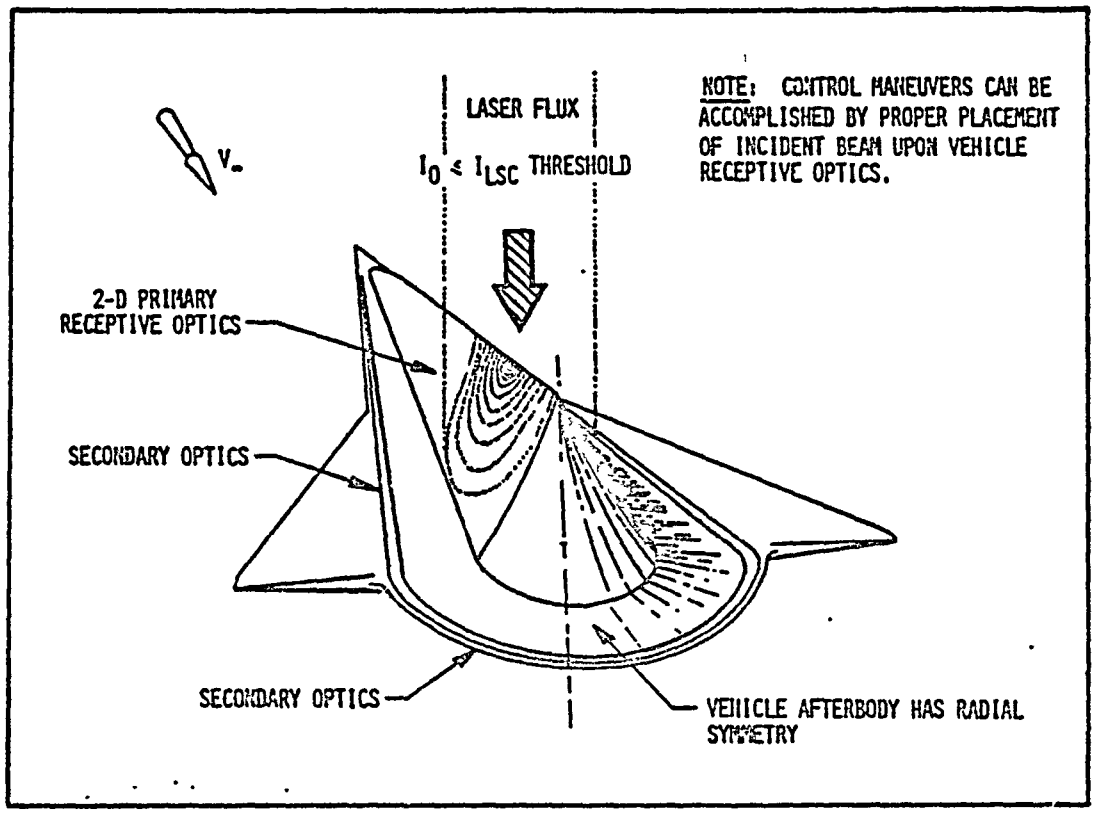

Figure IV-4. Small-Wing DELTA/ERH, Rear View, With Reflecting Primary Lens (Subsonic and VTOL Capability)

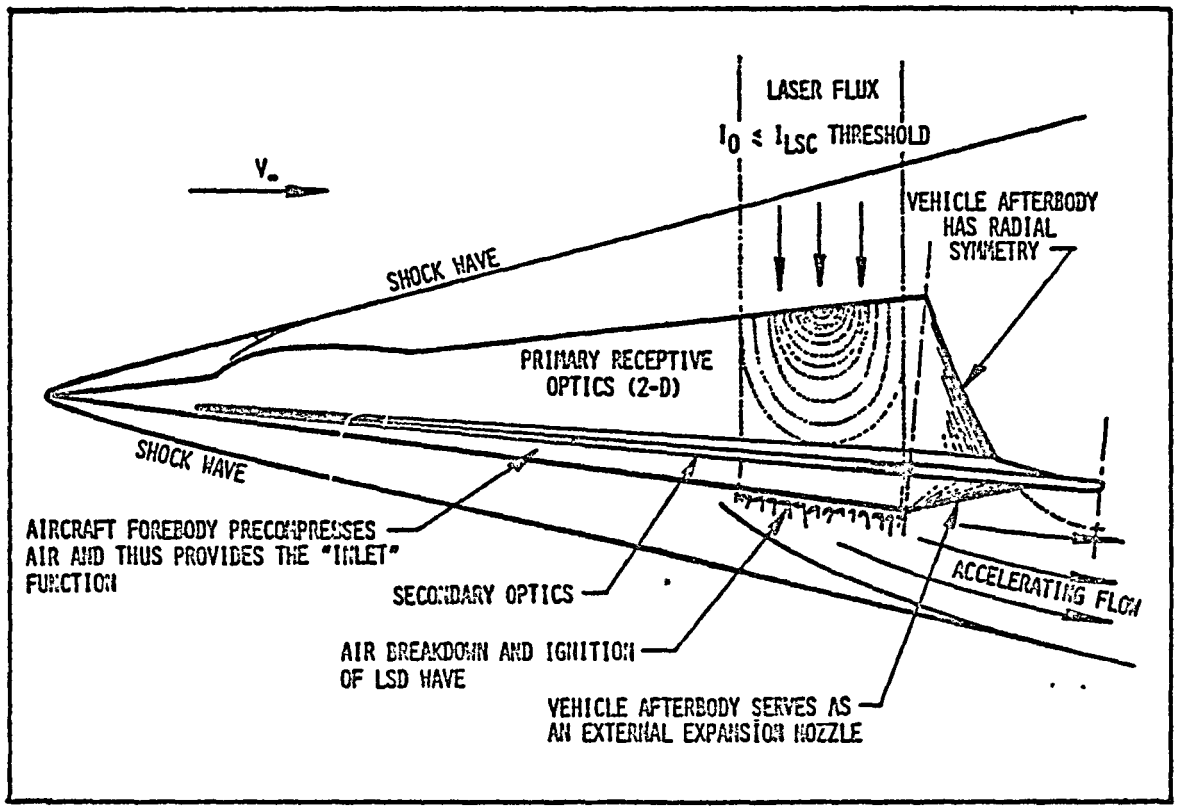

Figure IV-5. Small-Wing DELTA/ERH, Side View (Subsonic and VTOL Capability)

Figure IV-6 shows a variation-on-a-theme of the vehicle introduced in Figures IV-4 and IV-5, based upon the location of the ERH thruster surfaces. As before, a reflecting primary optical surface is integrated with the vertical stabilizer. However, the concept employs grazing-incidence secondary optical surfaces to flash power outward underneath the wing tips, instead of projecting the beam back towards the vehicle centerline (like in Figures IV-4 and IV-5). As with the concept portrayed in Figure IV-3, electrical air breakdown occurs at the wing tips instead of the vehicle centerline. Much attention must be given to the detailed design of the airframe in order to eliminate internal and external aerodynamic drag caused by the various geometric shapes of the optics and beam-projection passageways.

E. SUMMARY

Covered up to now have been the particular optics/airframe/engine configurations employing 2-D primary receptive lenses integrated with traditional highly-swept-delta airframes typified by the space shuttle orbiter. We now move on to review configurations which integrate 3-D, radially symmetric primary receptive lenses with radially symmetric airframes that are more typical of the Apollo and Mercury spacecraft re-entry capsules, or perhaps, the Mars lander aeroshell disc.

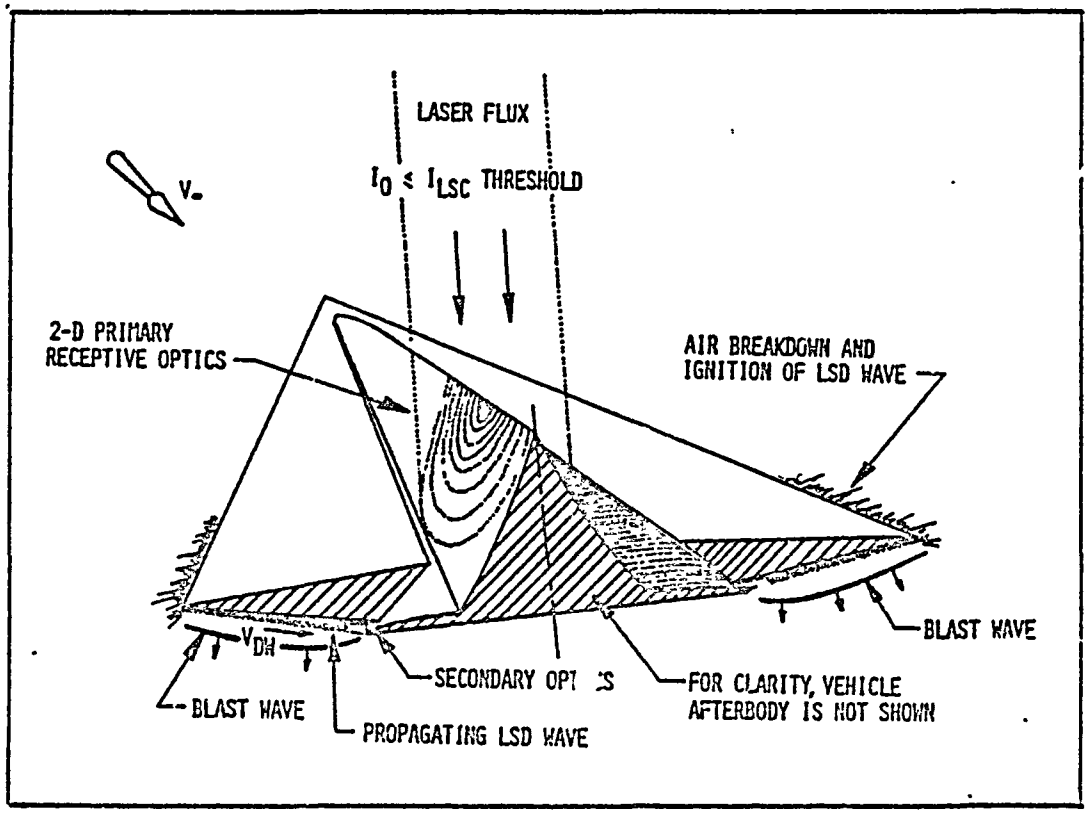

Figure IV-6. Large-Wing DELTA/ERH With Reflecting Primary Optics (Subsonic and VTOL Capability)

REFERENCES FOR CHAPTER IV

1. Kantrowitz, A. R. and Rosa, R. J., "Ram Jet Powered by a Laser Beam," US Patent No. 3,818,700.

CHAPTER V
LASER-THERMAL AIR-BREATHING PROPULSION: RADIAL CONFIGURATIONS

This chapter explores the prospects for air-breathing laser propulsion of radially symmetric shuttlecraft. Both internal and external radiation-heated (IRH and ERH, respectively) thrusters are considered. Large variations in airframe fineness ratio are examined, from the highly tapered geometry exemplifed by the NASA Hypersonic Ramjet Engine (HRE) pictured in Figure V-1, to lower fineness ratio geometries more typical of the Apollo command/re-entry module or the Mars lander aeroshell. Table V-1 displays the design concept classes for "radial" shuttlecraft configurations considered in this chapter. As with Chapter VI, the shuttlecraft introduced here are generally designed for efficient VTOL, subsonic, supersonic and hypersonic flight within an atmosphere. Furthermore, they can fly directly up, as well as perpendicular (i.e., lateral) to the beam.

A. THE NASA HYPERSONIC RAMJET TEST ENGINE

An excellent starting point for this study is the NASA HRE supersonic (chemical) combustion ramjet test engine shown in Figure V-1. As is evident from the profile, the engine is configured with a large isentropic inlet spike and a center body duct which is able to translate forward and aft a substantial distance--to insure that the Mach cone exactly touches the forward inlet lip, throughout a large range of flight Mach numbers. The length of the internal annular duct passageway is set by the requirements for supersonic (e.g., hydrogen) combustion and adequate mixing of the duct flow. The plug nozzle is of the external expansion/deflecting variety. The engine will not produce thrust at flight speeds below Mach 1, of course.

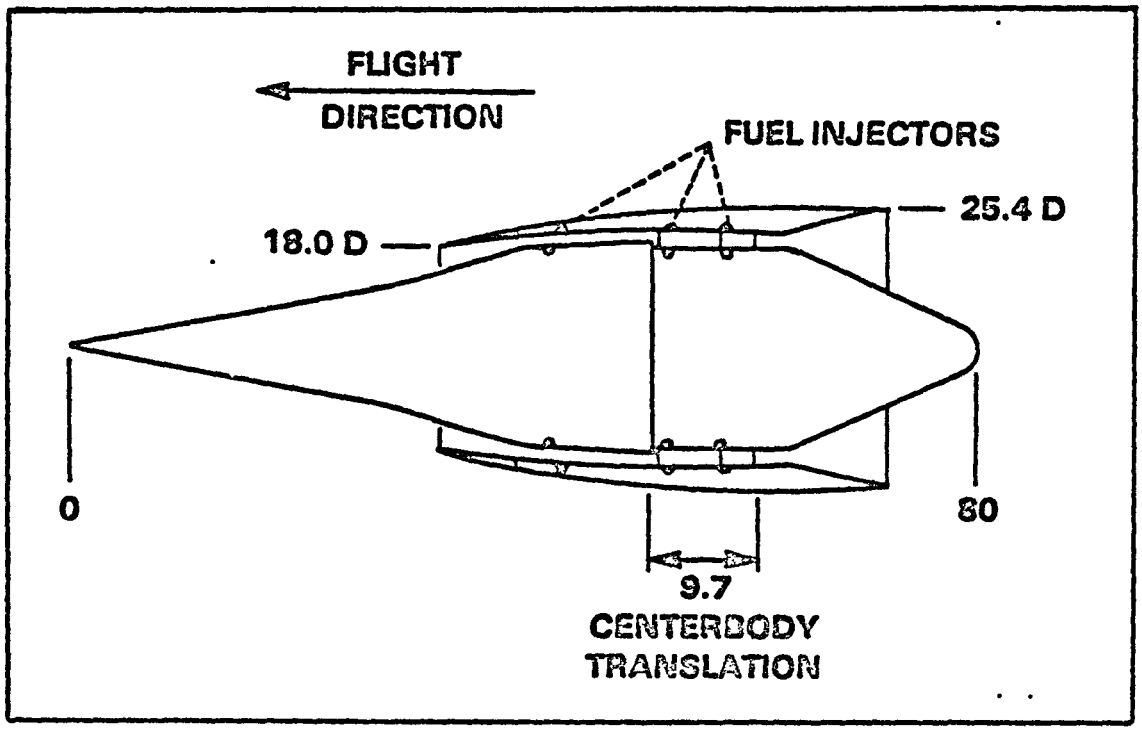

Figure V-1. Profile of Scramjet Test Engine Built by Garrett Corp. for NASA's Hypersonic Ramjet Engine Project

TABLE V-1. DESIGN CONCEPT CLASSES FOR "RADIAL" AIRFRAME CONFIGURATIONS

THRUSTER TYPE	FLIGHT MODE	
INTERNAL RADIATION-HEATED (IRH)	VTOL*	TRANSLATION+
EXTERNAL RADIATION-HEATED (ERH)	VTOL*	TRANSLATION+

* FLIGHT ALONG LASER BEAM

+ FLIGHT PERPENDICULAR TO LASER BEAM

B. "RADIAL" IRH/ERH CONFIGURATION (HIGH-FINENESS RATIO)

A laser-propelled version of the HRE engine is displayed in Figure V-2. This radially symmetric shuttlecraft is conceptually identical to the NASA scramjet engine, except that laser energy is used to heat the duct air working fluid. The forward isentropic inlet spike doubles as a parabolic primary receptive optic, so the shuttlecraft central axis of symmetry must always be aligned with the remote laser beam. Laser power is brought to a line focus that encircles the vehicle perimeter; the line focus is completely enclosed by the inlet duct. The annular duct is adjustable to produce a wide variety of throat areas and nozzle expansion ratios for efficient hypersonic operation. No fuel, other than that required for emergency operation (e.g., by a back-up chemical rocket engine) would be carried aboard the vehicle. The shuttle payload would be housed within the vehicle centerbody.

The laser propulsion engine is of the combination power plant variety, utilizing both IRH and ERH thruster modes. Figure V-3 is a schematic diagram of the IRH propulsion mode. The isentropic inlet spike completely "swallows" the low-intensity laser beam and brings it to a circular-line focus within the duct--in the process generating a standing absorption wave which is delicately balanced within the internal air flow field. The heated exhaust flow then expands aftward through the plug nozzle, producing thrust.

Because of the high temperatures generated by LSC waves, the IRH thruster may have to operate in the LSD regime in order to minimize frozen flow losses. A severe reduction in engine efficiency will result from significant levels of gas dissociation produced at temperatures beyond 3000 K, unless the constituents re-combine while the gas still resides in the duct. Hence, the thruster may have to operate in a rapidly pulsed mode using LSD-wave heating to control the peak "combustor" temperatures.

However, in order to successfully reach the highest flight Mach numbers, "combustion" temperatures may have to be pushed to the maximum.

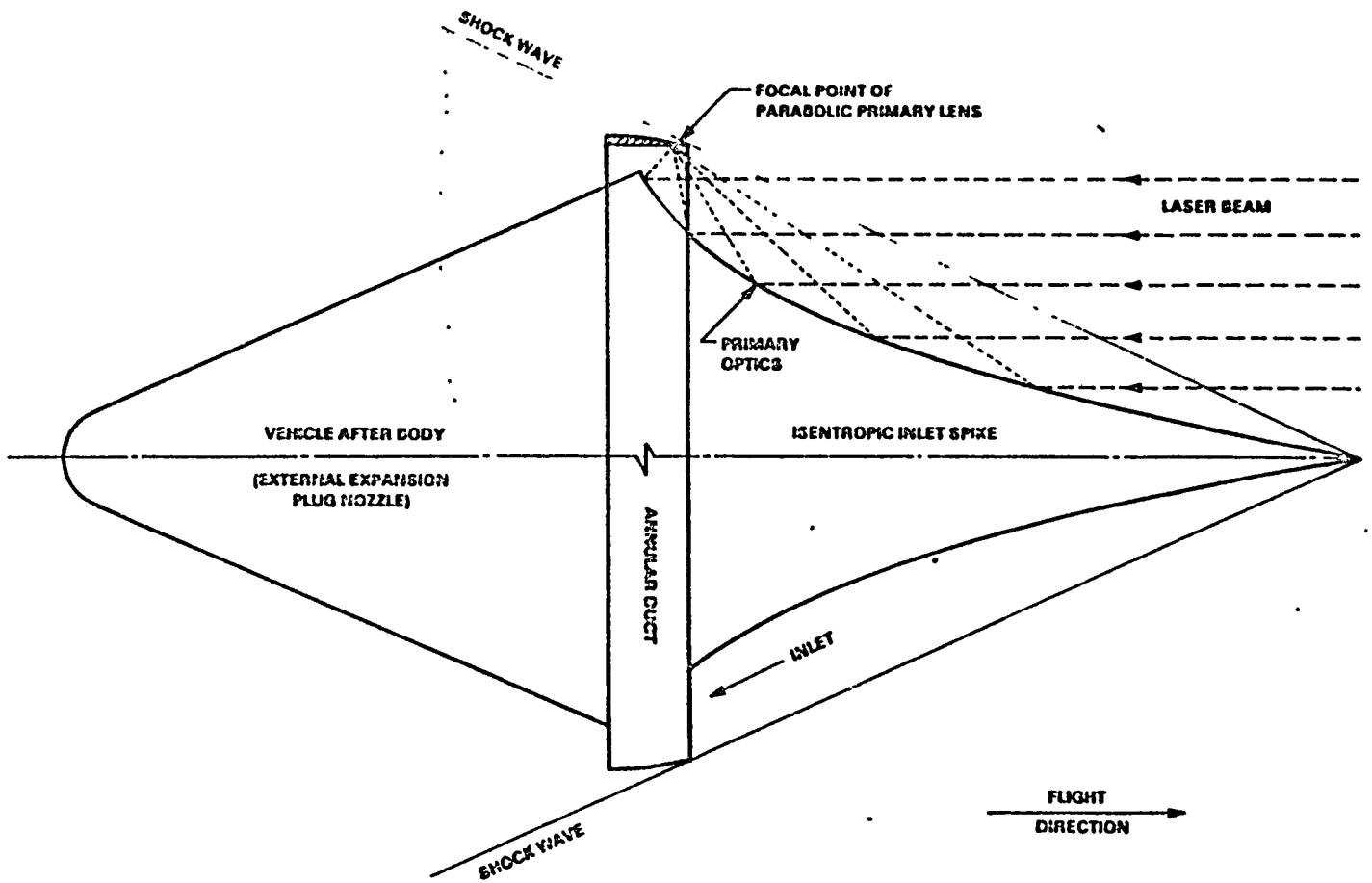

Figure V-2. Radial IRH/ERH Configuration with Isentropic Inlet Spike (High Fineness Ratio)

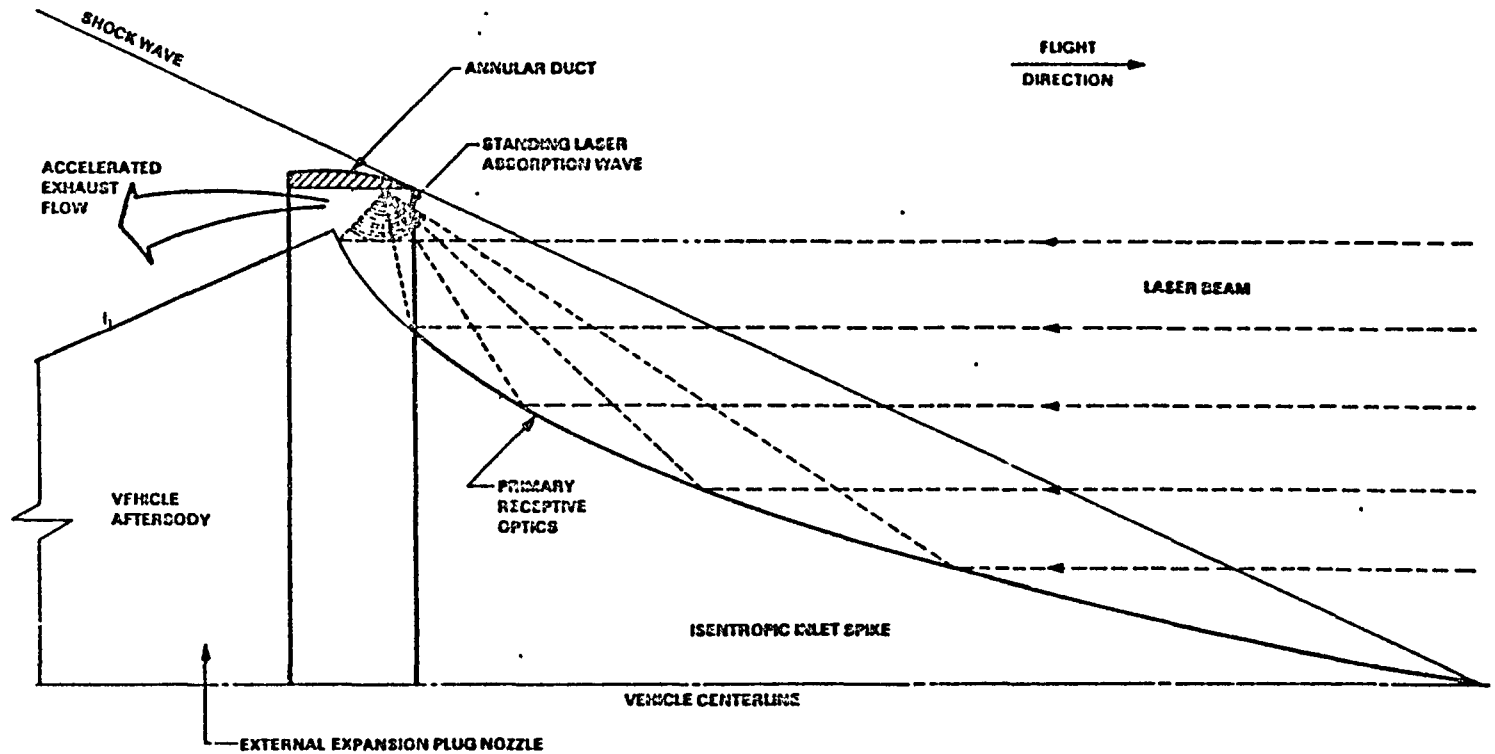

Figure V-3. IRH Propulsion Mode

In this eventuality, frozen flow losses would be accepted as a matter-of-course penalty for operating in this stressing flight regime. Because of the combustion temperature limitations of hydrocarbon fuels, the highest attainable hypersonic flight velocity is about Mach 7. With laser-heating comes the potential for substantial improvements in "combustion" temperatures, and peak hypersonic air-breathing propulsion speeds.

A few additional comments should be made regarding the inlet and plug nozzle design considerations for laser shuttlecraft. The shuttle would normally fly at zero angle of attack to stabilize inlet diffuser for maximum efficiency. ("Pitch" and "yaw" maneuvering forces could be generated by non-symmetric operation of the ERH or IRH thrusters.) Also, the plug exhaust nozzle has the inherent advantage of automatically adjusting to changes in atmospheric pressure; consequently, it can exhibit high performance at sea level, as well as at very high altitudes.

One final note should be made about the above-described IRH propulsion mode. The IRH thruster portrayed in Figure V-3 might (in concept) operate just as well without the annular duct housing--in effect, becoming an "external-burning" ramjet. However, the elimination of the annular duct would also deny the capability for VTOL and subsonic flight, as will now be described.

Figure V-4 is a schematic diagram of the ERH propulsion mode. Basically the duct would provide the additional function of housing a set of retractable secondary (reflecting) optics. In the ERH thruster mode, the secondary optics would be extended into the focal region of the laser beam, and thereby reproject a very intense laser beam parallel to (and just below) the vehicle afterbody--to focus near the vehicle, as shown in Figure V-4. Here an LSD wave is ignited (e.g., by laser-induced air breakdown or an electric spark), and the wave races all the way up the laser beam, parallel to the lower afterbody surface. Just before the LSD wave contacts the secondary optics, the laser pulse is terminated. Finally, the hot, high-pressure layer of air (generated by passage of the LSD wave) expands off the vehicle afterbody, producing thrust. Asymmetric operation of the ERH thruster would cause the vehicle to translate in directions

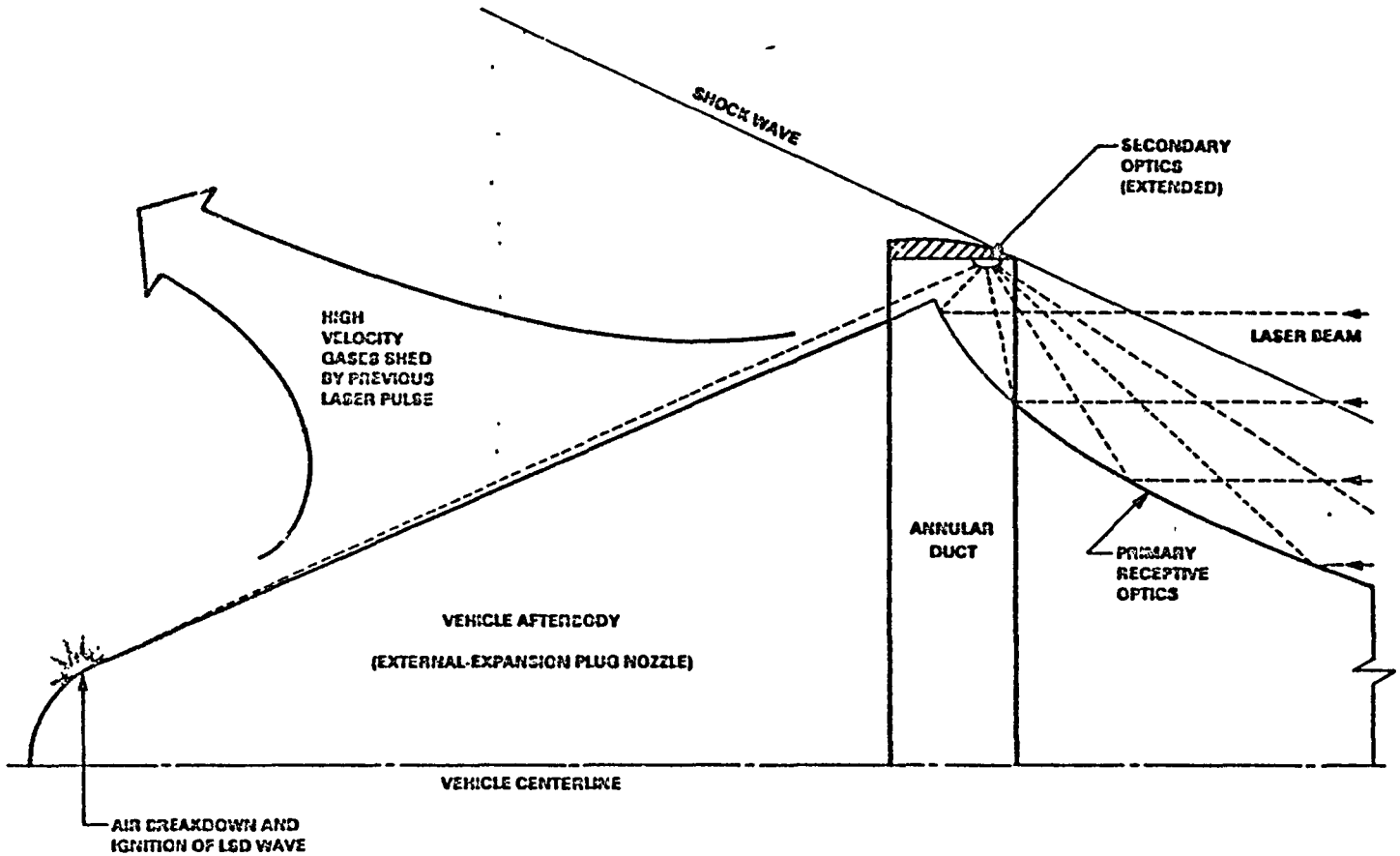

Figure V-4. ERH Propulsion Mode

lateral to the beam, and could also provide flight maneuvering and control forces.

Whereas the radial IRH/ERH vehicle pictured in Figure V-2 was designed for a high-fineness ratio, other useful lower-fineness ratio configurations can be envisioned as variations on the basic theme. Although the entire inlet spike of the Figure V-2 vehicle serves as a primary optics, other inlets which have only a portion of the total area serving as optics are possible. The remaining inlet area could be a greatly fore-shortened double-cone, or possibly a rounded/truncated cone.

The radial IRH/ERH configurations in Figures V-5A and V-5B serve to demonstrate some of these possibilities. Note that the vehicle afterbody has been severely shortened to facilitate efficient operation in the VTOL propulsion mode with ERH thrusters. The Figure 5A geometry is designed to receive an annular laser beam onto its parabolic primary optics; only 75 percent of the area represented by the beam's external diameter is actively used. For this shuttlecraft geometry, the inactive (i.e., non-optical) portion of the inlet is simply fitted with a rounded aerodynamic fairing. Figure V-5B illustrates a similar vehicle of even lower fineness ratio, which is designed for an annular propulsive laser beam with only 50 percent "active area."

C. RADIAL IRH/ERH CONFIGURATIONS WITH ISENTROPIC-SPIKE/CONE CENTERBODY INLETS

Whereas the low-fineness ratio radial IRH/ERH shuttlecraft pictured in Figure V-5 utilized rounded isentropic-spike center-body inlets, the configuration in Figure V-6 is designed around a combination isentropic-spike (again doubling as a primary receptive optic) and truncated cone center-body inlet. As before, the primary optical surface is mathematically generated by rotating a parabola about an off-center axis which coincides with the vehicle centerline. The active laser beam contours associated with various truncations of the primary optics (e.g., the "isentropic" spike) are indicated in Figure V-6. Note that the focus of the parabola is just outside the vehicle rim, and that the focused beam is intercepted by

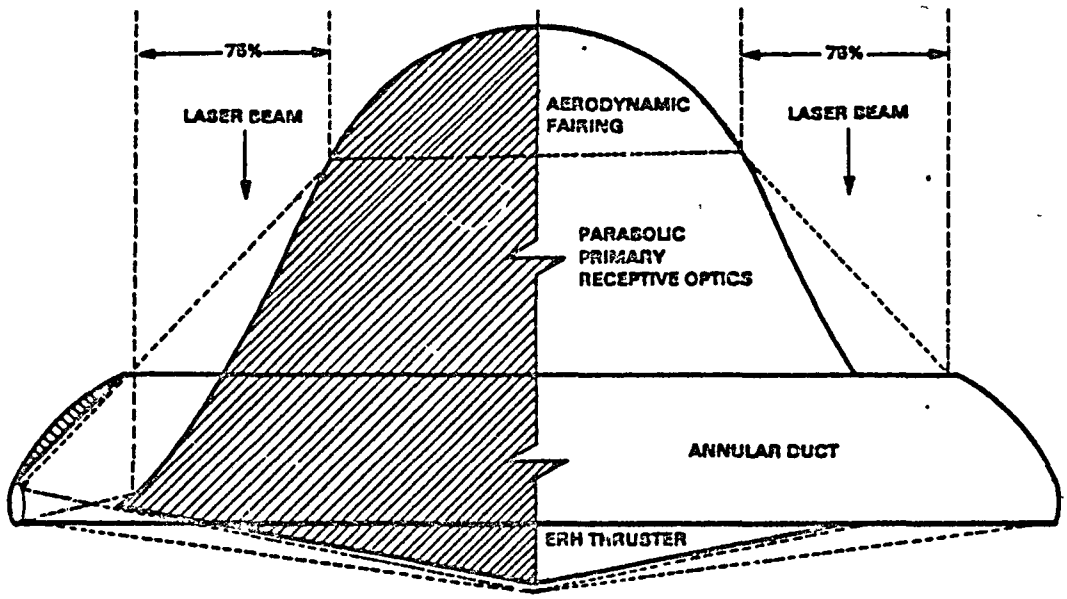

A) 78% ACTIVE AREA (ANNULAR BEAM)

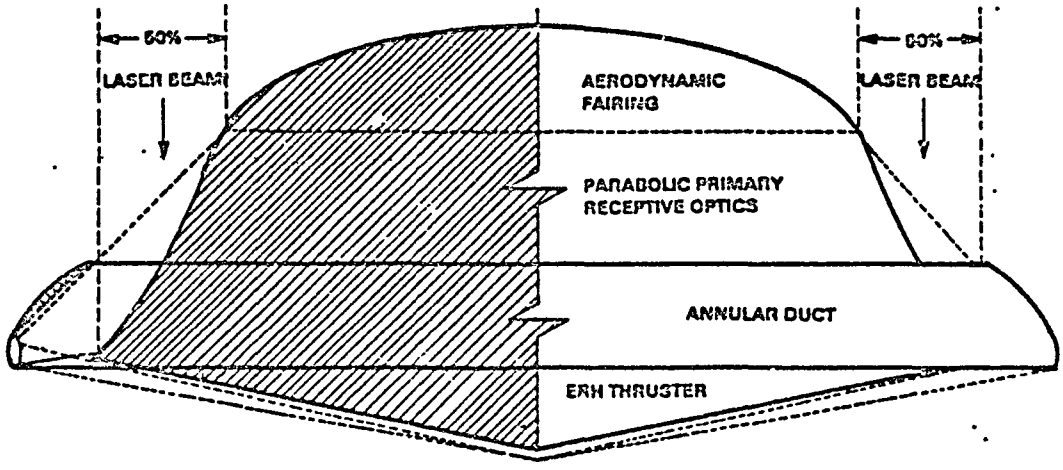

B) 50% ACTIVE AREA (ANNULAR BEAM)

Figure V-5. Radial IRH/ERH Configuration with Rounded Isentropic - Spike Center Body Inlets (Lower Fineness Ratio)

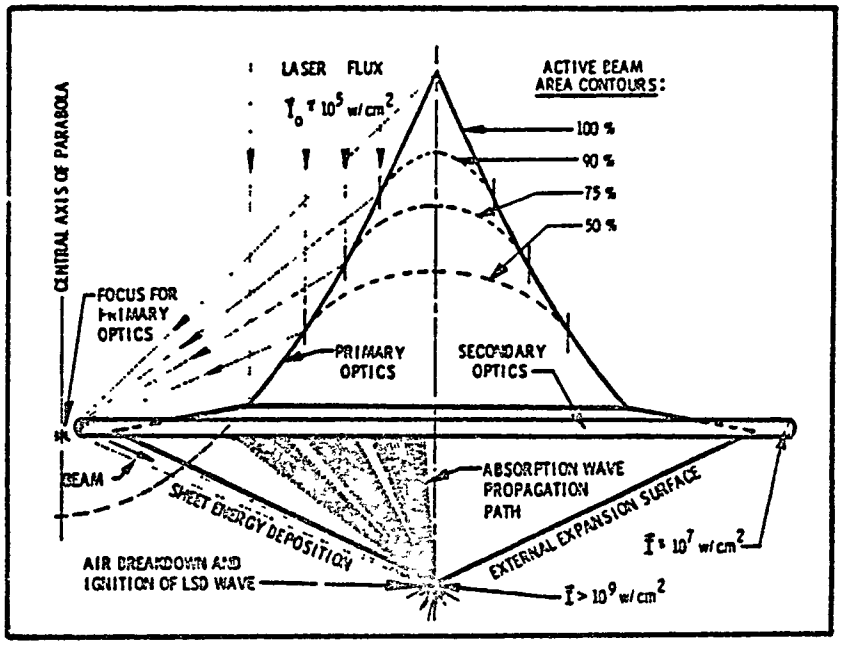

Figure V-6. Small-Wing Radial IRH/ERH in the Translation Flight (Central Focus)

secondary optics (located at the rim) just prior to reaching that point. Subsequently, the intense beam is projected back across the entire lower surface of the vehicle, which acts as an ERH thruster. Note that the vehicle afterbody is less foreshortened than that of the shuttlecraft pictured in Figure V-5.

The vehicle configuration is particularly suitable for atmospheric re-entry, but its low lift/drag (L/D) shape would indicate a limited potential for conventional maneuverability using aerodynamic lift. Although the shuttle could generate a small amount of aerodynamic body lift in the lateral flight mode, the ERH propulsive engine is envisioned to provide the dominant share of flight-supporting lift.

In principle, the external expansion surface contour would be set at the proper inclination to cause the resultant ERH thrust vector to exactly pass through the vehicle center of gravity. With this alignment, no unintentional pitch or roll torques would be placed upon the vehicle--regardless of the lateral thrust developed by the ERH engine. Laser illumination of the primary optics will result in electrical air breakdown at the vehicle central axis, followed by ignition of LSD waves which will "burn" across the ERH thruster surface. (As before, the beam would be shut off just before the LSD wave contacts the secondary optics.) Uniform illumination of the primary optics will generate a radially symmetric pattern of hot, high-pressure plasma fingers. These high-pressure regions will expand across the entire lower vehicle surface, generating vertical thrust. Repetitive pulsing of the beam will levitate the vehicle into the air.

In the VTOL mode, the ERH thruster is likely to generate a great deal of acoustic noise, probably sounding much like a mammoth loud speaker when producing audible frequencies of several hundreds to thousands of Hertz. An essentially quiet alternate scheme for VTOL using LSC waves can be postulated with the plasma model portrayed in Figure III-7B. Basically, a much reduced level of laser radiation would maintain a continuous LSC wave "plasmoid torch" at the very center of the lower vehicle ERH thruster surface. Sufficient thermal power levels would be injected into this lower

surface air volume to maintain an overpressure of 0.01 to 0.1 atmospheres (i.e., 10^3 to 10^4 Newtons/m^2), easily sufficient to support these radial IRH/ERH shuttlecraft in the hover mode.

When operating in the ERH thruster mode, unsymmetrical illumination of the primary optics will propel the vehicle in a direction opposite to that of the illuminated surface, and perpendicular to the laser beam. Nonuniform deposition of beam energy (e.g., by varying pulse shape, duration, and energy) during the propagation of the LSD absorption wave can cause pitch or roll torques to be placed upon the vehicle, thereby generating flight maneuverability and control forces.

Cooling requirements of the secondary mirrors will be significantly more severe than that for primary mirrors, due to higher flux loadings on these surfaces. Therefore, during lateral flight when only a small portion of the entire secondary lens is illuminated, there may be some advantage to rotating the rim optics so that the heating load would be more uniformly distributed. This may be accomplished by supporting the rim upon a separate bearing system and driving it with a small auxiliary engine. In reaction, the vehicle centerbody would rotate slowly in the opposite direction at a slower speed because of its larger aerodynamic drag. As a result, a more uniform heating of <u>all</u> optical surfaces will occur, thereby causing lower temperature-gradient-induced stresses, and perhaps permitting simpler, lighter weight optical cooling systems. One additional fortuitious result of spinning the rim optics could be the generation of a strong gyroscopic moment--which could greatly increase the stability of the receptive optical platform.

It should be noted that the vehicle may change its direction of lateral flight simply by re-orienting the azimuthal placement of the laser beam upon the receptive optics. This will automatically vector the propulsive ERH thrust. Hence, the vehicle need not bank and turn like more conventional aircraft which depend on aerodynamic lift to negotiate turns. Such a banking turn maneuver would destroy the critical beam/optics alignment of laser-propelled shuttlecraft.

D. ALTERNATE GEOMETRIES FOR RADIAL/ERH THRUSTERS

Figure V-7A is a bottom view of the vehicle shown in Figure V-6, with the ERH thruster operating in the VTOL mode. The illustration captures the thrust generation process at the beginning, when laser-induced electrical air breakdown is triggered at the vehicle center. (Recall that the secondary optics are configured about the rim, and act to reflect radiation inward towards the vehicle center.)

Figure V-7B shows an alternative optics/airframe/engine configuration that flashes the collected radiation radially outward below a large annular wing--which acts as the ERH thrust surface. The secondary optics are of the grazing-incidence variety and are slightly scalloped to cause the radiation to come to a series of point focii about the rim. This enhances the ability of the engine to easily trigger electrical air breakdown at, for example, several dozen focii.

E. RADIAL/ERH CONFIGURATIONS WITH PERIMETER FOCUS

Figure V-8 illustrates two variations in airframe geometry derived for the perimeter-focus secondary optics case. The first (Figure V-8A) takes on much of the appearance of a dinner plate--with a center cone structure which serves as the primary optics and contains the payload. Aerodynamic lift is generated off a planar surface; this variation is the flatest possible airfoil. The second variation, shown in Figure V-8B, has a thicker airfoil with a symmetric contour and little camber. Since it has a larger cross-sectional volume, it is able to enclose a much larger payload within the squashed toroidal volume distributed over the ERH thruster. The fatter airfoil permits substantially different aerodynamic characteristics from that of the planar airfoil.

It should be noted here that as the vehicle accelerates laterally from subsonic to supersonic flight speeds, the center of lift on the airfoil moves aft from the 25 percent chord to the 50 percent point--which is exactly aligned with the center of gravity for this radially symmetric

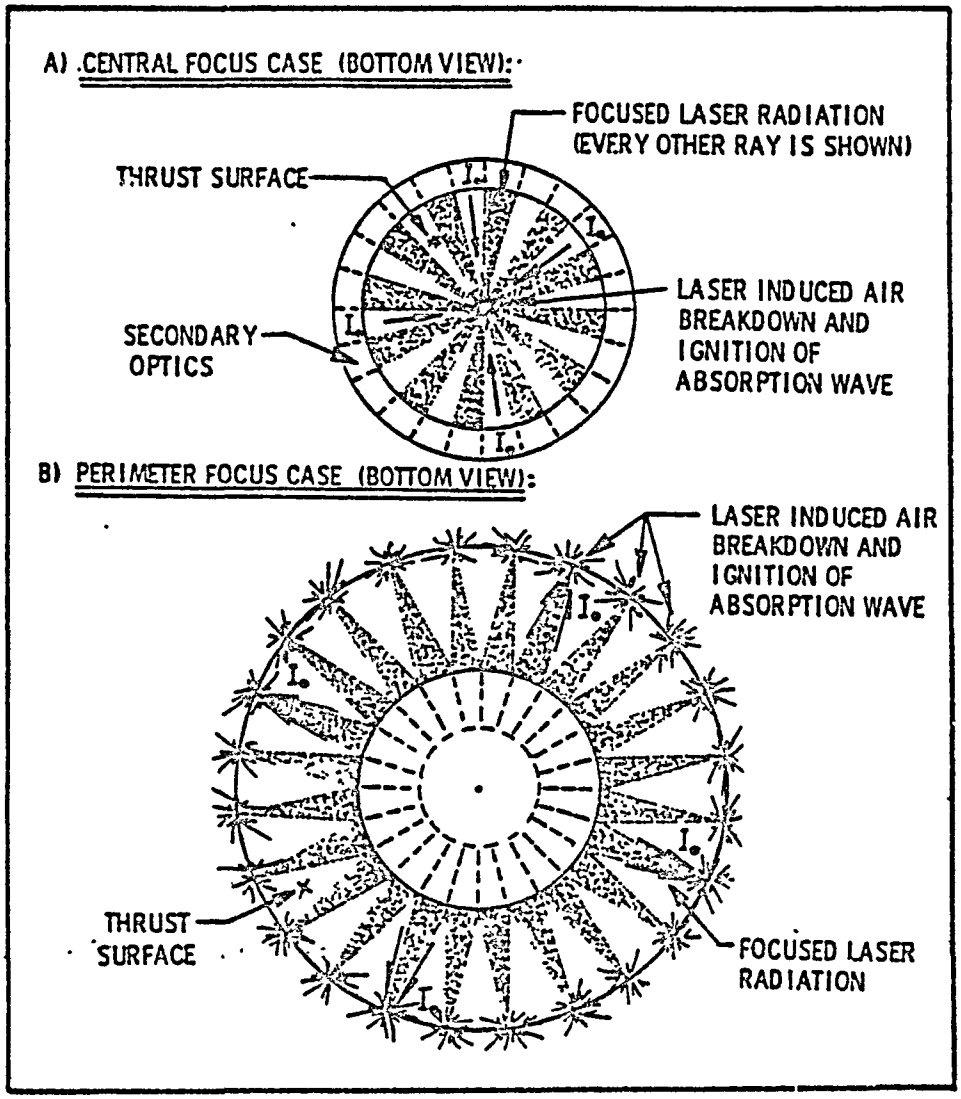

Figure V-7. Alternative Geometries for Radial/ERH Thrusters: Central vs. Perimeter Focus (Small vs. Large Wing)

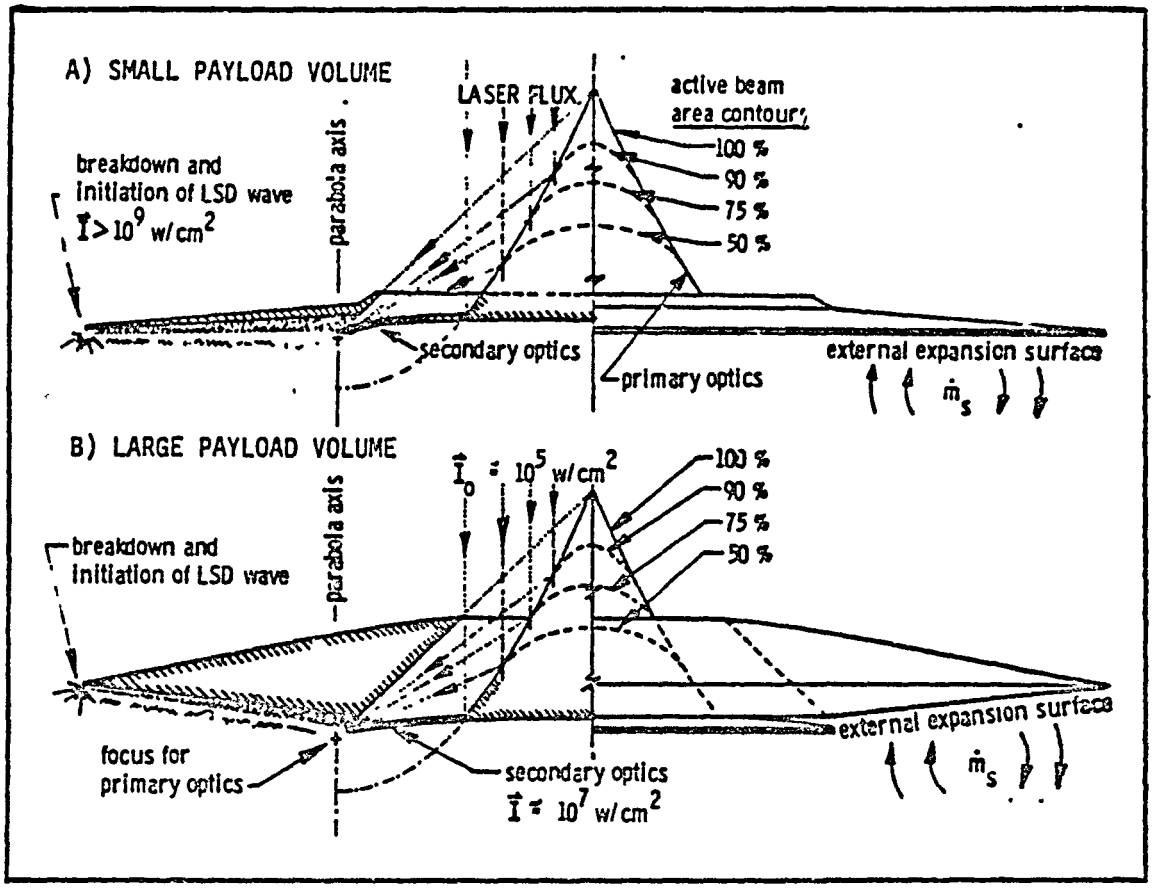

Figure V-8. Large-Wing Radial/ERH Configuration (Perimeter Focus)

vehicle. During vertical take-off and landing, the ERH thruster must create a vertical thrust distribution which is centered on the 50 percent point. At subsonic lateral speeds, the ERH thruster pressure distribution must be altered to complement aerodynamic lift--so that the resultant thrust vector always acts at the 50 percent chord.

Portrayed in Figure V-9 are the different incident beam irradiation patterns representative of subsonic and supersonic flight regimes. In subsonic flight (Figure V-9A), the aft ERH thruster surface is activated to balance the forward-located aerodynamic lift vector. For example, Figure V-10 depicts the lower ERH surface for the Figure V-8B vehicle in lateral subsonic flight towards the left hand side of the page. However, in supersonic flight (Figure V-9B) the ERH thruster must be symmetrically activated about the pitch axis since the aerodynamic lift vector will have moved aft to the 50 percent chord point.

Figure V-11 demonstrates the simple process by which pitch and roll of this "perimeter-focus" vehicle can be controlled. The incident beam is simply directed to fall upon the proper side of the primary optical surface--thereby activating that associated portion of the ERH thruster surface. For example, to cause the shuttle to pitch down, the laser beam is projected upon the most rearward portion of the primary lens--as shown in Figure V-11A.

Figure V-12 illustrates the three basic steps of the lateral ERH propulsion cycle for the Figure V-8A vehicle. The cycle begins with the supersonic air being compressed to a higher pressure as it moves across the bow shock. Next, the pulsed laser beam uniformly illuminates the receptive optics, which in turn flashes power towards the vehicle rim. This injects thermal energy into the pre-compressed air underneath the vehicle, and heats it to a much higher pressure and temperature. Next, the high-pressure air expands across the vehicle undersurface as shown in Figure V-12B, generating thrust. Finally, fresh un-heated air again enters the ERH thruster volume, and the cycle is repeated. One final note can be made regarding the apparent flight motion of such a shuttlecraft. Depending upon the pulsing frequency of propulsive laser beam (i.e., several

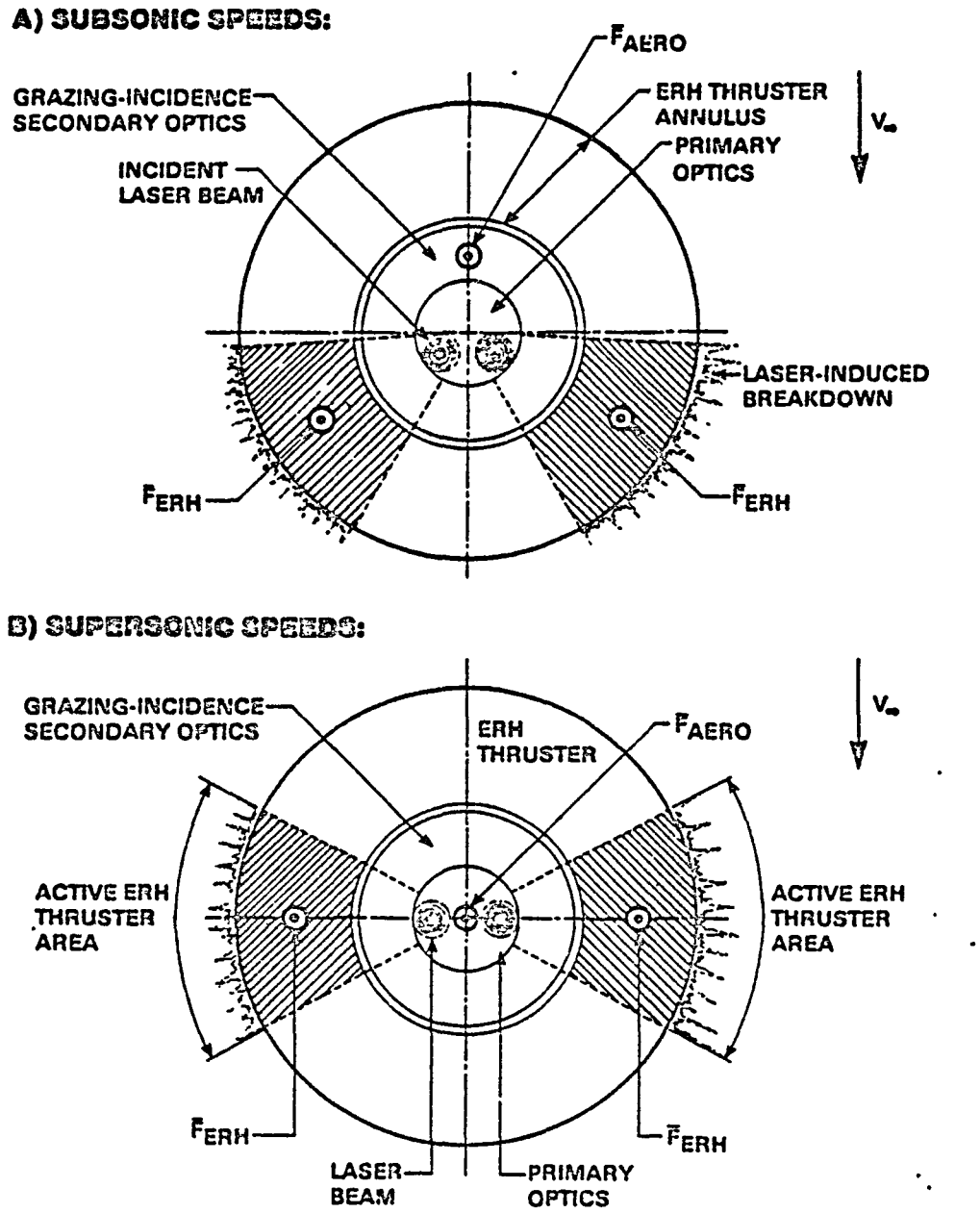

Figure V-9. Active ERH Thrust Distribution - Subsonic vs. Supersonic Flight (Top View)

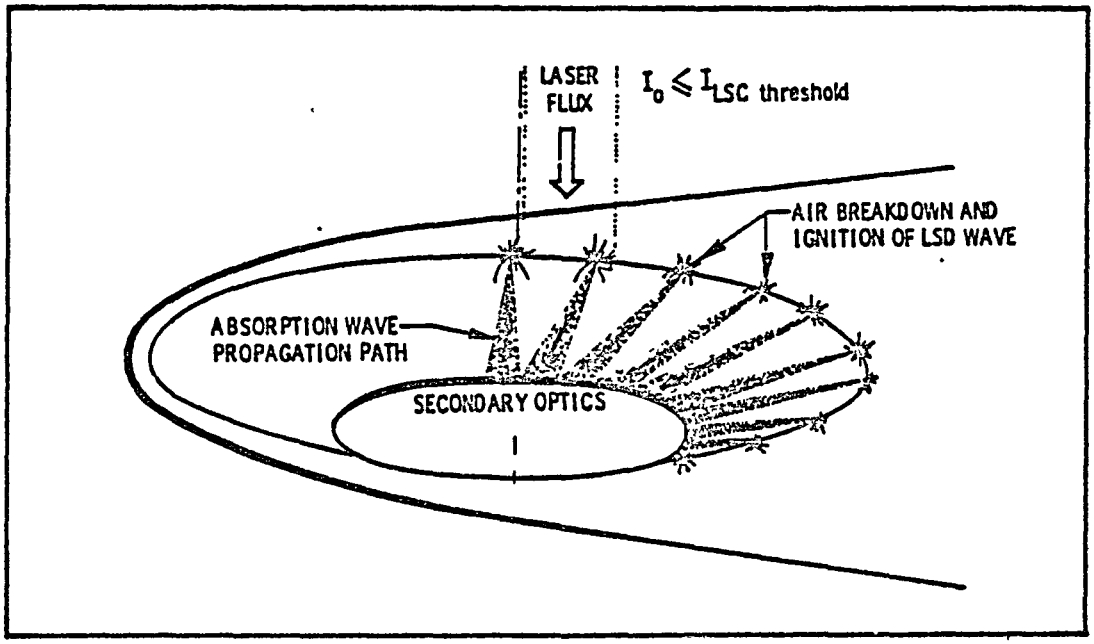

Figure V-10. Perimeter Focus, Radial/ERH Shuttle in Subsonic Translational Flight (Bottom View)

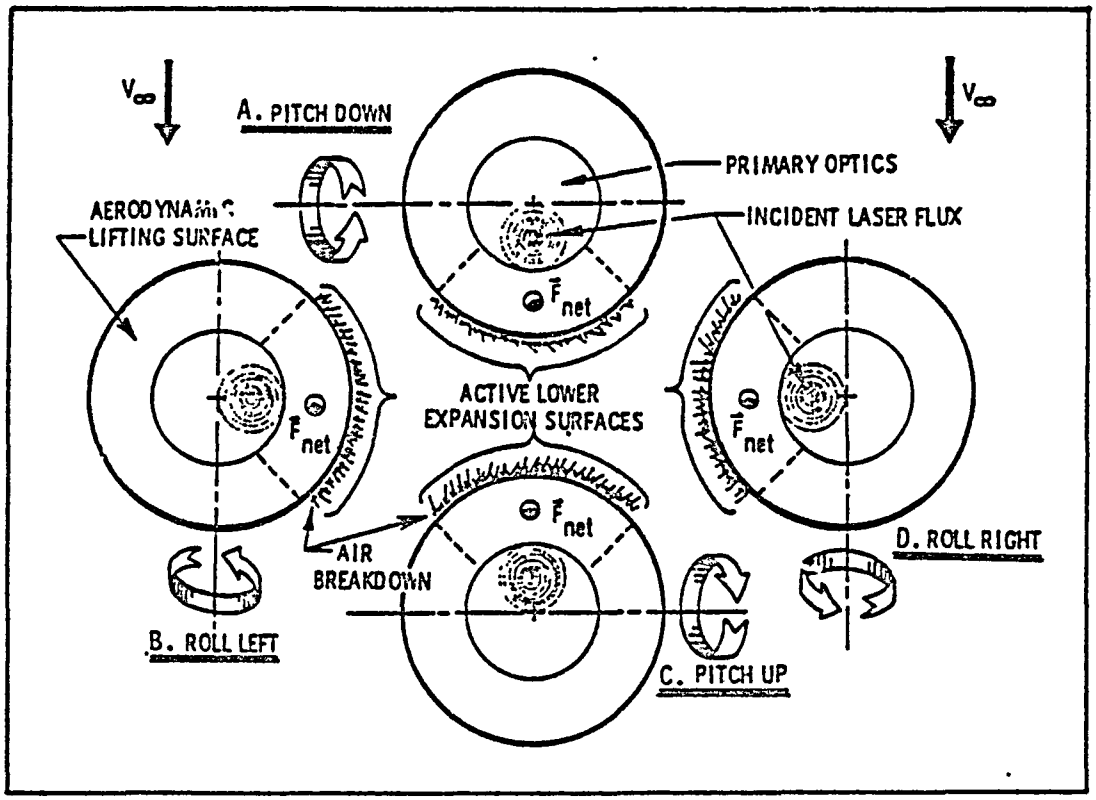

Figure V-11. Pitch and Roll Control for Radial/ERH (Perimeter Focus Case - Top View)

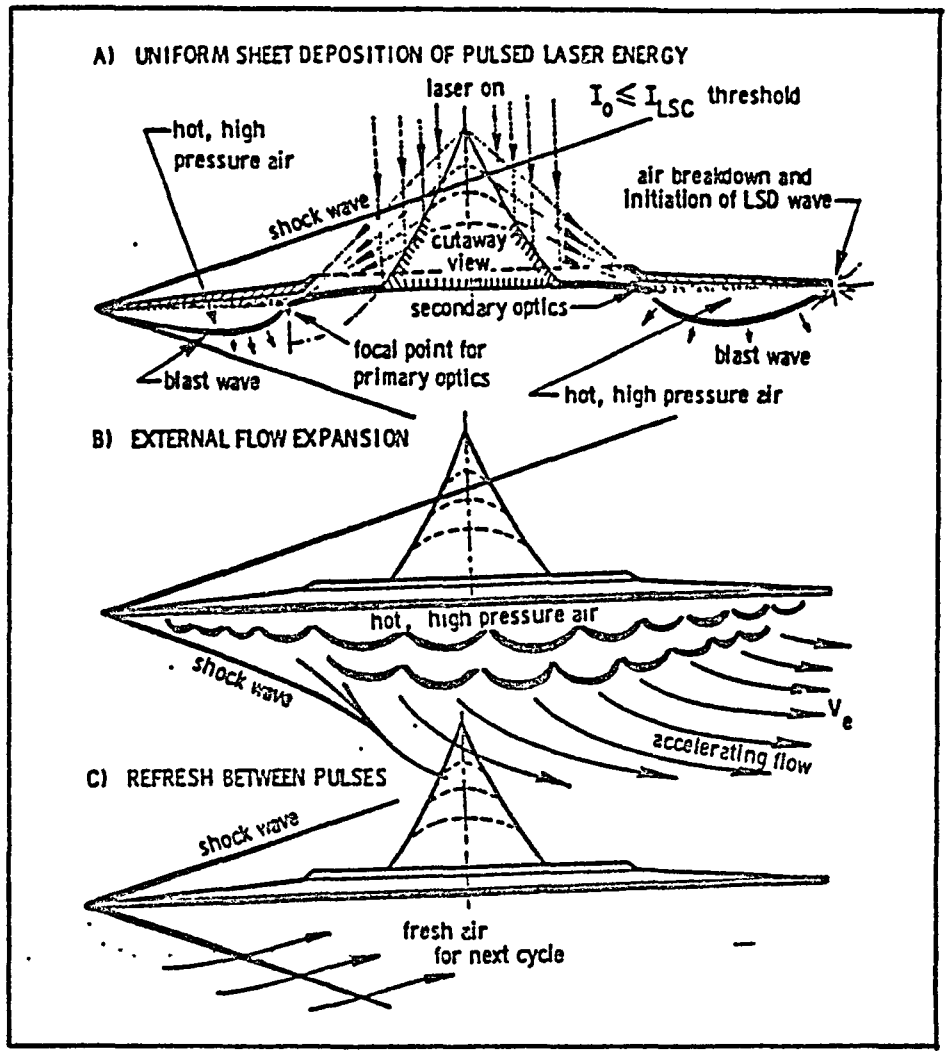

Figure V-12. Radial/ERH in Hypersonic Translation Flight (Perimeter Focus, Small Payload Volume)

Hertz vs. several hundreds to thousands of Hertz), the apparent motion of the vehicle might resemble that of a stone skipping over water--when viewed from a fixed point of reference.

F. ALTERNATE SUPERSONIC ERH PROPULSION MODES FOR RADIAL SHUTTLECRAFT WITH CENTRAL FOCUS SECONDARY OPTICS

Figure V-13 shows an alternate approach for supersonic flight propulsion of a radial vehicle with centrally focused secondary optics, such as those portrayed in Figures V-5 or V-6. First note that in Figure V-13, a radial shuttlecraft is being viewed from the underneath, and is moving towards the left side of the page in a direction lateral to the propulsive laser beam. During this ERH propulsive mode, the forward one-third of the primary optics is being illuminated by the remote laser beam, which therefore activates the forward 120° wedge of the rim-located secondary optics.

At the very beginning of this ERH thruster cycle, laser-induced breakdown is triggered at the central focal point. Next a large, nearly 2-D LSD wave races up the laser beam, its supersonic velocity slowing as the beam intensity drops upon the absorption wave. At some point, the velocity of advance for the LSD wave exactly equals the flight velocity of the vehicle--and the cresent-shaped absorption wave finally reaches a stationary position relative to the vehicle. The optical configuration produces a standing absorption wave with natural stability in the supersonic airstream. (The position of the secondary optics must be adjusted so that this LSD wave is completely outside the vehicle boundary layer.) Thus it may be possible to propel the shuttlecraft in an ERH thruster mode using a continuous, as opposed to a repetitively pulsed, laser beam.

Finally, it should be noted that much could be learned about the prospects for such RP and CW ERH thrusters from a thorough examination of current research on supersonic chemical "external burning" propulsion concepts. For example, as a result of this research it is known that thruster coupling (i.e., Newton/MW) and conversion efficiency (i.e., ratio of thermal-energy input to thruster-power output) can be maximized by insuring that: a) the "burning" process occurs completely outside of the

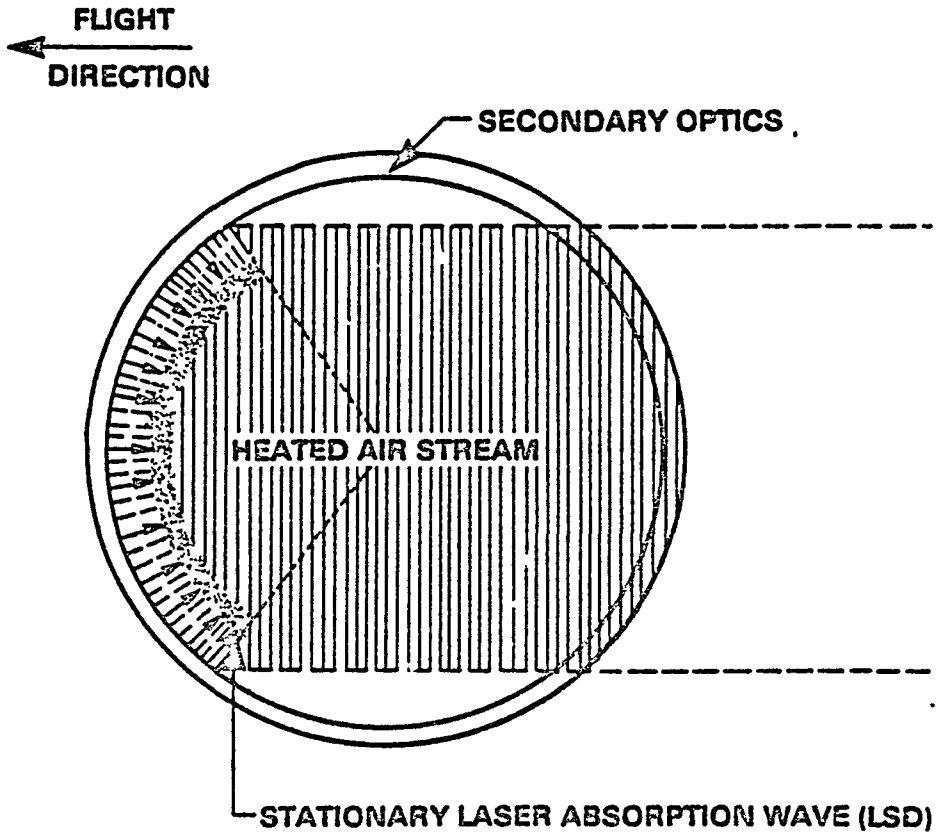

Figure V-13. ERH Thruster Mode with Stationary Laser Absorption Wave

boundary layer, b) the total thruster area is made as large as practical, and c) the ratio of heat input per unit thruster surface area (i.e., MW/M^2) is minimized.

G. ROTARY IRH PULSEJETS - REFLECTING PRIMARY OPTICS

This section explores the prospects for radial shuttlecraft which use rotary IRH thrusters to accomplish high lateral accelerations from a standing start or hover.

The concept for a rotary air-breathing pulsejet engine is introduced in Figure V-14. In horizontal flight, the propulsive engine operates in a pulsed fashion made quasi-steady by rotating a set of propulsion units. The rotating cascade of pulsejets operates in a manner similar to a gatling gun. Changes in lateral flight direction are simply accomplished by advancing or retarding the radiation-induced spark, which results in an immediate thrust-vectoring of engine exhaust gases. Gyroscopic stabilization of receptive optics (which are rigidly attached to the vehicle) permits accurate "lock-on" alignments with the remote beam. The overall optics/airframe/engine design allows radical changes in lateral flight direction with perfect beam alignment.

The rotary pulsejet engine in Figure V-14 is comprised of 12 separate propulsive units which rotate either on their own bearing system (i.e., independent of the rest of the vehicle), or as an intimate part of the entire craft. In the latter case, a central payload volume would be mounted on a separate bearing system, isolated from the vehicle rotation. As indicated in Figure V-14, each propulsion tube is sequentially energized with a pulse of beamed radiation as it rotates clockwise into the aft-most position; here, the high-velocity exhaust gases are ejected exactly opposite to the direction of flight.

The rotary pulsejet engine cycle is displayed in Figure V-15. The cycle begins as fresh air is taken into a thruster tube as it rotates from the 10:00 to 2:00 position (Figure V-15A). (Note that the 12:00 position in Figure V-15 is directly into the relative wind.) At the 5:00 position,

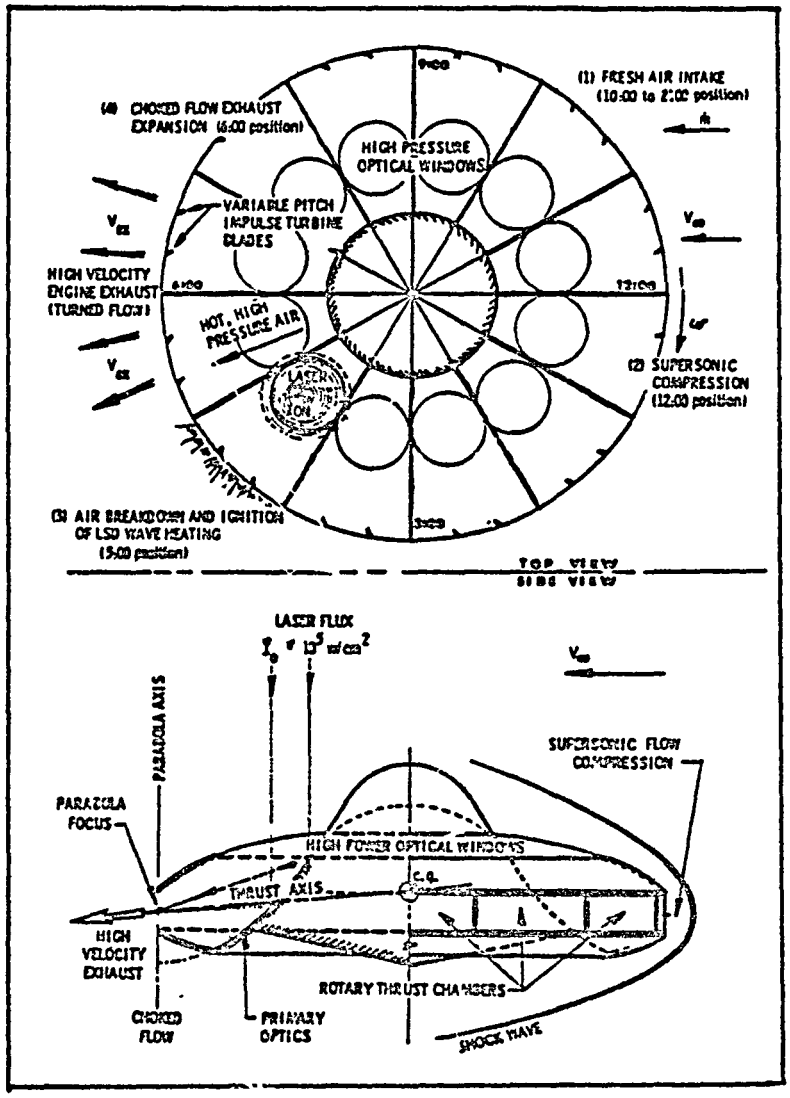

Figure V-14. Rotary IRH Pulsejet - Supersonic Lateral Translation Mode (Sonic Nozzle)

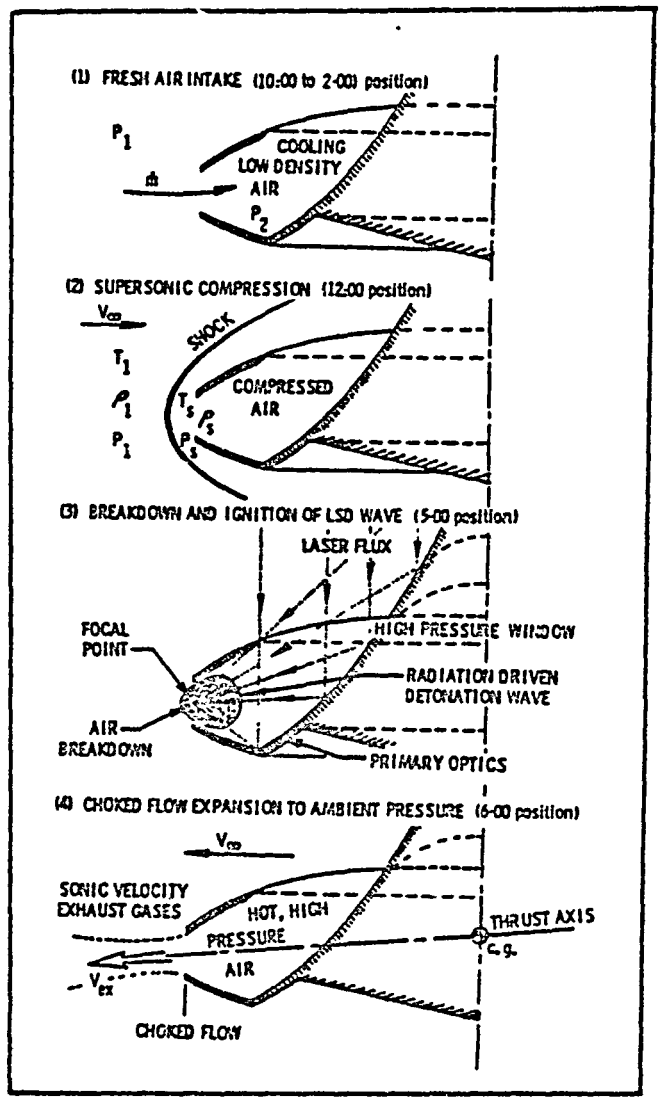

Figure V-15. Rotary Pulsejet Engine Cycle (Supersonic Compression)

a pulse of radiation is projected into the tube through a high-power optical window located near the closed end. As indicated in Figure V-15C, the radiation reflects off the primary optics and comes to a focus at the nozzle throat (i.e., minimum cross-section of the tube) where electrical air breakdown occurs and a LSD wave is ignited. Figure V-15C shows the LSD wave racing up the beam and processing all the enclosed air to a high temperature and pressure. Just before it contacts the primary optics, the beam is shut off and the LSD wave deteriorates to a very strong blast wave. Subsequently, the wave reflects off the closed end of the tube and expels all the high-pressure engine air (acting very much like a piston), thereby generating thrust.

The principal advantage to the rotary pulsejet propulsion system is that it is able to generate high levels of lateral thrust at zero forwrd velocity. The engine thrust vector is aligned horizontally in the intended direction of acceleration. The configuration should exhibit excellent performance in accelerating rapidly to supersonic horizontal flight speeds.

Once the vehicle attains supersonic lateral flight speeds, the rotary pulsejet engine cycle takes on many of the characteristics of a conventional 4-cycle Wankel internal combustion engine. Fresh air is taken into each tube from 10:00 to 2:00; supersonic compression peaks at 12:00; "ignition" occurs at 5:00; and finally, exhaust at 6:00. Each propulsion tube completes all four events within one 360 degree rotation of the vehicle.

1. Alternate Rotary Engine Concepts

Other varieties of rotary laser propulsion engines can be proposed for use with conventional turbomachinery: e.g., laser-heated turbojets. One might expect that the performance, in general, would suffer from a reduction of peak "combustion" temperatures as limited by even advanced turbine materials. However, the candidate engine/vehicle configurations proposed here might eliminate this restriction (in great measure) through the use of large regeneratively cooled turbine blades.

One possible laser-heated turbojet configuration is portrayed in Figure V-16. It is designed around the aerowindow concept (previously introduced in Figure III-12B) which uses a large single-stage

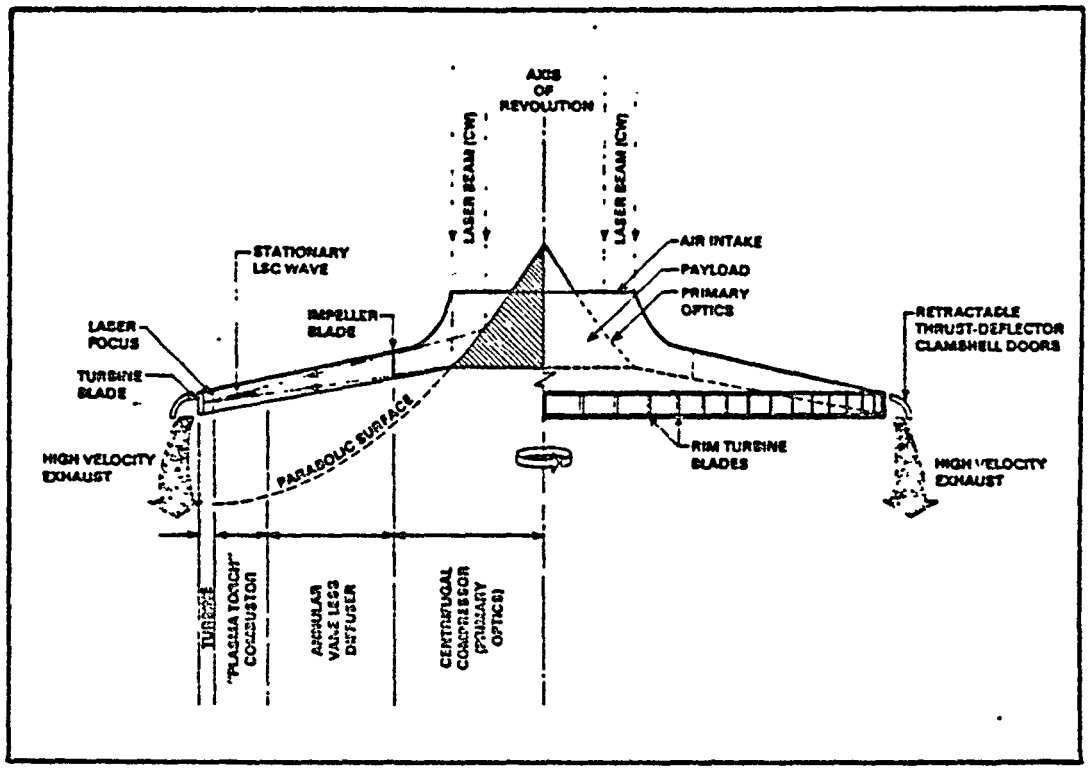

Figure V-16. Laser-Heated Turbojet Engine with Centrifugal Compressor and "Rim" Turbine (Subsonic VTOL Configuration)

centrifugal compressor. As described earlier, the upper surface of the centrifugal compressor (between the impeller blades) acts as a focusing primary reflecting lens to project the laser beam downstream into the "combustion" chamber. Since the beam is constrained to enter the engine through the compressor inlet, the use of an "inducer" section (which would more efficiently bring the flow into the compressor) is precluded. Hence, the compressor pressure ratio would be less than the 3:1 to 4:1 optimum value, unless the beam could be brought into the engine at a greater engine radius--perhaps through a material window in the compressor housing (i.e., the vehicle external skin).

In either case, the primary optics would bring the laser beam to a line focus in the "combustor" section, and a standing LSC-wave (or rapidly-pulsed LSD-wave) would be maintained in the subsonic pressurized air just downstream of the vaneless diffuser section, as shown in Figure V-16. As indicated, a set of turbine blades would be rigidly attached to the vehicle perimeter, thereby applying torque to the compressor by spinning the entire shuttlecraft.

By extending clamshell thrust-deflector "doors", as shown in Figure V-16, the laser-heated turbojet could be given VTOL capability. However, several catastrophic problems arise when one tries to provide the vehicle with lateral flight capability. Most serious is the compressor stall problem which would be caused by the extreme alignment angles of the oncoming airstream to the intake housing. Normally, the airstream would enter the intake at a relative angle aligned as close as possible to the turbomachine axis of rotation. The second problem relates to the production of lateral thrust. The only apparant means is to assymetrically illuminate the laser-heated "combustor" section. This would lead to a complicated gasdynamic flow situation that could greatly alter the flow stability through all upstream components--particularly within the diffuser and compressor sections. Furthermore, it is not immediatley evident that this approach could successfully generate a net lateral thruster vector. Hence this approach, although perhaps interesting, should be considered unpromising.

A highly promising approach can be described as follows. Let us assume that the radial shuttlecraft in Figure V-14 is equipped with an auxiliary airbreathing chemical-fueled gas generator (i.e., a turbo-compressor) which is able to deliver "cool" (compressor-bleed) air at tens of atmospheres pressure to the propulsion tubes. With this new engine concept, the remote laser beam (10X to 100X more powerful than the auxiliary engine) would be dumped into the propulsion tubes--using them like "after-burners" (either CW or RP). This could be an exceedingly powerful laser-heated turbojet engine.

2. VTOL Propulsion of Rotary Pulsejet Shuttles

Clearly, if each propulsion tube of the radial IRH shuttle pictured in Figure V-14 were to be fitted with an extendable clamshell door, the high-velocity gases (ejected by the laser-heated "after-burner") could successfully levitate the vehicle--giving it VTOL capability.

However, a significantly more elegant approach would be to integrate an ERH thruster with the lower vehicle centerbody surface, as shown in Figure V-17. ERH thruster would operate exactly as described previously for the delta shuttlecraft vehicle in Chapter IV. That is, a series of portholes or slits would be opened in the primary optics to allow projection of very intense beams of concentrated radiation from a series of retractable secondary optics, which are deployed during VTOL operation.

Several minor variations in the optical train configuration are possible. First, the primary optical surface can be an exact parabola of revolution which would project towards a line focus and require the use of cylindrical secondary optics. For this alternative, the focal region is actually a point centered at the vehicle centerline--permitted by an azimuthal curvature of the secondary optics. This approach requires a slit opening in the primary optical surface to allow passage of the beam to the ERH thruster. The second approach is to slightly scallop the primary optics as shown for the vehicle in Figure V-14. This brings the radiation to a point focus near the nozzle throat of each propulsion tube. Hence a set of spherical-contoured secondary optics would be used for this approach, and round portholes would permit radiation to be beamed to the

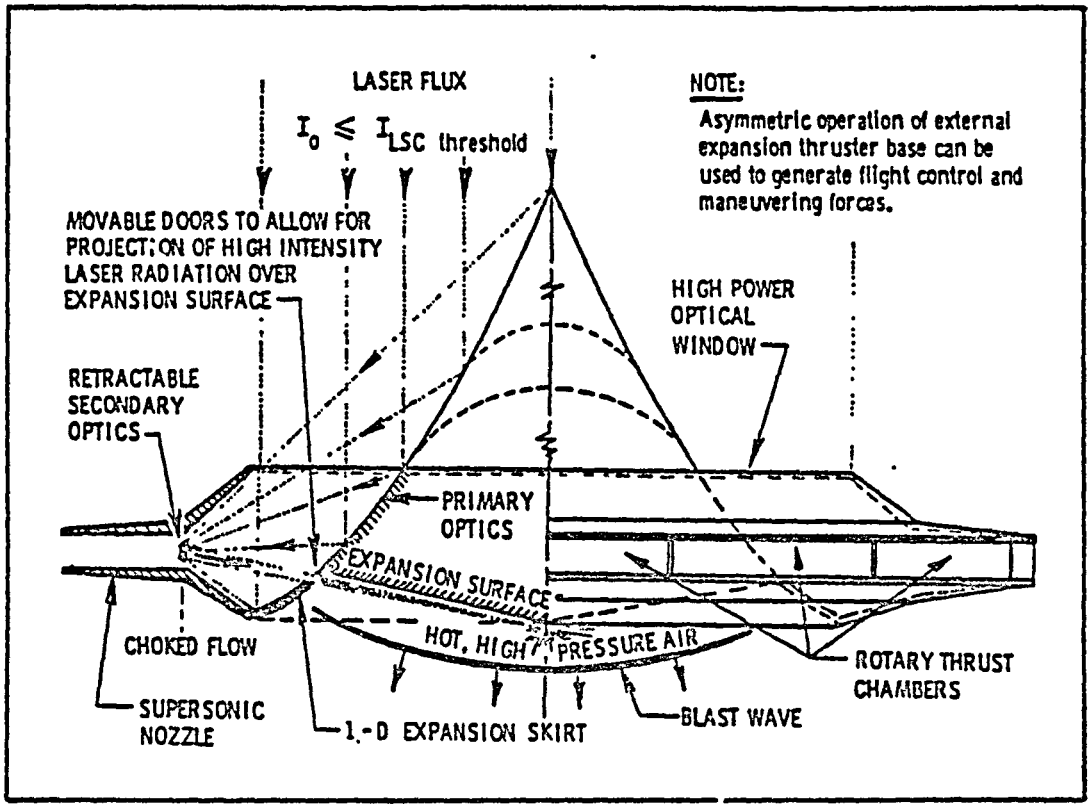

Figure V-17. Rotary IRH Pulsejet - VTOL Mode with ERH Thruster (Supersonic De Laval Nozzle)

ERH thruster. This alternative results in the creation of a set of hot, high-pressure plasma "fingers" that are generated across the ERH thruster surface.

Several additional comments should be made about the radial optics/airframe/engine configuration presented in Figure V-17, before moving on. Note that the high-power optical window lies in a single plane. This configuration is suggested as a potential variation-on-a-theme, even though it may not be optimum for a light beam to enter the HEL window at normal incidence--because of losses due to reflected radiation. As shown in Figure V-18, theory suggests that with plane polarized light, the highest transmittance (and hence the lowest reflectance) can be obtained by setting the window at the Brewster angle (~55°).

Finally, we note that a rotary pulsejet may be furnished with pitch and roll maneuverabilty by two distinctively different approaches. For example, unsymmetric irradiation of the ERH thruster surface can give rise to pitch and roll forces as shown in Figure V-9. The alternative is to use a variable geometry exit nozzle on certain rotary pulsejet configurations (e.g., most easily obtained with an expansion-deflection nozzle type), or through the use of retractable clamshell doors as shown in Figure V-16. With this approach, the high-velocity exhaust gases are non-symmetrically deflected downward, thereby producing a torque on the vehicle. (For that moment, of course, the exhaust thrust vector does not pass through the vehicle center-of-gravity.) The proper rotary pulsejet thrust tubes would be energized just as they arrive at the location required to exert the proper torque. In summary, either of the above two measures could conceptually generate adequate flight control and maneuvering forces. Finally it should be noted that torques exerted on vehicles with a large gyroscopic moment will cause a natural precess in a plane 90° off axis from that of the applied torque.

3. General Comments on IRH Rotary Pulsejet Exhaust Nozzles

There are any number of rim nozzle designs which can be proposed for rotary pulsejets: a) sonic nozzles which terminate at the minimum cross-sectional flow area (as shown in Figure V-14), b) conventional

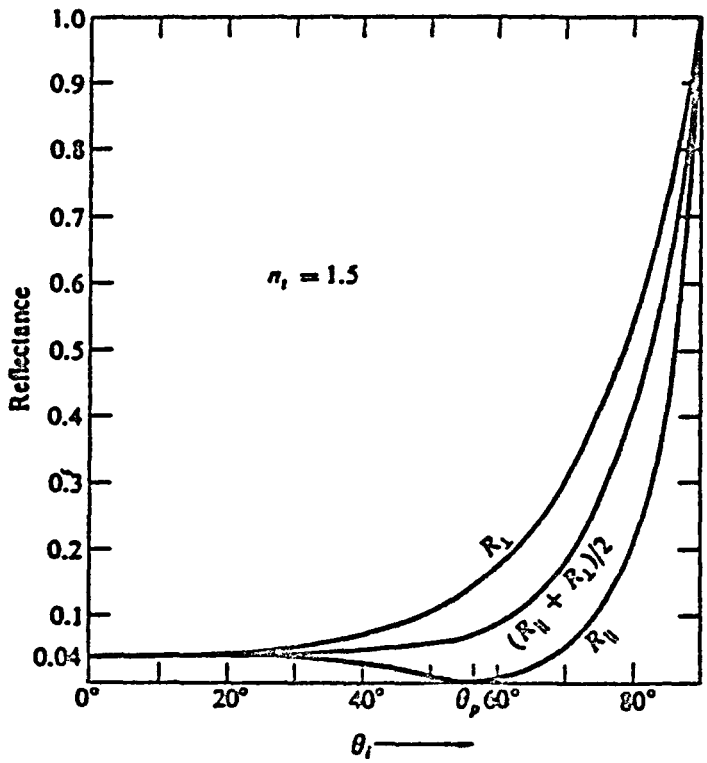

Figure V-18. Reflectance vs. Incident Angle, Showing That the Optimum Transmission Through a Window is Accomplished at the Brewster Angle (~55°) for Plane Polarized Light

converging-diverging "Bell-type" DeLaval nozzles which further accelerate sonic "throat" gases to supersonic velocities (see Figure V-17), c) expansion/deflection supersonic nozzles, d) "plug"-type supersonic nozzles, and e) "grid" supersonic nozzles. Each rim nozzle design configuration will, of course, affect the aerodynamics of the vehicle. Furthermore, it should be noted that the exhaust nozzle becomes an inlet with another 180° rotation of the vehicle.

Finally we note that additional gains in performance of the rotary pulsejet engine might be secured by incorporating nozzles with variable exit area. Such a feature may greatly improve flight performance at supersonic speeds, and will certainly be required if the engine is to operate on several propellants: e.g., air or H_2(rocket mode).

H. ROTARY IRH PULSEJETS - FRESNEL PRIMARY OPTICS

This section reviews other variations of rotary pulsejet shuttlecraft which incorporate Fresnel lenses for primary optics, and ERH thrusters or IRH-"afterburning" thrusters for VTOL. Although both reflecting and refracting configurations can be envisioned (see Figure V-19), this study will concentrate on possibilities for refracting varieties.

Figure V-20 portrays a radial shuttlecraft with a "3-D" primary fresnel lens, based upon the 2-D delta shuttle shown earlier in Figure IV-3B. The refracting Fresnel lens simultaneously acts as an HEL optical window, high-pressure enclosure (for the IRH rotary pulsejet mode in Figure V-21), and the aerodynamic skin. This vehicle incorporates two sets of secondary optics: one which is engaged for the rotary pulsejet mode in lateral flight (SO#1); the other in VTOL (SO#2). The SO#1 optics are firmly attached to a central piston-actuated "foot" (looking much like a toad-stool stem), which drops down in preparation for a vertical landing with ERH thrusters. This process automatically disengages SO#1, allowing SO#2 to be rotated into position for reflecting the high-intensity beam towards the vehicle rim. (The vehicle under-surface rim is used as an ERH

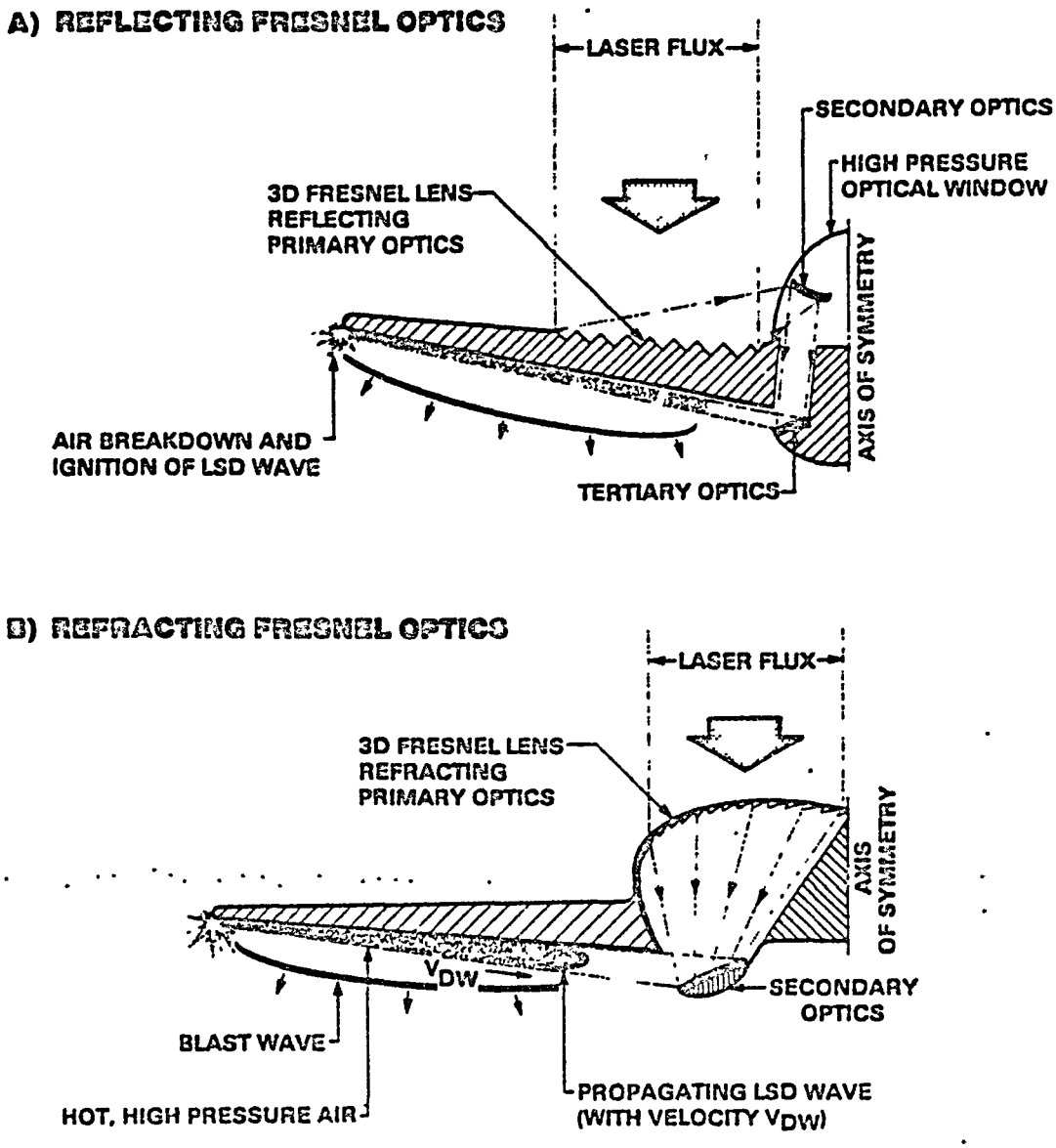

Figure V-19. Integration of Laser Power Into Rotary Pulsejets With Fresnel Optics (Cross-Sectional View, ERH Thruster Mode)

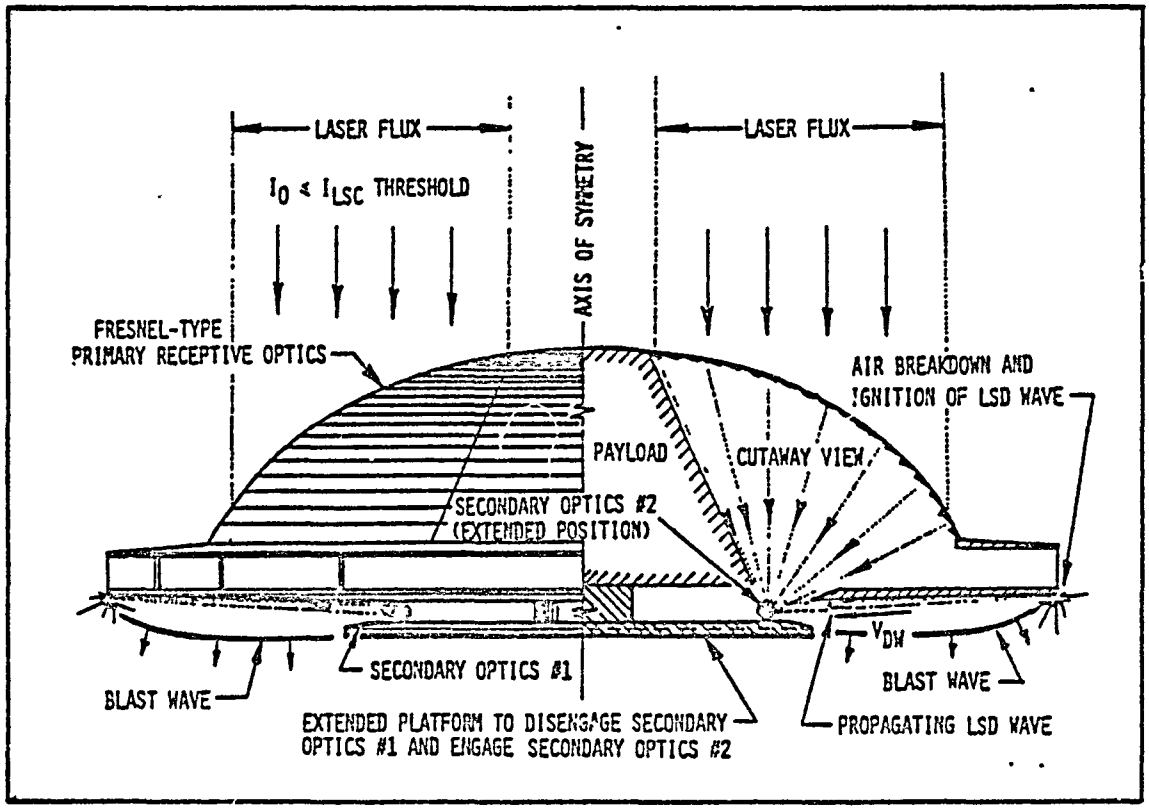

Figure V-20. Rotary IRH Pulsejet with Supersonic De Laval Nozzle (VTOL Mode with ERH Thrusters)

thruster.) Finally, note that the Figure V-20 vehicle has a conventional supersonic type of nozzle on the pulsejet propulsion tubes.

The vehicle "support stem" may also be designed to serve as a landing gear and entrance into the payload area. In addition, by a hydraulic piston action it could elevate the ERH thruster surfaces to a sufficient height above the ground prior to takeoff--in order to minimize injestion and recirculation of dust contaminants. Also, the stem could be easily isolated from the rotary motion of the vehicle. This would permit spinup and (de-spin) of the rotary pulsejet chambers while the vehicle is resting on the ground--a possible advantage for vertical takeoff (and landing) operations.

Figure V-21 is a variation of the Figure V-20 concept, shown in lateral flight towards the left side of the page. The conventional DeLaval nozzle of the rotary pulsejet engine is replaced with an expansion-deflection nozzle, thereby changing the appearance of the vehicle to resemble a "squashed" planet Saturn. As shown, the primary optic focuses the incident beam to a higher intensity upon the secondary optics (SO#1 in Figure V-20), which in turn causes the beam to focus at the geometric center of the pulsejet propulsion tube--thereby triggering air breakdown and the initiation of the IRH thruster cycle. An ERH thruster for VTOL could be integrated with either the central lower-surface area, or the circumferential ring/nozzle. This pulsejet configuration has one additional unique feature. When the expansion-deflection nozzle is rotated 180° to the "intake" position, the specific inlet geometry can serve as an efficient induction system for supersonic flight; the bow shock can be made to attach to the lower lip of the pulsejet chambers.

Figure V-22 portrays another rotary pulsejet configuration which incorporates a flat Fresnel primary lens and a supersonic "grid" nozzle. This shuttle concept takes on the appearance of a thick coin (or perhaps a short column section of a Greek temple). The vehicle is shown in high-speed flight towards the right side of the page. Note that the shuttle-craft has 12 pulsejet chambers arranged in pie-shaped fashion, and that the exhaust gases are rapidly expanded through a "grid" nozzle. (Grid nozzles

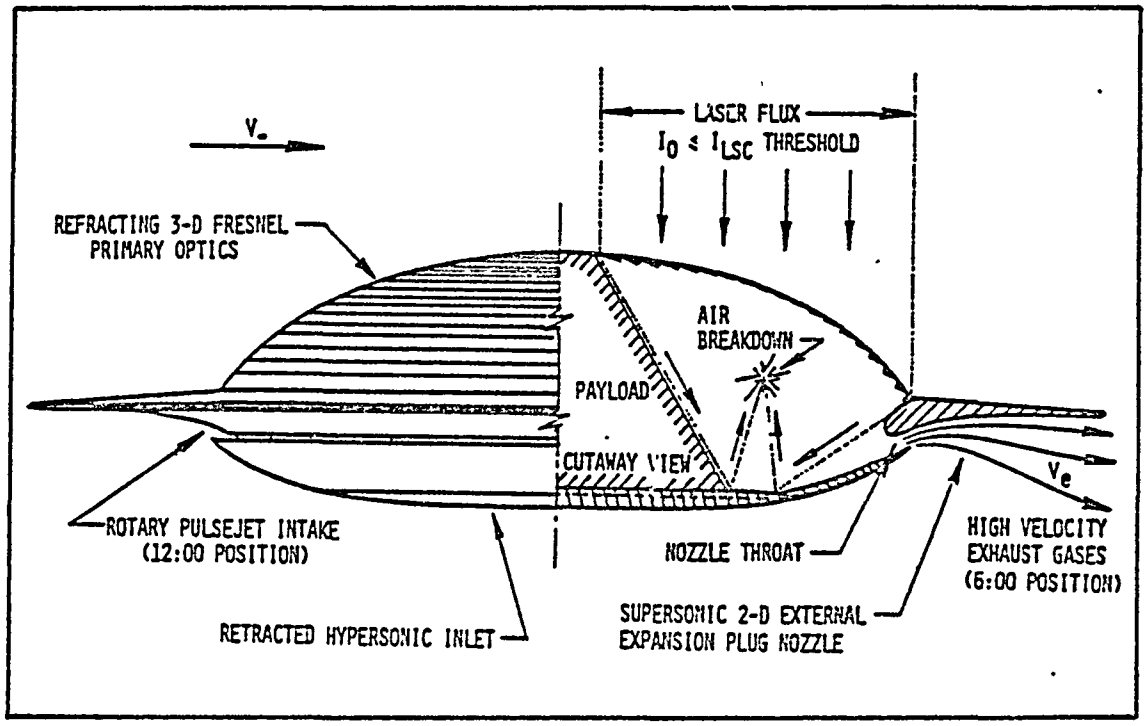

Figure V-21. Rotary IRH Pulsejet with Expansion/Deflection Nozzle (Translation Flight Mode)

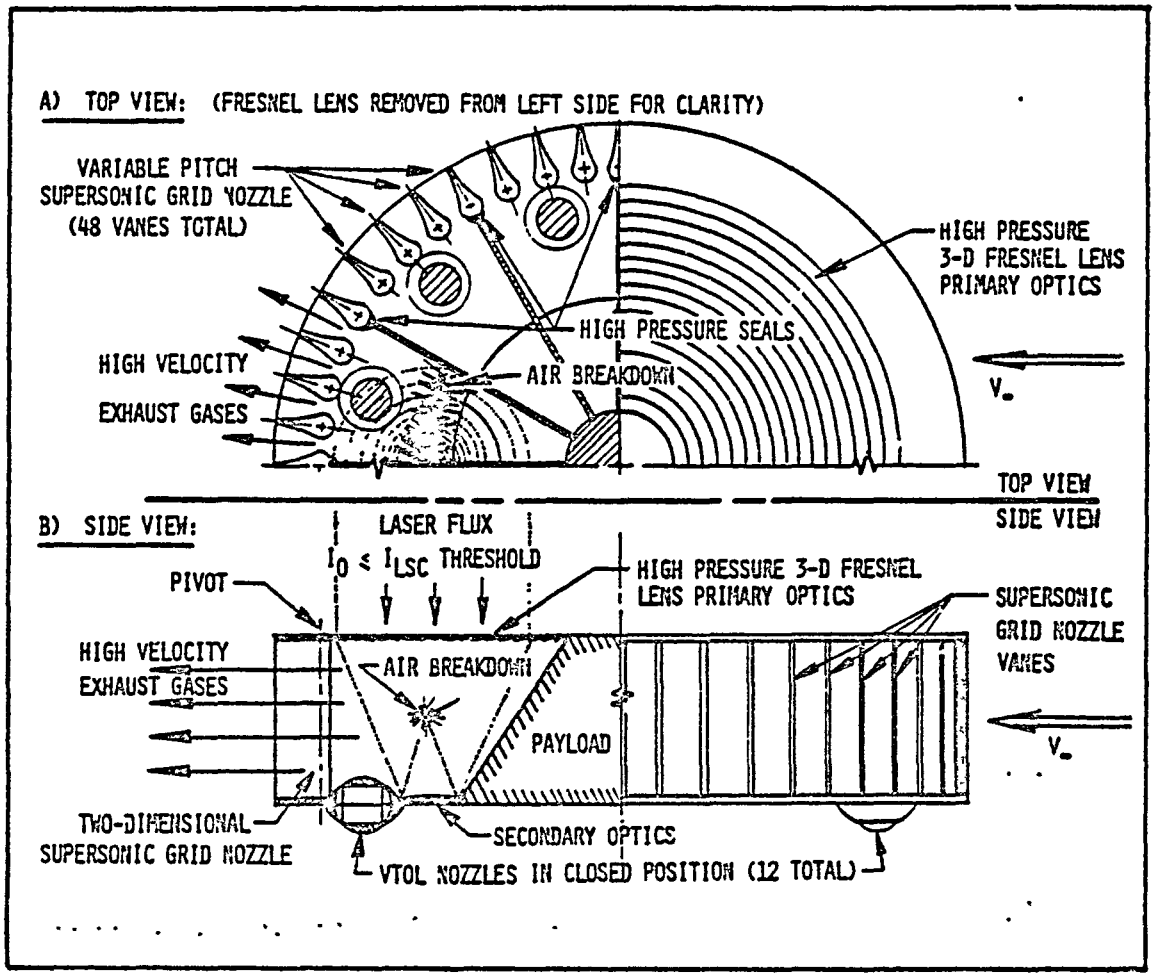

Figure V-22. Rotary IRH Pulsejet with Supersonic Grid Nozzle (Lateral Translation Flight Mode)

have been applied in current high-power chemical lasers to expand high-pressure flows to large supersonic velocities across unusually short nozzles.) The 2-D grid nozzle can be used to vector exhaust flow simply by turning the vanes uniformly in a clockwise or counter-clockwise direction (as viewed from the top); this creates a turbine wheel effect, and imparts a rotary motion to the entire vehicle.

Figure V-23 shows this shuttle in VTOL mode, with the grid nozzle rotated to the fully closed position; also, separate IRH engine exhaust valves (one per pulsejet chamber) are simultaneously opened in the lower surface of the vehicle. As described earlier, an auxiliary chemical-fueled turbo compressor would deliver high-pressure cold air to the IRH thruster tubes. To develop VTOL thrust, the remote beam (10X to 100X more powerful than the auxiliary engine) would superheat this cold air, using the IRH chambers as "afterburners." (Alternately, an additional set of secondary optics could enable the lower shuttle surface to be used as an ERH thruster.

I. DRAG REDUCTION MODE FOR ROTARY IRH PULSEJETS

Certain rotary pulsejet configurations, such as that shown in Figure V-24, may be able to utilize a unique mechanism for reducing drag at high supersonic to hypersonic velocities. One ideal application of this mechanism might be during a boost to planetary orbit when it would be preferable for a SSTO shuttlecraft to leave the sensible atmosphere much beyond 4 km/sec, in order to avoid excessive aerodynamic drag and heating. In this mode, it may be necessary to substitute internal liquid hydrogen propellant for air as the working fluid (i.e., reaction mass)--thereby converting the propulsion system into a rotary IRH rocket.

The details of this drag reduction scheme are portrayed in Figure V-25. With the pulsejet variable area nozzles in the partially closed position, a set of secondary optics can be engaged (see Figure V-26) to project very thin and wide, high-intensity beams laterally out any pulsejet chamber. If, for example, a single-pulsed beam is projected

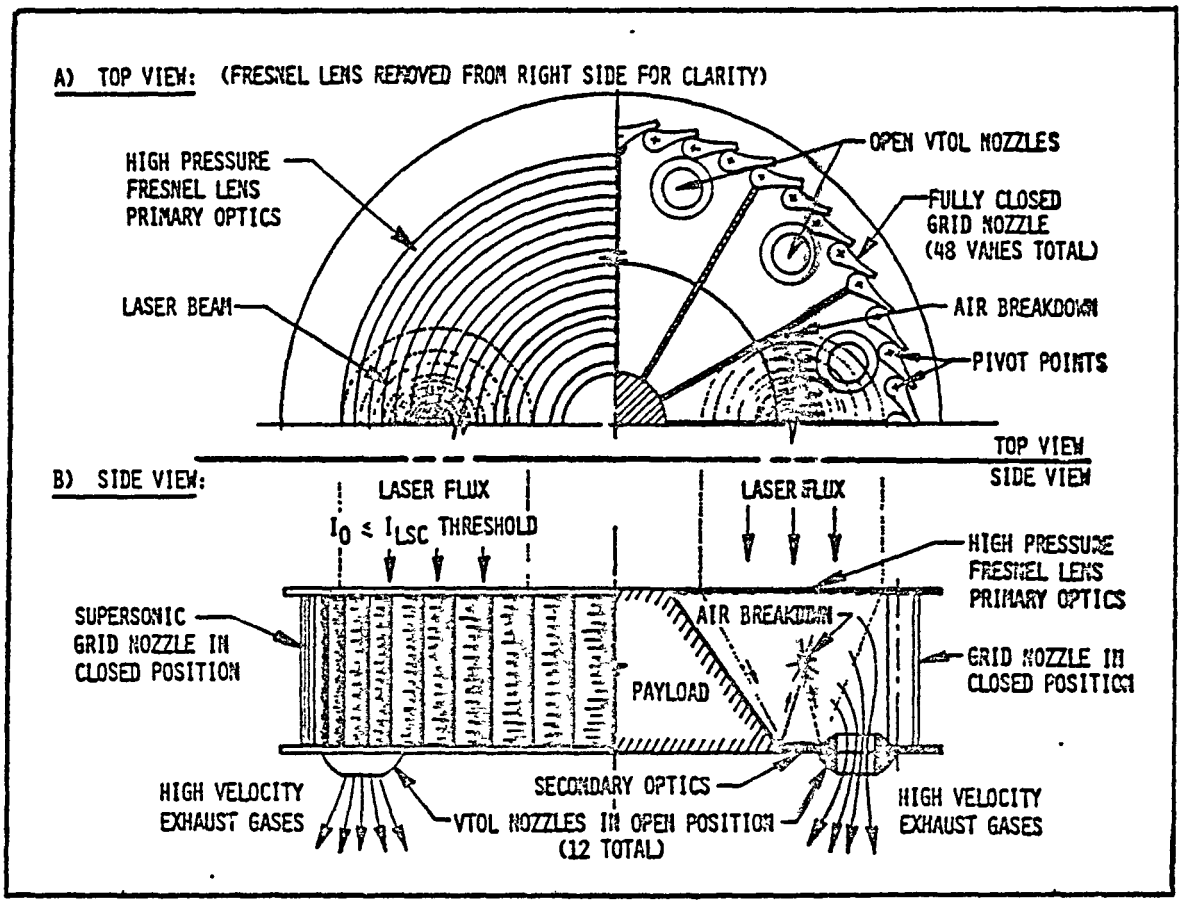

Figure V-23. Rotary Pulsejet Engine with Grid Nozzle - VTOL Flight Mode

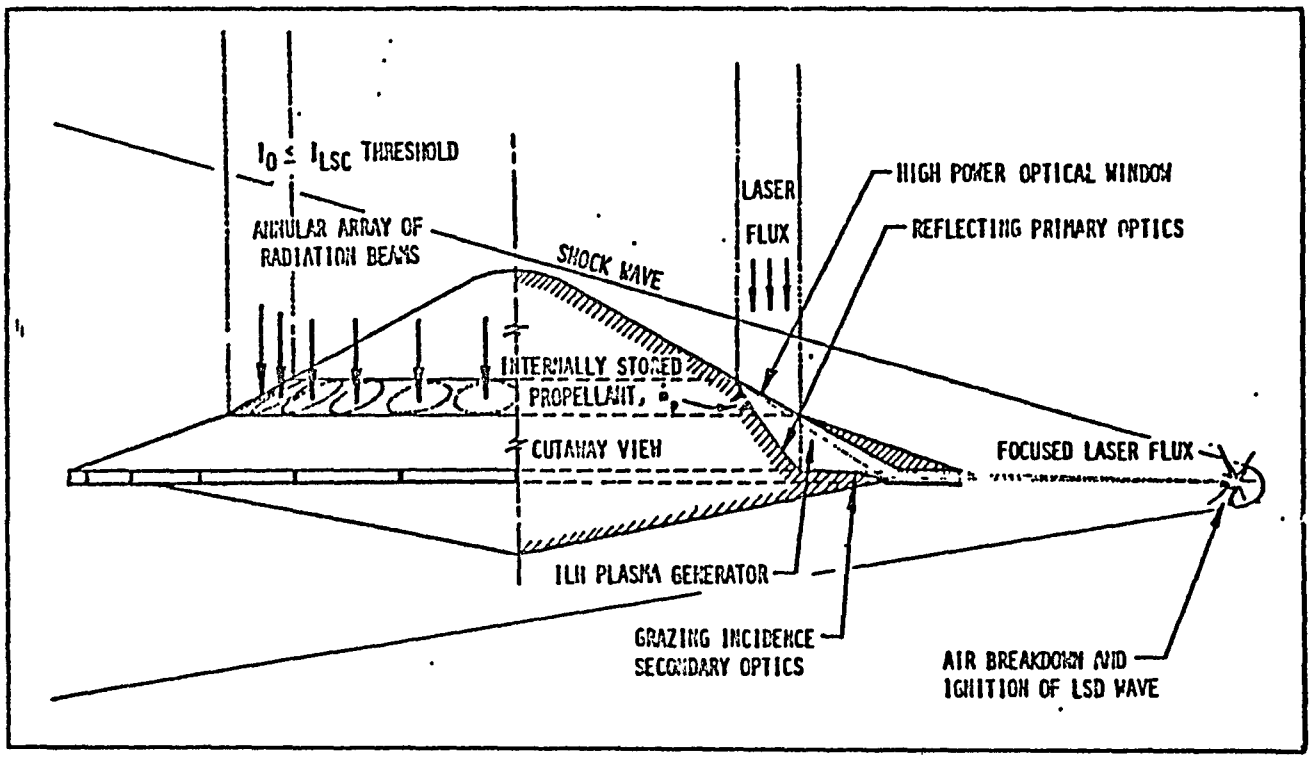

Figure V-24. Rotary IRH Pulsejet in Drag Reduction Mode

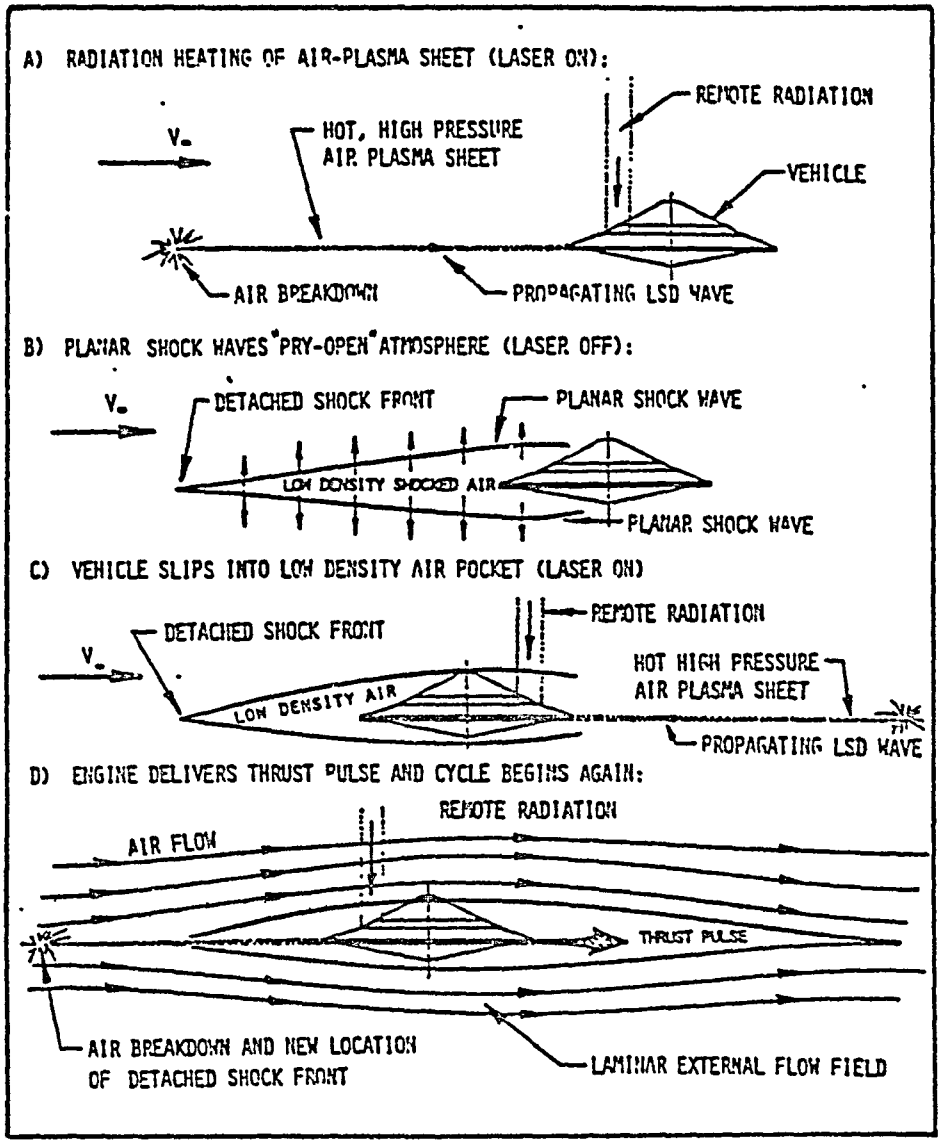

Figure V-25. Drag Reduction Scheme

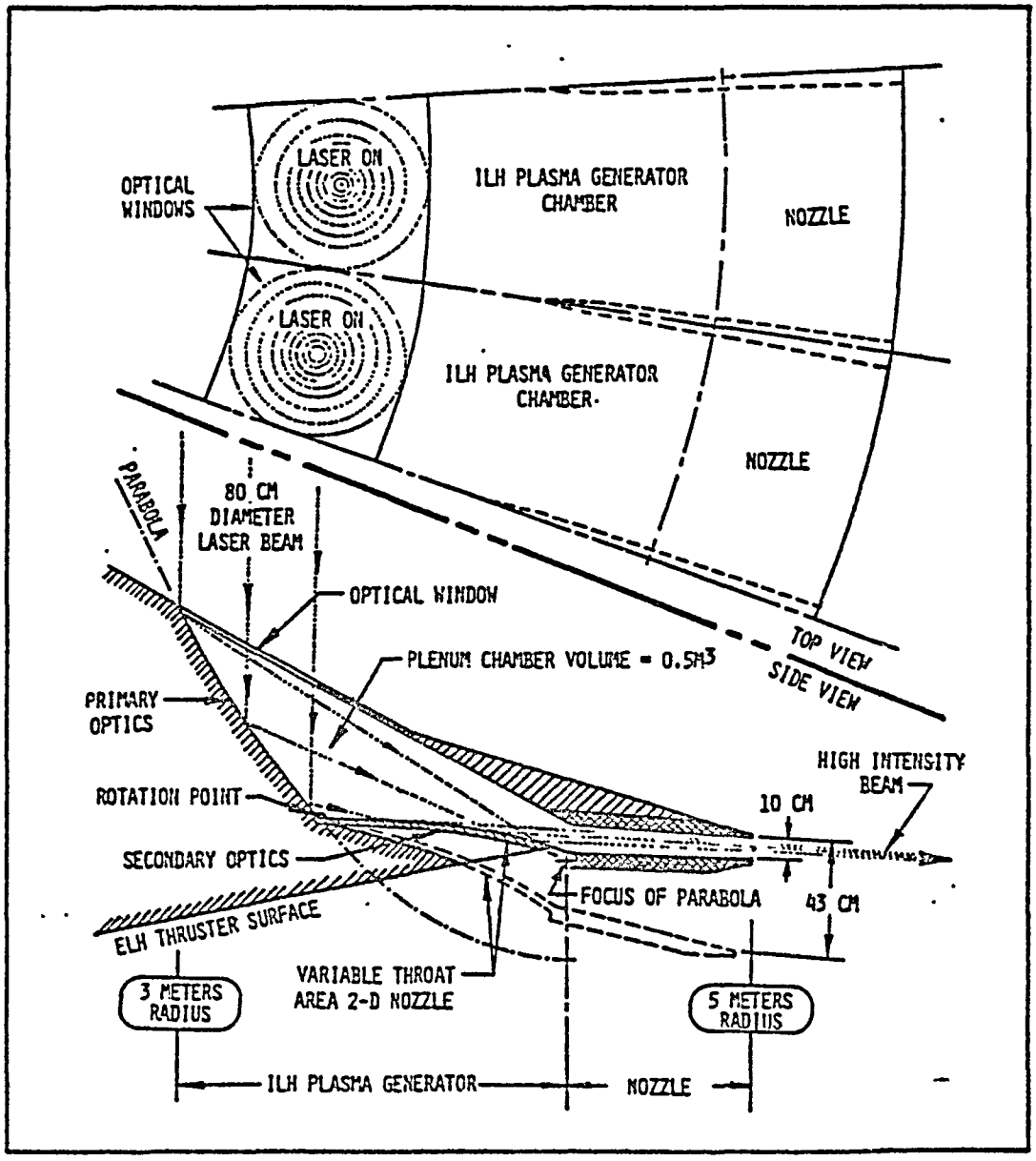

Figure V-26. Details of Pulsejet/Optics Geometry

forward in the direction of flight (Figure V-25A), then the beam will come to focus at some distance in front of the vehicle, trigger electrical breakdown, and ignite an LSD wave. Subsequently, the LSD wave will propagate rapidly back to the vehicle, and process all the air along its path into a hot, high temperature plasma. (Immediatley before the LSD wave enters the pulsejet nozzle, the laser pulse will be terminated.)

As the high-pressure plasma sheet begins to relax to ambient pressure, planar shock waves are driven off in both directions transverse to the vehicle flight path (Figure V-25B). The net result is that the forward projected beam effectively "pries open" the atmosphere and provides a lower density flight environment for the vehicle. With proper timing, the vehicle slips into this lower density air before the plasma temperature cools (see Figure V-25C), the "air pocket" pressure drops and high density surrounding air reclaims the temporary void. Hence, at hypersonic speeds, the vehicle may communicate its approach to the atmosphere by maintaining a detached shock at some distance in advance of the leading edge. The expanding plasma will do the work of pushing the atmosphere out of the way and thereby suppresses the formation of a strong bow shock and the associated wave drag.

On the back side of the rotary engine, the reverse process is carried out to preclude a turbulent collapse of the atmosphere. Unlike the front side, the LSD wave is allowed to propagate into the pulsejet chamber and heat the hydrogen gas before the laser pulse is terminated. The high-pressure gases are then expelled from the chamber with great force, and thereby propel the vehicle forward until the next pulsejet chamber rotates into proper "ignition" position (Figure V-25D). By this process, a smooth quasi-laminar flow may be provided about the vehicle, given the expenditure of some laser energy.

J. SPHERICAL ROTARY IRH PULSEJET CONFIGURATION

This section presents a whimsical point of departure from the compact, heavier-than-air design philosophy of rotary pulsejet configurations presented previously. Figure V-27 portrays the concept of a spherical laser-propelled vehicle which could "float," neutrally-buoyant in dense, low altitude planetary atmospheres. The intent of this approach is to minimize laser energy expenditure required in exploring a planet from aerial platforms.

The primary structure of this laser-propelled rigid airship would be a lightweight geodesic truss framework into which numerous refracting primary lenses and IRH pulsejet chambers would be mounted. About two-thirds of the exterior spherical surface would be covered with pulsejets, the rest with primary receptive optics. As shown in Figure V-27, the payload would be located in the upper one-third of the sphere, arranged in a toroidal-shaped volume that is clearly out of the internal laser beam path. The sphere would be filled with helium; the exterior skin would serve as the vehicles "gas bag."

The primary receptive optics could be of the Fresnel variety. However, considering the long focal path to the small secondary optics (located at the geometric center of the vehicle) "simple" 3-D refracting varieties might also be used. (The inspiration for this "compound" primary lens concept comes from the structure of an insect eye--pictured in Figure V-28.) Incident laser intensities would be low enough to permit the use of lightweight plastic film materials--with the appropriate laser wavelengths. The compound primary lens would be sufficiently versatile to receive any orbital beam with a zenith angle of ± 30 degrees (i.e., measured from a line perpendicular to the planetary surface.

As indicated in Figure V-27, the configuration of individual pulsejet engines is incredibly simple, essentially taking a paraboloid-of-evolution geometry introduced earlier in Figure III-10. The major difference is, of course, that the laser beam enters the pulsejet chamber from the "upstream" end, through a lightweight refracting "tertiary" Fresnel lens--which is of

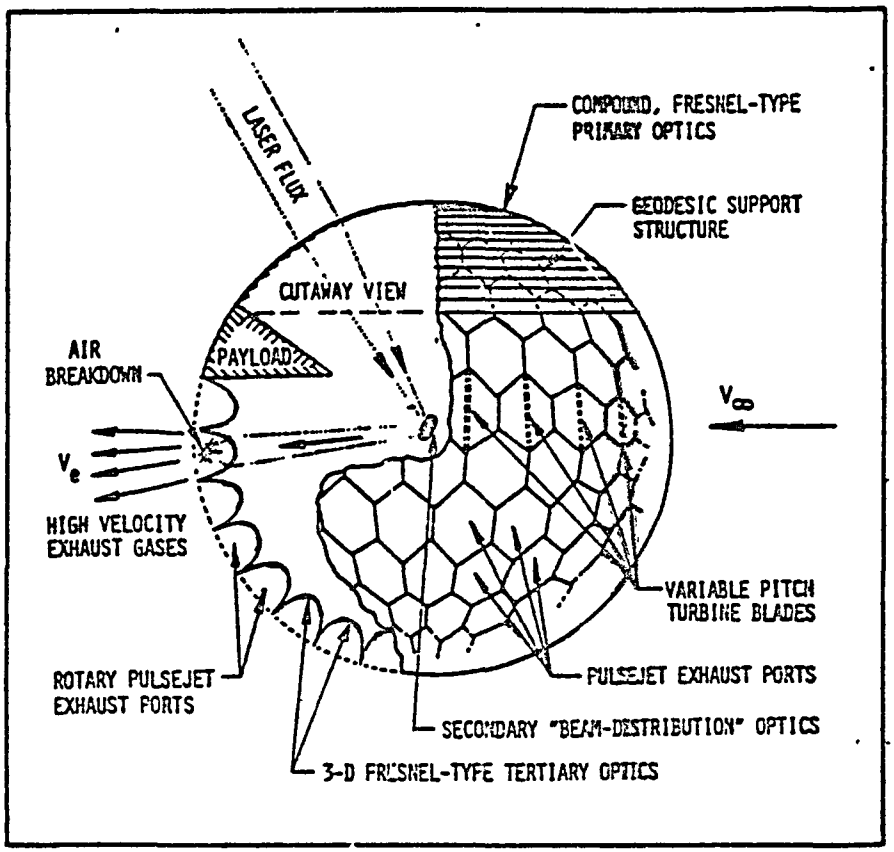

Figure V-27. Spherical Geometry Rotary IRH Pulsejet - Translation Mode

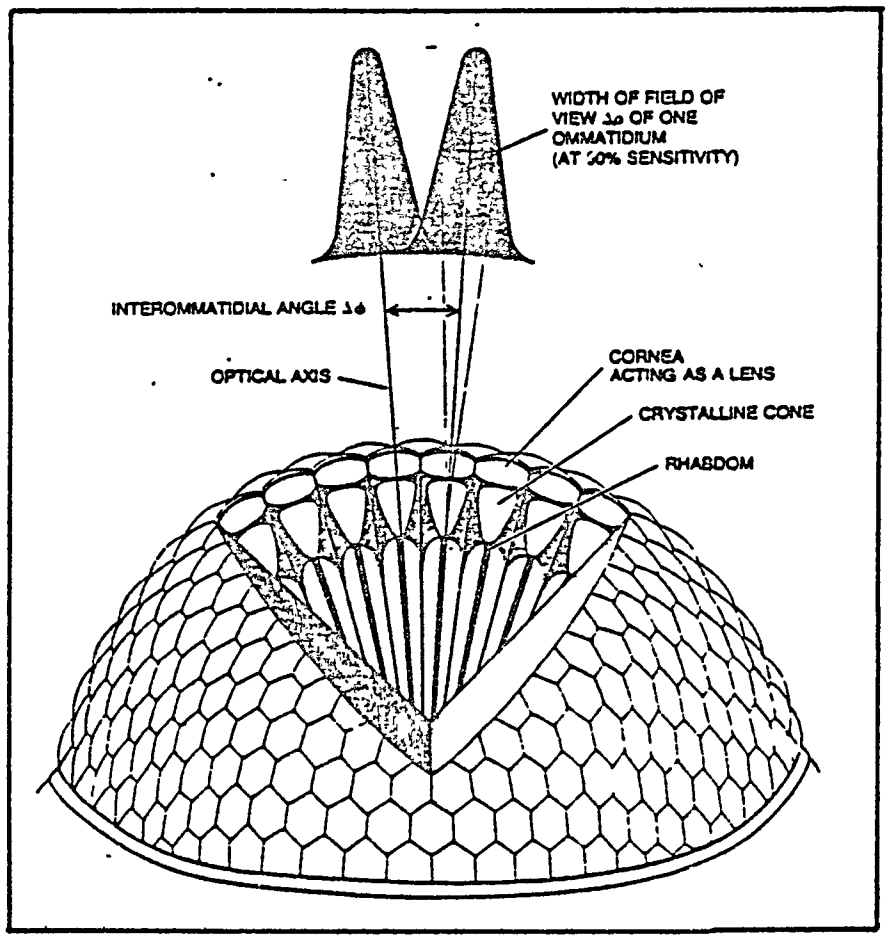

Figure V-28. Structure of insect eye determines how much detail the eye is capable of seeing. Each ommatidium has a cornea that also serves as a lens focusing light through a transparent cone onto a light-sensitive element: the rhabdom. The interommatidial angle is the angle between the optical axes of the adjacent ommatidia. The field of view of each of the ommatidia is defined as the angle subtended where the sensitivity has fallen to 50 percent of its maximum value. (From Scientific American)

integral construction with the pressure chamber itself. Individual pulsejet engines would operate with a very low duty cycle (made possible by their great number) so that they may be cooled radiatively. Thrust is generated by laser-induced gas-breakdown and the formation of a radiation-driven detonation wave, which ejects all the air residing in a pulsejet chamber.

One could imagine that the secondary reflective "beam-distribution" optics might be articulated much like an IBM typewriter ball. A continuous train of laser pulses would be concentrated upon the multi-faceted secondary optics, which in turn, would reflect the beam sequentially at a high rate to a great number of pulsejets. As the vehicle slowly rotates, all the cold thruster tubes can be accessed. (Rotary pulsejets located about the sphere's equator could be fitted with adjustable-pitch turbine blades to impart a rotary motion to the vehicle.) The shuttle could thereby be propelled in any desired direction, either lateral or vertical, simply by activating the appropriate pulsejets.

CHAPTER VI
AIR-BREATHING LASER-ELECTRIC PROPULSION OF RADIAL SHUTTLECRAFT

This chapter introduces two concepts for air-breathing laser-electric propulsion of radial shuttlecraft. The first concept requires repetitively pulsed (RP) laser radiation to drive an RP "MHD-fanjet" with variable intake diameter. The second utilizes continuous wave (CW) laser radiation to drive a quasi-steady "MHD-fanjet" accelerator with fixed inlet diameter.

A. PRINCIPAL ELEMENTS OF MHD-FANJET ENGINE

Principal elements of the MHD-fanjet engine are schematically illustrated in Figure VI-1. Basically, the engine produces thrust by facilitating momentum exchange with the atmosphere; i.e., mechanical energy is transferred from IRH rocket exhaust gases to the air inducted through an annular MHD-fan component. As shown in Figure VI-1, incident laser power is first received through high-power optical windows "O", then concentrated within laser-heated rocket burners "H" by reflective primary mirrors. The laser energy is absorbed by a high-pressure gaseous working fluid (e.g., H_2 fed from internal tanks) which subsequently expands to a high velocity. The partially ionized, high-pressure gases drive MHD generators "T" into action, which in turn produces electric power to excite the MHD-fan "F". The annular fanjet developes thrust by propelling an electromagnetic "actuator disk" into the annular accelerator volume. A supersonic diffuser section "D_s" for MHD fan air is provided by the entire vehicle forebody. It is useful to note that MHD generator gas conductivity, pressure and temperature can be held constant and independent of flight Mach number, since it is fed with internal propellants.

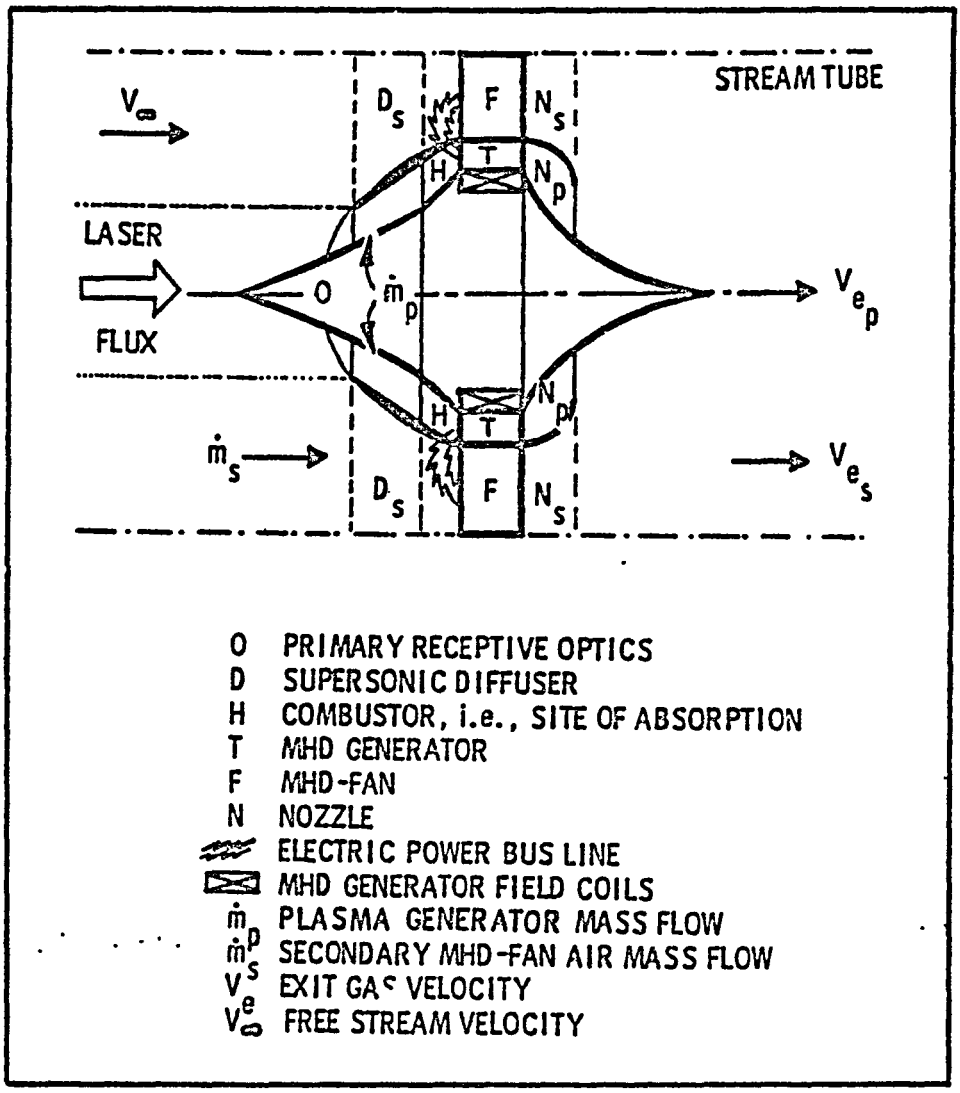

Figure VI-1. Principal Elements of MHD-Fanjet Engine

B. BRIEF INTRODUCTION TO MHD-FANJET PHYSICS

Basically, the MHD fanjet engine uses Lorentz forces to couple reaction thrust from an accelerating electric-arc "actuator-disk" to the vehicle, i.e.,

$$F_m = j \times B = \left(\frac{\mu_o J^2}{4\pi^2 \delta}\right)\left(\frac{1}{r^2}\right) \qquad (1)$$

where j is the electric current density within the actuator disk, δ is the actuator disk thickness, μ_o is the permeability of free space, B is the strength of the self-induced magnetic field, and F_m is the electromagnetic body force on the annular MHD fan actuator disk at the radius "r". Note that since the body force is a function of $1/r^2$, the slipstream air closest to the vehicle will be accelerated with the greatest force--a condition necessary for minimization of the wave drag created at supersonic flight speeds.

Figure VI-2 displays the basic thermodynamic cycle of the MHD fanjet which is similar to that of a conventional air-turborocket (see curve "b"). The incorporation of an MHD generator instead of a turbine makes it possible to use a rocket-type gas generator that delivers gas at a significantly higher initial energy than that envisioned for turborockets (which would use conventional turbines); this permits a higher utilization of internally stored propellant. Hence, substantially improved levels of thrust and specific impulse (e.g., 10,000 seconds) may be attained. As indicated in Figure VI-2, a small mass flow of primary IRH rocket fluid $\dot{m}_p$ (hydrogen) experiences a great reduction in enthalphy Δh_p which is then transferred to the much larger mass flow rate of secondary MHD-fan air $\dot{m}_s$ (i.e., greater by a factor of 100 or more),--thereby raising the fan air enthalpy by a small about Δh_s, such that $\dot{m}_p \Delta h_p \approx \dot{m}_s \Delta h_s$. The result is a great reduction in stagnation pressure of rocket exhaust gases and a small increase in stagnation pressure of fan air during the electrical energy transfer process.

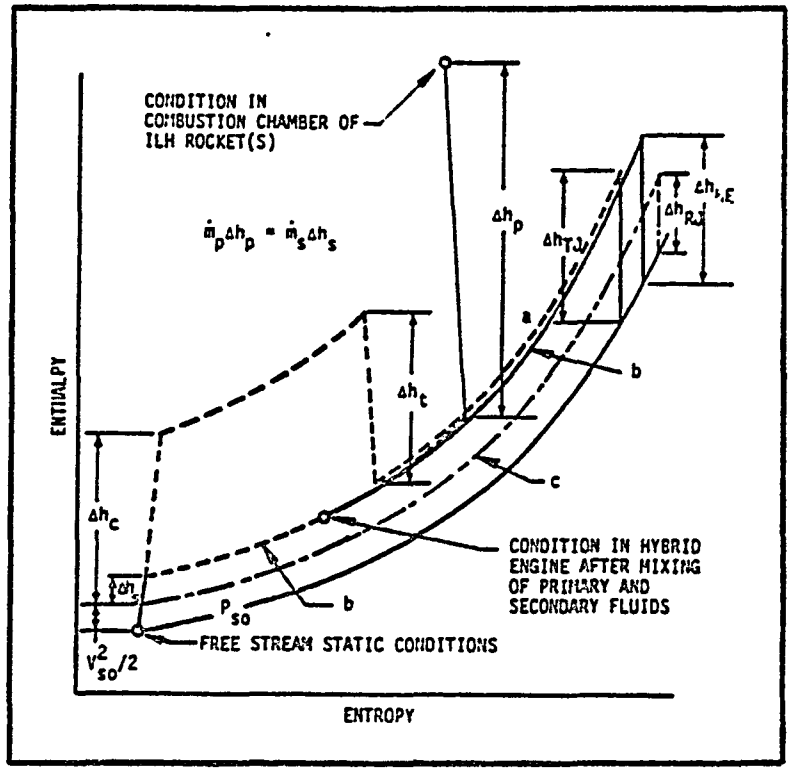

Figure VI-2. Mollier Diagram for MHD-Fanjet
(From Reference 7)

The overall laser-power-to-thrust-power conversion efficiency η_o for the MHD fanjet is equal to the product of the efficiencies of each component, i.e.,

$$\eta_o = \eta_{AD}\ \eta_{MG}\ \eta_{FAN}\ \eta_{PE} \quad (2)$$

$$= (.92)\ (.51)\ (.90)\ (.95) = \underline{40\%}$$

where AD, MG, and FAN refer to the actuator disk, XMHD generator, and MHD-fan; η_{PE} is the propulsive efficiency of the engine. Typical efficiencies for each component are listed below Equation VI-2; all together, they indicate an overall efficiency of 40 percent. It is assumed that 8 percent of the laser pulse energy is required to create the actuator disk in the first pace, so η_{AC} is set to 92 percent. The XMHD generators are assumed to be 51 percent efficient. The choice of efficiencies for the rest of the components is justified below.

The MHD-fan may be likened to a propeller or rotor which is designed for optimum efficiency of operation in the rarefied upper atmosphere at supersonic to hypersonic Mach numbers. The basic propulsion principle has been demonstrated with MHD-augmented shock tunnels[1-4] which have shown that it is feasible to add significant enthalphy to hypersonic flow directly. MHD-augmentation enables most of the input electric energy to be added as direct kinetic energy rather than thermal energy, such as by arc heating. Subsequently, the resulting gas stream is at a higher total pressure than would have resulted from other methods--which normally convert much of this available electric energy into chemical dissociation of the moving air stream. Such hypersonic wind tunnels have demonstrated electrical efficiencies with air up to 90 percent.

The theoretical maximum efficiencies attainable by the MHD-fanjet itself may be assessed by the use of simple Rankine-Froude momentum theory.[5] Basically, this theory assumes that the fan disk may be physically replaced by an "actuator disk" having an infinite number of blades

and able to create uniform change in velocity of the air stream flowing through the disk. The thrust acting on the disk is then given by,

$$F = m \frac{dV}{dt} = A \rho (V + \Delta V/2) \Delta V, \quad (3)$$

where A is the disk area, ρ is the density of the airstream, V is the speed of advance, and ΔV is the induced velocity change. The average change in pressure over the disk is often referred to as the disk loading, and is equal to F/A.

The ideal propulsive efficiency of the MHD fanjet is a measure of how efficiently the engine propulsive energy is used; it is calculated by comparing the thrust power output to the power input. The useful thrust power output is simply the thrust multiplied by the velocity of advance of the actuator disk, i.e., F V. The power input to the actuator disk is the thrust produced by the pressure of the air on the disk multiplied by the airflow velocity through the disk, i.e., $F(V + \Delta V/2)$. The ideal propulsive efficiency, η_{PE} is then given by

$$\eta_{PE} = \frac{\text{Useful Thrust Power}}{\text{Available Propulsive Power}} = \frac{FV}{F(V+\Delta V/2)} \quad (4)$$

The coupling coefficient of an actuator disk is equal to the ratio of thrust to available propulsive power, and in equation form appears as

$$C = \frac{F}{P} = 10^5/(V + \Delta V/2) \quad (5)$$

where C is the coupling coefficient in dynes/Watt and V is measured in m/s. Equation 5 is plotted in Figure VI-3 as a function of flight velocity V, assuming (for example) that the induced velocity change ΔV is equal to 10 percent of V. (This condition would result in an ideal propulsive efficiency of 95 percent.)

In order to secure high propulsive efficiencies and good coupling coefficients over a great range of supersonic flight speeds, the MHD-fan must be able to vary its actuator disk diameter, pulse repetition

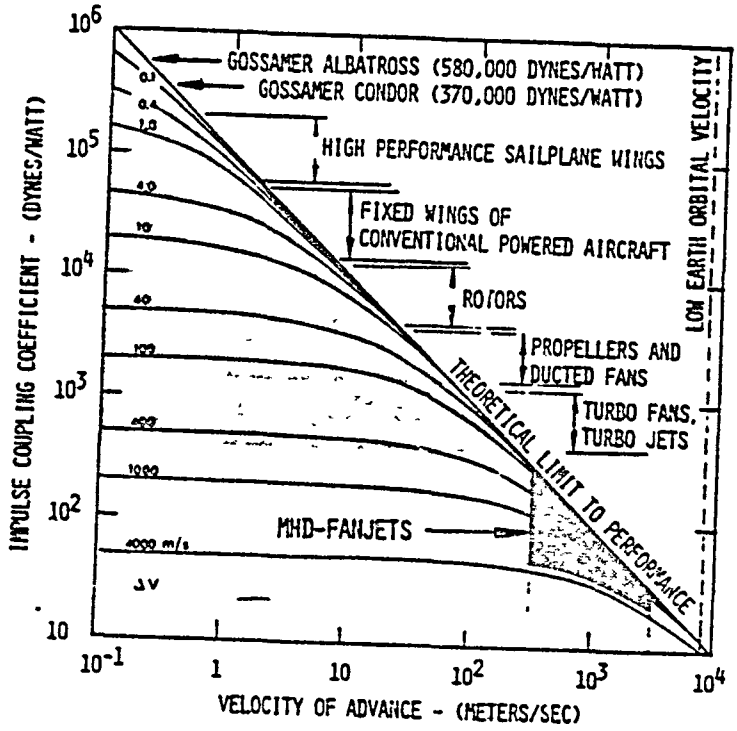

Figure VI-3. Coupling Coefficient vs. Velocity of Advance for Air Breathing Engines

frequency, and disk loading. The MHD-fan electric load will change significantly with actuator disk diameter and flight velocity. Therefore, the gas state conditions (i.e., pressure, temperature, PRF, etc.) delivered by the IRH plasma generator to the XMHD generator must be varied also. Hence, XMHD generator output would be changed in accordance with a precise "acceleration schedule" similar in concept to that used in present day turbojet engines to prevent "flameout" when the power loading is changed drastically. Such precise operations must be computer controlled and monitored because of the numerous variables involved.

Coupling coefficient vs. the velocity-of-advance for the complete range of air-breathing propulsive engines (including aerodynamic lifting surfaces, which can be interpreted in the light of air-breathing thrust-augmentation devices) is portrayed in Figure VI-3. Since coupling coefficients anticipated for the MHD fanjet are in the range of 30-280 d/w_e, they fall into the regime just below turbofans and turbojets. Shown in Figure VI-4 are the coupling coefficients vs. disk loading for these same airbreathing engines. It is interesting to note that the MHD-fanjet creates an entirely new class of its own--with coupling coefficients less than turbojets, but disk loadings more typical of large helicopters rotors (e.g., 1 to 50 lbs/ft^2 at altitudes of 16 km and higher).

C. REPETITIVELY-PULSED "MHD-FANJET" CONCEPT

Figure VI-5 shows a cutaway view of an RP MHD-fanjet-propelled shuttlecraft. Relatively minor revisions to the basic rotary pulsejet geometry are required to incorporate the RP MHD-fanjet engine as shown in the cutaway view, Figure VI-6. First, the 2-D exhaust nozzles from the IRH plasma generators must be provided with a mechanism to vary the minimum cross-section "throat" area and nozzle expansion ratio--in order to operate successfully with both air and hydrogen working fluids. Secondly, the nozzles must also serve as RP MHD generator ducts--complete with wall electrodes, wall insulators, and strong magnetic field coils (e.g., 2 to 10 Tesla) which can be energized on demand, as shown in Figure VI-7. (An

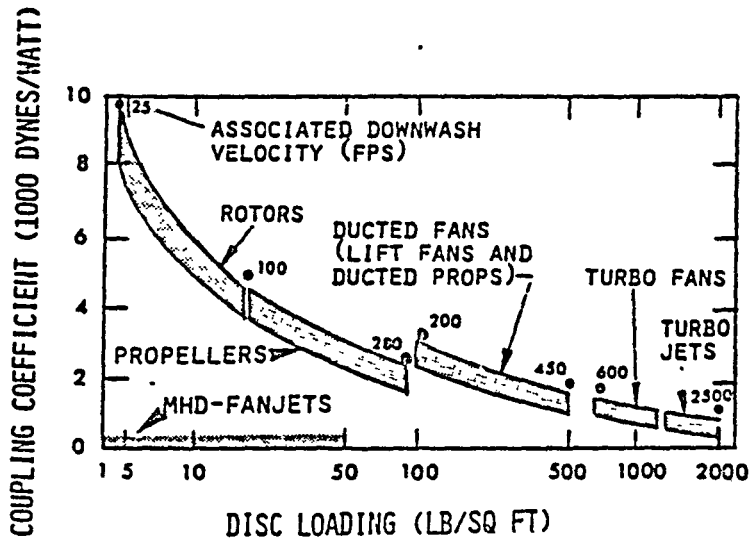

Figure VI-4. Coupling Coefficient vs. Disk Loading (From Reference 8)

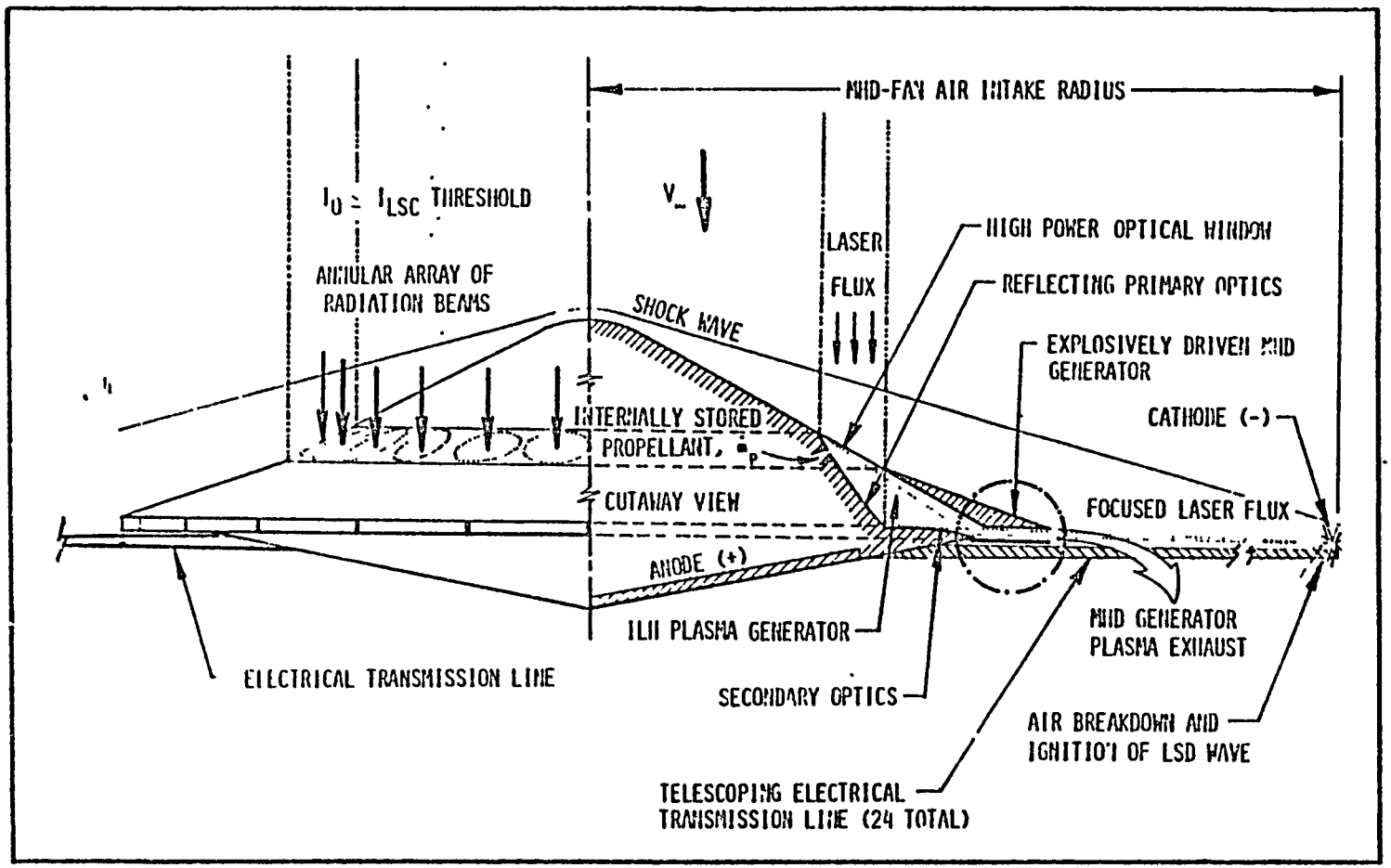

Figure VI-5. Cutaway View of Hypersonic MHD-Fanjet

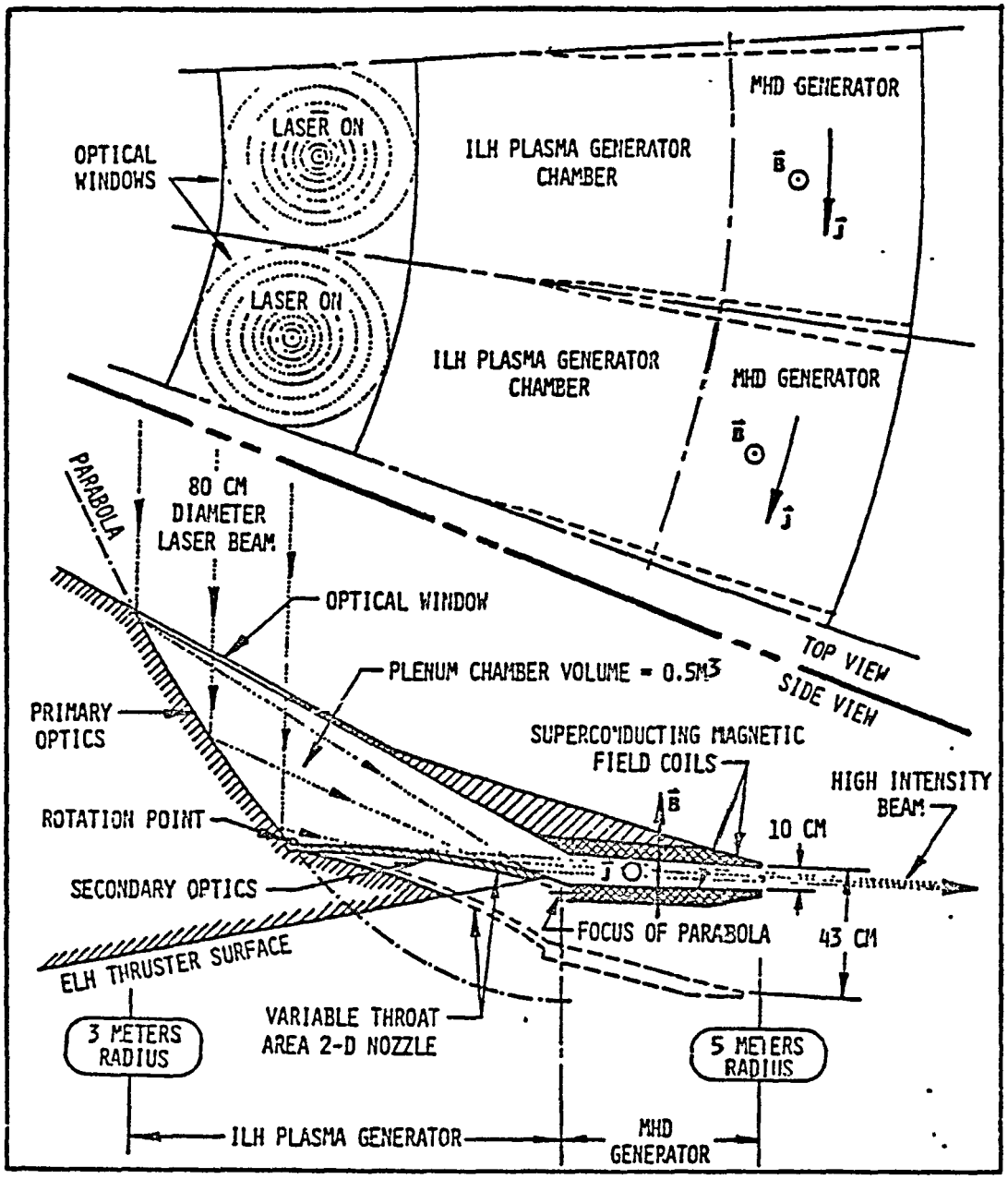

Figure VI-6. IRH Plasma Generator Geometry

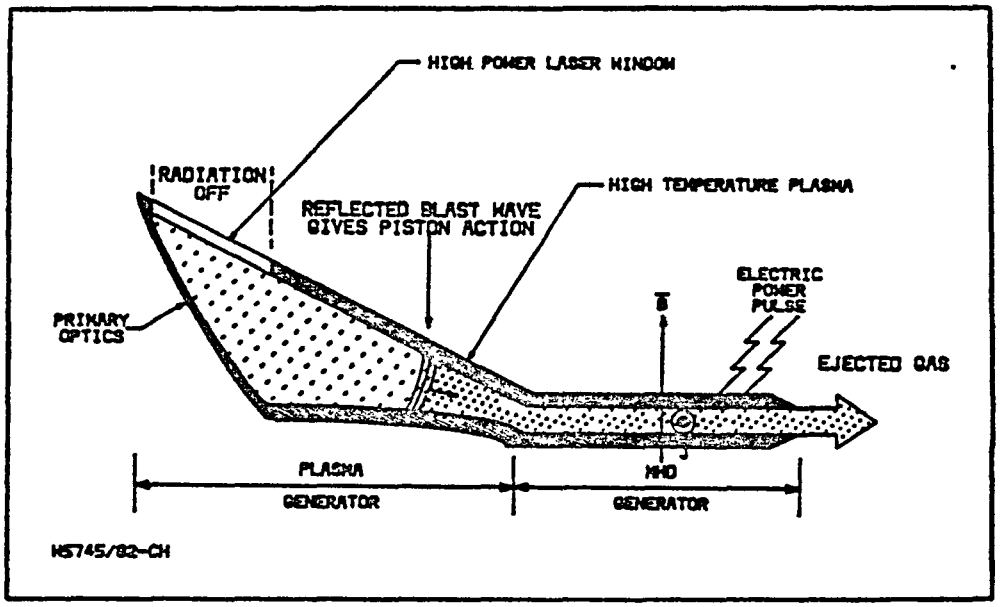

Figure VI-7. MHD Radiation-to-Electric Power Conversion

analysis of this device may be found in Appendix B.) Third, the vehicle structure must be modified to incorporate telescoping "fan" electrodes (which might also be superconducting). Fourth, a small rim portion of the vehicle undersurface must also serve as an anode electrode for the MHD-fan accelerator. Finally, as shown in Figure VI-6, the lower interior surface of the radiation superheater walls (i.e., downstream of the primary optics and upstream of the nozzle throat) becomes a grazing incidence secondary optic.

In the air-breathing rotary pulsejet mode, the variable area nozzle is in the wide open position; the primary opitic brings the beam to a line focus midway between the throat section. When this nozzle is slightly closed in preparation for the MHD-fanjet propulsion mode (which requires hydrogen propellant instead of air in the radiation superheater), the secondary optic is automatically engaged. As a result, the incident beam no longer comes to a line focus at the nozzle throat, but is re-projected by the secondary optics to focus at the outer ends of the transmission lines. The high-intensity focused radiation causes the air to electrically break down along the entire perimeter of the MHD fan. This triggers the initiation of the MHD-fan propulsion cycle shown in Figure VI-8, and described below.

At the beginning of each laser pulse, then, laser-induced air breakdown is triggered at the endpoints of the transmission lines, bathing them in a dense non-equilibrium ionized plasma. As this plasma toroid expands to make solid electric contact with the ends of the transmission lines, it acts as a large surface-area annular, gaseous-cathode electrode for the MHD-fan as portrayed in Figure VI-8A. By this mechanism, the effective electrode area is increased by several orders of magnitude over that represented by the hollow cathodes themselves, which are located at the endpoints of all transmission lines.

Following laser-induced air-breakdown, LSD waves are ignited at this MHD-fan slipstream tube perimeter and propagate inward at a high velocity in the rarefield upper altitude air. As pictured in Figure VI-8A, the propagating LSD waves slice a high-conductivity plasma disk through the

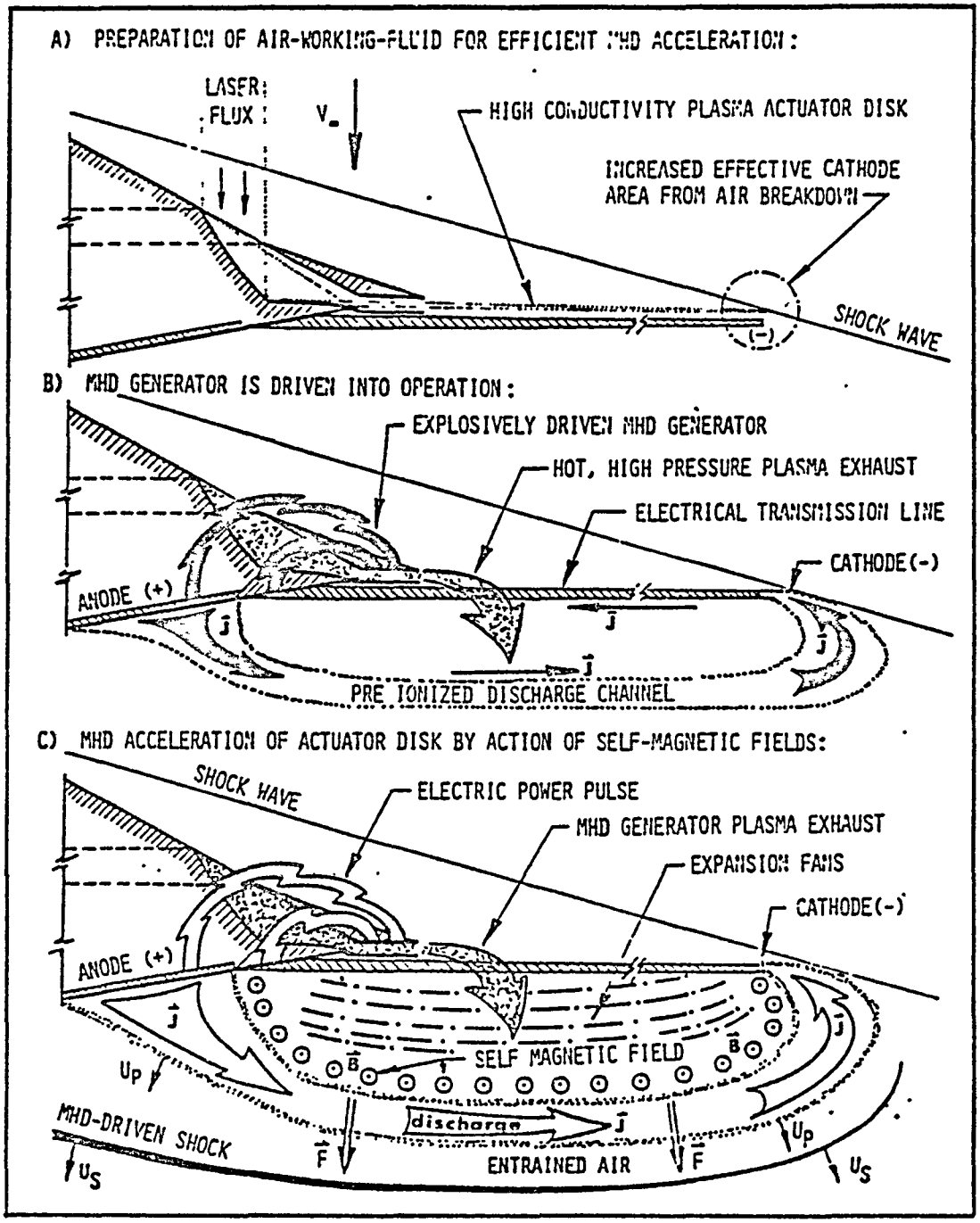

Figure VI-8. MHD-Fanjet Thrust Cycle

neutral MHD-fan airflow and thereby prepare the disk for electromagnetic acceleration. As the LSD waves arrive within the MHD generator ducts, they reflect off the secondary optics and propagate into the ILH combustion chambers. LSD wave heating of the injected H_2 propellant then produces a high temperature and pressure (e.g., 140 atmospheres) non-equilibrium ionized plasma, which then explosively drives the MHD generator into operation as the plasma expands down the duct. As illustrated in Figure VI-8B, the resultant high-power, short-duration electrical burst is then short-circuited through the high-conductivity "actuator disk."

As shown in Figure VI-8C, MHD acceleration of the high-conductivity actuator disk occurs by the action of self-magnetic field "Lorentz" forces. Following the transient startup process of the MHD generator, the initial MHD-fan electric current (arc) intensifies through the minimum inductance position predetermined by the laser-induced air-breakdown. Electrons are extracted from the cathode electron plasma, fall through the cathode-anode voltage drop and finally thermalize on the anode electrode. The electrical conductivity of the disk is expected to improve as the arc moves from an initial non-equilibrium ionized condition into a final thermalized phase when the current intensifies to its peak value. As the disk is accelerated, it entrains mass in "snow-plow" fashion ahead of the advancing current sheet.

Note that each cathode electrode of the several explosively-driven MHD generators can be electrically isolated from the others, and that great care in the design of the accelerator is given to first preparing a uniform, high-conductivity current path for the primary arc discharge. Hence, the MHD-fan accelerator is likely to avoid the "spoke discharge" geometry which severely degrades the theoretically attainable performance predicted for the axisymmetric, self-magnetic field category of MHD thrusters.

Because of the enormous rate at which electrons will thermalize on the anode electrode (10^6 to 10^7 Amperes), the anode may require transpiration or ablative cooling. For an ablatively cooled anode which gives off high-conductivity vapors, the effective anode electrode area may be substantially increased by recirculation of the vapors within the low-pressure

base area. As a result, the electron scavenging abilities of the thruster anode may be significantly improved over the non-ablative approach.

In summary, the RP MHD-fanjet thruster permits an RP electric current of sufficient intensity to accelerate the unionized slipstream air by driving an MHD shock wave into this fluid, entraining mass ahead of an electrically conducting wave.

D. QUASI-STEADY "MHD-FANJET" CONCEPT

This MHD-fanjet would be driven by a continuously-driven version of the RP laser-heated MHD generator pictured in Figure VI-7. Basically, the detailed optics and chamber geometry would be altered to maintain an LSC wave plasma just upsteam of the throat, right at the entrance to the MHD generator--as shown in Figure VI-9. The working fluid would be unseeded hydrogen, although He, Ar, or Ne could be considered. Continuous peak gas temperatures could range from 15,000 to 20,000 K. The upper and lower insulating walls of the MHD generator housing might be designed to function as high-temperature transparent "light bulb" radiators--in order to reduce the wall cooling load. It is quite possible that this radiant heat flux might be reduced to acceptable levels (i.e., and still maintain good laser-to-electric conversion efficiency) simply by proper design of the plasma "torch" properties (i.e., temperature, pressure, density, etc.), physical size, and overall geometry.

A shuttlecraft design which might be suitable for the CW laser-heated MHD generator and a quasi-steady MHD-fanjet engine is pictured in Figure VI-10. (It is a derivation of the earlier radial configuration portrayed in Figure V-2.) The propulsive CW laser beam would be, in this case, absorbed within a confined rocket plasma generator chamber after coming through a material window, as indicated in Figures VI-9 and VI-10.

Two different thruster modes of operation would be used by this MHD-fanjet--depending upon flight altitude and velocity (basically, low vs. high). Both modes fall within the class of "self-modulated" MHD accelerators, which are driven by continuous direct-current power supplies;

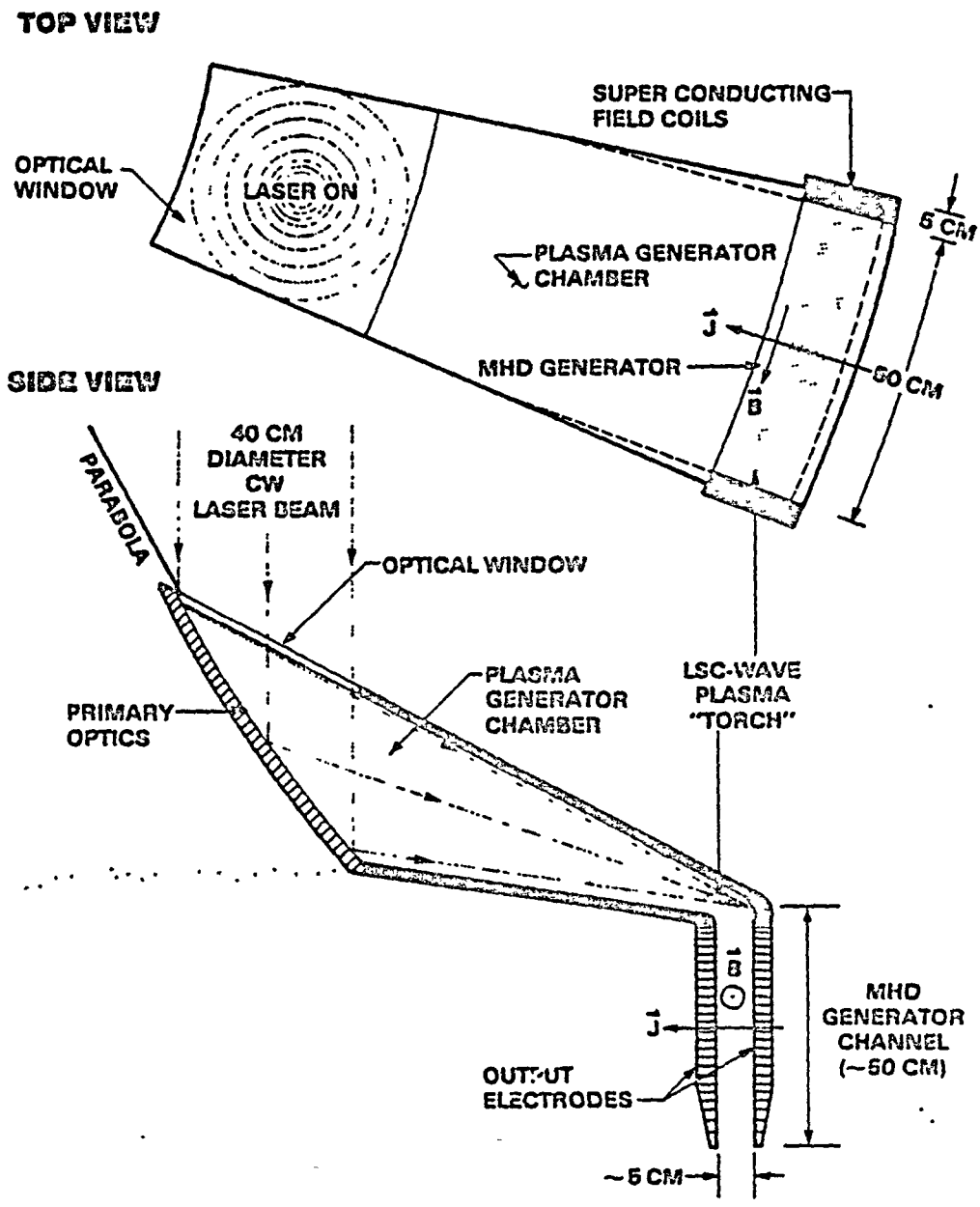

Figure VI-9. Concept for CW Laser-Heated MHD Generator

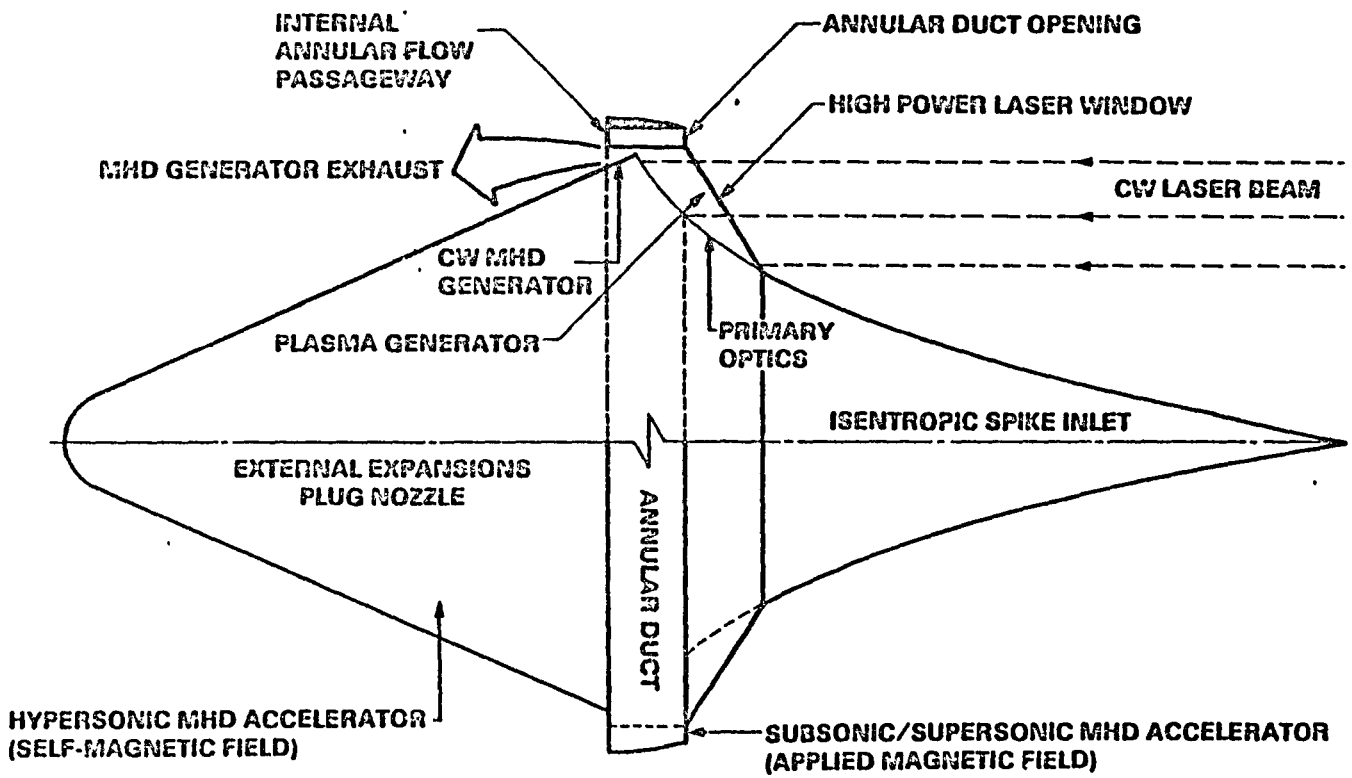

Figure VI-10. Shuttlecraft Configuration for Quasi-Steady MHD-Fanjet Engine

in our case, an MHD generator. (More definitive information on this category of electric propulsion engines may be found in Reference VI-6.) For the sake of argument, the two thruster modes described here are tied to a shuttlecraft with a 4.5 meter diameter annular duct of one meter length (in the flight direction). The axial dimension of the external-expansion plug nozzle is roughly set equal to the duct diameter. The overall shuttlecraft length for this engine might be 10 to 11 meters. Finally, as noted in Figure VI-10, the subsonic/supersonic MHD "ducted-fan" uses an applied magnetic field to accelerate the duct air; whereas, the hypersonic "external-expansion" accelerator uses self-magnetic fields.

1. Subsonic/Supersonic MHD Accelerator

Figure VI-11 shows an end view of the "subsonic/supersonic" low altitude MHD accelerator. Electromagnetic field coils are arranged azimuthally about the 4.5m diameter vehicle so that the applied magnetic field lines close upon themselves--in a toroidal configuration. As indicated, the individual magnetic coils are estimated to be 5 cm thick, and are to be shared with the MHD generators. The toroidal MHD accelerator duct is divided into 26 separate channels measuring 25 X 50 X 100 cm each. (The MHD generators measure 5 X 50 X 50 cm each, and are located directly below their accelerators.)

Figure VI-12 illustrates the "subsonic/supersonic" propulsion cycle. This cycle begins with a laser-initiated or electric-spark-initiated discharge at the duct MHD-accelerator inlet location. Thereafter, the discharge races to the end of the channel, accelerating all the air within the duct. The uniform discharge is assumed to be impermeable, acting much like a piston. Upon reaching the channel exit, the discharge disconnects itself, triggering the formation of a new discharge at the channel inlet.

2. Hypersonic MHD Accelerator

Figure VI-13 portrays the propulsion cycle for the "hypersonic," high altitude MHD-fanjet mode. The thrust cycle being exactly as shown in Figure VI-12A and VI-12B, but after the electric discharge arrives at the channel exit, it then emerges onto the plug nozzle as indicated in

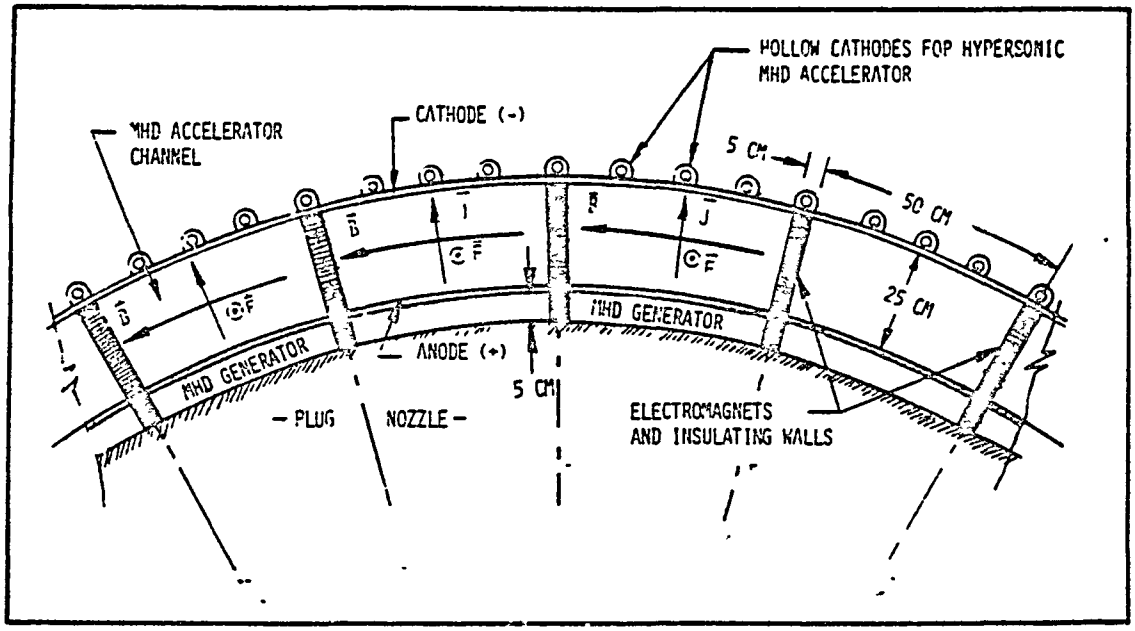

Figure VI-11. Subsonic/Supersonic MHD Accelerator

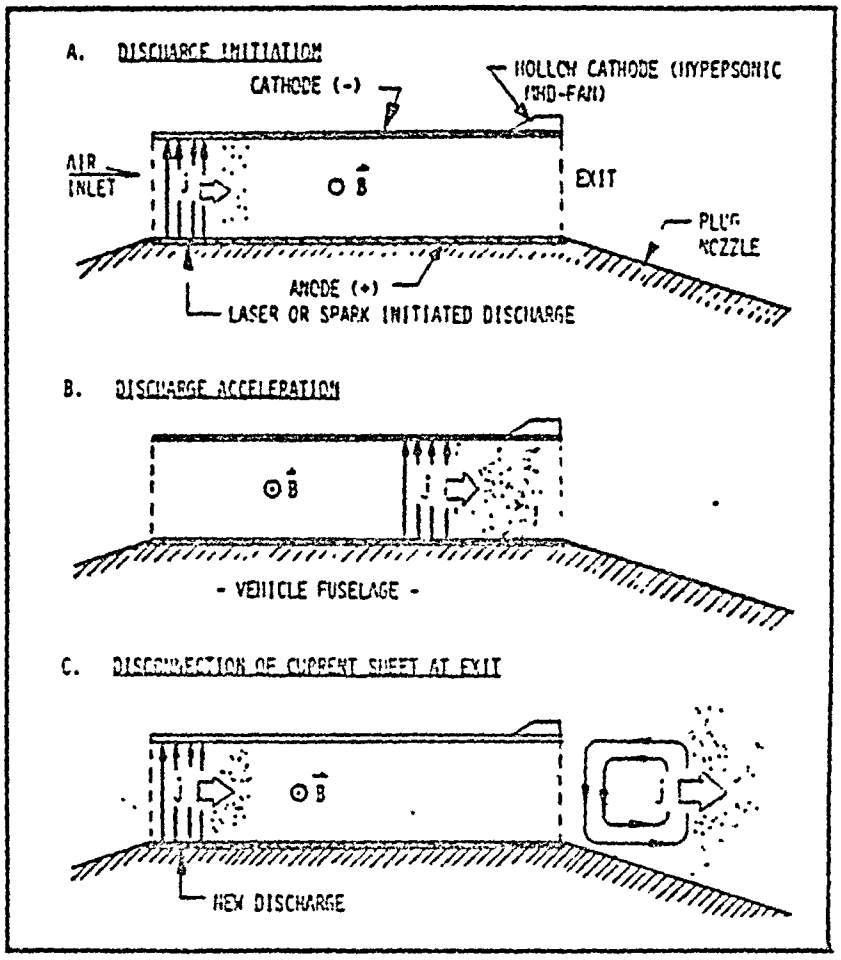

Figure VI-12. Self-Modulated MHD Accelerator Concept (Subsonic/Supersonic Mode)

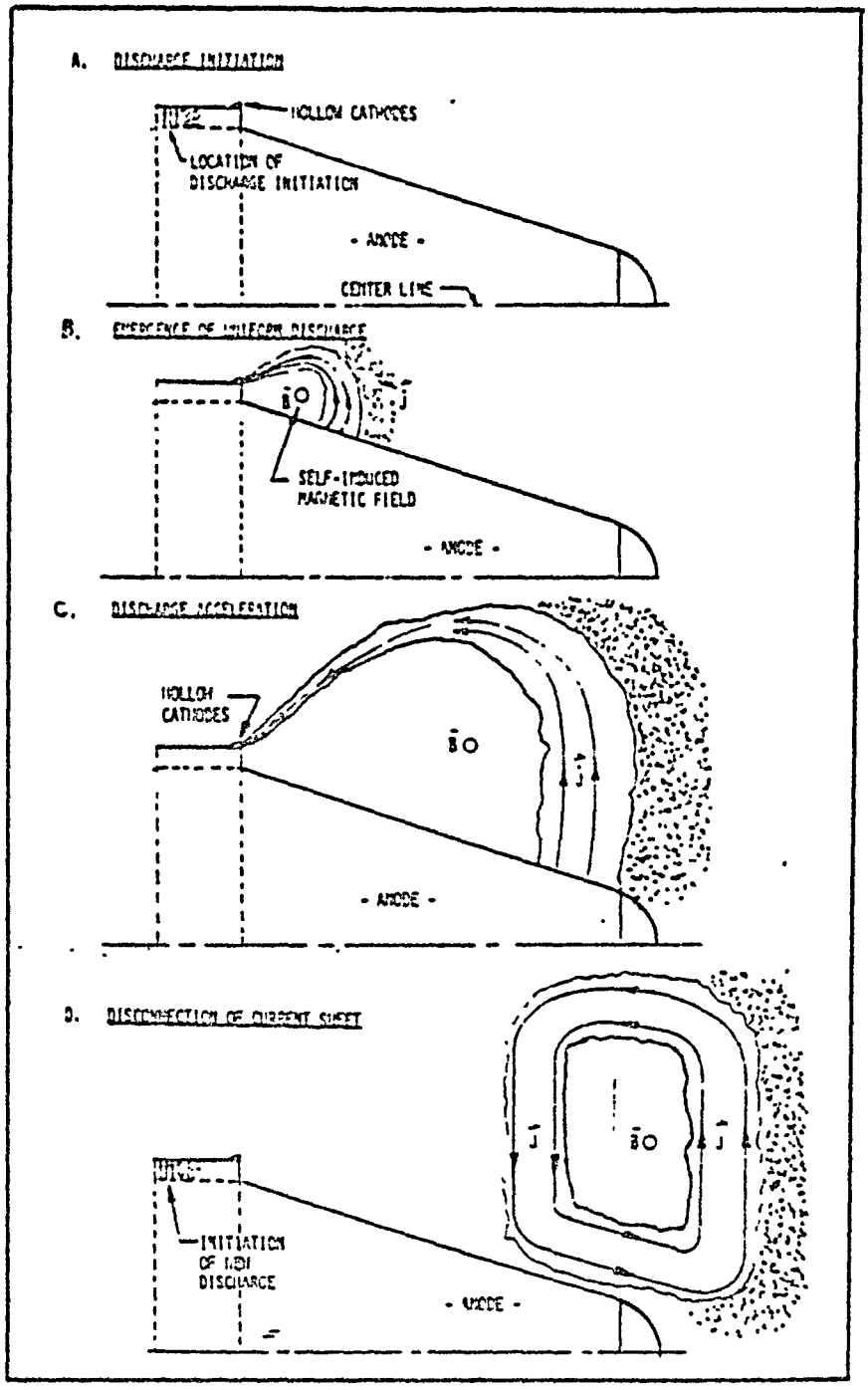

Figure VI-13. Self-Modulated MHD Accelerator Concept (Hypersonic Mode at High Altitude)

Figure VI-13B. Physically, this process is accomplished by electrically connecting the large external "plug nozzle" anode to the small "duct" anode, and by switching the outer "duct" cathode to rear-facing hollow cathodes (located upon the rear outer surface of the duct).

This first portion of the "internal" acceleration process, then, serves to produce a uniform electrical discharge with high conductivity, high velocity, and low permeability by the time it emerges from the channel exit. Due to the low density of the rarefied upper altitude air, this process occurs quickly.

Now the discharge continues to accelerate, as shown in Figure VI-12C, pushing all the air residing in the external "plug nozzle" region to the final "exhaust velocity." Again, the "snow plow" analogy applies as the air working fluid is processed by the action of self-magnetic field Lorentz forces. As indicated in Figure VI-13D, the cycle is complete when the toroidal current discharge expands to unwieldy proportions, then disconnects itself from the external MHD accelerator, simultaneously with the formation of a new discharge at the channel inlet.

Other than when an ERH thruster must be used for VTOL (as discussed in the previous chapter), this MHD fanjet engine should be capable of propelling the shuttlecraft along a typical orbital trajectory from sea level (subsonic) to 100 km altitude (hypersonic). (Beyond 70-100 km, the shuttlecraft would become a pure laser-heated rocket, and cease its air-breathing function.) It should be possible to demonstrate a thrust-to-electric-power coupling in low-subsonic speeds of at least 1000-1500 dynes/Watt(e); 500 dynes/Watt(e) at high-subsonic speeds; and 100 dynes/Watt(e) at Mach 3.

This Page Intentionally Left Blank

REFERENCES FOR CHAPTER VI

1. Harris, C. J., et al., "MHD Generator and Accelerator Experiments in Seeded and Unseeded Air Flows," Transactions on International Electricity from MHD Symposium, Vol. 1, International Atomic Energy Agency, Salzburg, 1966.

2. Harris, C. J., "Comment on Nonequilibrium Effects on High-Enthalpy Expansion of Air", AIAA Journal, Vol. 4, No. 6, June 1966, p. 1148-1149.

3. Pate, S. R., et al., "Development of an MHD-Augmented, High Enthalpy, Shock Tunnel Facility," AIAA Journal, Vol. 12, No. 3, March 1974, pp. 289-297.

4. Harris, C. J., and Marston, C. H., "MHD Augmented Shock Tunnel Experiments With Unseeded, High Density Air Flows," AIAA Journal, Vol. 13, No. 2, February 1975, pp. 229-231.

5. Dommasch, D. O., Sherby, S. S., and Connolly, T. F., Airplane Aerodynamics, Pitman Publ. Corp., New York, 1961.

6. Jahn, R. G., Physics of Electric Propulsion, McGraw-Hill Book Company, New York 1968, pp. 302-304.

7. Berner, F., "MHD Turborocket Engine for Recoverable Launch Vehicles", AERL Research Report 206, BSD-TR-64-183, Contract No. AF 04(694)-414, Avco Everett Research Lab., Everett, MA, March 1965.

8. Dulberger, L. H., "Advanced Rotary-Wing Aricraft," Space/Aeronautics, April 1967, pp. 68-82.

CHAPTER VII
PERFORMANCE EVALUATION OF SSTO RADIAL SHUTTLECRAFT

This Chapter investigates the single-stage-to-orbit performance of radial shuttlecraft using a variable cycle propulsion system with four different modes: three air-breathing, and one rocket. An external-expansion base thruster is utilized for air-breathing VTOL propulsion to perhaps 3km altitude and Mach 1. A rotary air-breathing pulsejet mode is applied in the regime from Mach 1 to 3, and 30km. The air-breathing MHD-fanjet mode carries the vehicle to 80km altitude and 4km/sec. Beyond 4km/sec, the vehicle leaves the atmosphere (possibly using the drag reduction scheme mentioned in Chapter V) and accelerates to 8km/sec low Earth orbital velocity in a rocket mode on strictly internal propellant (e.g., hydrogen). Figure VII-1 shows the interplay of these thruster flight regimes.

In order to gain some appreciation of shuttlecraft scaling relationships, three different diameters are analyzed: 5m, 10m and 20m, as shown in Figure VII-2. The first is able to carry a single man to orbit; the second, two men; and the third, a payload equal to half that of the current space shuttle orbiter (e.g., 15,000kg).

This chapter begins with a technical analysis of the propulsion physics for each thruster mode. Next, a weight estimate is assembled for three different shuttle vehicles. Finally, the laser power requirements for orbital boosting along a typical SSTO trajectory are calculated.

A. TECHNICAL DESCRIPTION OF PROPULSION PHYSICS

This section begins with a brief examination of pulsejet optical requirements, and the beam/vehicle interface shown in Figure VII-3. The pulsejet/optics geometry presented earlier in Figure V-26 is adopted as the design standard for use in all three shuttlecraft sizes. The pulsejet configuration (including MHD generator) measures roughly 2 meters in length and a meter in width; it has a plenum volume of $0.5m^3$. The MHD generator/

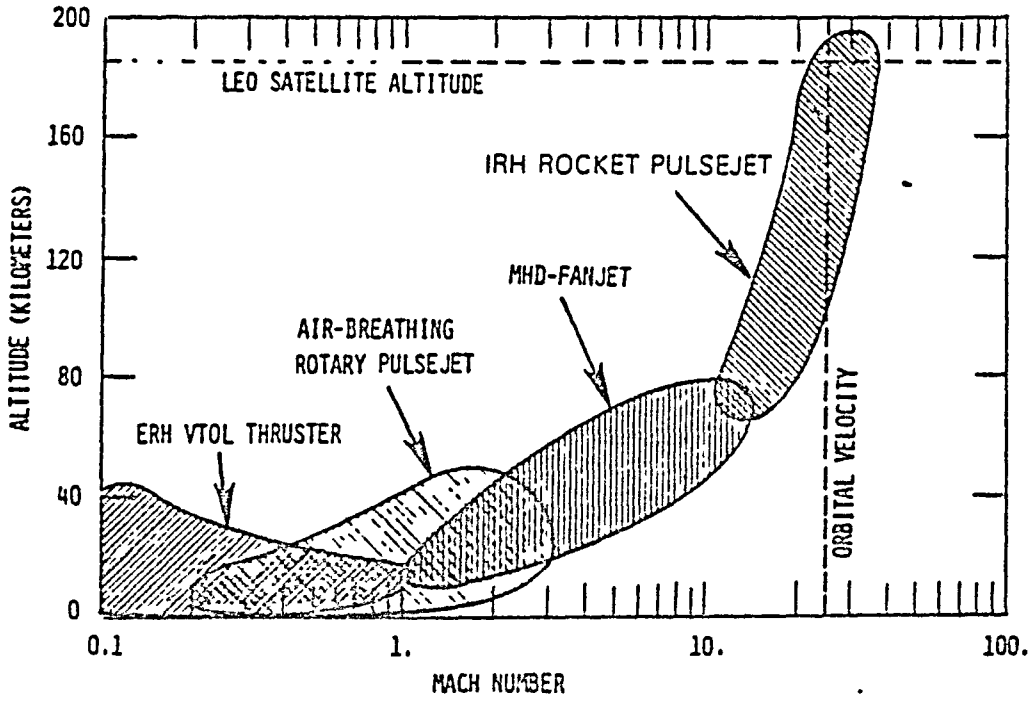

Figure VII-1. Flight Regimes for Various Thruster Modes

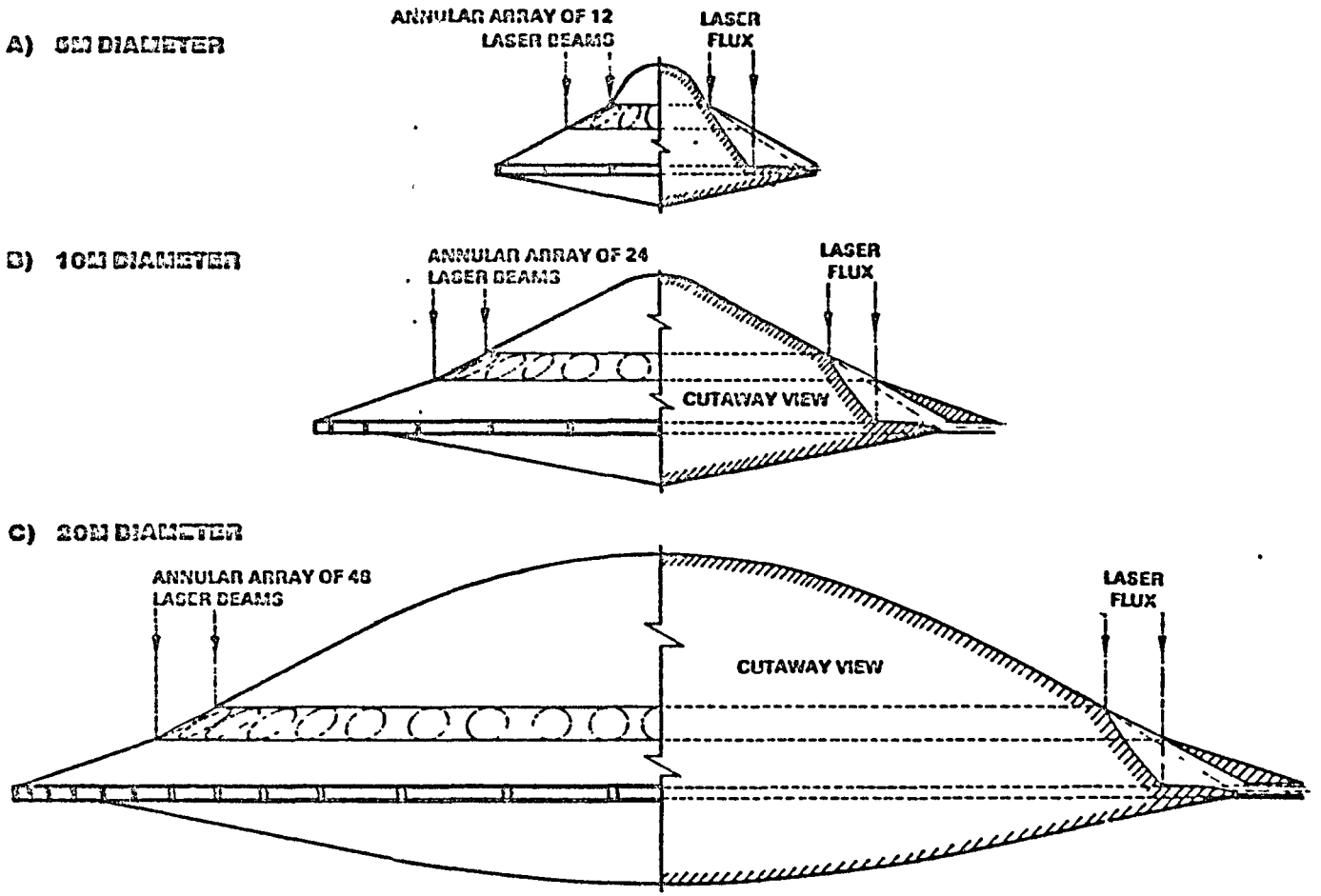

Figure VII-2. Scaling of Radial Shuttlecraft Configurations

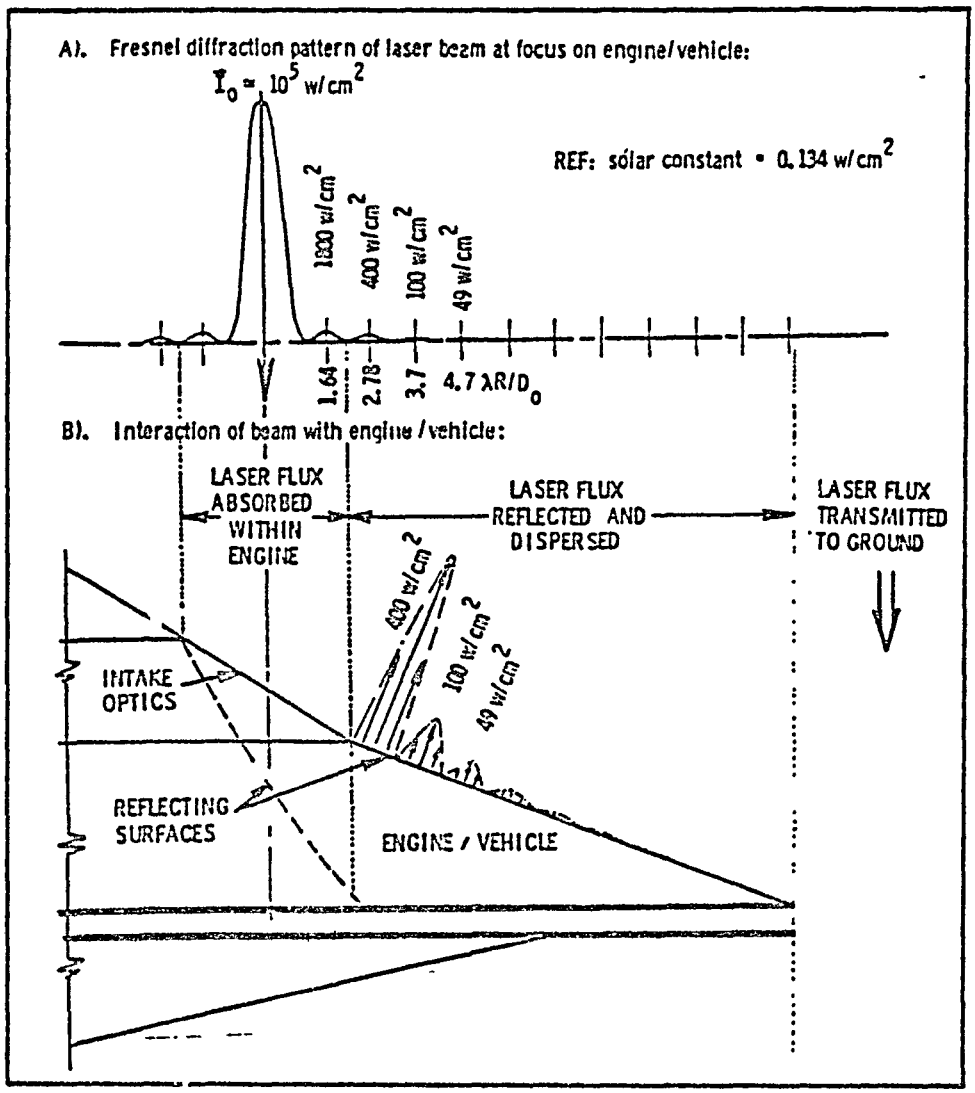

Figure VII-3. Optical Interface Between Beam and Vehicle

channel measures 1m X 1m X 10cm--which adds an additional $0.1m^3$ to the pulsejet internal volume. The exhaust nozzle is of the two-dimensional variety, and is able to vary its exhaust nozzle height from 10cm (minimum) to 40 - 50cm (maximum)--i.e., from 0.1 to $0.5m^2$.

1. High-Power Laser Optics

A propulsive beam pulse energy of 5 megajoules with a wavelength in the near infrared (e.g., 1.8 to 2.5 microns) is assumed for a beam diameter of roughly one meter. For a high-power optical window of 5 cm thickness with an absorption coefficient of 10^{-4}/cm, the transmission coefficient will be 99.95 percent; hence, of the incident 636.6 joules/cm^2, only 0.318 joules/cm^2 will be absorbed within the material window. At 100 Hz PRF, 31.8 watts/cm^2 over the entire high-power window must be carried away by liquid or gaseous coolant.

The peak pressures generated by the laser supported detonation wave within the IRH plasma chamber will approach 140 atmospheres. Crystalline sapphire windows should be able to sustain this severe temperature and pressure environment if supported in a rigid, cooled geodesic framework. To date, the largest single crystal sapphire measures 32 centimeters in diameter, has a mass of 48 kg, and was grown by Crystal Systems, Inc. in Salem, Massachusetts.[1] Therefore, one can probably assume that a 100 cm diameter window could successfully be fabricated from a half dozen smaller units. With a good anti-reflection coating applied to the exterior window surface, 99.9 percent of the incident energy will be transmitted into the pulsejet chamber.

Note in Figure VII-3 that the primary optic forms a parabolic surface whose average inclination is 35 degrees to the optical axis of the beam. Therefore, the beam strikes an effective surface area of 7854 cm^2/ cos (35°) or 13,690 cm^2. As a result, the mirror will see a single-pulse fluence of 365J/cm^2. Since the damage threshold for cooled metallic mirrors at near infrared wavelengths is roughly 10J/cm^2, the mirror must have a reflectivity of at least 97.3 percent to survive the first pulse. Reference 2 reports that the reflectivity of vapor deposited silver mirrors with 1.5 - 2.0 μm radiation ranges from 97.8 to 98.3 percent; for copper,

97.7 to 98.1; for gold 98.7 to 98.9 percent. It would seem that conventional metallic mirrors can survive single-pulse fluences predicted for the primary optics.

However, at 100 Hz PRF the absorbed flux would be 1000 Watts/cm^2, which exceeds the limits of liquid metal cooled mirrors by about a factor of five. Hence, the mirror-reflectivity must be improved to at least 99.45 percent in order to sustain the time-average flux load at 100 Hz. This requirement may possibly be met by a broad band metallic reflecting surface if it is diamond turned on a lathe. The only possible alternative requires the use of multi-layer high reflectivity coatings. These are typically good for 99.95 percent of reflectivity at one specific wavelength of laser radiation, but may not easily survive the abusive environment of the plasma generator chambers.

In the MHD fan mode, the grazing incidence secondary optic (refer to Figure VII-4) will see about 10 percent of the total pulse energy before the LSD wave reflects off the surface and propagates into the IRH plasma generator. However, the active area of the surface may be only 1/10 that of the primary mirror, so the above discussion on mirror limits applies here as well.

One final note which must be made regarding the actual diffraction-limited optical interface between the laser beam and the vehicle (see Figure VII-3). Diffraction effects do not permit a "top-hat" intensity distribution to be placed upon the engine high-power window by a laser source from several thousand kilometers away. The diffraction pattern will appear as shown, and low levels of laser radiation will unavoidably "spill" over the shuttle upper surface. If a time average flux of 400 w/cm^2 falls upon the vehicle skin, the surface must have a reflectivity of at least 92.5 percent in order to utilize regenerative water-cooled mirror technology. If a reflectivity of 99.7 percent can be maintained on the shuttle upper surface, the time-average absorbed flux falls to that of 10 solar irradiances; and the need for active cooling might be eliminated altogether.

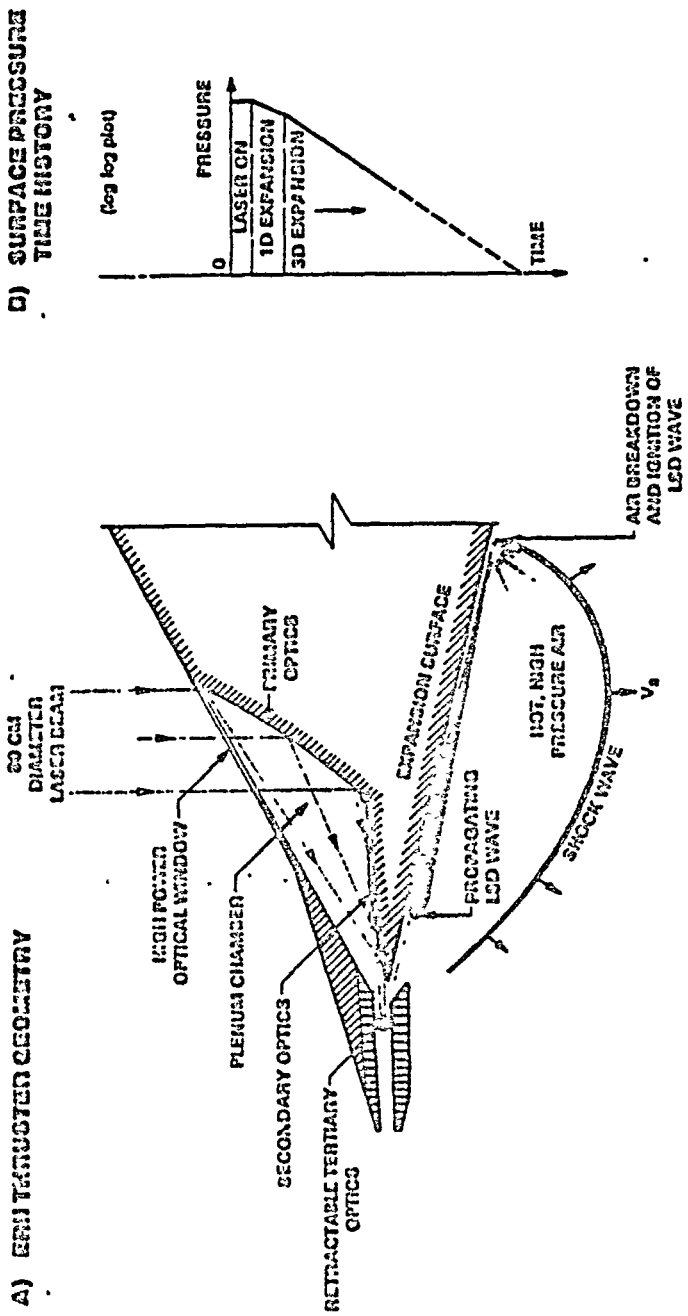

Figure VII-4. External Radiation-Heated Thruster Integrated With Vehicle Lower Surface

2. External-Radiation Heated VTOL Thruster Mode

Of the several methods by which the shuttle may accomplish VTOL operation, the simplest is to integrate a pulsed external radiated-heated thruster with the lower vehicle centerbody surface as shown in Figure VII-4. A series of slits would be opened in the primary optics to allow projection of very intense beams of concentrated radiation from a series of retractable tertiary optics which are deployed during VTOL. In operation, electrical air breakdown would occur at a point near the central vehicle axis, and a number of light sparks (e.g., 24 for the 10m vehicle) would rapidly "burn" their way across the ERH thruster surface and come to a halt at the entrance to the portholes just as the laser pulse is terminated. These "slabs" of hot, high-pressure air plasma (created in the process), would subsequently expand over the adjacent passive ERH expansion surface, thereby imparting momentum to the thruster base. This process is then repeated at a repetition frequency of ten to several thousand times a second, as required to levitate (or accelerate) the vehicle. Figure V-7A is a bottom view of the VTOL thruster in operation.

The performance of the ERH thruster is a strong function of the pressure created by laser supported detonation (LSD) waves as they race across the ERH surface (see Figure VII-4). As mentioned earlier, Raizer[3] was first to calculate the velocity and pressure produce by LSD waves. The detonation wave velocity is proportional to the cube root of the flux divided by the ambient air density in front of the wave. The pressure behind the detonation wave is proportional to the product of the ambient air density and the square of the detonation wave velocity.

The total impulse transmitted to the thruster surface is composed of contributions while the laser pulse is on and after the pulse has ceased. Let us assume that the laser energy is deposited into a thin sheet of air adjacent to the thruster surface so that while the pulse is on, the expansion flow geometry is completely one-dimensional. Let P_{s1D} represent the pressure generated at the thruster surface by passage of the LSD wave during the time the laser is on. After pulse termination, the shock-expansion flow field relaxes as a planar blast wave up to the time that the

flow geometry becomes two-dimensional. This time, τ_{2D}, is defined as the order of time it takes the leading edge of the plasma to travel a distance equal to the minimum width W of the irradiated plasma sheet. The total impulse delivered to the ERH thruster surface, then, is given by

$$I_T = \int_0^{\tau_p} p_{s1D} h V_{DW} t dt + p_{s1D} \tau_p^{2/3} A_s \int_{\tau_p}^{\tau_{2D}} \frac{dt}{t^{2/3}} + A_s \int_{\tau_{2D}}^{\tau_o} P_s dt \qquad (1)$$

where $\tau_p << \tau_{2D}$, A_s is the total "active" ERH thruster surface area, τ_p is the laser pulse length, and τ_o is the impulse delivery time. For large active ERH thruster surfaces and very thin irradiated plasma sheets, Equation 1 adequately describes the process since the total impulse delivered to the surface will occur much before the two-dimensional characteristic time τ_{2D} and only a small fraction of the high-pressure plasma will spill over the edges of the ERH thruster surface. For some ERH thruster geometries, secondary optical surfaces may act as 1-D skirts to help direct the 1-D gas expansion process.

Equation 1 addresses the case for a 100 percent "active" ERH thruster surface area, (i.e., $A_s = A_t$ where A_t is the total thruster surface area). Another approach is to propagate a set of very small diameter light sparks across the ERH thruster surface, resulting in the generation of several hot, high-pressure "fingers" of plasma which consequently expand over the "passive" ERH chruster surfaces. For this ERH thruster concept, the ratio passive/active surface area is very large (i.e., $A_s << A_t$), and essentially presents an infinitely large surface over which to spread. Hence, the very narrow high-pressure plasma fingers first expand one dimensionally over the active irradiated thruster surfaces while the laser is on, then relax as cylindrical blast waves over the passive thruster areas for the remainder of the time during which the impulse is imparted.

For this case, the total impulse delivered is given by

$$I_T = \int_o^{\tau_p} P_{s1D} h V_{DW} t dt + P_{s1D} \tau_p^{2/3} A_s \int_{\tau_p}^{\tau_o} t^{-2/3} dt +$$

$$\int_{\tau_{2D}}^{\tau_o} \int_o^{r_f(t)} p_s(t)(2L) dr dt \qquad (2)$$

For a given τ_p, flux, and pulse energy the choice of a line focus ERH thruster (Equation 1) or multi-finger-focus ERH thruster (Equation 2) is entirely dependent upon the engine/optics/airframe configuration. There is no reason to expect that one is inherently superior in performance to the other, at the present time.

Pirri[4] calculates the coupling coefficient for an infinite diameter target with a normal incidence beam (see Figure III-8) for the case of the LSD wave traveling exactly one beam diameter before the pulse is terminated (i.e., $\tau_p = \tau_{2D}$) as:

$$\left(\frac{I_T}{E}\right)_{max} = \frac{(p_{s1D})^2}{I_o p_o} = \left(\frac{\gamma+1}{2\gamma}\right)^{\frac{4\gamma}{(\gamma-1)}} \left(\frac{[2(\gamma^2-1)]^{4/3}}{(\gamma+1)^2}\right)\left(\frac{\rho_o^{2/3} I_o^{1/3}}{p_o}\right) \qquad (3)$$

From Equation 3, we can deduce that the maximum coupling coefficient has only a weak dependence upon flux and that it is completely independent of irradiated spot area, although Pirri emphasizes that the pulse time when this value is obtained is dependent upon the spot area through τ_{2D}. Coupling coefficients up to 50 dynes/Watt are theoretically predicted for fluxes of $10^8 W/cm^2$ and above. Some researchers believe 100 d/W is attainable.

In order to apply Equation 3 to the case for propagation of light sparks parallel and adjacent to an ERH thruster surface, we have only to assure that the LSD wave velocity is significantly greater than the plasma

sound speed (i.e., $V_{DW} >> V_p$) and that the perpendicular height of the irradiated light spark is less than or equal to the width. Let us assume the availability of a "rubber" laser (e.g., the free-electron laser) which can deliver laser pulses of any energy, duration and waveform (hence specifying V_{DW} across the ERH thruster surface). We could then define this pulse duration in relation to the maximum dimension L of the ERH thruster (across which the light spark must travel) as follows:

$$\tau_p = \int_0^L \frac{L}{V_{DW}} dx \ , \qquad (4)$$

where x is measured from the point of LSD wave ignition in the direction of the propagating light spark.

Much flexibility exists in the choice of laser intensity projected upon the absorption waves, LSD pressure ratio and coupling coefficient. However, the price for quiet ERH thruster operation is decreased coupling efficiency. The greatest coupling of 50 to 100 dynes/Watt occurs for the high laser intensities (e.g., $\geq 10^8$ W/cm^2) and pressure ratios, e.g., 10-100 atm. However, ERH thrusters may perhaps be operated at much lower intensities close to the LSC/LSD-wave transition intensity (i.e., 10^6 - 10^7W/cm^2 for 10.6 μm radiation), and lower average over-pressures of 1-10 atm, but with reduced coupling; 1-10 dynes/W. Whereas final air temperatures with the strong LSD wave regime may be 4000 K - 5000 K, temperatures within the transition regime will be several times greater, perhaps 10,000 K - 15,000 K.

Finally, we note that since LSD wave pressure (and hence ERH thrust) varies as indicated in Equation 2 of Chapter III, one would expect ERH thruster coupling coefficients to decrease with the cube root of the ambient atmospheric density, as the shuttle climbs to altitude. Figure VII-5 shows the results of such an altitude-climbing calculation. The coupling coefficient is seen to drop from 100 dynes/Watt at sea level to 25 d/W (equivalent to the air-breathing rotary pulsejet performance) at an

altitude of 30 km; then to 12.5 d/W (the performance expected from hydrogen-fueled laser-heated rockets) at about 43 km altitude. Although other dynamical effects (i.e., those not taken into consideration in this simplistic calculation) may enter to degrade the coupling performance with altitude faster than that shown in Figure VII-5, it presents an upper limit to the anticipated performance envelope.

We will now move on to a discussion of the rotary pulsejet propulsion physics as applied to shuttle vehicles of three different diameters; 5, 10, and 20 meters.

3. Rotary Pulsejet Thruster Mode

Figure VII-6 shows the 2-D pulsejet nozzle in the wide-open air-breathing mode. As mentioned earlier, the nozzle exhaust opening may be varied from 10cm to 40-50cm.

As with centrifugal impellers in rotating turbomachinery, the maximum attainable rates of rotation for rotary pulsejets are limited by the structural integrity of the materials incorporated, which is a direct function of the rim or tip speed. Recent advanced centrifugal impellers are now pushing tip speeds to 616 m/sec, or about Mach 2.0 at sea level standard conditions. Figure VII-7 shows the simple relationship between rim Mach number, rim velocity and rate-of-rotation for the vehicle diameters of interest. The rim velocity is given by

$$V_{RIM} = 2\pi W R_{VEH} \qquad (5)$$

where W is the rotation rate in revolutions/second, and R_{VEH} is the vehicle radius.

When operating in an air-breathing mode at subsonic flight speeds, the static pressure level within the rotary pulsejet chambers can be calculated on the basis of its great similarity to centrifugal compressor passageways. At zero flow through the passageways (which exactly models the thruster condition prior to irradiation by the laser pulse), the ambient pressure within the pulsejet chamber is solely a function of the centrifugal force acting upon the air within the pulsejet. The internal

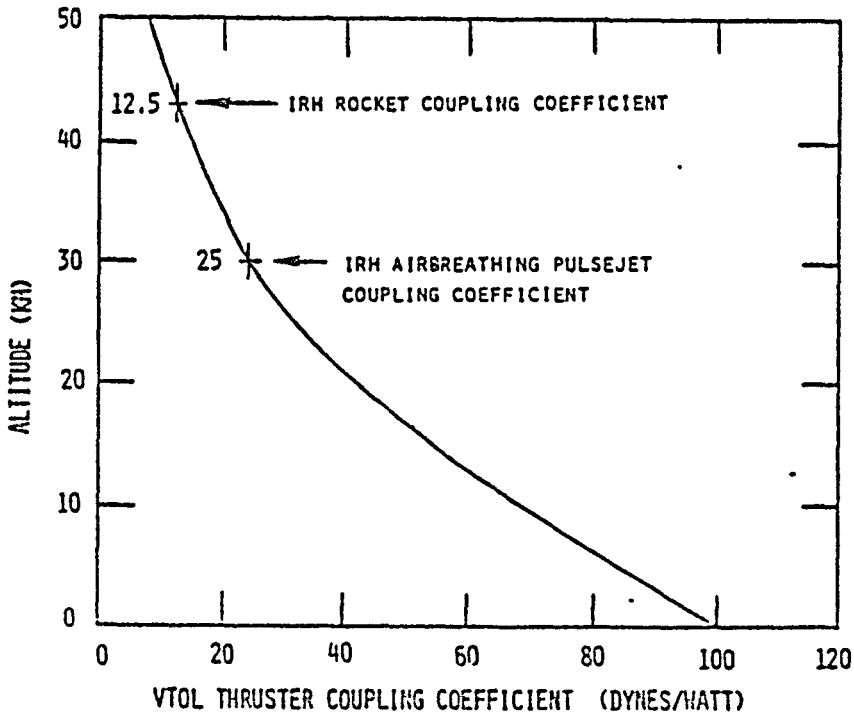

Figure VII-5. ERH Thruster Coupling vs. Altitude

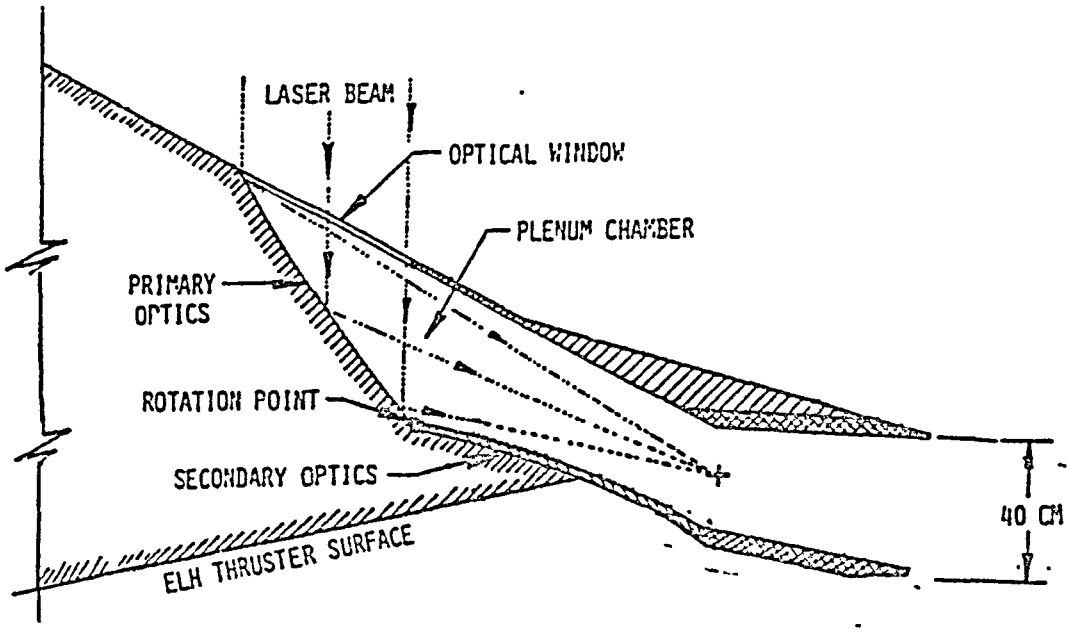

Figure VII-6. Nozzle Position for Air-Breathing Rotary Pulsejet Mode

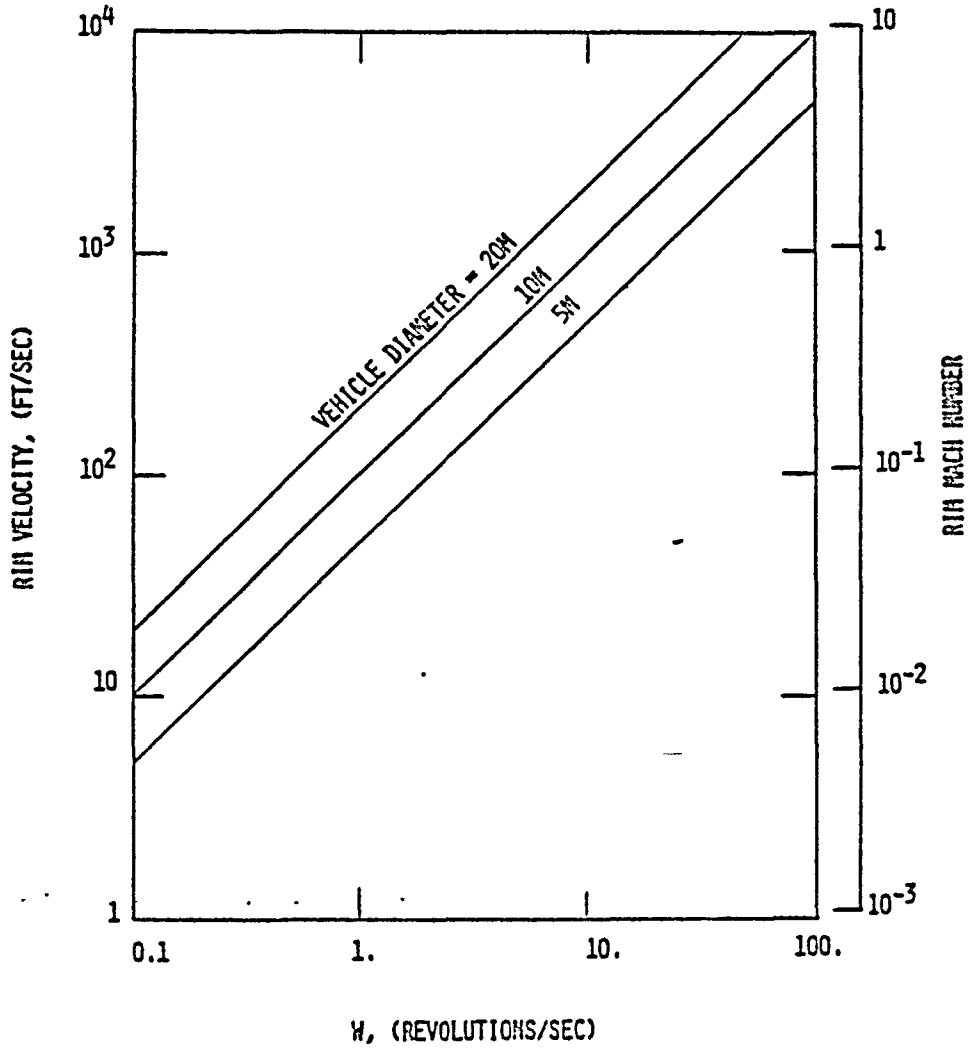

Figure VII-7. Rim Velocity vs. W

pressure ratio P_1/P_2 is theoretically dependent only on the tangential rim velocity V_2, the gas temperature T and the ratio of pulse jet chamber radii r_1/r_2, as given by

$$P_2/P_1 = \exp\left\{\frac{V_2^2}{2RT}\left[1-\left(\frac{r_1}{r_2}\right)^2\right]\right\} \qquad (6)$$

where P_2 is the ambient air pressure, P_1 is the chamber pressure at the innermost chamber location of r_1, r_2 is the radius at the vehicle rim, and R is the gas constant. Figure VII-8 displays a sample calculation of Equation 6 for pulsejet chamber diameter ratios from 0.4 to 0.95 and rim mach numbers up to 10.

Popper[5] has developed an algorithm for predicting the total impulse delivered by an enclosed cavity after irradiation by a pulse of laser energy. The approach considers impulse contributions from both sonic and subsonic venting of the cavity. Although the brevity of this study does not permit the analysis to be reviewed here, the results of a sample calculation are presented in Figure VII-9 for a pulsejet cavity volume of $0.5m^3$, nozzle exit area of 4400 cm^2, γ (ratio of specific heats for air at an elevated temperature of roughly 8000°K) of 1.18, and a plasma sound velocity of 4.5×10^5 cm/sec. Note that the impulse calculation assumes laser pulse energy is scaled linearly with pulsejet chamber pressure in order to keep the peak gas temperature roughly constant.

Figure VII-10 displays the absorbed laser power for 5 MJ laser pulses as a function of shuttle diameter and rotation rate. Shown in Figure VII-11 is the time-average thrust developed by a vehicle as a function of rotation rate for the several shuttle vehicle diameters of interest. Displayed in Table VII-1 are the results of a sample calculation for air-breathing rotary pulsejet performance for a ratio of P_1/P_2 of 0.8. As indicated, the 5m diameter shuttle is able to produce 1.37×10^5 Newtons thrust at a rotation rate of 14 RPS with a propulsive beam energy of 0.67 gigawatts (4.0 MJ pulses at 168Hz); the 10m shuttle generates 1.57×10^6 Newtons thrust at 8.0 RPS with 0.77 gigawatts; the 20m vehicle produces 1.95×10^6 Newtons thrust at 5 RPS with 0.96 GW. At these conditions, each

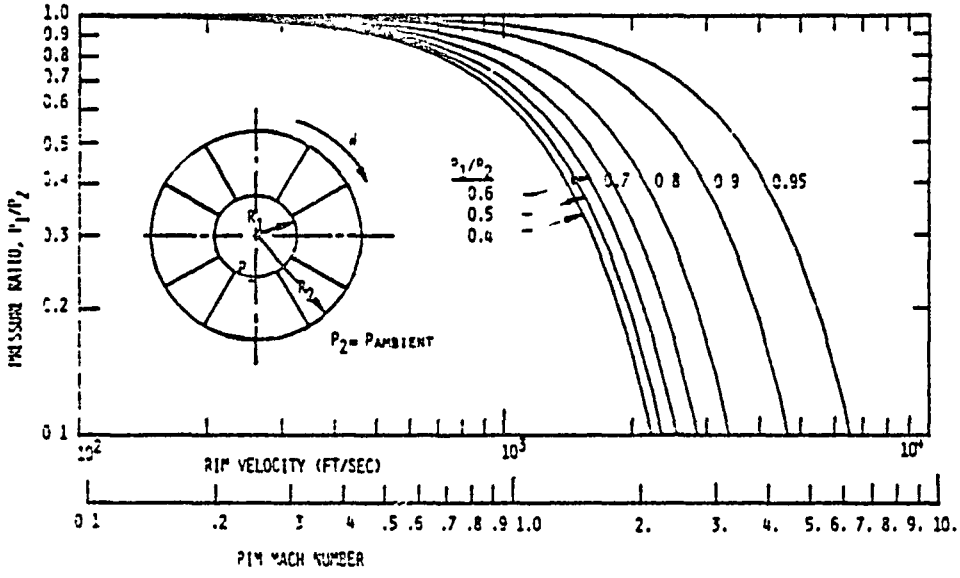

Figure VII-8. Pressure Ratio vs. Rim Velocity

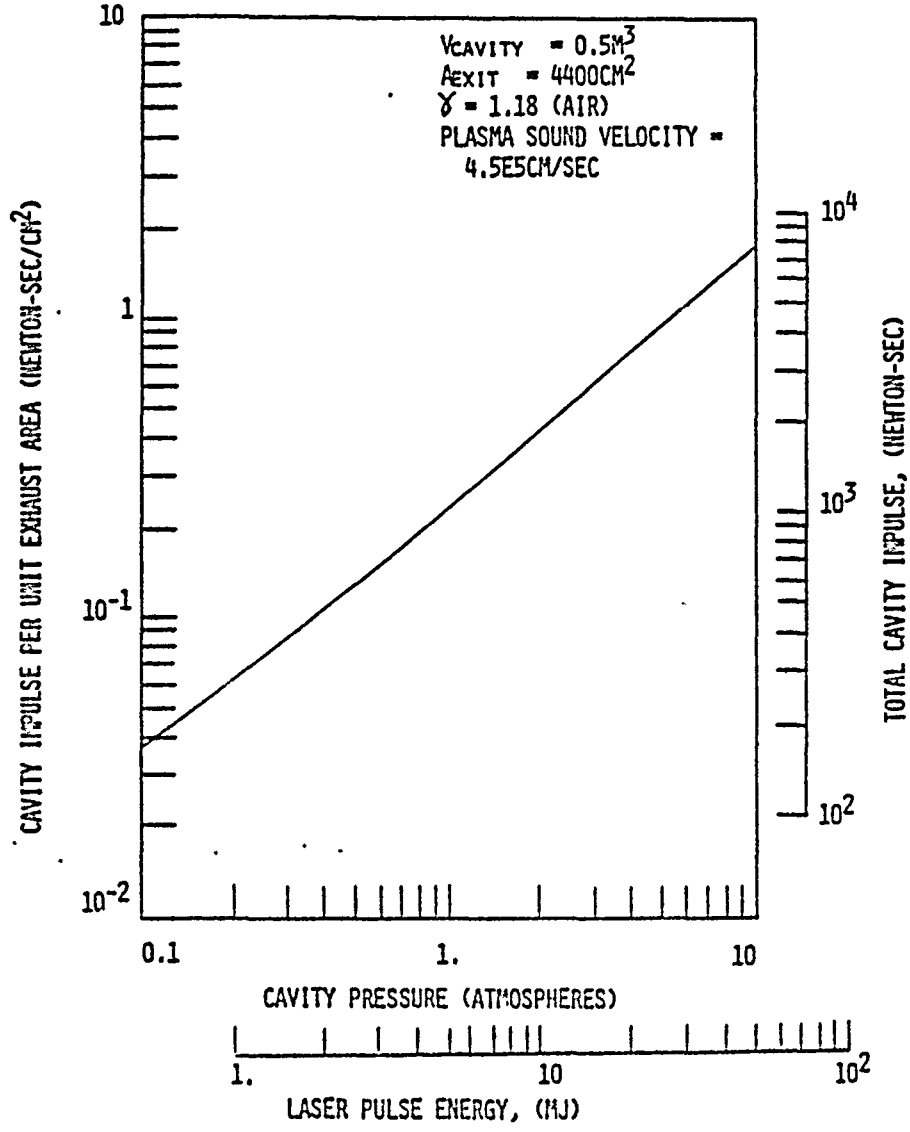

Figure VII-9. Cavity Pressure vs. Impulse

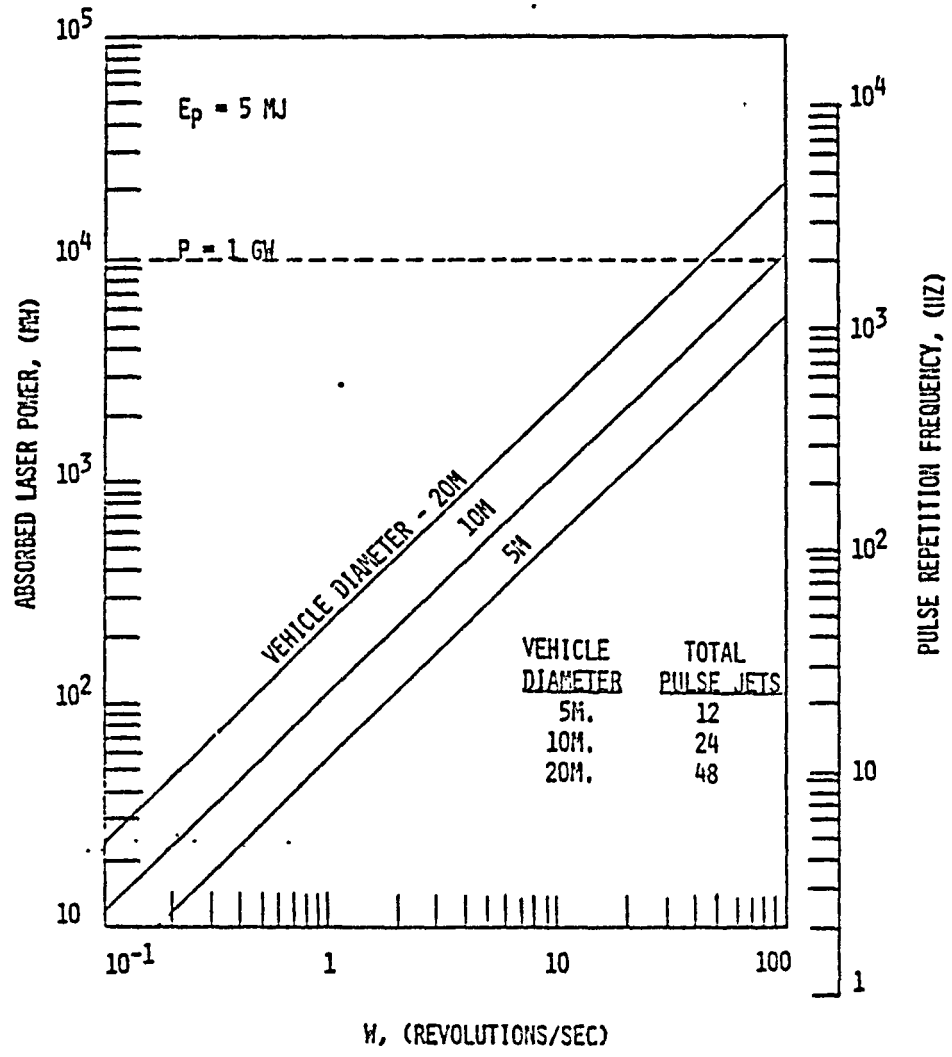

Figure VII-10. Absorbed Laser Power vs. W

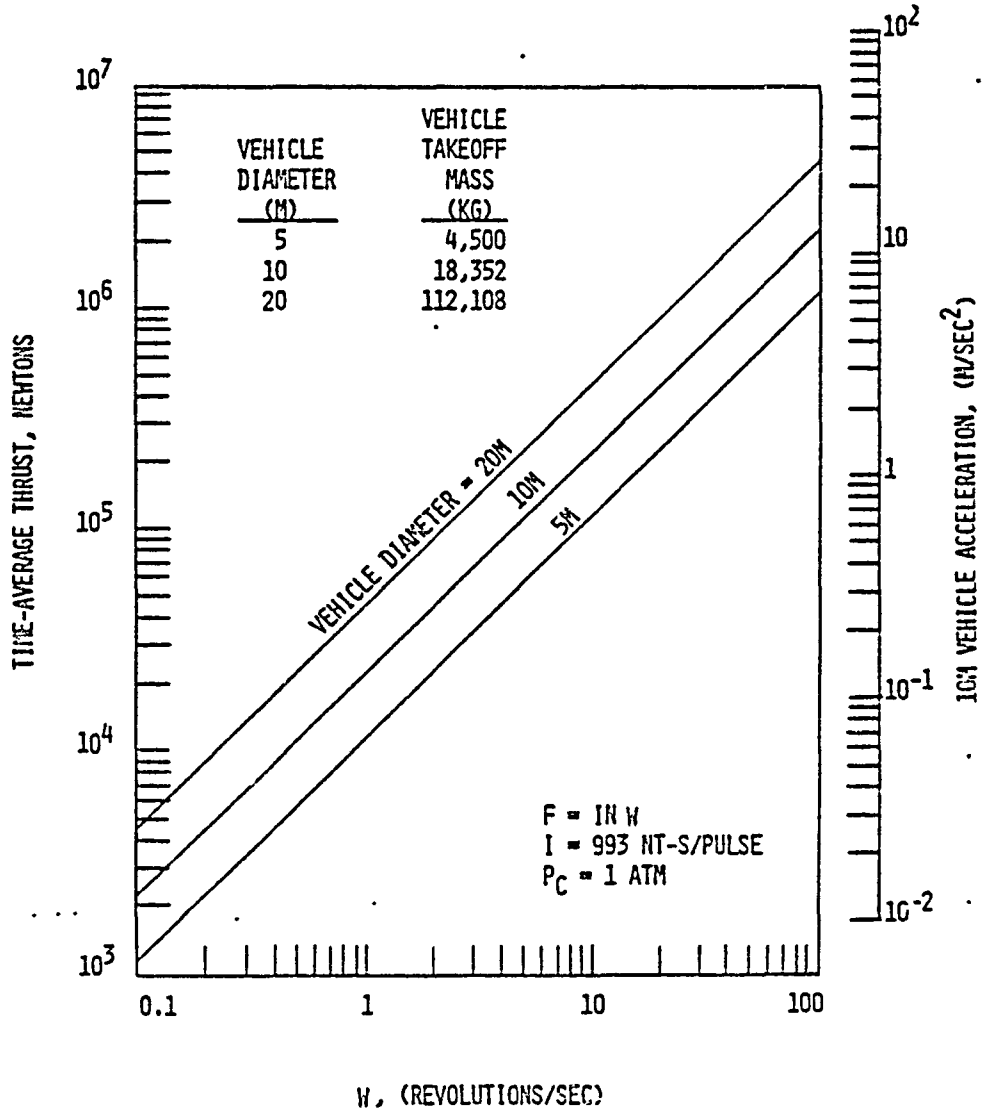

Figure VII-11. Thrust vs. W

TABLE VII-1. ROTARY PULSEJET PERFORMANCE

(SEA LEVEL AIR)

VEHICLE DIAMETER (m)	NUMBER OF PULSEJETS	R_1/R_2	P_1/P_2	RIM MACH NUMBER	REVOLUTIONS PER SECOND (sec^{-1})	LASER PULSE ENERGY (MJ)	PRF (sec^{-1})	LASER POWER (GW)	THRUST (10^5 Newtons)	COUPLING (dynes per Watt)
5	12	0.5	0.8	0.7	14	4.0	168	0.67	1.37	19.9
10	24	0.6	0.8	0.8	8	4.0	192	0.77	1.56	20.4
20	48	0.8	0.8	1.0	5	4.0	240	0.96	1.95	20.4

of the vehicles attains a thrust-to-laser-energy coupling of 20 dynes/Watt, which is about what has been demonstrated in small-scale experiments at AVCO Everett Research Lab.[6] The results of these tests with laser-heated pulsejets at one atmosphere were displayed earlier in Figure III-11.

Similar experiments have been performed with pulse laser-heated rockets and hydrogen propellant at very reduced ambient atmospheric pressures and typically exhibit conversion efficiencies (i.e., thrust-power-to-laser-power) of 50 percent, coupling coefficients of 12.5 dynes/Watt, and a specific impulse of 1000 seconds.[7]

4. MHD Fanjet Thruster Mode

The shuttlecraft are assumed to use the repetitively pulsed variety of MHD-fanjet engine first introduced in Chapter VI, Section C. As previously described in good detail, the RP MHD fanjet accelerator is driven by the XMHD generator pictured in Figure VII-12. A strong electromagnet (which is wrapped about the pulsejet nozzle) can apply a 2-10 Tesla magnetic field (B) to the high-velocity plasma flowing through the channel. This would result in the immediate generation of a powerful pulse of electric current, in exchange for creating a large pressure drop across the nozzle. This electromagnet is energized only when shuttlecraft are flying in the MHD-fanjet mode. A technical analysis of such XMHD generators can be found in Appendix B, and will not be further treated here.

To vary the intake diameter of the MHD-fanjet, shuttlecraft are assumed to be equipped with telescoping "transmission-line" cathodes. The exterior surfaces of these electrodes are electrically insulated except at their tips, which define the perimeter of an MHD-fanjet's intake area--as shown in Figure VII-13 for a 5m diameter shuttle. At the tip of each "transmission-line" is installed a hollow cathode electrode, designed to handle a current of 400KA. The ring anode of an MHD-fanjet engine is installed below the XMHD generator exhaust nozzle, as indicated in Figure VII-13.

a. Cathodes

The function of a cathode is to supply electrons in an amount nearly equivalent to the total arc current (about 10 percent of the

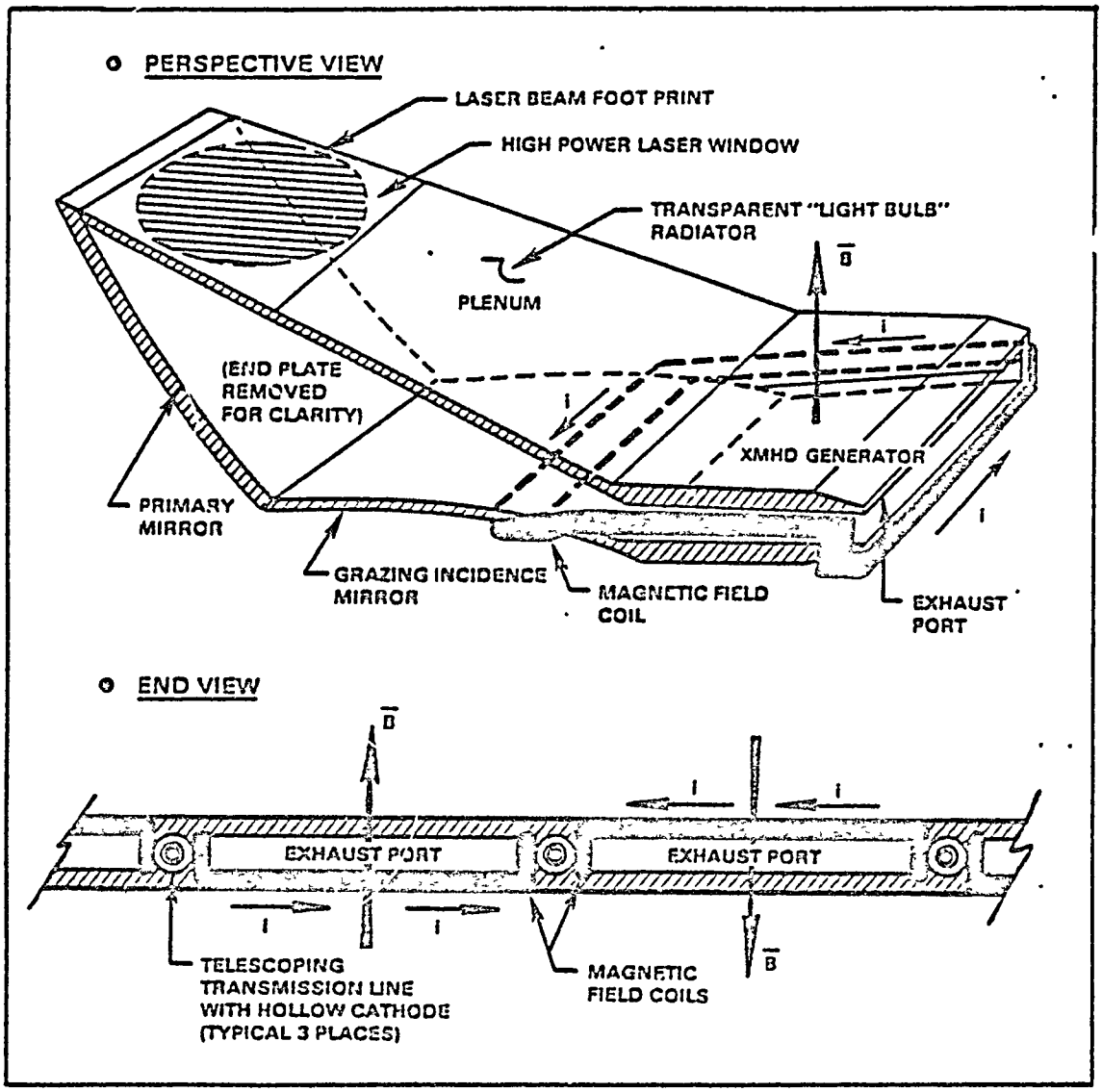

Figure VII-12. Magnet Configuration for XMHD Generator Channel

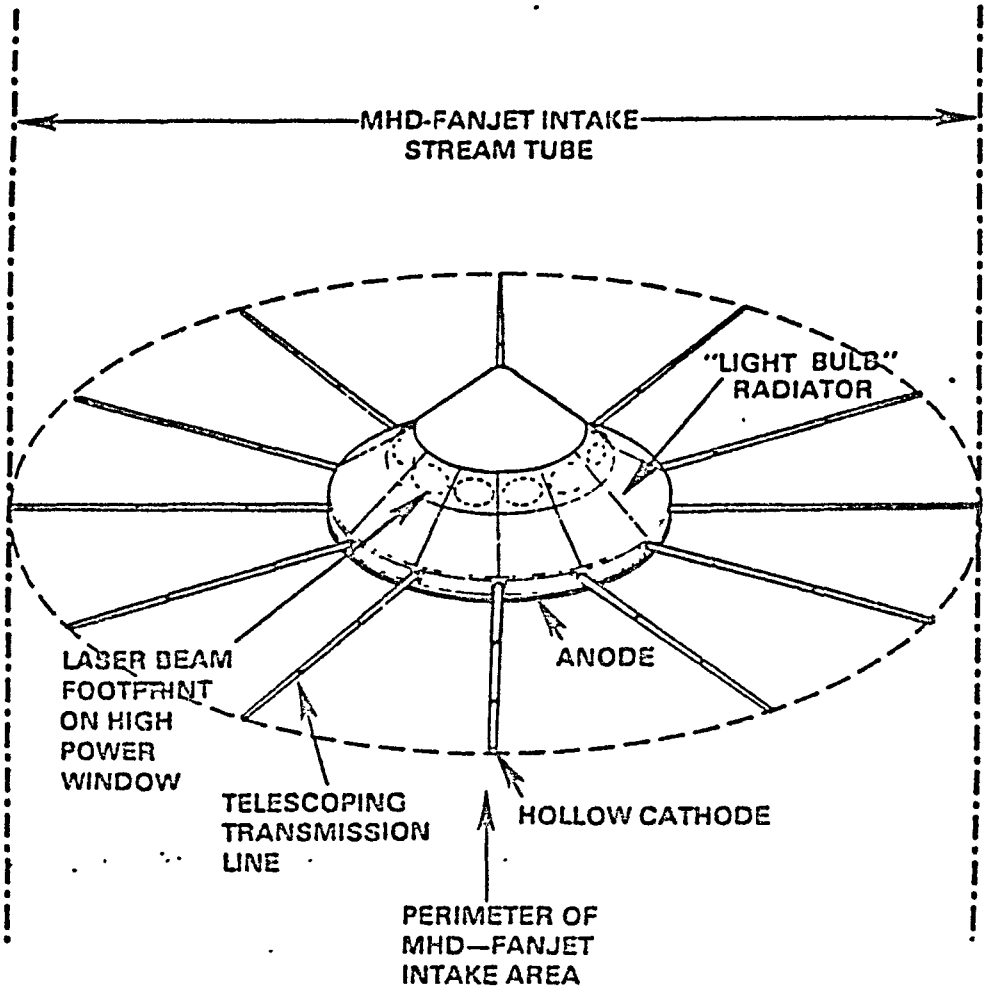

Figure VII-13. MHD-Fanjet Transmission Line Configuration (5m Shuttle)

current.may be ionic at the cathode). The most common type of cathode relies on thermionic emission from alkali-earth oxides which are coated or impregnated on a metallic matrix. Even with this low work function material, temperatures of over 1000 K must be maintained. In addition, these oxydies are known to be "poisoned" by atmospheric oxygen, losing their emissivity and oxidizing their substrate. Other emission mechanisms, such as field emission or photoelectric emission could be directly exploited, but would require complex devices.

A device that can uniquely meet the requirements of the electromagnetic fanjet is the hollow cathode. This is basically a cylindrical enclosure with an open end, and through which a certain amount of gas flow is maintained. Emission is from the inner surface of the enclosure, and can be extremely copious even when the surface is too cold to emit thermionically. The mechanisms responsible for this behavior are not yet understood, although Krishnan (Reference 8) strongly suggests photoemission due to hard UV photons from the enclosed, trapped plasma. A good review of the science and technology of hollow cathodes was given by Delcroix and Trindade in 1974 (Reference 9).

Figure VII-14 shows one of the several experimental hollow cathodes configurations reported in Reference 8. These experiments were conducted for millisecond single-pulse operation, and didn't require active cooling. For continuous or repetitive-pulse operation, a cooling system would be required; it could easily be accomplished with a regenerative approach using the same hydrogen consumed by the MHD generators. For an estimate of cooling loads, we assume a cathode voltage drop of 10 Volts--of which 50 percent ends up as a cathode heating. Using, for example, the 10m diameter shuttle, the peak total power dissipated is 10^7 Amp x 5 Volts, or 50 MW; however, the duty cycle at this current is about 1/10, and therefore the mean power dissipated is 5 MW. If the 22 kg/sec of H_2 per generator

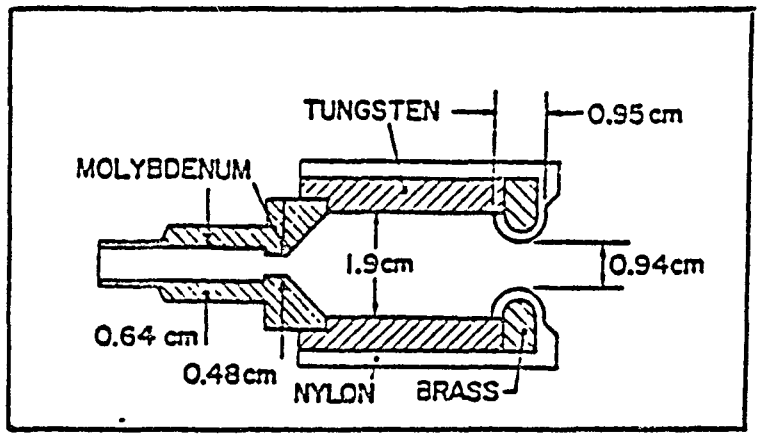

Figure VII-14. Experimental Hollow Cathode Configuration (From Reference 8)

were all passed through the cathodes, the temperature rise (assuming C_p = 14,000 J/kg - K) would be:

$$\Delta T = \frac{5 \times 10^6 \text{ Watt}}{0.1 \times 24 \times 22 \text{ kg/sec} \times 14{,}000 \text{ J/kg - K}} = \underline{7\ ^oK} \qquad (7)$$

Alternatively, if a ΔT of 1000 K is allowed, a fraction of 0.7 percent of the H_2 can accomplish the cathode cooling. This may be a better scheme given the remote location of the cathodes.

Turning to the sizing of the cathodes, Krishnan (Reference 8) showed that under optimum conditions, the current attachment region extends about 1 diameter into the cavity. In his experiments, satisfactory operation with minimum erosion was achieved at local current densities in this active region of the order of 1000-2000 A/cm^2. If we accept these figures as design guidelines, we can calculate the cavity diameter from

$$400 \times 10^3 \text{ Amp} = (\pi D) \times D \times 10^3 \text{ Amp/cm}^2 \qquad (8)$$

$$D = \underline{11.3 \text{ cm}}$$

Krishnan also found that the optimum amount of internal flow (of Argon, in this case) was 0.1 g/sec for a diameter of 1.9 cm. At this flow rate the current was spread internally the most evenly. Scaling this result with the diameter (to ensure equal free path/diameter ratio), we require a through flow of

$$\text{flow rate} = 0.1 \times (11.3/1.9) = \underline{0.6 \text{ g/sec}} \qquad (9)$$

or 0.06 g/sec per cathode on the average. This is a very small flow rate, and therefore it is quite possible to use Argon or other inert gas for the purpose thus preventing oxidation of the internal heated surfaces.

It is felt that the problem of designing efficient, lightweight cathodes is thus resolved satisfactorily. Anodes may pose a more severe challenge.

b. Anode

Two main requirements must be met here:

(1) Cooling of the anode to minimize erosion and corrosion.

(2) Avoidance of electrolytically accelerated anodic corrosion.

For efficient cooling, copper is usually preferred, since its good thermal conductivity minimizes hot spot formation and allows thicker, stronger sections. For a flight device, considerations of weight may favor other materials, provided corrosion problems are avoided (possibly carbon or carbon-based ion-intercalated compounds). The anode voltage drop ΔV in air-copper is 2-6 Volts (Cobine, Reference 10). The power deposited on the anode is approximately

$$\text{deposited power} = I\ (\Phi_a + \Delta V) \qquad (10)$$

where Φ_a is the work function of the anode material (4.5 Volts for Cu). Thus an effective drop of about 9-10 Volts can be expected, about twice that for the cathode. Regenerative cooling is therefore quite possible using modest amounts of hydrogen. Incidentally, the combined anode-cathode voltage drop is roughly 15 Volts. Comparing to the typical 6000 Volts overall for the discharge, this is only a 0.25 percent loss; the real importance of electrode losses is in the requirement for cooling rather than in the loss of efficiency.

The second requirement (corrosion avoidance) may be the most challenging, given the oxidizing atmosphere. In the presence of any molten microscopic salt or oxide layer deposited on the anode, ionic species such as $O^=$, $SO_4^=$, $S^=$, etc. are driven to the melt-metal interface, and produce strong and continuing corrosion upon discharge. This attack is strongly intensified at high temperature, so that a first line of defense must be the maintenance of anode temperatures below some 450 K. At this temperature, corrosion at a rate of 1-10 μg/Coulomb can still be expected. Assuming the current concentrates on the outer 20 cm of the anode (e.g., for the 10 m dia. shuttle, area = $2\pi \times 5 \times 0.2 = 6.3m^2$), the current den-

sity is of the order of 1.5×10^6 A/m^2, or 150 A/cm^2. At 10 μg/Coul, and with a density of 8.9 g/cm^3, this indicates a recession rate of:

$$\text{rate} = \left(150 \frac{\text{Coul}}{\text{sec-cm}^2}\right) \times \left(10^{-5} \frac{\text{g}}{\text{Coul}}\right) \times \left(\frac{1}{8.9 \text{ g/cm}^3}\right) = \frac{1.7 \times 10^{-4} \text{ cm}}{\text{sec}} \qquad (11)$$

Thus, during a typical firing duration of 60 sec, a loss of 0.1 mm could be sustained. This may become unacceptable if high reusability is desired. In that case, a possible modification could be the use of transpiration cooling using either hydrogen or another highly reducing agent; this would act as a "getter" for the oxidizing electrolytic agents, similar to the operation of the Bacon fuel cell anodes.

c. Electrode Integration with MHD-Fanjet

Figure VII-13 illustrates the geometry in which the telescoping transmission lines are attached to the center-body of a 5 m diameter shuttle. As indicated in Figure VII-15, each transmission line is equipped with a hollow cathode at its tip. The anode ring is attached to the outermost 20-50 cm of the lower shuttle surface. At hypersonic flight speeds, the shock wave formed off the vehicle center-body is used by the MHD-fanjet electric arc as an extended anode sheath as shown in Figure VII-15.

d. Dynamics of a Propulsive Electric Current Sheet

An analysis was performed on the dynamics of a propulsive current sheet representative of an MHD-fanjet RP actuator disk; it is included as Appendix C of this report. Two specific calculations were made, using input gas conditions that would be seen at the endpoints of an exemplary orbital fanjet flight trajectory: i.e., Cases I and IV in Figure VII-16. The "nominal" trajectory used for calculations of MHD-fanjet performance begins at 31 km (100,000 ft) altitude and 800 m/s velocity, and ends at 4 km/s and 68 km.

A first-order model of the transient behavior of high current plasma sheets used to accelerate gas in electromagnetic thrusters is one in which the sheet is assumed impervious to gas, and is reduced to a

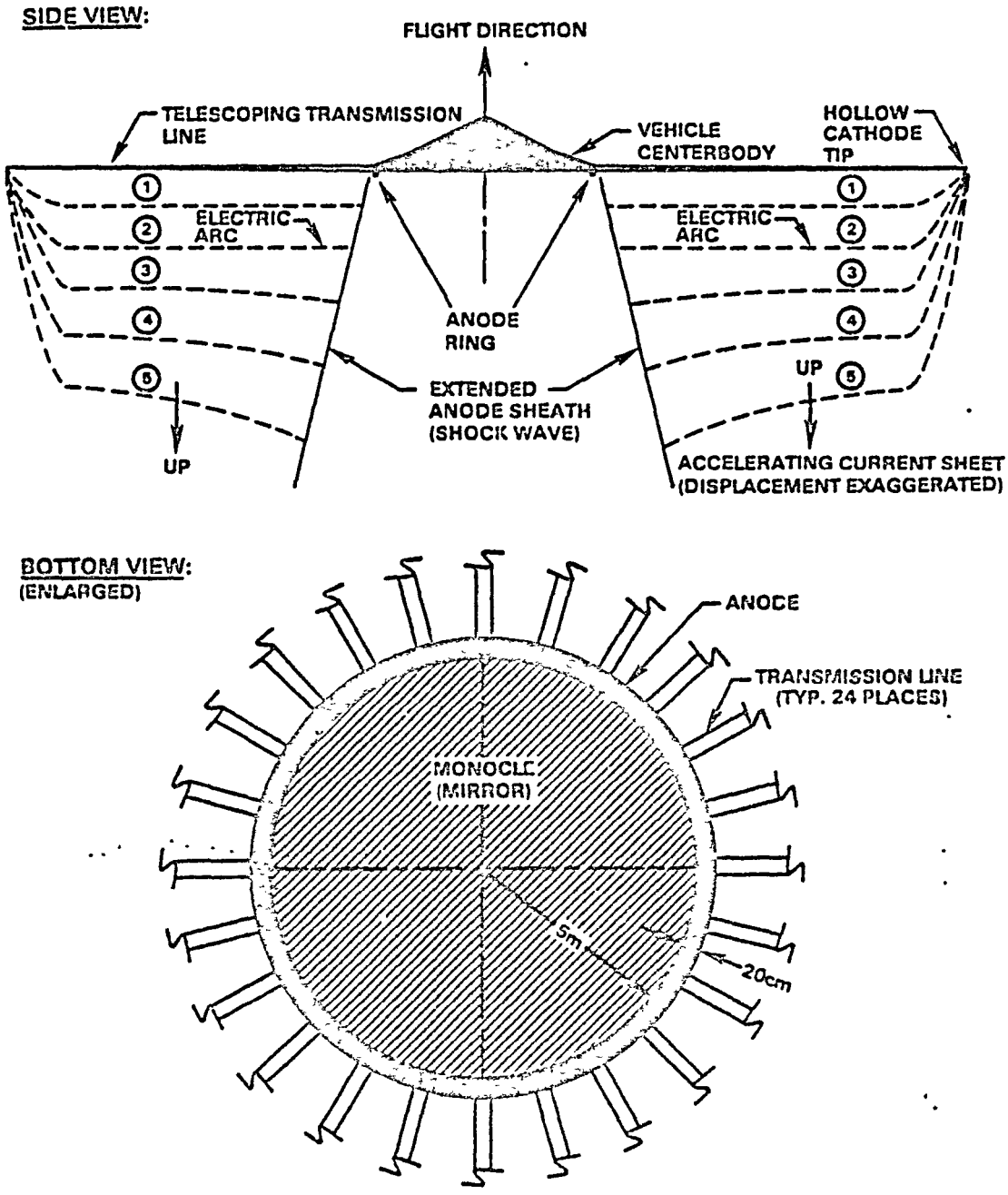

Figure VII-15. Electrodes for MHD-Fanjet (10m Shuttle)

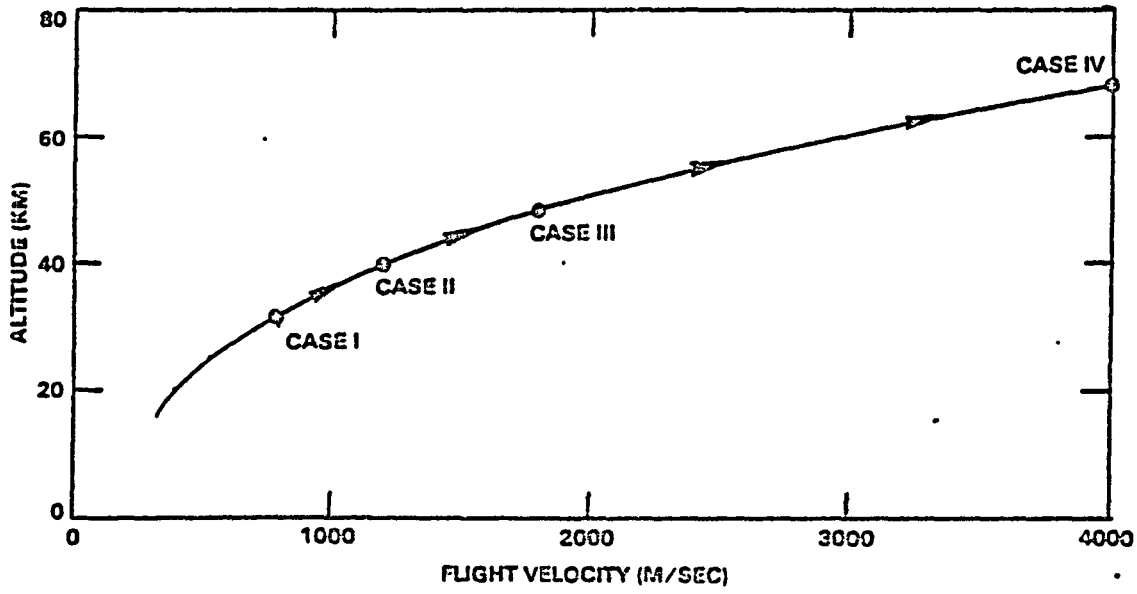

Figure VII-16. Exemplary Orbital Flight Trajectory for MHD Fanjet

geometrical surface acting as a piston. This is an improvement over the elementary "snowplow" model, in that it allows some insight into the gas behavior in front of and behind the advancing current sheet, but it still cannot by itself give information about the physics of the current sheet itself--its conductivity, temperature, permeability to the gas, thickness, etc.

Discussed in Appendix C is a model in which the piston approximation is used as a first order solution, establishing the basic flow field "far" from the current sheet. Also the structure of the current sheet itself is examined in some detail. In the interest of simplicity, several important approximations are still introduced (such as perfect gas behavior, one-dimensionality, etc.), but the model provides much insight into the factors controlling the sheet dynamics, and yields some quantitative information as well.

The major conclusions of this analysis are as follows. For good "gas sweeping" performance, permeability of the current sheet must quickly be reduced to the level of a few percent, and the gas temperature within the sheet quickly driven above 18,000 K (in order to reach the maximum gas conductivity) shortly after initiation of the electric discharge. Since the "point design" for a laser driven XMHD generator output calls for a 0.5 to 1.0 msec duration pulse, peak current sheet sweeping performance should really occur within 50 microseconds or earlier. The analysis suggests that any current sheet driven hard enough to reach 18,000 K (and very low permeability) in the first 10 microseconds will probably have a piston velocity (u_p) of at least 330 m/s--anywhere along the nominal MHD fanjet flight trajectory.

e. Fanjet Intake Radius vs. Flight Speed

Figure VII-17 shows the relationship of flight velocity and piston speed (u_p) as a function of propulsion efficiencies from 0.65 to 0.95. Since the analysis in Appendix C indicates that the propulsion concept may not work efficiently at u_p's less than sonic, we shall assume a fixed relative "piston speed" of 330 m/s.

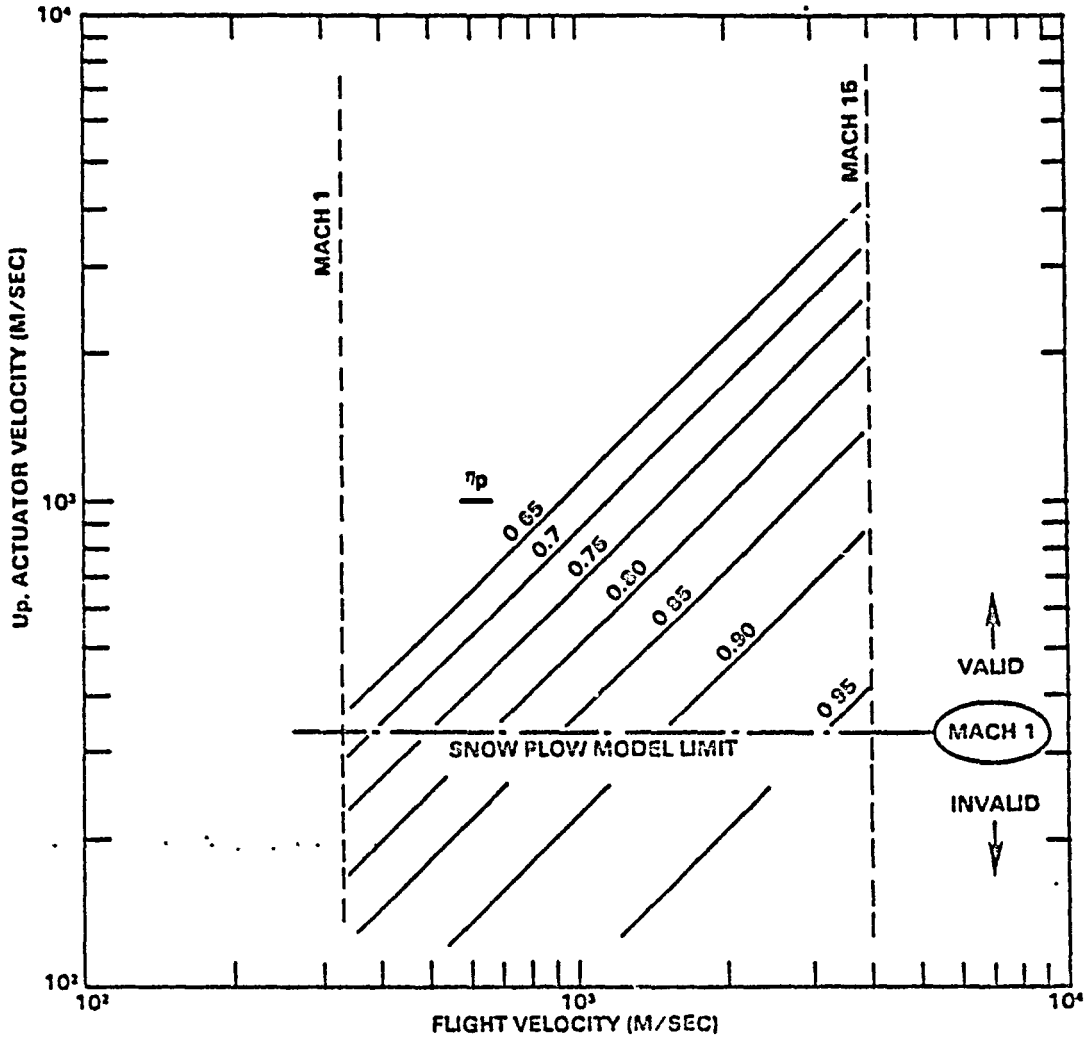

Figure VII-17. Actuator Speed as a Function of Flight Velocity for Various Propulsive Efficiencies

The fanjet intake radius (R_F) for a fixed value of time-average input electric power and u_p can be expressed as

$$R_F = \left[\frac{P_e}{\pi\rho\ (V + u_p/2)^2\ u_p}\right]^{1/2}, \text{ (m)} \qquad (12)$$

where R_F is the fan radius in meters, P_e is the available electric power in Watts, ρ is the atmospheric density in kg/m^3 and V is the flight velocity in m/s. For example, Figure VII-18 is a plot of Equation 12 for various altitudes from 16 to 68 km, assuming a fixed time-average input power of 2 GWe for the 10 m diameter shuttlecraft.

f. Exemplary 2-D "Snow Plow" Calculations

Exemplary two-dimensional, radially-symmetric "snow plow" calculations were performed for two points (Cases II and III) along the orbital trajectory in Figure VII-16 for the 10 m diameter shuttle; the mathematical model is reported in Appendix D. Table VII-2 gives the input trajectory data set for these MHD fanjet calculations. A number of other input parameters which do not exactly agree with the conditions assumed in Appendix C are displayed in Table VII-3.

"Snow plow" calculations were carried out using five material points. Two points (0 and 6) were placed at 5.0 m (the vehicle rim/anode location), and at the cathode tips (ends of electrical transmission lines), respectively. These points were forced to have zero velocity (relative to the vehicle) throughout the thrust pulse. No account was made for the mass flow intercepted by the vehicle centerbody area (25π m^2) in these calculations. The simulation was run for a total pulse duration of 1 millisecond in time steps of 10^{-4} seconds for Cases II and III.

Figure VII-19 shows the results of the simulation for Case II. The location of the current sheet is captured at intervals of 0.2 msec. As the pulse develops, the actuator disk deforms as expected, with higher changes in velocity towards the anode/rim (r = 5m). The current sheet reached a velocity (u_p) of 330 m/sec after 0.6-0.7 msec, and

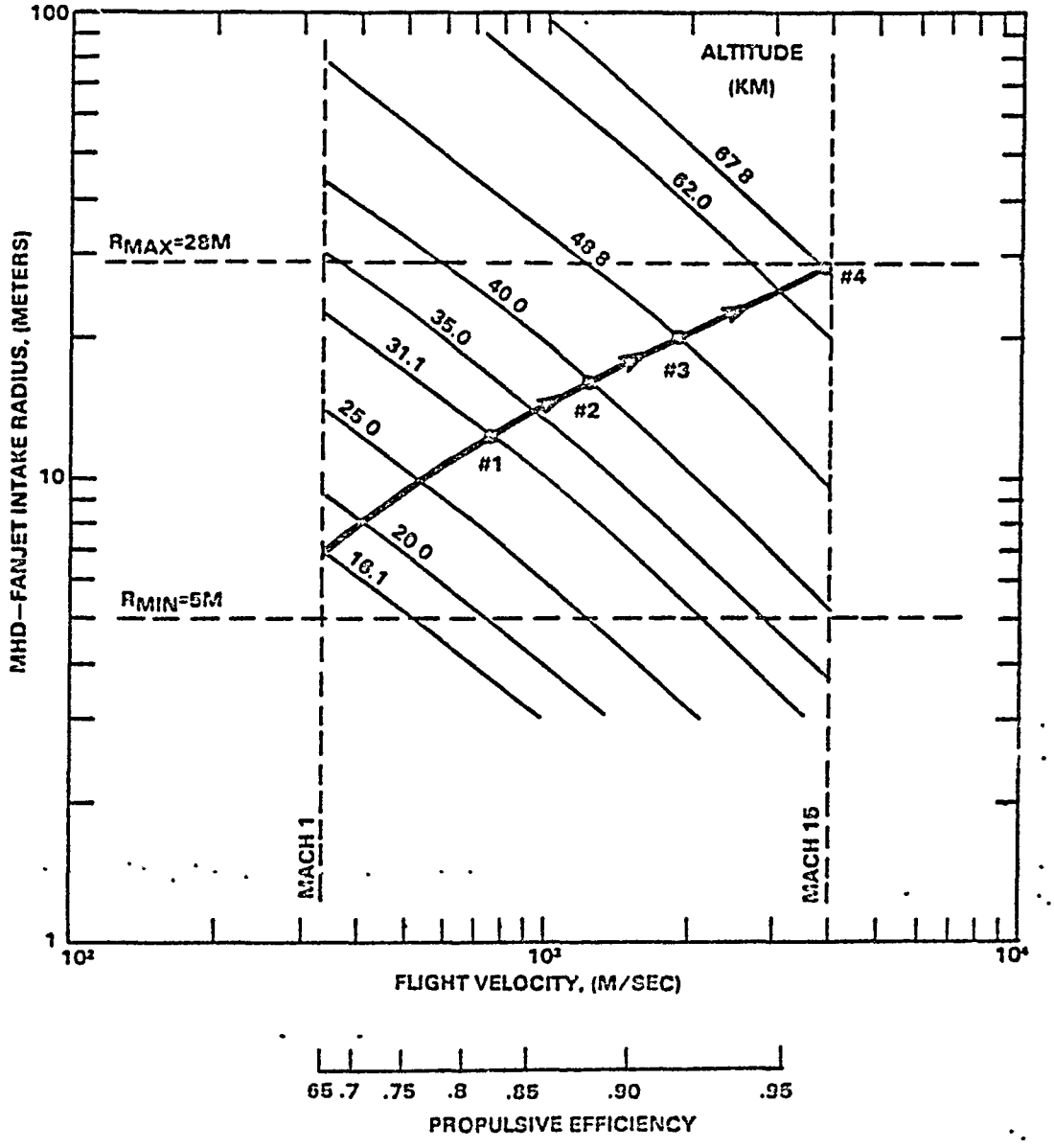

Figure VII-18. MHD-Fanjet Intake Radius vs. Flight Velocity

TABLE VII-2. DATA FOR MHD-FANJET PERFORMANCE CALCULATION

CASE	ALTITUDE (km)	DENSITY (kg/m^3)	FLIGHT VELOCITY (m/s)	FAN DIAMETER (m)	PROPULSIVE EFFICIENCY η_p	PISTON SPEED UP (m/s)
I	31.1	.01504	800.	24.	0.81	330
II*	40.0	4.020×10^{-3}	1200.	32.	0.87	↓
III*	48.8	1.254×10^{-3}	1800.	40.	0.91	↓
IV	67.8	1.486×10^{-4}	4000.	56.	0.95	330

*Chosen for numerical simulation.

TABLE VII-3. ASSUMED INPUT VALUES

PARAMETER	VALUES	
	APPENDIX C	APPENDIX D
σ-current sheet conductivity, (mho/m)	80.	200.
Current sheet thickness, (cm)	40. (initial)	50. (fixed)
Sheet thickness assumed for initial fanjet inductance (L_o), (cm)	40.	100.
Sheet representation	1D	2D-Toroid
Anode radius, (m)	$-\infty$	5
Cathode radius, (m)	$+\infty$	24 to 56 (31 km) (68 km)

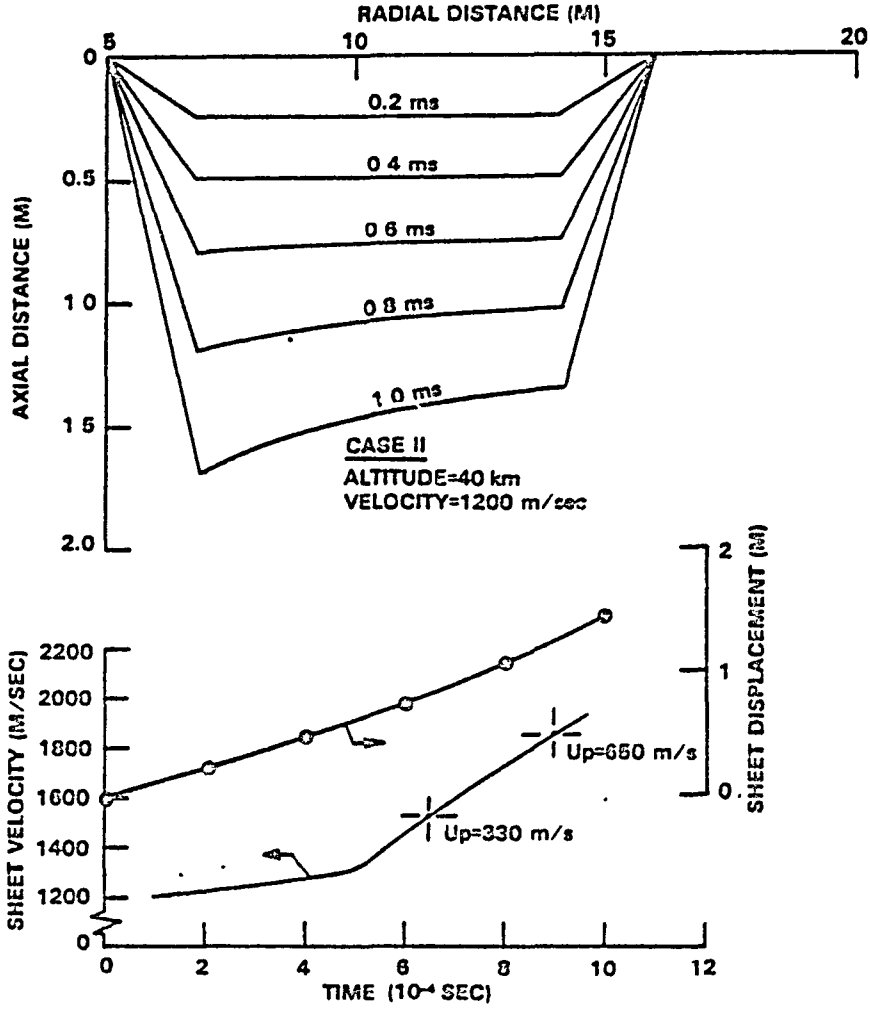

Figure VII-19. "Snow Plow" Results for Case II

650 m/sec at the end of the 1 msec simulation. The arc reached sonic velocity after moving roughly 0.8 m; 650 m/sec in 1.44 m--measured relative to the vehicle.

The simulation for Case III is displayed in Figure VII-20. As with Case II, the arc reached Mach 1 after 0.6-0.7 m/sec. Total displacement of the current sheet is roughly 1 m at u_p = 330 m/sec, and 2.08 m at 750 m/sec.

A summary of the model output is assembled in Table VII-4. For Case II, the MHD-fanjet arc discharge consumed 10.3 MJ of electric power to generate an impulse of 1800 N-sec; this translates to a coupling coefficient of 17.5 dyne-sec/Joule. The MHD-fanjet performance was substantially better in Case III, using 7.01 MJ to develop 2150 N-sec--for a coupling coefficient of 30.7 dyne-sec/Joule. Supplied with a nominal time-average input power of 2 GWe, the MHD-fanjet would operate at 194 Hz at 40 km altitude, and 285 Hz at 50 km.

Simple calculations were used to check the validity of the MHD-fanjet impulse values computed by the "snow-plow" model (see Table VII-5). To agree with the 2-D snow-plow model, the mass flow intercepted by the vehicle centerbody ($A = 25\pi$ m^2) is ignored. This represents 9.8 percent of the total intake area for Case II; 6.3 percent, for Case III. If one assumes that the mass flow through the remaining annular MHD fanjet intake area is accelerated smoothly from V_o (flight speed) to $V_o + u_p$, and that the static gas pressure at the exit of the fanjet is equal to ambient, then the time-average thrust (F_{ave}) can be expressed as

$$F_{ave} = \rho_o A_{fan} V_o u_p, \text{ (Newtons)}, \qquad (13)$$

where ρ_o is the ambient air density in kg/m^3, A_{fan} in m^2, V_o and u_p in m/sec. The average thrust in Table VII-4 is calculated using the final current sheet velocities predicted by computer simulations. As indicated, the time-average thrust calculated by the snow-plow model roughly agrees with that of Equation 13.

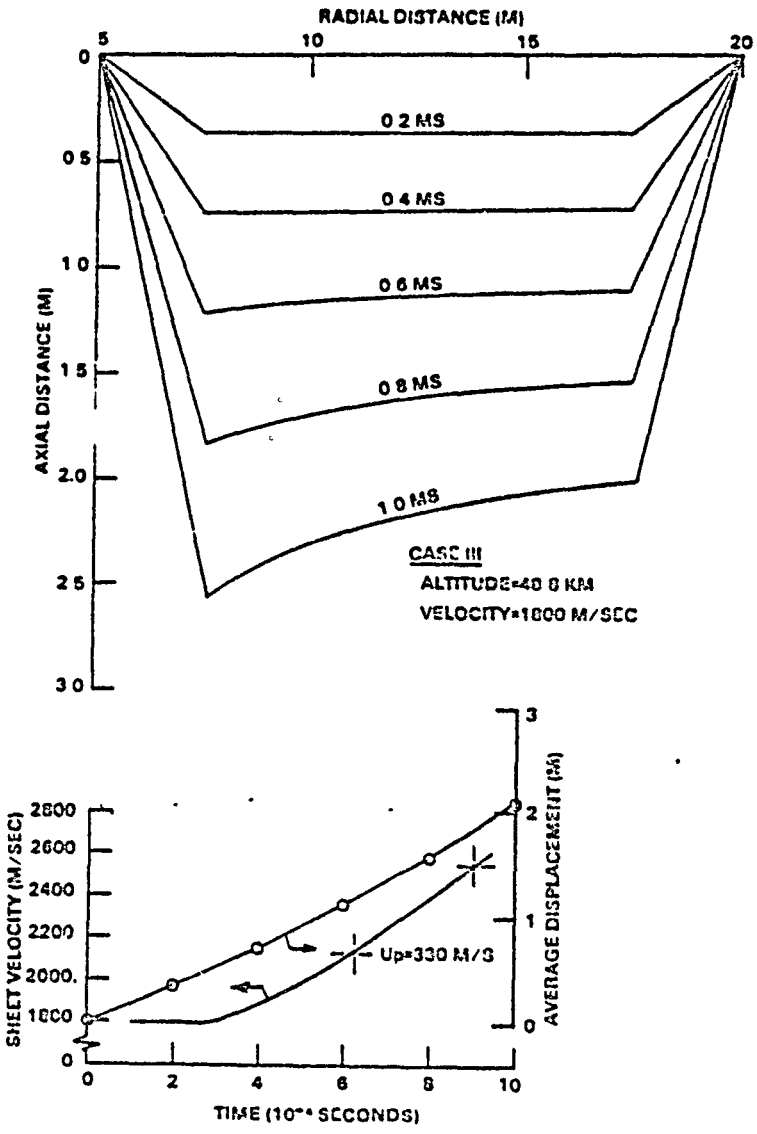

Figure VII-20. "Snow Plow" Results for Case III

TABLE VII-4. SUMMARY OF MODEL OUTPUT

Case #	Altitude (km)	Piston Speed u_p (m/s)	ΔX_{max} (m)	Thrust F_{ave} (10^6N)	Energy E_{tot} (10^6J)	PRF for 2 GWe (Hz)	Actual Coupling Coefficient (d-s/J)
II	40.0	650.	1.44	1.8	10.3	194.	17.5
III	48.8	750.	2.08	2.15	7.01	285.	30.7

TABLE VII-5. ANALYTICAL CHECK OF MOMENTUM FLUX

Case #	Altitude (km)	Fan Intake Area (m^2)	Mass Flow Rate (kg/m^2)	Piston Speed u_p (m/s)	Thrust F_{ave} (10^6N)	Ideal coupling Coefficient (d-s/J)	Coupling Efficiency $\left(\frac{\text{actual}}{\text{ideal}}\right)$
II	40.0	726.	3500.	650.	2.28	65.6	27%
III	48.8	1180.	2660.	750.	1.99	46.2	66%

For an air breathing engine, it can be easily shown that the coupling coefficient is

$$C = F_{ave}/P_e = 10^5/(V_o + u_p/2), \text{ (dyne-sec/Joule)} \qquad (14)$$

where P_e is the time-average input power in Watts. As shown in Table VII-4, the ideal theoretical coupling coefficient of 65.6 d-s/J for Case II is a factor of 3.75 greater than predicted by the simulation. This would suggest a poor coupling between the MHD generator output and the fanjet's accelerating current sheet. The agreement for Case III is substantially better, indicating a coupling efficiency of 66 percent ideal. There is little doubt that such coupling efficiencies could be improved to the 80-90 percent level through proper matching of MHD accelerator and generator electrical parameters.

B. SHUTTLECRAFT WEIGHT-SCALING ESTIMATE

In order to evaluate the flight performance of SSTO shuttlecraft, first-order weights analyses must be made for the three point designs: 5m, 10m, and 20m diameter vehicles. Each vehicle is equipped for four propulsion modes: ERH thruster, rotary pulsejet, MHD-fanjet, and IRH rocket. Each of the vehicles utlizes a standardized propulsion module, the IRH pulsejet (also referred to elsewhere as a plasma generator) which is able to absorb 5MJ laser pulses at a repetition frequency of 20-60 Hz. Therefore, each pulsejet module is able to develop a time-average thermal power of 100 to 300 megawatts. As mentioned earlier, these engines are distributed linearly about the vehicle rim, and laterally measure about 1 meter; hence, 12 will fit on a 5m vehicle, 24 on a 10m vehicle, and 48 on a 20m diameter vehicle. As mentioned above, the 5m vehicle is able to carry a 1 man payload (90 kg) to orbit; the 10m vehicle, 2 men (182 kg); and the 20m vehicle, 15000 kg--equal to half the capability of the space shuttle orbiter. The relevant descriptive shuttle data is summarized in Table VII-5.

Internal vehicular volume for the craft pictured in Figure VII-2 is calculated generally assuming a 120^{o} apex right cone for definition of the upper surface and a 160^{o} apex right cone for the lower heat shield surface. Internal volume for the 5m diameter vehicle comes to $30m^3$; $100m^3$ for the 10m diameter; and $300m^3$ for the 20m diameter. Spacecraft structural weight is estimated from these volumes by assuming an average density of 40 kg/m^3 (2.5 lb/ft^3). This value is based upon an observed density history in body structure weight design of US spacecraft as reported in Reference 11.

The mass of a typical pulsejet chamber is estimated from data in Reference 12 to be 93 kg/chamber (204 lbs). The calculation is based on an ideal spherical plenum chamber (volume of 0.5 m^3) with an allowable yield stress of 200,000 psi, which is reasonable for advanced pressure vessel materials. The chamber is designed to contain a blast wave with a face-on pressure of 2,000 psi (136 atm) with a factor of safety of 2. The superconducting coil weight for each XMHD generator is estimated from projections in Reference 13 for a generator having a peak power output of 2.75 GW and a value of 4×10^{10} for $U^2B^{1/2}$. A coil specific mass of 4.3×10^{-5} kg/kW results in a mass of 118 kg/coil.

The telescoping electrical transmission lines are assumed to be fabricated of composite superconductors with a matrix ratio of superconductor to normal metal of 1:4 by mass. The self-magnetic field of the MHD-fan (as defined by Equation 1 in Chapter VI) is seen to bathe the superconductor at the rim of the 10m diameter vehicle in a peak magnetic field of only 6 kilogauss, for a peak current through the toroid discharge path of 1.5×10^7 Amperes. Hence, we will assume that a superconductor can be found which will remain superconducting in this relatively weak self-magnetic field and still exhibit a current density of 10^5 $Amps/cm^2$.

If we assume that each transmission line is designed to carry a maximum of 10^6 Amperes, the conductor cross-sectional area must be one square centimeter. The mass of each transmission line is then obtained by multiplying the total volume of the conductor by its density, then quadrupling the result to account for the normal metal. The length of a transmission

line is obtained by substracting the vehicle radius from the maximum MHD-fan intake radius presented in Table VII-6. A superconductor density of 8.4 gm/cm^3 is assumed in the calculation. For the 10m diameter vehicle, we find that each 23m long transmission line has a mass of 78.4 kg, giving 1882 kg total for all 24.

Laser-powered shuttles can easily exhibit a mass ratio of 1.5 where only 33 percent of the initial launch mass is dedicated to liquid propellants. Equation 14 below shows the relationship between engine specific impulse (I_{sp}), velocity change, and mass ratio:

$$m_i/m_f = \exp\ (\Delta V/I_{sp}\ g) \qquad (14)$$

where m_i is the launch mass and m_f is the final mass after making the velocity change (ΔV). It is assumed that a shuttlecraft will accelerate from a velocity of 4 km/sec in largely air-breathing modes which consume less than 10 percent of the total on-board propellants. Listed in Table VII-7 are the propellant requirements for each shuttle in accelerating from 4 km/sec up to 8 km/sec low earth orbital velocity (i.e., ΔV = 4 km/sec) with an IRH rocket (I_{sp} = 1000 seconds).

Incidentally, Rom and Putre[14] have performed theoretical calculations that indicate the optimum specific impulse for laser-heated rockets: "The greatest payload delivered to low earth orbit per total energy consumed at the laser power station lies with rocket engines having an I_{sp} in the range of 1200 to 2000 seconds." As mentioned earlier, the lower end of this range has already been demonstrated in small-scale experiments with hydrogen-fueled, pulsed laser-heated rockets.

Summing the various component masses listed in Table VII-6, we find that the 5m diameter vehicle has a lift-off mass of 5550 kg; the 10m diameter vehicle 18,350 kg: and the 20m vehicle 70,480 kg. Note that the "wing loading" at lift-off for the smallest vehicle is 283 kg/m^2, and 202 kg/m^2 for the largest. These wing loadings are not far removed from that of conventional light jet aircraft.

TABLE VII-6. SHUTTLE VEHICLE DATA

PARAMETER \ VEHICLE DIAMETER	5m	10m	
NO. OF PLASMA GENERATORS	12.	24.	48.
LASER ENERGY PER PULSEJET (MJ)	5.	5.	5.
PEAK POWER PER PULSEJET (MW)	100.-300.	100.-300.	100.-300.
PAYLOAD TO LEO (kg)	90.	180.	15,000.
VEHICLE HEIGHT (m)	1.8	3.	5.3
INTERNAL VEHICLE VOLUME (m^3)	30.	100.	303.
VOLUME OF LH_2 (m^3)	26.4	78.6	303.
ERH THRUSTER AREA* (m^2)	19.6	78.5	314.
MAX. DIA. OF MHD-FAN (m)	28.	56.	80.

* ERH THRUSTER AREA IS SET EQUAL TO ENTIRE VEHICLE BASE AREA.

TABLE VII-7. VEHICLE MASS ESTIMATE

VEHICLE DIAMETER / PARAMETER	MASS (kg)		
	5m	10m	20m
AIRFRAME & STRUCTURE	1250.	3890.	12,300.
PLASMA GENERATORS	1210.	2220.	4440.
XMHD GENERATOR MAGNETS	690.	2840.	5680.
TRANSMISSION LINES	460.	1880.	4910.
PAYLOAD	90.	180.	15,000.
VEHICLE DRY MASS	3700.	11,000.	42,300.
PROPELLANT TO LEO*	1850.	5,500.	21,200.
MASS AT LIFT-OFF	5550.	16,500.	63,500.

*ASSUMES MASS RATIO OF 1.5, for ΔV = 4km/sec.

C. LASER POWER REQUIREMENTS

We will now summarize the laser power requirements for the four variable-cycle propulsion modes. As mentioned before, the external-expansion base thruster is utilized for air-breathing VTOL propulsion to perhaps 3 km and Mach 1. The rotary pulsejet air-breathing mode is applied in the regime from Mach 1 to 3, and 16 to 30 km. The air-breathing MHD-fan carries the vehicle to 80 km and 4 km/sec. Beyond 4 km/sec, the vehicle leaves the atmosphere and accelerates to the 8 km/sec low earth orbital velocity in the IRH rocket mode on strictly internal propellant (e.g., hydrogen).

Proper operation of an ERH thruster should result in a maximum coupling of the order of 100 dynes/Watt. Hence, a laser power of 162 MW (e.g., 10 MJ pulses at 16.2 Hz) is required to levitate the 10m vehicle, and 1.62 GW (10MJ Pulses at 162 Hz) will boost it vertically at 10 g's acceleration. The hover condition can be maintained with a time-average base over-pressure of only 0.03 atm. Table VII-8A summarizes laser power requirements for all three vehicles in this mode.

After a shuttle climbs to a substantial altitude, it may transition to lateral acceleration in the rotary air-breathing pulsejet mode. Calculations of the maximum sea level static thrust for rotary air-breathing pulsejets were made earlier and are summarized below in Table VII-8B. Note that thrust is approximately constant for all three vehicles, varying between 1.37 to 1.95 X 10^5 Newtons. As indicated, the maximum thrust to weight ratio is 2.54 for the 5m vehicle, 0.96 for the 10m vehicle and 0.3 for the 20m vehicle. The acceleration of the 20m vehicle will be quite sluggish compared to the 5m, unless the laser pulse energy can be significantly increased above 5 MJ; however, this will substantially increase air temperatures, and may somewhat reduce the coupling coefficient.

At supersonic flight velocities from Mach 2-3 up to about Mach 12, and altitudes from 30 to 80 km where insufficient air exists for air-breathing rotary pulsejet operation, the shuttle will propel itself in the MHD-fan mode. For example, the 10m vehicle may fly at a velocity of 800 m/s and an

TABLE VII-8. PERFORMANCE ESTIMATE

A. ERH THRUSTER (Sea Level, Zero Velocity)

PARAMETER \ VEHICLE DIAMETER	5m	10m	20m
COUPLING COEFFICIENT $(d\text{-}s/J)_L$	100.	100.	100.
MASS AT LIFT-OFF (10^3kg)	5.55	16.5	63.5
"WING LOADING" (kg/m^2)	283.	210.	202.
REQUIRED LASER POWER (MW)			
o HOVER (1g)	54.	162.	622.
o 3 g's ACCELERATION	162.	485.	1867.
o 10 g's ACCELERATION	539.	1620.	6220.

B. AIR-BREATHING ROTARY PULSEJET (Sea Level Altitude)

PARAMETER \ VEHICLE DIAMETER	5m	10m	20m
MAX LASER PRF (sec^{-1})	168.	192.	240.
COUPLING COEFFICIENT $(d\text{-}s/J)_L$	20.	20.	20.
MAX REVOLUTIONS/SECOND	14.	8.	5.
VEHICLE MASS (10^3kg)	5.5	16.5	63.5
MAX ABSORBED LASER POWER (MW)	670.	770.	960.
MAX THRUST (10^5 Newtons)	1.37	1.56	1.95
MAX THRUST/WEIGHT RATIO	2.54	0.96	0.31

TABLE VII-9. PERFORMANCE ESTIMATE

A. MHD-FANJET (31.1 KM, 300 M/S)

PARAMETER \ VEHICLE DIAMETER	5M	10M	20M
VEHICLE MASS (10^3 Kg)	5.55	16.5	63.5
ELECTRICAL COUPLING COEFFICIENT $(d\text{-}s/J)_e$	95.	95.	95.
LASER COUPLING COEFFICIENT $(d\text{-}s/J)_L$	47.5	47.5	47.5
CENTER-BODY DRAG (GW)	0.124	0.496	1.98
ACTUATOR VELOCITY (M/S)	330.	330.	330.
PROPULSIVE EFFICIENCY (%)	81.	81.	81.
REQUIRED LASER POWER (GW)			
o 1g ACCELERATION	0.239	0.836	3.29
o 3 g's ACCELERATION	0.467	1.52	5.91
o 10 g's ACCELERATION	1.27	3.90	15.1

B. IRH ROCKET PULSEJET (>70 km, >4 km/s)

PARAMETER \ VEHICLE DIAMETER	5M	10M	20M
VEHICLE MASS (10^3 Kg)	-5.55	-16.5	-63.5
LASER COUPLING COEFFICIENT $(d\text{-}s/J)_L$	12.5	12.5	12.5
REQUIRED LASER POWER (GW)			
o 1g ACCELERATION	0.435	1.29	4.98
o 3 g's ACCELERATION	1.31	3.88	14.9
o 10 g's ACCELERATION	4.35	12.9	49.8

altitude of 31 km with an electrical coupling coefficient of 95 d/We, an MHD-fan diameter of 24 meters, and a propulsive efficiency of 81 percent. For an electrical conversion efficiency of 50 percent, the laser coupling coefficient would be 47.5 dynes/Watt$_L$. With a total laser input power of less than 3.5 GW, the engine is able to process an air mass flow rate of 5440 kg/s through an induced velocity change of 330 m/s and thereby produce a gross thrust of 2.24 X 10^6N. The 10m diameter 120^o apex cone body will produce a drag force of 6.2 X 10^5N (i.e., 496 MW) at this flight velocity and altitude. Ignoring the additional parasite and wave drag caused by the transmission lines, we find that the net thrust of 1.62 X 10^6N is enough to accelerate the 16,500 kg vehicle at 10 g's. Similar calculations for the 5m and 20m shuttle are displayed in Table VII-9A.

Much beyond 4 km/s, it may be preferable for the vehicle to leave the atmosphere in order to avoid excessive aerodynamic heating, and to convert to the use of internal hydrogen propellant in a IRH rocket propulsion mode. As mentioned above, a hydrogen-fueled pulsed laser rocket engine has demonstrated a coupling coefficient of 12.5 dynes/Watt, a specific impulse of 1000 seconds and an overall laser-to-thrust-power conversion efficiency of about 50 percent. Hence Table VII-9B assumes these values in calculating laser power requirements for the three shuttlecraft.

D. POTENTIAL LAUNCH TRAJECTORY FOR 10M SHUTTLE

Using the above weights data and the altitude-cependent coupling coefficients of the various propulsion modes, one can attempt to describe a typical altitude/velocity trajectory to low earth orbit for the 10m shuttle. One sample trajectory is shown in Figure VII-21.

The large-area laser-heated VTOL thruster integrated with the shuttle lower surface permits a rapid jump to supersonic flight velocities. At launch, the 10 meter diameter shuttle is delivered 24 separate beams which contain 5 MJ pulses at a PRF of 30 Hz--for a combined laser power of 3.6 gigawatts. This power is transmitted to the ERH thruster, thereby

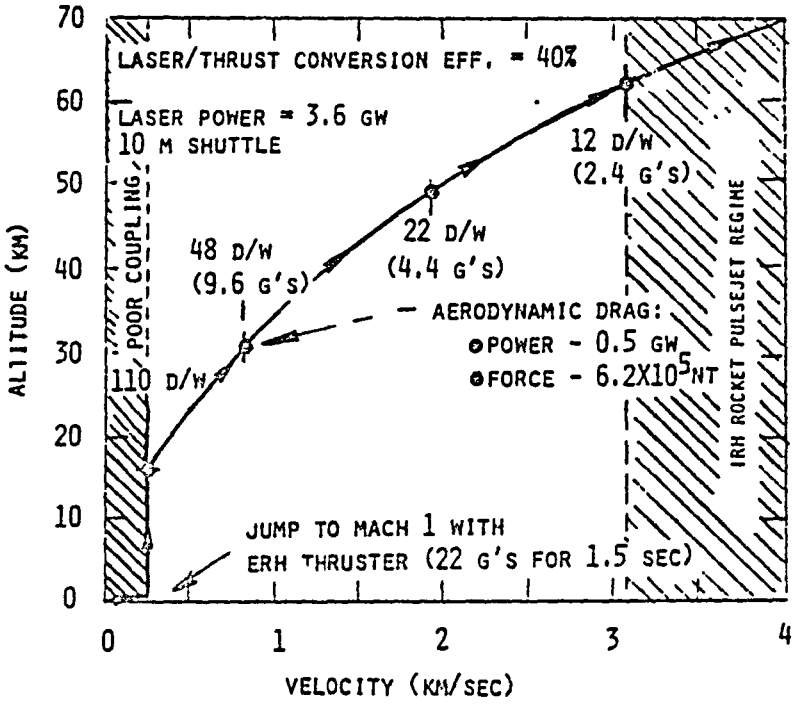

Figure VII-21. Typical SSTO Trajectory for 10m Diameter Shuttle

generating 4 X 10^6 Newtons of thrust, which is sufficient to accelerate the shuttle at 22 g's. Within 1.5 seconds, the vehicle has reached sonic velocity, having climbed only 250m on the energy from 46 laser pulses. (With a properly tailored impulse, today's jet pilots could sustain the g-load if reclined horizontally.)

From here, the 10m shuttle proceeds to climb vertically at sonic velocity using the rotary air-breathing pulsejet and/or ERH thruster to an altitude of 16 km--where the MHD-fanjet is engaged.

Here the vehicle extends its "transmission-line" electrodes to a diameter of 14 meters and continues to climb vertically at increasing supersonic velocities--until reaching an altitude of 70 km and speed of 4 km/sec. At this altitude, the MHD fan electrodes (which have now been extended to 28M) are completely retracted and the vehicle now changes to the IRH rocket mode. It then leaves the atmosphere, and accelerates to orbital velocity.

Following re-entry, the air-breathing rotary pulsejet mode is utilized for maneuvering prior to a VTOL landing, which again is accomplished with the ERH thruster.

E. ACKNOWLEDGEMENT

The sections on MHD-fanjet electrode design requirements and the dynamics of a propulsive current sheet were provided by M. Martinez-Sanchez; D. Heimerdinger computed the "snow plow" model results in Figures VIII-19 and VIII-20.

This Page Intentionally Left Blank

REFERENCES FOR CHAPTER VII

1. Laser Focus, August 1978, p. 104.

2. AMERICAN INSTITUTE OF PHYSICS HANDBOOK, McGraw Hill Book company, 1980.

3. Raizer, Y. P., "Heating of a Gas by a Powerful Light Pulse," J. Expt. Theoret. Physics, Vol. 48, May 1965, p. 1508-1519; also, Sov. Phys.-JETP, Vol 21, 1965, pp. 1009ff.

4. Pirri, A. N., "Theory for Momentum Transfer to a Surface with a High-Power Laser," The Physics of Fluids, Vol. 16, No. 9, September 1973, pp. 1435-1440.

5. Popper, L., "Gas Escape from an Enclosed Cavity (Supersonic and Subsonic Flow)," Memorandum to J. P. Reilly, dated 29 May 1974, AVCO Everett Research Laboratory, Inc., Everett, Masachusetts.

6. Pirri, A. N., et. al., "Propulsion by Absorption of Laser Radiation," AIAA Journal, Vol. 12, No. 9, September 1974, pp. 1254-1261.

7. Nebolsine, P. E., Pirri, A. N., Goela, J. S., and Simons, G. A., "Pulsed Laser Propulsion," Proceedings of 1978 JANNAF Conference, Incline Village, Nevada, 14 February 1978.

8. Krishnan, M., and Jahn, R. G., "Physical Processes in Hollow Cathodes in High Current Discharges," AMS Report 1293, Princeton University, 1976.

9. Delcroix, J. L. and Trindade, A. R., "Hollow Cathode Arcs," Advances in Electronics and Electron Physics, Vol. 35, L. Marton ed., Academic Press, 1974.

10. Cobine, J. D., GASEOUS CONDUCTORS, THEORY AND ENGINEERING APPLICATIONS, Dover Publications, Inc., New York, 1958.

11. Heineman, W. Jr., "A Total Perspective Weight Technique for Advanced Manned Spacecraft", SAWE Paper No. 793, 28th Annual Conference of the Society of Aeronautical Weight Engineers, San Francisco, CA, 5-8 May 1969.

12. Teno, J. and Sonju, O. K., "Development of Explosively-Driven MHD Generator and Short Pulse Aircraft High Power," Interim Technical Report, No. 1, AERL Report AFAPL-TR-74-48, Avco Everett Research Laboratory, Everett, MA, June 1974.

13. Rosa, R. J., MAGNETOHYDRODYNAMIC ENERGY CONVERSION, McGraw-Hill Book, Co., New York, 1968.

14. Rom, F. E. and Putre, H. A., "Laser Propulsion," TM-X-2510, NASA, April 1972.

CHAPTER VIII
LASER-THERMAL AIR-BREATHING PROPULSION OF CYLINDRICAL CONFIGURATIONS

This chapter investigates promising laser-thermal propulsion modes for cylindrical shuttlecraft configurations which would utilize either heavier-than-air or lighter-than-air structures technology. The former category might apply to vehicles with lengths from 10 to 100 meters; the latter to a larger class of shuttles measuring 100 to 1000 m in length. (These would be neutrally buoyant only in the low altitude planetary atmosphere, e.g., less than 3 km.) Air-breathing laser pulsejet engines augmented by aerostatic, aerodynamic, and free-vortex-induced lift would be used to propel these cylindrical shuttlecraft out through the densest portion of the atmosphere. Within this flight regime, low flight velocities could permit the attainment of exceptionally high ratios of thrust-to-laser power, while keeping aerodynamic drag to a minimum.

A. ENGINE/OPTICS/AIRFRAME CONFIGURATION

The general configuration proposed for cylindrical shuttlecraft is pictured in Figure VIII-1A. The airframe structure has a fineness ratio (i.e., length/diameter) of roughly 10:1. Attached to one (or both) ends of the vehicle is a laser-driven power head module. The geometry of these modules is configured similarly to the rotary pulsejet engine pictured in Figure V-14.

The proposed optical train configuration for cylindrical shuttlecraft is shown in Figure VIII-1B. To enhance clarity, optical elements are displayed greatly enlarged in proportion to vehicle diameter. For example, the radial dimensions of high-power primary optics need be as little as 2 meters for a shuttle with an external diameter of 10 meters (and vehicle length of 100 meters). As shown in Figure VIII-1B the laser beam is received through an opening in the upper vehicle skin onto a "beam catcher"

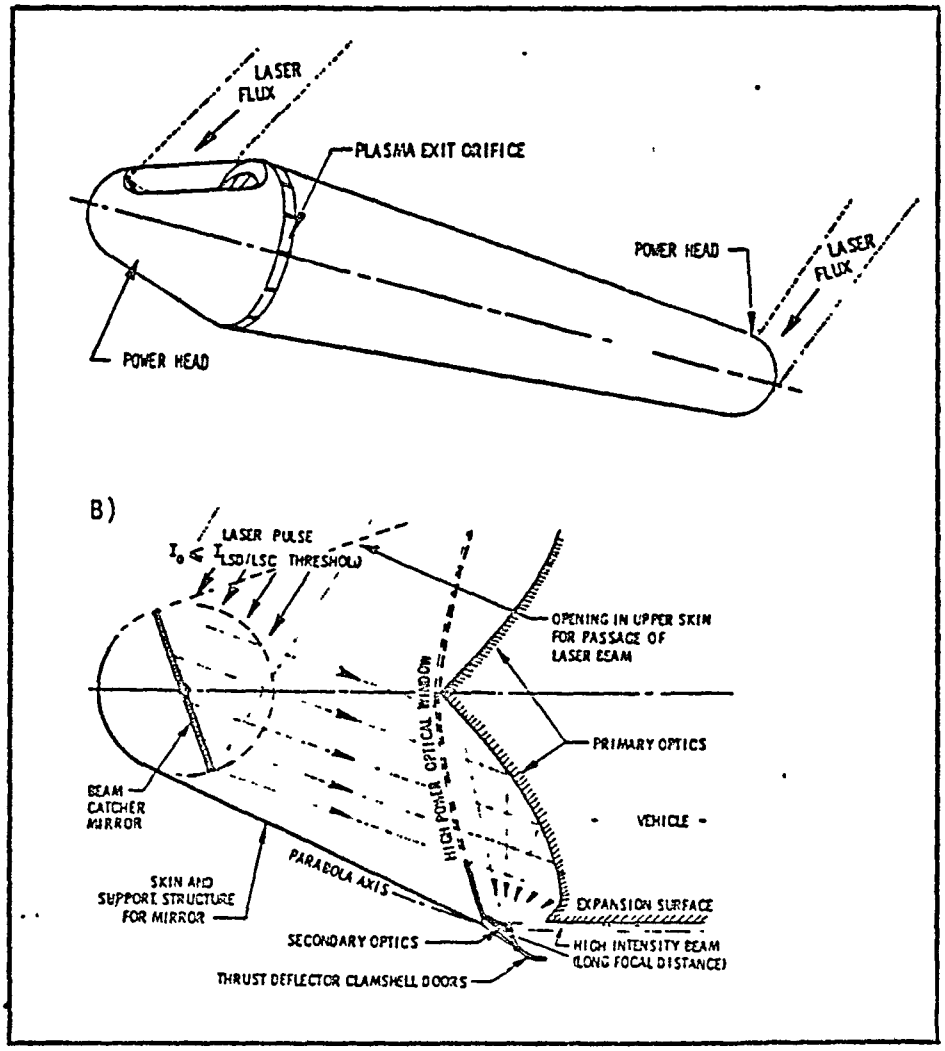

Figure VIII-1. Engine/Optical/Airframe Configuration for Cylindrical Shuttlecraft

mirror. This articulated mirror is able to project the reflected beam onto any azimuthal location around the radially symmetric primary optical surface. Before contacting the parabolic primary optics, the beam passes through a high-power window. The primary optics and high-power window constitute a donut-shaped high-pressure structural envelope for the absorption of laser energy. For the 10 m diameter shuttle, the donut-shaped envelope would be divided radially into 24 independent absorption chambers.

Upon reflecting off the primary optics, the beam is either a) focused to a high intensity upon the secondary optics, then reflected to a remote location for absorption (as shown in Figure VIII-1B), or b) the secondary optics are retracted away from the focal region and the beam is subsequently allowed to come to a line focus (around the vehicle perimeter) midway between the exhaust ports of individual absorption chambers. The functional logic for this optical train configuration will become more apparent with subsequent discussions in this chapter.

B. ERH PULSEJET MODE

The use of propagating LSD waves (long path-length) and pulsed external expansion thrusters can permit highly distributed surface pressures to be placed along the cylindrical shuttle exterior; hence, longitudinal bending moments produced on shuttlecraft structure during maneuvers are reduced to a minimum.

The ERH thruster mode necessitates the use of secondary optics which are rotated into a position near the focal region of the primary optics. As illustrated in Figure VIII-1B, the low intensity beam incident on the primary lens is brought nearly to a "point" or "line" focus upon the secondary optics. In turn, the secondary lenses project the high intensity beam (now with a very long focal length) towards the opposite end of the vehicle. The optical axis of this beam is aligned with the longitudinal axis of the shuttle and is spatially located just a few centimeters above the vehicle external skin, as shown in Figure VIII-2.

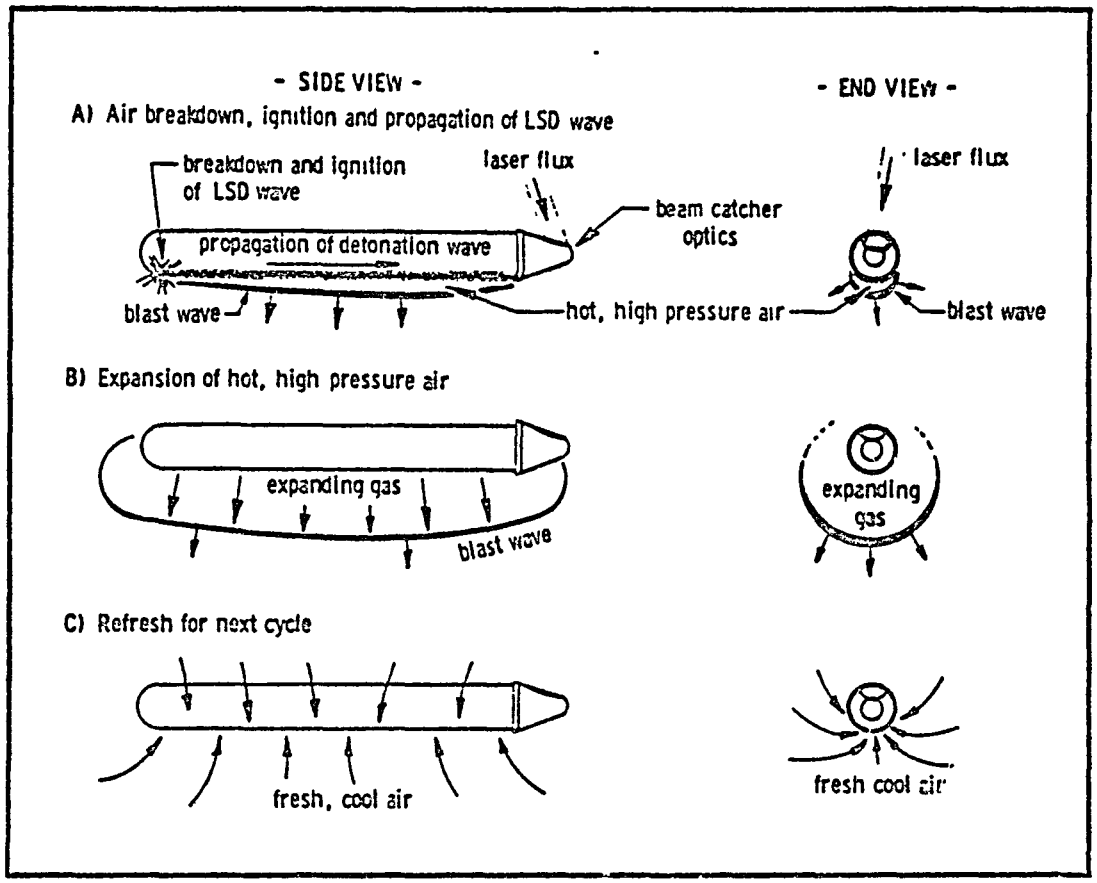

Figure VIII-2. Pulsed External Expansion Thruster Cycle

The ERH thruster cycle begins when electrical breakdown is triggered by a) an electrical spark, b) the ejection of an easily ionized vapor (or particulate), or c) laser-induced breakdown absorption at a precisely controlled "ignition" location. Subsequently, LSD absorption waves propagate the length of the vehicle and leave in their wake cylinders of hot, high-pressure air. The rapid expansion of this plasma drives a cylindrical blast wave into the surrounding air, and shoves it aside. In the process, a reaction force is applied to the vehicle, lifting it into the air. A short time later fresh, cooler air rushes back to the lower surface of the vehicle, the laser pulse is reinitiated, and the cycle begins again.

As shown in Figure VIII-3A, the vehicle is able to move in a lateral direction (i.e., perpendicular to the longitudinal axis)--right, left, up or down simply by positioning the laser beam into the proper pulsejet chamber at the 9:00, 3:00, 6:00 or 12:00 positions, respectively. Yaw and pitch maneuverability are facilitated by terminating the laser pulse early as indicated in Figure VIII-3B. The alternative approach of triggering ignition points at the vehicle center and propagating LSD waves to the vehicle ends will generate equivalent results. Therefore, it is clear that the LSD wave ignition point must be carefully controlled, lest the vehicle be imparted with an unexpected asymmetric thrust.

Since instantaneous pressures generated by passage of the LSD wave may be as high as 100 atmospheres, "hard" reinforced thrust-bearing surface plates must be attached to the external shuttlecraft structure in order to transmit this load directly to the longeron structure. Rapid deterioration of the pressure within the expanding cylindrical plasma will eventually result in its re-distribution to a much larger surface area; as a result, a significantly lower-pressure impulse is finally communicated to the substantially weaker vehicle skin. These "hard" ERH thruster pads must also be designed to operate without deterioration in the elevated gas temperatures generated by the LSD waves.

The physics of ERH thrusters has been treated in Chapters III-VII and will not be pursued further here--other than to point out that the maximum coupling coefficient obtainable by the air-breathing ERH thruster is

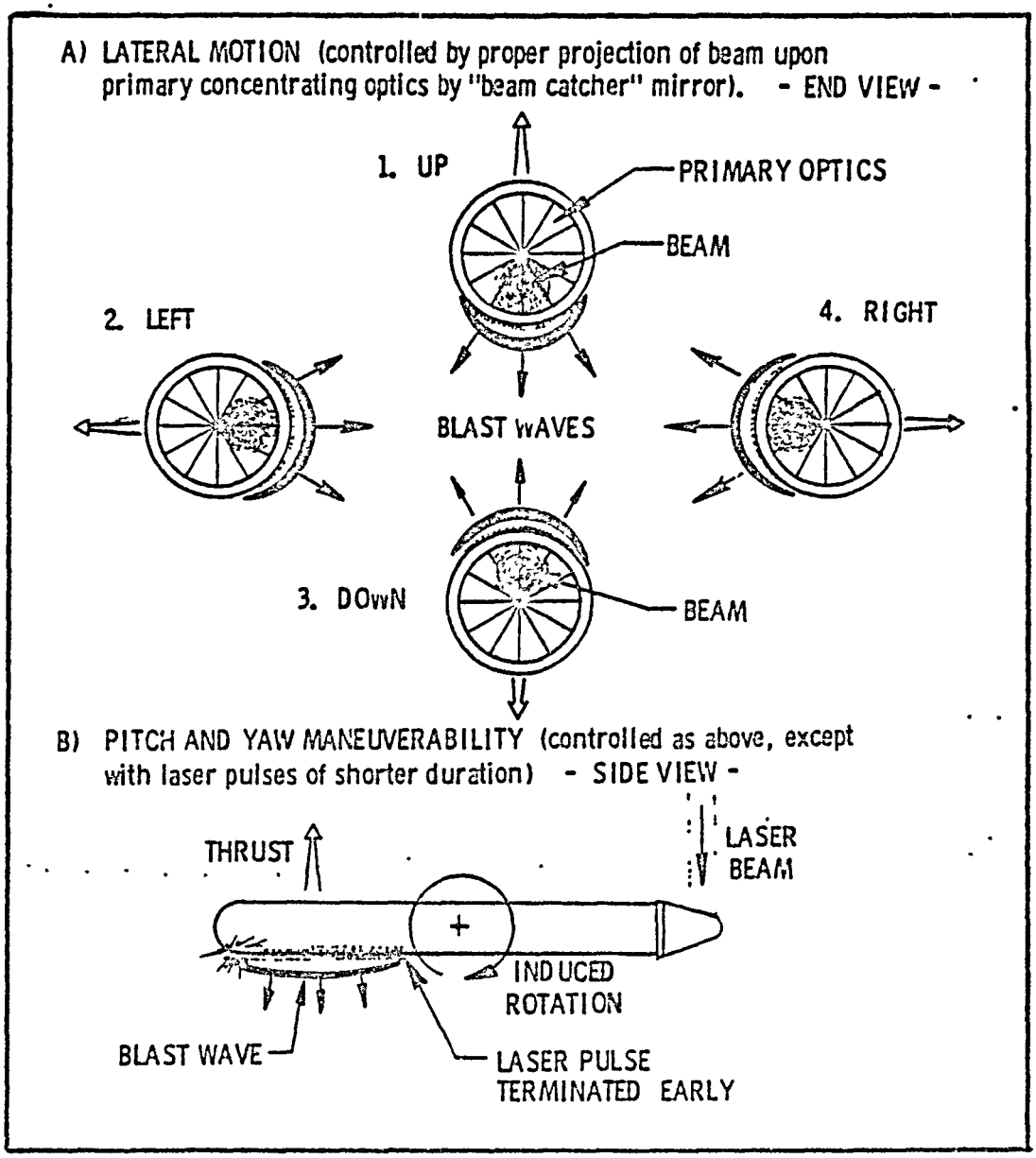

Figure VIII-3. Flight Maneuverability and Control for Cylindrical Shuttlecraft

roughly 50 dynes/Watt, as compared with that of air-breathing IRH thruster which may be noticeably less.

C. IRH PULSEJET MODE

The basic physics of the IRH propulsive mode has been introduced in Chapters III and VII. Therefore, additional discussions presented here are limited to the specific pecularities that arise from the integration of IRH pulsejet powerheads with cylindrical shuttlecraft.

As indicated earlier, the articulated "beam-catcher" mirror is able to reflect laser power pulses into any azimuthal chamber of the annular engine. Rapid fire, "gatling-gun" operation of the powerhead can provide quasi-steady axial propulsive thrust, as shown in Figure VIII-4A, when thrust-vectoring clamshell doors are used to deflect the high-velocity pulsed exhaust gases aft. This propulsive mode might also be accomplished with quasi-CW laser power, using an auxiliary chemical-fueled turbo-compressor to deliver high-pressure cold air into the IRH chambers--which would then be used as laser-heated afterburners.

In addition to providing axial-aligned thrust, the powerheads can enable complete pitch, yaw and roll maneuverability. With the clamshell doors retracted as shown in Figure VIII-4B, the pulsejet exhaust gases are exhausted radially (at right angles to the vehicle longitudinal axis) thereby enabling the shuttlecraft to perform yaw or pitch maneuvers. Care must be taken not to overstress the shuttle structure since the maneuvers may place large longitudinal bending moments on the vehicle.

Finally, the pulsejet powerheads can produce rolling torques upon the shuttlecraft through the use of variable pitch turbine blades located in each pulsejet exhaust port. Reaction forces caused by turning the exhaust flow, enable the vehicle to perform a roll maneuver (or to control its rate of spin) about the longitudinal axis.

Finally, as indicated earlier, the pulsejet powerheads are designed to operate both in an air-breathing mode (dense, low altitude air) and in a IRH rocket mode (rarefied upper atmosphere and space).

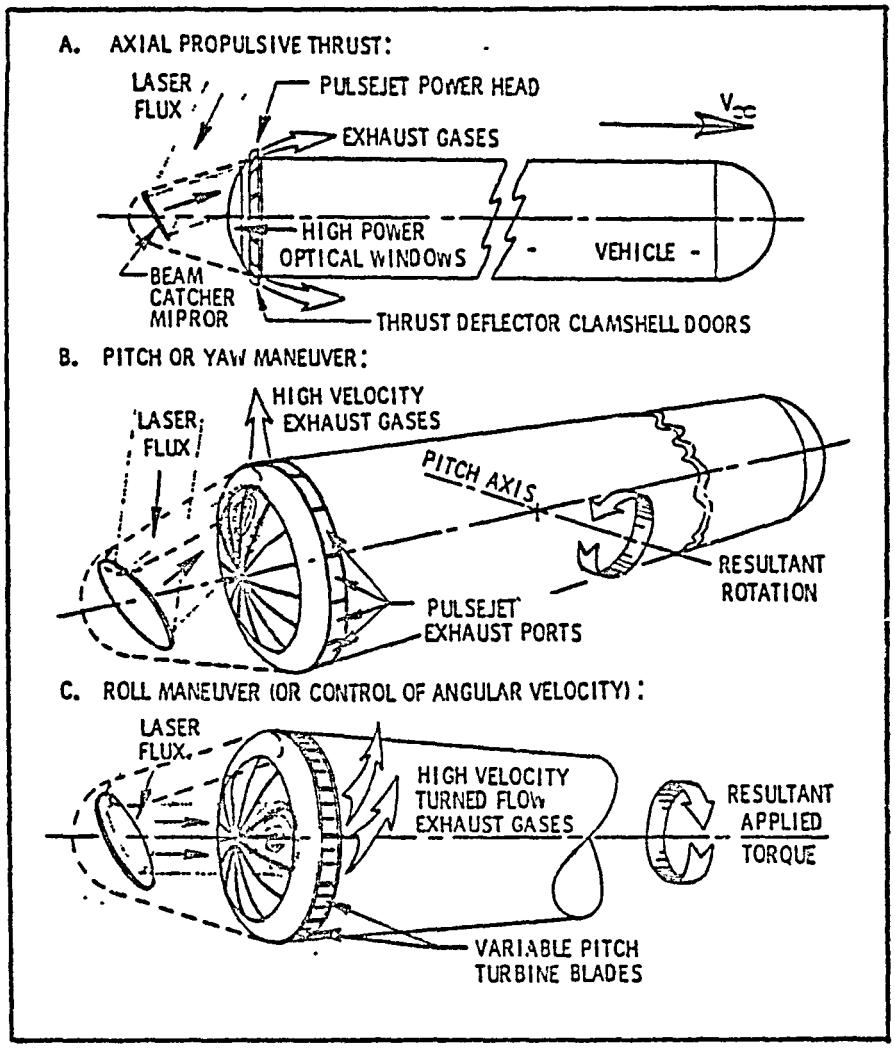

Figure VIII-4. IRH Pulsejet Mode

D. CONVENTIONAL AEROSTATIC/AERODYNAMIC VS. VORTEX-AUGMENTED LIFT

In this mode, laser energy would be beamed to a powerhead at one end (possibly both) of the vehicle as shown in Figure VIII-5. High-velocity exhaust gases from the rotary pulsejets would be mechanically deflected aft by adjustable vanes or 2-D vectorable nozzles. To generate additional aerodynamic lift from the cylindrical fuselage, the vehicle could fly (along its major axis) at a nose-high altitude. This technique was often used by the old airships to climb to an altitude higher than that which would support the craft with aerostatic forces alone. Airships were also commonly flown in nose-high or nose-low attitudes to compensate for changes in the crafts' neutral buoyancy.

Portrayed in Figure VIII-5B is an augmented-lift concept that utilizes a huge "spanwise" (i.e., aligned with the major axis) vortex which is formed over the entire shuttle vehicle. The vortex is maintained by the span-wise "blowing" action of axial-aligned exhaust gases ejected from IRH pulsejet engines. The active lift-generating mechanism utilizes the artificially induced span-wise pressure gradient to evacuate the vortex core, which in turn organizes the angular momentum about the vehicle into a conically-shaped vortex that is trapped in place. The external effect of the augmented lift concept is that of a swept-back tornado moving into the local wind vector and producing a lift force in a direction perpendicular to the plane defined by the local wind vector and central vortex axis.

The vortex-augmented lift (VAL) concept is, in effect, a thrust augmentation mechanism whereby the propulsive thrust originally developed by the IRH pulsejet power heads is then amplified to support a static load (i.e., the vehicle gross weight) which could not be maintained directly by the engine exhaust thrust (acting alone) at an equivalent input power level. Hence, the VAL concept embodies a momentum exchange process that is carried out with the atmosphere as follows: (a) a relatively small mass flow rate of high-velocity exhaust gases from the pulsejet engine is used to excite an externally bound vortex, (b) the vortex, in turn, processes an enormous mass flow of free stream air, generating lift while imparting to

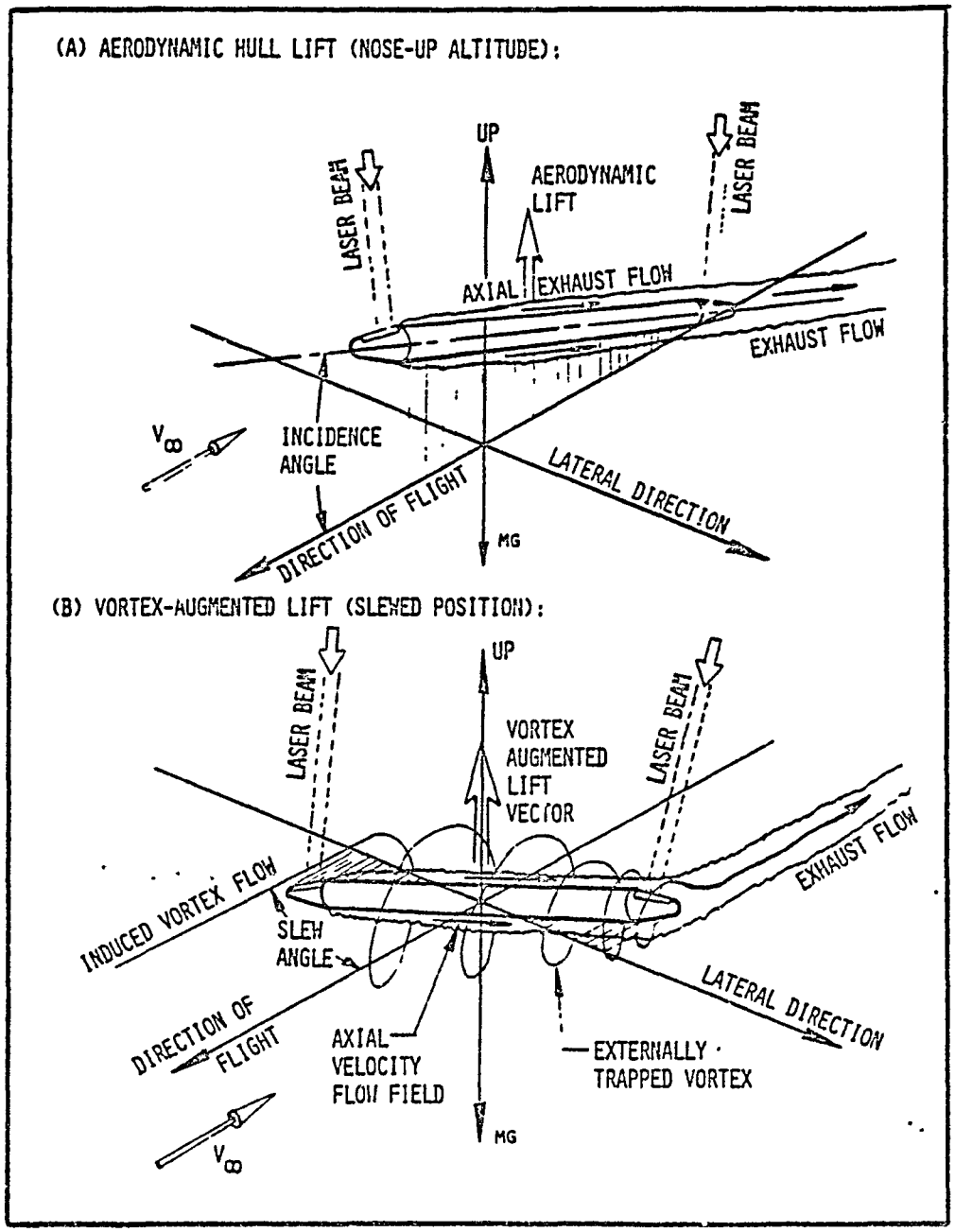

Figure VIII-5. Aerodynamic Lift Mode

it a very small downwash velocity ΔV upon passage of the "wing." The approach has much in common with the horizontal-take-off single-stage-to-orbit (SSTO) winged vehicles which have been proposed in the past. The purpose of this mode is to maximize vehicle rate-of-climb.

E. DISCUSSION OF FREE-VORTEX-INDUCED LIFT

A comprehensive review of the various methods which have been used to generate and stabilize a span-wise vortex over the upper surface of a wing (for purposes of lift enhancement)--is given in Ref. 1. The least complicated scheme for generating super-circulation and high lift coefficients over swept wings involves the blowing of an air jet along the upper wing surface--span-wise, toward the wing tip.[1-7] Other schemes have replaced the vortex with a rotating cylinder which is located either on top of the wing, or in a cavity within the wing. All of these lift enhancement techniques use an externally trapped vortex to simulate a thickening of the wing. Augmented lift is produced by lowering the pressure in the immediate vicinity of the vortex, and hence, over the upper wing surface.

1. Experimental Evidence

Kasper[8-9] was first to confirm the lift enhancement effect of externally trapped vortices in full-scale aircraft. His approach utilized leading and trailing edge flaps to trigger formation of the vortex and to trap it in place. The Kasper BKB glider was repeatedly able to reduce its sink rate and stalling speed to half its normal value--when the lift-producing vortex was engaged. This requires a lift coefficient of several times the normal capability of unaugmented wings.

Recent wind tunnel tests of the vortex-augmented lift concept were made by Clareus and Westesson[4,10] with swept wings and moderate degrees of span-wise blowing (wing aspect ratio of 4; flow Reynolds number of 150,000). For each semispan wing, air was blown span-wise from a single nozzle which protruded a short distance beyond the fuselage external surface. The nozzle was located at the exact core of the vortex. They were able to achieve maximum lift coefficients in the range of 4.45 to 5.5,

which substantially exceeds the maximum C_L of 3.5 attainable with even slotted flaps on conventional wings. The researchers noted a significant improvement of C_L with increasing flow Reynolds number.

In his theoretical study, Rossow[1] has shown that section lift coefficients up to 10 can be achieved if the vortex can be adequately stabilized and if the mechanism used to evacuate the vortex core can be generated efficiently. At the end of his study, Rossow briefly addresses the effects of wing sweep and free stream Mach number on the strength and position stability of a lift-enhancing vortex. He indicates that the combined effects of wing sweep and angle-of-attack provide the needed vortex stabilizing agents; i.e., the naturally-occurring span-wise pressure gradient provides the suction required to evacuate the vortex core, in order to organize and maintain its motion. In discussing various other flow-field restraints, he points out that lift is achieved in an externally trapped vortex because the free-stream velocity over the upper part of the system is accelerated by as much as a factor of 10. Rossow concludes that if compressibility effects (and the attendant inefficiency and noise produced by the shock waves, buffet, etc.) are to be avoided at the top of the vortex bubble, the vehicle flight velocity envelope must be restricted to relatively low Mach numbers.

2. Application to Cylindrical Shuttlecraft

Therefore, use of the externally trapped vortex concept for cylindrical shuttlecraft lift enhancement will most likely be restricted to the low subsonic portion of the launch trajectory and may enable the vehicle to climb efficiently to the highest possible ceiling altitude in an "air-breathing" mode. For some shuttlecraft sizes, the augmented flight regime may possibly be extended to the high subsonic speeds and beyond by spinning the vehicle rapidly about its longitudinal axis--thereby utilizing the Magnus lift effect. (Two excellent examples of the phenomenon known as the Magnus effect are the curve pitch in baseball, and the hook or slice shot in the game of golf.)

The vortex core region for the aerodynamic lift augmentation mode is rigidly defined by the vehicle extremities. Consequently, the vehicle itself will tend to (a) provide a central attachment axis for the vortex, and (b) protect and stabilize the vortex from being dislodged by the oncoming airstream.

3. Vortex Motion and Aerodynamic Wing Theory

A brief discussion of vortex motion and its relation to elementary aerodynamic wing theory will serve to further clarify the propulsion concept.

Naturally occurring examples of free vortex motion in air and water are commonly referred to as tornadoes, whirlwinds, cyclones, maelstroms and whirlpools. The rotary behavior of fluids is quite well understood and follows well-defined physical laws. The earliest treatments of vorticity addressed the more simplified case of two-dimensional, non-viscous flow. More recent investigations have included real three- and four-dimensional effects (time), as well as those of a finite viscosity. At present, vortex motion has become the subject of much controversy in studies of the generation and decay of aircraft trailing vortex systems.[11-16] (Powerful trailing vortices shed by large commercial jet aircraft are known to pose a great hazard to the safe passage of light aircraft.)

Displayed in Figure VIII-6 are two- and three-dimensional physical models for free vortex flow. Figure VIII-6A is an end view showing the vortex center and lines of equal flow velocity which are inversely proportional to the distance from the center (i.e., $V_2 = V_1 (r_1/r_2)$. The two-dimensional model in Figure VIII-6B predicts an infinite tangential flow velocity at the vortex center which cannot occur because of finite viscosity effects. In contrast, Figures VIII-6C and VIII-6D present the three-dimensional "bathtub drain" or "corner eddy" model for free vortex flow. Note that the vortex core in Figure VIII-6D occupies a finite cylindrical volume of radius R_1 which contains an axial flow field. Fluid is pulled into the vortex with a predominately radial velocity until it reaches the

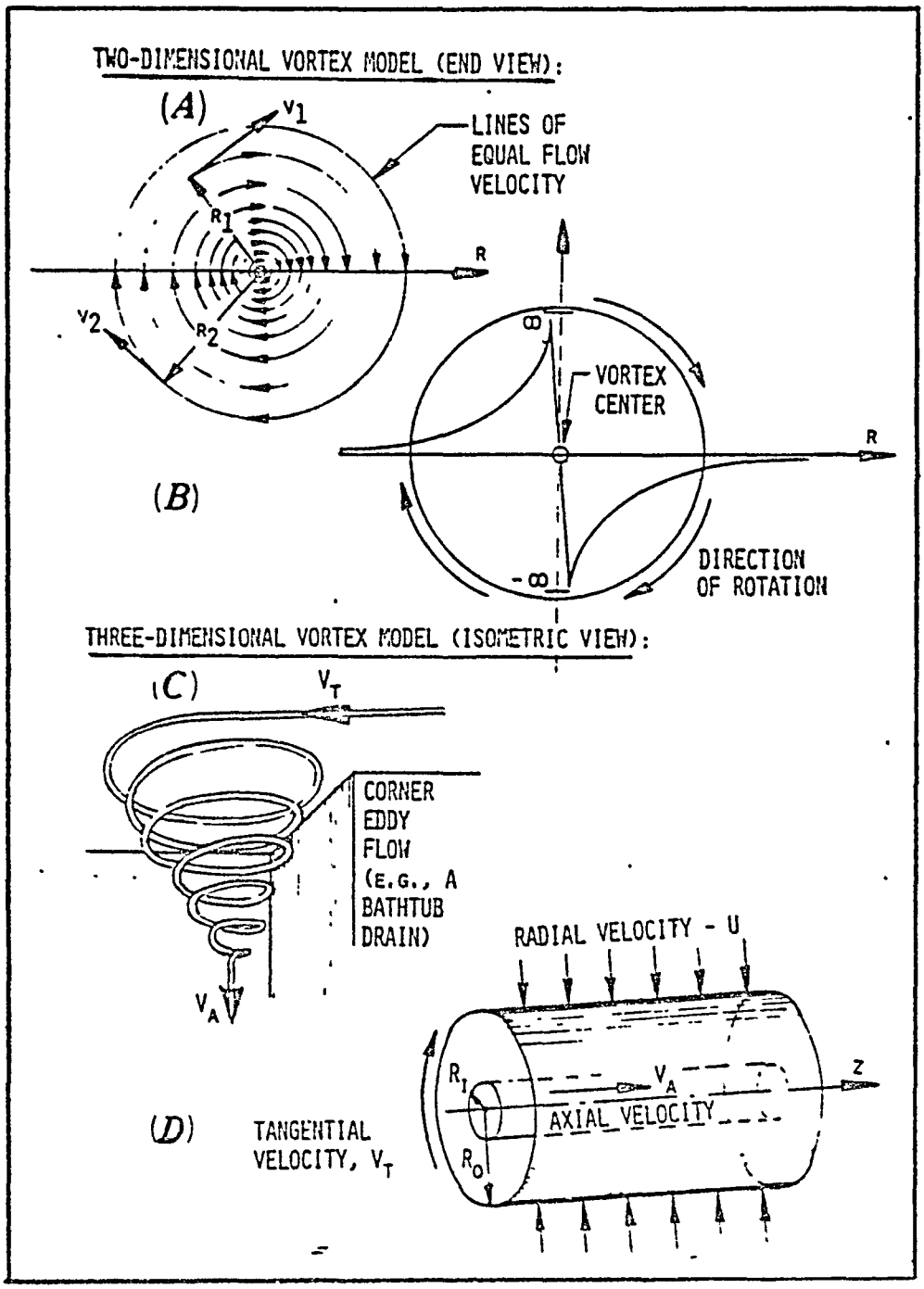

Figure VIII-6. Simplified Models for Free Vortex Flow

outer vortex envelope at radius R_o, where it begins to pick up a significant tangential velocity V_t. Upon reaching R_i, the particle has already seen its highest tangential velocity. It then enters the axial flow vortex core region. From the laboratory reference frame, the particle moves in a three-dimensional spiral trajectory of decreasing radius and increasing velocity until it enters the axial flow core region, where it is then pulled out axially as shown in Figure VIII-6C.

Conservation of mass dictates that the rate of mass entrainment must equal the rate of bleed out the core. Reduced fluid pressures due to the high tangential velocities near the vortex core are balanced by centrifugal forces acting on the fluid particles themselves. If the flow is interrupted at any point along the trajectory, the vortex will begin to decay downstream of the disturbance.

The vortex strength or "circulation" Γ is given by the following expression

$$\Gamma = \oint \bar{V} \cdot d\bar{s} \qquad (1)$$

where the line integral is taken over any closed curve S containing the vortex, and $\bar{V}$ is the local flow velocity at any given point.

The Kutta-Joukowsky relation may be used to determine the lift force L generated by a vortex with circulation strength Γ immersed in a linear flow field of velocity V. As adapted for the case of variable sweep angle, the relation becomes

$$\bar{L} = \rho \bar{V} \times \Gamma \bar{\ell} \qquad (2)$$

where the vector $\bar{\ell}$ is the length (or span) of the vortex whose orientation is derived from the "right hand rule" as applied to the tangential circulation direction (see Figure VIII-7).

A free vortex cannot abruptly end in a real fluid, so the rotational flow field continues in the form of tip vortices which emerge from the ends of the "bound" (or attached) primary vortex much like two

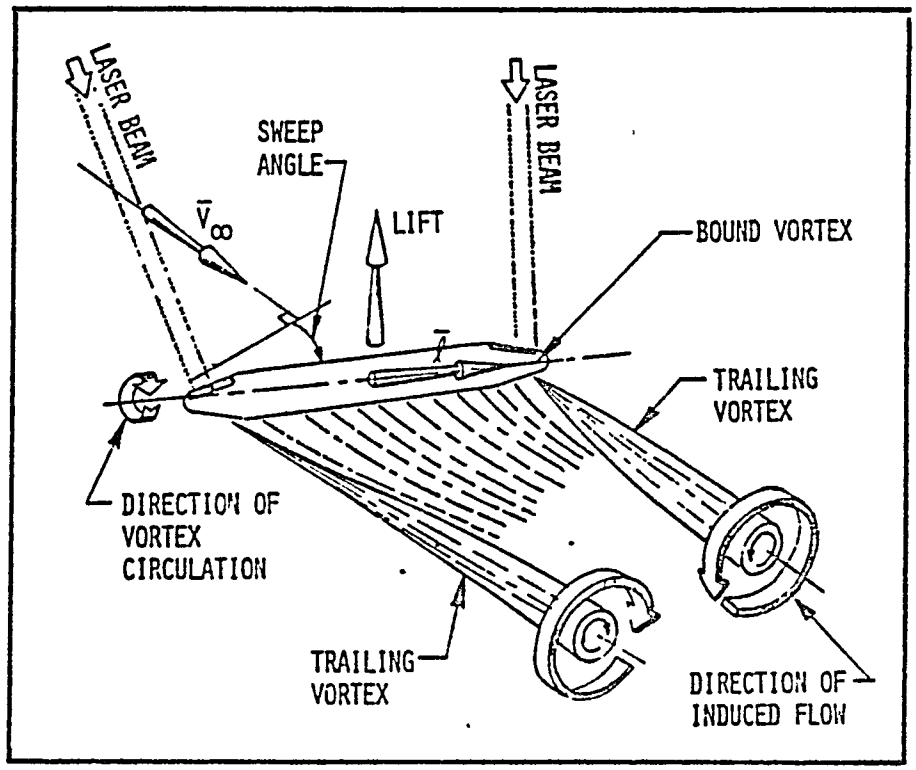

Figure VIII-7. Generation of Trailing Vortex System

horizontal tornadoes. As illustrated in Figure VIII-8, decay of the vortex flow system occurs in several stages.[15,16] In the near wake (Figure VIII-8A), viscosity effects tend to increase the vortex core radius, which in turn cause a decrease in tangential flow velocity. In the intermediate wake (Figure VIII-8B), the two oppositely rotating vortex filaments grow to large proportions and interact to cause a mutual breakdown. At the far wake, filament instability effects result in the dramatic interaction of the trailing vortex pair. The two filaments break up into segments and form rings of highly turbulent flow as shown in Figure VIII-8C.

The penalty for the production of lift is "induced" drag, which manifests itself by a rearward tilting of the lift vector. (The lift vector is defined as a force which always acts in a direction perpendicular to the local air stream.) The action of the trailing vortices is to superimpose a vertical down-wash velocity distribution upon the flow field moving by the "bound vortex." Hence, the local air flow at the site of the bound vortex core is actually inclined downward with respect to the flight path direction, and as a result the lift vector leans aft--thereby causing induced drag.

4. Lessons From MacReady's Gossamer Wings

Several lessons for minimizing flight propulsive power requirements (those which are a direct result of lift production) can be gleaned from the Gossamer Condor/Albatross experience.[17] The very limited capabilities of the human powerplant necessitates the use of a flight platform which exhibits an extremely high coupling coefficient "C" (Lift/Flight Power). The coupling coefficient for a flight platform may be defined as follows:

$$C = L/P = (L/D)/V \qquad (3)$$

where P is the flight propulsive power, D is the total vehicle drag, and V is the flight velocity. Since the required flight power is equal to the product of the total vehicle drag and the flight velocity, the velocity

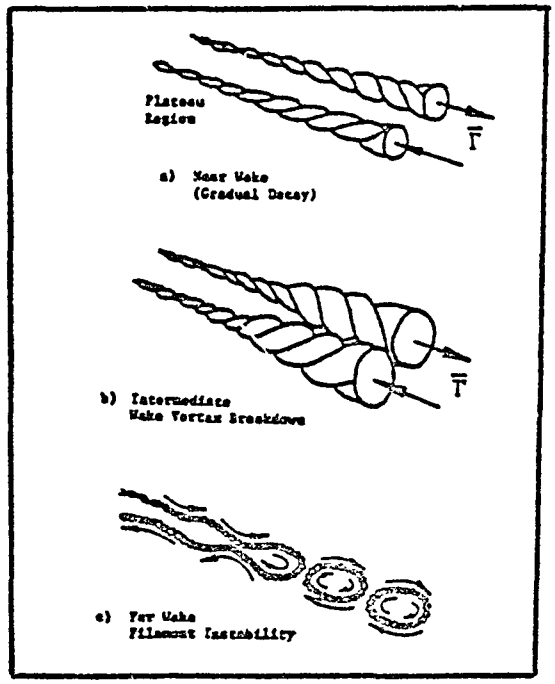

Figure VIII-8. Decay of Vortex Flow System
(From References 15, 16 and 18)

must be relatively slow and the overall L/D high. To obtain a high L/D at a very low flight velocity, MacReady chose a high aspect ratio, externally stiffened wing with a moderately low lift coefficient (C_L = 1.0), in order to reduce the induced drag coefficient which varies as C_L^2. The overall drag coefficient C_D of an aircraft is composed of a parasitic drag term C_{D_o} and the induced drag term which varies with C_L^2 as follows,

$$C_D = C_{D_o} = C_L^2/\pi ARe, \tag{4}$$

where AR is the aspect ratio and e is the span efficiency factor.

Furthermore, MacReady[17] shows that if vehicle shape and lift coefficient are kept constant and only size and weight are permitted to vary, then the required flight power varies as $W^{3/2B-1}$ (where W is the total vehicle weight and B is the wingspan). Hence, extremely lightweight vehicles with very large spans will consume the least flight propulsive power. Finally, MacReady indicates that his design approach did not have as a foregone conclusion that the vehicle be very streamlined, but that the penalty for non-streamlined construction must be assessed. The coupling coefficient achieved by the Gossamer Condor is roughly 374,000 dynes/Watt and exceeds by a good margin the capability of today's finest high performance sailplanes. In great measure, this accomplishment is permitted by the substantially lower flight envelope (~ 4.48 m/sec) of the Condor.

F. SUMMARY

In conclusion, the cylindrical shuttlecraft configurations may be able to use vortex-augmented lift and high coupling coefficients to efficiently climb under laser power to the upper reaches of the atmosphere. In so doing, aerodynamic lift/thrust forces (i.e., those resulting in a positive rate of climb upward) are applied linearly along the vehicle structure--and hence do not result in the production of large structural bending stresses.

This Page Intentionally Left Blank

REFERENCES FOR CHAPTER VIII

1. Rossow, V. J., "Lift Enhancement by an Externally Trapped Vortex," Paper No. 77-672, AIAA 10th Fluid and Plasmadynamics Conference, Albuquerque, New Mexico, 27-29 June 1977.

2. Dixon, C. J., "Lift Augmentation by Lateral Blowing Over a Lifting Surface," AIAA Paper 69-193, February 1969.

3. Cornish, J. J., III, "High Lift Applications of Spanwise Blowing," ICAS Paper No. 70-09, Seventh ICAS Congress, Rome, September 1970.

4. Clareus, Ulf, and Westesson, Rold A., "FORSOK MED VIRVELLYFT," Institutionen for Flygteknik SAAB-SCANIA, 1973.

5. Dixon, C. J., Theisen, J. G., and Scruggs, R. M., "Theoretical and Experimental Investigations of Vortex-Lift Control by Spanwise Blowing," Experimental Research, Vol. I, Lockheed Aircraft Corporation, LG73ER-0169, September 1973.

6. Bradley, R. G., Smith, C. W., and Wray, W. O., "An Experimental Investigation of Leading-Edge Vortex Augmentation by Blowing," NASA CR-132415, April 1974.

7. Campbell, James F., "Augmentation of Vortex Lift by Spanwise Blowing," AIAA Journal of Aircraft, Vol. 13, No. 9, September 1976, pp. 727-732.

8. Kasper, W., "Vortex Motion and its Application to Aircraft," 14 May 1970; also "Stability and Control of the BKB-1 Tailless Airplane," undated; Both available from the author, 1853 132 S.E., Bellevue, Washington, 98005.

9. Cox, J., "The Revolutionary Kasper Wing," 10 July 1973, Sport Aviation, pp. 10-16.

10. Ridder, KTH, Ingelman-Sundberg FFA, Loyd LiH, Westesson, Clareus, "Virvellyft. Kommentarer till nagra preliminara vindtunnelprov.," SAAB-SCANIA, 1974-03-01.

11. McCormick, B. W., Tangler, J. L., and Sherrieb, H. E., "Structure of Trailing Vortices," Journal of Aircraft, Vol. 5, No. 3, 1968.

12. McCormick, B. W., "Aircraft Wakes: A Survey of the Problem," Presented at the FAA Symposium on Turbulence, Washington, D.C., March 22-24, 1971.

13. Brandt, S. A. and Iverson, J. D., "Merging of Aircraft Vortices," Paper No. 77-8, AIAA 15th Aerospace Sciences Meeting, Los Angeles, CA, 24-26 January 1977.

14. Meng, J. C. S., "The Physics of Vortex Ring Evolution in a Stratified and Shearing Environment," Paper No. 77-12, AIAA 15th Aerospace Sciences Meeting, Los Angeles, CA, 24-26 January 1977.

15. Groenenboom, J. and Ievalts, J., "Wing Vortex Visualization and Vortex Interference Patterns," Paper No. 77-309, AIAA 13th Annual Meeting and Technical Display Incorporating the Forum on the Future of Air Transportation, Washington, D.C., 10-13 January 1977.

16. Tartaglioni, J. J., "An Analysis of the Aircraft Trailing Vortex System," Paper No. 78-312, AIAA 14th Annual Meeting and Technical Display, Washington, D.C., 7-9 February 1978.

17. MacReady, P. B., "Flight on 0.33 Horsepower: The Gossamer Condor," Paper No. 78-308, AIAA 14th Annual Meeting and Technical Display, Washington, D.C., 7-9 February 1978.

CHAPTER IX
AIR-BREATHING LASER-ELECTRIC PROPULSION: CYLINDRICAL CONFIGURATIONS

This chapter investigates air-breathing electrically augmented thruster concepts which might be useful in propelling cylindrical shuttle craft to orbit. These propulsion modes are portrayed for use in the rarefied upper atmosphere and ionosphere, where shuttlecraft are no longer aided by aerostatic or aerodynamic lift. The engine/optics/airframe configuration for these vehicles was introduced earlier in Figure VIII-1.

A. INTRODUCTION

Within the dense atmosphere, pulsed air-breathing laser-heated engines augmented by aerostatic, aerodynamic, and free-vortex-induced lift can be used to propel the cylindrical vehicle to the outer reaches of the atmosphere. By design, the shuttlecraft uses the planetary atmosphere to greatest advantage by flying at a low velocity in order to obtain the greatest impulse-to-laser-power coupling and to reduce aerodynamic drag to the minimum. These concepts were covered in Chapter VIII.

At higher flight velocities within the rarefied upper atmosphere and ionosphere, the shuttles may use several other high specific impulse electrically augmented thrusters reviewed in this chapter. These propulsive units, which (in operation) send large electric current levels through their superconducting longeron structure (see Figure IX-1) permit the shuttle to gain a positive propulsive advantage over conventional unaugmented rocket systems. For example, in one such thruster mode, the electromagnetic engines might warp the local geomagnetic field out to a radius of several tens of kilometers, and thereby communicate a reaction force to the planetary mass itself, by way of a perturbation to the local planetary magnetic field.

When flying in one of several electric propulsion modes, the shuttle requires lightweight laser-heated explosively driven magnetohydrodynamic (XMHD) generators which are compatible with the pulsed radiation

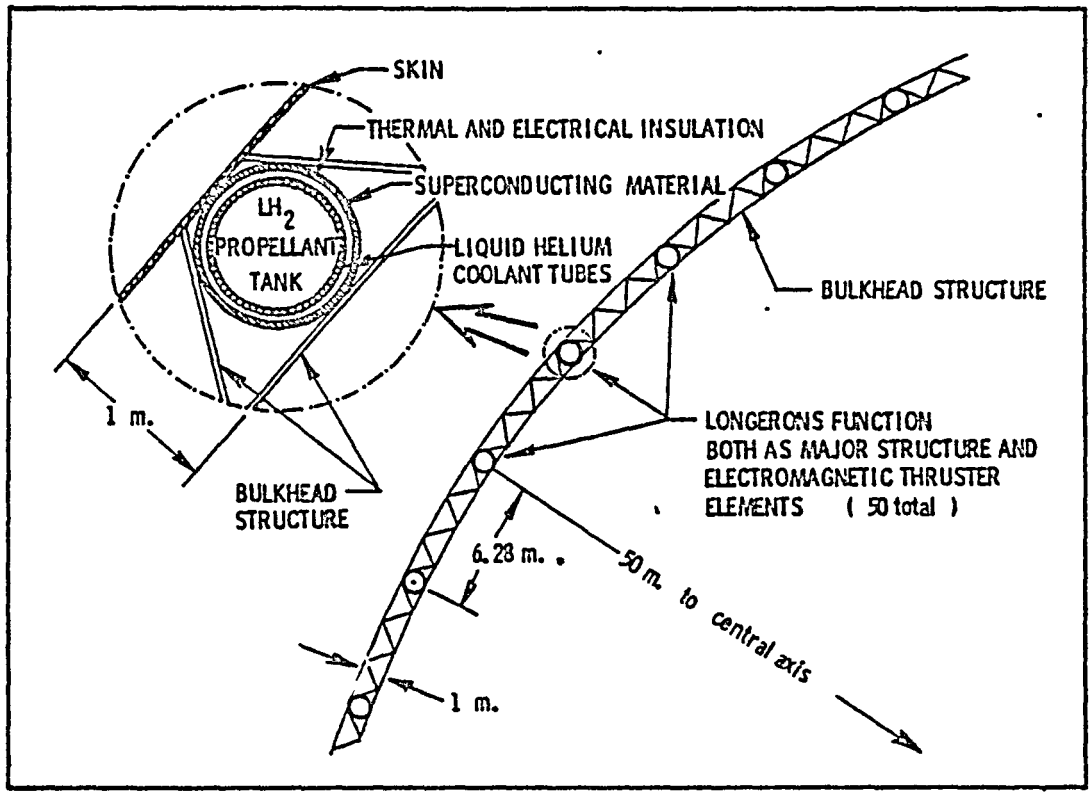

Figure IX-1. Superconducting, Longeron Structure for 1000m Long Shuttle

superheaters used in the powerheads (e.g., see Figure V-14). Normally, the purpose of the pulsejet exhaust section is to accelerate the high pressure gases generated within the radiation superheater to produce high-velocity exhaust gases (i.e., thereby producing the maximum attainable thrust from a minimum mass flow rate of propellant). However, in the electric propulsion modes, energy must be extracted from this high-velocity plasma exhaust, and converted to pulsed electrical power. This may be accomplished by inserting a magnetohydrodynamic (MHD) generator at the output of the pulsejet chamber as shown in Figure IX-2. A MHD generator is, of course, simply a hollow duct of square cross section, composed of two opposing walls which are insulators and another two which are used as electrodes. When a very strong magnetic field (e.g., 2 to 10 Tesla) is applied across the duct in a direction perpendicular to both the insulating walls and the electrically conducting plasma stream, electrical power will flow from the electrodes to an external resistive load.

Based upon preliminary studies (included in Appendix B), the pulsed XMHD conversion concept shows excellent promise for handling high average power levels (e.g., 10^9 Watts) at efficiencies in the range of 40 to 50 percent. Simplicity in design of such XMHD generators can be inferred from studies of pulsed laser-heated rocket technology, and chemical-fueled explosively driven MHD generators[1-3], neither of which utilize moving parts. The nature of pulsed converter operation eliminates the plasma stability constraints typical of CW radiation-heated systems. In addition, the converter has simple working fluid requirements: a) pulsed injection at low repetition rates, and b) continuously fed gas at repetition rates much above 100 Hz. The successful development of such a converter technology will require the intimate integration of: the physics of a) radiation-driven absorption waves, b) high-temperature gasdynamics, c) explosively driven MHD generation, d) high-power laser windows and mirrors, and e) lightweight actively cooled pressure vessels.

The configuration for a XMHD which is compatible with the shuttle powerhead is illustrated in Figure IX-2. The only major change from the pulsejet configuration previously introduced in Figure V-14 is the addition

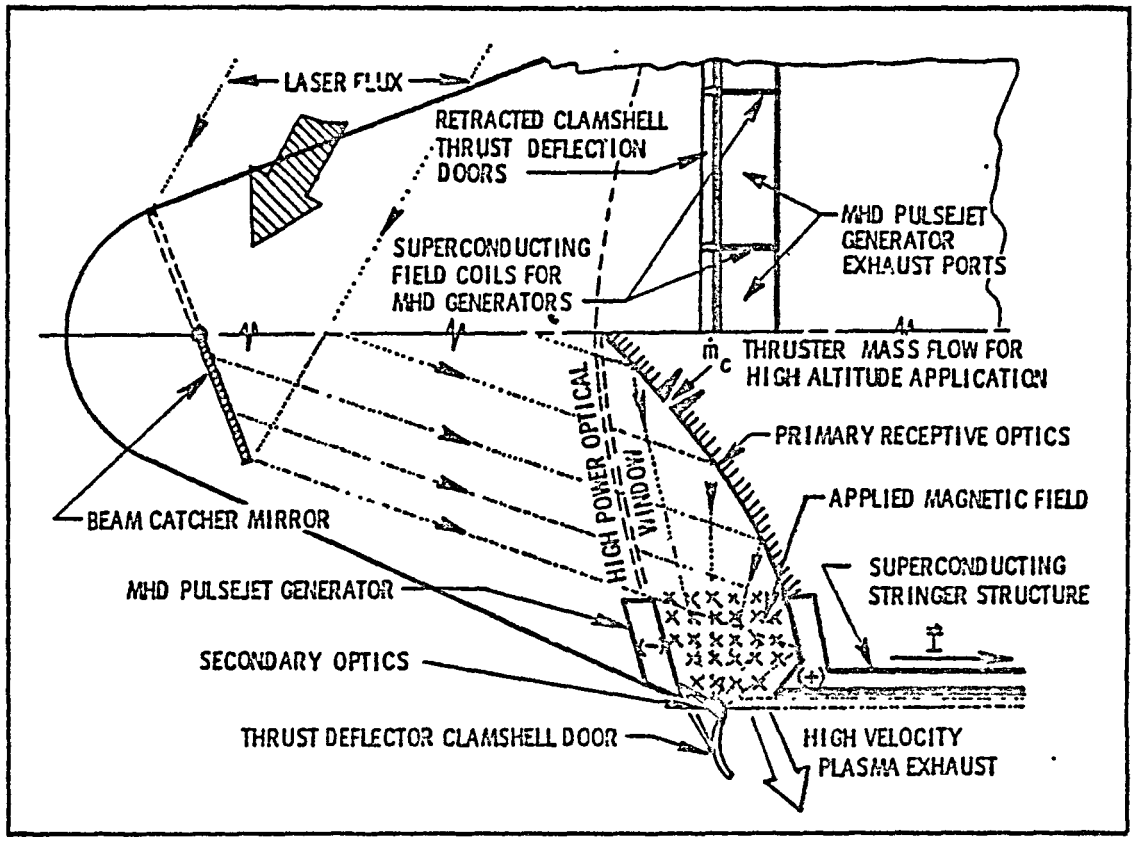

Figure IX-2. Detonation Wave Driven MHD Generators for Short Pulse, High Power Requirements (Not to Scale)

of powerful superconducting electromagnets, insulating walls, and electrodes in the pulsejet nozzle region. When electric power is required from the power head, the superconducting magnets are energized and strong magnetic fields are applied at right angles through the exhaust section in the direction indicated by $\bar{B}$ in Figure IX-2; power is extracted directly out of the page as suggested by the current vector $\bar{J}$.

The XMHD generator cycle is identical to that portrayed in Figure V-15 except that the electrical power pulse becomes the functional output of the device, instead of reaction thrust. A schematic diagram of the cycle is given in Figure B-4 of Appendix B. LSD wave heating of the injected propellant produces a high temperature and pressure non-equilibrium ionized plasma which then explosively drives the MHD generator into operation. The XMHD generator is designed for open-cycle operation with hydrogen as the working fluid, and is a very lightweight converter for the flyable electric power plant application. A gigawatt-level electrical converter may have a specific weight/power of better than 1 kg/MW.

In summary, the electrically augmented thruster cycles receive power from explosively driven magnetohydrodynamic generators fitted to the exhaust nozzles of the IRH pulsejet engines. The following propulsion modes suggest only a few of the possibilities; some are more speculative than others.

B. "ELECTRICAL STORM" ATMOSPHERIC COUPLING MECHANISM

In concept, this thruster attempts to artificially reproduce several of the physical processes which occur naturally in electrical storms. As portrayed in Figure IX-3, remote-beamed power is used by high-energy linear accelerators (LINAC) which eject several Coulombs (e.g., 1-10) of electric charge (proton beams from one vehicle end, electron beams from the other). This charge is then temporarily stored in oppositely charged

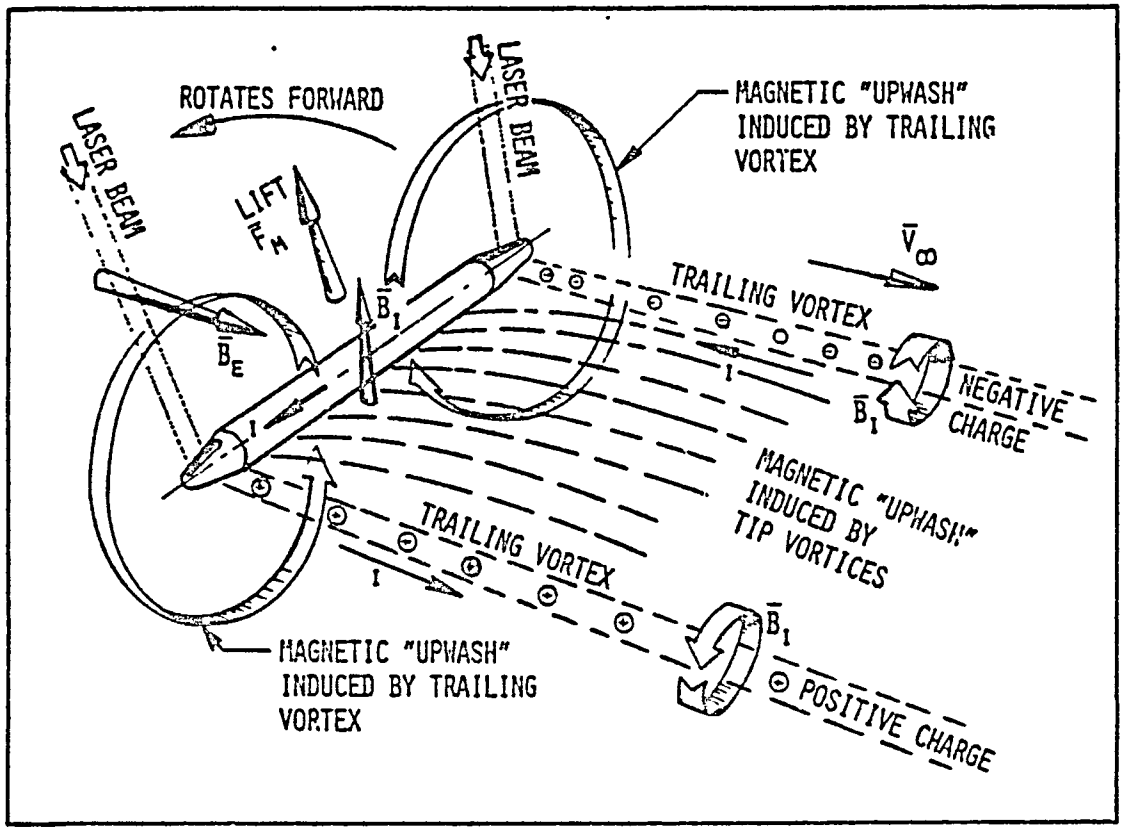

Figure IX-3. "Electrical-Storm" Atmospheric Coupling Mechanism

"clouds" at a distance of several vehicle lengths.* Space charge dispersion effects cause a large atmospheric reaction mass to be trapped within these large-area-electrode "clouds." Continued charge pumping of these "electrode-clouds" soon initiates a glow discharge across the inter-cloud volume. At this time, the XMHD generators fire up and deliver 10^6 to 10^9 Amps of current through this circuit causing a very large atmospheric mass to be accelerated away from the vehicle through the action of self-magnetic field derived Lorentz forces.

Physically, the thruster concept is the electromagnetic (EM) analogy to aerodynamic lift production. Aerodynamic vortex strength Γ becomes the electrical current I; local circulation velocity V becomes the local magnetic field B; wing span becomes the length of the shuttle superconductor stringer (or long·ron) structure. This analogy is further clarified in Table IX-1, which presents the representative equations for vortex-induced lift from either case. As illustrated in Figure IX-3, the flow tubes of free charge from both vehicle ends act as electromagnetic "tip vortices" to cause a strong self-induced magnetic field B_I to appear at the site of the shuttle "bound vortex."

The magnetic field B generated near a long cylindrical current element (the EM trailing vortex core) is:

$$B = \frac{\mu_o I}{2\pi r} , \qquad (1)$$

where I is the charge rate of flow (i.e., electrical current), r is the radial distance from the EM vortex core and μ_o is the permeability constant equal to $4\pi \times 10^{-7}$ Weber/Amp-meter. The strength "I" of an EM vortex may be obtained from Ampere's law:

$$I = \frac{1}{\mu_o} \oint \bar{B}_i \cdot d\bar{s} , \qquad (2)$$

*In a recent paper, Alfven[6] reminds us that a thundercloud can store 10 to 50 Coulombs.

TABLE IX-1. EQUATIONS FOR VORTEX-INDUCED LIFT

	AERODYNAMIC VORTEX SYSTEM	ELECTROMAGNETIC "VORTEX" SYSTEM
FREE VORTEX	$v = \frac{(\text{constant})}{r}$	$B_f = \frac{(\text{Constant})_m}{r}$
VORTEX STRENGTH	$\Gamma = \oint \bar{v} \cdot d\bar{s}$	$I = \frac{1}{\mu_o} \oint \bar{B}_f \cdot \bar{ds}$
VORTEX-INDUCED LIFT (SCALAR FORM)	$F_a = \rho V \Gamma \ell$ (Kutta-Joukowsky Relation)	$F_m = I \ell B_e$
VORTEX-INDUCED LIFT (VECTOR FORM)	$\bar{F}_a = \rho \bar{V} \times \Gamma \bar{\ell}$ (accounts for wing sweep)	$\bar{F}_m = I \bar{\ell} \times \bar{B}_e$ (THE LORENTZ RELATION)
INDUCED THRUST OR DRAG (T_f AND D_f, RESPECTIVELY)	$D_f = F_a (\sin \alpha_f)$	$T_f = F_M \text{ SIN } (\frac{\mu_o I}{\pi \ell B_e})$
POWER EXPENDED (IN PRODUCING LIFT)	$P = F_a(\sin \alpha_f) V_{wing}$	$P = I (\ell \bar{V}_- \times \bar{B}_e + V_D)$ (where V_D is an additional voltage drop required to generate the vortex)

where the closed integral is taken about any closed path S which contains the vortex core, and B_l is the local magnetic field encountered along the path. Finally, the Lorentz relation gives the lift force generated by the EM bound vortex of strength "I" which is immersed in a uniform external magnetic field B_E:

$$\bar{F}_M = \bar{I}L \times \bar{B}_E \qquad (3)$$

where L is the length of the bound EM vortex whose direction is aligned with the flow of positive charge carriers. The vector form of Eq. (3) permits the analysis of the slewed (or swept) EM "bound" vortex.

For the sake of argument, assume the cylindrical shuttle is at some point in time moving in a direction directly into the local external geomagnetic field vector B_E as shown in Figure IX-4B. Note that the external effect of the trailing EM vortices is to cause a magnetic "upwash" behind the EM bound vortex, as illustrated in Figure IV-4A. Physically, the trailing vortices cause an induced magnetic field B_I to appear at the site of the bound vortex. The orientation of B_I is at right angles to the plane defined by the bound and trailing EM vortices, and the magnitude of the induced magnetic field at the bound vortex site is:

$$B_I = \mu_o I/\pi L \qquad (4)$$

Much the same as in the case of aerodynamic lift, the trailing vortices within a distance of one wing span L behind the vehicle are responsible for generating over 95 percent of the induced field seen by the bound vortex.

The end result of all this is that the magnetic lift vector F_m in Figure IX-4B is rotated forward. In other words, the mere existence of EM trailing vortices causes an induced thrust upon the bound vortex, rather than an induced drag effect as is the case for aerodynamic vortex systems.

Once generated, the trailing EM vortex system is envisioned to breakdown and decay into EM vortex rings similar to that portrayed in Figure VIII-8 for the aerodynamic vortex flow system. An analysis of an EM

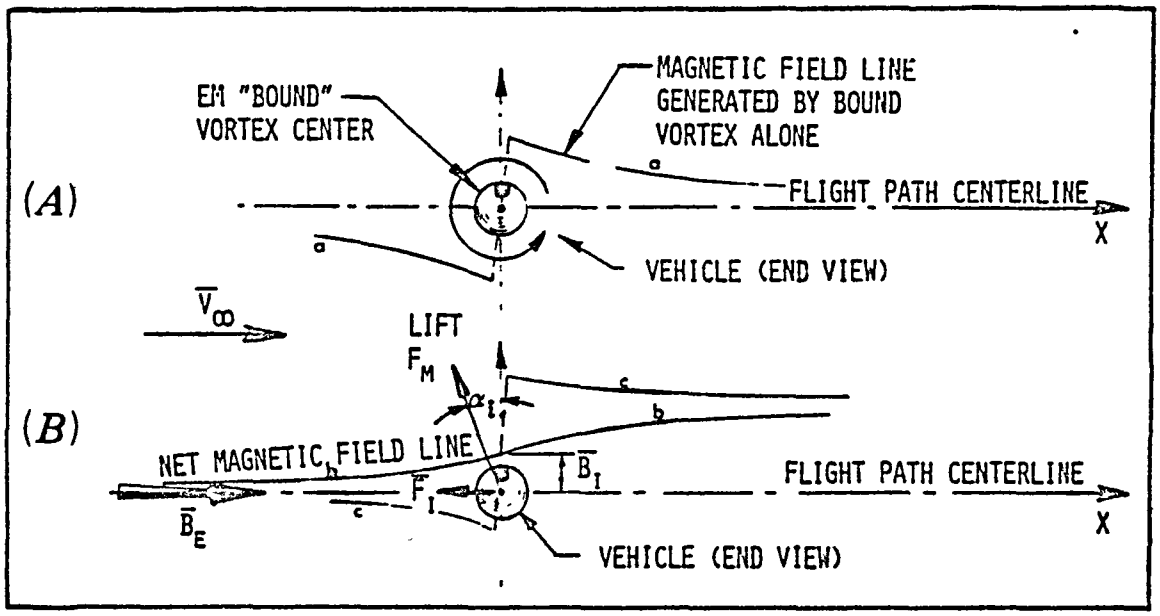

Figure IX-4. Induced Magnetic "Upwash" Due to Tip Vortices

vortex ring (i.e., an electrical current loop) system will reveal the origin of the induced thrust component. It is commonly known that for the case of powerful electromagnets, the induced magnetic field generated by one-half the current loop at the site of the other--tends to explode the magnet radially outwards. Since the only physical load-bearing component of the current loop is provided by the shuttle superconducting longeron structure itself, it is certainly clear that the entire trailing vortex system will be "blown away" by electromagnetically derived forces. During this "momentum-exchange" process with the atmosphere, reaction forces are first communicated from the bound EM vortex through the action of electromagnetic fields to moving charged particles, then to an acceleration of neutral atmospheric particles as a result of collisional processes with the charged particles. At the end of a thrust pulse, EM and plasma instabilities in the trailing vortex system will result in subsequent breakdown and decay of the system, probably first evidenced by huge electrical discharges in the wake.

The induced angle of tilt α_i for the electromagnetic lift vector in Figure IX-4B is given by

$$\alpha_i = \tan^{-1}\left(\frac{B_I}{B_E}\right) \simeq \tan\left(\frac{\mu_o I}{\pi L B_E}\right) \qquad (5)$$

For example, assume that an induced magnetic field of 10 times the strength of the Earth's surface field of 0.5 Gauss is to be generated. From Eq. (5) it is found that α_i would be roughly 84^o, and from Eq. (4) that "I" going through the vortex system must be 1.25×10^6 Amps (for the 1000m long shuttle). This magnitude of electrical current has been observed in naturally occurring electrical discharges (i.e., lightning).

Portrayed in Figure IX-5 is a cross section of the EM bound and trailing vortex ring system during the breakdown and decay process. As noted in Figure IX-5A by the location of the trailing vortex system and the free system velocity vector V_∞, the shuttle is assumed to be moving towards the left side of the page. Regardless of the original flight direction and

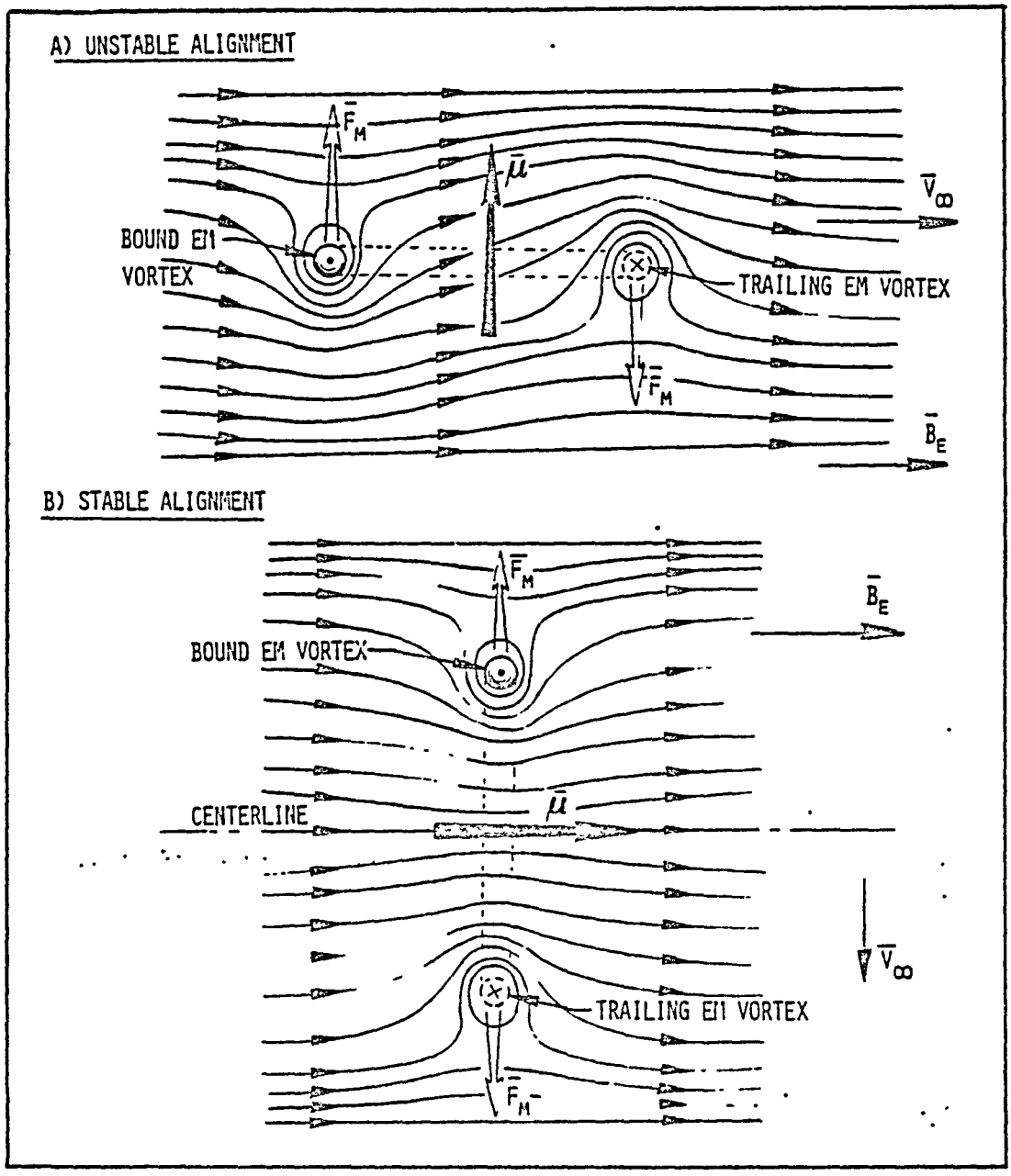

Figure IX-5. Decay of EM Trailing Vortex System

hence the orientation of the trailing EM vortex system, the ring EM vortex has a finite magnetic dipole moment equal to

$$\bar{\mu} = I\bar{A} \tag{6}$$

where A is the total area enclosed by the current loop. This dipole will experience a torque due to the action of the external magnetic field B_E, and eventually tip into a stable alignment of the μ and B_E vectors as shown in Figure IX-5B. The magnitude and direction of the torque vector ψ is given by

$$\bar{\psi} = \bar{\mu} \times \bar{B}_E \tag{7}$$

A straightforward calculation reveals that low voltage, non-relativistic ejection of charged particles from shuttle active emission electrodes (at the vehicle ends) is space charge limited to very low net electrical current levels and hence thrust (barring, of course, the use of some other clever approach to non-relativistic physics of which the author is presently unaware). The electrical field E at the external surface radius r of a cylindrical rod of electrical charge may be determined with the aid of Gauss's law as follows

$$\bar{E} = q/2\pi c_o k \ell r \tag{8}$$

where q is the total charge within a length ℓ, k is the dielectric constant of the atmospheric medium, and ϵ_o is the permittivity constant equal to 8.85×10^{-12} Farad/m. Assuming, then, that the shuttle active emission electrodes eject charge at a constant average rate I and velocity V equal to the flight velocity (such that the charge remains approximately at rest with respect to the atmosphere), we have:

$$E = I/2\pi\epsilon_o KrV \tag{9}$$

Sea level air has a dielectric strength and breakdown strength of 1.00 and 3×10^5 V/m, respectively. For a charge tube radius of 100m and a flight velocity of 100 m/s, Eq. (9) reveals that the maximum electrical current flow rate is 0.445 Amperes. Above this current rate, electrical breakdown of the atmosphere will occur.

There are two obvious approaches to circumventing this physical limitation on the maximum charge flow rate. Both involve the mechanisms for active charge emission from the electrodes.

1. Emission of "Seed Gas"

The first approach involves the simultaneous emission of a "seed" gas along with the flow of electrical charge. The "seed" gas molecule would be one with a sizeable electric dipole moment - (e.g., a water molecule has a dipole moment of 6.1×10^{-30} Coul-m*). For such molecules, the effective center of positive charge does not coincide with the effective center of negative charge. Therefore, the external effect of ejecting electrical charge with the dielectric vapor would be such that the electrical field at the external vortex tube is reduced. The "seed" gas acts as a distributed dielectric within the charge flow field.

The dielectric strength of liquid state water at zero degrees centigrade is 88, and the breakdown strength can be greater than 2×10^6 V/m for submicrosecond pulse lengths. The dielectric characteristics of water vapor are significantly reduced from these values. However, even if water could be used as a distributed dielectric with the same properties as exhibited in the liquid state, the maximum charge flow rate would at most be increased by a factor of only 100 to 1000. Barring the use of some super dielectric "seed" gas, all the evidence seems to point away from the use of charge ejection at sub-relativistic velocities.

2. Relativistic Charge Emission--"Glow Discharge" Propulsion

The second approach eliminates any need for "seed" material but requires that the electrical charge be emitted in high current, low voltage relativistic bolts. The ambient atmosphere can provide complete space

* Molecular dipole moment is $P = 2aq$, where "a" is the separation distance of the charge and "q" is the charge magnitude in Coulombs.

charge neutralization of the charge particle beam when moving at velocities approaching the speed of light. Devices for accelerating electrons and ions to 100 MeV - 1 GeV are presently being examined for use as beam weapons. (A review of this research is provided in Refs. 7-9.)

This propulsion mode would more accurately be described as a "Glow Discharge" electromagnetic thruster, designed for use in the stratosphere with 100 to 1000m long orbital shuttles. The basic propulsion cycle is portrayed in Figure IX-6, for a reference 1000m vehicle. The cycle begins with the atmospheric charging step shown in Figure IX-6A. On-board particle accelerators are used to create charged clouds (e.g., 1-10 Coulombs each) with overall dimensions of several kilometers--at a distance of at least 1000m from the vehicle. Simultaneous ejections of both protons and electrons (from opposite ends) leave the vehicle electrically neutral at all times. The goal is to produce an increasingly large electric field, almost to the point of electrical breakdown in this step.

The next step in the propulsion cycle sequece is the "onset of glow discharge," indicated in Figure IX-6B. At this point, a uniform glow electric discharge begins to form between the two charged clouds.

Immediately following the onset of glow discharge, a large current (i.e., megamperes to gigamperes) is driven through the stratospheric plasma. The strong self-magnetic fields generated by the discharge then acts to drive away the air trapped within the glow discharge region--through the action of Lorentz J x B forces, as shown in Figure IX-6C. An equal and opposite reaction force upon the vehicle itself causes the vehicle to be propelled away. The goal is to entrain a quantity of air that equals or exceeds the mass of the vehicle--so that the velocity change of the air working fluid is a small fraction (e.g., 10 percent) of the vehicle velocity. (This condition yields a high propulsive efficiency for the thruster.) The cycle is then repeated with a new volume of working fluid which is convected into the active E/M interaction region.

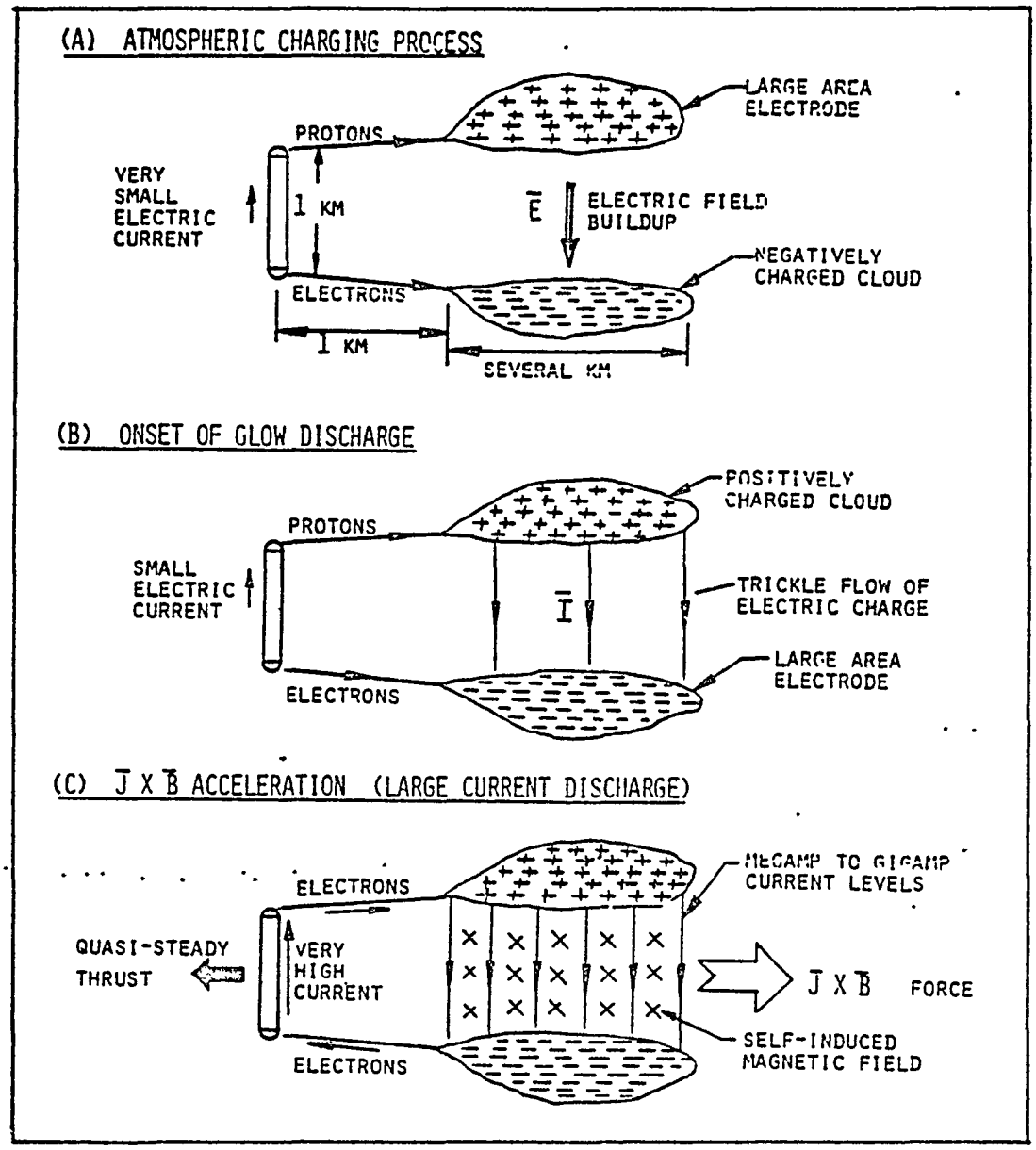

Figure IX-6. Stratospheric "Glow Discharge" Propulsion Concept (20 to 100 km Altitude)

C. MHD-FAN PULSEJET PROPULSION MODE

The MHD-fan pulsejet propulsion mode is envisioned for use by the HLLV primarily at altitudes exceeding 20 km and flight Mach numbers of at least 1.

1. Basic Engine Cycle

The basic engine cycle is portrayed in Figure IX-7. The direction of flight is at right angles to the longitudinal axis (towards the top of the page). The cycle begins when laser pulses received by both power heads are projected along the underside surface of the shuttle at very high intensities close to the breakdown threshold. Focus by both beams occurs at the vehicle center-section where air breakdown and ignition of LSD waves occur. LSD wave fronts propagate rapidly up the beams and into the pulsejet chamber exhaust ports, creating in the process a high conductivity air plasma sheet as shown in Figure IX-7A.

Meanwhile, a fresh slug of internal propellant has been injected into the radiation superheater and expands to fill the chamber just as the advancing LSD wave propagates into the powerhead, thereby heating the propellant to a high temperature and pressure. It then expands out the exhaust ports and through the XMHD generators. Subsequently, large pulses of electric power are simultaneously generated as the XMHD generators are energized. These electrical power pulses are then short-circuited through the lower longeron superconductors and through the high conductivity air plasma sheet. MHD acceleration of this current-carrying sheet occurs by the action of self-magnetic fields generated by the return current flow through the superconducting shuttle longerons, as shown in Figure IX-7B. As a result, this current sheet is pressed into the surrounding air, entraining air ahead of the MHD-driven shock and forcing it away from the vehicle.

As indicated in Appendix C, adequate current sheet inductance required for an efficient acceleration process will occur for current sheets traveling at an initial velocity of at least 330 m/s. However, since the propagating LSD waves will shed a cylindrical shock wave which

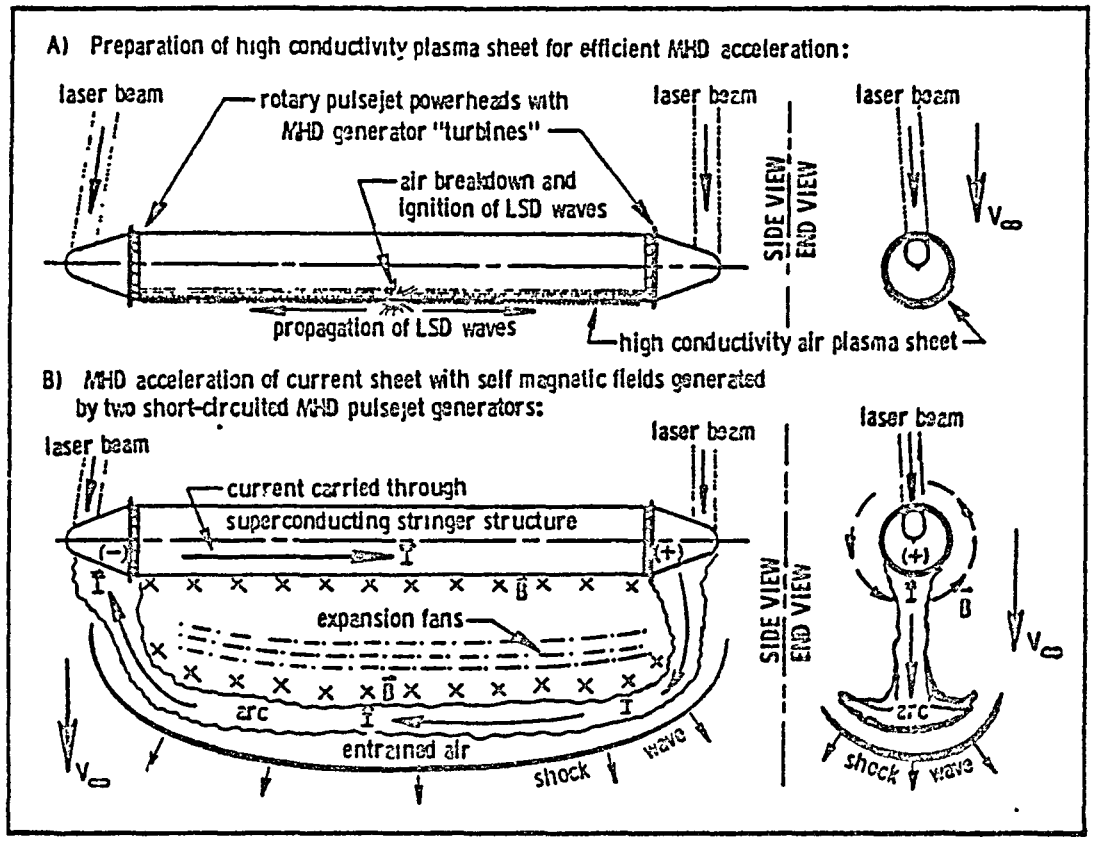

Figure IX-7. Twin Beam LTAV With MHD-Augmented Thruster

will move away from the shuttle lower surface at a velocity of Mach 1, and since the main electrical discharge is likely to initially intensify along this shock front, it is likely that the MHD-Fan propulsion system may successfully operate at flight velocities somewhat below 330 m/s, although the efficiency of operation should increase with flight speed.

Air through which the vehicle is flying is compressed at the leading edge, then flows around the outside of the cylinder, and into the active MHD thruster volume in preparation for the next accelerator pulse. In this manner. fresh air is ingested around the cylindrical shuttle as the thruster operates in repetitively pulsed fashion to accomplish momentum exchange with the atmosphere.

2. Analysis of Thruster Physics

In principle, the propulsion concept is closest to that of the air-turborocket. Electrical energy is removed from a rocket high velocity plasma exhaust flow by MHD generator "turbines." This electrical power is then used to accelerate a much larger mass flow rate of air (i.e., large compared with that which flows through the MHD generators) processed by an electrical "fan" accelerator having a configuration similar to the "parallel rail" or "button gun" type of linear MHD accelerator treated by Jahn in Ref. 10. Some care must be given to preventing the spoke-discharge pitfall evidenced in some experimental MHD accelerators. To eliminate such problems for the cylindrical thruster, the pre-ionized discharge path should be a large-area crescent (see Figure IX-6B) with uniform electrical conductivity. The physics of the MHD fan accelerator may be found in Appendices C and D; hence, it will not be repeated here.

The MHD-Fan approach does not require relativistic emission of electrical charge. The electrons simply drift through the current sheet with some finite velocity, as occurs in most any gaseous or solid conductor. The laser pre-ionized path (along which the main electric discharge later intensifies) is conceptually similar to the "stepped leader" and "return stroke" processes exhibited by natural atmospheric lightning. For the largest of such electrical discharges, air/plasma temperatures are rapidly driven to 30,000K and pressures to 100 atm as the arc intensifies

to the peak current value. Such air/plasma state conditions generally exhibit a conductivity of 215 mhos/cm. Hence, the intensity of laser radiation used in the LSD-wave pre-ionizing "stepped leader" should be high enough to generate these gas conditions within the starting crescent-shaped cylindrical shock wave.

For the sake of argument, let us assume that the thruster operates with a duty cycle of 100:1 and that the instantaneous thrust upon the current sheet is 1000 times the weight of the shuttle; hence, for the 1000m long vehicle, F_{peak} is 7.37×10^{10} Newtons. (See Chapter XII for an analysis of "lighter-than-air" vehicle weights.) The electric current which must flow through the arc at initiation in order to generate this force may be estimated by examining the magnetic interaction between two very long parallel electrical current elements with a separation distance D equal to the vehicle diameter, i.e.,

$$I = \left[2\pi F_I D/\mu_o L\right]^{1/2} \tag{10}$$

where F_I is the initial thrust upon the current discharge. It is found that $I = 1.9 \times 10^8$ Amps for the 1000m long shuttle.

At the end of the thrust pulse, the electric arc will have expanded to a roughly circular geometry, and the final force F_f upon the current element is

$$F_f = \mu_o I^2/2 \tag{11}$$

or 2.27×10^{10} Newtons for the 1000m long shuttle.

The crescent-shaped discharge region illustrated in Figure IX-7 is subjected to electromagnetic pressures from behind and reaction forces from the entrained air ahead, as the front advances in "snow plow" fashion into ambient air. Assuming that the total frontal area of the arc is equal to the vehicle length times the diameter, the arc has a distributed magnetic pressure of 730 atmospheres applied to it at initiation, and 225 atm at the end of the thrust pulse. For various reasons the arc may

not experience this total pressure, but the indicated order-of-magnitude illustrates that current sheet conductivity is likely to be maintained throughout the thrust pulse.

Determining a rough order-of-magnitude thickness for the current sheet is a more difficult matter. However, it is possible to estimate the maximum diameter of a circular cross-sectional arc attached to the vehicle ends (electrodes) which will permit a self-generated gas pressure of 100 atm required for adequate plasma electrical conductivity. The magnetic self-constriction pressure P of an electric arc upon its own conduction channel may be determined from Eq. 12.

$$P = \frac{\mu_o j^2}{4} (r_1^2 - r^2) + P_o \qquad (12)$$

where P_o is the ambient pressure outside the arc, j is the assumed uniform current density, r is the radius within the arc where the pressure is to be determined and r_1 is the outside edge of the current channel. Assuming that P_o is negligible and that the self-magnetic pressure at a radius of 0.707 r_1 (the mid-point radius which divides the cross-sectional conduction area into two equal parts) must be 100 atmospheres, it is easy to show that r_1 must be 7.5 meters for an arc discharge of 1.9×10^8 Amps required by the 1000m shuttle. Hence, the current density must be 1.08×10^6 Amps/m^2 which represents a total arc cross-sectional area of 177 m^2. Therefore, the current sheet thickness for a rectangular (or crescent-shaped) discharge region with a width equal to the vehicle diameter is 1.77m. This thickness represents an aspect ratio for the current sheet of about 56:1. Incidentally, the self-magnetic constriction force at the center of an 1.9×10^8 Amp arc with circular cross-section is about 200 atm.

The electrical resistance of the arc discharge path of length ℓ, (which is set equal to the vehicle length L at initiation, and roughly 3L at termination) is given by

$$R = \ell/A\sigma \qquad (13)$$

where A is the cross-sectional area of the electric arc and σ is the gas conductivity. At discharge initiation for the 1000m shuttle, the current sheet resistance is 263 micro-ohms; at the end, 788.0 micro-ohms.

The "end plate" electrodes of the linear shuttle MHD accelerator are not sufficiently broad so that the edge effects of the magnetic and electric fields and mass flow may be neglected. However, if edge effects are minimal, the inductance contributed to the electric circuit is simply μ_o (L/D)X, where L is the vehicle length, D is the electrode width (equal to the vehicle diameter), and X is the downstream displacement of the current sheet measured from its initial discharge location at the vehicle skin. The inductance contributed by this moving current sheet increases with X and is the only time-varying contribution to the total circuit inductance. The time rate of change of the circuit inductance is then

$$\dot{L} = (\mu_o L/D)\,\dot{X} \qquad (14)$$

where $\dot{X}$ is the velocity of the current sheet relative to the shuttle. Assuming the dimensions of the 1000m long shuttle and setting $\dot{X}$ = 300m/sec, it is found that L is 3.77×10^{-3} Ohm.

Therefore, the electrical resistance within the MHD generator power plant including that of the discharge itself must be small compared with 3.77×10^{-3} Ohm if the majority of the available electrical power is not to be wasted in Joule heating. Hence, $\dot{L}$ is seen to be greater by a factor of 14.3 (i.e., at pulse initiation) than the resistance of the current sheet itself. Therefore, it is anticipated that the potential for an effcient acceleration process appears good. However, the peak and average accelerator power requirements are exceptionally formidable for the 1000m vehicle: $\dot{L}J^2/2 = 6.8 \times 10^{13}$ Watts peak or 6.8×10^{11} Watts average, assuming a 100:1 duty cycle. The 1000m shuttle would consume the combined output of sixty-eight 10 GW solar power stations in this propulsion mode.

D. MHD-PUMPED VORTEX-INDUCED LIFT

The purpose of a MHD-Pumped Externally Trapped Aerodynamic Vortex (MPETAV) is to provide a means of lift augmentation and drag reduction for a cylindrical shuttle climbing through the more rarefied upper altitudes at supersonic velocities. The concept of MPETAV-augmented lift is conceptually identical to the subsonic vortex-induced lift concept introduced in Chapter VIII, except for the external vortex-pumping mechanism and the applicable flight velocity regime. Instead of using span-wise blowing to pump the vortex, the MPETAV approach uses electric arc "paddle wheels" as shown in Figure IX-8 to accelerate the supersonic airstream flowing over the upper surface of the cylinder--thereby increasing the circulation strength of the aerodynamic vortex and therefore lift. The magnetic dipole moment of each electric arc "paddle" (given by Eq. 6) interacts with the Earth's magnetic field in a manner that resembles the operation of a direct current electric motor. The commutating action is provided by the pulsed supply of electric power from the XMHD generators. The longitudinal axis of the shuttle is aligned directly at right angles to the flow stream, or in a slightly slewed position. Since the shuttle flight direction must be roughly aligned with the Earth's magnetic field, polar boost trajectories may be required in order to use the MPETAV principle.

The physics of the MPETAV electrical acceleration cycle are quite similar to that introduced for the MHD-Fan concept in the previous section, except that the pre-ionizing LSD wave-generated "stepped leader" is struck directly along the upper vehicle surface at the maximum cross section presented by the shuttle to the flow. The MPETAV cycle begins in Figure IX-8A as the XMHD-driven electric arc intensifies along the pre-ionized path, and thereby creates a magnetic dipole which momentarily has a neutrally stable orientation with respect to the external magnetic field. As the electric arc continues to intensify and self-magnetic fields begin to propel the electric discharge in a direction radially away from the vehicle skin, the magnetic dipole moment grows rapidly stronger. Simultaneously, the supersonic airflow about the shuttle sweeps the electric discharge downstream

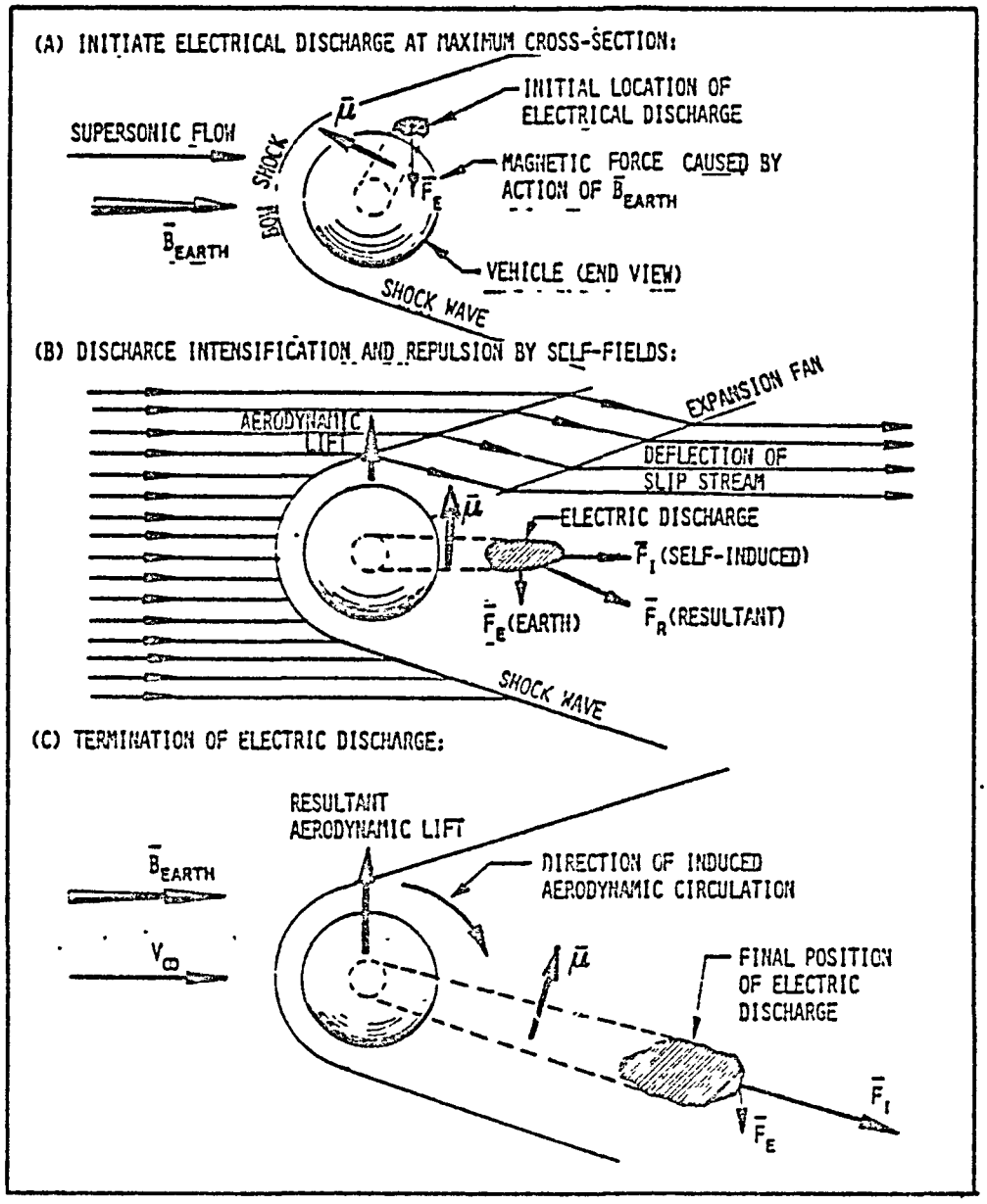

Figure IX-8. MHD-Pumped Externally Trapped Aerodynamic Vortex

and in the process disturbs the neutrally stable alignment of the magnetic dipole moment and the Earth's magnetic field.

As illustrated in Figure IX-8B, the arc experiences a net force which can be broken into two components, each the direct result of an applied magnetic field. The self-magnetic field always acts to create a force upon the current sheet in a radially outward direction from the vehicle longitudinal axis. The earth's magnetic field always acts to generate a torque in the $\bar{\mu} \times \bar{B}_e$ direction (i.e., towards the bottom of the page in Figure IX-8). As shown in Figure IX-8C, the self-magnetic forces quickly become orders of magnitude larger than those due to the Earth's field. Early termination of the electric current prevents the magnetic dipole moment vector μ from rotating into complete alignment with the Earth's field.

The net effect upon the external aerodynamic flow field by the passage of rapidly pulsed electric discharges (i.e., "paddles") is that flow is accelerated over the upper surface of the vehicle, thereby augmenting lift. In addition, a momentum exchange process is carried out with the atmosphere through the action of self-magnetic fields, and this causes an acceleration of the cylindrical shuttle in an analogous fashion to the MHD-fan system described in the previous section.

E. WAY'S ELECTROMAGNETIC PROPULSION CONCEPT

1. Historical Context

The air-breathing electromagnetic propulsion mode introduced in this section is a variation-on-a-theme of a MHD propulsion concept originally proposed for submarines (e.g., see Refs. 11-20). Way[11,16-20] has done the most extensive theoretical and experimental research on the concept and has built a 10 foot operating model which is pictured in Figure IX-9A. He used a single electromagnetic field coil of rectangular configuration; the largest dimension was aligned with the longitudinal axis of the vehicle. A constant electric current conducted within the coil created a strong magnetic field which enveloped the vehicle and reached far

A) Two Pole Electromagnet Geometry

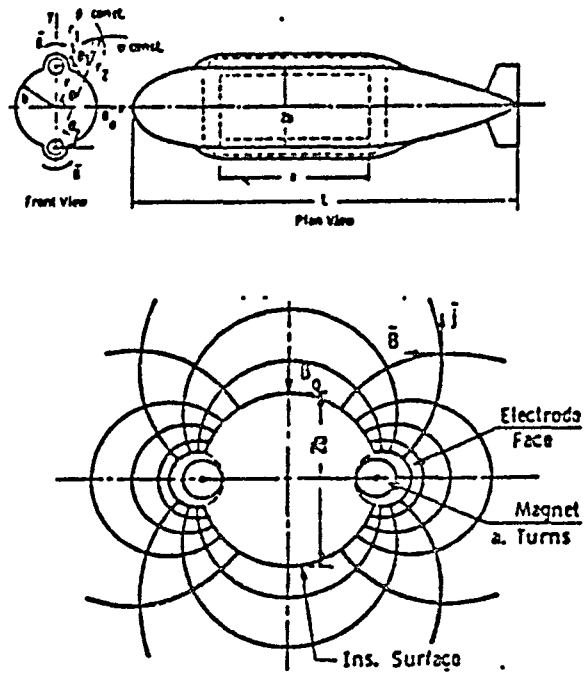

B) Multiple Pole Electromagnet Geometry

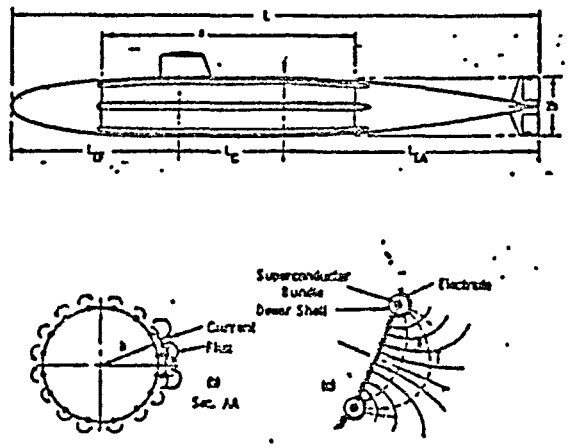

Figure IX-9. Configurations of Magnetic Field and Current Flow Pattern for Way's Pronulsion Concept (From References 50, 51 and 53)

out into the surrounding sea water. An electrical power plant within the vehicle is used to apply a potential across the two long electrodes which are mounted on the vehicle exterior surface directly over the longitudinally aligned portions of the coil. A sizeable continuous electric current is made to flow through the external conducting medium, since the ocean is a saline solution and has a finite conductivity. Water is entrained within the electric arc path and is subsequently accelerated aft by the action of JxB Lorentz forces. Hence, a momentum exchange process is carried out with the external fluid, resulting in a forward thrust upon the vehicle.

2. Shuttle EM Thruster Cycle

The air-breathing E/M thruster envisioned for the cylindrical shuttle is closest to Way's multiple pole electromagnet geometry pictured in Figure IX-9B. The continuously operating approach of Way is discarded in favor of a quasi-steady rapidly pulsed mode of electrical generation. The sea water external medium (having a constant low value of electrical conductivity) is replaced by the atmosphere which is subjected to transient ionization at close proximity to the shuttle, as schematically diagrammed in Figure IX-10. A major change to the cylindrical shuttle configuration proposed previously is the inclusion of a dozen or more longitudinally oriented electrodes which run the entire length of the shuttle external surface, one electrode per superconducting longeron (refer to Figures IX-9B and IX-10).

Physically, this transient ionization process is carried out through the use of remote beamed laser radiation, as follows. The forward end of the vehicle is equipped with the optical train configuration displayed in Figure VIII-1. These internal optics permit a "beam catcher" mirror to distribute laser power onto parabolic "primary" mirrors. In turn, each primary mirror condenses the beam upon a "secondary" mirror--which then reprojects the high-intensity beam along the outer vehicle surface, to a focus at the aft end of the vehicle as shown in Figure VIII-1B.

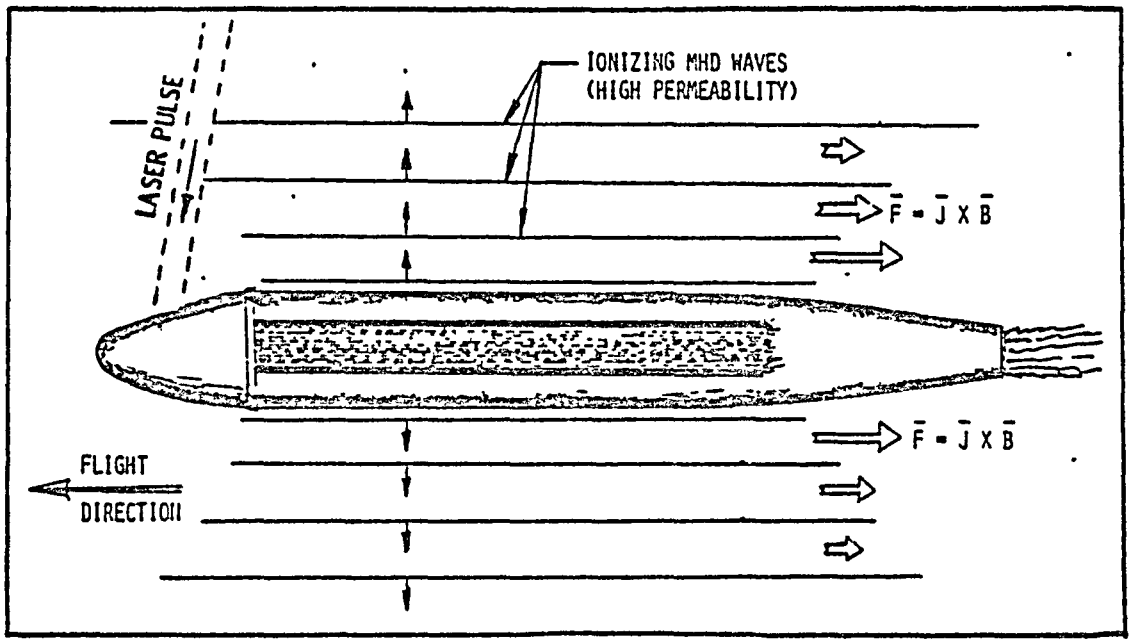

Figure IX-10. Transient Ionization Concept

The cycle begins with a new laser pulse-train which is received at the "beam catcher" mirror and distributed in gatling-gun sequence into all the primary optical chambers (say perhaps, in a clockwise rotation). Air breakdown is followed by ignition and propagation of LSD waves which race up the beam, converting all the air in its path (close to the vehicle surface) to a hot, high-pressure plasma. As indicated in Figure IX-11, each propagating LSD wave generates a strong cylindrical blast wave, which moves rapidly away from the vehicle at the speed of sound.

As shown in Figure IX-12, an energetic power supply (e.g., the laser-heated XMHD generator) then drives a large electric discharge from one longitudinal electrode through the conducting air plasma to the adjacent electrode. As the cylindrical discharge intensifies, the advancing front takes on the characteristics of a detonation wave. Joule heating (I^2R losses to the resisting plasma) of the air behind the shock wave transforms it into an electrically supported detonation wave. This process increases the conductivity and propagation velocity of the discharge.

Only a small strip of air is an electrically conducting plasma at any given moment. That which is entrained within the electric current volume is accelerated aft by the action of Lorentz forces ($\bar{F}_M = \bar{J} \times \bar{B}$) in gatling-gun fashion as shown in Figure IX-13. As a whole, the supersonically advancing detonation waves process all the air within a large cylindrical radius (e.g., 30 to 50 percent greater than the vehicle diameter), imparting it to a velocity increment in the aft direction. (Note that the ionizing current wave must have a <u>good permeability</u>, and that the accelerating Lorentz forces are applied at <u>right angles</u> to the direction of wave propagation.) Fresh air is convected into the annular accelerator volume by the forward motion of the vehicle.

By this means, a momentum exchange process is carried out with the atmosphere; and the shuttle is accelerated forward. Fresh air is convected into the annular accelerator volume by the forward motion of the vehicle - and is subsequently accelerated by the next pulse. Shuttle flight velocities may need to be at least sonic in order that acceptable current sheet inductance can permit good E/M thruster efficiencies.

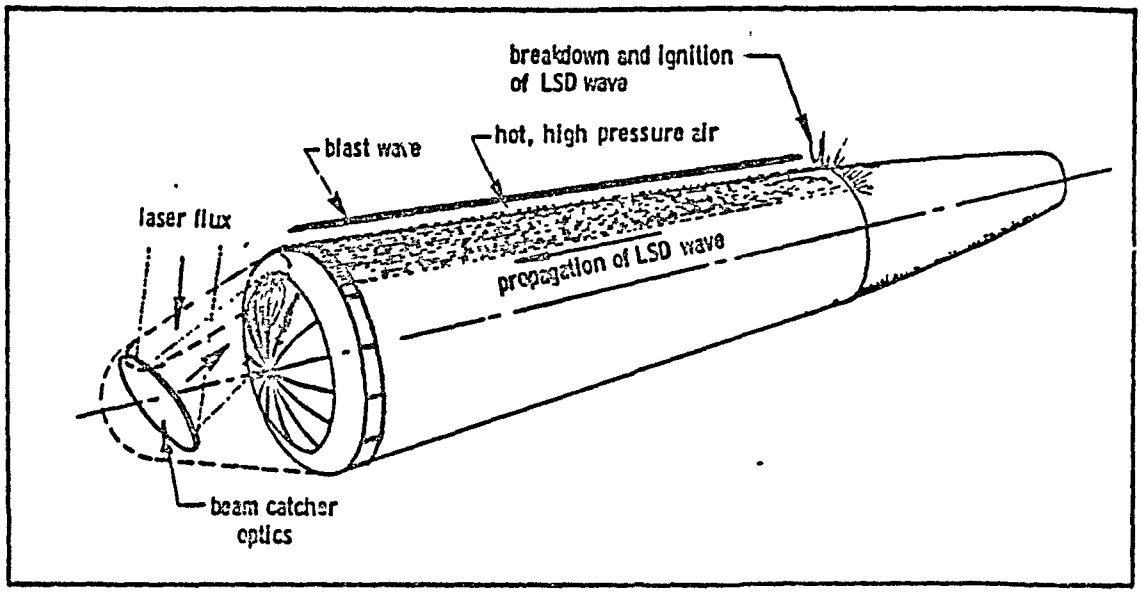

Figure IX-11. Laser Generation of Strong Cylindrical Blast Wave

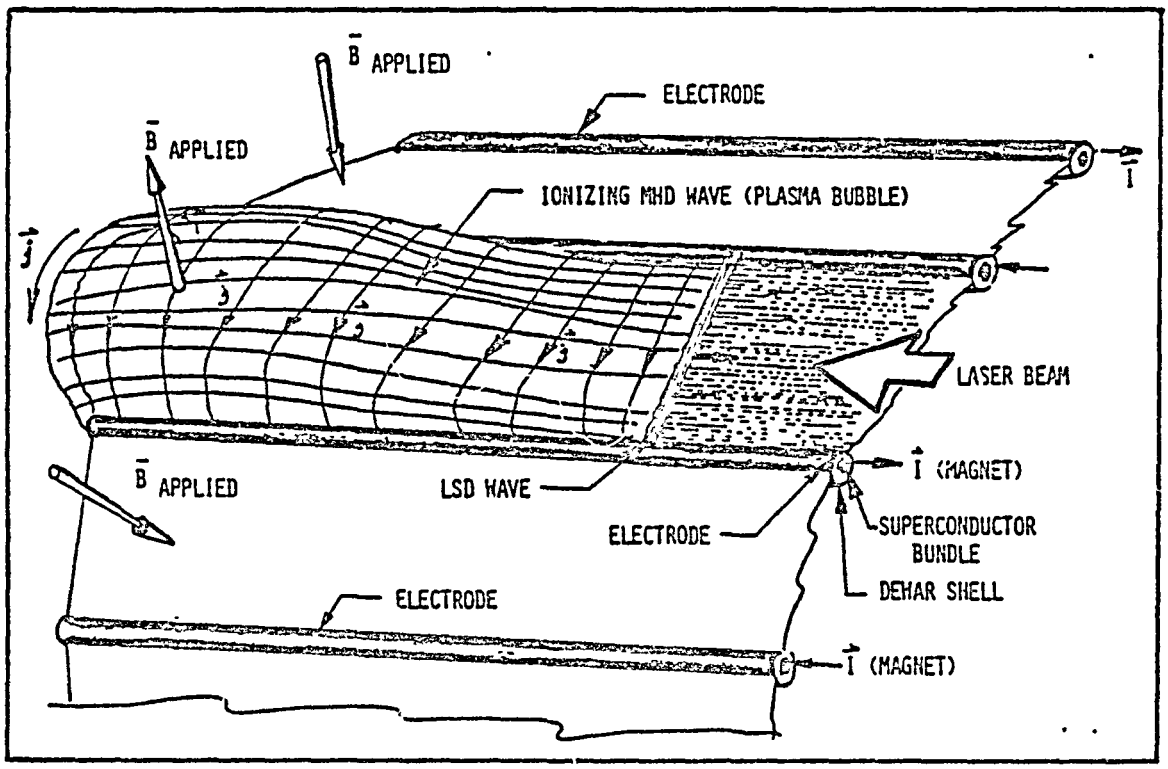

Figure IX-12. Electrical Discharge Configuration

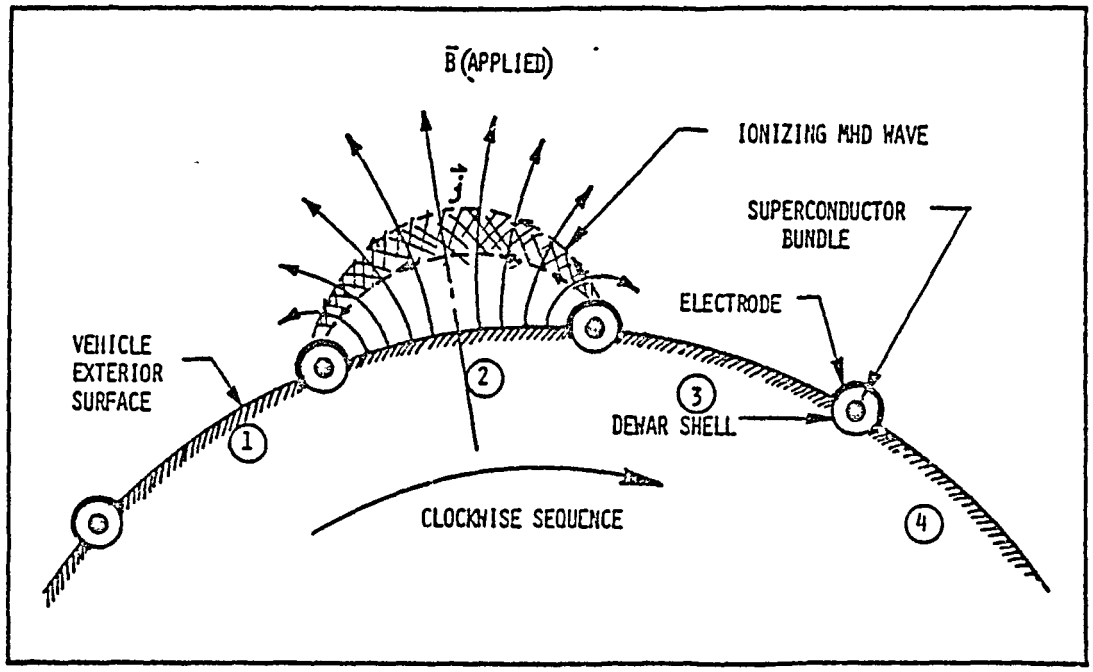

Figure IX-13. "Gatling Gun" Acceleration Process (Vehicle End View - Looking Aft)

The suggested multiple pole electromagnetic field geometry for the shuttle should prevent the development of a strong rolling torque (due to the Earth's magnetic field) which would certainly be experienced by a shuttle having the simpler two pole electromagnetic field geometry portrayed in Figure IX-9A. By purposeful design, then, potential restrictions upon the shuttle flight velocity orientation with respect to the local planetary magnetic field are circumvented.

F. LARGE AMPLITUDE ALFVEN WAVE THRUSTER MODE

The last electrically augmented propulsion system to be discussed for the shuttle is the large amplitude "Alfven-wave" thruster which uses the Earth's geomagnetic field and internal propellant (for the XMHD generators) to accelerate through the ionosphere to orbital altitudes and velocities. This high specific impulse (up to 10^5 sec for the 1000m long shuttle) engine concept develops thrust by warping the local geomagnetic field out to a radius of several tens of kilometers, and thereby communicates a reaction force to the planetary mass by way of a perturbation to the local planetary field.

To develop significant thrust-to-weight ratios, the concept requires active emission electrodes which permit the generation of sizeable electric currents through the shuttle superconducting longerons and out the ends of the vehicle, as portrayed in Figure IX-14. In operation, the XMHD generators (being fed with internally stored hydrogen propellant) develop pulsed electrical power and eject charged plasma clouds with a significant residual aft-directed velocity. The external surfaces of the powerheads act as large surface area electrodes or "plasma contactors" to ensure good electrical contact with the ionospheric magneto-plasma. The entire exterior shuttle surface between the power-head ends serves as an electrically insulated skin to protect the superconducting longerons from shorting-out through the ionospheric plasma. As shown in Figure IX-14, the positively charged end of the vehicle is engulfed in a large positive ion cloud which

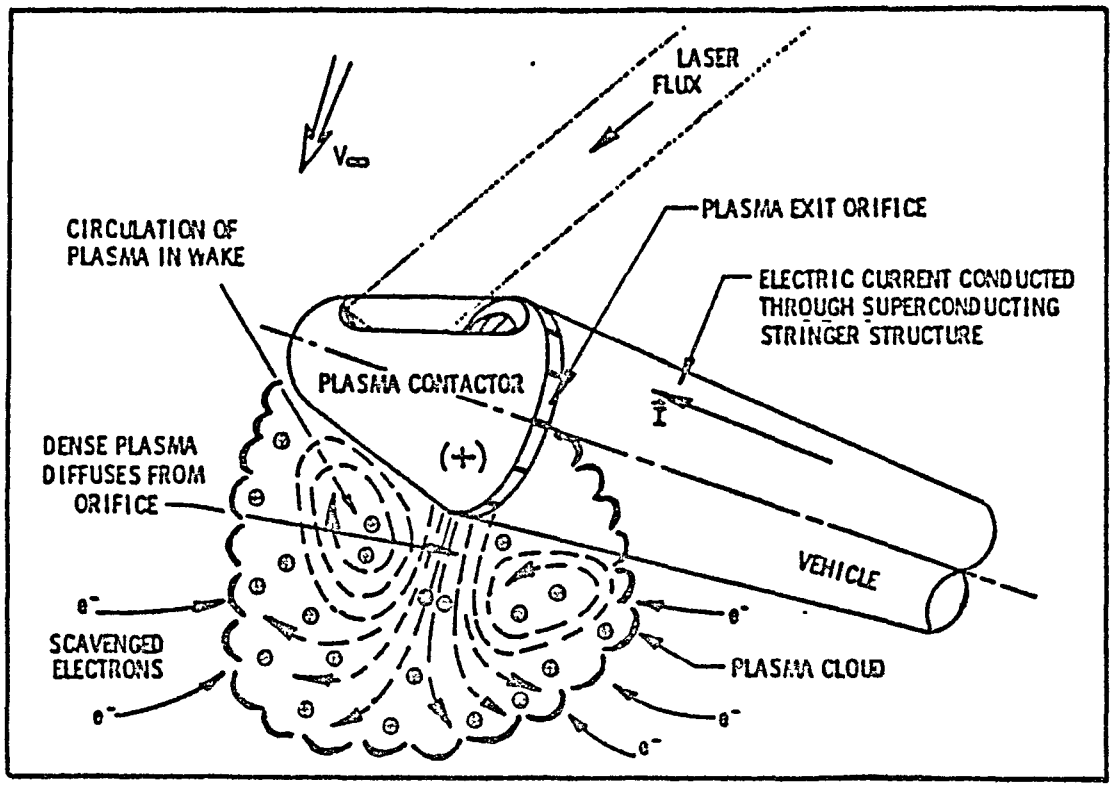

Figure IX-14. Plasma Contactor for Production or Collection of High Electron Currents by MHD-Augmented LTAV Thruster

scavenges electrons from the ambient background plasma. The other end of the vehicle (see Figure IX-15) emits quasi-steady repetitively pulsed low-voltage high-current electron beams; it is shown foreshortened as it recedes into the distance.

The electrons and ions are then carried away from the vehicle electrodes by large amplitude Alfven waves in a manner analogous to the operation of E/M transmission lines. These electric currents fall in rough alignment with the geomagnetic field lines. No thrust or lift augmentation is anticipated from the generation of the trailing E/M vortices. Thrust is developed by Lorentz forces ($\bar{F}_M = i\bar{L} \times \bar{B}_E$) developed upon the superconducting longerons in a direct E/M interaction with the Earth's magnetic field. In Figure IX-15, the Earth's magnetic field vector $\bar{B}_{EARTH}$ is shown directed towards the right side of the page; therefore, the E/M thrust is oriented towards the top of the page. This resultant load is linearly distributed along the superconductor length and is thereafter transmitted directly to the shuttle longeron primary structure. However, the acceleration forces developed by this thruster are likely to be small, i.e., several tenths of a "g", and most suitable for orbital maneuvering applications--unless some way can be found to increase electric current levels by many orders-of-magnitude.

Figure IX-16 shows the electromagnetic interaction with the earth's geomagnetic field in greater detail. It illustrates in top, bottom, front, and side views the orientation geometry of the plasma Alfven-wave wings generated by an accelerating conductor in the geomagnetic field. The Alfven wave velocity vector is $\bar{V}_a$; the applied electric field, $\bar{E}$; the induced magnetic field generated by the E/M "bound vortex" (i.e., the electric current carried through the superconducting longerons), $\bar{B}_{IND}$; the Earth's magnetic field vector, $\bar{B}_{EARTH}$.

1. Theoretical Basis

The theoretical basis for the operation of a geomagnetic propulsion engine within the ionosphere (altitudes greater than 100 km but less than 10,000 km) is quite well understood[21-25]. When a conductor traverses through a magnetic field, various electrodynamic and plasma processes are

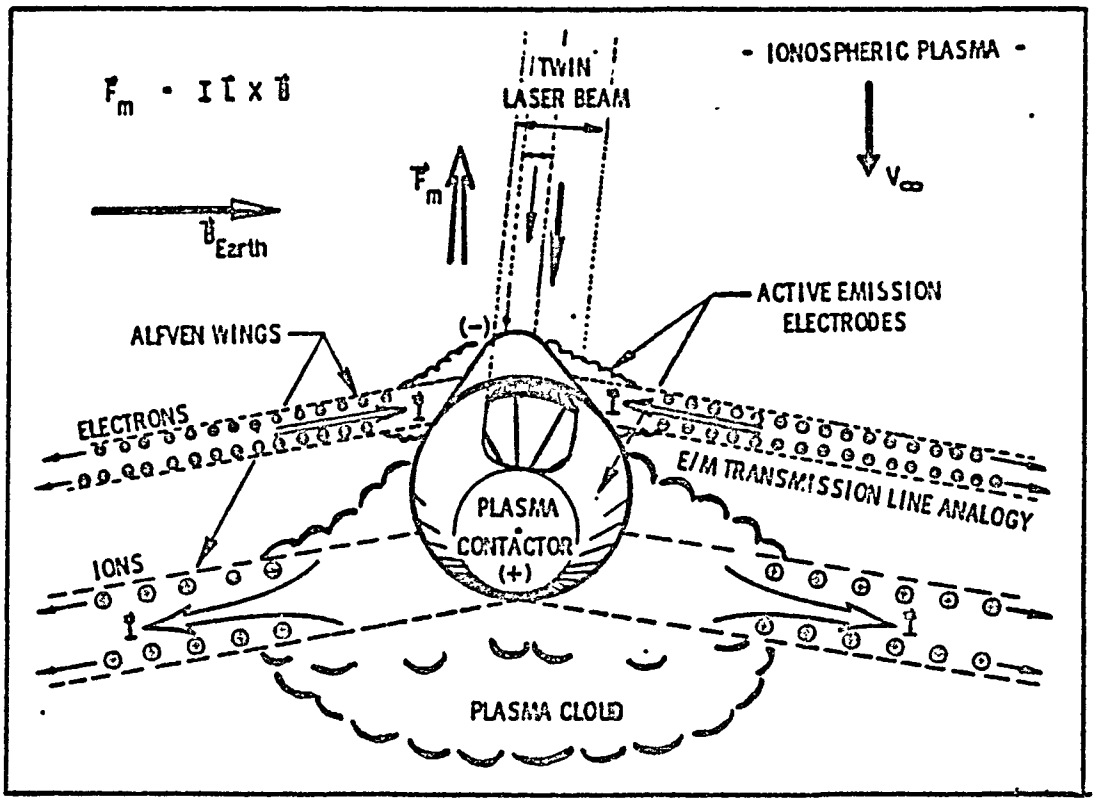

Figure IX-15. Ionospheric Coupling Mechanism for Large LTAV Alfven Wave Geomagnetic Thruster (End View)

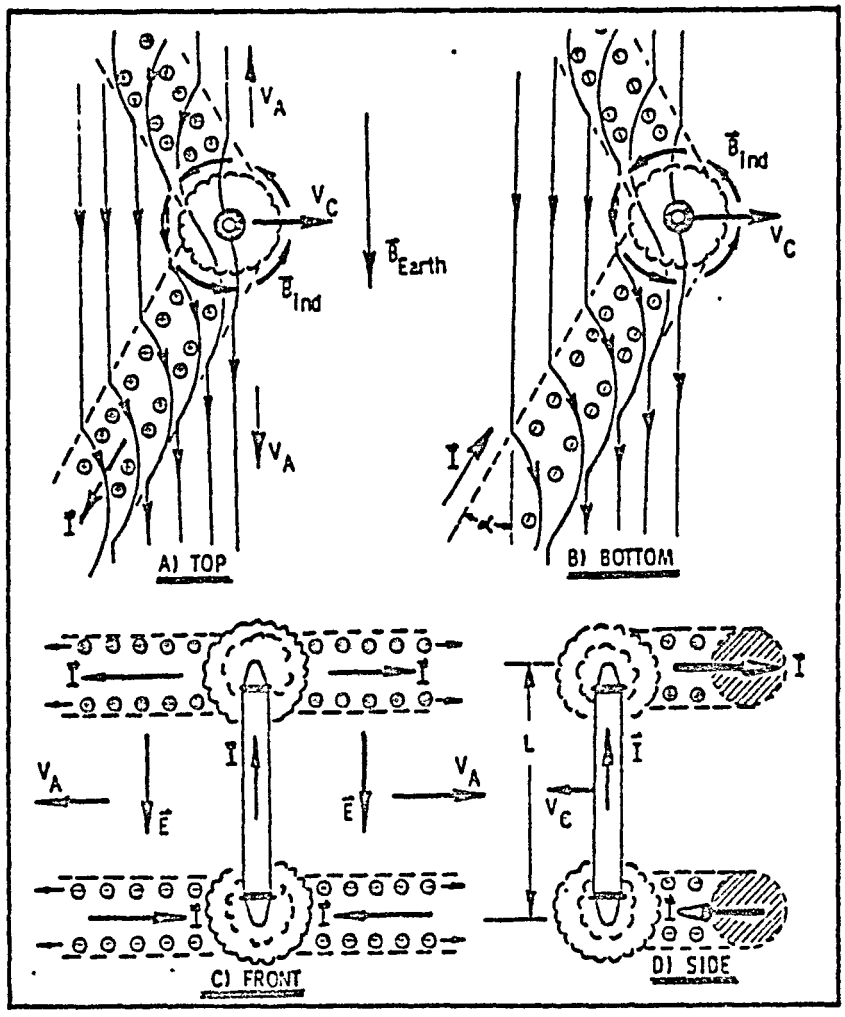

Figure IX-16. The Generation of Alfven Wave Wings From an Accelerating Conductor in the Geomagnetic Field Within the Ionosphere

in evidence. A conductor moving in a vacuum develops a motional electric field $\bar{E}_c$ (in the vehicle reference frame) given by:

$$\bar{E}_c = \bar{V}_c \times \bar{B}_p \qquad (15)$$

where the electric field $\bar{E}_c$ is measured in the conductor reference frame, V_c is the conductor velocity, and $\bar{B}_p$ is the planetary geomagnetic field. The action of this electric field causes a polarization of the conductor, and following a brief transient period, no current flows through the conductor.

However, within the ionosphere, a return current path can be provided by the dilute and anisotropic plasma which is quite a good conductor of electricity along the magnetic field lines. In this case, the existence of the magnetic field and the plasma allow a flow of electric charge to be transferred between the ends of the conductor and the ambient medium. The result is a steady flow of charge through the conductor. Electrons are scavenged from the plasma at one end of the conductor and emitted by the other. Electric power can be removed from this circuit in exchange for conductor (or vehicle) kinetic or potential energy.

Operated in reverse, an electric field provided by on-board power can increase the kinetic or potential energy of the vehicle, thereby acting as a geomagnetic propulsion engine. Outside the conductor (as shown in Figure IX-16), large amplitude Alfven waves are created as electric currents flow in the plasma outwards along the planetary magnetic field lines. A resulting warpage of the ambient magnetic field in the immediate vicinity of the conductor (see Figure IX-16A) occurs from a superposition of the 'circular' magnetic field (labeled as $\bar{B}_{ind}$) created by the flow of current through the conductor. The local disturbance then propagates away along the local magnetic field lines at the Alfven velocity V_a. As a result, the Alfven "wing" disturbances are swept back at an angle α to the conductor (see Figure IX-16A) given by:

$$\text{Tan } \alpha = V_c/V_a \qquad (16)$$

Then the Alfven velocity is given by

$$V_a = (B_p^2/4\pi\rho_i)^{1/2} \tag{17}$$

where B_p is the magnetic field strength, and $\rho_i = nM_i$, which is the ionic mass density.

2. Alfven Waves

The disturbance which is created in the wake of the cylindrical shuttle conductor as it moves perpendicularly through a magnetized plasma consists largely of a) electric charge injection (electrons and positive ions) from active emission electrodes, b) magnetic field, and c) electric field perturbations at the primary frequency ω which is equal to

$$\omega = V_c/d \tag{18}$$

where d is the dimension of the electrodes in the direction perpendicular to $\bar{B}$, and V_c is the component of the conductor velocity perpendicular to the magnetic field. These disturbances produce Alfven or hydromagnetic waves, which are shear waves in both the ambient magnetic field and the mean ion velocity. The waves travel at the Alfven velocity V_a when the primary frequency is much less than the ion gyro frequency Ω_i (i.e., $\omega << \Omega_i$). Banks and Williamson[23] suggest that certain engine configurations may be capable of generating waves on the order of the ion gyrofrequency and higher, and possibly waves with frequencies well below the ion gyrofrequency.

3. Theoretical Limits to Ionospheric Current Coupling

There exists an upper limit to the current which is available to a given passive-electrode system for the purposes of power removal or generation. However, Banks and Williamson[23] point out that this is not an inherent limitation on the magnitude of the Alfven wave which can be generated nor on the current which can be made to flow along the field lines when internal power in the system is used. However, the only practical systems expected to approach the Alfven limit are systems with active

electron and ion emitters. Otherwise, current flow within the system will be limited by internal resistance of the conductor, skin effects of the electrode-plasma interface, or perhaps finite parallel conductivity of the ambient plasma.

Assume that the ambient plasma conductivity perpendicular to the magnetic field line is near zero and that the parallel conductivity is finite. The "flux tube" of field lines passing into one electrode of the conductor comprises an electromagnetic transmission line in a medium where the dielectric permittivity is the plasma dielectric constant $\varepsilon_\perp$, and may be expressed by

$$\varepsilon_\perp \cong 1 + (C/V_a)^2 \tag{19}$$

where C is the propagation velocity of light. The conductor effectively "shorts out" the magnetic field lines passing through the conductor, since the tangential electric field at the electrode surface (in the conductor reference frame) must be zero.

Banks and Williamson[23] propose an idealized system which consists of two spherical electrodes of diameter d connected by a long conducting wire of length L (where $L << d$). The impedance of an open 2-wire transmission line for such a system is approximately

$$Z_o = 120\, \varepsilon_\perp^{1/2} \cosh^{-1}(L/d) \tag{20}$$

The impedance for systems of reasonable dimensions can be shown to fall within the range of 0.2 - 1.0 ohms.

A voltage is developed between the two electrodes, given by $\Delta V = E_c L$, where E_c is given by Eq. (15). Therefore, the electric current delivered to the Alfven wave is

$$I = \Delta V/Z_o = V_c B_p L/Z_o = \frac{V_c LC\sqrt{4\pi\rho_i}}{120 \cosh^{-1}(L/d)} \tag{21}$$

where again V_c is the relative velocity of the conductor with respect to the ambient plasma.

4. Prospects for Gigampere Current Levels

To the author's knowledge, all of the Alfven wave engines proposed to date have relied solely upon the sparse ionospheric plasma for a source of ion and electron charge flow required by the engine. Moore[22] was first to propose the emission of enormous "plasma contactor" clouds to greatly enlarge the effective electrode area for scavenging electrons from the ionospheric plasma. This scheme may increase the total current generation abilities of a given system by at best 1 or 2 orders of magnitude. Given the maximum cross-sectional area A_e of the cloud electrode (area perpendicular to the flight velocity vector V_c), the limiting electron current collectable by a passive system may be expressed as

$$I_{Limiting} = \rho_e V_e A_e \qquad (22)$$

where ρ_e is the ionospheric electron density. To further increase the electric current level beyond the 10 to 100 Ampere limit collectable by even very large electrodes (e.g., 100 meter diameter conducting ballons[23]) requires active emission electrodes and a source of on-board propellant to provide the associated charge flow.

Clearly, megampere-and-beyond current pulses may be generated using relativistic beam ejection techniques presently being developed for fusion and beam weapon applications[7-9]. However, such a system would pay heavy penalties in terms of peak power demands upon the power supply in order to develop the required megavolt acceleration voltages; hence, the increased probability of lower duty cycles and reduced average thrust.

Recent conversations[26] have shed light on one additional prospect for a very high current, low voltage discharge mechanism within the ionospheric magneto-plasma. The cycle has certain physical similarities to that portrayed in Figure IX-7. To minimize plasma arc kinking instabilities during initiation of a low voltage discharge, the arc path would initialize just above the vehicle skin, thereby minimizing the magnetic

dipole field and interaction with the earth's magnetic field. As the discharge intensifies, active emission of low voltage ions and electrons from the vehicle electrodes is gradually increased. Simultaneously, the electron density within the electric arc volume is increasing and hence improves the conductivity of the accumulated plasma. Self-magnetic constriction pressures upon the plasma arc discharge channel prevent this plasma from escaping too rapidly.

Once the discharge is pushed away from the vehicle in the aft direction, the strength of the magnetic dipole grows and much energy is stored within the magnetic field; thereafter, little additional energy is required to sustain it. Eventually, the expanding "solar flare" arc grows to unwieldy proportions, the current level is reduced to zero, the trapped plasma within the discharge channel is blown away, a new arc is struck next to the vehicle, and the cycle begins again.

In summary, if plasma instabilities (e.g., arc "kinking") do not develop along the discharge channel, this emission mechanism will perhaps allow the generation of high enough electron densities within the 10^6 to 10^9 Ampere discharge channel (while limiting the space charge effects) to greatly increase the channel conductivity and therefore reduce the voltage requirements (to perhaps 5 ~ 100 Volts?) as the arc is blown away by self-magnetic forces. As the dimensions of the discharge loop grow large, the reduced electron densities and long plasma conductor lengths will drive voltage requirements up to a point where it becomes more efficient to initiate a new discharge path close to the vehicle skin.

REFERENCES FOR CHAPTER IX

1. Sawle, D. R. and Bosserman, H., "Analysis and Test of Explosively Driven Magnetohydrodynamic Pulse Generator," Report No. AL-TDR-64-11, Contract No. AF33(657)-11562, February 1964, Air Force Avionics Lab., Research and Technology Division, AFSC, Wright-Patterson AFB, Ohio.

2. Pape, R., "Multimegajoule, Pulsing, Explosive Driven MHD Feasibility Study," Technical Report AFAPL-TR-71-11, November 1971, Air Force Aeropropulsion Laboratory, Wright-Patterson AFB, Ohio.

3. Teno, J. and Sonju, O. K., "Development of Explosively Driven MHD Generator and Short Pulse Aircraft High Power," Interim Technical Report No. 1, AERL Report AFAPL-TR-74-48, Avco Everett Research Laboratory, Everett, MA, June 1974.

4. Decher, R., "End Loop Shorting in Nonequilibrium MHD Generators," AIAA Journal, Vol. 10, No. 8, August 1972, pp. 983-984.

5. Houben, J.W.M.A., Blom, J. H. and Rietjens, L.H.T., "End Effects in Faraday Type MHD Generators with Nonequilibrium Plasmas," AIAA Journal, Vol. 10, No. 11, November 1972, pp. 1513-1516.

6. Alfven, H., "Space Craft Propulsion: New Methods", Science, Vol. 176, No. 4, April 1972, pp. 167-168.

7. Robinson, C. A., Jr, "US Pushes Development of Beam Weapons," Aviation Week and Space Technology, 2 October 1978, pp. 14-22.

8. Robinson, C. A., Jr, "Key Beam Weapons Tests Slated," Aviation Week and Space Technology, 9 October 1978, pp. 42-53.

9. Robinson, C. A., Jr, "Army Pushes New Weapons Effort," Aviation Week and Space Technology, 16 October 1978, pp. 42-52.

10. Jahn, R. G., Physics of Electric Propulsion, McGraw-Hill Book Co., New York 1968.

11. Way, S., "Examination of Bipolar Electric and Magnetic Fields for Submarine Propulsion," preliminary Memorandum Communication tc US Navy Bureau of Ships, 15 October 1958.

12. Rice, W. A., US Patent 2997013, 12 August 1961.

13. Friauf, J. B., "Electromagnetic Ship Propulsion," A.S.N.E. Journal, February 1961, pp. 139-142.

14. Phillips, O. M., "The Prospects for Magnetohydrodynamic Ship Propulsion," Journal of Ship Research, March 1962, pp. 43-51.

15. Doragh, R. A., "Magnetohydrodynamic Ship Propulsion Using Superconducting Magnets," Transactions of the Society of Naval Architects and Marine Engineers, Vol. 71, 1963, pp. 370-386.

16. Way, S., "Propulsion of Submarines by Lorentz Forces in the Surrounding Sea," ASME paper 64-WA/ENER-7, Winter Meeting, New York City, 29 November 1963.

17. Way, S. and Devlin, C., "Construction and Testing of a Model Electromagnetically Propelled Submarine," Proc. Eng. Aspects of Magnetohydrodynamics, Stanford Univ., CA, 1967.

18. Way, S., and Devlin, C., "Prospects for the Electromagnetic Submarine," AIAA Paper No. 67-432, AIAA 3rd Propulsion Joint Specialist Conference, Washington, DC, 17-21 July 1967.

19. Way, S., "Electromagnetic Propulsion for Cargo Submarines," Journal of Hydronautics, Vol. 2, No. 2, April 1968, pp. 49-57.

20. Way, S., "Research Submarines with Minimal Ocean Disturbance," SAE Paper No. 69-028, presented at SAE Conference on 13-17 January 1969.

21. Drell, S. D., Foley, H. M. and Ruderman, M. A., "Drag and Propulsion of Large Satellites in the Atmosphere: An Alfven Propulsion Engine in Space", Journal of Geophysical Research, Vol. 70, No. 13, 1 July 1965, pp. 3131-3145.

22. Moore, R. D., "The Geomagnetic Thrustor - A High Performance Alfven Wave Propulsion System Utilizing Plasma Contracts," AIAA Paper No. 66-257, AIAA Fifth Electric Propulsion Conference, San Diego, CA, 7-9 March 1966.

23. Williamson, P. R. and Banks, P. M., "The Tethered Balloon Current Generator--A Space Shuttle-Tethered Subsatellite for Plasma Studies and Power Generation," final report to National Oceanic and Atmospheric Administration, Environmental Research Laboratories, Space Environmental Laboratories, Boulder, Colorado, 16 January 1976.

24. Morrison, P. J., Thompson, W. B. and Williamson, P. R., "Current Collection by a Long Wire in Near-Earth Orbit," presented at the 1976 IEEE International Conference on Plasma Science, Austin Texas, 24-26 May 1976.

25. Williamson, P. R., Banks, P.M. and Oyama, K., "The Electrodynamic Tether," Proceedings of the UAH/NASA Workshop on the Uses of a Tethered Satellite System, University of Alabama in Huntsville, Huntsville, Alabama, 2-3 May 1978, pp. 163-173.

26. Communication with P. R. Williamson.

NOMENCLATURE

A	area of wing or lifting surface; area enclosed by current loop; electric arc cross-sectional area
A.R.	wing aspect ration (A/c)
b	vehicle length or wing span
B	magnetic field strength
c	wing cord
C	coupling coefficient (thrust/power); propagation velocity of light
C_D	overall drag coefficient
C_{D_0}	parasitic drag coefficient
C_L	section lift coefficient
d	electrode dimension (usually equal to external diameter of cylindrical shuttle)
D	aerodynamic drag; vehicle diameter
e	span efficiency factor
E	electric field strength
F	resultant force; thrust
F_i	initial thrust
F_f	final thrust
i,I	electric current
I_o	intensity of electromagnetic radiation
j,J	electric current density
K	dielectric constant; a dimensionless constant
ℓ	wing span; length of arc discharge
L	lift; length of bound vortex

$\dot{L}$	time rate of change of circuit inductance
$\dot{m}$, $\dot{m}_c$	mass flow rate of propellant
P	flight propulsive power; gas pressure or pressure differential
q	dynamic pressure head ($\rho V^2/2$)
r	radial dimension
R	electrical resistance
s	a closed curved path
S	factor of safety
t	thickness of fabric skin
T	gas temperature
V	velocity
V_a	Alfven wave velocity
V_D	additional voltage drop
W	vehicle weight
$\dot{X}$	velocity of current sheet relative to shuttle
Z_o	impedence of open 2-wire transmission line
α	induced angle
γ	ratio of specific heats
ϵ_o	permittivity constant
ϵ_1	plasma dielectric constant
μ	magnetic dipole moment
μ_o	permeability constant
ρ	gas density
ρ_e	ionospheric electron density
ρ_i	ionic mass density

σ	fiber working stress; gas conductivity
Γ	vortex "circulation" or strength
ψ	torque vector
Ω_i	ion gyro frequency
ω	frequency

Subscripts

a	aerodynamic
c	conductor
DW	detonation wave
e	external; earth; electrode
ex	exhaust gas conditions
i,ind,I	self-induced
LSC	laser-supported combustion
LSD	laser-supported detonation
m,M	magnetic
o	ambient conditions
P	planetary
S	conditions behind shock wave
1	conditions ahead of shock wave
∞	ambient conditions

CHAPTER X
MONOCLE SHUTTLE: SSTO LASER RELAY CRAFT*

A. INTRODUCTION

The primary objective of this chapter is to: (1) investigate the concept of a manned reusable single-stage-to-orbit (SSTO) air/spacecraft propelled by laser energy beamed from powerful remote space-based (or ground-based) power plants, (2) identify requirements/criteria necessary for integration of a high-energy laser (HEL) with robust tactical and strategic fire power into this conceptual advanced space shuttle design, (3) examine the defense effectiveness of the HEL-integrated design, and (4) calculate the mass of the Monocle laser-relay shuttlecraft and compare it with that projected for radial craft of Chapter VII.

The study applies innovative techniques and advanced technologies to the flight-platform/laser integration problem. Stark excursions from present air/spacecraft baseline designs are permitted in the accomplishment of this integration process.

The "Monocle Shuttle" concept, satisfies all of the above-mentioned goals and objectives. The concept is conceived as an enabling shuttle technology for the new Space Command, a lightweight "fighter" for the space superiority mission. A squadron of these advanced SSTO vehicles would have the ability to defeat today's most awesome nuclear offensive threat: a massive ballistic missile attack.

B. HIGH-ENERGY LASERS IN FUTURE USAF MISSIONS

New weapon development is undertaken to increase the USAF's capability to carry out its mission. In the past few years, the HEL has developed very rapidly and has shown great potential for unique and revolutionary defense applications. In particular, high-energy laser systems offer many

* This study was performed with support from the Defense Advanced Research Projects Agency under Contract No. 555713-S to the BDM Coproration.

possibilities for essentially instantaneous, long-range projection of military force. Since the USAF is interested in the HEL as a future weapon, increasing emphasis is being placed upon its integration into flight vehicles. This favorable ground swell of support has resulted in construction of the experimental Airborne Laser Laboratory (ALL), much prototype HEL-related hardware, and several detailed analytical studies of future HEL-equipped fighters for the air-superiority mission. With the creation of Space Command, integration of HELs into future space shuttle and orbital-transfer vehicles will become of paramount interest.

Because the HEL is still in the early stages of development, the revolutionary implications of such future defense systems are just beginning to emerge. For example, from within the atmosphere or from the Earth's surface, lasers could provide area defense or limited anti-satellite (ASAT) capabilities; whereas, relay mirrors in space, or lasers based in space could (in principle) direct lethal energy to any strategic or tactical target on the Earth or in cislunar space. Whether in space or within the atmosphere, the impact of successful HEL deployment could be immense, and might strongly affect the world balance of power.

C. HEL-INTEGRATED FLIGHT VEHICLE CONCEPTS

Much has been learned about HEL-integrated flight vehicles from the ALL, HEL prototype hardware, and analytical studies. A significant realization is that HEL effectiveness can be severely compromised by retrofitting current laser devices into existing flight vehicles. Conventional flight vehicle design practice normally tends to optimize such parameters as thrust-to-weight, maneuverability, range, payload capability, direct operating cost, or life cycle cost. However, with the introduction of revolutionary weapons, these standard design procedures no longer apply.

A whole new group of critical questions must be addressed. For example, how does the HEL affect requirements for the flight platform's structure, electrical power supply, and propulsive engine? Can the ability of the platform to maneuver be used to minimize requirements on the laser optics? What sophisticated techniques can be employed to isolate HEL

optics from vibrations of the platform structure? How can advances in the technological areas of structures, aerodynamics, and flight control be applied to facilitate innovation in the HEL-integration process? What innovative approaches can be taken to HEL beam control, advanced fire control systems, and HEL device technology? What locations for engine, optics, laser, and power supply can simplify the HEL/platform installation? It must be recognized that revolutionary weapon concepts can have a predominant impact on the figures-of-merit (FOM) employed in flight vehicle design.

Figure X-1 attempts to portray the evolution of HEL-integrated flight vehicles into the future. The cartoon begins in 1983 with the concept of a fighter-borne HEL (laser powers of 0.1 - 1.0MW) designed for the air superiority mission. The conventional approach physically mates the HEL device with the flight vehicle (e.g., as in the ALL experiment). The other major alternative places the laser at a remote location and requires the integration of an appropriate "fighting mirror" with the flight platform, to relay and properly focus this beam upon the target. Adaptive HEL mirrors with high-reflectivity coatings can relay enormous levels of laser power, and yet can be made relatively light weight. By 1990-1995, aerostat "fighting mirrors" could be used to relay 1-10MW from ground-based transportable or ship-based HEL equipment. Low earth orbital relay satellites and massive 50-100MW mountain top laser installations should become feasible by the year 2000 or 2010. Space-based HEL battle stations with laser powers greatly exceeding the 100MW level may appear by 2020.

Figure X-2 presents an investigative framework for the derivation of future HEL-integrated flight vehicle concepts. This flowchart summarizes the thought processes along the two major branches mentioned above: fighter-borne, and "fighting mirror" approaches. The following discussion explores these alternatives in somewhat greater detail.

1. Fighter-Borne HEL Approach

The fighter-borne HEL alternative could produce highly specialized aircraft which demand major design concessions in the integration of on-board laser devices and/or associated power systems. An excellent contemporary analogy is the British Harrier aircraft, for which

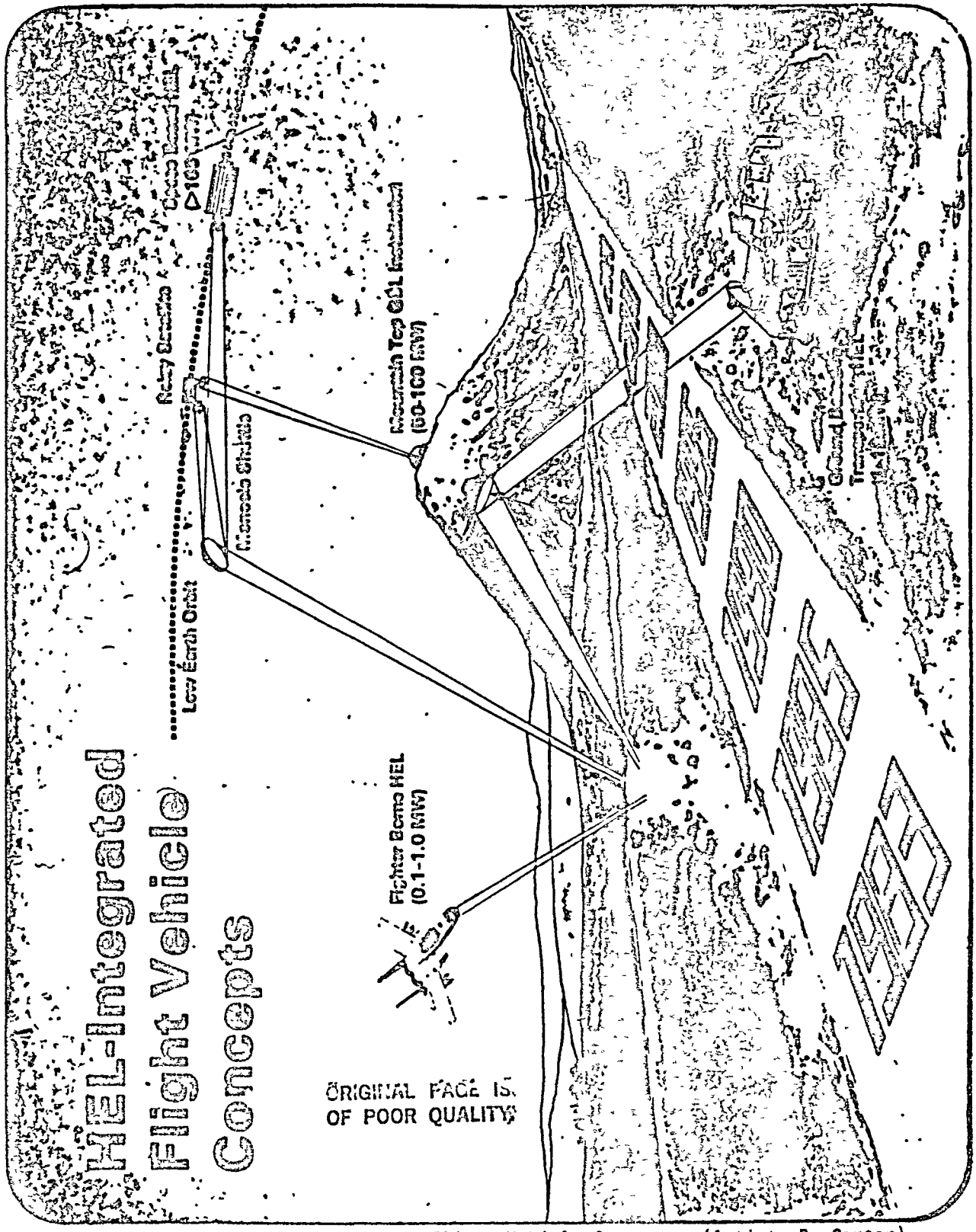

Figure X-1. HEL-Integrated Flight Vehicle Concepts (Artist, R. Carter)

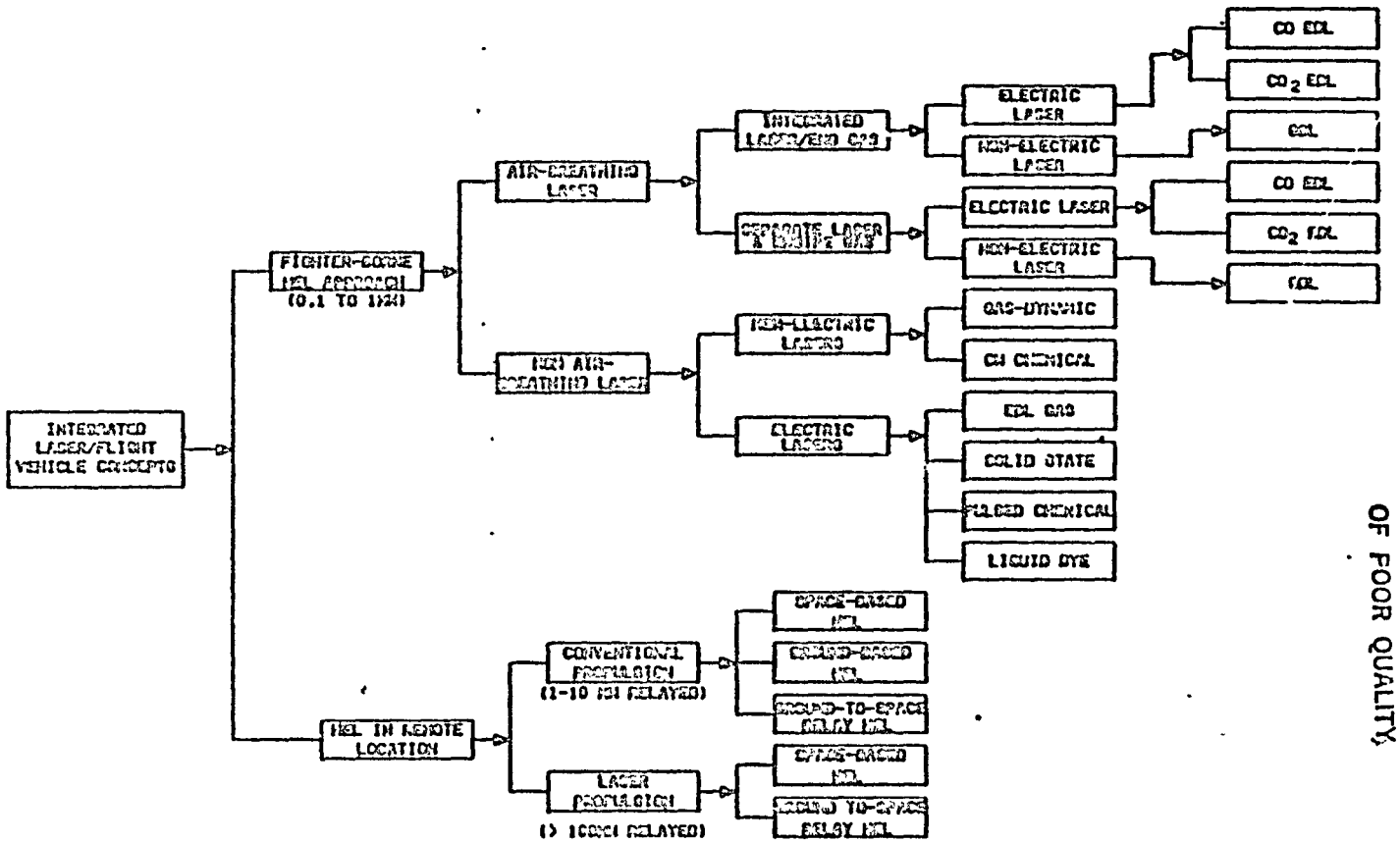

NS745/82-AC

Figure X-2. Investigative Framework for HEL-Integrated Flight Vehicles

major sacrifices in the potential top end flight speed were made in exchange for superior VTOL capability. The aircraft is sometimes described as a mammoth turbojet engine with stubby flying surfaces stuck onto it.

For HEL-integrated aircraft, a similar design approach could lead to the use of powerful "over-designed" (i.e., from the standpoint of flight requirements) turbomachine engines which can alternately produce laser power or propulsive thrust. Here, the laser or associated power supply could put extreme demands upon the engine, just as the stressing requirement for VTOL vectored thrust does in the Harrier.

Two main divisions in the logic stream for the fighter-borne HELs can be identified as shown in Figure X-2. Fundamentally, the major division can be made on the basis of whether or not the laser is air-breathing. For the air-breathing laser variety, a further division can be distinquished by whether or not the laser gas stream is in any way shared with the air-flow through the fighter's turbojet engines. An example of the "shared" variety is the "ram air-breathing laser" recently studied by AERL, Grumman and others. The "unshared" alternative would be accomplished with independent air inlet and exhaust ducts. Even though most air-breathing laser concepts to date have utilized strictly gas-dynamic excitation processes, the prospects for electrically-excited CO or CO_2 lasers should probably be re-examined.

The other major division, non-air-breathing lasers, can be readily divided into those requiring, and those not requiring electrical power. Examples of the latter are chemical lasers and, again, gas-dynamic lasers. Those requiring electric power might be EDL-gas, solid state, liquid dye, or pulsed chemical lasers. (Pulsed chemical lasers are volumetrically initiated by an electric discharge.) Many of today's most promising high-efficiency gas lasers require electric discharge pumping. Therefore, a thorough examination of mechanisms for generating high peak and average power aboard fighter aircraft is in order.

Figure X-3 shows an investigative framework leading to innovative approaches for such aircraft high-power systems. The major division occurs according to whether or not the prime power is developed by a separate auxiliary power unit (APU) or pulled directly off the propulsive turbine

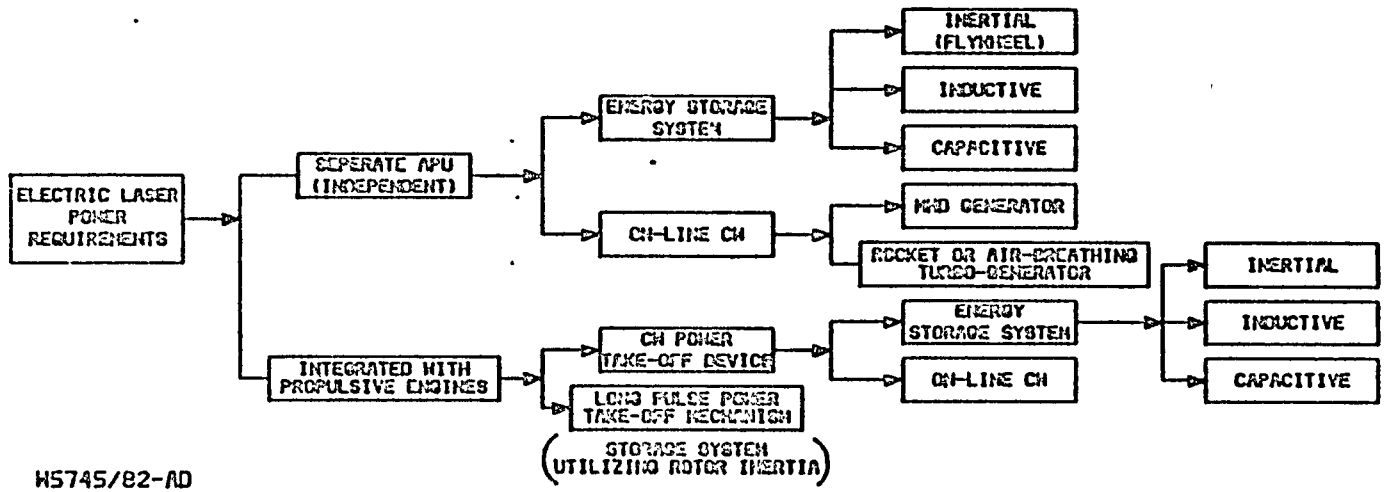

Figure X-3. Advanced Power Supplies for Electric Lasers

engines by means of some power take-off device. The power take-off approach is further divided into two categories: one presents a continuous load; another makes use of the rotational energy stored in the engine rotor(s). The latter option would involve first overspinning the engine RPM, then pulling out a short duration "laser firing" load which would be significantly greater than the engine could ever withstand continuously.

The continuous power take-off approach can be further divided as follows: the output of the power take-off device can either drive the laser directly, or "recharge" an advanced energy storage system--which would later be "discharged" at a very high rate. Examples of such storage devices include lightweight inertial flywheels, inductive stores (e.g., superconductors), and capacitive stores.

The alternative approach of using APUs can be further divided into storage and non-storage systems. For example, the storage variety may be driven by air-breathing or rocket turbogenerator prime power supplies, utilizing various energy storage schemes mentioned above. Non-storage systems would draw continuously from turbogenerator or MHD generator prime power units.

Finally we note that the fighter-borne HEL approach follows the ALL experiment in a linear, one-dimensional thought process which affirms that the laser device must be carried onboard the flight platform. Such fighter-based concepts will clearly be able to serve important tactical missions, but for the foreseeable future will be limited to laser powers of less than 1MW. Heavy-lift jet transports (e.g., C-5A or B-747 class) should eventually be able to extend onboard laser powers to the range of 1-10MW. (Some researchers believe that HEL-integrated transports may be the air-superiority "fighters" in the near future.) HELs are simply heavy devices whether using open or closed-cycle gas flow systems, and are more difficult to redesign into light-weight combat-ready equipment than originally thought.

2. "Fighting Mirror Approach"

For the "fighting mirror" approach, two major divisions in the logic stream are identified. One somewhat unlikely alternative involves

the use of HELs installed in ground-transportable and shipboard platforms which will probably deliver, at most, 1-10MW of beam power. Relay flight vehicle configurations utilizing this beam power may closely resemble existing baseline aircraft (or their lighter-than-air counterparts)--modified for carrying agile fighting mirrors. This approach avoids penalizing a lightweight fignter with its own massive laser and laser power supply--in favor of complicating the beam transport/optical-train. Laser power would be projected in short, near vertical paths up through the atmosphere, then relayed and properly focused upon the target. Target engagement range will be severely limited by beam power losses suffered through long atmosphere slant range paths.

The above approach has several potential technical bottlenecks which will prevent realization of the full strategic and tactical potentials of future HEL-integrated flight vehicles. However, the major problems can be circumvented by taking the optical relay platform to space, and by putting the massive laser at a remote location. The benign environment of space results in an extremely stable, low vibration platform which is exceedingly difficult to emulate by high-speed jet aircraft moving through a turbulent atmosphere--even with the most sophisticated vibration isolation technology. Secondly, whether repetitively pulsed or continuous, high-energy lasers and their associated power supplies are inherently powerful sources of vibration which can cause significant jitter of HEL optics which are mounted to the same structural platform. Third, strategic scenarios are associated with very long ranges (e.g., >1000KM), high laser power levels (e.g., 10-100MW), and small spot sizes (e.g., <1m) that require extremely good pointing and tracking. These requirements suggest that the space-relay "fighting mirror" approach may provide an ideal solution for strategic laser applications.

Informed estimates predict the feasibility of prototype 50-100MW mountain top GBL installations by the year 2000 to 2010 time frame, if not before. If a full-scale weapon system based upon the ground-to-space relay concept is deployed, then 2-4 GBLs on each of 10 mountain top sites may be able to project HEL power by way of relay satellites to anywhere on or

above the earth. This power system would be able to propel fighting mirrors into orbit with the very same laser power that can also be reprojected to destroy targets: i.e., laser propulsion to create an extended HEL optical train. However, such a feat would certainly take the combined effort of a dozen GBLs to supply the necessary beam power required for the launch of even a small, one-man "fighting mirror" shuttlecraft. Further in the future, powerful space-based laser "battle stations" generating several hundred to several thousands of megawatts will be able to single-handedly "beam up" substantially larger shuttlecraft from the earth's surface.

Three kinds of space relay devices (i.e., "fighting mirrors") have been examined: the "Monocle" and "Binocle" configurations proposed by Lockheed, and the "Perinocle" proposed by BDM--all pictured in Figure X-4.

The "Monocle" approach (Refs. 1 and 2) is the simplest in concept, but perhaps the most difficult in execution. The advantages of one large aperture with no secondary transfer mirrors for the high-energy laser beam are offset by several problems. There is no demagnified beam available for fine beam steering, and implementation of a secondary focus (e.g., by an etched holographic grating on the surface) to address this problem would be difficult because of the need for front access over a large, rapidly changing angle of incidence. Fine pointing would have to be accomplished with a large number of adaptive elements in a high resolution phased array. Sensing of the relative element positions would be done from the mirror backside by a technique developed by Lockheed. However, it is not clear how the feedback loop would be closed to optimize the beam on the target. The large and varying oblique angles would produce effective variations in mirror coating thickness, leading to considerable changes in the absorbed energy fluence, with significant consequences for the mirror figure. Finally, it should be noted that the monocle geometry does not permit self protection in an attack from the backside. Protection would have to come from other monocles elsewhere in space.

The "binocle" has a completely different set of problems. There are many possible configurations using a variety of optical trains. Various concepts have been proposed employing from 4 to 12 secondary

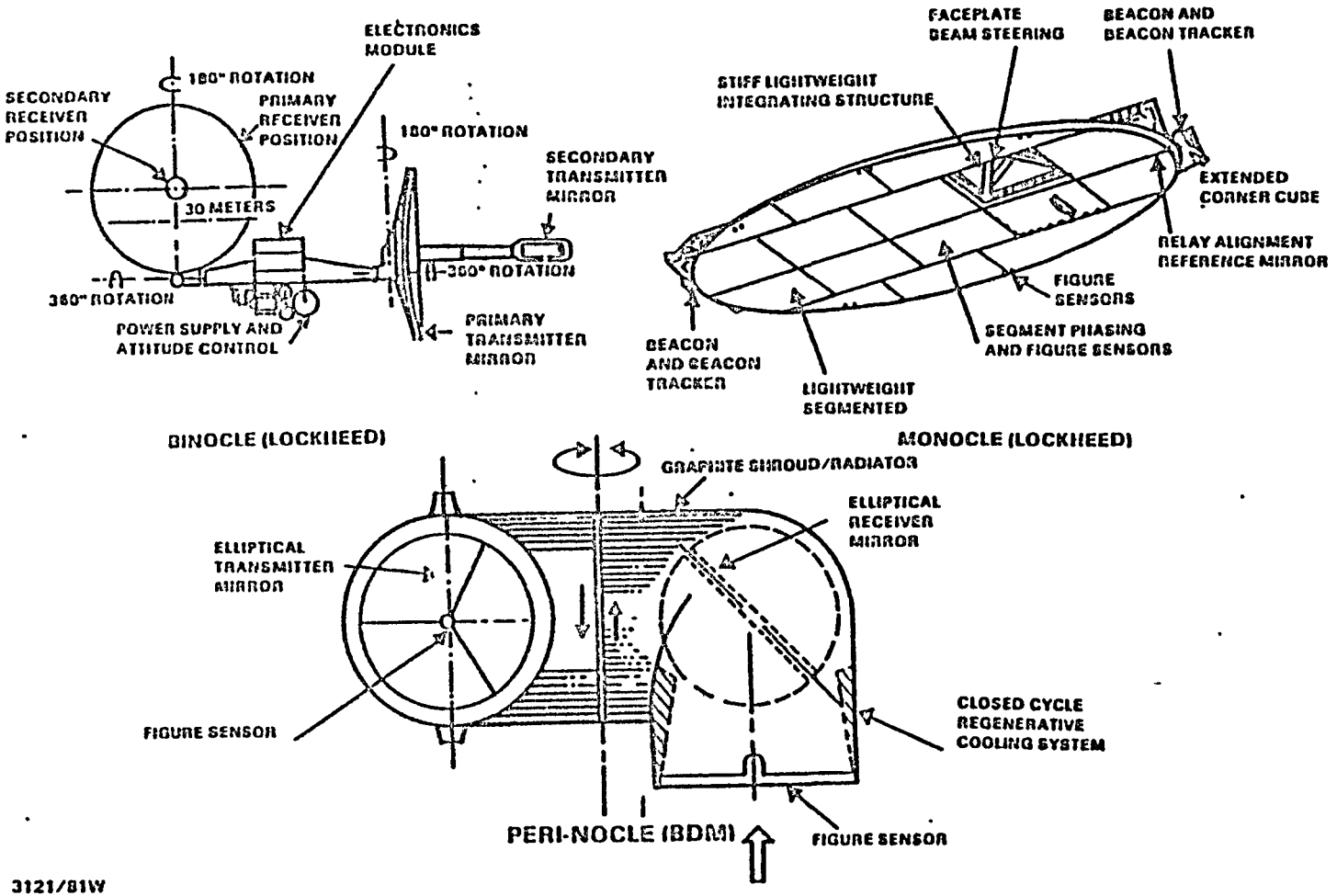

Figure X-4. Relay Device Configurations

mirrors in the beam path, in addition to the two primary mirrors. The secondary mirrors would provide excellent optical isolation of dynamical perturbations, thus greatly simplifying the micro-pointing and permitting the primary mirrors to maintain relatively low moments of inertia necessary for rapid, agile slewing. The major disadvantages of the binocle relate to the very high flux densities on the small secondary mirrors, and the buildup of stray heat from scattered radiation inside the system. Depending upon the wavelength, the secondary mirror survival would be highly dependent upon very advanced mirror coating and active cooling techniques.

Much like a periscope with a rotary joint in the center, the "perinocle" contains only two large mirrors, one or both being adaptive phased arrays. A holographic grating would provide a low-power sample (i.e., of the main beam impinging on each mirror) which could be analyzed from a fixed point in the optical train. Full access to all 4π directions is achieved by rotating the two mirrors about their common optical axis, and by slewing the entire device about the local axis vertical to the earth. This produces minimum perturbations to the moment of inertia of the entire system. The waste heat internal to the system is minimized by having only two large mirrors, with no high flux-density associated with internal focussing of the main laser beam. The entire device is encapsulated in an ablative, graphite filament-wound shell which provides protection and a strong low-weight main-frame for the mirrors.

Although shuttle configurations could be designed around each of the relay mirror concepts (whose properties are summarized in Table X-1), the monocle was chosen for its low weight, compactness, and the ease with which it could be integrated with a shuttle vehicle's lower external surface. Two shuttle configurations were considered: (1) a highly swept delta "lifting body" geometry used in the Space Shuttle Orbiter, and (2) a radially symmetric, discoid geometry used in the Apollo command module re-entry vehicle. Since more innovative propulsion options were in evidence for the latter option, it was selected for use in this study. An artist's illustration of the resulant "monocle-shuttle" configuration is presented in Figure X-5.

TABLE X-1. SUMMARY OF PROPERTIES FOR THREE RELAY CONCEPTS

CONCEPT	PROPOSED BY	NO. OF OPTICAL ELEMENTS	ADVANTAGES	DISADVANTAGES
MONOCLE	LOCKHEED	1 (SEGMENTED)	• LOW FLUX LOADING • RADIATIVE COOLING ? • ONE MIRROR DOES IT ALL • COMPACT, LOW VOLUME • LIGHT WEIGHT	• MAY HAVE BEAM ALIGNMENT PROBLEMS • VULNERABLE TO ATTACK FROM BEHIND
BINOCLE	LOCKHEED	6 TO 14 DEPENDING UPON CONFIGURATION	• ONE "EYE" ON TARGET, ONE "EYE" ON SOURCE • LOW INERTIA FOR RAPID SLEW • GOOD DYNAMIC ISOLATION FOR FINE POINTING	• HIGH FLUX LOADING ON SMALL MIRRORS • REQUIRES MAJOR ACTIVE COOLING CAPACITY • BULKY, HIGH VOLUME • HEAVY
PERI-NOCLE	BDM	2	• LOW FLUX LOADING • ONE "EYE" ON TARGET, ONE "EYE" ON SOURCE • "HARD" SHROUD TO PROTECT OPTICAL SURFACES	• MODERATE MOMENT OF INTERIA • BULKY, HIGH VOLUME • HEAVY

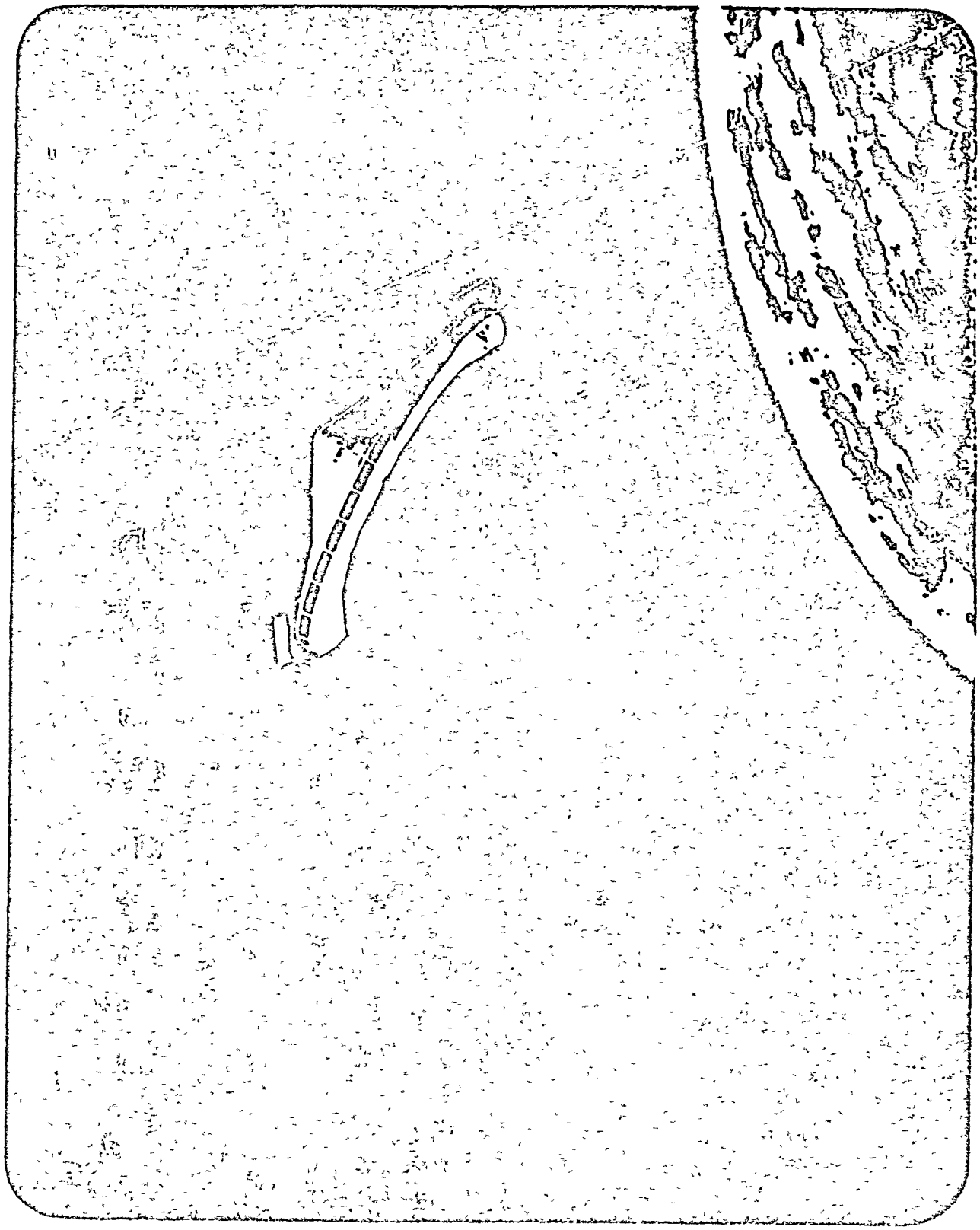

Figure X-5. Monocle Shuttle Configuration (Artist: R. Carter)

D. HEL MIRROR TECHNOLOGY FOR MONOCLE

The ability of a monocle "fighting mirror" to handle a given level of laser power depends heavily upon its diameter, total reflectivity, as well as the cooling method.

For power levels of interest for strategic laser systems, actively cooled bare metal mirrors will be unable to maintain the required figure at all interesting wavelengths, due to excessive levels of thermal absorption. One exception is in the case of very large mirrors which dilute the energy fluence to a tolerable value. In this instance, aluminum is best at 0.35μm, giving 92 percent reflectivity; silver is best at 1.0μm, yielding 99 percent reflectivity.

Mirror coatings to achieve reflectivities better than 99.5 percent appear feasible at all but the shortest visible wavelengths, where atomic dimensions become significant in determining the achievable uniformity of layer thickness. Multi-layer thin films will be necessary to achieve reflectances of 99.5-99.9 percent. For example, at 0.35μm twenty layers are required, maintaining an overall thickness uniformity consistent with $\lambda/40$ total figure. Layer thickness uniformity must be controlled to 0.1nm, which is less than the diameter of an atom. At 1.0μm, fewer layers are required because of better underlying metal reflectivity. Required layer uniformity ~1.0nm is readily achievable.

Mirror cooling constraints are very severe, but new innovations appear to be providing the needed advances in the state of the art for all but the shortest visible wavelengths. Consistent with $\lambda/40$ optical distortion, 4 J/cm^2 per pulse appears to be a hard upper limit on present state-of-the-art for coated mirrors for pulsed laser systems.* In the CW limit, water cooled mirrors have been demonstrated successfully at 30 W/cm^2 absorbed sustained flux (heat transfer coefficient = 5 W/cm^2K). In the CW limit, liquid metal cooled (NaK) mirrors with 0.12 inch thick tungsten carbide

* This data is based on a 45 layer MgO/MgF_2 dielectric stack on aluminized molybdenum substrate 0.5mm thick, heat transfer coefficient 5 W/cm^2-K; 0.35μm wavelength; 1μ second pulse length at 100 pps.

faceplates have successfuly withstood 200 W/cm^2 (heat transfer coefficient = 35 W/cm^2K). Gaseous or cryogenic cooling appears unpromising due to the low thermal conductivity of the gaseous layer at the mirror surface. Heat pipe mirrors with wicking grooves theoretically may yield effective heat transfer coefficients of 350 $W/cm^2<$. A good review of HEL mirror coating and cooling technology can be found in Reference 3.

Shown in Figure X-6 are the limits on total incident laser power imposed by the properties of mirrors using various representative cooling schemes mentioned above: i.e., (1) water, (2) liquid metal using sodium/potassium eutectic (NaK), and (3) wick-type heat pipes. Boundaries are shown on 99 percent and 99.9 percent surface reflectivity. A line is also indicated for 92 percent reflective bare aluminum at 0.35μm. The 99 percent figures represent bare metal at 1.0μm. As indicated, a 5 meter diameter monocle with 99.9 percent reflective coating and heat pipe cooling system can handle (at near normal incidence) a 50MW laser beam; 10m monocle - 200MW; 20m monocle - 800MW.

E. BMD CAPABILITY OF THE MONOCLE RELAY

Figure X-7 from Reference 4 is a mapping of representative laser parameters into beam brightness, the best measure of overall laser system effectiveness. The map reveals the interplay of equivalent mirror aperture (diameter), wavelength, jitter, and laser power. An expression for brightness (B) is given as follows:

$$B = (P/2\pi\sigma_T^2)\ L, \text{ (Watts/sterradian)} \qquad (1)$$

where P is the laser power in Watts, σ_T is the total beam spread in radians, and L is the beam quality.*

* Beam quality (L) is a measure of the distortion (at the aperture) from a perfectly flat wavefront with a "top hat" intensity distribution.

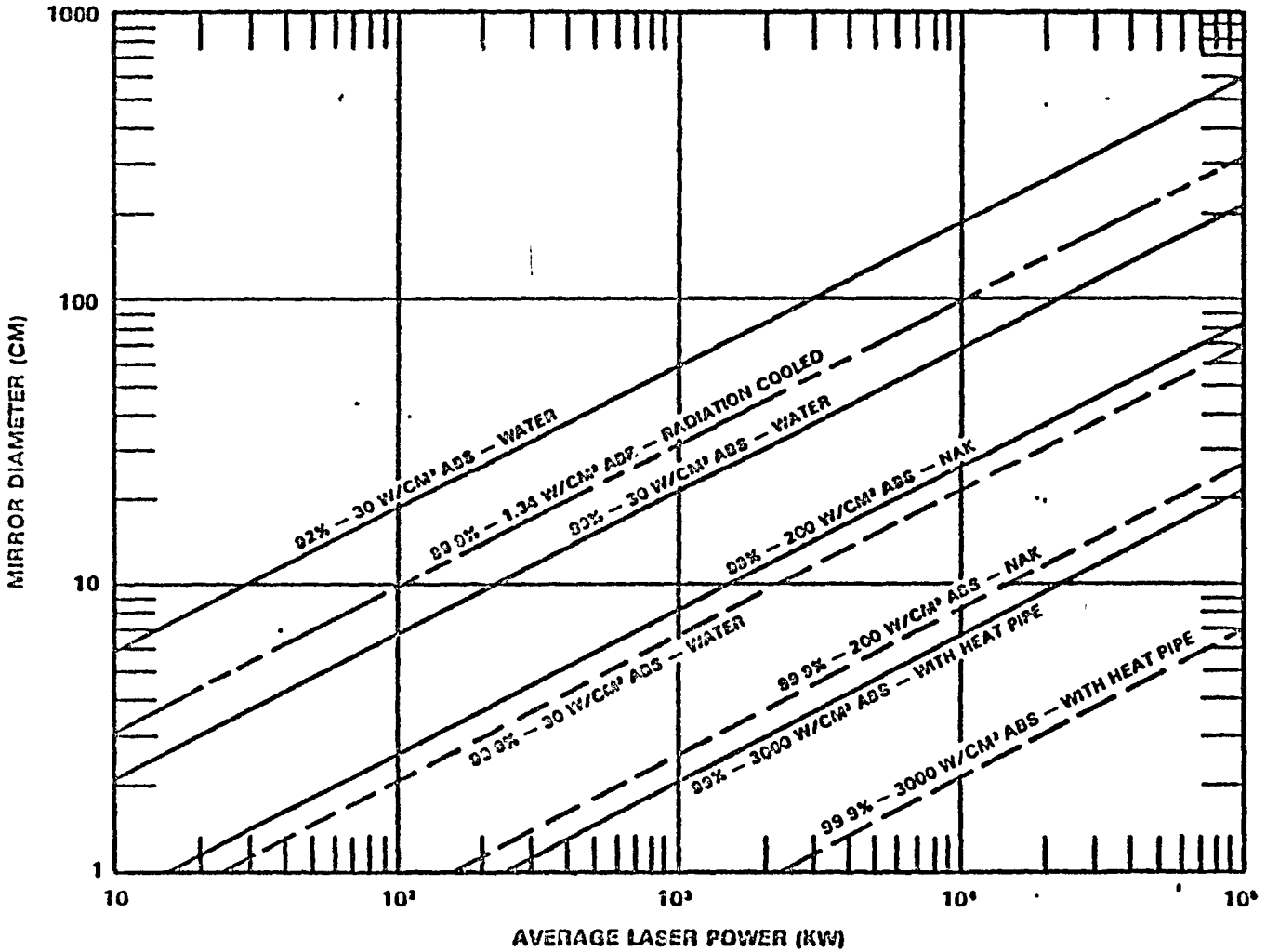

Figure X-6. Power Handling Capabilities of HEL Mirrors
(From Reference 6)

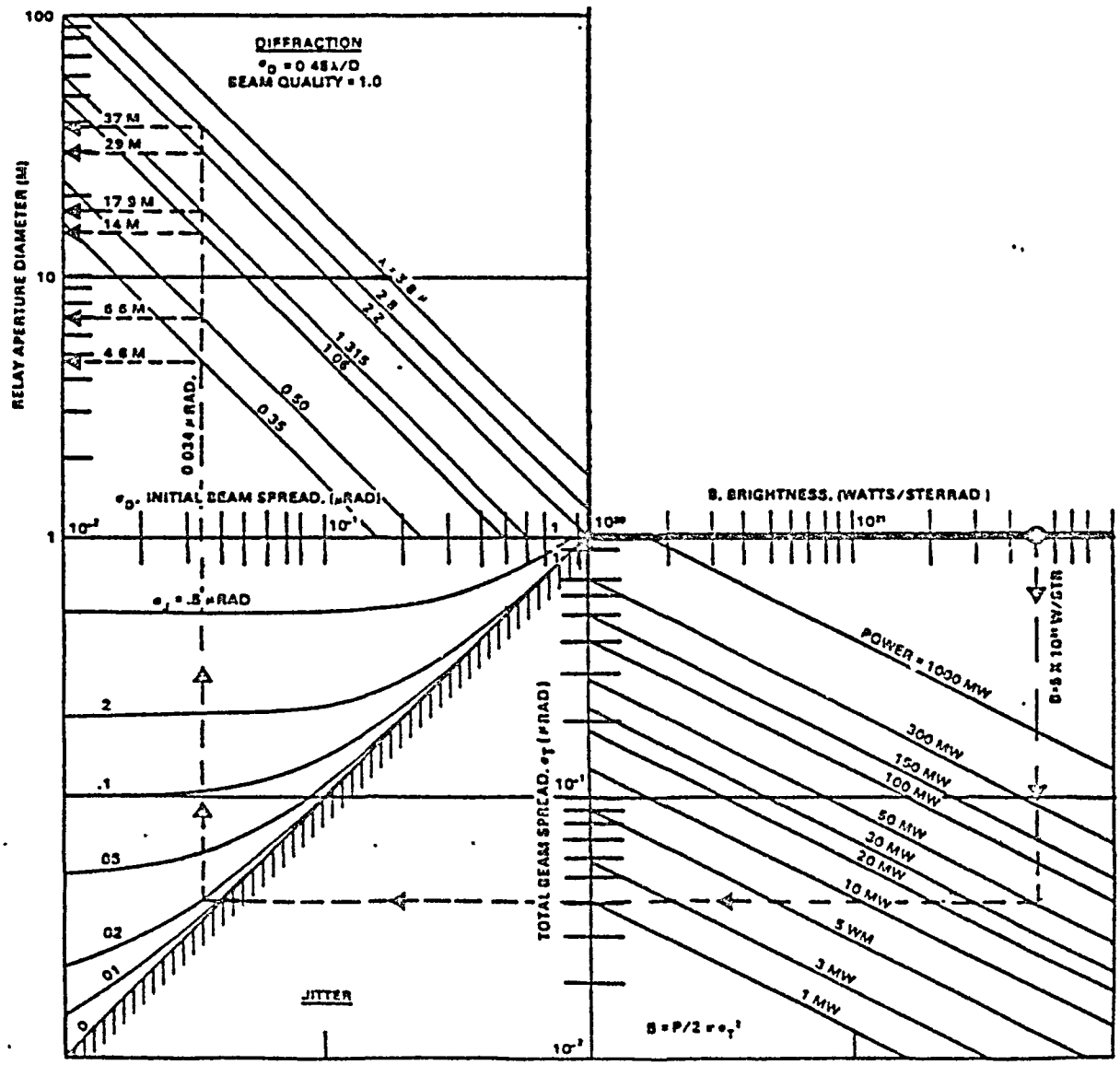

Figure X-7. Mapping of Laser System Parameters
(From Reference 4)

As indicated in Figure X-7 a 50MW, 0.35μm beam will give a brightness of $5X10^{21}$ Watts/sterradian with a 5 meter aperture, a very low value of jitter and perfect beam quality. A beam of this brightness appears to be the minimum useful level in the ballistic missle defense (BMD) mission.

Figure X-8, also from Reference 4 shows the interplay of beam brightness with target range, target hardness, and irradiation time. The flux (ϕ) deposited on target is given by:

$$\phi = B/R^2, \text{ (Watts/cm}^2\text{)} \qquad (2)$$

where R is the range to the target. Lethal fluence "F" depends upon the "hardness" of the target and is related to irradiation time "Δt" by the following expression:

$$F = \phi \Delta t, \text{ (Joules/cm}^2\text{)} \qquad (3)$$

The total energy (E_x) required to disable the target is related to the minimum beam spot area (A) by:

$$E_x = FA, \text{ (Joules)} \qquad (4)$$

A number of studies on the potentials for ground-to-space relay and space-based laser weapon systems have been carried out (e.g., see References 5 and 6). Given the required HEL technology, the ability of such systems to successfully counter the BMD threat has already been well substantiated, and will not be further treated here.

F. WEIGHT ESTIMATION

The mass of a Monocle beam director mirror is estimated by Scherfflins and Lush[7] to scale directly with laser power, and mirror size raised to

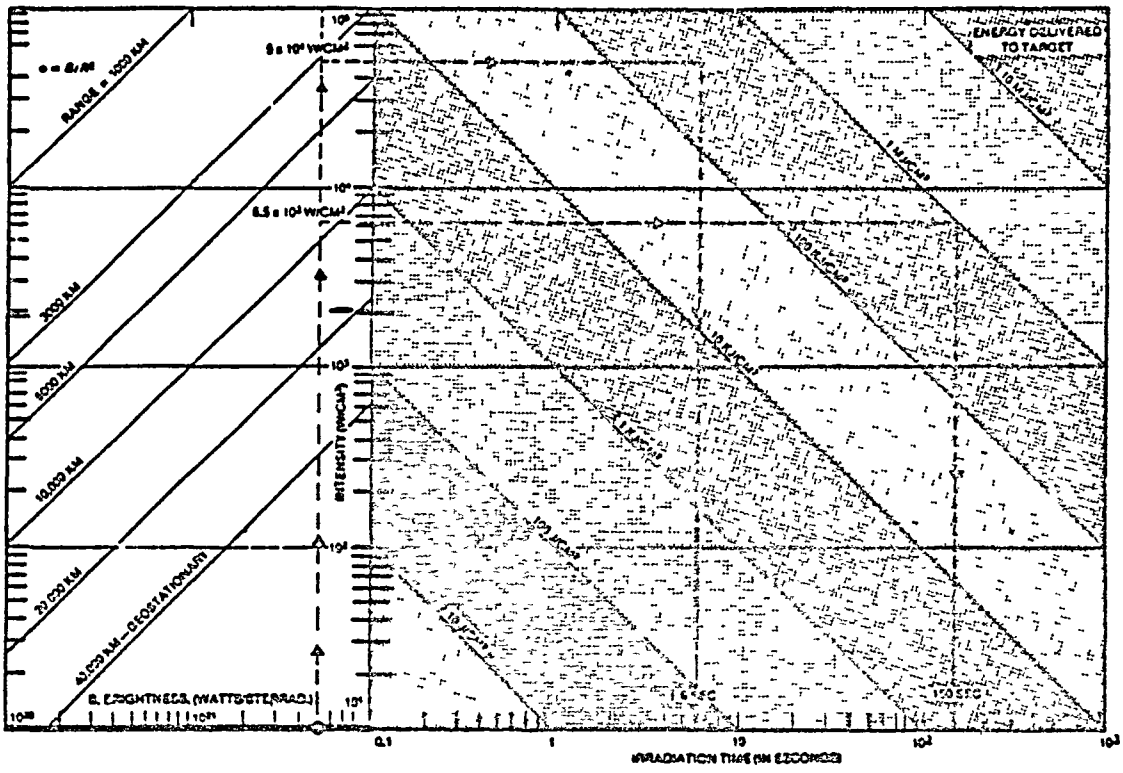

Figure X-8. Mapping of Target Engagement Parameters
(From Reference 4)

the 1.65 power as follows:

$$W = 9P + 76D^{1.65} + 800, \text{ (kg)} \qquad (5)$$

where P is the directed laser power in megawatts, and D is the monocle minor axis in meters. The original monocle design in Reference 7 was of elliptical configuration and has a minor axis equal to 60 percent the major axis. Since the Monocle Shuttle is circular in planform, an equivalent elliptical mirror of the same area was calculated in order to use Equation 5 to obtain a realistic weight estimate. These dimensions along with the calculated mirror mass are shown in Figure X-9. It is important to note that the Monocle beam director mass would include all primary spacecraft structure, pointing and tracking systems, mirror faceplates, figure sensors, mirror actuators, and reaction jets (used for gross mirror pointing).

Note that the mass of the basic Monocle in Figure X-9 is identically equal to that predicted for the airframes of the SSTO radial shuttlecraft in Chapter VII. Therefore, one would conclude that comparable performance could be demonstrated by the Monocle Shuttle, once integrated with advanced laser-propulsion engines. As previously described, these propulsive engines would utilize multiple 100-300MW beams (e.g., 5MJ pulses at 20-60Hz). Twelve laser beams could boost a 5m Monocle Shuttle to LEO; whereas 48 beams would boost a 20m Monocle carrying 15,000kg of payload (i.e., equivalent to one-half that of the Space Shuttle Orbiter). Finally, Monocles could perform their function as either manned, or unmanned platforms.

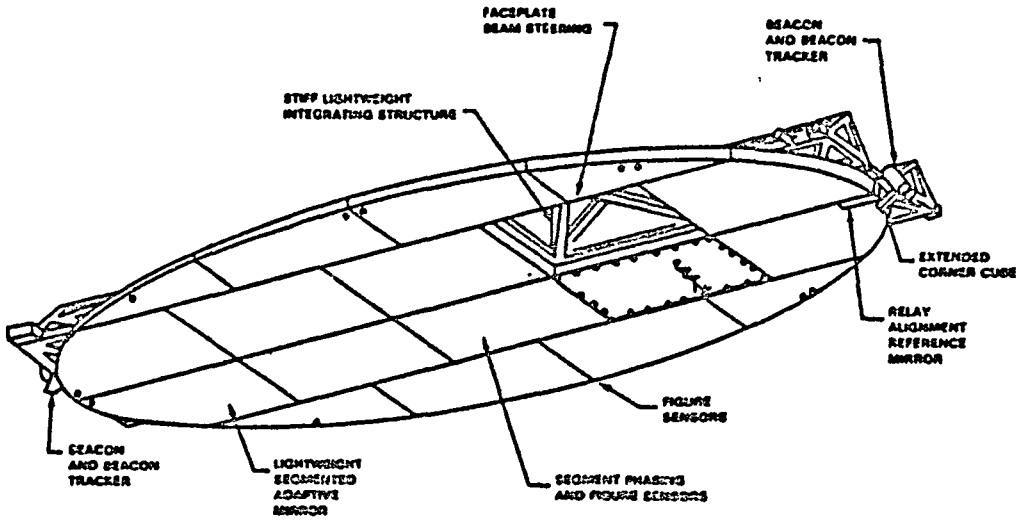

TECHNOLOGY LEVEL 1*: $W = 9\,P + 76\,D^{1.65} + 800$ (KG)
WHERE P IS LASER POWER IN MW AND
D IS MIRROR MINOR AXIS IN M

	5M	10M	20M
REFLECTED LASER POWER (MW)	50	100	500
EQUIVALENT MINOR AXIS (M)	3.88	7.76	15.52
MONOCLE MASS (KG)	1250.	3930.	12,300
MIRROR AREA (M^2)	19.6	78.5	314.2

* FROM REFERENCE 7.

Figure X-9. Monocle Beam Director Mass

REFERENCES FOR CHAPTER X

1. Scherfflins, J. H. and Lush, K. J., "ARIS Aperture Relay", LMSC-L030203, Contract No. DAAK90-76-C-DADE, 30 July 1977.

2. Decker, L., Aspinwall, D., Pohle, D., Dotson, R. and Bartosewcz, M., "Aperture Relay Experimental Definition", LMSC-L048510, Contract No. DASG60-78-C-0100, Lockheed Palo Alto Research Laboratory, California, 28 August 1979.

3. Sparks, M., "Assessment of Materials and Coatings Requirements for UV Laser Optics", BDM/W-81-447-TR, Contract No. MDA903-81-C-0151, BDM Corporation, McLean, VA, 7 August 1981.

4. Henderson, W. D., "Space-Based Lasers--Ultimate ABM System?", Astronautics and Aeronautics, Vol. 20, No. 4, May 1982, p.44ff.

5. Rather, J. D. G. and Myrabo, L. N., "Alternative Laser Initiatives in Space", Report No. BDM/W-2180-81-S, Contract No. DAAH01-80-C-1587, BDM Corporation, McLean, VA, October 9, 1981.

6. Rather, J. D. G., Myrabo, L. N. and Henderson, W. D., "Free-Electron Lasers in Space," Report No. BDM/W-1217-82-S, Contract No. DAAH01-80-C-1587, BDM Corporation, McLean, VA, April 1982.

7. Scherfflins, J. H. and Lush K. J., "ARIS Aperature Relay," LMSC-L030203, Contract No. DAAK90-76-C-DADE, 30 July 1977; See also Decker, L., Aspinwall, D., Pohle, D., Dotson, R., and Bartosewcz, M., "Aperture Relay Experiment Definition," LMSC-L048510, Contract No. DASG60-78-C-0100, Lockheed Palo Alto Research Laboratory, Palo Alto, California, 28 August 1979.

CHAPTER XI
FUTURE GLOBAL AEROSPACE TRANSPORTATION SYSTEMS

A. INTRODUCTION

As is widely known, the commercial airplane industry has developed from a US government-sponsored technology base which principally owes its origin to the 1950's. Aircraft design has focused upon performance until quite recently, and this has been its most unyielding requirement. In this single-valued problem, aircraft design sought the minimum takeoff weight to meet a desired performance level, since weight indicated acquisition cost. Fuel, after all, was relatively inexpensive and abundant then, and accounted for a small percentage of direct operating costs.

The Arab oil crises of 1973 signaled an abrupt end to that simple design world, and the commercial airline industry is now faced with rapidly escalating fuel costs and changing requirements in aircraft design. Present design requirements demand equal consideration for life cycle cost and environmental impact. Whereas convention has seen technology applied to improve performance, system utility, and economics, it is now equally related to social values. No longer must commercial air transportation be acceptable to merely the users, it must be made acceptable to civilization as a whole.

Quite unlike the past, the cost of operation and support of an aircraft system over its useful life of 15 to 25 years is now exceeding the initial acquisition cost. Operating costs are rising in all areas, with fuel leading the way. Fuel represented only 24.5 percent of the direct operating costs for US trunk airlines in 1968. In 1977 this percentage was 28.1 percent and may grow to as much as 61 percent to 70 percent by 1987.[1] The latter estimate assumes that the price of fuel in 1987 will be $1.60 to $2.42/gallon, respectively.

In the mid 1980's, sophisticated Air Traffic Control computers and satellite surveillance/communication systems may completely eliminate stacking and loitering of aircraft at destination airports--cutting fuel

waste. Strict fuel conservation measures are already preventing many commercial transports from taking off prior to receiving confirmation of an entry corridor time slot at the destination airport. However, the cost of fuel throughout the 1980's is not expected to dominate direct operating cost (DOC) and life cycle cost (LCC) sufficiently to require rapid evolution in aircraft configuration to the minimum fuel design.

Great uncertainties in the price and availability of conventional jet fuel are anticipated for the 1990's. The dominant consideration in future commercial aircraft design will be the fuel issue. Fuel costs in some algorithmic form will certainly be the principal measure-of-merit. Typical measures-of-merit include actual fuel expense, DOC, LCC, and LCC/ton-mile-12 hr day (i.e., LCC/productivity).

The chosen measure-of-merit drives the aircraft design selection. For example, Jensen et. al.[2], demonstrate that the aircraft design for minimum fuel is not necessarily the best design for either minimum DOC or LCC/productivity. As one would expect, the minimum-fuel aircraft will optimize at lower cruise velocities, wing loadings, and thrust-to-weight ratios, whereas, the minimum DOC and LCC/productivity aircraft optimize at higher values. However, it should be noted that as the range requirement increases and fuel cost heavily dominates DOC and LCC, then the aircraft design for minimum DOC and LCC/productivity does indeed approach the minimum-fuel design.

With this introduction, then, it may now be possible to predict how technology development will influence the design and configuration of commercial flight transport in the more distant future.

B. PRIOR CONCEPTS FOR BEAMED ENERGY AIR TRANSPORT VEHICLES

Figure XI-1 illustrates an air-transportation scheme proposed by Beckey and Mayer[3] of Aerospace Corporation. The concept utilizes a space-mirror complex (two-hundred clusters of 169 mirros, each 15 ft in diameter, in 300 n-mi orbit) with either ground or orbital nuclear power plants to beam energy to a fleet of 2000 laser-powered aircraft operated at one-third

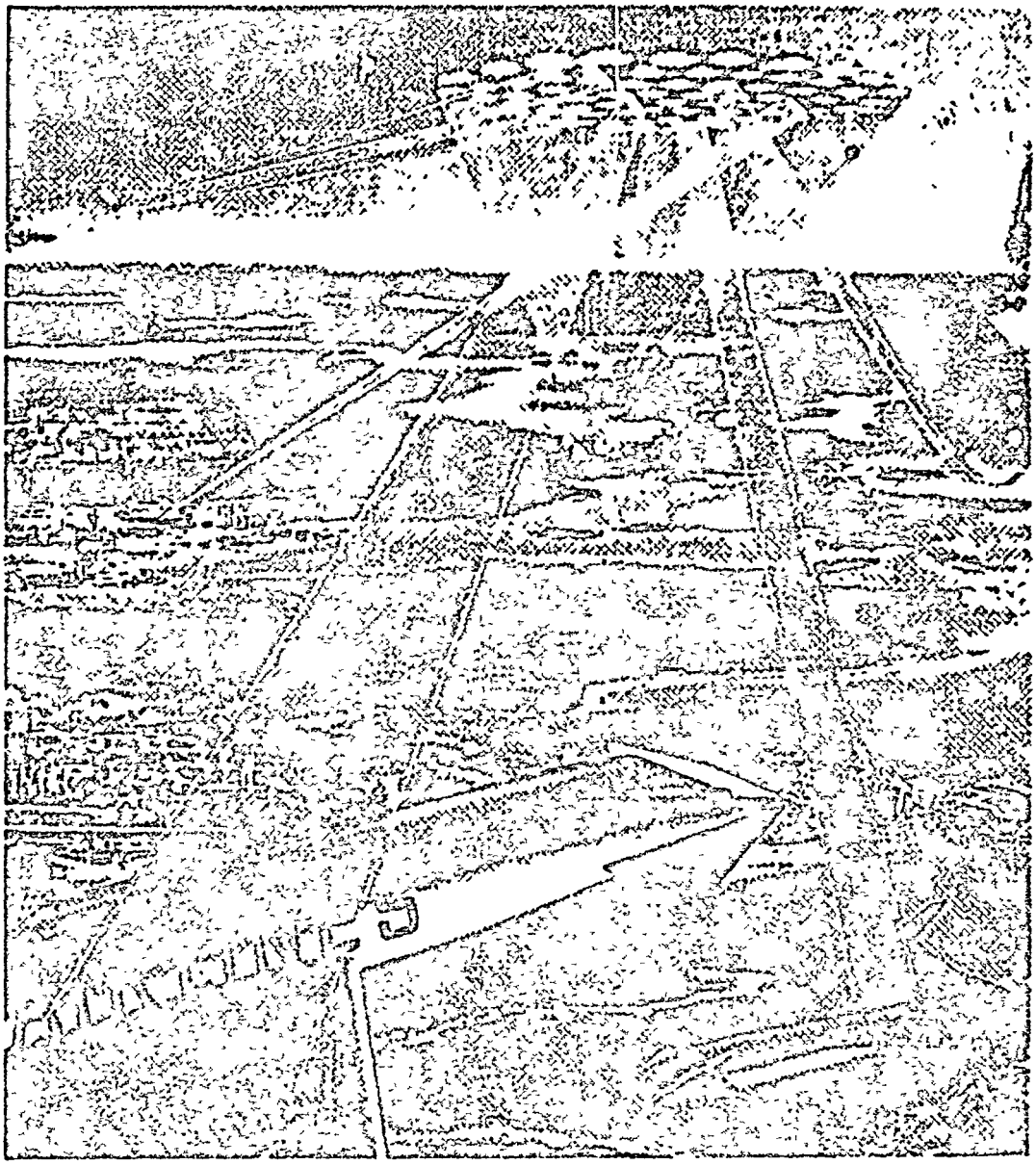

Figure XI-1. Concept for Laser-Powered Aircraft
(Beckey & Mayer, Reference 3)

duty cycle. No specifics are mentioned for integrating roughly 10-50 MW of remote laser power into each aircraft propulsion system. The authors briefly suggest that the energy would be collected by a lens on the upper wing surface near the root chord (as shown in the artist's sketch), and then focused into the engine heating chambers. Presumably, laser-driven gas turbine (Brayton cycle) engines of the type alluded to by Garbuny and Pechersky[4] would be used as main propulsive engines. The authors anticipate that these engines must operate on internal kerosene fuel for short periods when encountering excessive cloud cover at landing and takeoff.

Rom and Putre[5] suggest that laser propulsion engines might be used with ground-based electric power plants to facilitate transcontinental, transoceanic or worldwide transportation. In this scheme, remote laser power would be used to boost vehicles into free-flight ballistic trajectories, and perhaps to provide braking thrust at the destination.

An air transportation system utilizing microwave power is suggested by Miller[6] who envisions that energy might be transmitted to "fuel-less aircraft" in flight from multiple microwave transmitting stations distributed along the flight path. Presumably this system would necessitate the use of close-by power stations located either on the ground or in low earth orbit (thereby constraining the aircraft to fly along the satellite path), since beam spread angles with microwave wavelengths are large compared with that of lasers.

Detailed descriptions of methods for integrating remote laser power into aircraft propulsion systems are very scarce in the literature. The author is aware of only two complete airframe/optical/thruster concepts. One of those, by Hertzberg and Sun,[7] proposes the use of space-based CO or CO_2 electric-discharge lasers (with autonomous solar thermo-electric power plants) to beam 42 MW of radiation direct to aircraft in flight. The scheme, intended as a near-term demonstration of air-breathing laser propulsion, is based on the radiation-powered turbofan concept in Figure XI-2, and the conventional airframe in Figure XI-3. Three laser turbofan engines would be clustered in a common propulsion pod housing. On top of the pod,

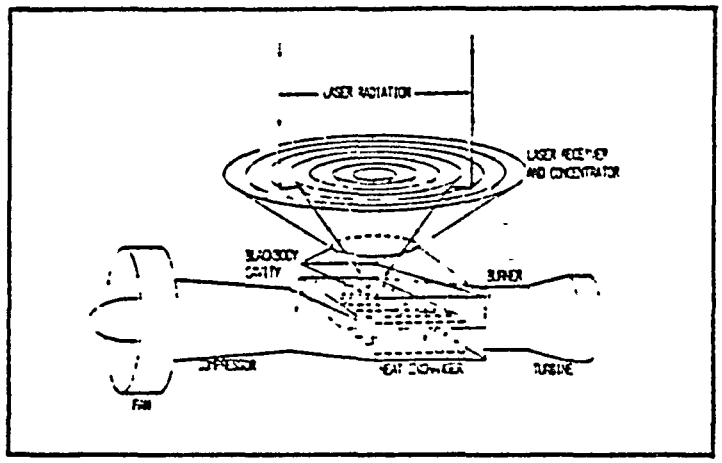

Figure XI-2. Laser-Powered Turbofan Concept
(From Reference 7)

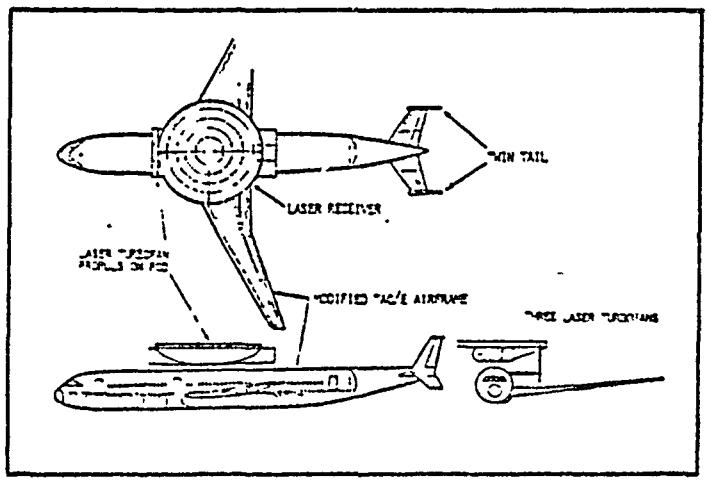

Figure XI-3. Baseline Laser-Powered Airplane, From Reference 7
(Based on Boeing's TAC/E Airplane)

a 15 m diameter reflecting/concentrating receiver lens would direct the laser beam into a heat exchanger. (A thin transparent window covers the receiver optics to minimize skin friction drag.) As shown in Figure XI-2, this heat exchanger is placed within a blackbody cavity (5 m diameter opening); a system of "light pipes and mirrors" is used to illuminate the interior of heat exchanger tubes with laser radiation. Except for the laser-heated "combustor" section, the rest of this engine concept uses conventional turbo-fanjet technology. The most serious liability of this propulsion scheme is that peak working gas temperatures, and hence performance, is limited by the melting temperatures of heat exchanger materials.

Kantrowitz and Rosa[8] in a recent patent have suggested an alternative concept which completely avoids this limitation. The patent describes a ramjet vehicle which focuses a beam of CW laser radiation into the "combustion chamber" by way of a highly polished expansion-deflection nozzle, which also acts as the primary receiving lens. Inverse Bremsstrahlung absorption of this propulsive beam (directly into the engine air) is triggered by the injection of alkali seed, just upstream of the "combustion" section. This alternative engine/optics/airframe concept, described more completely in Chapter IV, has one serious flaw: It cannot produce thrust at subsonic velocities.

Reported here, in Chapters III through IX are the results of an extensive search by the author for other unconventional air-breathing thruster concepts which are compatible with remote beamed power. The author believes that these engine/optics/airframe configurations are most promising for future use in global aerospace flight transportation systems--since they can a) develop thrust at subsonic speeds, b) absorb laser energy directly in the working gas, and c) avoid the use of seed materials by utilizing the inverse Bremsstrahlung absorption mechanism.

C. WINDOW TO AN ALTERNATIVE FUTURE

At the turn of the century, a new commercial Aerospace-Line industry can be expected to materialize, developing (in part) from government-sponsored Space Shuttle Orbiter technology and beamed-energy research. Flight transport vehicles at this time are not likely to draw a sharp distinction between air and space environments. They will perceive it as a continuum. This will be an era of beamed energy, generated in orbit and transmitted directly to vehicles in flight. Aerospace planes will no longer carry their own propulsive energy source, but will need reaction propellant (e.g., water, or liquid hydrogen, nitrogen, argon, etc.) for powered jaunts outside the atmosphere. The price of hydrocarbon-based jet fuels will have skyrocketed, making their use for propelling more conventional flight transports economically prohibitive.

Laser (or microwave) energy will be sold by satellite power station consortiums to the Aerospace-Line industry on a contract basis. Unconventional trajectories for atmospheric and exo-atmospheric flight will be developed to minimize total energy consumption (i.e., minimum "fuel") in transporting a given payload over any given route. Trajectories are likely to be of the boost-glide variety with very little energy addition during cruise, as shown in Figure XI-4. For transcontinental and intercontinental flights, most of the trajectory will be outside the atmosphere and will therefore completely eliminate atmospheric "cruise" drag. The familiar high aspect ratio wings are certain to be replaced by stubby delta or "lifting body" geometries typified by the space shuttle orbiter.

Given an expected competitive operating cost, the laser-powered shuttle would first compete on the longest route segments (5-15,000 mile routes). It is conceivable that the longest route segments serviced by, say, the 747-SP would be the first focus of a radical new technology that would replace equipment already in service. This possibility is beyond the year 2000, but certainly before 2020.

An artist concept of a future Laser Space Port is presented in Figure XI-5. Due to the high-intensity radiation projected from space to

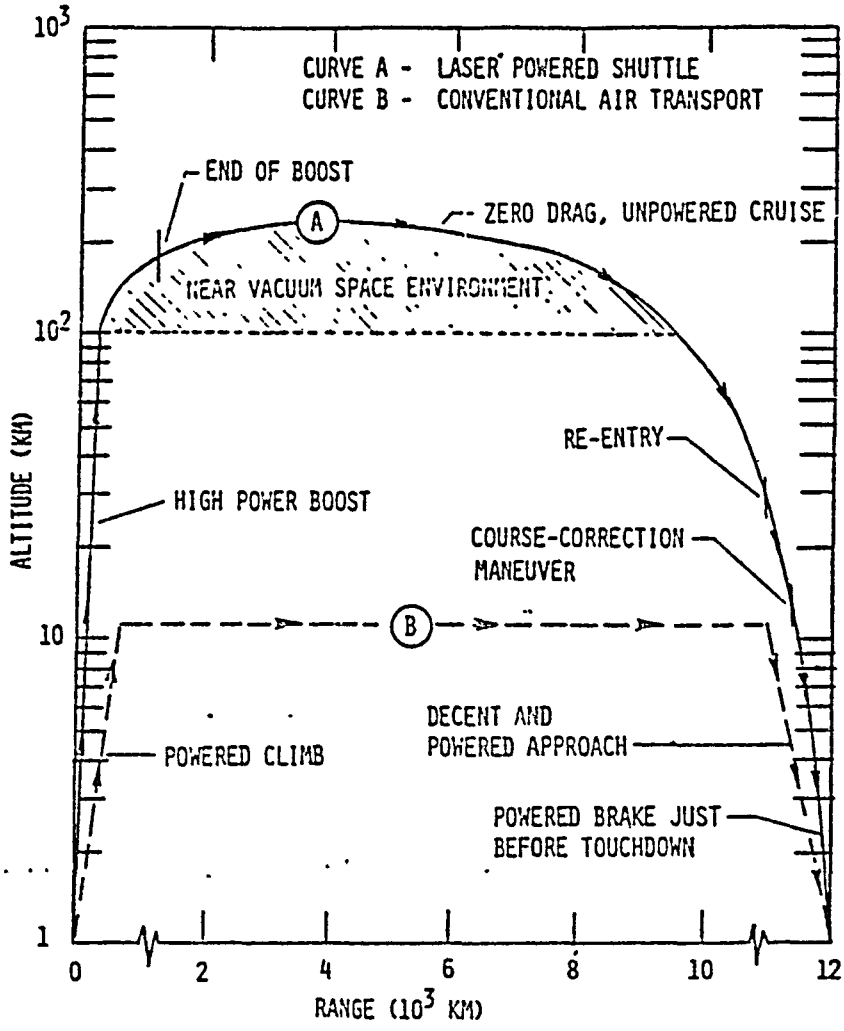

Figure XI-4. Mission Profile for Laser-Powered Shuttle vs. Conventional Air Transport Vehicle

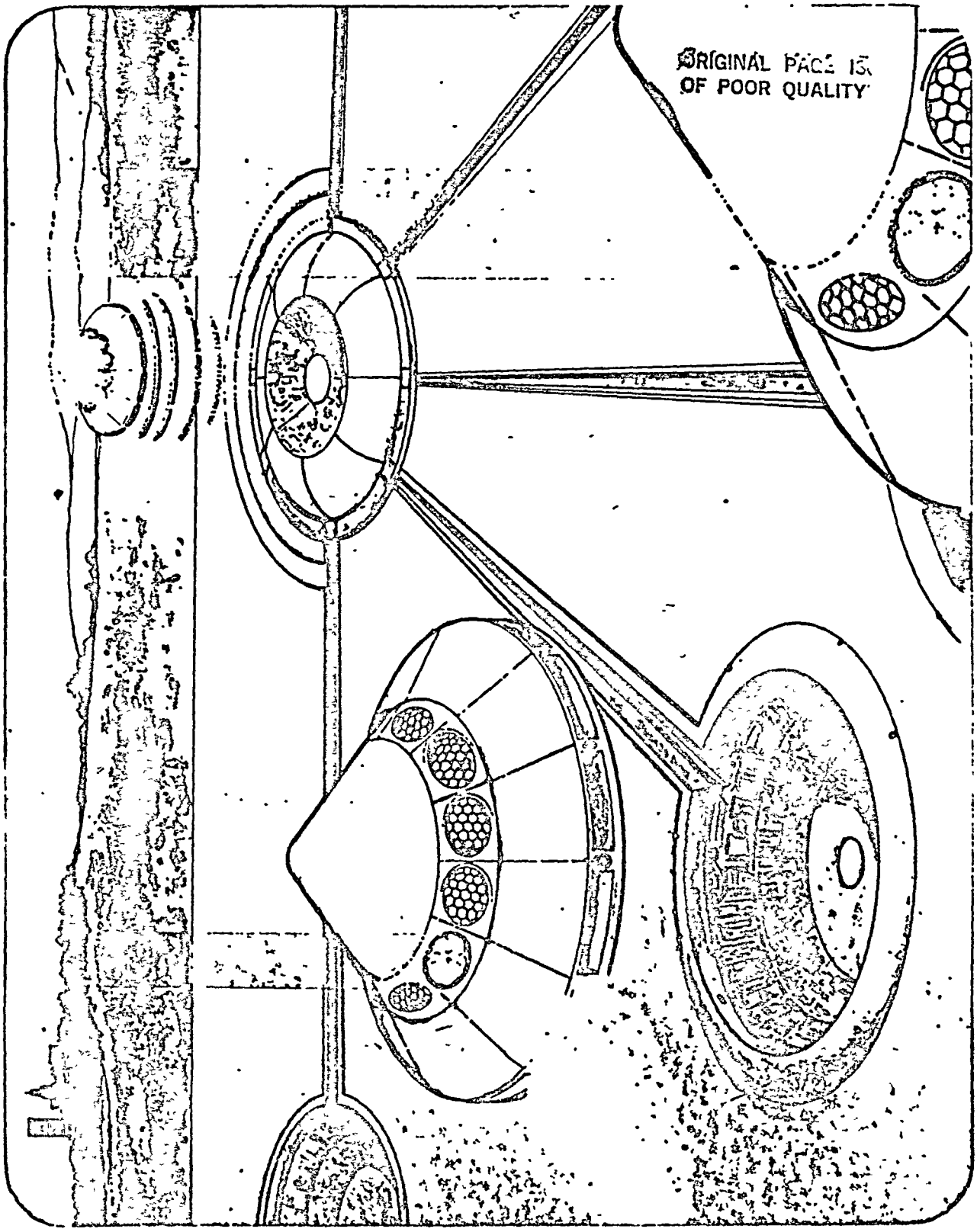

Figure XI-5. Launch Facility for Laser-Powered Shuttles (Artists: R. Rue and R. Carter)

the flight vehicles, and the finite probability of an occasional misdirected pulse of energy reaching the ground, the launch facility is located at the remote edges of the densely populated area it serves. Passengers enter the terminal at controlled locations removed from the immediate vicinity of the launch pads, and proceed to the various pads through underground corridors. These corridors have no windows, and are well protected from accidental flux impingement. Launch pads are fitted with clamshell doors which completely enclose a shuttle vehicle during passenger loading and unloading to provide a light-tight shelter with adequate laser flux protection capability.

The laser wavelengths for civilian propulsion applications must be longer than 1.6um - 1.7um to prevent accidental eye damage from glints reflected off the vehicles. At these longer wavelengths, the flux is absorbed at the cornea instead of being transmitted and focused by the lens upon the retina. Hence, upper vehicle surfaces must be highly reflective convex mirrors to sharply defocus incident radiation energy, which is not transmitted into the high-power engine windows, but falls upon the vehicle skin.

Portrayed in the air above the laser launch facility in Figure XI-5 are three smaller shuttlecraft. The most distant vehicle is illustrated in a VTOL propulsion mode with the entire vehicle base serving as an external expansion thruster surface, activated by pulsed beams entering the upper-surface windows in a radially symmetric fashion. The launch pad for this vehicle is shown with its protective clamshell door partially closed. In the foreground are two other vehicles flying laterally in the rotary pulsejet mode. Note that the beam enters only the aftward-most thruster window. The rotary engine for this vehicle contains radially directed pulsejet chambers which are energized in gatling gun fashion similar in concept to the Wankle rotary internal combustion engine. Laser pulses are projected into each high-power window as it rotates to the aftward most position. This rotary motion gives gyroscopic stability to the receptive optics--sufficient to withstand the most severe atmospheric turbulence.

Figure XI-6 shows one of the laser shuttle vehicles in the MHD-fanjet pulsed propulsion mode, as it climbs out through the rarefied upper

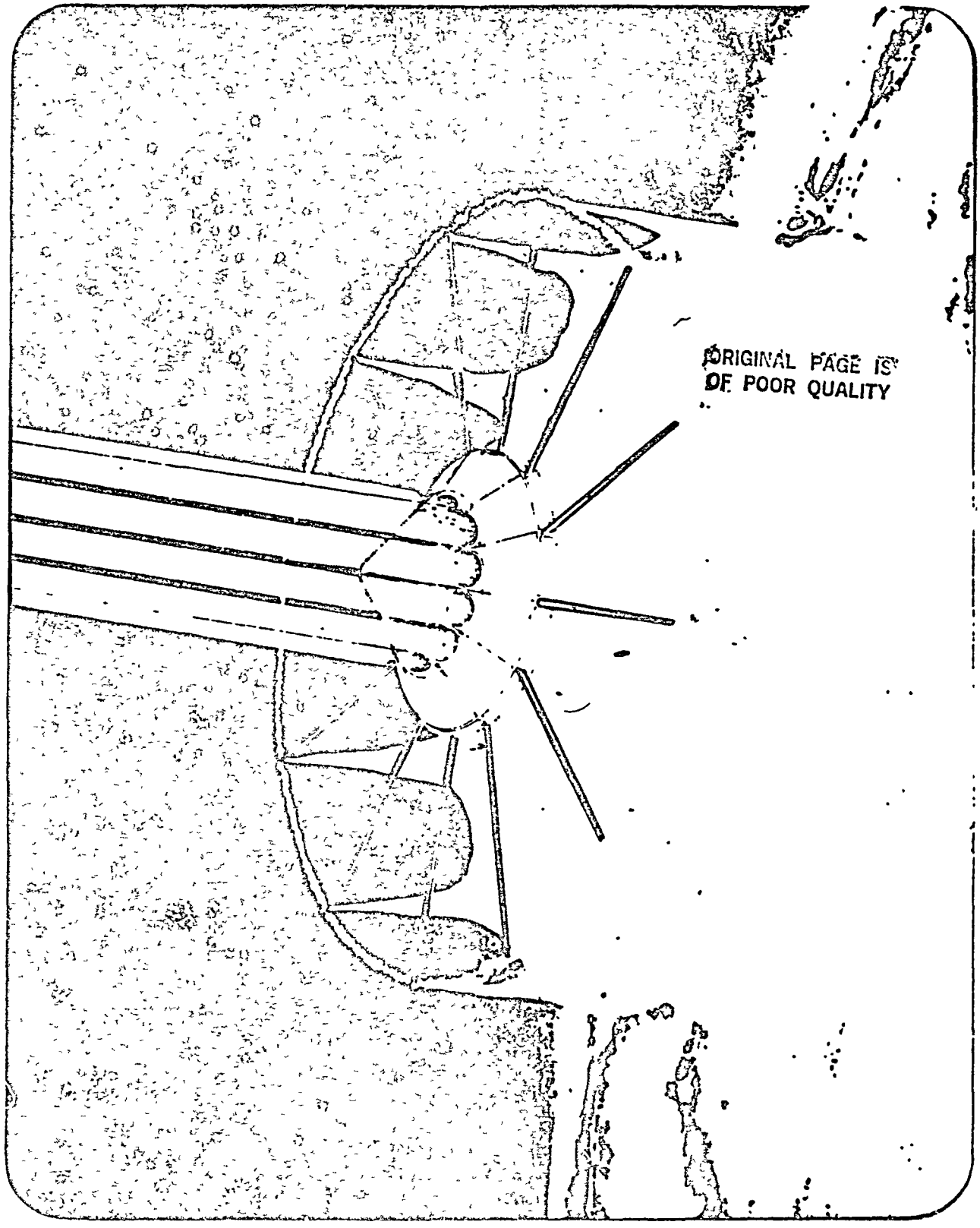

Figure XI-6. Shuttle in MID-Fanjet Propulsion Mode (Artist: R. Carter)

atmosphere (e.g., 30 to 80 km). The MHD-fanjet is a pulsed electromagnetic equivalent to the helicopter, or more exactly, the air-turborocket. Since many laser beams are pulsed simultaneously into all of the thruster windows, the MHD-fanjet is able to absorb an order-of-magnitude more peak laser power than the rotary pulsejet. At altitudes beyond 80 km, the vehicle leaves the atmosphere and is propelled in a laser-heated rocket mode, using internal propellants.

By 2020, flights into low Earth orbit will be as common as flights to the other side of the globe are today. The industry which made air transport a reality will have expanded its realm to include space shuttle service, an event which has long been prophesied in the film, "2001."

REFERENCES FOR CHAPTER XI

1. Swihart, J. M. and Minnick, J. I., "A Fresh Look at Aviation Fuel Prices," Astronautics and Aeronautics, Vol. 18, No. 3, March 1980, p. 34.

2. Jensen, S. C., et al. "The Role of Figures-of-Merit in Design Optimization and Technology Assessment," AIAA paper 79-234, January 1979.

3. Bekey, I. and Mayer, H., "1990-2000: Raising Our Sights for Advanced Space Systems," Astronautics and Aeronautics, July/August, 1976, pp. 34-63.

4. Garbuny, M. and Pechersky, M. J., "Laser Engines Operating by Resonance Absorption," Applied Optics, Vol. 15, No. 5, May 1976, pp. 1141-1157.

5. Rom, F. E. and Putre, H. A., "Laser Propulsion," TM-X-2510, NASA, April 1972.

6. Miller, R. H., "Air Transportation: The Unlimited Potential of a Beleaguered Industry," Astronautics and Aeronautics, Vol. 15, No. 12, December 1977, pp. 24-25.

7. Hertzberg, A., Sun, K. C., and Jones, W. S., "Laser Aircraft," Astronautics and Aeronautics, Volume 17. No. 8, March 1979, pp. 41-49; see also, Hertzberg, A., Sun, K. C., and Jones, W. S., "A Laser-Powered Flight Transportation System," AIAA preprint 78-1484, AIAA Aircraft Systems and Technology Conference, 1978.

8. Kantrowitz, A. R. and Rosa, R. J., "Ram Jet Powered by a Laser Beam", U.S. Patent No. 3,818,700.

CHAPTER XII
LASER-BOOSTED HEAVY LIFT LAUNCH VEHICLE

A. INTRODUCTION

This chapter introduces a heavy lift launch vehicle (HLLV) concept proposed for the large-scale transport of materials into orbit for use in space industrialization and colonization. Major concessions are made in the geometry of individual launch vehicles to facilitate the building of highly specific large-scale space structures; the HLLV center-section is designed to function as a ground-mass-produced structural module, and is boosted to space by "tug" power heads--for immediate connection to other modules. The shuttle design is based upon lighter-than-air-vehicle (LTAV) structures technology and innovative variable-cycle laser propulsion engines which are attached to the shuttle ends as removable power-heads. Once the payload is deployed, these power-heads then return to the Earth's surface for another "load."

As an example of what can be done, this study investigates the specialized HLLV structural modules which would be suitable for constructing photovoltaic satellite solar power stations (SSPS); alternatively, they could also be used for space colonies. It is assumed that the first SSPS is already in place, built with materials delivered to orbit with the current space shuttle orbiter, or some near-term derivative which has a greater payload capability. Therefore by using laser power-beaming, this SSPS would be able to boost HLLVs of the variety considered here into low Earth orbit--thereby greatly improving the economics of building all <u>future</u> SSPSs, because of a substantial reduction in launch costs. (Note that roughly <u>one-hundred</u> 10 GWe SSPSs measuring 20 km by 5 km will fit in geostationary orbit; these large satellites roam about in their orbits and space must be allowed to prevent collisions.) The prospective payoffs for this new HLLV concept are, then, a significant reduction in <u>number</u> and <u>cost</u> of shuttle launches required to build an SSPS--because of an enhanced high-volume low-density, launch-vehicle "payload" configuration.

Neutral buoyancy at sea level altitudes facilitates pre-launch preparation and handling of LTAV shuttles. Air-breathing laser-heated pulsejet engines augmented by aerostatic, aerodynamic, and free-vortex-induced lift propel the vehicle out through the dense portion of the atmosphere. Within this flight regime, low flight velocities permit the attainment of high ratios of impulse-to-laser-power while keeping aerodynamic drag to a minimum. Additional high specific impulse electrically augmented thruster modes (which incorporate the use of superconductors into structural propulsive elements) are used to attain a positive propulsive advantage over unaugmented rocket propulsion modes. These electric propulsion modes are portrayed for use at higher flight velocities within the rarefied upper atmosphere and ionosphere where the HLLV is no longer aided by aerostatic lift. (Two of the promising space applications for the construction modules necessitate the use of superconducting cables which are housed within the HLLV primary longeron structure.)

The physics for a number of innovative variable cycle propulsion modes was reviewed in Chapters VIII and IX. This chapter begins with a discussion of propulsion/vehicle systems integration, and potential low-dynamic-pressure launch trajectories. Next, the masses of three different HLLV sizes are estimated (100, 333 and 1000 m in length) to obtain some understanding of the mass-scaling relationship. Finally, the vehicle/engine performance and laser power requirements are assessed for each of several speculative propulsive modes, and vehicle sizes.

B. APPROACHES TO BUILDING LARGE SPACE STRUCTURES

There are only three basic approaches to building large-scale structures in space: a) deployment, b) erection, or c) fabrication. In the deployment approach, the entire structure is assembled on Earth, then somehow compressed or folded into a small high-density package, launched into space, and finally unfolded to the operational state. The erection approach necessitates the use of spacebound human/robot workers to assemble large prefabricated structural components. These structural units would be

manufactured on Earth, then lifted to orbit in uncompacted or slightly compacted states (e.g., telescoping structural beams like the Astro-Mast). The third approach, direct fabrication in space, has received the most attention by NASA and aerospace industries.[1-6] Direct fabrication requires, for example, the use of beam-building machines to manufacture standardized structural elements which are then joined together to produce the final assembled structure. This approach permics the basic construction materials to be delivered to space in a highly compressed state: e.g., rolls of thin metal sheet or carbon/fiberglass epoxy-impregnated cloth.

The building of kilometers-long photo-voltaic SSPSs will be an exceptionally formidable task involving hundreds of space shuttle flights to deliver enough construction materials to orbit. Furthermore, the presently favored "fabrication" approach will require great numbers of beam manufacture, transport, and joining operations in space. Ongoing rehearsals for construction in the zero G environment have indicated that even the simplest tasks becomc complex under weightlessness.[6] For this reason, the author favors the erection approach using ground pre-assembled 100-1000 meter, high-aspect-ratio structural elements; such elements are inherently more suitable for building kilometers long structures in space, since the number of handling and joining operations are minimized.

Whereas conventional wisdom would have rocket launch shuttle vehicles disgard lightweight, high-volume fuel tanks along the launch trajectory in order to place a small volume, high-density payload into orbit, the HHLV concept suggested here inserts the entire primary vehicle structure into orbit. A portion of the hydrogen or helium propellant required to propel the HLLV structural modules to orbit would be contained in a gaseous state at one atmosphere pressure within lightweight spherical bags. These bags would be composed of high-strengh-filament fabric with a low permeability coating--much in the manner of the rigid airships of past history. (However, the bulk of the propellant, -90 percent, would be held as a cryogenic liquid within insulated cylindrical-tank longeron members). Once in orbit, the gas bags are collapsed, removed and recycled (e.g., as hemispherical shelters).

C. BASIC HLLV AIRFRAME CONFIGURATION

Figure XII-1 shows the basic HLLV airframe geometry which has a fineness ratio (length/diameter) of 10:1. The detailed structural design is of conventional bulkhead and longeron construction, and is identical to the approach taken in rigid airships. The primary difference is that the major structural material would be high-strength carbon or boron filaments in an epoxy composite matrix. The cylindrical fuselage shape is more akin to the very early Zepplins, only with the rear stabilizing fins removed. Superconductors are housed within the HLLV longerons, as shown in Figure XII-1 for the 1000 m long vehicle. During the boost phase, these superconducting cables serve as part of the vehicle electric propulsion system.

After being separated from the HLLV, powerheads operate in an autonomous rotary pulsejet propulsion mode and return to Earth for the next payload. With few exceptions, the powerhead configuration is conceptually identical to that presented earlier in Figure V-14; the major difference is the addition of a beam-catcher optics to the vehicle central upper surface, mounted on a retractable mast. Within the atmospheric flight environment, the rotary engine operates in an air-breathing fashion; in space it becomes a laser-heated hydrogen-fueled rocket. As mentioned before, changes in lateral flight direction are accomplished simply by advancing or retarding the radiation-induced spark, which results in an immediate thrust-vectoring of engine exhaust gases. To provide the powerhead with VTOL capabiltiy for easy access to launch pads, a radially symmetric ERH pulsejet thruster is incorporated with the lower vehicle surface.

As mentioned above, this chapter examines three different HLLV sizes: 100, 333, and 1000 m. The smallest HLLV has displaced volume of 0.27 million cubic feet (MCF). The medium-sized 333 meter long vehicle has a displacement of 10 MCF and is roughly 30 percent larger than the Hindenburg or its sister ship the Graf Zepplin II (244m and 7 MCF). The 1000 meter long craft has a volume of 270 MCF. To the author's knowledge,

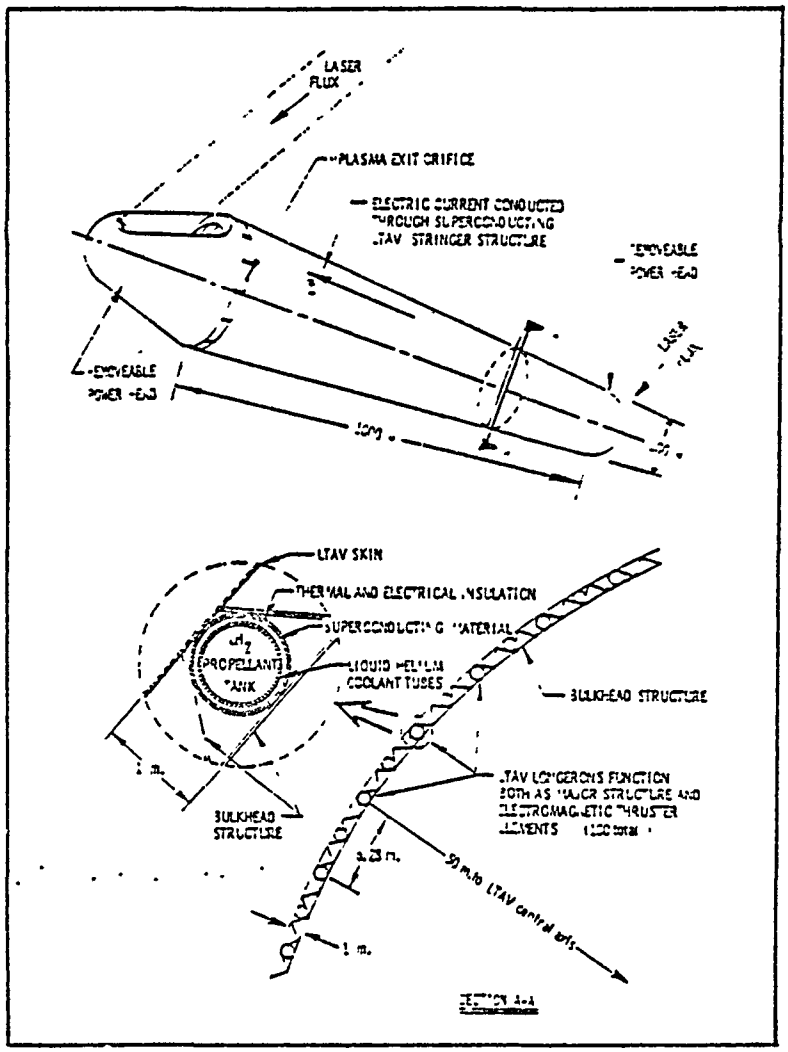

Figure XII-1. MHD-Augmented LTA Vehicle Structure for O'Neill Model 1 Space Colony

the largest airship which has received examination to date is 100 MCF. This study was performed by the Aerospace Development Company and funded by Shell Oil International[7] to determine the feasibility of oversized airships for transporters of natural gas.

In actual practice, these ultra-light "airframe" structures would be developed with computer-aided-design (CAD) techniques, and would take advantage of the fairly dormant archives on lighter-than-air vehicle (LTAV) technology. Design of the basic structural module, propulsion system, and light flexible skin subcomponents would be carried out in an integrated fashion to produce an advanced rigid airship-type launch vehicle with minimum weight and maximum payload carrying capability. Clearly this structure must be strong enough to sustain the aerodynamic launch loads which promise to be the largest loads subjected to the structure along the orbital flight trajectory. As proposed here, the relatively fragile structural elements are to be sheathed in metalized mylar (or Teflon) coated boron/carbon filament fabric which acts as a stressed skin to reduce aerodynamic loads transmitted to the primary longeron/bulkhead structure.

D. HLLV SYSTEMS INTEGRATION CONSIDERATIONS

Several major preliminary design considerations for the single-stage-to-orbit HLLV play an essential role in the systems integration process. First, the HLLV is designed from inception to deliver all its structure into orbit as payload. With the exception of propulsive fuel, no mass is brought nearly to orbital velocity, and then disgarded. (Only the removeable, lightweight powerheads are flown back to Earth.) All other major structure is designed for reuse at the orbital construction site. For example, the vehicle skin envelope is stripped off and recycled as either thin film reflecting material (i.e., mirrors) in solar-concentrating SSPS schemes, or as supporting fabric for the direct mounting of solar cells within edge-supported bays of the non-concentrating SSPS schemes. The spherical gas bags themselves are collapsed (after residual propellant is pumped out and stored), withdrawn from the vehicle structure, and used

to contain a breatheable one-atmosphere pressure environment suitable for construction crews. Depending upon the projected working stress requirements of the recycled gas bags and vehicle skin envelope, skin thicknesses may change substantially from vehicle to vehicle; also, the option of spherical gas bags may be entirely eliminated in favor of a significantly thicker vehicle skin envelope.

Three major applications have been identified for the basic HLLV skeletal structure: (a) standardized structural beams for building large space structures, (b) vertebrae in an electrically conducting backbone of an SSPS, (c) stripped skeletal structure for a cylindrical space colony (installation of the remaining hardware and interior furnishings would occur at the L5 or L4 final resting location). For the second application, it is envisioned that superconducting cables will be housed within the primary longerons of the HLLV structure. This superconducting longeron structure could also be used to great advantage for protecting space colonies from solar flares, as described below.

It is known that two cylindrical space colonies (each spinning about the longitudinal axis) must be connected to each other at the ends by cables--in order to counteract gyroscopic precess forces that would disturb the colony's critical alignment with the sun. Superconducting longerons could conduct continuous closed-loop currents as high as 10^9 Amperes through the exterior shell structure of two finished colonies (connected in series), with minimal resistive losses. In the process, strong electromagnetic fields would be generated, reaching a strengh of 60 kilogauss just outside the external skin. Ampere's law indicates that the magnetic field will remain at negligible levels within the colony itself. The net external result is the creation of a large electromagnetic dipole which can provide significant radiation shielding from solar flares and other high velocity charged particles streaming through space. Conceptually, the mass requirements for radiation protection of the occupants could be greatly reduced and hence cause a reduction in colony construction costs.

The additional mass contributed by superconducting longerons is likely to be significant and will place additional requirements upon the HLLV

systems integration approach. Preliminary investigations (in this chapter) indicate that such superconductors can be incorporated into innovative HLLV pulsed electric propulsion engines which may attain a competitive advantage over strictly rocket concepts. (In operation, liquid helium is circulated about the external surface of the cylindrical superconducting cables; within each hollow cable, liquid H_2 propellant may be stored.) Optimum design occurs when the peak electrical current and power requirements of the HLLV propulsive engine exactly match the intended space application of the conducting bus lines. Inherent in such a match is the understanding that is may be impractical to maintain a helium bath for the longerons during extended periods in space; hence, the conductor may have to operate in a normal or non-superconducting state when finally installed in the large space structure. The most stringent requirement, either the intended space structure application or boost-phase propulsion requirement, will determine the total cross-sectional conductor area--once the superconducting material properties are chosen.

Several factors influence the choice of the overall HLLV dimensions. First, the length-to-diameter (i.e., fineness) ratio of basic structural module must be adequate to the task of building the large-scale space structure for which it is designed. It must be a large enough module to minimize the number of handling and joining operations, but not so large as to exceed the mass-boosting capabilities of the remote laser SSPS power supply. Secondly, its overall mass-to-volume ratio must be sufficiently small so that the HLLV can aerostatically support itself in the dense sea level air with hydrogen or helium filled gas bags. The craft must be designed for neutral buoyancy at sea level altitude to enhance pre-launch preparations and handling of an extremely delicate and cumbersome structure.

One final consideration involves the powerheads which will boost the central structural module into orbit. Overall weight and balance factors may necessitate the use of two powerheads--one at each end of the vehicle. For certain HLLV configurations, one powerhead may be entirely adequate if the vehicle is suitably counterbalanced at the opposite end; others may

require no mass counterbalancing. An insight to the characteristics of representative HLLV powerheads may be gleaned from Chapter VII.

E. LASER PROPULSION OF HLLV TO ORBIT

Ten promising thruster concepts for propelling HLLVs to orbit on remote beamed laser power are catalogued in Chapters VIII and IX. The applicable altitude regimes for utilizing these propulsion modes are displayed in Figure XII-2. The following attempts to describe the launch procedure for a HLLV, and its acceleration to orbit.

The relatively fragile shuttle vehicles are assembled on the ground within large weather-tight dirigible-type hangers, then carefully removed before the temporary water ballast is dumped. They would be launched only on the fairest of pre-dawn weather conditions. Next the vehicles are free-floated out to a safe altitude of perhaps 1 km using aerostatic lift. Since aerostatic lift rapidly fall off to negligible levels above 3 km altitude, the vehicle must depend upon dynamic propulsive lift throughout the rest of the launch trajectory, using variable-cycle laser propulsion engines.

Within the dense atmosphere, pulsed air-breathing laser-heated engines augmented by aerostatic, aerodynamic, and free-vortex-induced lift propel the vehicle to the outer reaches of the atmosphere. By design, the HLLV uses the planetary atmosphere to greatest advantage by flying at a low velocity in order to obtain the greatest impulse-to-laser-power coupling and to reduce aerodynamic drag to the minimum. At the higher flight velocities within the rarefied upper atmosphere and ionosphere, the HLLV may use several additional high specific-impulse, electrically augmented thrusters such as the "electrical storm" propulsion mode shown in Figure XII-3. These propulsive units, which in operation send large electric current levels through longeron superconductors, permit the HLLV to attain a positive propulsive advantage over unaugmented rocket systems. Using another thruster mode, the electromagnetic engines are able to warp the local geomagnetic field out to a radius of several tens of kilometers,

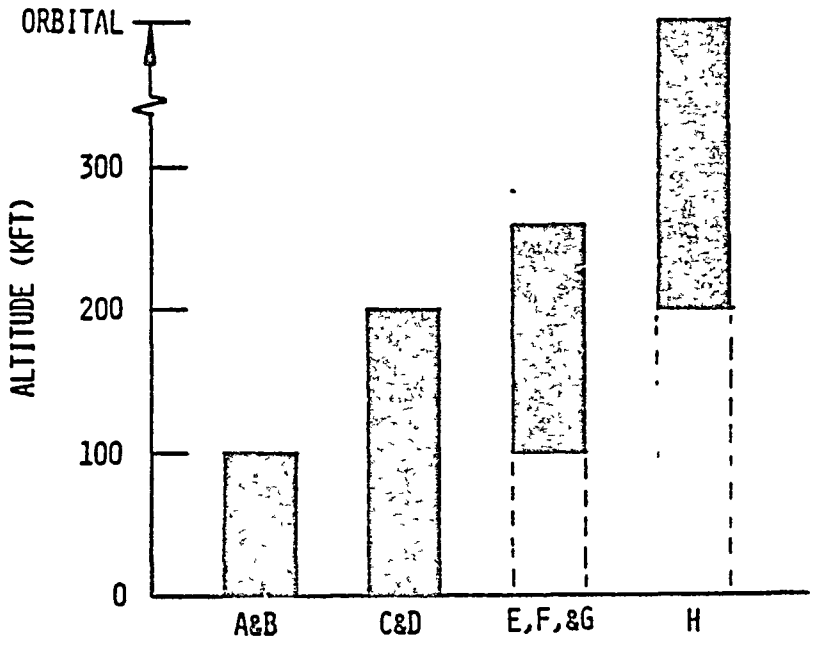

KEY TO PROPULSION MODES:

A. AEROSTATIC AND AERODYNAMIC HULL LIFT
B. VORTEX LIFT AUGMENTATION
C. LASER PULSEJET
D. "ELECTRICAL STORM" ATMOSPHERIC COUPLING MECHANISM
E. MHD-FAN PULSEJET
F. MHD-PUMPED VORTEX-INDUCED LIFT
G. WAY'S ELECTROMAGNETIC PROPULSION CONCEPT
H. LARGE AMPLITUDE ALFVEN WAVE THRUSTER

Figure XII-2. Regimes of Propulsion Mode Utilization

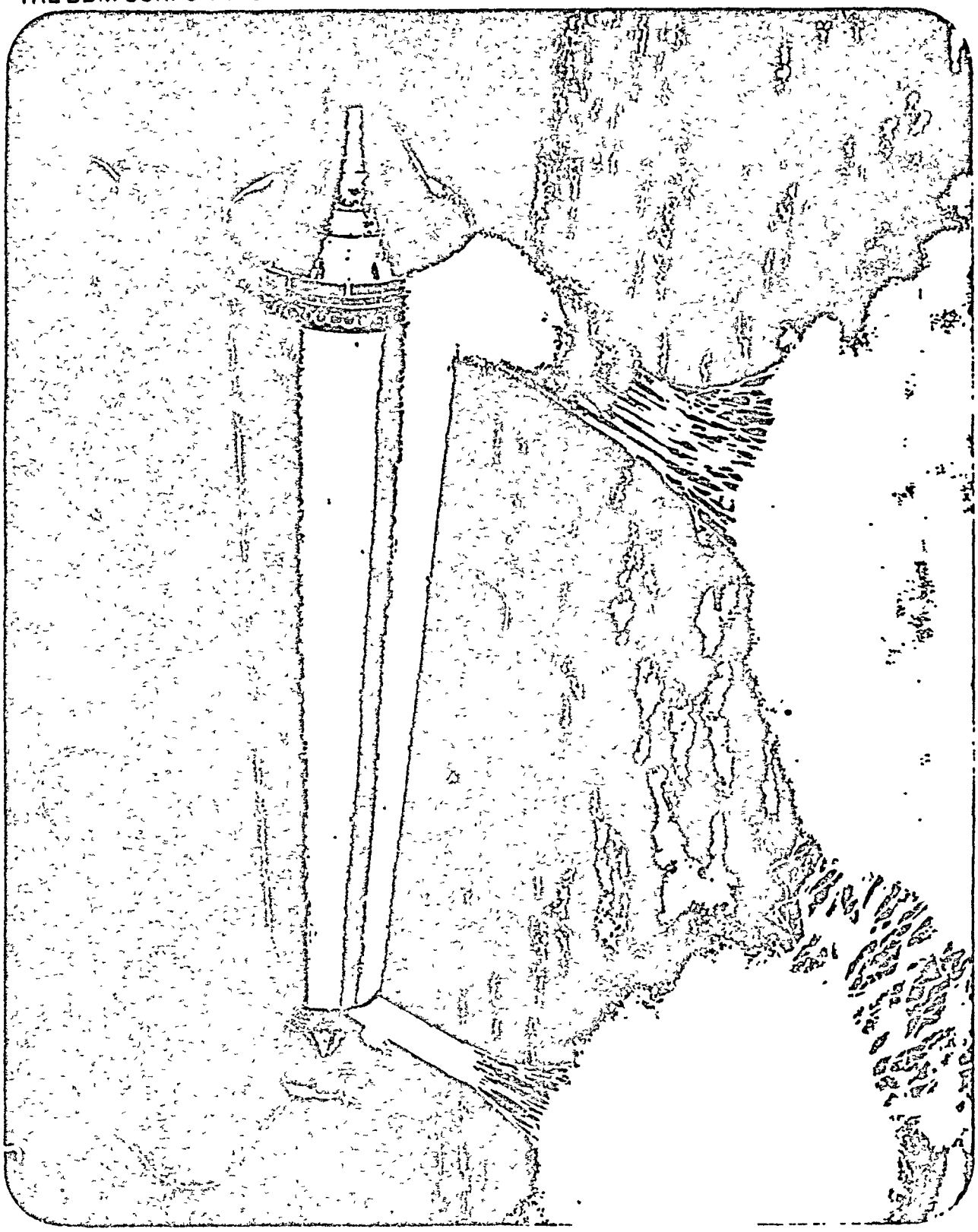

Figure XII-3. Laser-Boosted HLLV in "Electrical Storm" Propulsion Mode

and thereby communicate a reaction force to the planetary mass by way of a perturbation to the local planetary magnetic field: e.g., using the "Alfven-Wave" propulsion mode in Figure XII-4. Once in orbit, the HLLV "powerheads" are detached from the ends of the vehicle and flown back to Earth much in the manner of the space shuttle orbiter--to prepare for the next launch operation.

Introduced in the following sections are the details of the airframe, optics and propulsion system design, and finally the basis for their integration into a unified HLLV concept.

F. BEAMED POWER AND OPTICS

The idea of generating electricity from sunlight in space and then beaming the captured energy (by microwaves or lasers) to boost heavy payloads from the Earth's surface, is an attractive alternative energy option--especially since sunlight is a non-depleteable resource that can be exploited in space without producing harmful byproducts on Earth. Growing interest in the concept of 10,000 MWe space-based solar power stations may eventually make inexpensive bulk power a reality. (Power would be beamed either by direct line-of-sight, or indirectly by way of low Earth orbital relay stations.) Laser beaming of propulsive power has one additional advantage over conventional, chemically fueled launch vehicles. The vehicles need carry only enough fuel for the exoatmospheric portion of the flight trajectory, and for emergency operations. This allows launch vehicles to have a substantially higher payload fraction (i.e., payload weight/gross weight at takeoff) than with present systems.

For the launch vehicle application treated here, rapidly pulsed flight propulsive electromagnetic (EM) power would be delivered in a tightly controlled feedback loop system. Before a propulsive power pulse train is delivered by the SSPS, a pulsed "beacon" signal beam must have previously been transmitted by the HLLV flight vehicle. The signal beam would contain information on the precise location, velocity and projected trajectory of

Figure XII-4. MLV Maneuvering in "Alfven-Wave" Propulsion Mode

the shuttle. If any foreign object interrupts the signal beam transmission, the next power pulse is not delivered to the vehicle. Hence, the propulsive energy is precisely delivered, pulse-train by pulse-train. The accidental miss of a single power pulse (i.e., when the flight vehicle does not capture the full energy of the pulse, and some of it reaches the ground) would be termed a catastrophic failure of the system, analogous to the crash of an airliner today.

Highly collimated propulsive beams will be projected only along specific launch corridors. (The required pointing and tracking accuracies do not exceed that in current use by radio astronomers.) Such flight corridors for beam-riding launch vehicles must be rigidly controlled, as they presently are in the vicinity of sensitive military airports. Transmission of power would not take place until totally clear airspace existed along the boost trajectory. In this future era, airspace logistics problems should be virtually eliminatd, since the position of every flight vehicle in global airspace is likely to be known by several large computer facilities specifically dedicated for use by launch/flight controllers.

The proposed HLLV optical train configuration is shown in Figure XII-5. For purposes of functional clarity, optical elements are displayed greatly enlarged in proportion to the vehicle diameter. The laser beam is received through an opening in the upper vehicle skin onto a "beam catcher" mirror. This articulated mirror is able to project the reflected beam onto any azimuthal location around the radially symmetric primary optical surface. Before contacting the parabolic primary optics, the beam passes through a high power window. The primary optics and high power window constitute a donut-shaped high-pressure structural envelope for the absorption of laser energy. For example, the donut-shaped envelope might be divided radially into 24 independent absorption chambers for the 100 m long HLLV.

Upon reflecting off the primary optics, the beam is either focused to a high intensity upon the secondary optics, then reflected to a remote location for absorption (as shown in Figure XII-5), or the secondary optics are retracted away from the focal region and the beam is subsequently

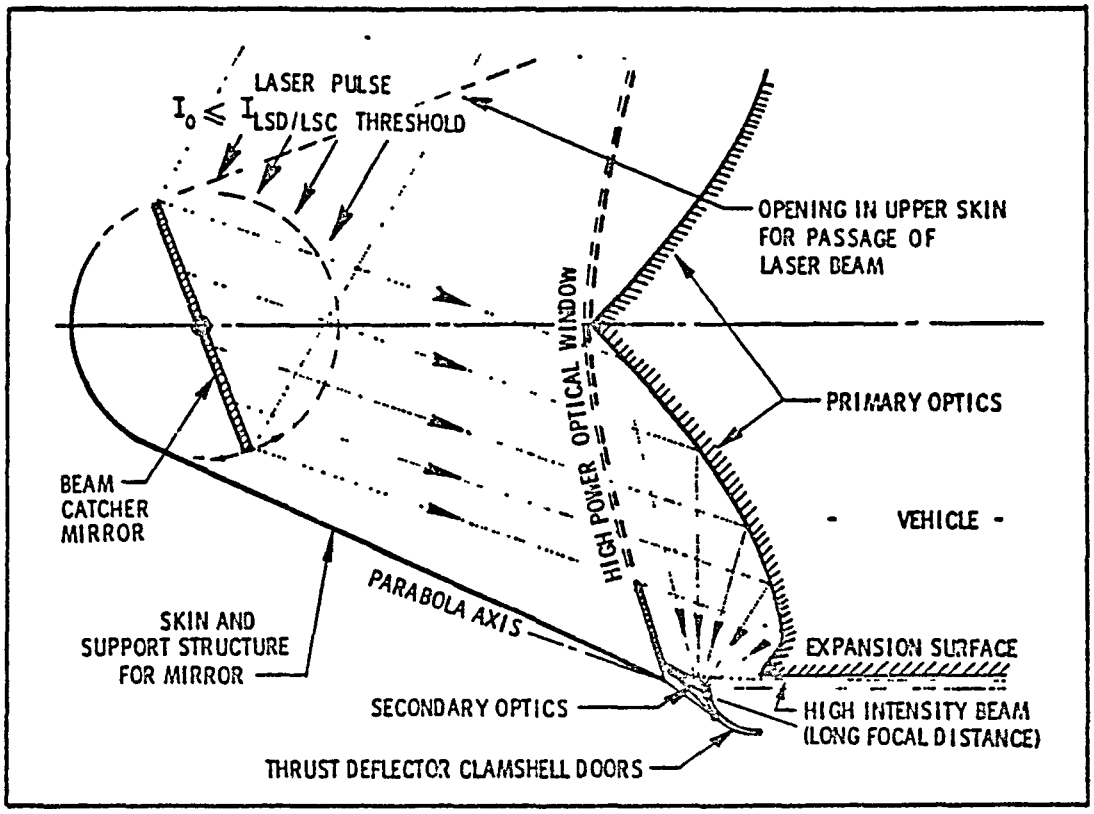

Figure XII-5. HLLV Optical Train Configuration

allowed to come to a line focus around the HLLV vehicle perimeter, midway between the exhaust ports of individual absorption chambers. The logic for the HLLV optical train configuration was developed previously in Chapters VIII and IX.

G. POTENTIAL LAUNCH CORRIDORS

Due in part to the enormous size and fragility of the central structural module used in the HLLV concept, unconventional approaches may be required to propel the vehicle into Earth orbit. Several of these propulsive schemes are able to use the unwieldy configuration of the assembled vehicle to a positive propulsive advantage.

The potential HLLV launch corridor, i.e., 5 to 50 psf dynamic pressure, is presented in Figure XII-6. Since the vehicle is designed to fly at right angles to the longitudinal axis (i.e., broadside) in certain flight propulsion modes, care must be taken not to overstress the pressure and temperature limitations of the shuttle's external skin. Although 50 psf is representative of only 140 mph at sea level, it also represents Mach 2.0 at 30 km altitude, Mach 12 at 60 km, Mach 22 at 70 km, etc., as shown in Figure XII-6. High equilibrium skin temperatures generated at the higher velocities may drive the vehicle to lower dynamic pressure trajectories--which in turn will reduce the problems of aerodynamic heating.

H. HLLV MASS SCALING ESTIMATE

In the absence of any substantive weight data on past supersonic rigid airships with orbital capability, it is assumed that the weight breakdown per component will remain roughly the same as for the old airships. In addition, it is assumed that significant advances in propulsion and structures technologies will permit orbital capability with no increase in mass. The hypothetical weight breakdown in Table XII-1 is based on a HLLV

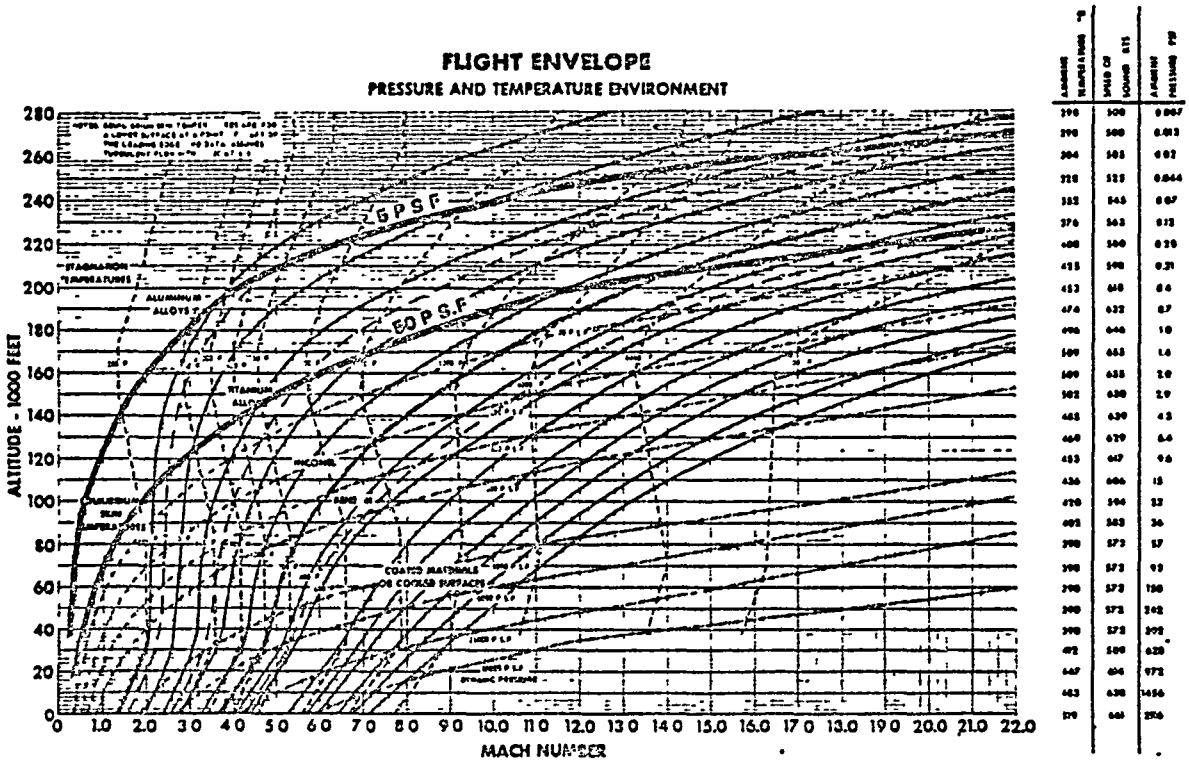

Figure XII-6. HLLV Launch Corridor: Pressure and Temperature Environment

TABLE XII-1. HLLV WEIGHT SUMMARY

VEHICLE	METRIC TONS (1000 KG)		
COMPONENT	1000M	333M	100M
STRUCTURE: HULL, ENVELOPE, BALLONETS	2580.0	95.3	2.58
SUBSYSTEMS AND EQUIPMENT: POWERHEADS, SUPERCONDUCTORS, CONTROLS, COMMUNICATION, GUIDANCE, NAVIGATION	1290.0	47.6	1.29
CREW, PASSENGERS AND DISPOSABLES, SPARES BAGGAGE, TOOLS, INITIAL BALAST	430.0	15.9	0.43
OPERATING EMPTY WEIGHT	4300.0	158.0	4.30
GASEOUS/LIQUID FUEL, RESERVES, OTHER CONSUMABLES*	3224.0	119.0	3.22
GROSS OPERATING WEIGHT	7520.0	277.8	7.52

*VEHICLE MASS RATIO DESIGN POINT = 1.75 = $M_{INITIAL}/M_{FINAL}$

geometry with a length-to-diameter ratio of 10:1 and spherical end caps. For each of the 100, 333 and 1000 m long vehicles, the Gross Operating Weight (GOW) is assumed equal to mass of air that would be displaced by the external hull envelope at sea-level altitude.

The first entry in Table XII-1 includes the mass of the skeletal structural module, the external skin envelop and the ballonets (spherical gas bags). These three items comprise the HLLV payload and represent 34 percent of the GOW at launch. The next entry, Subsystems and Equipment, is dominated by the mass of the propulsion system; i.e., the powerheads (which contain the flight deck and all controls, communication, guidance and navigation systems), the superconducting longerons (if any), and the cryogenic refrigeration equipment. The third entry includes most everything else except gaseous and liquid fuel, reserves, and other consumables--which are grouped into the fourth component category. Note that the ratio of Gross Operating Weight to Operating Empty Weight (GOW/OEW) represents a design point mass ratio of 1.75 for the HLLVs. Clearly, it is the specific impulse of the propulsion system which will dicatate how much fuel is actually required by a HLLV for an orbital flight. (The subject of engine specific impulse is addressed at the end of this chapter.)

Listed in Table XII-2 are the masses of several major subsystem components for the 1000 m HLLV. The first mass item, vehicle external skin (or envelope), is derived primarily from the anticipated stresses to be placed upon the membrane when installed in the large-scale space structure. (The mass of the spherical gas bags assumes an intended space application as shelters for construction crews, and are therefore designed to maintain a one-atmosphere pressure differential across a boron filament reinforced membrane.) The envelope must also be strong enough to withstand the gas-dynamic pressures experienced along the launch trajectory. Hence, the envelope mass presented in Table XII-2 assumes that both design conditions will be met for a dynamic pressure trajectory of 50 psf (which at sea-level altitudes is equivalent to a flight velocity of 140 mph). The method of

TABLE XII-2. PARTIAL SUBCOMPONENT MASS BREAKDOWN FOR 1000 M HLLV

SUBCOMPONENT	METRIC TONS (1000 KG)
VEHICLE EXTERNAL SKIN	42.0
SPHERICAL GAS BAGS (10 TOTAL)	726.0
SUPERCONDUCTORS	504.0
XMHD GENERATORS	283.0

analysis of both the envelope and the spherical gas bags is described below.

The shuttle vehicle is assumed to have ten gas bags or ballonets which contain hydrogen or helium propellant at one-atmosphere pressure. Assuming that Teflon-coated boron fibers (e.g., with a diameter of 8-mil) are woven into fabric in order to provide a gas bag construction material with a tensile strengh of 530 KSI, a modulus of 58 x 10^6 psi, a specific gravity of 146 lb/ft^3, and a factor of safety of 1.5, the weight of the bags can be calculated as follows. The thickness t of the high-strength spherical gas bag is given by

$$t = \frac{PrS}{2\sigma} , \qquad (1)$$

where P is the maximum pressure differential across the spherical enclosing surface of radius r, σ is the working stress and S is the safety factor. For the above given conditions, t is 0.041 in (or five fiber diameters), thereby resulting in a weight of 1.6 X 10^6 lb for ten 100 meter diameter gas bags.

Let us assume that the cylindrical aerodynamic "skin" is a) designed to support an absolute pressure differential of 50 psf (0.0236 atm), b) has a safety factor of 2, and c) uses the same boron fiber as addressed above. Hence, the required thickness t of the cylindrical gas bag can be expressed as

$$t = \frac{PrS}{\sigma} \qquad (2)$$

For the 100 m diameter vehicle, then, the cylindrical gas bag thickness is 0.00258 in. or 2.58 mil (i.e., less than the fiber diameter). The weight of material to enclose the craft is 93,000 lbs.

Summarizing then for the 1000 m HLLV, ten 100 m diameter bags comes to a mass of 726 metric tons. The total gas bag volume comes to 5.24 x 10^6 cubic meters, which can enclose 471 metric tons of hydrogen gas at one-atmosphere pressure. In comparison, the mass of conventional short-term

cryogenic storage tanks, typified by the shuttle orbiter external tank, equals roughly 10 percent of the enclosed fuel mass; the mass of long-term LH_2 cryogenic storage tanks is roughly equal the contained fuel. Subsequently, the mass efficiency of the 100 m diameter HLLV "gas bag" fuel tanks is more representative of the long-term type of cryogenic storage tanks, since the mass of the enclosure is 154 percent of the enclosed fuel. Smaller gas bags may have somewhat different performance.

As shown in Figure XII-1, the superconducting longerons also function as a cryogenic LH_2 fuel tanks for liquid hydrogen. For the 1000 m vehicle, the total LH_2 storage volume provided by the cylindrical longeron tanks is sufficient for 5000 metric tons; i.e., almost twice the required capacity. Note that the superconductor mass in Table XII-2 for the 1000 m HLLV is 10 percent of the projected maximum LH_2 mass capacity, or 20 percent of the actual required fuel. It is assumed that the combined peak current which is driven through all the superconducting longerons by the electric propulsion system for the 1000 m HLLV is 1.5×10^9 Amperes; also, the Nb_3Ge (sputtered film) superconductor with the critical characteristics pictured in Figure XII-3 is chosen for the sample calculation.

The magnetic field generated at the external skin for the 1000 m long HLLV by an electric current of 1.5×10^9 Amps (carried through the superconducting longerons) may be determined with the aid of Equation (9) in Chapter IX, by setting $r = 50$ m. It is found that the outermost edges of the superconductor are bathed in a self-magnetic field of 6 Webers/m^2 (i.e., 60 kilogauss). If it is now assumed that 100 longerons provide the total current-carrying capacity, then each would conduct 15 million Amperes. Again using Equation (9), it can be shown that the minimum cable diameter should be 1 meter in order to limit the self-field at the cable circumference to 6 Webers/m^2. Figure XII-7 indicates that for liquid helium temperatures, the Nb_3Ge superconductor exhibits a critical current density of approximately 2.5×10^6 Amps/cm^2. A conductor cross-sectional area of 6 cm^2 longeron can carry the current. The total volume of superconducting material must be 60 m^3. Assuming a conductor mass density of

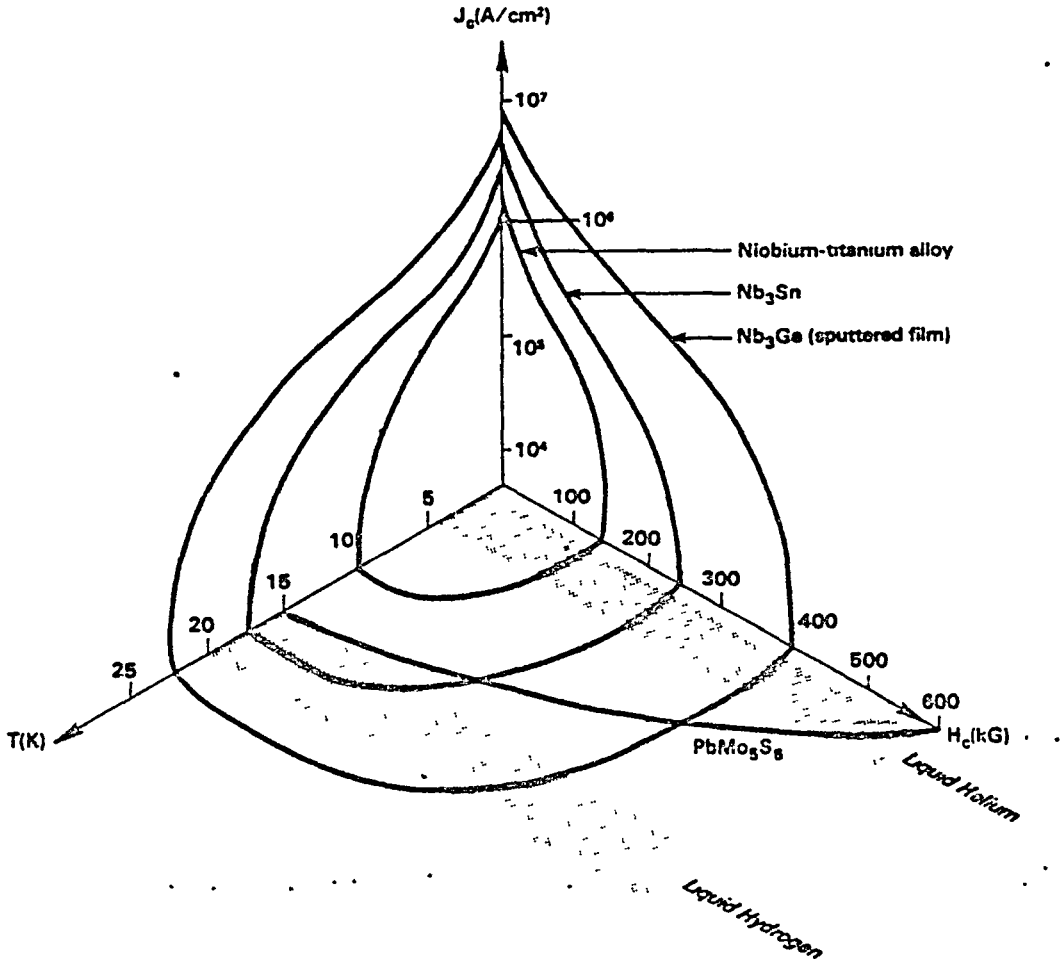

Figure XII-7. Critical Characteristics of High-Field Superconductors (From Reference 8)

8.4 gm/cm^3, 504 metric tons of material are required for the 1000 m HLLV longerons. This figure represents 6.7 percent of the GOW.

The final major subcomponent weight addressed in Table XII-2 is that of the explosively driven XMHD generators. As shown in Figure XII-5, the XMHD generators are distributed uniformly about the vehicle rim, intimately connected to the powerhead. They represent a major portion of the overall power plant mass. The XMHD generators for the 1000 m shuttle would be roughly similar to that introduced in Appendix B. However, since the HLLV peak power, voltage, the electric pulse duration requirements are clearly different than that for the rotary pulsejet addressed in Chapter VII, the XMHD performance (and mass) characteristics must be modified to fit the HLLV application.

It is assumed here that a peak electric power of 6.8×10^{13} Watts is demanded from the powerhead when propelling the 1000 m HLLV in the MHD-Fan mode. Reference 9 indicates that an experimental 5 MJ XMHD generator exhibited a peak power output of 1.46×10^{10} Watts, pulse duration of 10^{-4} seconds, peak voltage of 16.2 kV, and peak current of 9 megamps. Let us assume that a similar 5 MJ XMHD generator can be developed to run on remote laser energy at an identical peak power level, but with voltage, current, and pulse duration characteristics which are compatible with the 1000 m HLLV propulsion system. Clearly, 466 of the 5 MJ XMHD generators could generate the 6.8×10^{13} watt peak power requirement. However, the actual generators for a 1000 m HLLV would probably fall in the range of 10-50 MJ (or larger) capacity, thereby bringing the total number of units down to 250 or 50, respectively. However, for the purposes of weight scaling calculations, the 5 MJ units will suffice.

A method was suggested in Chapter VII for estimating the major XMHD generator components (i.e., radiation superheater chamber, superconducting field coil mass and MHD generator channel with electrodes). It is found that a suitable 5 MJ radiation superheater could weigh 370 kg; compatible field coil with MHD generator channel, 236 kg. This gives a total of 606 kg per 5 MJ XMHD generator, and represents a total mass of 283 metric tons for the required generating capacity: roughly 3.8 percent of the GOW.

Previous sections of this chapter have introduced the details of the HLLV airframe and optics design, HLLV mass breakdown, and have catalogued ten propulsion system modes which are worthy of further examination as prime movers for the HLLV concept. The next section provides a discussion of power requirements for various laser propulsion modes--as a function of HLLV lifting capacity.

I. POWER REQUIREMENTS AND MASS RATIOS

The fuel consumed by the variable cycle laser propulsion system in boosting a given HLLV into orbit is directly dependent upon the specific impulse, thrust-to-weight ratio, impulse coupling coefficient and thrust duration of the various propulsion modes used along the orbital flight trajectory. Table XII-3 attempts to quantify the performance potential of the ten most promising propulsion modes.

Let us begin with a general discussion of the impulse coupling coefficient which is defined as the ratio of engine thrust to input power. The highest coupling coefficients are attainable by air-breathing (as opposed to rocket) engines which propel themselves by momentum exchange with the atmosphere. Within this engine class, even a winged rocket may be considered an air-breathing engine if the aerodynamic lifting surface is viewed as a "thrust augmentation" device. The object would be to attain a resultant lift that greatly exceeds the rocket thrust. (Even though rocket thrust may be only a fraction of the total vehicle weight, it would still be adequate to support the vehicle in flight. Viewed in this light, the winged rocket is a close cousin to the air-turbo-rocket engine.

All aerodynamic lifting surfaces (e.g., fixed wings, rotary wings (helicopters), large ducted-fans, and compressors) can be subjected to a performance analysis of their impulse coupling coefficient. For example, the coupling coefficient C for the fixed wing of an aircraft may be expressed as follows

$$C = \frac{L}{P} = \frac{L}{D} \frac{10^5}{V_{wing}} , \qquad (3)$$

TABLE XII-3. PERFORMANCE POTENTIAL FOR HLLV PROPULSION SYSTEMS

	SPECIFIC IMPULSE (SECONDS)	THRUST TO WEIGHT RATIO	COUPLING COEFFICIENT (DYNES/WATT)
NON-ELECTRIC THRUSTERS:			
A. AEROSTATIC LIFT	∞	1	∞
B. AERODYNAMIC LIFT	--	1	300,000
C. VORTEX-INDUCED LIFT	--	>1	10,000
D. ROTARY IRH PULSEJET (ROCKET MODE)	1,000	10	25-50
E. ERH PULSEJET (AIR-BREATHING MODE)	∞	10	50-100
ELECTRICALLY-AUGMENTED THRUSTERS:			
A. "ELECTRIC STORM" ATMOSPHERE COUPLING	--	--	--
B. MHD-FAN PULSEJET	10,000	10	100
C. MHD-PUMPED VORTEX-INDUCED LIFT	--	>1	--
D. WAY'S ELECTROMAGNETIC PROPULSION CONCEPT	--	>1	--
E. LARGE AMPLITUDE ALFVEN-WAVE ENGINE	100,000	0.1	--

where L/D is the dimensionless lift-to-drag ratio, V_{wing} is the "blade" forward velocity in m/s, and C is the coupling coefficient in dynes/Watt. The coupling coefficient does not seriously degrade in performance until the "blade" velocity approaches sonic conditions where Mach divergence effects greatly increase drag.

A more convenient expression for the coupling coefficient of rotary wings, propellers, ducted fans, turbo-fans, turbojets and all other air-breathing thrusters is given by

$$C = \frac{F}{P} = 10^5/(V + \Delta V/2), \qquad (4)$$

where V is the velocity of advance of the engine, and ΔV is the velocity increment imparted to the air moving through the engine. Equation (4) may be used to analyze the performance of a fixed-wing aircraft by setting V equal to the rate-of-climb of the wing, and ΔV equal to the vertical down-wash velocity imparted to the air upon passage of the wing.

In contrast, the coupling coefficient for a rocket propulsion system is

$$C = \frac{F}{P} = 2 \times 10^5/V_{ex} \qquad (5)$$

where V_{ex} is the rocket exhaust velocity in m/s, and C is again in dynes/Watt.

Equation (4) is plotted in Figure XII-8 for various ΔV's. The theoretical limit to coupling performance is indicated by the diagonal cross-hatched line, and is obtained by setting ΔV equal to zero. Superimposed upon the plot are the performance regimes of various categories of air-breathing thrusters. The highest coupling exhibited to date by man-made machinery is that of MacCready's Gossamer Albatross which has demonstrated a phenomenal 580,000 dynes/Watt.* In second place is his Gossamer Condor, with a coupling of 370,000 dynes/Watt.

---

* No doubt the coupling performances of many winged insects (e.g., butterflys, dragonflys, etc.) equal or exceed this value.

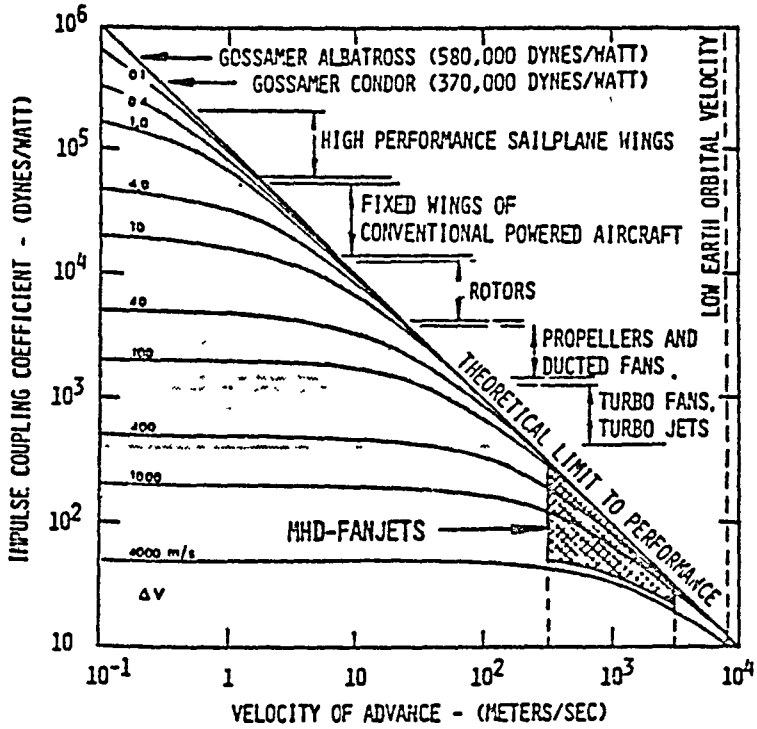

Figure XII-8. Coupling Coefficient vs. Velocity of Advance For Air-Breathing Engines

Below MacCready's creations fall the regimes of high performance sailplanes, then fixed-wing aircraft, followed by rotary wing vehicles, and finally conventional propellers. The Sikorski S-64E "Aerial Crane" exhibits 2500 dynes/Watt. Other large diameter rotors for VTOL and STOL aircraft have produced as much as 9000 to 12,000 dynes/Watt. Conventional aircraft propellers typically exhibit from 1500 to 1800 dynes/Watt at takeoff. As the advance velocity is increased beyond the regime where conventional propellor-driven thrusters deliver optimum performance, the maximum attainable coupling continues to decline. In order of decreasing coupling performance, these regimes are occupied by ducted-fans, turbofanjets, turbojets, ramjets, scramjets, and air-turbo-rockets. At flight velocities much beyond 2000 m/s, the coupling performance of air-breathing engines begins to rapidly deteriorate, and rocket engines fall into a more favorable light. Their low level of coupling performance is entirely independent of flight speed, and is soley a function of rocket exhaust velocity.

Figure XII-9 (from Reference 10) presents another way of analyzing the coupling coefficient performance of air-breathing engines. Here the coupling coefficient is plotted as a function of disk loading (rotor thrust divided by rotor disk area, or exhaust exit area) for various categories of thrusters. Note that as disk loading increases, the associated downwash velocity ΔV increases, coupling performance decreases, and larger percentages of flight propulsive power are thrown away in generating noise. As shown in Figure XII-5, only rotary wing aircraft with under 14 psf loading generate downwash velocities below hurricane winds.

The remarkable insect-like flying machines of MacCready have evolved from something more powerful than an entirely logical, rational approach to aircraft design.[11] While pursuing many other design challenges which are unrelated to the human-powered flight problem, MacCready was able to extract, every now and then, new insights which permitted him to view the problem from several vastly different perspectives. He was then able to use many, seemingly unrelated bits of information to intuitively leap to a solution that fitted them all together. Such bridges of the immagination are not normally accessible from the strictly rational approach.

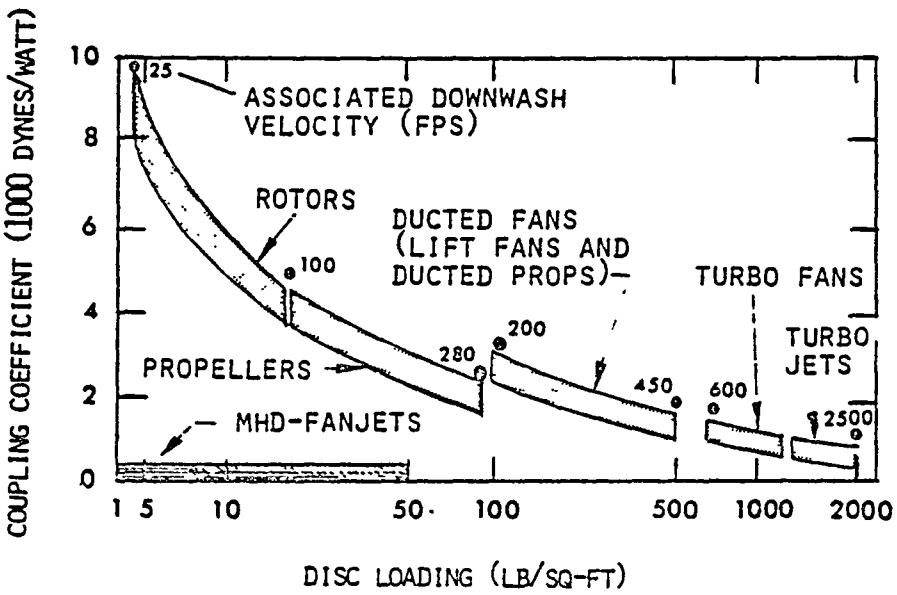

Figure XII-9. Coupling Coefficient vs. Disk Loading (From Reference 10)

MacCready has shown that the key to staying aloft with very little flight propulsive power is to make the aircraft large, lightweight and able to fly at relatively low speeds. He found that for his application, flight propulsion power requirements are simply inversely proportional to the wing span. No matter how miniscule the power of the human engine, it is possible to achieve the required flight efficiency simply by making the vehicle big enough. Certainly, there are obvious penalties facing large-scale vehicles which must fly slowly: e.g., construction difficulties, hangering problems, the frailty in the face of weather. Hence, MacCready's flights were carried out where weather was suitable.

As MacCready points out,[11] the success of his vehicles does not unconditionally imply that its strategy can be used to create aircraft to achieve different goals than that of the Gossamer Condor or Albatross. However, there are major similarities between the approach taken by MacCready, and what might be used in the design of heavy lift launch vehicles of the type proposed here. Such HLLVs must climb to the upper reaches of the atmosphere while consuming the least possible flight propulsive power, at low flight velocities where the impulse coupling coefficients are highest. Flight velocity should be low because of aerodynamic drag generated by the very large HLLV surface areas and because drag increases with the square of the flight velocity.

The importance of engine coupling coefficient in relation to HLLV lifting capacity can be exemplified by applying the performance figures for the Albatross and the Sikorski "Aerial Crane" to the proposed HLLV. As mentioned earlier, the Albatross attains 580,000 dynes per Watt; the "Aerial Crane", 2500 dynes per Watt. Assuming these coupling coefficients, the 1000 meter HLVV would require 12.7 megawatts (Albatross coupling) versus 2.95 gigawatts ("Aerial Crane" coupling) to support a GOW of 7520 metric tons. The 333 meter vehicle requires 1/2 megawatt versus 1/10 gigawatt; the 100 meter vehicle, 0.01 megawatt versus 2.95 megawatts. The importance of processing a very large mass flow rate of air through a small ΔV, then, is clearly apparent from these calculations.

The need for a HLLV thrust-to-weight (T/W) ratio greater than 1 through the atmospheric portion of the launch trajectory is not necessarily

mandatory. Wings or trapped-aerodynamic-vortices can be used throughout the lower velocity regime with propulsion systems having a T/W less than one which accomplish a "thrust augmentation" process by momentum exchange with the atmosphere. Furthermore, at the other end of the launch trajectory where flight velocities finally become a substantial fraction of orbital, centrifugal forces upon the vehicle will begin to unload the vertical lift force requirement. Hence, at the highest Mach numbers where electrically augmented thrusters are used, engine T/W ratios may be significantly smaller than one.

The importance of engine specific impulse (I_{sp}) in relation to vehicle mass ratio (GOW/OEW) becomes readily apparent with a few straightforward calculations using Equation (6)

$$GOW/OEW = \exp\left[(\Delta V)_{vehicle}/gI_{sp}\right], \qquad (6)$$

where $\Delta V_{vehicle}$ is the velocity increment, and g is the acceleration due to gravity. The results for two space missions are displayed in Table XII-4: "earth escape" (about 11 km/s), and "moon landing from Earth departure" (roughly 16 km/s). Since the HLLV introduced here is designed for a mass ratio of 1.75, it is evident that fulfillment of these missions requires engine specific impulses that exceed 1000 seconds. Note that if variable cycle laser propulsion engines can exhibit a net specific impulse of 10,000 seconds, the entire HLLV could fly several times into orbit and back again on the available fuel.

J. SUMMARY

This Chapter introduces the concept of a heavy lift launch vehicle whose configuration is intimately tied to the standardized building module requirements of a specific large-scale space structure for which it is designed. The HLLV payload is the vehicle structural shell itself, and it is delivered into orbit intact and ready to be joined to other identical modules at the space construction site.

TABLE XII-4. ENGINE SPECIFIC IMPULSE VS. MASS RATIO

	MISSION MASS RATIO	
I_{sp} (SECONDS)	EARTH ESCAPE	MOON LANDING
10^3	3.07	5.11
10^4	1.12	1.18
10^5	1.01	1.02

The vehicle payload itself is a low mass, large volume structure which more conventional launch vehicles usually drop off (i.e., in the form of expendable fuel tanks) along a high dynamic pressure orbital trajectory. In contrast, the launch corridor proposed for this vehicle is one of low dynamic pressure. The structural payload module is protected from the hurricane force winds (generated on the way into orbit) by a lightweight, high-strength envelope which is later stripped off and recycled for other purposes. The overall vehicle configuration takes on much of the appearance of old rigid airships.

C-5

REFERENCES FOR CHAPTER XII

1. Covault, C., "Structure Assembly Demonstration Slated," Aviation Week and Space Technology, 12 June 1978, pp. 49-53.

2. Covault, C., "Platform Design for Numerous Uses," Aviation Week and Space Technology, 19 June 1978, pp. 67-73.

3. Covault, C., "Tank Tests Validate Structure Assembly," Aviation Week and Space Technology, 26 June 1978, pp. 55-62.

4. Covalut, C., "Views Change on Power Satellite Work," Aviation Week and Space Technology, 17 July 1978, pp. 42-46.

5. "Building Large Structures in Space," entire issue of Astronautics and Aeronautics, Vol. 16, No. 10, October 1978.

6. Schefter, J., "Giant Space Structures - how we will build them," Popular Science, Vol. 214, No. 3, March 1979, pp. 78-83.

7. Shell Oil International study, (examines the feasbility of airships up to 100 million cu-ft capacity as transporters of natural gas), Shell Centre, London, SE1 7NA, England, - company proprietary report dated about 1976-77.

8. Schwartz, B. B. and Foner, S., "Large-Scale Applications of Superconductivity," Physics Today, July 1977, pp. 34-43.

9. Teno, J. and Sonju, O. K., "Development of Explosively Driven MHD Generator and Short Pulse Aircraft High Power," Interim Technical Report No. 1, AERL Report AFAPL-TR-74-48, Avco Everett Research Laboratory, Everett, MA, June 1974.

10. Dulberger, L. H., "Advanced Rotary-Wing Aircraft," Space/Aeronautics, April 1967, pp. 68-82.

11. MacCready, P., "The Gossamer Condor," Astronautics and Aeronautics, Vol. 17, No. 6, June 1979, pp. 60-63.

CHAPTER XIII
ELECTROSTATIC PROPULSION CONCEPTS

This chapter contains some of the most speculative propulsion concepts in the entire collection. However, they also have excellent potential for high payoffs, in that they explore the realm of extremely high coupling coefficients (thrust/input-power)--previously explored only by MacCready's Gossamer Albatros and Condor aircraft. Instead of using propellors, fans, jets, or rockets for generating flight propulsive thrust, this new class of aircraft would use high electrostatic fields. Revolutionary new territory is revealed by the liason of "action-at-a-distance" forces upon the atmosphere (i.e., still using momentum exchange) and lighter-than-air vehicle structures technology.

A. BASIC CONCEPT

This analysis assumes the existence of very large (e.g., 100-1000 m long) rigid airships capable of generating artificial charged clouds (e.g., 1-1000 Coulombs) within the atmosphere. This type of lighter-than-air vehicle (LTAV) is described in Chapter XII. These "rigid airships" would be equipped with 100 MeV to 1 GeV accelerators for emitting relativistic charged particle beams (electron or proton); they would also carry other necessary cloud-charging equipment. The charged particle beams are assumed to propagate 100 m - 10 km at low altitude; tens to hundreds of km within the ionosphere.

Figure XIII-1 illustrates three candidate endo-atmospheric charging concepts. Figure XIII-1A shows an approach using on-board electron accelerators to create a large negatively charged cloud several kilometers across--at an altitude of, say perhaps, 1,500 m above the ground. Simultaneous ejection of a proton beam (again from a vehicle-based accelerator) into the ground plane leaves the region below the cloud with a net positive charge. The goal is to produce a very strong electric field

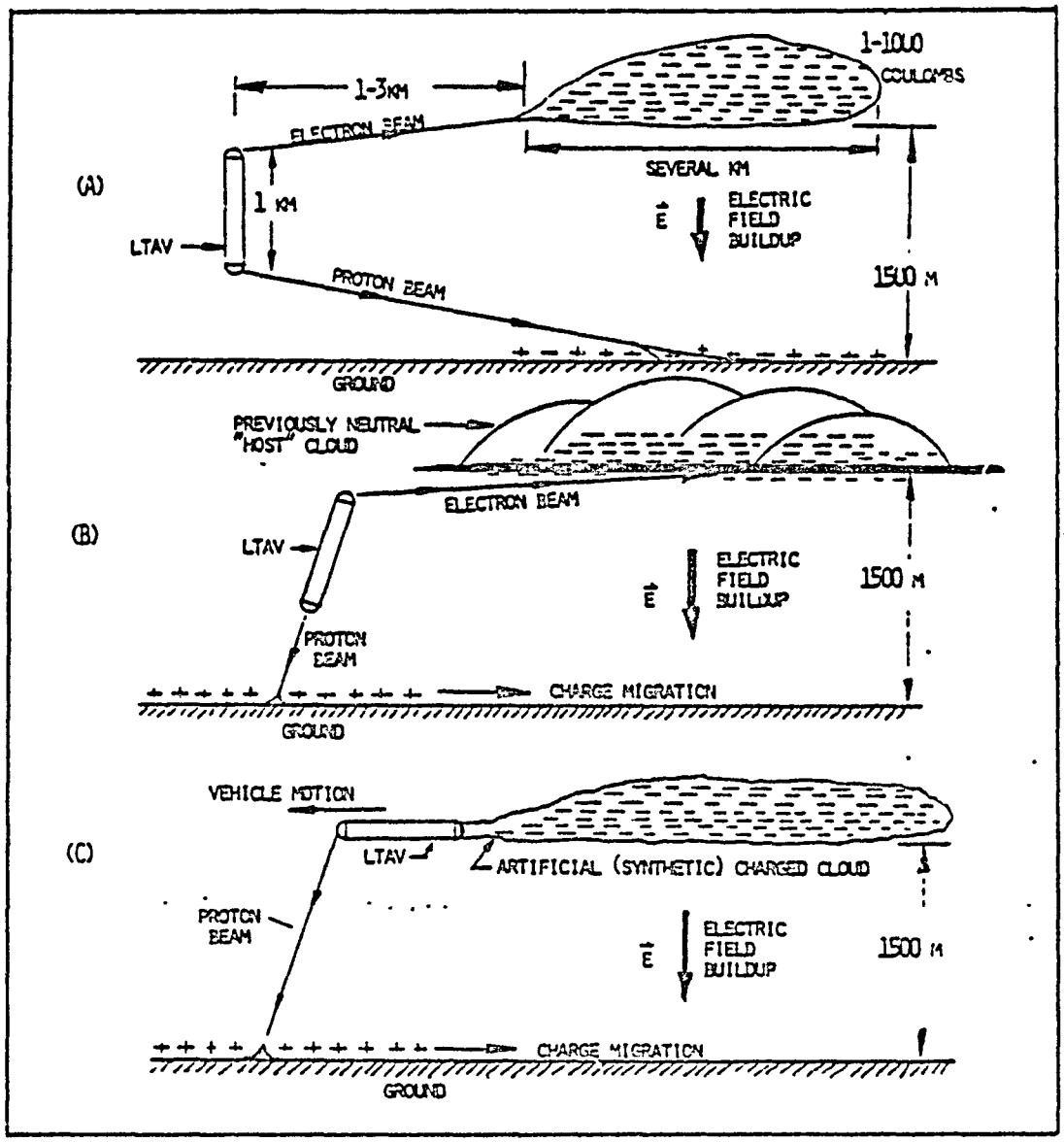

Figure XIII-1. Atmospheric Charging Concepts

within the volume just below the cloud--while leaving the rigid airship electrically neutral at all times.

Several important technical issues are begging answers. First, after the electrons have decelerated and have subsequently attached themselves to neutral molecules such as oxygen, what is the resultant probable ion concentration or density--as a function of altitude? Secondly, will the protons indeed leave their net positive charge upon the ground as they impact and scavenge electrons from the soil/plants--as the model suggests? Third, must there be some mechanism created to act as a rectifier so that electron charge will not "short-circuit" from the cloud, back through the ionized beam path, and discharge through the vehicle to the ground?

In the search for answers to these questions, current research on charged particle beam propagation in the atmosphere should prove useful (e.g., see Reference 2). Figure XIII-2 presents a basic endo-atmospheric propagation model for an atmospheric charging analysis. Incidently, it is presently thought that electron beam propagation might be substantially enhanced by using a pulsed high power laser beam to "bore" a high conductivity, pre-ionized channel through the atmosphere--just prior to electron beam injection (i.e., thereby forming the electrical circuit).

Several other approaches might avoid the "short-circuit" pitfall. One idea, indicated in Figure XIII-1B is to fire the electron beam into a previously uncharged, natural H_2O-vapor cloud--so that the electrons rapidly attach to H_2O vapor or to micron-sized droplets (mist). In addition, the proton beam would be directed in a long slant-range path, perhaps being distributed in several smaller bolts over a very large ground area. This alternative would cause some delay in the transit of positive charge to the area directly beneath the cloud. Figure XIII-1C shows an additional alternative of depositing the negative charge (emitted by the vehicle) onto artificial fog (e.g., high pressure H_2O mist generators), or onto extremely fine dielectric fibers which are chopped off at regular intervals from electrode "spinneretts". High electrostatic forces would drive free electrons to the end of these fibers, prior to their being sheared off. The goal would be to produce a large surface area, high charge per mass

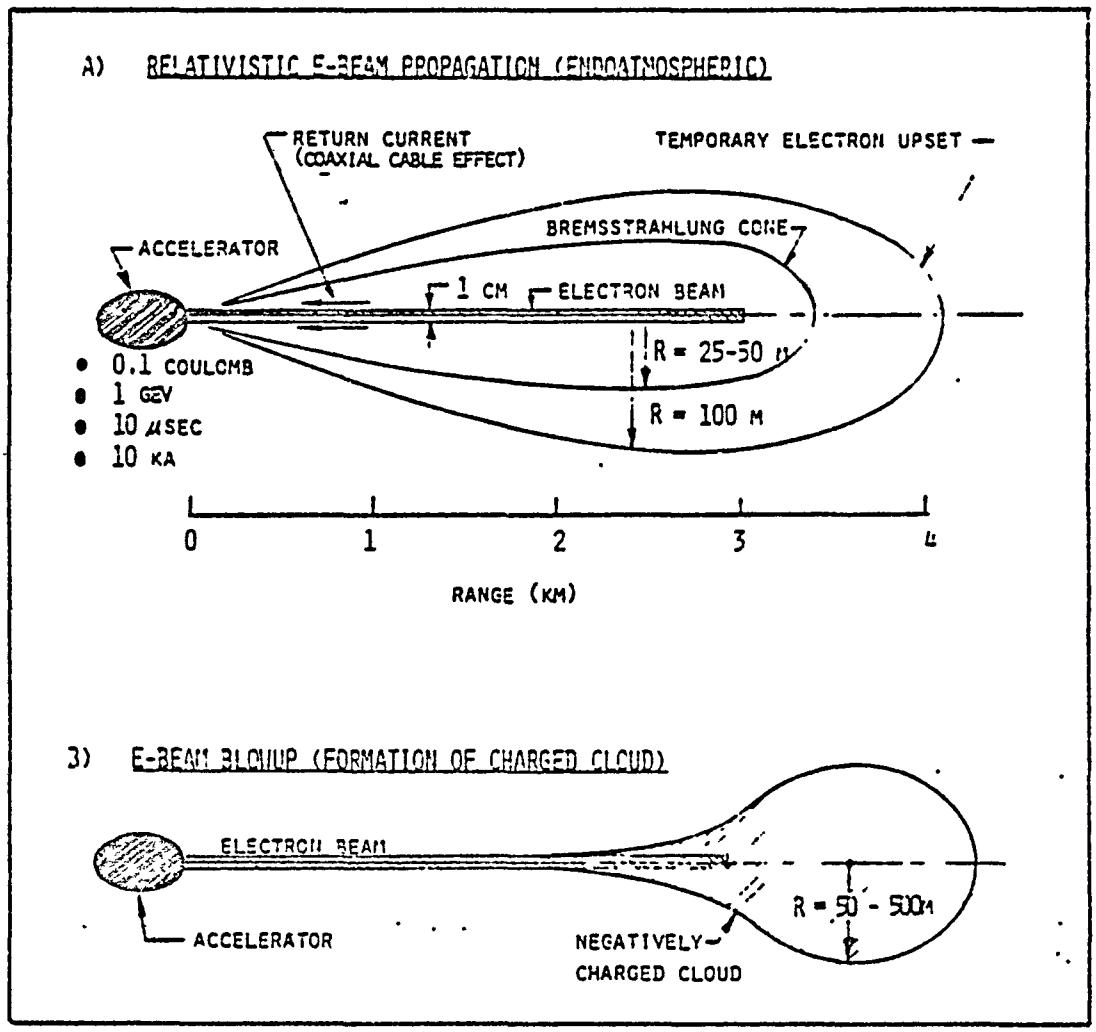

Figure XIII-2. Generation of Negatively-Charged Cloud

ratio emission--whose rate of descent within the atmosphere would be extremely slow (e.g., like spider webs carried off by the winds to great distances).

B. ELECTROSTATIC "CARTESIAN DIVER" (ECD) CONCEPT

The "Cartesian Diver" vehicle is a neutrally bouyant, rigid metalized sphere which is equipped with a very lightweight particle accelerator (see Figure XIII-3) and powered by remote beamed microwave radiation. The accelerator would have sufficient power only to adjust the potential of the ECD surface (either negative or positive) up to the breakdown limit. It may be possible for a 10 m sphere to accelerate upward at 1 g, in electric fields which have already been measured under thunderstorms--when the ECD's surface is charged to the breakdown limit. Figure XIII-4 shows the orientation of electrostatic fields for this propulsion concept.

Clearly, the "Cartesian Diver" vehicle need not be filled with helium or hydrogen to become neutrally buoyant, this could all be accomplished electrostatically, and become the first large scale application of the Millikan "oil drop" experiment. Figure XIII-5 portrays a concept by which the heavier-than-air "Cartesian Diver" vehicle might support itself in "ground effect." The scheme would be used to the break downward motion in preparation for landing, or to enable hover just above the ground. Basically, the vehicle would take on a positive charge while simultaneously directing positive beams into the ground. Hence, the vehicle would be supported in "ground effect" by mutual repulsion of the two positively charged entities.

Figure XIII-6 illustrates a motive concept which might be used for lateral propulsion of the ECD vehicle. The large LTAV vehicle uses its particle accelerators to deposit a series of charged clouds along the flight path of the ECD. Each cloud has an order of magnitude or two (10X or 100X) more charge than that carried by the ECD. The propulsive principle is similar to that of a linear electrostatic motor, whereby the "stator" is provided by a series of charged clouds, and the armature is the

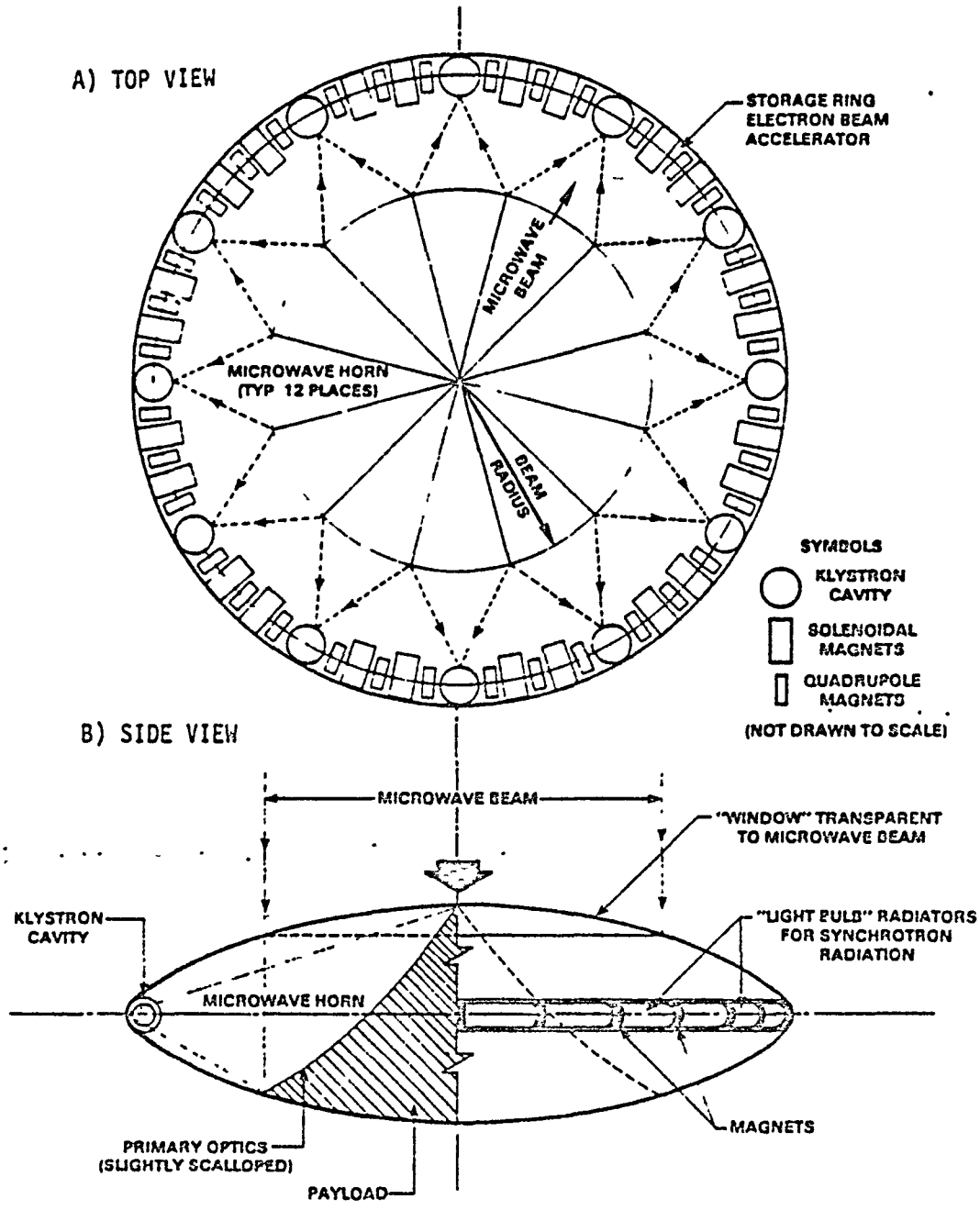

Figure XIII-3. Schematic Diagram of Lighter-Than-Air Electrostatically Propelled Vehicle

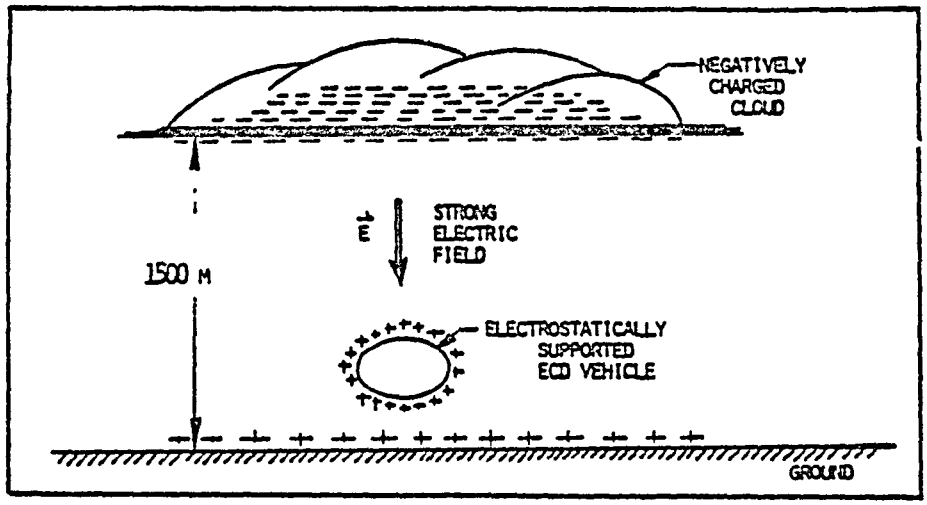

Figure XIII-4. Electrostatic "Cartesian Diver" (ECD) Concept

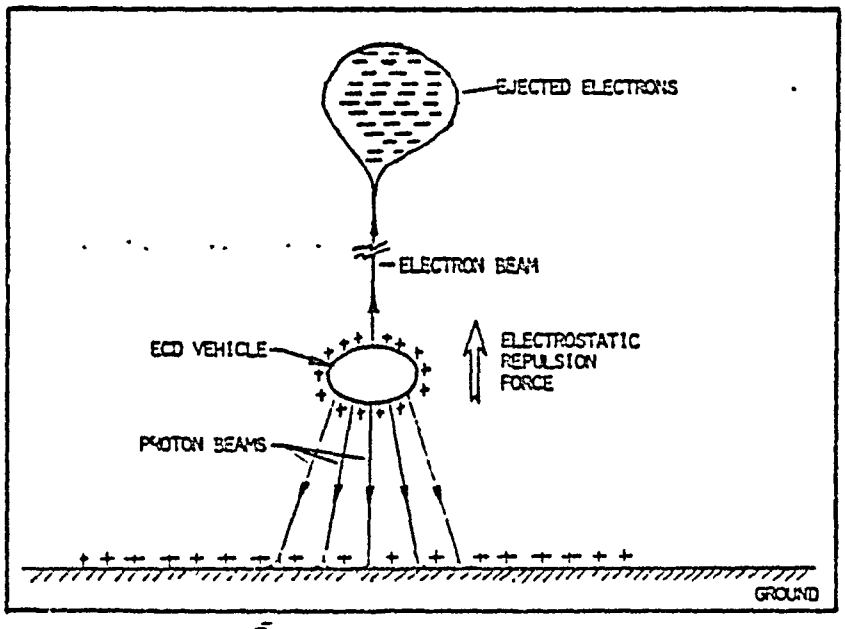

Figure XIII-5. Electrostatic "Gound Effect" Concept

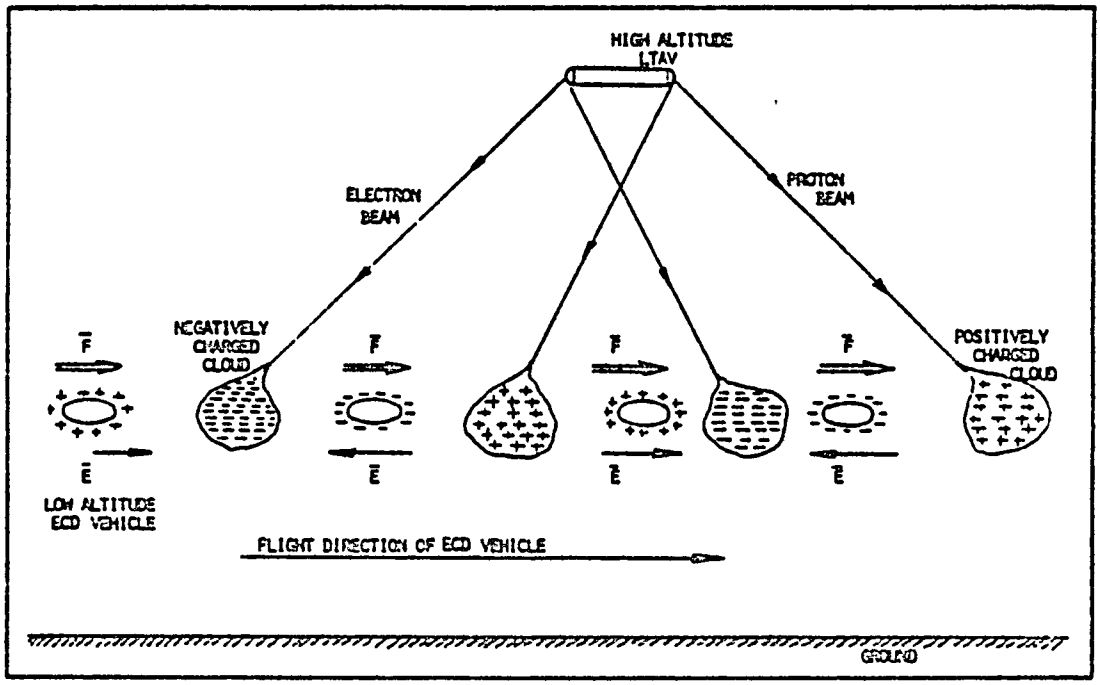

Figure XIII-6. Dependent ECD Propulsion--Linear Electrostatic Motor Concept

ECD vehicle itself. As shown in Figure XIII-6, flight propulsion is accomplished by alternate electro-static attraction and repulsion forces acting on the ECD vehicle.

Figure XIII-7, illustrates a single representative ECD/cloud encounter. Once it is attracted into a negatively-charged cloud (Figures XIII-7A and XIII-7B), the positively charged ECD vehicle scavenges electrons from the cloud to become electrically neutral (Figure XIII-7C). Just prior to exiting from the other side of the cloud, the ECD emits a proton beam to take on a high negative potential (See Figure XIII-7D). Hence, Figure XIII-7D shows the negatively-charged ECD being repelled by the previous negative cloud, while being attracted to the next positive cloud.

C. SELF-MOTIVATED ELECTROSTATIC PROPULSION CONCEPTS

This concept involves self-motivated electrostatically propelled vehicles. Basically it treats a class of flight vehicles equipped with charged particle beam accelerators that have significantly more power (i.e., 10-1000X) than that of the ECD vehicle. Figure XIII-8 is an artist concept of such a vehicle in flight.

1. Within the Atmosphere (Endo-Atmospheric)

To generate a propulsive force within the atmosphere, the vehicle would first eject a relativistic charged particle beam of electrons (e.g., 100 MeV to 1 GeV) in the desired direction of motion. This process would, of course, leave the vehicle with a net positive charge.) At some distance from the vehicle, the electron beam slows down and expands, due to the effects of coulomb repulsion. (The relativistic space charge neutralization processes no longer apply as the beam stops its forward motion.) The electrons then attach themselves to previously netural air molecules and in the process create a massive charged cloud (not unlike that which occurs naturally in thunderstorms). Hence, this cloud becomes the "reaction mass" against which the vehicle pulls itself through the atmosphere.

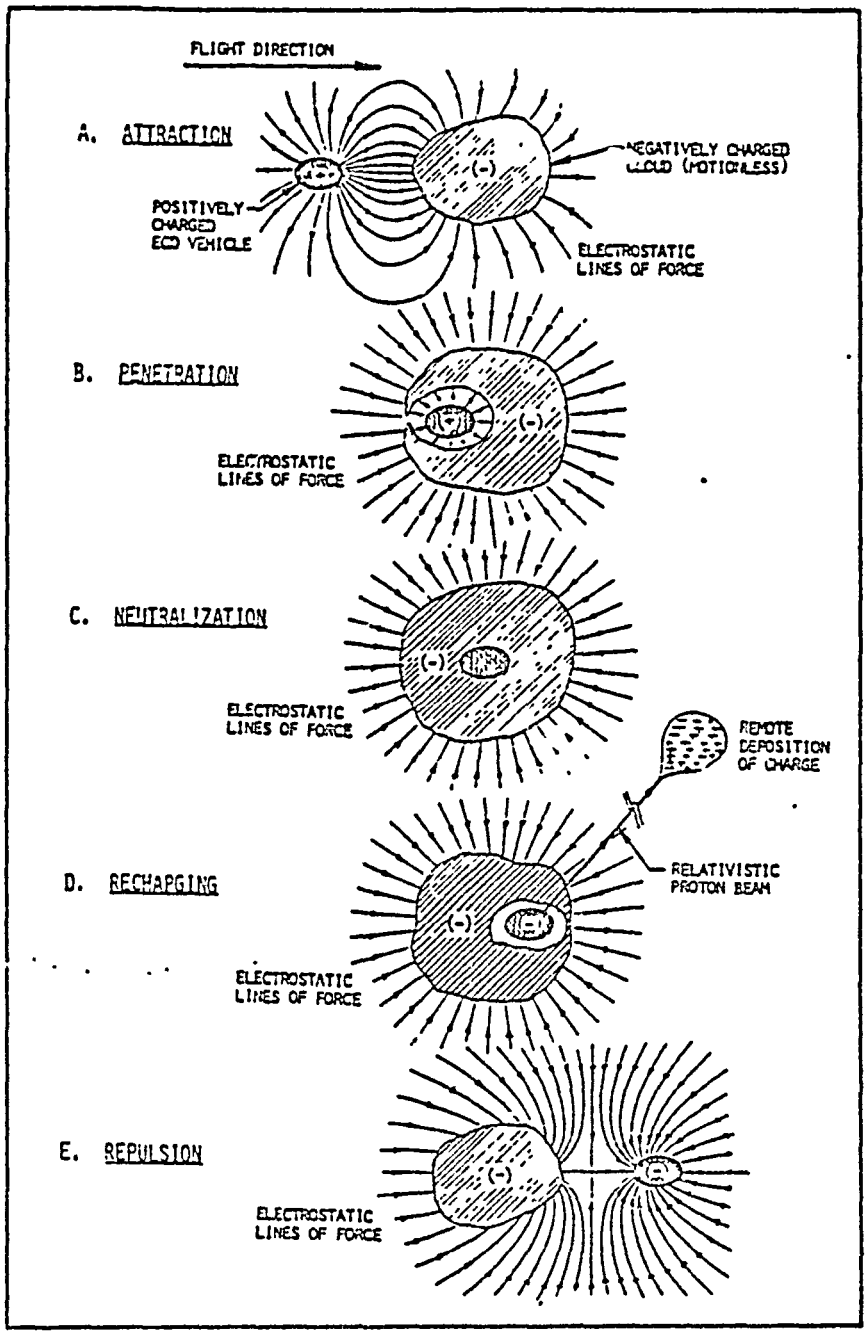

Figure XIII-7. Electrostatic Propulsion of ECD Vehicle Through Charged Cloud

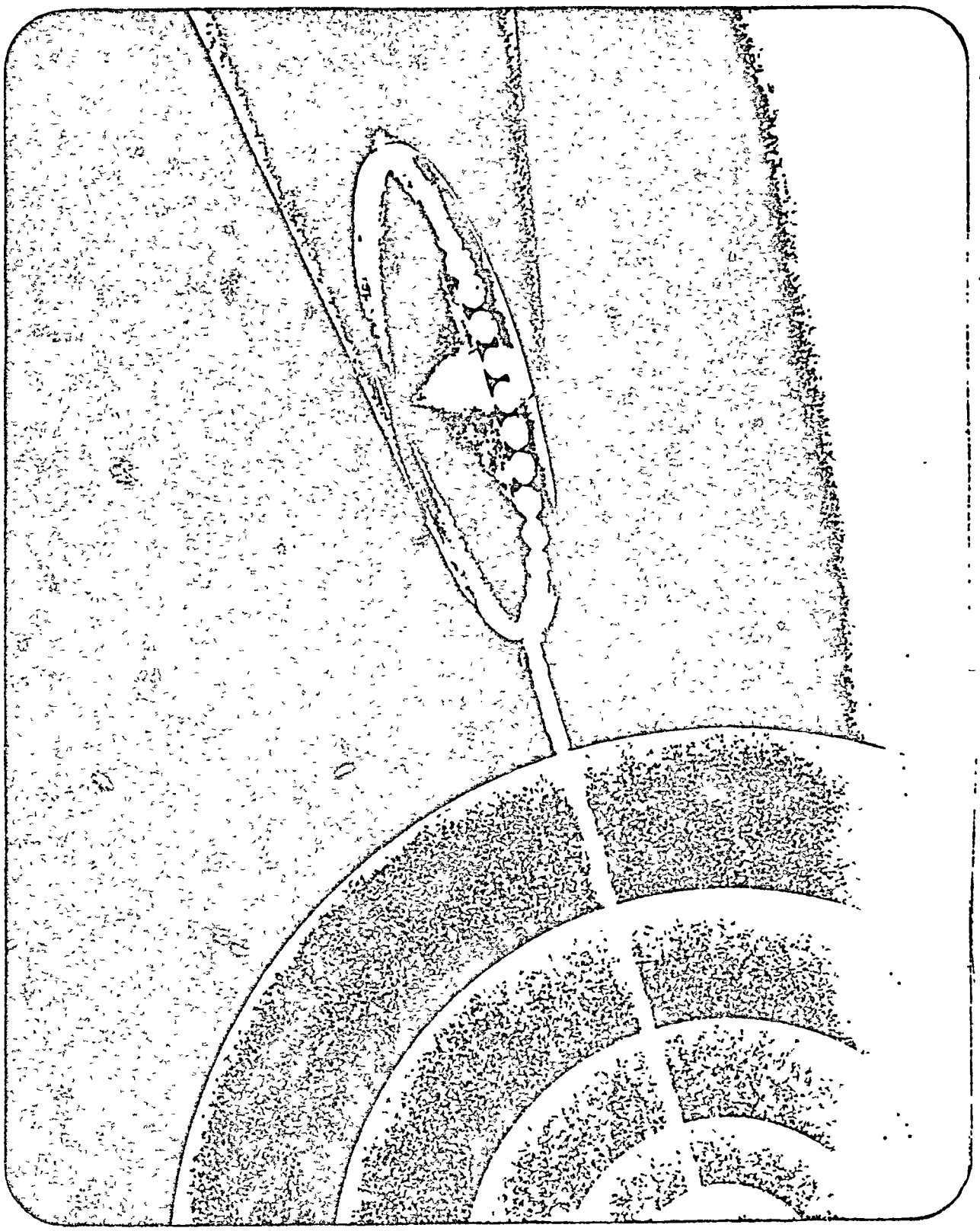

Figure XIII-8. Lighter-Than-Air Electrostatically Propelled Vehicle (Artist: R. Carter)

Figure XIII-9 illustrates three conceptual approaches to self-motivated electrostatic propulsion within the atmosphere. It is assumed that the vehicle always charges itself to the maximum potential--limited by the breakdown threshold at a given altitude. However, as indicated in Figure XIII-9A, this assumption sets an upper limit on the quantity of charge that can be placed upon the vehicle (q_1), as well as the remote cloud (q_2)--since q_1 must equal q_2, and since q_1 is fixed by the vehicle dimensions.

Further increases in flight propulsive forces can possibly be generated by several means. It is possible to increase q_2 beyond the above-mentioned limit by allowing charge to "leak off" the vehicle surface through the processes of corona discharge (i.e., the generation of q_3 in Figure XIII-9B). A further increase in leakage rate may be accomplished by: (a) convection of positively charged ions off the vehicle surface, enhanced by high forward flight velocities, or (b) artifically-induced convection by rapid vehicle rotation, or (c) by providing large numbers of pointed grids attached to the smooth vehicle exterior surface, to preferentially enhance corona discharge in the aft direction. As an alternative to the corona discharge process, excess positive charge could be placed upon ejected "carrier" molecules (e.g., H_2O vapor), or on actively-grown synthetic fibers which are sequentially chopped off when they reach an appropriate length. Another approach (shown in Figure XIII-9C) would be to eject proton beams in the aft direction. Regardless of the approach, it is clear that $q_1 + q_3 = q_2$ in Figures XIII-9B and XIII-9C.

Figure XIII-9 illustrates the one-step process of generating a single charged "stator" cloud (q_2) for a self-propulsive mode that can be likend to a linear electrostatic motor. The full concept is identical to that previously described in Figure XIII-6 for the dependent ECD, where the vehicle itself serves as the armature. Here, the major difference is that the self-propelled vehicle has particle beam accelerators powerful enough to generate its own "stator" clouds in rapid-fire succession as shown in Figure XIII-10. This propulsive scheme could be useful at altitudes from the earth's surface out to the ionosphere.

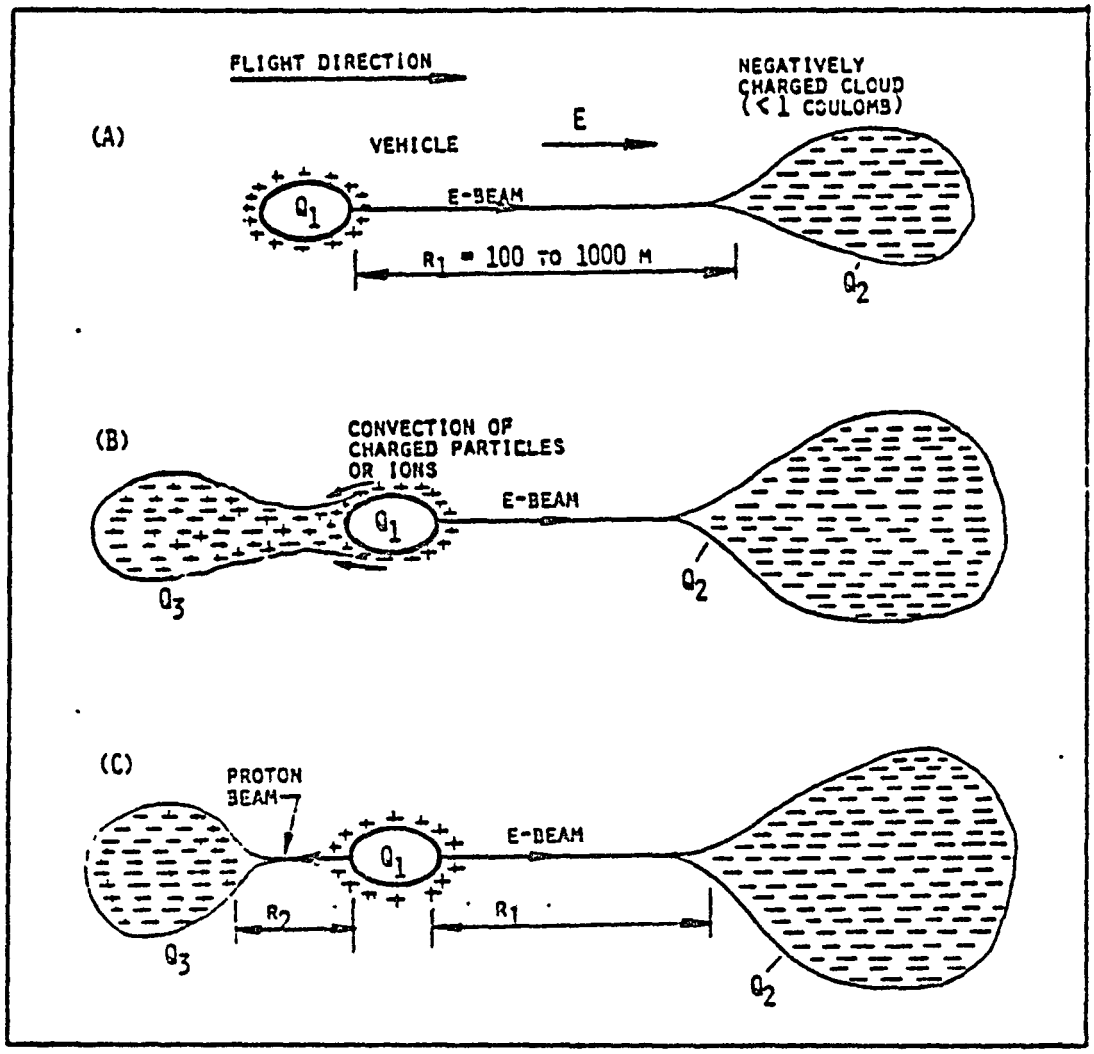

Figure XIII-9. Self-Motivated Electrostatic Propulsion Concepts

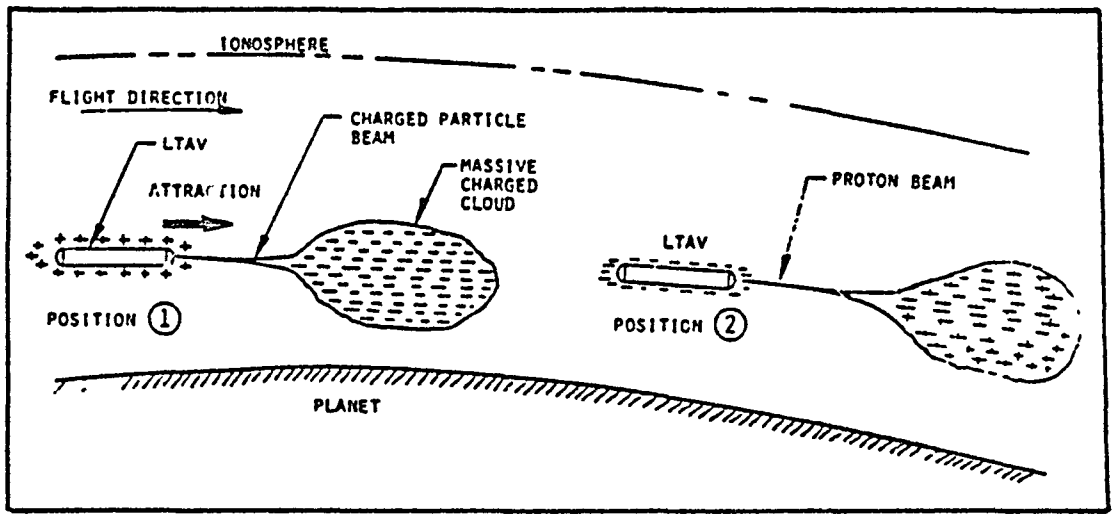

Figure XIII-10. Endoatmospheric Electrostatic Propulsion Concept

2. Beyond the Ionosphere

A similar propulsion scheme in Figure XIII-11 might be used by very large LTAV vehicles flying at high sub-orbital velocities (e.g., 4 to 8 km/sec) at altitudes beyond the ionosphere. The vehicle first emits a relativistic E-beam to charge up a large reaction mass of ionospheric air. In the process, the vehicle becomes positively charged and is attracted towards the negatively charged cloud. Upon moving over the cloud, the vehicle neutralizes itself, then reverses its potential, repelling the charged cloud. Later it repeats the beam ejection procedure to generate a new positively-charged cloud ahead of the vehicle's flight path. As with the previous example in Figure XIII-6, the vehicle creates a linear electrostatic "motor" within the atmosphere, where the charged clouds become the "stator" and the vehicle itself is the "armature." (The concept is similar to that introduced in Reference 2 where the vehicle endeavors to charge up a "piece" of an entire asteroid or the moon.)

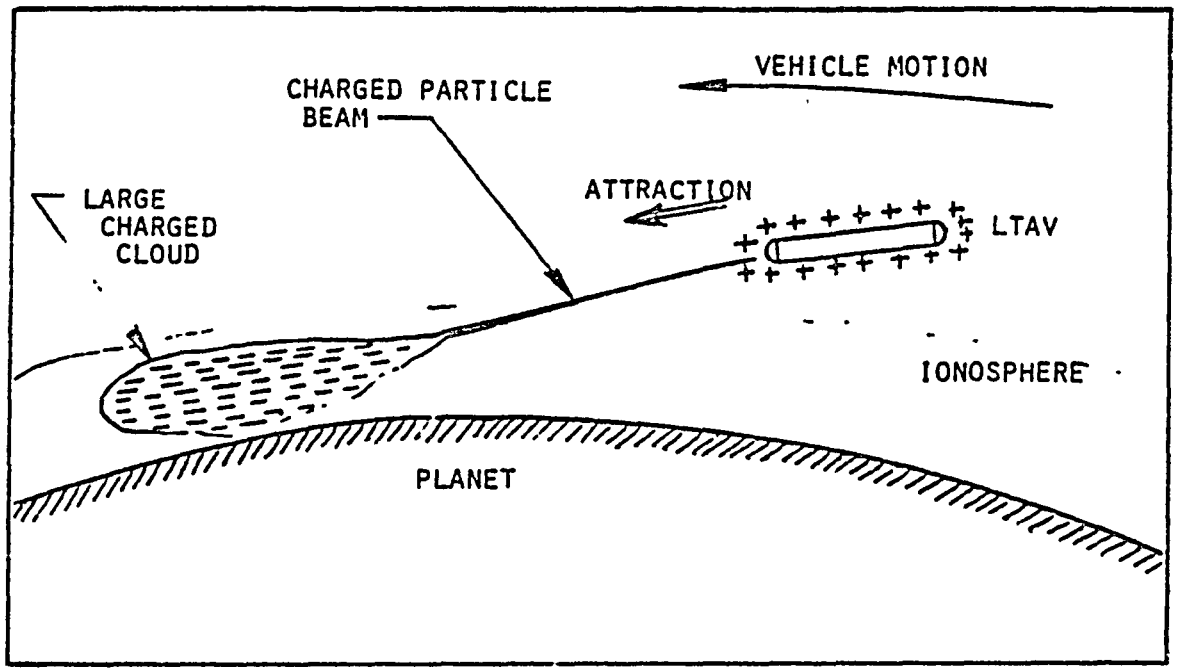

Figure XIII-11. Transatmospheric Electrostatic Propulsion Concept

REFERENCES FOR CHAPTER XIII

1. Barletta, W. A., "Charged Particle Beam Weapons," UCRL-87288, Lawrence Livermore Laboratory, Livermore, California, 9 December 1981.

2. Cook, J. C., "Electrostatic Lift for Space Vehicles," Fifth Symposium of Ballistic Missile and Space Technology.

CHAPTER XIV
MANNED SPACE BATTLE CRUISERS: NEAR TERM*

This chapter attempts to assess the state-of-readiness of multi-mode nuclear reactors for use in manned battle cruisers by the Space Command in the year 2000 or earlier. The hypothetical battle cruiser configuration in Figure XIV-1 is introduced to set the stage for subsequent discussions. This nuclear-powered vehicle would be equipped with a powerful free-electron laser, particle beam weapon, electromagnetic cannon (gun) and, possibly, microwave weapon. These weapons require high electric power, possibly in the range of tens of megawatts to a few gigawatts in a "burst" mode that may run from one to a hundred seconds in duration. Multi-mode nuclear reactors would provide not only primary high-thrust propulsion (as a nuclear rocket), but also peak electric "payload" power (generated in an open-cycle mode with MHD generators or turbogenerators) and low levels of stationkeeping electric power.

A. SPACE NUCLEAR POWER PLANT TECHNOLOGY

Military space weapons (e.g., free electron laser (FEL), neutral particle beam (NPBW), electromagnetic gun/cannon, and possibly microwave) will demand instant--i.e., within several seconds--delivery of hundreds to thousands of MWe which must be generated in the open cycle mode for the foreseeable future.[1,2] Required durations for peak power could range from several seconds to several hundred seconds, depending upon the weapon type and mission scenario.[1] To conserve precious onboard coolant, such multi-mode reactors must then flash back into closed-cycle operation for the removal of reactor decay heat--which will range from 3-4 percent reactor power for "burst" mode generation.[2]

The required levels of weapon peak electric power can be generated by fixed and rotating particle bed reactors--but not by the solid core

* This study was performed with support from the Defense Advanced Research Projects Agency under Contract No. DAAH01-80-C-1587 to the BDM Corporation.

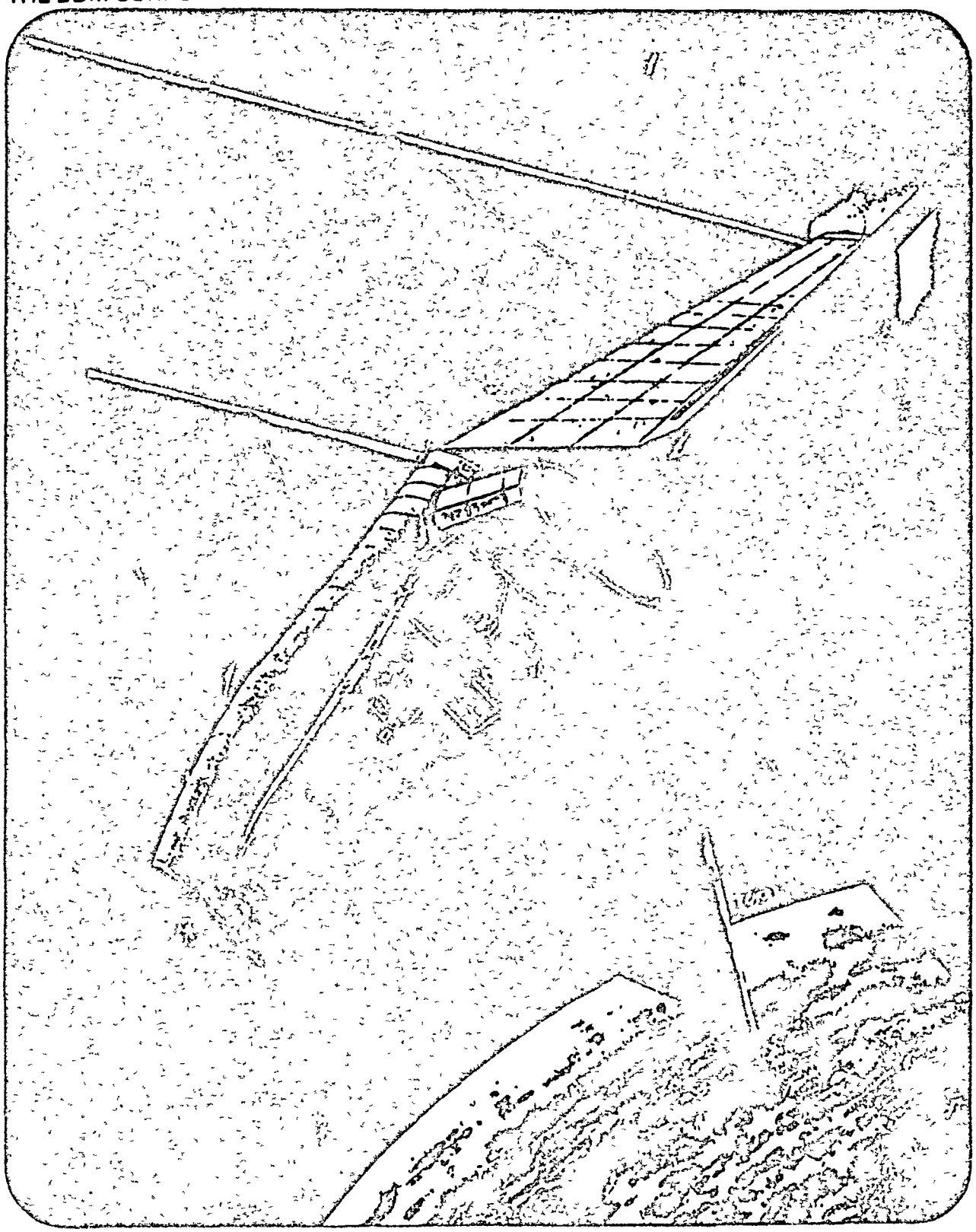

Figure XIV-1. Hypothetical Battle Cruiser Configuration (Artist: R. Carter)

reactors developed during the NERVA program.[2] High thermomechanically-induced stresses on solid core fuel elements during "burst-mode" high electric power generation will cause immediate core failure--unless large amounts of precious open-cycle coolant are ejected through the reactor and into space while slowly ramping the reactor power level up to peak weapon power, and then back down to stationkeeping power levels.[2]

For the sake of argument, let us assume the use of multi-mode, particle bed reactor power plants of the varities shown in Figure XIV-2 with a peak power level of 2500MW(th).* In the high-power mode, such a reactor could generate 1000MW(e) with advanced turbogenerators (Figure XIV-2B, ~40 percent enthalphy extraction), or 500MW(e) with MHD generation (Figures XIV-2A or XIV-2C, - 20 percent extraction). Following "burst" mode operation, the decay heat would reach 0.04 X 2500MW(th) or 100MW(th).

Compatible closed-cycle auxiliary (i.e., station-keeping) electric systems can exhibit 25-35 percent thermal-to-electric conversion efficiencies with Brayton or Rankine approaches. Hence, this decay heat could be used to generate 25MW(e) for housekeeping purposes. The most critical component in this conversion system is the space radiator: it must be lightweight and have a high survivability, in a military sense. Because of the large amounts of waste heat, the use of present radiator technology (e.g., heat pipe or finned-tube designs) could result in heat-rejection radiators being a major, if not dominant, mass component.

Also since the weapon systems themselves will be far from 100 percent efficient, waste heat rejection from these devices becomes a problem of paramount importance--largely because of the prodigious power levels. The only way to effectively cool these weapons during "burst" mode operation is with open cycle coolant--at very high flow rates. For example, to minimize electrical power requirements, the particle accelerators in FELs and PBWs will probably be maintained at cryogenic temperatures (e.g., 40 K). An effective coolant might be liquid hydrogen, since it would also be used as a propellant in the nuclear rocket thruster mode, i.e., for orbital

* The Nerva-1A was 1500MW(th); PEWEE, 514MW(th); Pheobus was planned for 4000-5000MW(th).

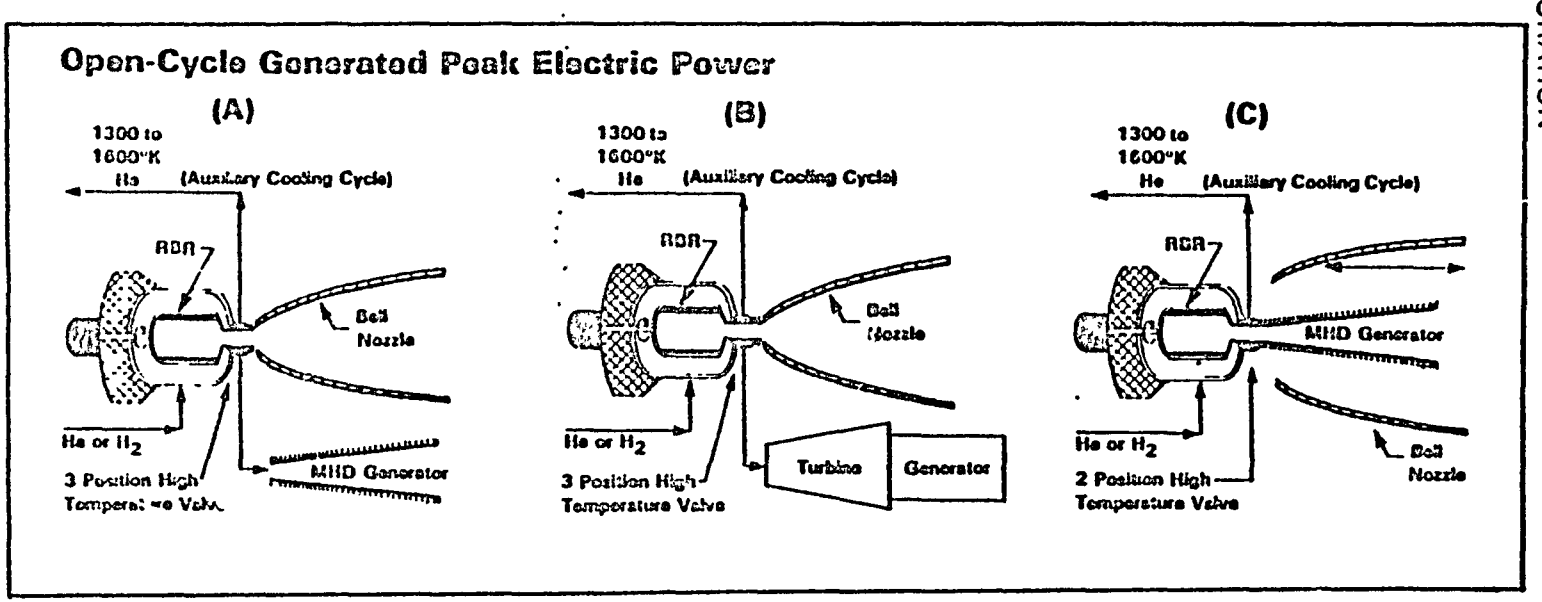

Figure XIV-2. RBR Concepts for Shared Power/Propulsion (From Reference 2)

transfer. Logically then, a battle cruiser must be equipped with a number of large volume cryogenic tanks containing LH_2 used for both propulsive and weapon applications. Finally, one would expect that the mass of tank insulation be traded off against the capacity of a cryogenic reliquifaction system running off stationkeeping power.

B. LIQUID DROPLET RADIATOR

The practicality of closed-cycle nuclear-electric stationkeeping systems can be greatly improved with the development of lightweight heat-rejection systems--such as the liquid droplet radiator (LDR) proposed by Mattick and Hertzberg.[3] The concept of a radiating particulate stream was first suggested by Hedgepeth and Knapp,[4] and has been the focus of substantial investigations at the Astro Research Corporation[5,6] and at the University of Washington.[3]

The key element of the LDR concept is, of course, the use of streams of liquid droplets to provide an enormous radiating surface area with a small amount of coolant mass. Herein lies the potential for reducing overall radiator system mass by an order of magnitude compared to finned tube or heat-pipe radiators. A wide variety of droplet materials (oils, eutectics, metals) are presently being investigated, and cover a wide range of operating conditions.

There are several other outstanding features to LDR systems. First, the systems can be easily packaged for earth-to-orbit launch, and facile deployment and retraction. Second, the droplet stream is immune to meteor damage and has a high survivability. It is also the only known radiator system that could be "hard" in the military sense. Clearly there are technology issues that might increase the risk of implementation of LDR systems, but the potential payoff is very high.

1. Major LDR Technical Issues

Several of these major technical issues can be enumerated as follows. The first relates to the technical challenge to be met in constructing the droplet generator. A very large number of orifices must be assembled into a distributed area "shower head" that is somehow able to

accurately direct hundreds of these streams into a droplet collector device located at a distance of tens of meters away. Active focusing of these streams may be required; electrostatic and electromagnetic techniques for accomplishing this are presently being explored.

The second issue relates to the problem of droplet stream collection by a physical device. A collector for liquid metals might take the configuration of a spinning funnel-shaped device with an anti-splash surface that throws collected liquid radially outward to a rim-located centrifugal pump. The collecting diameter may have to be 2 to 3 times larger than the focused droplet stream to collect inadvertant sprays resulting from pressure variations in the cooling system or from spacecraft motion. Sufficient fluid must always be present to prime the collector pump.

Another interesting approach can be taken with oil coolants, e.g., DOW 705. Minute (i.e., Angstrom size) magnetic particles can be emulsified in the oil coolant to form ferro-fluids. This approach enables magnetic field confinement and focusing of the droplet stream at the collector--thereby greatly reducing the specific mass of that component.

A third technical issue is related to the problem of droplet emissivity. Some researchers are quite concerned about the low values of emissivity for uncoated tin, lithium or eutectic droplets. Carbon coating of metal droplets presently appears unlikely, and recent preliminary calculations indicate that the available emissivities of metal droplets may result in total LDR radiator weights which exceed that for heat pipes. Also, a principal concern is the mass of liquid metals which must be carried in the cooling system.

It is clear that highly doped oils will be a favored, high emissivity LDR coolant for lower radiated power levels. Although operating temperatures are substantially lower than metals, oils do hold the promise for increasing the cycle efficiency of auxiliary space-based heat engines.

There is generally high confidence that all of the foregoing problems are solvable within a 3 to 4 year time frame.

2. Triangular LDR Configuration

As displayed in Figure XIV-3, a 60° equilateral triangle LDR configuration is chosen for this battle cruiser study. The droplet collector

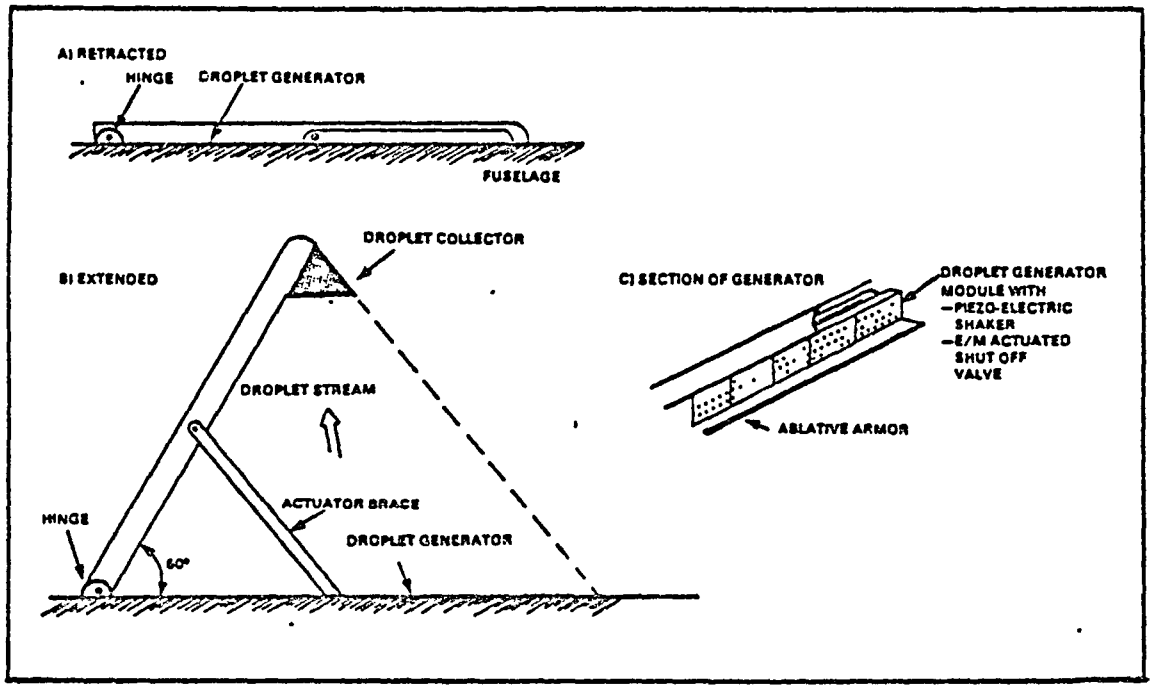

Figure XIV-3. Chosen Liquid-Droplet Radiator (LDR) Configuration

is hinged in order to retract into the spacecraft fuselage during earth-to-orbit launch. The generator itself is rigidly mounted to the spacecraft, and is divided into a large number of droplet generator modules; each has its own piezo-electric shaker and an electromagnetically activated shut off valve--in order to insure redundancy, graceful degradation, and high survivability of this critical element. Each reactor would be furnished with one triangle radiator, sized to absorb the peak reactor decay heat. As the reactor power is scaled back to zero, the droplet generator modules on each triangle radiator would be sequentially shut off until the whole radiator was completely inoperative--then the generator arm could be retracted. Hence, in operation, the coolant delivered to each droplet generator module can be held to a constant temperature, and would not "freeze out" before reaching the collector.

Figures XIV-4 and XIV-5 from Reference 7 give the size of triangular-geometry LDRs as a function of radiated power at various peak coolant temperatures--for tin and o , respectively. Figures XIV-6 and XIV-7 (also from Reference 7) present coolant evaporation losses as a function of initial droplet temperature.

C. SPACE COMMAND BATTLE CRUISER

1. Hypothetical Spacecraft Configuration

Figure XIV-8 portrays top, side and rear-end views of a hypothetical Space Command battle cruiser based on the use of three multi-mode nuclear reactors and liquid droplet radiators. The overall size of the spacecraft can be appreciated by comparing it to the scale of a docking space shuttle orbiter. The 150 m length of the battle cruiser is comparable to that of the nuclear-powered "Discoverer" (200 m long) used for voyages to the outer planets in the film "2001." The Discoverer is shown in Figure XIV-9.

The multi-mode powerplants (shown in Figure XIV-10) incorporate the rotating bed particle reactor design. Each develops 2,500 MW(th) and has its own 100 MW(th) LDR with closed-cycle conversion system. The high temperature, liquid metal LDRs are 100 m on a side. Referring to

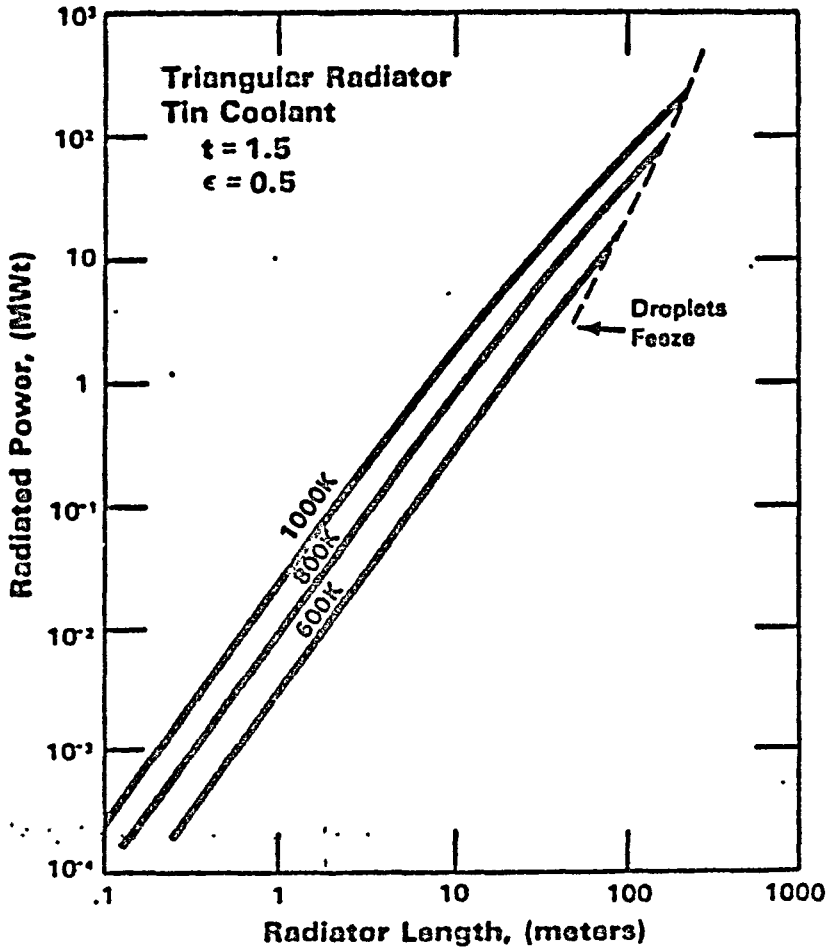

Figure XIV-4. Liquid Droplet Radiator Size vs. Radiated Power: Tin (From Reference 7)

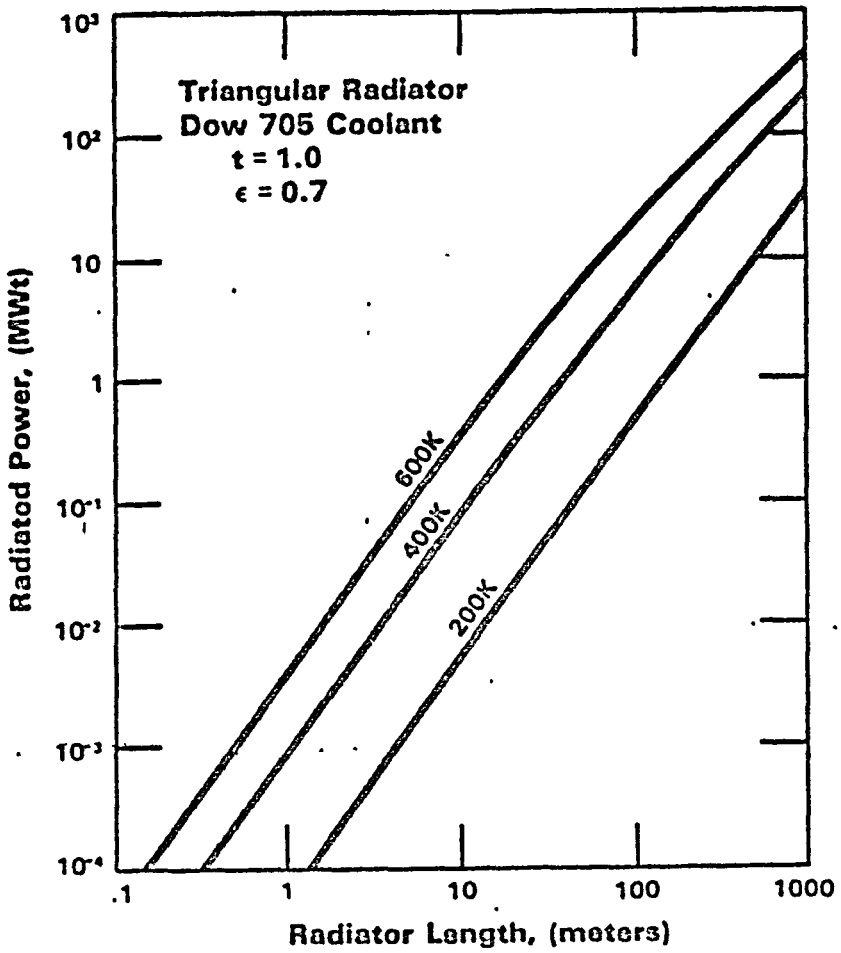

Figure XIV-5. Liquid Droplet Radiator Size vs. Radiated Power: Oil (From Reference 7)

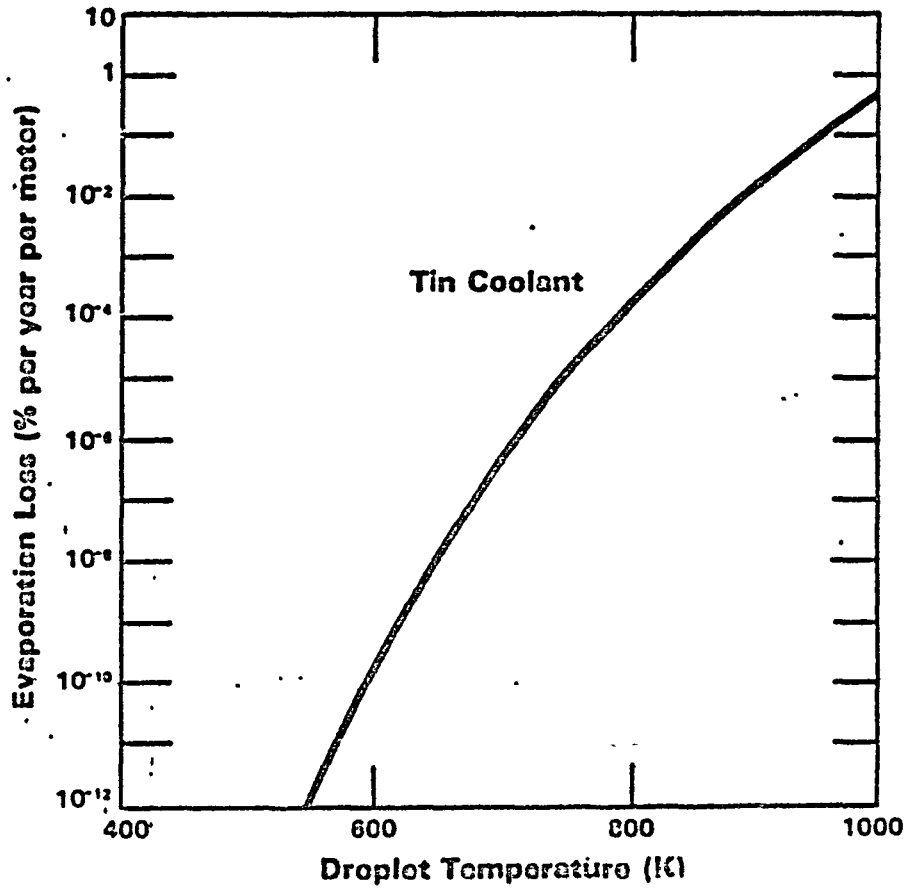

Figure XIV-6. Evaporation Loss From Liquid Droplet Radiator: Tin (From Reference 7)

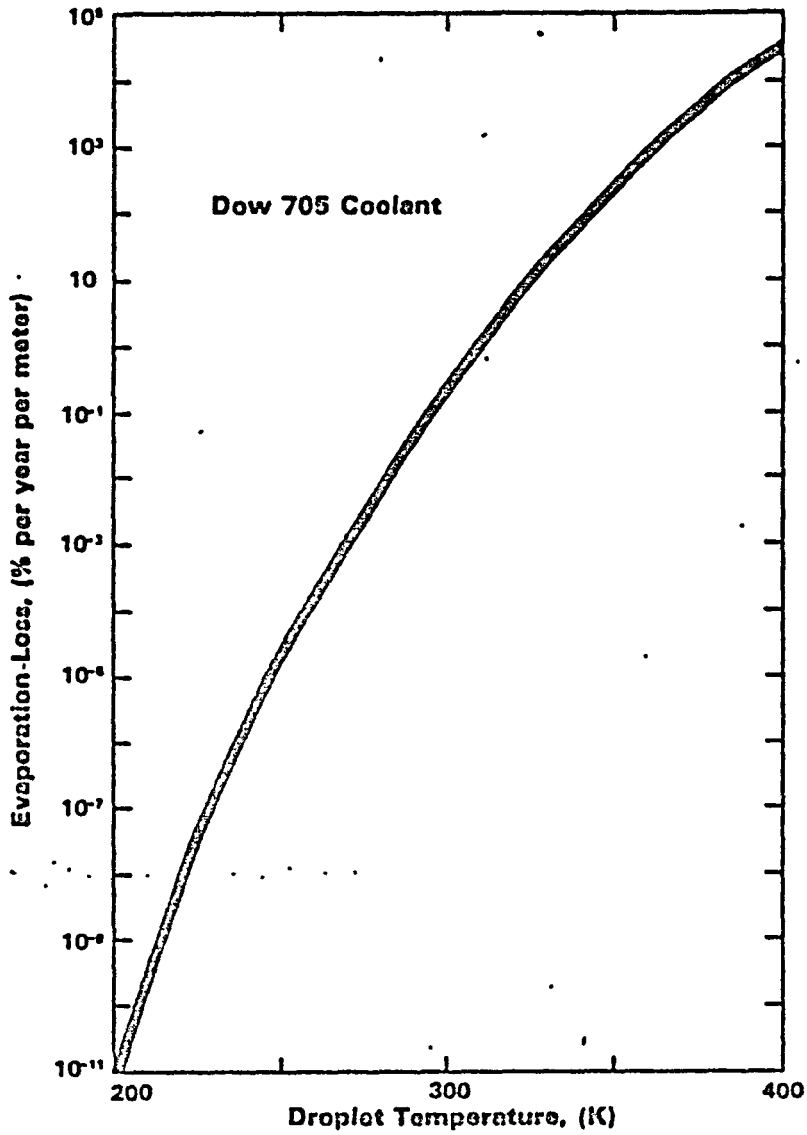

Figure XIV-7. Evaporation Loss From Liquid Droplet Radiator: DOW 705 (From Reference 7)

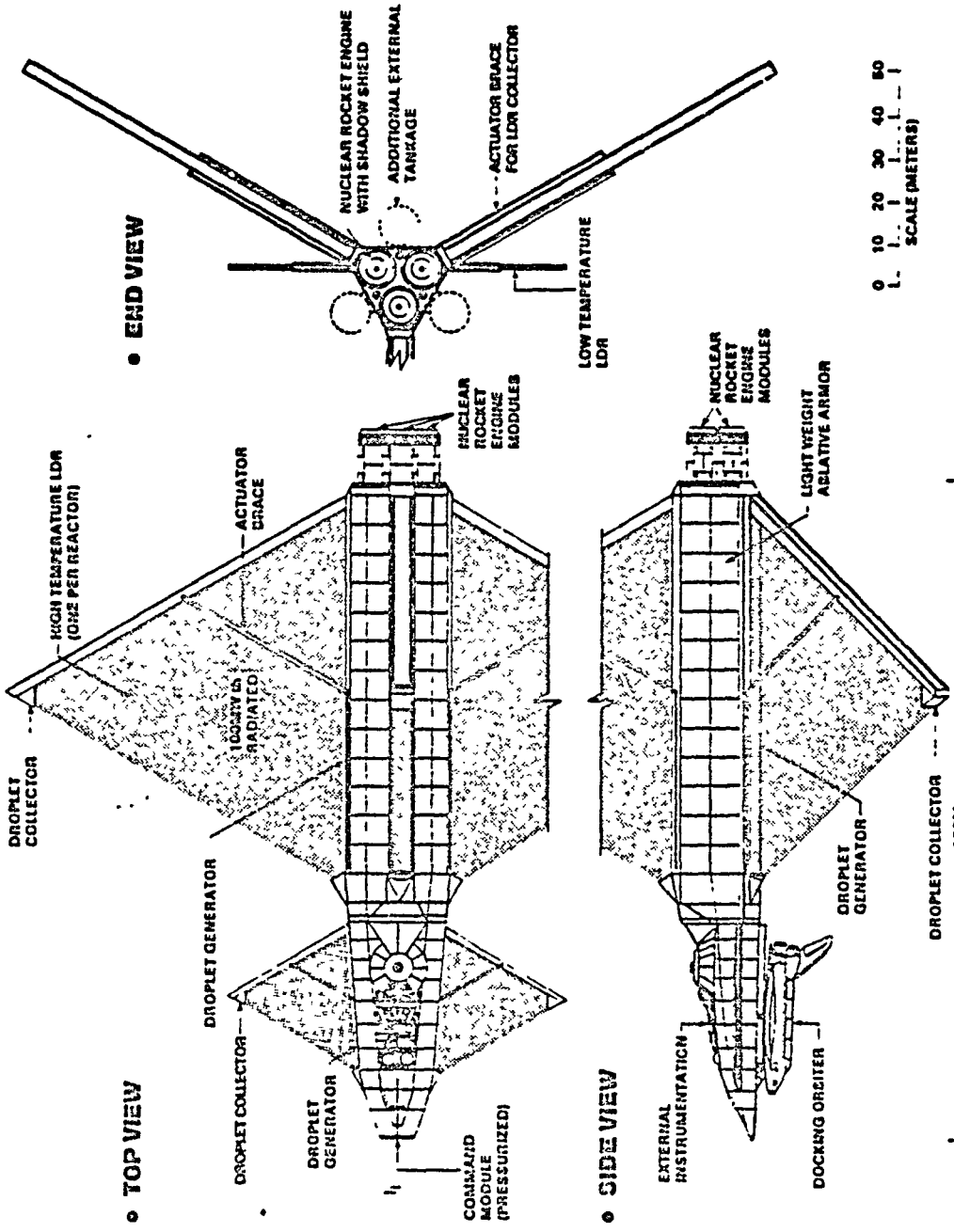

Figure XIV-8. Manned Space Battle Cruiser: Post 2000 Era

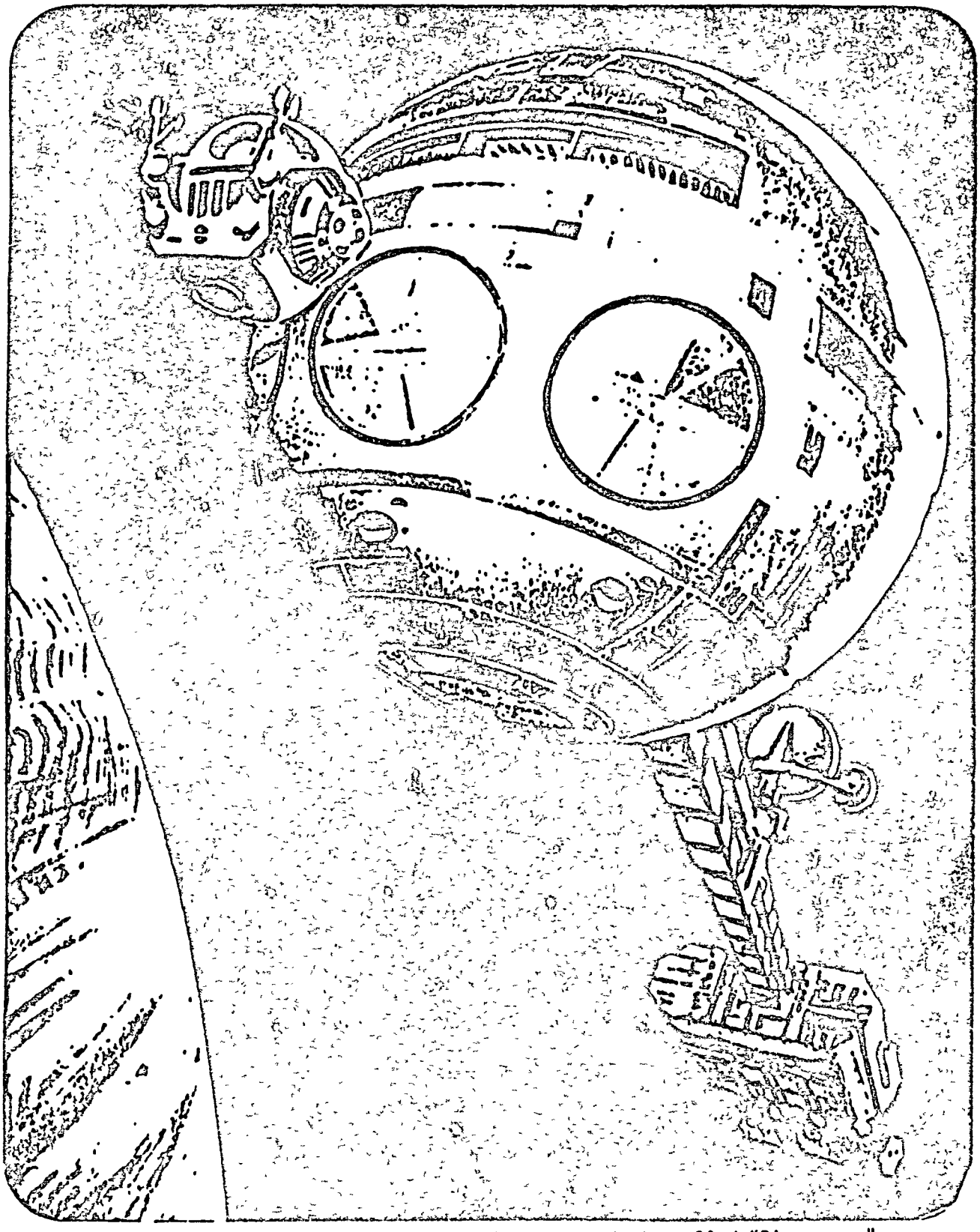

Figure XIV-9. The 200m Long Nuclear-Electric Propelled "Discoverer" From the Film "2001" (From Reference 9)

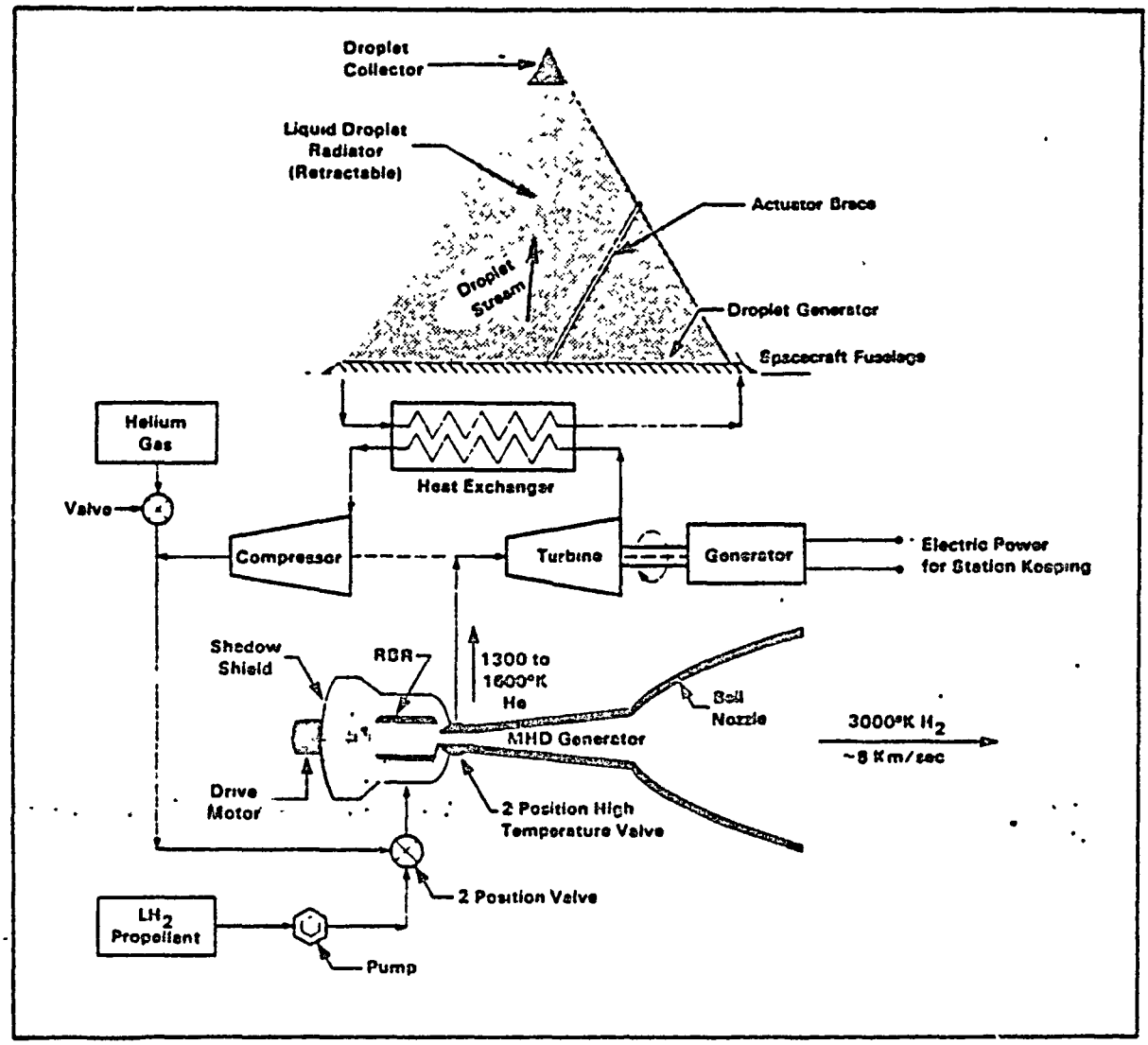

Figure XIV-10. Multimode RBR Powerplant for Battle Cruiser

Figure XIV-4, we find that if tin is used as the coolant, the peak temperature must be 1000°K. (This calculation assumes a droplet sheet emissivity of 0.5.)

The three multi-mode power plants could put out a combined total of 75 MW(e) in the auxiliary closed-cycle mode. Besides satisfying "housekeeping" power needs, it could be used by auxiliary electric propulsion engines for maneuvering and orbit-raising.

As indicated in Figure XIV-11, the high-temperature LDRs are mounted to the aft 100 meters of the 150 m long spacecraft. Housed within that 100 m long cavity are six LH_2 cryogenic ET tanks. These fuel tanks and the multi-mode reactor powerplants (with shadow-type radiation shields) are joined together with space-frame trusses, and protected with lightweight ablative laser-countermeasure "armor."

2. Manned Element

The forward-most 50 m of the spacecraft is a pressurized manned "command module," which has its own 40 m long LDR's for environmental temperature control. If ferrofluids are used (i.e., iron pigment in DOW 705), the two LDR's could reject 2 MW(th) waste heat with a peak coolant temperature of 400 K (127°C).

As indicated in the cutaway view (Figure XIV-11), the "command module" is separated from the aft "propulsion" module with a secondary radiation shield. The command module contains two "bridges": A 1-G twenty meter diameter centrifuge (see Figure XIV-12 for a cutaway view), and a smaller heavily shielded area used during PBW or FEL operation. This forward-most "bridge" is massively protected against a worst case accident with the PBW, wherein the beam is misdirected back at the crew. The total thickness of this shield is calculated on the basis of the maximum dose which could be accumulated before the PBW is automatically shut down.

Radiation environments for an exemplary PBW and FEL have been calculated, and can be reduced to acceptable levels with proper shielding design.[8] During PBW operation, all the crew must be moved to the heavily shielded forward "bridge." (However, for FEL operation, the radiation shield at the aft end of the command module might be sufficient.) One must

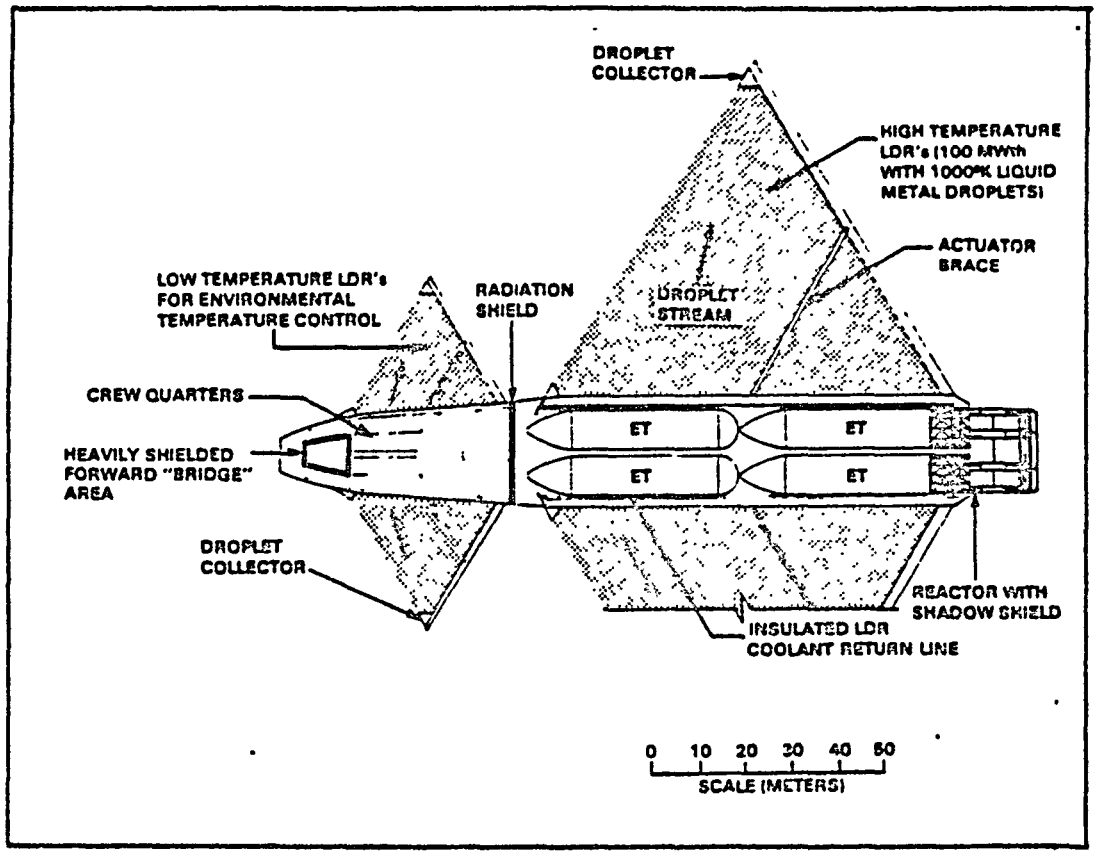

Figure XIV-11. Cutaway View of Space Battle Cruiser

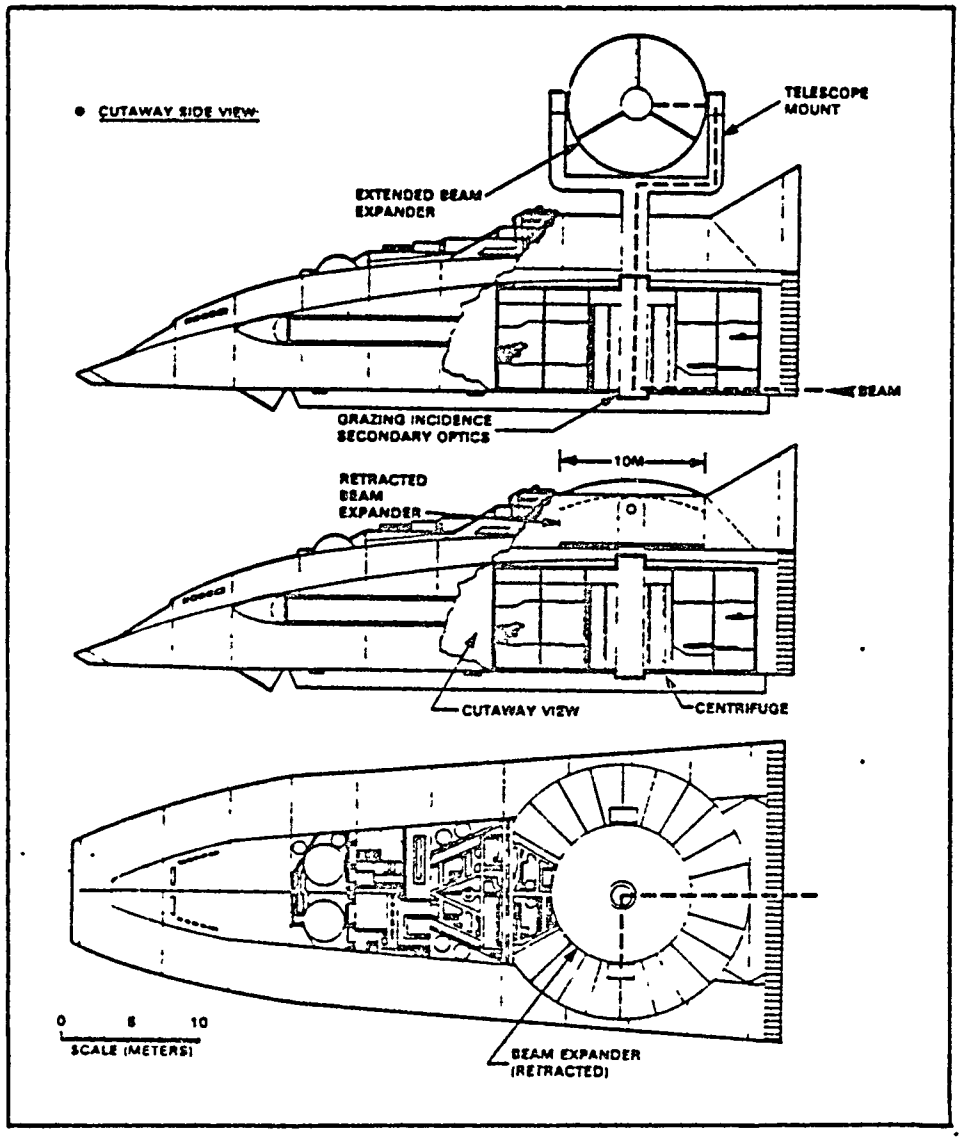

Figure XIV-12. FEL System Integration: Telescope

be careful to include considerations of "radiator shine": i.e., radiation that is scattered off the liquid metal droplet generators and off the droplet stream itself. Finally, the multi-mode reactors must be mounted to short structural booms extended aft of the locations as portrayed in Figure XIV-11, and equipped with large angle shadow shields that keep the 60° droplet generators within the "cone of radiation protection."

3. Weapon System Integration

Figure XIV-13 indicates how a free electron laser weapon might be integrated with the exemplary battle cruiser configuration. Viable accelerator options include the RF LINAC, storage ring, and induction LINAC varieties. Accelerators would be positioned between the LH_2 tanks, and removed as far as possible from the command module. The FEL wiggler magnet would be located at the midpoint between the aft end of the vehicle and the telescope, where grazing incidence optics are used to form a resonator cavity. A 10-12 meter final beam expanding mirror (with "hardened" back side) is designed to be retractable--to protect the delicate high-reflectivity, multi-layer film coating from nuclear detonations (E/M pulse threat).

The accelerator and optics for a neutral particle beam weapon would also be located between the LH_2 tanks. The NPBW final output optics would project the beam in the aftward direction, away fromm the crew.

Figure XIV-14 relates E/M gun projectile velocity to accelerator rail length for several realistic rates of acceleration (15,000 to 50,000 G's)--as shown in comparison with battle cruiser overall dimensions.

4. Launch and Assembly in Orbit

The battle cruiser is designed to be boosted piecemeal from the Earth's surface, then assembled in orbit. Major spacecraft components are designed with aerodynamically smooth contours to facilitate the boost to orbit: e.g., the entire 50 m long forward command module (Figure XIV-12), and the shuttle external tanks (Figure XIV-15).

As indicated in Table XIV-1, the existing shuttle propulsion system can deliver 104.3 tons to low earth orbit (LEO); other shuttle-derived vehicles have been proposed for boosting 140 to 200 tons in a

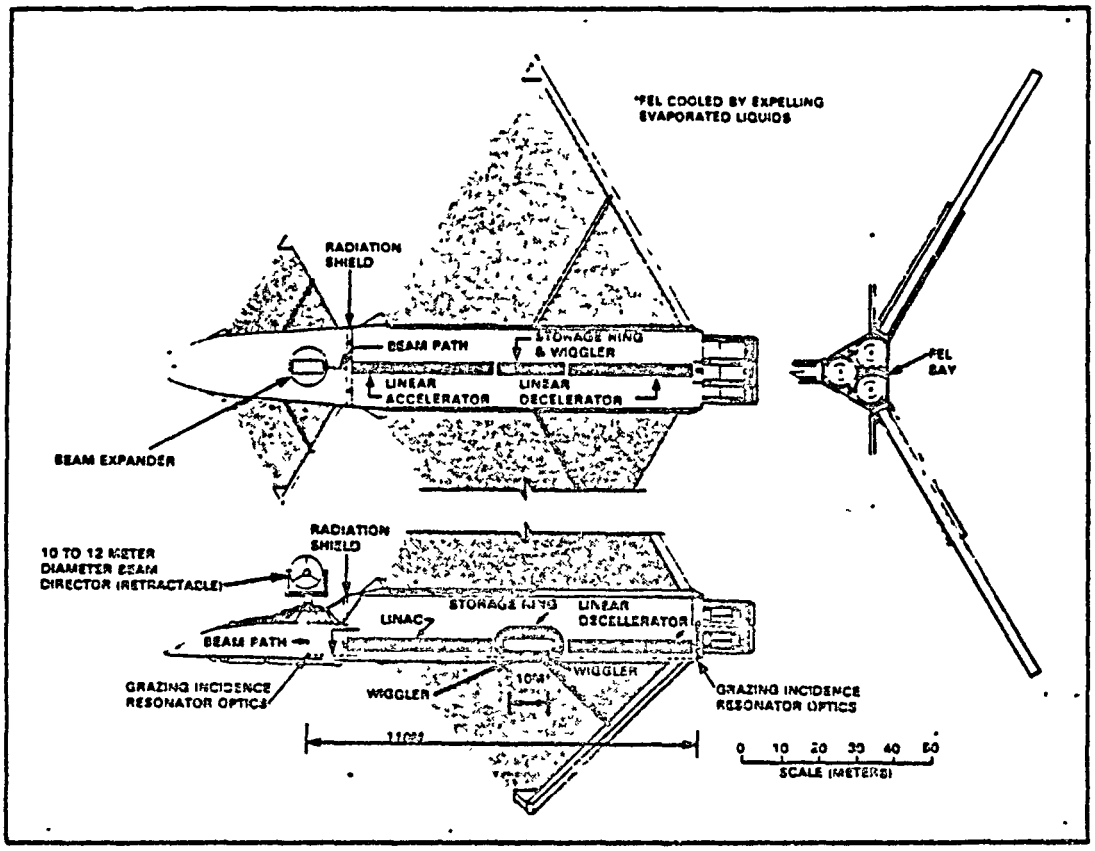

Figure XIV-13. FEL System Integration: Accelerator Alternatives

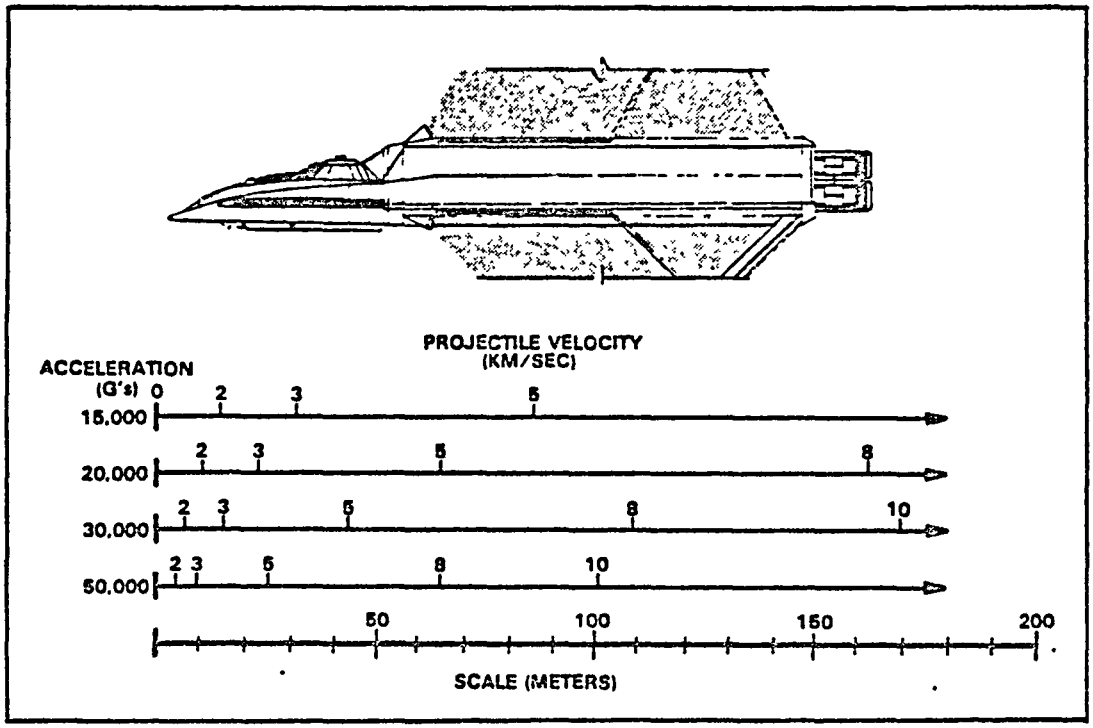

Figure XIV-14. EM Gun Length

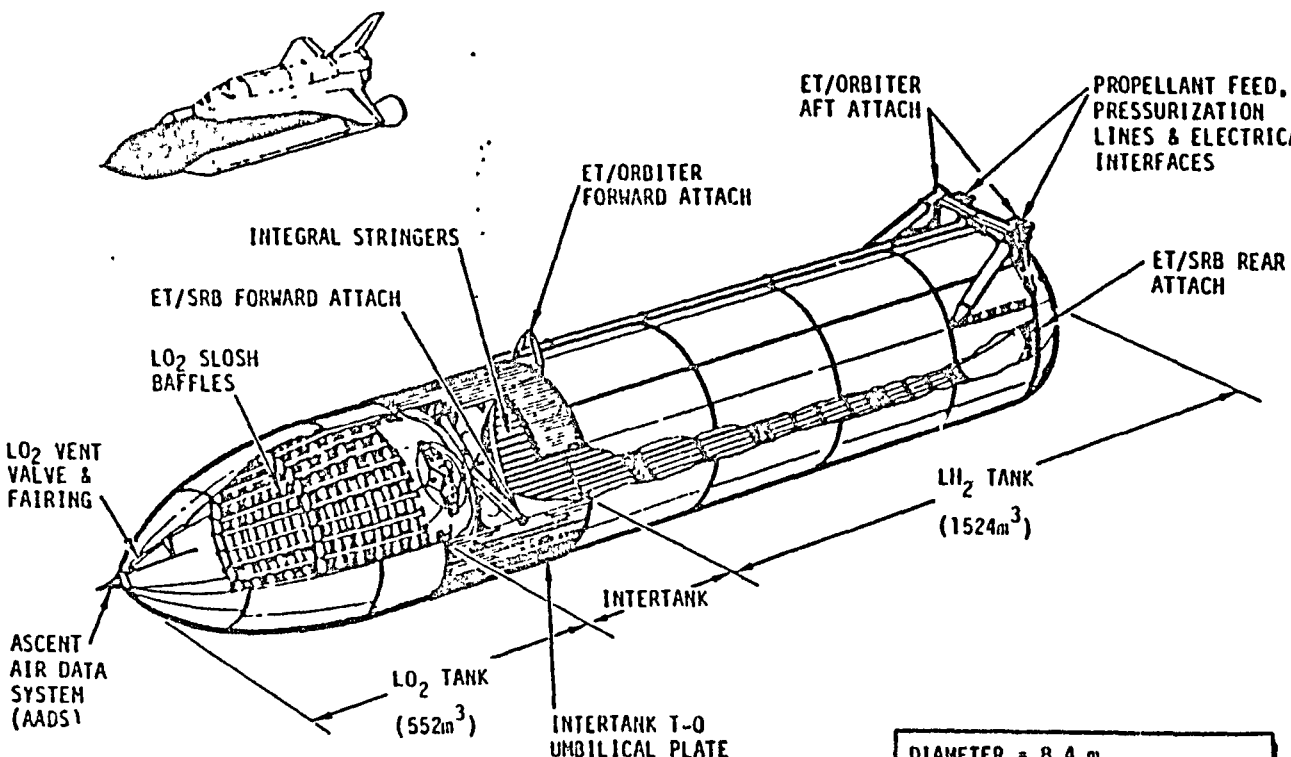

* IF FILLED COMPLETLY WITH H_2, CAN HOLD 138 TONS

** THE ET IS COVERED WITH A PROTECTIVE INSULATION THAT WILL ENSURE THE SUPERCOLD FLUIDS INSIDE REMAIN IN THE LIQUID STATE

Figure XIV-15. External Tank

TABLE XIV-1. SHUTTLE ORBITER DATA*

COMPONENT	MASS (METRIC TONS)
SSME ENGINES	9.25 T
THERMAL PROTECTION	7.26 T
BARE ORBITER	58.32 T
MAXIMUM PAYLOAD	29.50 T
SUBTOTAL	104.3 T
FUELED MAIN TANK	756. T
SOLID PROPELLANT ROCKETS	1179. T
LAUNCH MASS	2039. T

EMPTY ET TANK = 35.4 T
LIGHT WEIGHT ET TANK = 32.2 T
*NASA SHUTTLE PUBLIC AFFAIRS OFFICE, 4-20-82.

single package. Hence to use existing shuttle propulsion technology, the forward command module must be lightweight-designed for 100 tons at lift-off. It is possible that additional fuel could be temporarily carried within internal compartments of the "command module," and that additional SSME engines be added to its aft bulkhead as required for the boost to LEO. The launch configuration for such a scheme is portrayed in Figure XIV-16. Once in orbit, the rest of the internal equipment, radiation shields, and external hardware would be installed on the "command module."

It is presently known that by accepting a 5 percent payload reduction in the shuttle orbiter (i.e., 1.5 tons), the empty shuttle external tank (ET) could be flown into orbit. Therefore, empty LH_2 tanks could be "purchased" by the miltiary at a good price (i.e., from flights largely paid for by others), then incorporated into the battle cruiser as is, or with just the aft LH_2 tank. The first option entails the use of 6 ETs for the battle cruiser. The latter, which requires 9 tanks, discards the 552 M^3 LO_2 tank and intertank T-0 umbilical plate.

Note that if filled entirely with LH_2, the shuttle ET tank can contain 138 tons. Future lightweigh versions of the ET tank are expected to weight 32.2 tons; this would represent a tankage penalty of 23.3 percent. By using only the aft 1524 m^3, the tankage penalty can probably be reduced to 15-20 percent. Advanced cyrogenic tankage designed especially for the space cruiser (and not having to survive a 10 G launch environment when filled to capacity) could probably attain 10 percent. Although battle cruiser acceleration performance could be maximized by use of the lightest weight tank, its "hardness" to attack can be expected to suffer.

Figure XIV-17 portrays a military hanger in low earth orbit, built for the purpose of constructing space battle cruisers.

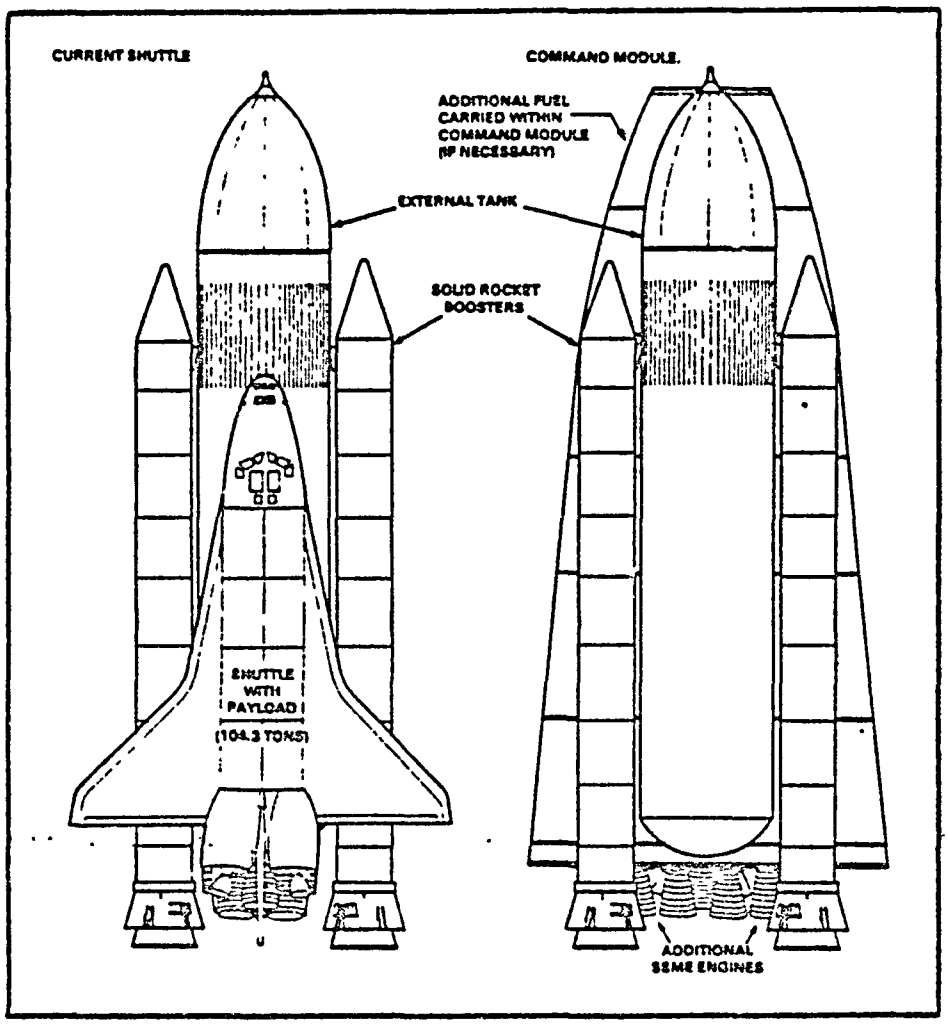

Figure XIV-16. Command Module Launch Configuration

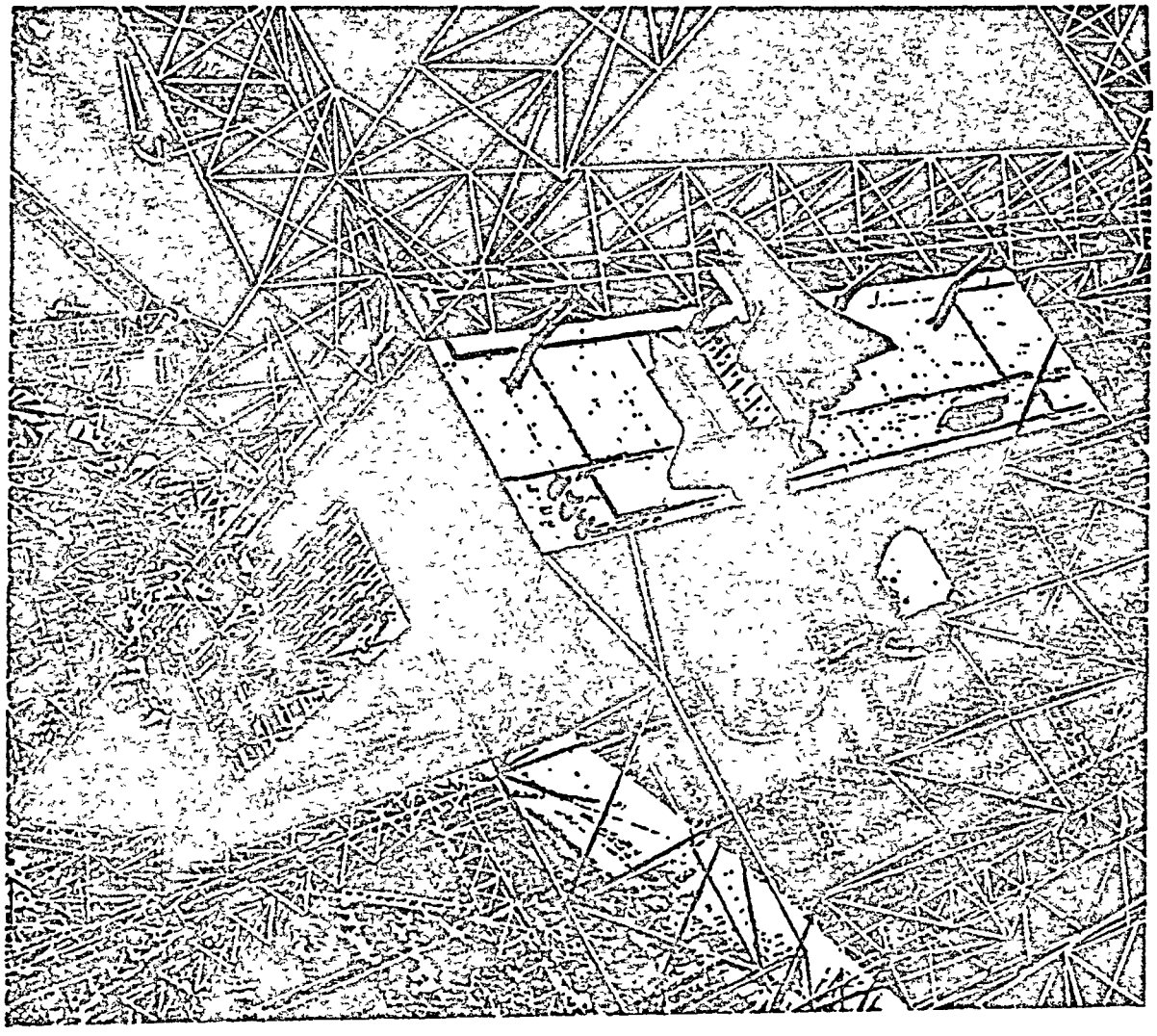

Figure XIV-17. Military Hanger for Space Construction of Battle Cruiser (From Reference 10)

REFERENCES FOR CHAPTER XIV

1. Powell, J. R. Botts, T. E., and Myrabo, L. N., "Advanced Reactor Designs for High Power Generation", presented at the Symposium on Advanced Reactor Systems, NRC, Washington, DC., 15-17 November 1982.

2. Myrabo, L. N., Stickley, C. M., Powell, J. R., and Botts, T. E., "Space Nuclear Prime Power and Propulsion", BDM/W-83-114-TR, The BDM Corporation, McLean, VA, January 1983.

3. Mattick, A. T. and Hertzberg, A., "Liquid Droplet Radiators for Heat Rejection in Space," presented at the 15th Intersociety Energy Conversion Engineering Conference (AIAA operated), Seattle, Washington, 18-22 August 1980.

4. Hedgepeth, J. M. and Knapp, K., "Preliminary Investigation of a Dust Radiator for Space Power Systems", ARC-TN-1054, Astro Research Corporation, 1 March 1978.

5. Knapp, K., "A Parametric Study of Liquid-Droplet Stream Radiators," ARC-TN-1095, Astro Research Corporation, 10 December 1980.

6. Knapp, K. K., "Lightweight Moving Radiators for Heat Rejection in Space," AIAA Paper No. 81-1076, AIAA 16th Thermophysics Conference, Palo Alto, California, June 23-25, 1981.

7. Myrabo, L. N., Stickley, C. M., and Meth, S., "Analysis of RBR/FBR Mission Applications", Volume 1, BDM/W-2755-82-S, The BDM Corporation, McLean, Virginia, 28 October 1982.

8. Knowles, H. B., "Direct Shielding Calculations," Internal BDM Memorandum, The BDM Corporation, McLean, Virginia, 7 May 1982.

9. Aldiss, B., Compiler, Science Fiction Art, Bounty Books, NY, 1975, p. 121, (front cover illustration for Science Fiction Monthly, Vol. 1, No. 1).

10. Schefter, J., "Giant Structures - How We'll Build Them", Popular Science, Vol. 214, No. 3, March 1979, p. 79.

CHAPTER XV
INTERPLANETARY CARRIERS: FAR TERM

A. INTRODUCTION

Since powerful advanced electric power plants are an "a priori" part of most currently envisioned large manned interplanetary vehicles, a most attractive alternative use of this power would be to remotely propel shuttlecraft to and from the planetary surface. Such shuttles, powered by laser or microwave energy, can be designed to use the atmosphere to advantage (i.e., by momentum exchange) and thereby out-perform conventional rocket-powered shuttles. From an integrated systems standpoint, the beamed-energy dependent shuttle would appear to be the most energy and fuel efficient transport--necessitating the least power plant redundancy in interplanetary missions. The logistics of such a system is explored in this chapter.

Also, the availability of a powerful electric power plant has other implications for extraterrestrial propellant resupply in advanced manned missions. As pointed out by Heppenheimer,[1] converting water to hydrogen propellant at the landing site offers a potential means to keep down the size of interplanetary spacecraft, and permits mission operations out to Jupiter's system. This hydrogen could be used both by the interplanetary vehicle as well as by single-stage-to-orbit (SSTO) shuttlecraft.

B. BEAMED-ENERGY TRANSMISSION NETWORK

Figure XV-1 is a schematic diagram of a beamed-energy network for a large-scale manned planetary expedition. Orbital laser or microwave power is beamed to MFG shuttlecraft either a) direct from mammoth interplanetary carriers, or b) first bounced off a relay satellite. Clearly, power could also be beamed direct from the interplanetary carrier vehicle to L/S craft.

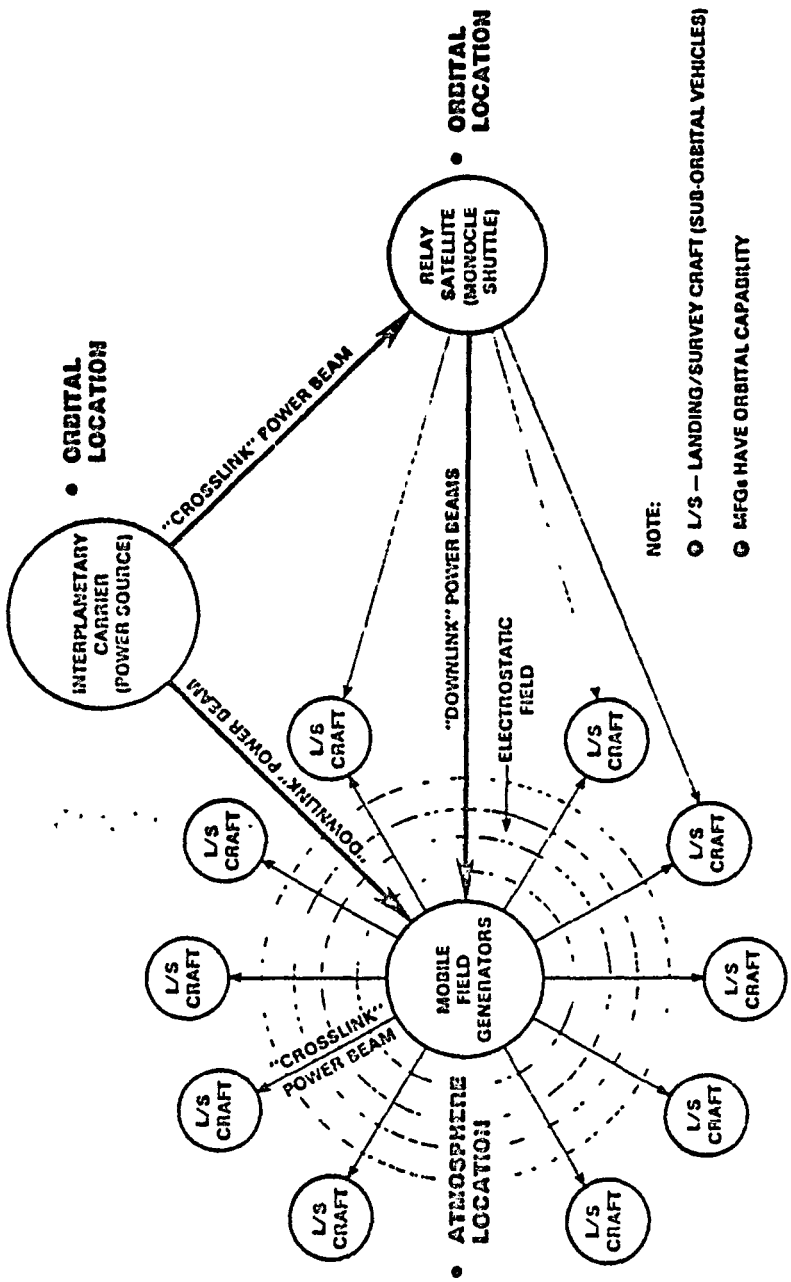

Figure XV-1. Beamed-Energy Network for Large-Scale Planetary Exploration Mission

1. Relay Satellite Stations

These self-propelled (or laser-propelled) relay satellites would be deployed in great numbers about the destination planet, enabling the interplanetary cruisers to beam laser power to shuttlecraft or MFG carrier vehicles located anywhere around the entire globe. The "Monocle Shuttle", described in Chapter X is an example of such a relay station for laser frequencies.

2. Mobile Field Generator (MFG) Shuttlecraft

After placing relay satellites in appropriate orbits, the interplanetary cruiser would deploy large SSTO shuttlecraft to the planet surface. These Mobile Field Generator (MFG) vehicles are designed to float, neutrally-buoyant, in the dense low-altitude atmosphere. The primary function of MFG vehicles is to carry numerous smaller landing/survey (L/S) craft, which do not have SSTO flight capability. Next the SSTO shuttle, acting as a "mobile electrostatic field generator", would artificially charge up a portion of the planet's atmosphere (as shown in Figure XIII-1), then deploy the L/S craft to fly on this field--in order that they may conduct their explorations largely from the air.

The MFG shuttlecraft are envisioned as lighter-than-air vehicles (LTAV) of the variety described in Chapter XII, equipped with aerial docking and interior storage (i.e., hanger) provisions for L/C craft. Figure XV-2 is an artist concept of a MFG carrier, deploying L/S craft.

When the decision is made to return to the interplanetary cruiser, the L/C craft would be gathered up and the MFG carrier vehicle would be boosted back into orbit on laser power beamed from the interplanetary cruiser.

3. Landing/Survey (L/S) Craft

The L/S craft could be either of the heavier-than-air or lighter-than-air variety. They could either a) fly on large electrostatic fields generated by artificial atmospheric charging (i.e., the MFG carrier vehicle function), as introduced in Chapter XIII, or b) fly with laser-thermal or laser-electric engines of the types described in Chapters IV - IX. These craft would be designed for efficient atmosphere-based, planetary exploration, and would not have SSTO capability.

Figure XV-2. MFG "Carrier" Vehicle, Deploying Shuttlecraft (Artist: R. Carter)

4. Interplanetary Spacecraft

Figure XV-3 portrays the essential features of an interplanetary spacecraft suitable for large scale solar system expeditions. It is modeled after the cylindrical geometry of 10 km long O'Neill Model 3 space colonies,[2] and would contain superior space laboratory and observatory facilities. (The laser power-beaming mirror might be shared for space telescope applications.) An advanced gas core reactor, fusion, or matter-antimatter anihilation power source would produce prodigeous levels of electricity for use in power beaming or electric propulsion engines. Propellant and tankage are placed between the reactor and the manned portions of the cruiser to reduce the radiation exposure. MFG shuttlecraft would occupy the space between propellant tanks and the 1-G centrifuge crew compartment.

The interplanetary cruiser would be kept in high orbits around the destination planet and would never venture into the planetary atmosphere; it would not have SSTO capability.

The exterior contours of the interplanetary cruiser would be smoothly rounded, so that it could be charged up to a very high potential. By this means, large numbers of "escort" shuttlecraft may be propelled great distances from the cruiser electrostatically, using the cruiser as the reaction mass as shown in Figure XV-4. This would also enable the interplanetary cruiser to provide an electrostatic tractor field for escort "fighters". (The concept is similar to that introduced in Reference 3 where the vehicle endeavors to charge up an entire asteroid or the moon.)

Finally, we note that the laser-power beaming equipment may be used for self-protection of the interplanetary cruiser. High velocity astronomical threats (e.g., meteorites, etc.) may be vaporized, fractured into small pieces, or laser-propelled away to avoid the danger of impacting the vehicle. "Monocle" fighting-mirror escorts could provide the function of re-focusing the cruiser's laser beam, thereby greatly increasing the lethal range.

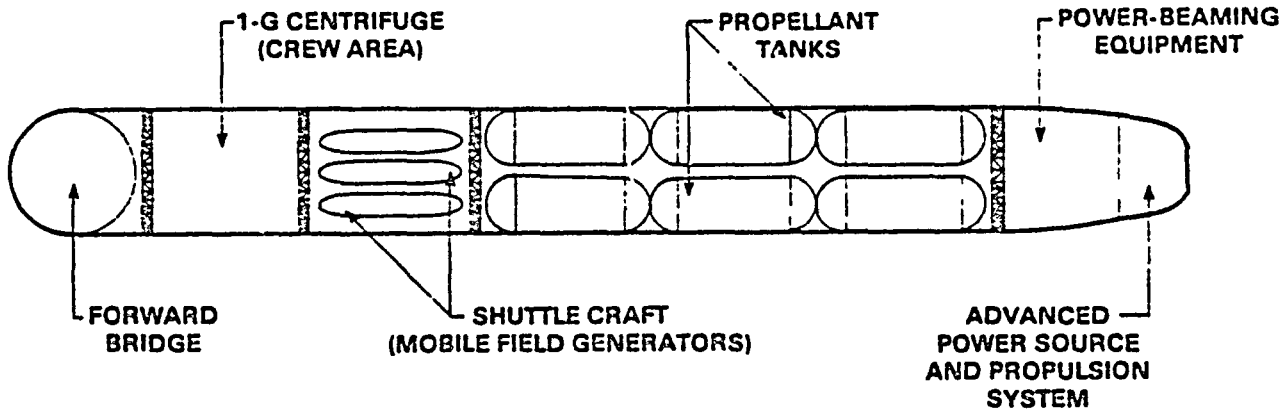

Figure XV-3. Schematic Diagram of Interplanetary Carrier

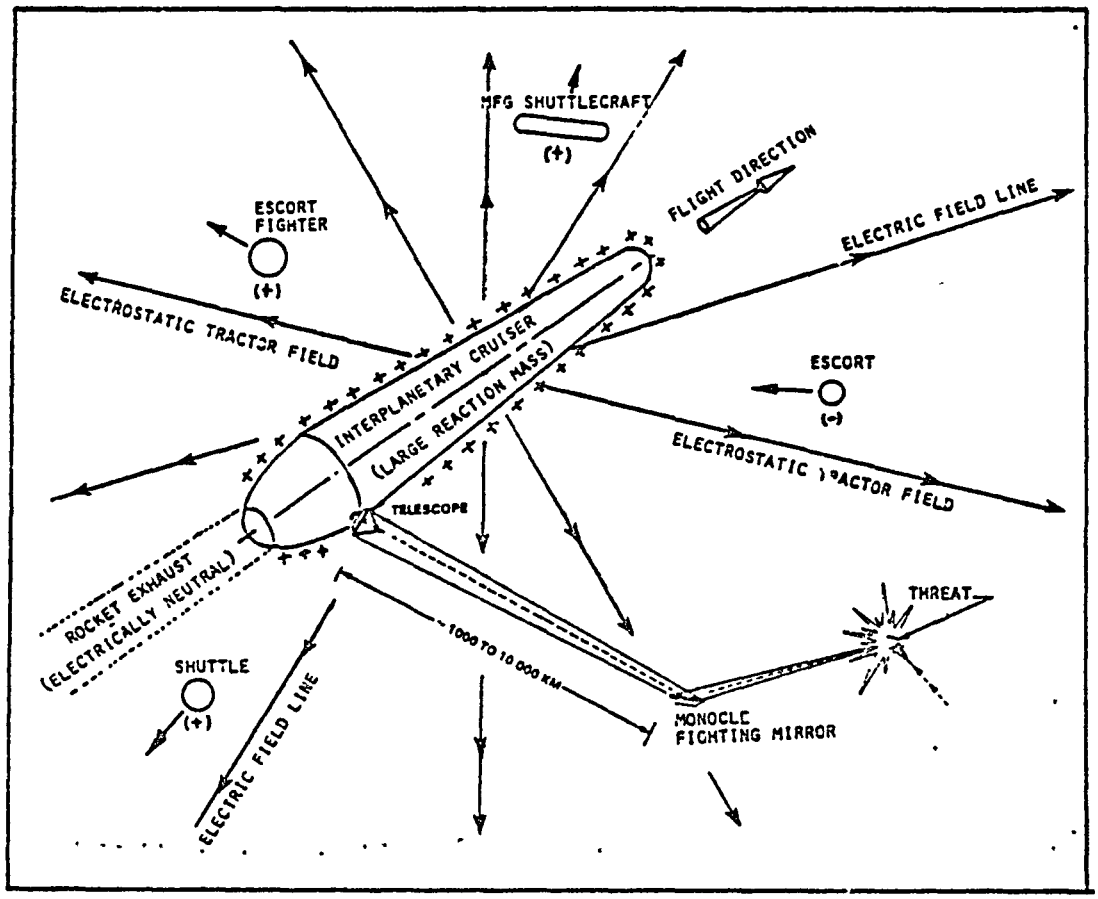

Figure XV-4. Interplanetary Carrier Provides Reaction Mass and "Electrostatic Tractor Field" For Escort Shuttlecraft

This Page Intentionally Left Blank

REFERENCES FOR CHAPTER XV

1. Heppenheimer, T. A., "Extraterrestrial Propellant Resupply for Advanced Manned Missions", Astronautics and Astronautics, November 1972, pp. 60-67.

2. O'Neill, G. K., "The Colonization of Space", Physics Today, Volume 27, No. 9, September 1974, pp. 32-40.

3. Cook, J. C., "Electrostatic Lift for Space Vehicles" Fifth Symposium on Ballistic Missile and Space Technology, pp. 203-239.

APPENDIX A

BIBLIOGRAPHY ON BEAMED-ENERGY PROPULSION

Compiler: L. N. Myrabo, Ph.D.

APPENDIX A

BIBLIOGRAPHY ON BEAMED-ENERGY PROPULSION

Willinski, M. I., "Beamed Electromagnetic Power as a Propulsion Energy Source", AMERICAN ROCKET SOCIETY JOURNAL, Vol. 29, Aug. 1958, pp. 601-603.

Marx, G., "Interstellar Vehicle Propelled by Terrestrial Laser Beam", NATURE, Vol. 211, 2 July 1966, pp. 22-23.

Redding, J. L., "Interstellar Vehicle Propelled by Terrestrial Laser Beam", NATURE, 11 Feb. 1967, pp. 588-589.

Forward, R. L., "Ground Based Lasers for Propulsion in Space", Hughes Research Laboratories internal paper, Malibu, CA, 19 May 1967.

Bonneville, J. M., "Propulsion Assisted by Microwave Power," The Journal of Microwave Power, Vol. 3, No. 4, December 1968, pp. 187-193.

McLafferty, G. H., "Laser Energy Absorption in the Exhaust Nozzle of a Laser-Powered Rocket", United Aricraft Research Laboratories Report UAR-G256, 15 Jan. 1969.

Norem, P. C., "Interstellar Travel, A Round Trip Propulsion System with Relativistic Velocity Capabilities", American Astronautical Society Paper No. 69-388, June 1969.

Kantrowitz, A., "The Relevance of Space", ASTRONAUTICS & AERONAUTICS, Vol. 9, No. 3, March 1971, pp. 34-35.

Klass, P. J., "Laser Propelled ABM Studied", AVIATION WEEK, 17 April 1972.

Minovitch, M. A., "The Laser Rocket - A Rocket Engine Design Concept for Achieving a High Exhaust Thrust with High I_{sp}", Jet Propulsion Laboratory, TM 393-92, 18 Feb. 1972.

Arno, R. D., MacKay, J. S. and Nishioka, K., "Applications Analysis of High Energy Lasers", NASA Technical memorandum, NASA TM X-62, 142, March 1972.

Rom, F. E. and Putre, H. A., "Laser Propulsion", NASA Technical Memorandum, NASA TM-X-2510, April 1972.

Kantrowitz, A., "Propulsion to Orbit by Ground-Based Lasers", ASTRONAUTICS & AERONAUTICS, Vol. 10, No. 5, May 1972, pp. 74-76.

"Advanced Propulsion Concepts - Project Outgrowth", Tech. Report AFRPL-TR-72-31, Mead, F. B., Jr., editor, Air Force Rocket Propulsion Laboratory, United States Air Force, Edwards, CA, June 1972.

Pirri, A. N. and Weiss, R. F., "Laser Propulsion", AIAA Paper No. 72-719, Boston, MA., 26-28 June 1972.

Minovitch, M. A., "Reactorless Nuclear Propulsion - The Laser Rocket", AIAA Paper No. 72-1092, New Orleans, Louisiana, 1972.

Nakamura, Y. et. al., "Interim Progress Report on Propulsion Concepts for Advanced Systems", NASA No. 113-31-08-00, Sept. 1972, (JPL internal document).

Kizner, W., "Optimization of a Thrust Program for an Orbiting Laser Rocket Using One Ground Based Laser Generator--Maximum Eccentricity with Minimum Fuel and Time:, Phaser Telepropulsion, Inc., Technical Report No. 101-1, Sept. 1972.

Harstad, K. G., "Review of Laser-Solid Interaction and Its Possibilities for Space Propulsion:, Technical Memorandum 33-578, Jet Propulsion Laboratory, Pasadena, CA, Nov. 1972.

Moeckel, W. E., "Propulsion by Impinging Laser Beams", J. SPACECRAFT AND ROCKETS, Vol. 9, Dec. 1972, pp. 942-944.

"Laser-Energy Conversion Symposium", NASA Technical memorandum X-62,269, Proceedings of the First NASA Conference on Laser Energy Conversion, Billman, K. W., editor, Ames Research Center, Moffett Field, CA, Jan. 1973.

Garbuny, M., "Laser Engine Operating by Resonance Absorption" at Laser-Energy Conversion Symposium, NASA-Ames, 18-19 Jan. 1973, NASA TM X-62,269.

Buonadonna, V. R., Knight, C. J. and Hertzberg, A., "The Laser Heated Wind Tunnel - A New Approach to Hypersonic Laboratory Simulation", AIAA Paper 73-211, Washington, D.C., 1973.

Bloomer, J. H., "The Alpha Centauri Probe", PROC. 17th INT. ASTRONAUTICAL CONGRESS (Propulsion and Re-Entry), Madrid, 1966; Gordon and Breach, Inc., New York, 1967, pp. 225-232.

Chapman, P. K., "Laser Propulsion to Relativistic Velocities for Interstellar Flight," PROC. 24th I.A.F. CONGRESS, Baku, U.S.S.R., 7-13 Oct. 1973.

Buonadonna, V. R., Knight, C. J. and Hertzberg, A., "The Laser-Heated Hypersonic Wind Tunnel", AIAA JOURNAL, Vol. 11, No. 11, Nov. 1973, pp. 1457-1458.

Baty, R. S., "Space Propulsion - Let's Do it Better Electrically", AIR UNIVERSITY REVIEW, Nov.-Dec. 1973, pp. 10-25.

Cohen, W., "New Horizons in Chemical Propulsion", ASTRONAUTICS AND AERONAUTICS, Vol. 11, No. 12, Dec. 1973, pp. 46-51.

Poole, J. W. and Thorpe, M. L., "Seeded Gas Thrusters and Related System Components", Report No. NASA-CR-2364, Contract NAS3-17192, Humphreys Corp., Concord, N.H., Jan. 1974.

Pirri, A. N., Monsler, M. J. and Nebolsine, P. E., "Propulsion by Absorption of Laser Radiation", AIAA JOURNAL, Vol. 12, No. 9, Sept. 1974, pp. 1254-1261.

PROCEEDINGS, SECOND NASA CONFERENCE ON LASER ENERGY CONVERSION, NASA SP-395, Billman, K. W., editor, NASA Ames Research Center, Moffett Field, CA, Jan. 1975.

Byer, R. L., "Intial Experiments with a Laser Driven Stirling Engine", at Second Symposium on Laser Energy Conversion, NASA-Ames, CA, Jan. 1975.

Caledonia, G. E., Wu, P. K. S. and Pirri, A. N. "Radiant Energy Absorption Studies for Laser Propulsion", Physical Sciences Inc., PSI TR-20, NASA CR-134809, March 1975.

"Frontiers in Propulsion Research: Laser, Matter-Antimatter, Excited Helium, Energy Exchange and Thermonuclear Fusion", NASA Technical Memorandum 33-722, Papailiou, D. D., editor, 15 March 1975.

Forward, R. L., "Advanced Propulsion Concepts Study: Comparative Study of Solar Electric Propulsion and Laser Electric Propulsion", Under JPL Contract No. 954085, Subcontract under NASA contract NAS7-100, Task Order No. RD-156, Hughes Research Laboratories, Malibu, CA, June 1975.

Moeckel, W. E., "Optimum Exhaust Velocity for Laser-Driven Rockets", J. SPACECRAFT, Vol. 12, No. 11, Nov. 1975, pp. 700-701.

Minovitch, M. A., "Performance Analysis of a Laser Propelled Interorbital Transfer Vehicle", Final Report, Contract NAS 3-18536, NASA CR-134966, Feb. 1976.

Caledonia, G. E., Root, R. G., Wu, P. K., Kemp, N. H. and Pirri, A. N., "Plasma Studies for Laser-Heated Rocket Thruster", Physical Sciences Inc., PSI TR-47, 1976.

Barchukov, A. I., Bunkin, F. V., Konov, V. I. and Prokhorov, A. M., "Laser Air-Jet Engine", JETP LETT., Vol. 23, No. 5, 5 March 1976, pp. 213-214.

Wu, P. K. S. and Pirri, A. N., "Stability of Laser Heated Flows", AIAA JOURNAL, Vol. 14, No. 3, March 1976, pp. 390-392.

Garbuny, M. and Pechersky, M. J., "Laser Engines Operating by Resonance Absorption", APPLIED OPTICS, Vol. 15, No. 5, May 1976, pp. 1141-1157.

Kemp, N. H., Root, R. G., Wu, P. K. S., Caledonia, G. E. and Pirri, A. N., "Laser-Heated Rocket Studies", NASA CR-135127, May 1976.

Pirri, A. N., Simons, G. A. and Nebolsine, P. E., "The Fluid Mechanics of Pulsed Laser Propulsion", ARPA Order No. 3176, PSI TR-60, Physical Sciences Inc., Woburn, MA, July 1976.

Bunkin, F. V. and Prokhorov, A. M., "Use of a Laer Energy Source in Producing a Reactive Thrust", SOV. PHYS. USP., Vol. 19, No. 7, July 1976, pp. 561-573.

Larson, V. R., "Future Propulsion Options for Performance Growth", AIAA Paper No. 76-708, AIAA/SAE 12th Propulsion converence, Palo Alto, CA, July 26-29, 1976.

Bekey, I. and Mayer, H., "1980-2000: Raising our Sights for Advanced Space Systems", ASTRONAUTICS AND AERONAUTICS, July/Aug. 1976, pp. 34-63.

Myrabo, L. N., "MHD Propulsion by Absorption of Laser Radiation", J. SPACECRAFT & ROCKETS, Vol. 13, No. 8, Aug. 1976, pp. 466-472.

Huberman, M. et al., "Investigation of Beamed Energy Concepts For Propulsion: Systems Studies - Volume I", AFRPL-TR-76-66, TRW Defense and Space Systems Group, Redondo Beach, CA, Oct. 1976.

Huberman, M. et al., "Investigation of Beamed Energy Concepts For Propulsion: Laser/Propellant Coupling Analysis - Volume II", AFRPL-TR-76-66, TRW Defense and Space Systems Group, Redondo Beach, CA, Oct. 1976.

Huberman, M., et al., "Investigation of Beamed Energy Concepts For Propulsion: (Classified) - Volume III", AFRPL-TR-76-66, TRW Defense and Space Systems Group, Redondo Beach, CA, Oct. 1976.

Lo, R. E., "Propulsion by Laser Energy Transmission", IAF-76-165, 27th International Astronautical Federation Congress, Anaheim, CA, 10-16 Oct. 1976.

Selph, C. and Horning, W., "Laser Propulsion", IAF-76-166, 27th International Astronautical Federation Congress, Anaheim, CA, 10-16 Oct. 1976.

Shoji, J. M. and Larson, V. R., "Performance and Heat Transfer Charcteristics of the Laser-Heated Rocket - A Future Space Transportation System", AIAA Paper No. 76-1044, AIAA International Electric Propulsion Conference, Key Biscayne, FL, Nov. 1976.

Wu, P. K., "Similarity Solution of the Boundary-Layer Equations of Laser Heated Flows", AIAA JOURNAL, Vol. 14, No. 11, Nov. 1976, pp. 1659-1661.

Wu, P. K., "Real Gas Effect in a Laser Heated Thruster", AIAA JOURNAL, Vol. 14, No. 12, Dec. 1976, pp. 1766-1768.

Kantrowitz, A. R. and Rosa, R. J., "Ram Jet Powered by a Laser Beam", U.S. Pat. No. 3,818,700.

Caledonia, G. E., "Conversion of Laser Energy to Gas Kinetic Energy", J. ENERGY, Vol. 1, No. 2, March-April 1977, pp. 121-124.

Wu, P. K., "Convective Heat Flux in a Laser Heated Thruster", PSI TR-80, Physical Sciences Inc., Woburn, MA, April 1977.

Simons, G. A. and Pirri, A. N., "The Fluid Mechanics of Pulsed Laser Propulsion", AIAA Paper No. 77-699, AIAA 10th Fluid and Plasma Dynamic Conference, Albuquerque, N. Mex., June 1977.

Kemp, N. H. and Root, R. G., "Nozzle Flow of Laser-Heated, Radiating Hydrogen With Applications to a Laser-Heated Rocket", AIAA Paper No. 77-695, AIAA 10th Fluid and Plasma Dynamics Conference, Albuquerque, N. Mex., June 1977.

Weyl, G. M. and Shui, V. H., "On Water-Vapor Plumes, Condensation, and Their Effect on Laser Propagation in the Laser Propelled Rocket", AIAA Paper No. 77-696, AIAA 10th Fluid and Plasma Dynamics Conference, Albuquerque, N. Mex., June 1977.

Legner, H. H. and Douglas-Hamilton, D. H., "CW Laser Propulsion", AIAA Paper No. 77-657, AIAA 10th Fluid and Plasma Dynamics Conference, Albuqueruqe, N. Mex., June 1977.

Whitmire, D. P. and Jackson, IV, A. A., "Laser Powered Interstellar Ramjet", JBIS, Vol. 30, No. 6, June 1977, pp. 223-226.

Chapman, P. K., "Optimal Trajectories for Laser-Powered Launch Vehicles", AAS/AIAA Astrodynamics Specialist Conference, Jackson Lake Lodge, Grand Teton National Park, Wyoming, 7-9 Sept. 1977.

Molmud P., "Laser Assisted Propulsion-Coupling Mechanisms", R&D Status Report 6, Contract F04611-76-C-0003.

Shojhi, J. M., "Laser Heated Rocket Thruster", Contract No. NAS3-19728, (Final Report To Be Published).

Sellen, J. M., Jr., "Laser Receiver System Study", R&D Status Report 6, Contract F04611-76-C-0003.

Weber, R., "Laser Powered Propulsion for Aircraft," Memorandum to NASA Headquarters, Research Div., dated June 11, 1976.

"Laser Rocket Systems Analysis Study," Lockheed Missiles and Space Co., LMSC-D564671, October 1977.

Dyson, F. J. and Perkins, F. W. Jr., "JASON Laser Propulsion Study, Summer 1977," Stanford Research Institute, Menlo Park, CA, Technical Report JSR-77-12, December 1977.

Felber, F. S., "Laser Acceleration of Reactor-Fuel Pellets," General Atomic Project 2101, EPRI Contract RP-323-2, December 1977.

Hertzberg, A., Sun, K. C. and Jones, W. S., "A Laser-Powered Flight Transportation System," AIAA preprint 78-1484, AIAA Aircraft Systems and Technology Conference," See Also GAS FLOW AND CHEMICAL LASERS, J. F. Wendt, Ed., McGraw Hill, 1978.

Nebolsine, P. E., Pirri, A. N., Goela, and Simons, G. A., "Pulsed Laser Propulsion," Proccedings of 1978 JANAF Conference, Incline Village, Nevada, 14 February 1978; See also Report No. PSI-TR-108 submitted under DARPA Order No. 3176, February 1978.

Myrabo, L. N., "Solar-Powered Global Air Transportation",, presented at the AIAA/DGLR 13th International Electric Propulsion Conference, San Diego, CA, 25-27 April 1978.

Nebolsine, P. E., Pirri, A. N., Goela, J. S., Simons, G. A. and Rosen, D. I., "Pulsed Laser Propulsion," Physical Sciences, Inc., TR-142; presented at the AIAA Conference on Fluid Dynamics of High-Power Lasers, October 1978.

Jones, W. S., "Laser-Powered Aircraft and Rocket Systems with Laser Energy Relay Units," RADIATION ENERGY CONVERSION IN SPACE, Progress in Astronautics and Aeronautics, Vol. 61, 1978, p. 264-270.

Douglas-Hamilton, D. H., Kantrowitz, A. R. and Reilly, D. A., "Laser Assisted Propulsion Research," RADIATION ENERGY CONVERSION IN SPACE, Progress in Astronautics and Aeronautics, Vol. 61, pp. 264-270, 1978.

Ageev, V. P., Barchukov, A. I. Bunkin, F. V., Konov, V. I., Korobeinikov, V. P., Putryatin, B. V. and Hudyakov, V. M. (1978) "Experimental and Theoretical Modeling of Laser Propulsion", Paper 78-221, presented at the XXIX-th Congress of the International Astronautical Federation, Dubrovnik, 1978; ACTA ASTRONAUTICA (1980), 7, 79-90.

Weiss, R. F., Pirri, A. N. and Kemp, N. H., "Laser Propulsion," ASTRONAUTICS AND AERONAUTICS, Vol. 17, No. 3, March 1979, pp. 50-58.

Jones, W. S., Forsyth, J. B. and Skratt, J. P., "Laser Rocket System Analysis," Lockheed Missiles and Space Co., NASA CR159521, 15 March 1979.

Chapman, P. K., "Laser Propulsion from the Moon," Arthur D. Little, Inc., SPACE MANUFACTURING III, Proceedings of the 4th Princeton/AIAA Conference, Princeton, NJ, 14-17 May 1979.

Pages B1 and B34 Missing

which lowers the gas temperature to the range of 500-1000 K, and a pressure of perhaps 2 to 10 atmospheres.

At the appropriate moment in the engine cycle, the rotary "intake" valve opens, the flow chokes at the minimum section, and the XMHD generator channel is filled with a fresh load of argon at 1 atmosphere and 500 K (or perhaps 2 atm and 1000 K). Subsequently, the intake valve closes and a LSD wave is ignited at the far end of the XMHD generator channel. The wave then races across the channel and processes all the argon gas to 60 atm and 30,000 K in the next 75 microseconds. (Meanwhile the 660 atm blast wave is shed and pushes all the "spent" argon from the previous pulse--out the rotary exhaust valve.) For the next 750 microseconds, this 60 atm driver gas expands into the plenum at supersonic velocities, suffering a large pressure drop through the 6-10cm electric discharge at the end of the XMHD generator channel.

As mentioned above, the radiation emitted by the 30,000 K "driver gas" is transmitted directly out of the two actively-cooled refractory windows which serve as confining walls for the XMHD generator. (The other two orthogonal walls are the MHD generator electrodes, of course.) When these driver gases expand through the electric discharge into the diffuser/plenum section they continue to radiate. This 0.5m^3 cavity is also a one-sided "light blub" radiator; the other major surface comprises the primary and secondary lenses. Here the gases radiatively cool to a temperture of perhaps 2000-3000 K, and await ejection by the next blast wave "piston".

One final note should be made with regard to the fifth side of the XMHD generator channel which is the location of the rotary intake valve. (The sixth side is the open exit end where the discharge resides.) This valve must also allow for projection of the preionizing LSD wave discharge for creating the MHD-fan activator disk. Hence, it must also serve as an aero-window to counteract the pressure differential for those 1-10 microseconds it takes to perform those functions. It is estimated that 1-10 percent of the argon working fluid may be vented to the atmosphere during this operation.

C - 6

This Page Intentionally Left Blank

REFERENCES FOR APPENDIX B

1. Myrabo, L. N., "A Concept for Light-Powered Flight," AIAA Paper No. 82-1214, AIAA/SAE/ASME 18th Joint Propulsion Conference, Cleveland, OH, June 21-23, 1982.

2. Myrabo, L. N., "Solar-Powered Global Air Transportation," AIAA Paper No. 78-689, AIAA/DGLR 13th International Electric Propulsion Conference, San Diego, CA, April 1978.

3. Tate, E., Marston, C. H., and Zauderer, B., "Large Enthalpy Extraction Results in a Non-Equilibrium MHD Generator," Proceedings of the Sixth International Conference on MHD Electrical Power Generation, Washington, DC, June 1975, pp. 89-104.

4. Blom, J., Veefkind, A., Houben, J., and Rietjens, L., "High Power Density Experiments in the Eindhoven Shock Tunnel MHD Generator," Proceedings of the Sixth International Conference on MHD Electrical Power Generation, Washington, DC, June 1975, pp. 73-88.

5. Bangerter, C. D., et al., "Pulsed Magnetohydrodynamic Program," Final Technical Report, AFAPL-TR-76-34, Hercules, Inc., July 1976.

6. Bangerter, C. D., and Hopkins, B. D., "Explosively Driven MHD Power Generation - A Progress Report," Proceedings of the Sixth International Conference on Magnetohydrodynamic Electrical Power Generation, Washington, DC, June 9-13, 1975, p. 155-170.

7. Jones, M. S., and McKinnon, C. N., "Explosive-Driven Linear MHD Generator," Conference on Megagauss Magnetic Field Generation by Explosives and Related Experiments," September 1965, Frascati, Italy.

8. Jones, M. S., Bangerter, C. D., Peterson, A. N. and McKinnon, C. N., "Explosive Magnetohydrodynamics," AFAPL-TR-67-64, August 1967.

9. Kirillin, V. A., Al'tov, V. A., Asinovskiy, E. I., Dremin, A. N. Dubovitskiy, F. I., Zenkevich, V. B., Kuznetsov, Yu. A., Lebedev, Ye. F., Savrov, S. D. and Sheindlin, A. Ye., "Explosively-Driven MHD Generator with a Superconducting Magnet System," ANSSR, Doklady, Vol. 185, No. 2, 1969, p. 316-319.

10. Asinovskiy, E. I., Ye. F. Lebedef and V. Ye. Ostashev, "Investigation of Processes Determining the Efficiency of Energy Conversion in a Linear Explosive MHD Generator," 7th International Conference on MHD Electrical Power Generation, Volume II, Pages 605-612, Cambridge, MA, June 16-20, 1980.

11. Jones, M. S., Jr., and V. H. Blackman, "Parametric Studies of Explosive-Driven MHD Power Generators," Proceedings of the International Symposium

on Magnetohydrodynamic Electrical Power Generation, Paper 51, Paris, July 1964.

12. Jones, M. S., Jr., V. H. Blackman, R. C. Brumfield, E. W. Evans, C. N. McKinnon, "Research on the Physics of Pulsed MHD Generators," MHD Research, Inc., Report 646, Final Report under ARPA Contract Nonr-3859(00).

13. Jones, M. S., Jr., "The Use of an Explosively Driven MHD Generator for Laser Pumping," MHD Research, Inc., Report 672, a paper presented at The Second Laser Conference on Laser Technology, April 6-8, 1965.

14. Jones, M. S., McKinnon, C. N., and Blackman, V. H., "Generation of Short-Duration Pulses in Linear MHD Generators," 5th Symposium on Engineering Aspects of MHD, April 1964.

15. Asinovskiy, E. I., Kuznetsov, Yu. A., Lebedev, E. F., Maksimov, A. M., and Ostashev, V. E., "Motion of a Plasma Driven by a Non-Conducting Piston in a Magnetic Field," 6th International Conference on MHD Electrical Power Generation, June 1975, Washington, DC.

16. Asinovskiy, E. I. and Ostashev, V. Ye., "Limiting Possibilities of a Pulsed MHD Power Generator to Generate Electrical Power into an Ohmic Load," Teplofizika Vysokikh Temperature, Vol. 14, No. 5, 1976, p. 1079-1082.

17. Bangerter, C. D., "Explosive Magnetohydrodynamic Program," Hercules Incorporated Systems Group, Technical Report AFAPL-TR-73-16, May 1973.

18. Teno, J., and Sonju, O.K., "Development of Explosively Driven MHD Generator for Short Pulse Aircraft High Power," Interim Technical Report No. 1, AVCO Research Laboratory, Inc., Technical Report AFAPL-TR-74-48, June 1974.

19. Baum, D. W., Gill, S. P., Shimmin, W. L., and Watson, J. D., "Dense Nonindeal Plasma Research," Annual Report 130, Final report for Period 15 April 1979 to 14 March 1981 under US Navy Contract No. N00014-78-C-0354, 30 April 1981.

20. Pain, H. T., and Smy, P. R., "Experiments on Power Generation from a Moving Plasma," Journal of Fluid Mechanics, Vol. 10, No. 1, 1961.

21. Ostashev, V. Ye., Maksimov, A. M., Lebedev, Ye. F., Kuznetsov, Yu. A., and Davydon, A. N., "Non-stationary Interaction of Plasma Flow Behind a Strong Shockwave with a Magnetic Field," Teplofizika Vysokikh Temperature, Vol. 13, No. 1, 1975, p. 110-115.

22. Bichenkov, E. I., "Explosive Generators," Soviet Physics - Doklady, Vol. 12, No. 6, December 1967, p. 567-569, translated from Doklady Akademii Nauk SSSR, Vol. 174, No. 4, p. 779-782, June 1967.

23. Burenin, Yu. A. and G. A. Shvetsov, "Energetic Characteristics of Pulsed MHD Systems," Fizika Goreniya i Vsryva, Vol. 11, No. 3, p. 433-437, May-June 1975.

24. Brumfield, R. C., Evans, E. W., and McKinnon, C. N., "Pulsed MHD Power Generation," 4th Symposium on Engineering Aspects of MHD, April 1963, Berkeley, CA.

25. Spitzer, L., Jr., "Physics of Fully Ionized Gases," Number 3, Interscience Tracts on Physics and Astronomy, Interscience Publishers, 1962.

26. McWhirter, R. W. P., "Rates of Recombination in Hydrogenic Plasmas," Nature, Vol. 190, p. 902, June 1961.

27. Bates, D. R., Kingston, A. E., and McWhirter, R. W. P., "Recombination Processes Between Electrons and Atomic Ions," I. "Optically Thin Plasmas," Proc. Soc. A., Vol. 267, p. 297, II. "Optically Thick Plasmas," Proc. Roy. Soc. A., Vol. 270, p. 155, 1962.

28. Park, C., "Calculation of Radiative Properties of Nonequilibrium Hydrogen Plasma," J. Quant. Spectrosc. Rad. Transfer, Vol. 22, p. 101-112, 1979.

29. Rosa, R. J., Magnetohydrodynamic Energy Conversion, McGraw-Hill, New York, 1968.

30. Crompton, R. W., Gibson, D. K., and McIntosh, A. I., Australian J. Phs., 22, 715 (1969)

31. Argyropoulos, G. S. and Casteel, M. A., "Tables of Interaction Parameters for Computation of Ohm's Law Coefficients in Various Gases," J. Applied Phys., 41, 10, pp. 4162-4165, September 1970.

32. Oliver, D. A., Swean, T. F., Bangerter, C. D., Maxwell, C. D., Demetriades, S. T., "A Computer Study of High Magnetic Reynolds Number MHD Channel Flow," STD Research Corp., Final Report under Contract No. N00014-77-C-0574, Work Unit NR 099-415, October 31, 1980.

33. Oliver, D. A., Swean, T. F., Markham, D. M., and Demetriades, S. T., "Strong Interaction Magnetogasdynamics of Shock-Generated Plasma," AIAA Paper No. 80-0027, AIAA 18th Aerospace Sciences Meeting, Pasadena, CA, January 1980.

34. Oliver, D. A., Swean, T. F., Markham, D. M., Maxwell, C. D., and Demetriades, S. T., "High Magnetic Reynolds Number and Strong Interaction Phenomena in MHD Channel Flows," Proceedings of the 7th International Conference on MHD Electrical Power Generation, Volume II, Pages 565-572, Cambridge, MA, June 16-20, 1980.

35. Argyropoulos, G. S., Demetriades, S. T., and Kendig, A. P., "Current Distribution in Nonequilibrium J X B Devices," J. App. Phys., Vol. 38, No. 13, December 1967.

36. Lackner, K., Argyropoulos, G. S., and Demetriades, S. T., "Relaxation Effects in J X B Devices," AIAA J., Vol. 6, No. 5, pp. 949-951, May 1968.

37. Demetriades, S. T., Oliver, D. A., Swean, T. F., and Maxwell, C. D., "On the Magnetoaerothermal Instability," AIAA 19th Aerospace Sciences Meeting," St. Louis, MO., Paper No. 81-0248, January 1981.

38. Maxwell, C. D., et al., "Three-Dimensional Effects in Large Scale MHD Generators," AIAA 14th Fluid and Plasma Dynamics Conference," Palo Alto, CA, Paper AIAA-81-1231, June 1981.

39. Drellishak, K. S., Knopp, C. K., and Cambel, A. B., "Partition Functions and Thermodynamic Properties of Argon Plasma," Phys. Fluids, ser. 6, vol. 9, p. 1280, 1963.

APPENDIX C

DYNAMICS OF A PROPULSIVE CURRENT SHEET

AUTHOR:

M. Martinez-Sanchez
Associate Professor
Department of Aeronautics and Astronautics
Massachusette institute of Technology
Cambridge, MA

This study was performed for the Defense Advanced Research Projects Agency under contract No. 555713-S to The Brookhaven National Laboratory.

APPENDIX C

DYNAMICS OF A PROPULSIVE CURRENT SHEET

A first-order model of the transient behavior of high current plasma sheets used to accelerate gas in plasma thrusters is one in which the sheet is assumed impervious to gas, and is reduced to a geometrical surface acting as a piston. This is an improvement over the elementary "snowplow" model, in that it allows some insight into the gas behavior in front of and behind the advancing current sheet, but it still cannot by itself give information about the physics of the current sheet itself--its conductivity, temperature, permeability to the gas, thickness, etc. We discuss here a model in which the piston approximation is used as a first order solution, establishing the basic flow field "far" from the current sheet. Also the structure of the current sheet itself is examined in some detail. In the interest of simplicity, several important approximations are still introduced (such as perfect gas behavior, one-dimensionality, etc.), but the model provides much insight into the factors controlling the sheet dynamics, and yields some quantitative information as well.

1. Gas Dynamic Effects of Impermeable "Piston" Model

When a large current sheet is established, the magnetic force acting on it accelerates a certain mass of gas, and this can be used for propulsion. In calculating the propulsive effect of the sheet, the simplest approximation is the "snowplow" model which contains several assumptions:

(1) The layer is infinite in extent (edge effects and in-plane flows neglected).
(2) The sheet is impermeable to the flow of gas.
(3) As the current sheet advances, the overtaken gas "piles up" in a thin region ahead of it, in effect instantaneously acquiring the sheet velocity. Vacuum is created behind the sheet.

The thrust per unit area when the sheet speed u_p is constant is easy to calculate from this model. If the gas density ahead of the sheet is ρ_0 one finds

$$F = \rho_0 u_p^2 \qquad (1)$$

which is basically the incoming momentum flux "destroyed" by the sheet, when viewed from the sheet itself.

Without modifying assumptions (1) and (2) above, one should reexamine assumption (3) when the relative sheet speed is not much higher than the undisturbed speed of sound, since then the sheet disturbance, travelling at that sound speed, can affect gas regions of considerable thickness.

The situation can now be described as follows: A "piston" (the current sheet) advances at u_p to the right into undisturbed air at ρ_0, T_0. The forward-travelling sound waves coalesce into a leading shock which itself advances at some speed V_{shock} higher than u_p, creating a growing layer of shocked gas at uniform ρ, T, higher than ρ_0, T_0 between shock and piston. The backward-travelling sound waves diverge (since they travel faster as they recede) more and more into the warmer (unchilled) rear gas. This creates an expansion fan behind the piston; there is a region of variable gas speed and pressure whose leading edge moves backwards at $-a_0$, the undisturbed speed of sound, and which extends forward either to where the gas has reached the piston speed u_p, or where its pressure has dropped to zero (this latter condition prevailing at high piston speeds). Between this point and the piston itself, there is either vacuum (for high u_p) or a uniform region at some density below ρ_0 and moving at u_p.

We will omit the derivations, which are fairly straightforward using the method of characteristics (Ref. 1), and quote the results for the different regions. In the following, $a = \sqrt{\gamma RT}$ is the local speed of sound, a measure of local gas temperature, and u is the forward local gas velocity. The piston (and gas) moves to the right, and the regions are listed in order, from the rear forward in Table C-1.

TABLE C-1. GAS REGIONS FOR IMPERMEABLE PISTONS

	Region 1 (Far behind)	Region 2 (Expansion fan)	Region 3 (Behind piston)	Region 4 (Shocked gas)	Region 5 (Undisturbed)
$u =$	0	$\frac{2}{\gamma+1}\left(a_o + \frac{x}{t}\right)$	u_p if $u_p < \left(\frac{2a_o}{\gamma-1}\right)$ Undefined if $u_p > \frac{2a_o}{\gamma-1}$	u_p	0
$a =$	a_o	$\left(\frac{2}{\gamma+1}\right) a_o - \left(\frac{\gamma-1}{\gamma+1}\right) \frac{x}{t}$	$a_o - \left(\frac{\gamma-1}{2}\right) u_p$ if $u_p < \left(\frac{2a_o}{\gamma-1}\right)$ 0 if $u_p > \left(\frac{2a_o}{\gamma-1}\right)$	See shock expressions (Eq. 16).	a_o

The shock velocity U_{shock} is found from the Rankine-Hugoniot relations as

$$V_{Shock} = \left(\frac{\gamma+1}{4}\right) u_p + \sqrt{\left(\frac{\gamma+1}{4}\right)^2 u_p^2 + a_o^2} \xrightarrow[u_p >> a_o]{} \left(\frac{\gamma+1}{2}\right) u_p \qquad (2)$$

and then conditions after the shock (subscript "1") are

$$\frac{\rho_1}{\rho_o} = \frac{a_o^2 + \left(\frac{\gamma+1}{4}\right) u_p^2 + u_p \sqrt{\left(\frac{\gamma+1}{4}\right)^2 u_p^2 + a_o^2}}{a_o^2 + \frac{\gamma-1}{2} a_o^2} \xrightarrow[u_p >> a_o]{} \frac{\gamma+1}{\gamma-1}. \qquad (3)$$

$$\frac{P_1}{P_o} = 1 + \gamma \frac{u_p}{a_o^2}\left[\left(\frac{\gamma+1}{4}\right)u_p + \sqrt{\left(\frac{\gamma+1}{4}\right)^2 u_p^2 + a_o^2}\right] \xrightarrow[u_p >> a_o]{} \frac{\gamma(\gamma+1)}{2}\left(\frac{u_p}{a_o}\right)^2 \qquad (4)$$

$$\frac{T_1}{T_o} = \left[\frac{P_1}{P_o}\frac{\rho_o}{\rho_1}\right] \xrightarrow[u_p >> a_o]{} \frac{\gamma(\gamma-1)}{2}\left(\frac{u_p}{a_o}\right)^2 \qquad (5)$$

$$a_1 = \sqrt{\gamma R T_1} \xrightarrow[u_p >> a_o]{} \sqrt{\frac{\gamma(\gamma-1)}{2}}\, u_p \qquad (6)$$

A schematic representation of these solutions is given below for cases <u>without</u> a vacuum (Figure C-1), and <u>with</u> a vacuum behind the piston (Figure C-2).

The derived thrust equals the force that must be applied to maintain the piston motion, i.e.,

$$F = \int \frac{\partial(\rho u)}{\rho t}\, d(\text{Vol.}), \qquad (7)$$

Per unit piston area, d(Vol)=dx. Also, since the only independent variable is $\eta = x/t$, $\frac{\partial(\rho u)}{\partial t}\, dx = -\eta \frac{\partial(\rho u)}{\partial \eta}\, d\eta$

and we calculate

$$F = -\int_{-a_o}^{V_{shock}} \eta \frac{\partial \rho u}{\partial \eta}\, d\eta = -\left[\eta\, u\, \rho\right]_{-a_o}^{V_{sh.}} + \int_{-a_o}^{V_{sh.}} \rho u\, d\eta \qquad (8)$$

0

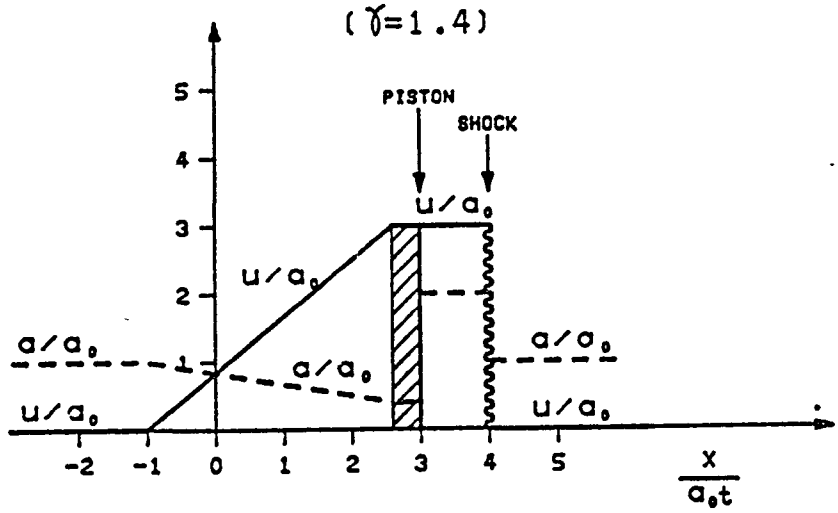

Figure C-1. Case With $\frac{up}{a_0}$ =3

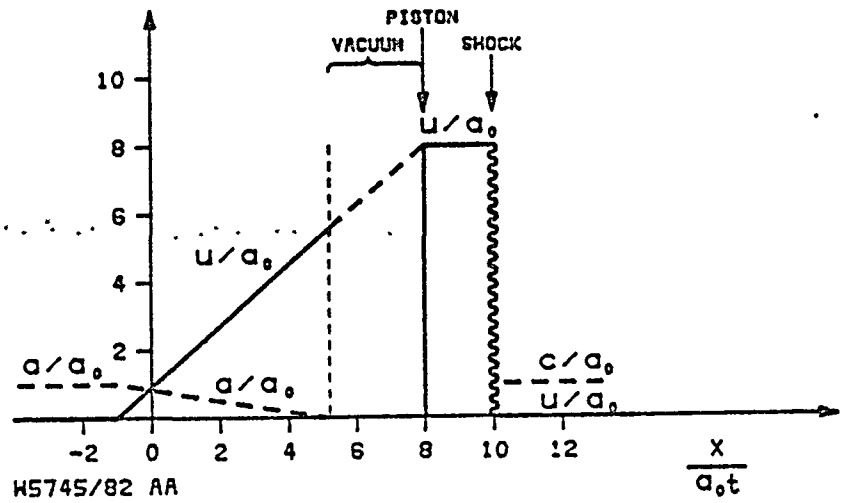

Figure C-2. Case With $\frac{up}{a_0}$ =8

Using the solutions in Table C-1, we can then calculate the contributions F_1, F_2, F_3 due respectively to gas between shock and piston, gas in the uniform region behind the piston (for low piston speeds), and gas in the trailing expansion fan. These are summarized in Table C-2, where $M_p = u_p/a_o$ is the piston "Mach number," and we have defined $C_f = F/\rho_o u_p^2$. Numerical results for $\gamma = 1.4$ are given in Table C-3.

Notice, for reference, that the pure snowplow model (Equation 1) predicts simply $C_f = 1$. The gas dynamic model predicts $C_f = (\gamma+1)/2$ (1.2 for $\gamma = 1.4$) at hypersonic piston speeds, but it indicates considerably higher thrust at low relative piston speeds (notice that velocities here are to be super-imposed on whatever flight speed there may be). The effect is due to the fact that the mass of air affected at low piston speeds is not governed by that piston speed, but rather by the speed of sound, which is then much greater. On the other hand, low piston speeds imply (Equation 4) low pressure ratios, and hence a weak current sheet. Under these conditions, the assumption of an impermeable, thin piston is also questionable. In addition, finite size effects (in-plane velocities, for example) are also likely to appear in such cases.

Altogether, then, the snowplow model is reasonable for $u_p/a_o \geq 2$-3, and, with some correction to account for the finite shock-piston distance, for $u_p/a_o \geq 1$.

Given that the propulsion efficiency is

$$\eta_{prop} = \frac{2V}{u_p + V}, \tag{9}$$

where V is the flight speed, and that we desire $\eta_{prop} \geq 0.9$, it appears that the use of the snowplow model should be restricted to flight Mach numbers M above

$$M = \frac{\eta_p}{2(1-\eta_p)} \simeq 5$$

or to flight speeds above some 1500 m/sec. At speeds lower than this (with $\eta_{prop} \geq 0.9$), the model can still provide qualitative insights on the discharge behavior, but more refined methods appear necessary for quantitative accuracy.

TABLE C-2. SUMMARIZED EXPRESSIONS

$M_p = \frac{u_p}{a_o} \leq \frac{2}{\gamma-1}$	$M_p = \frac{u_p}{a_o} \geq \frac{2}{\gamma-1}$
$C_{f_1} = \frac{\gamma+1}{4} + \sqrt{\left(\frac{\gamma+1}{4}\right)^2 + \frac{1}{M_p^2}}$	$C_{f_1} = \frac{\gamma+1}{4} + \sqrt{\left(\frac{\gamma+1}{4}\right)^2 + \frac{1}{M_p^2}}$
$C_{f_2} = \frac{\left(1 - \frac{\gamma-1}{2} M_p\right)^{(\gamma+1)/(\gamma-1)}}{M_p^2}$	$C_{f_2} = 0$
$C_{f_3} = \frac{1 - \left(1 + \frac{\gamma+1}{2} M_p\right)\left(1 - \frac{\gamma-1}{2} M_p\right)^{\frac{\gamma+1}{\gamma-1}}}{\gamma M_p^2}$	$C_{f_3} = \frac{1}{\gamma M_p^2}$

TABLE C-3. NUMERICAL RESULTS FOR $\gamma = 1.4$

M_p	0.25	0.5	1	1.5	2	2.5	3	4
C_{f_1}*	4.645	2.688	1.766	1.497	1.381	1.321	1.2864	1.2500
C_{f_2}**	11.761	2.126	0.261	0.052	0.012	0.003	0.0005	4×10^{-6}
C_{f_3}***	0.507	0.428	0.302	0.213	0.150	0.107	0.0779	0.0446
C_f	16.913	5.242	2.331	1.762	1.543	1.431	1.3647	1.2946

Table 3a (for $M_p < \frac{2}{\gamma-1} = 5$)

M_p	5	6	8	10	20	∞
C_{f_1}*	1.2325	1.2227	1.2129	1.2083	1.2021	1.2
C_{f_2}**	0	0	0	0	0	0
C_{f_3}***	0.0286	0.0198	0.0116	0.0071	0.0018	0
C_f	1.2610	1.2426	1.2245	1.2154	1.2039	1.2

Table 3b (for $M_p \geq \frac{2}{\gamma-1} = 5$)

* Between piston and shock.

** Entrained behind piston.

*** Entrained in rarefaction fan.

Finally, we note that if the relative velocity of the current sheet is always greater than sonic, then the model could be reasonably extended to flight Mach numbers as low as 2.2 if η_{prop} is relaxed to 0.8; to Mach 1 for $\eta_{prop} = 0.65$.

2. Summary of the Piston Model

As explained in detail above, when a one-dimensional "piston" moves after an impulsive start at a constant speed v_p into stagnant gas at pressure p_o and temperature T_o, several distinct regions can be distinquished in the gas. From front to rear, these are:

(a) Undisturbed gas upstream

(b) A leading shock wave moving at $v_s > v_p$, given by

$$-M_s = \frac{\gamma+1}{4} M_p + \sqrt{\left(\frac{\gamma+1}{4}\right)^2 M_p^2 + 1} \qquad (10)$$

where

$$M_p = \frac{v_p}{a_o}, \quad M_s = \frac{v_s}{a_o}, \quad a_o = \sqrt{\gamma R T_o} \qquad (11\ a, b, c)$$

(c) Uniform, shock-compressed gas between the piston and the shock. Denoting its properties with a subscript,

$$\frac{p_1}{p_o} = 1 + \gamma M_s M_p \qquad (12)$$

$$\frac{T_1}{T_o} = 1 + \frac{\gamma - 1}{2} M_p (2M_s - M_p) \qquad (13)$$

$$v_1 = v_p \qquad (14)$$

(d) The piston itself

(e1) If $M_p \geq \frac{2}{\gamma - 1}$, a trailing vacuum region, bounded between the piston and a trailing surface which advances at a speed

$$\frac{2}{\gamma - 1} a_o \ (< v_p).$$

(e2) If $M_p \leq \frac{2}{\gamma - 1}$, a uniform trailing region between the piston and a surface advancing at a speed $\frac{\gamma + 1}{2} u_p - a_o$. If conditions in this region area are labeled (2), we have

$$\frac{P_2}{P_o} = \left(1 - \frac{\gamma - 1}{2} M_p\right)^{\frac{2\gamma}{\gamma - 1}} \tag{15}$$

$$\frac{T_2}{T_o} = \left(1 - \frac{\gamma - 1}{2} M_p\right)^2 \tag{16}$$

$$v_2 = v_p \tag{17}$$

(f) A trailing expansion fan extending downstream between the end of region (e) and a surface moving backwards at the undisturbed speed of sound, a_o. Measuring x and t from the location and instant where the piston started (impulsively) to move, this region satifies

$$a = \frac{2}{\gamma + 1} a_o - \frac{\gamma - 1}{\gamma + 1} \left(\frac{x}{t}\right), \quad (a = \sqrt{\gamma RT}) \tag{18}$$

$$v = \frac{2}{\gamma + 1} \cdot \left(a_o + \frac{x}{t}\right) \tag{19}$$

$$P/\rho^\gamma = \text{const.} = P_o/\rho_o^\gamma \tag{20}$$

(g) Undisturbed Gas Downstream

If the "piston" is actually a thin current sheet carrying a current J per unit depth, and the circuit arrangement is such that the magnetic field is zero upstream of this current sheet, then its value just downstream of it is

$$B_2 = \mu_o J , \tag{21}$$

and we can establish one more relationship by the mechanical equilibrium condition

$$P_1 - P_2 = \frac{B_2^2}{2\mu_0} \tag{22}$$

3. Assumptions for Local Sheet Model

a. We assume $M_p < \frac{2}{\gamma - 1}$. For air, $M_p < 5$, which covers most cases of interest. Thus, no trailing vacuum arises.

b. The gas is perfect throughout, and the specific heat ratio γ is constant.

c. Radiation cooling is neglected. This is appropriate for pressures of the order of (or less than) one atmosphere.

d. Simple profiles of current density and temperature are assumed, as shown in Figures C-3 and C-4.

e. Far upstream and downstream, the conditions prevailing are those calculated from the "piston" model. This implies in particular that the current sheet is immersed in gas which moves with the sheet (regions (c) and (e) of Section 2). The region in front being compressed and the one in back being rarefied by the push of the "piston". However, the model will now allow finite gas velocities u(x) relative to the piston. although with the restriction

$$u^2/2 \ll h \tag{23}$$

and, implicitly, $|u| \ll v_p$ as well.

4. Governing Equations

After exploiting the assumptions of the previous section (which, in particular, reduces the momentum equation to a quasi-static force balance), the equations can be written in the frame of the advancing current sheet. To be precise, since the sheet is itself deforming and

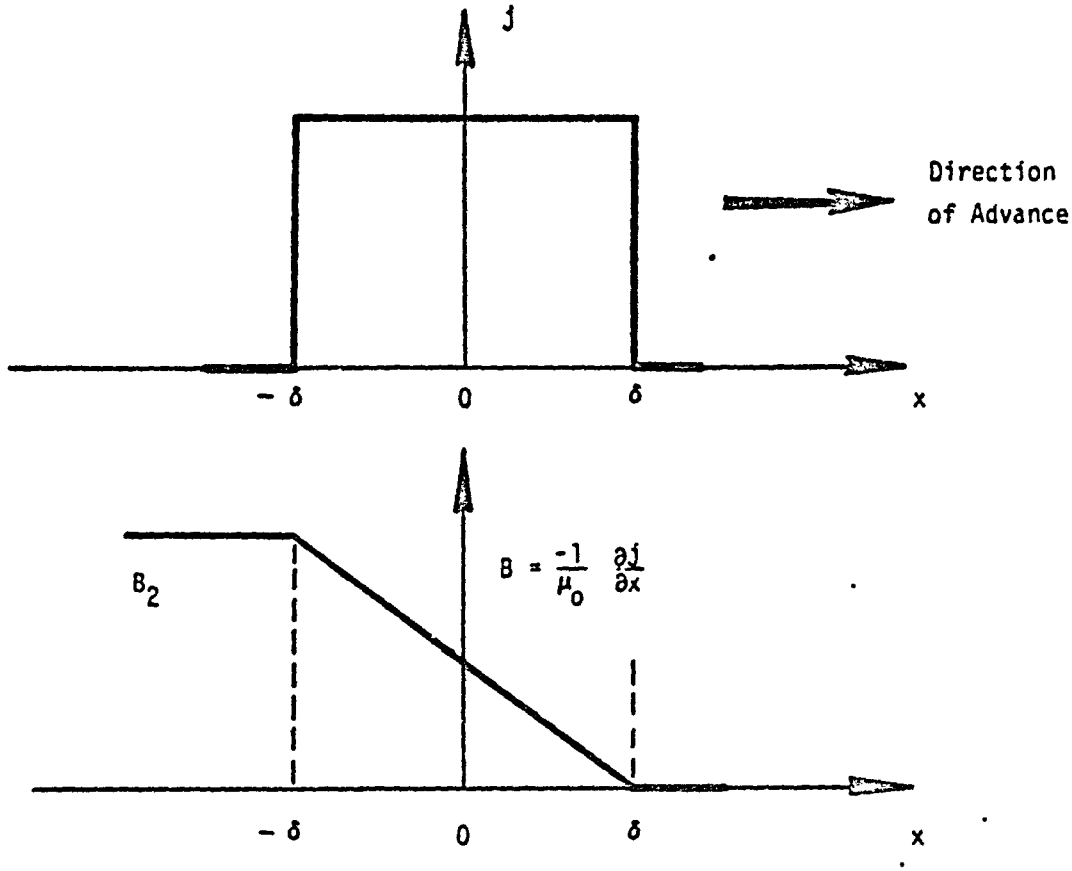

Figure C-3. Current and Magnetic Field Profiles

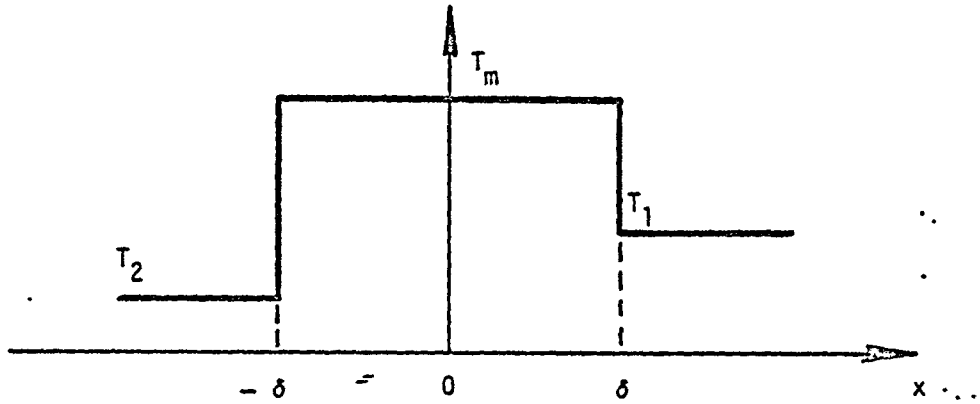

Figure C-4. Temperature Profile

widening, we follow a frame in which

$$\int_{-\infty}^{\infty} \left(\frac{\partial B}{\partial t}\right) dx = 0 \tag{24}$$

i.e., one in which only distortion, but not shifting of the B-field profile is allowed. From Faraday's equation

$$\frac{\partial B}{\partial t} = -\frac{\partial E}{\partial x} \tag{25}$$

it then follows that $E(\infty) = E(-\infty)$; since at $x \to \infty$ there are presumed to be no electrodes imposing a voltage, the rest-frame $E(\infty)$ is zero, and the same is true of any other frame ($B(\infty) = 0$). Therefore, we reach the important result

$$E_1 = E_2 = 0 \tag{26}$$

Of course, this result applies to the particular frame chosen only. For one moving at any speed u relative to it (including the rest frame). the field would be $E' = E - uB$, and is not necessarily zero far from the sheet.

The equations are now

Continuity: $$\frac{\partial \rho}{\partial t} + \frac{\partial (\rho u)}{\partial x} = 0 \tag{27}$$

Momentum: $$p + \frac{B^2}{2\mu_0} \simeq P_1 \tag{28}$$

Energy: $$\frac{\partial(\rho h)}{\partial t} + \frac{\partial(\rho h u)}{\partial x} = \frac{\partial}{\partial x}\left(k \frac{\partial T}{\partial x}\right) + \frac{\partial P}{\partial t} - \underbrace{\frac{E}{\mu_0}\frac{\partial B}{\partial x}}_{(= \vec{E} \cdot \vec{J})} \tag{29}$$

(where $h \simeq h_0 = h + \cancel{\frac{u^2}{2}}_{\,0}$)

Faraday: $$\frac{\partial B}{\partial t} = -\frac{\partial E}{\partial x} \tag{30}$$

Ampere: $$B = -\frac{1}{\mu_o}\frac{\partial j}{\partial x} \tag{31}$$

Ohm's Law: $$j = \sigma(E - uB) \tag{32}$$

State: $$P/\rho = RT \text{ and } h = C_p T \tag{33}$$

For our purposes, the energy equation can be rewritten with the help of equations (28), (30), and (33) as follows:

From (24)

$$\rho h = \rho C_p T = \rho\left(\frac{\gamma}{\gamma - 1}\right) R T = \left(\frac{\gamma}{\gamma - 1}\right) p \tag{34}$$

and from (28) and (30)

$$\frac{\partial p}{\partial t} = -\frac{B}{\mu_o}\frac{\partial B}{\partial t} = \frac{B}{\mu_o}\frac{\partial E}{\partial x} \tag{35}$$

Hence, the group

$$\frac{\partial(\rho h)}{\partial t} - \frac{\partial p}{\partial t} + \frac{E}{\mu_o}\frac{\partial B}{\partial x} = +\left(\frac{\gamma}{\gamma - 1} - 1\right)\frac{B}{\mu_o}\frac{\partial E}{\partial x} + \frac{E}{\mu_o}\frac{\partial B}{\partial x}$$

$$= \frac{1}{\gamma - 1}\frac{\partial}{\partial x}\left(\frac{E B}{\mu_o}\right) - \left(\frac{2 - \gamma}{\gamma - 1}\right)\frac{E}{\mu_o}\frac{\partial B}{\partial x} \tag{36}$$

Giving for the energy equations

$$\left(\frac{\gamma}{\gamma - 1}\right)\frac{\partial}{\partial x}(pu) - \frac{\partial}{\partial x}\left(k\frac{\partial T}{\partial x}\right) + \left(\frac{1}{\gamma - 1}\right)\frac{\partial}{\partial x}\left(\frac{EB}{\mu_o}\right) - \left(\frac{2 - \gamma}{\gamma - 1}\right)\frac{E}{\mu_o}\frac{\partial B}{\partial x} = 0 \tag{37}$$

We will use an integrated form of this equation. In particular, integrating between x and ∞, we obtain

$$\frac{\gamma}{\gamma-1}(p_1u_1 - pu) + k\frac{\partial T}{\partial x} - \left(\frac{1}{\gamma-1}\right)\frac{E\,B}{\mu_0} - \left(\frac{2-\gamma}{\gamma-1}\right)\int_x^\infty \frac{E}{\mu_0}\frac{\partial B}{\partial x}\,dx = 0 \qquad (38)$$

where use has been made of $\left(k\frac{\partial T}{\partial x}\right)_\infty = 0$ and $E(\infty) = 0$. If the lower limit x is now set at $x \to -\infty$, we obtain a global energy balance:

$$\frac{\gamma}{\gamma-1}(p_1u_1 - p_2u_2) = \frac{2-\gamma}{\gamma-1}\int_{-\infty}^{\infty}\frac{E}{\mu_0}\frac{\partial B}{\partial x}\,dx \qquad (39)$$

Notice that, since for an expanding sheet $E \geq 0$ (to be shown) and $\frac{\partial B}{\partial x} \leq 0$, this last equation implies a continued advection of thermal power <u>into</u> the sheet region. This is somewhat contrary to intuition, but can be understood by examining in detail the structure of the expanding current layer. In regions where $\frac{\partial B}{\partial t} > 0$ (ahead of the layer centroid), we have $\frac{\partial p}{\partial t} < 0$ (by (35)). Thus, while the magnetic energy density $\frac{B^2}{2\mu_0}$ is increasing there, the thermal energy density $ph = \frac{\gamma}{\gamma-1}p$ is decreasing, and because of the factor $\frac{\gamma}{\gamma-1} > 1$ (3.5 for air), this thermal energy is dominant and the net result (wherever $\frac{\partial B}{\partial t} > 0$) is to take net energy "out of storage". However, the reverse happens behind the layer centroid, where $\frac{\partial B}{\partial t} < 0$ due to the layer growth; and since $\frac{\partial B^2/2\mu_0}{\partial t} = \frac{B}{\mu_0}\frac{\partial B}{\partial t}$, the more or less symmetric profile of $\frac{\partial B}{\partial t}$ is more heavily weighed (by the $\frac{B}{\mu_0}$ factor) in this region. Overall, then, energy is being "stored" in the growing layer, and this must be convected from the regions far from it (and even more so if radiation losses were included).

5. <u>Application of Assumed Profiles</u>. We now use the profiles of Figure C-3 and C-4 to obtain more detailed equations involving the unknown parameters δ, $\frac{d\delta}{dt}$, T_m, $\frac{dT_m}{dt}$, as well as the <u>relative</u> velocities u_1, u_2 far from the layer.

The profile of B in Figure C-3 is given by

$$B = \begin{cases} B_2 & \text{——} \quad \frac{x}{\delta} < -1 \\ \frac{B_2}{2}\left(1 - \frac{x}{\delta}\right) & \text{——} \quad -1 < \frac{x}{\delta} < 1 \\ 0 & \text{——} \quad \frac{x}{\delta} > 1 \end{cases} \tag{40}$$

Therefore, using $\frac{\partial B}{\partial t} = -\frac{\partial E}{\partial x}$ and $E(\infty) = E_1 = 0$,

$$E = \int_x^{\infty} \frac{\partial B}{\partial t}\, dx \tag{41}$$

Notice that, since the B profile is continuous (if "kinky"), the time derivative is simply

$$\frac{\partial B}{\partial t} = \begin{cases} 0 & \text{——} \quad x/\delta < -1 \\ +\frac{B_2}{2}\frac{x}{\delta^2}\frac{d\delta}{dt} & \text{——} \quad -1 < x/\delta < 1 \\ 0 & \text{——} \quad x/\delta > 1 \end{cases} \tag{42}$$

and, integrating,

$$E = \begin{cases} 0 & \text{——} \quad x/\delta < -1 \\ \frac{B_2}{4}\left(1 - \frac{x^2}{\delta^2}\right)\frac{d\delta}{dt} & \text{——} \quad -1 < x/\delta < 1 \\ 0 & \text{——} \quad x/\delta > 1 \end{cases} \tag{43}$$

Equation (43) shows (as anticipated) that $E \geq 0$ if $\frac{d\delta}{dt} > 0$. Figure C-5 shows the shape of the E- profile.

In the following, we will save writing by using

$$\xi = \frac{x}{\delta} \tag{44}$$

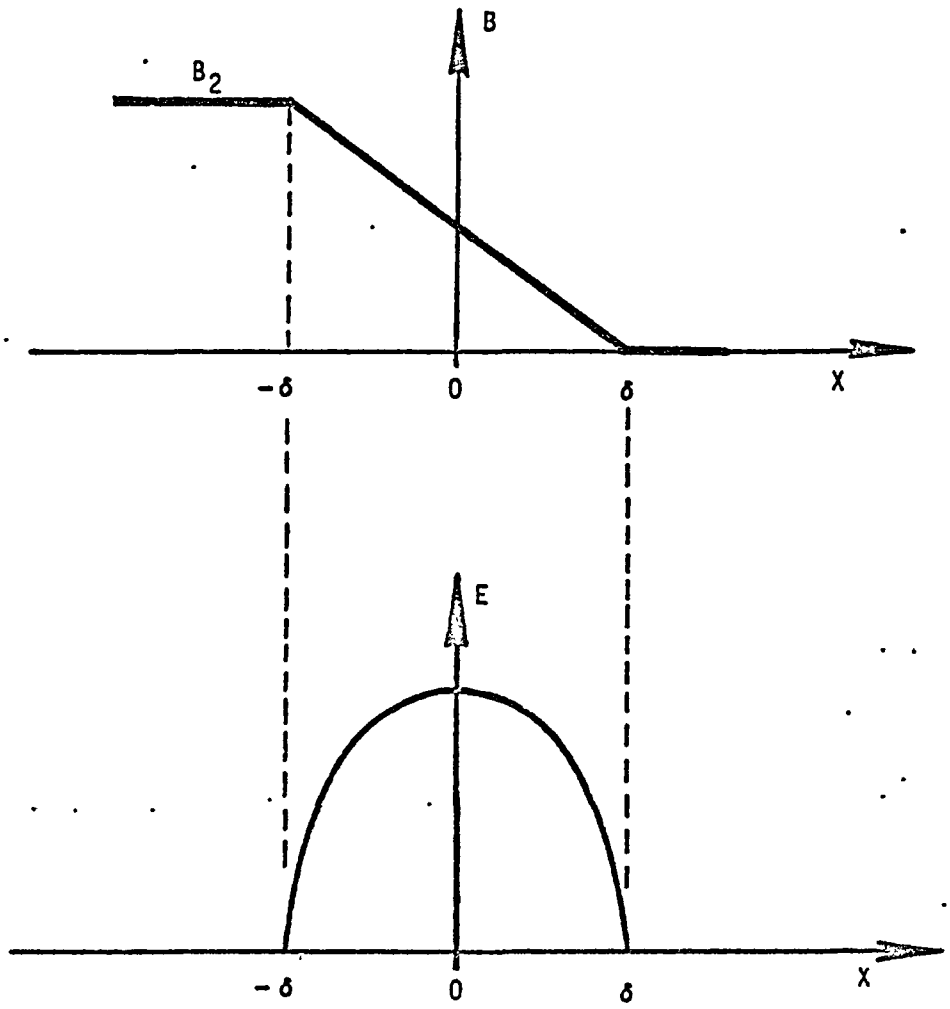

Figure C-5. Local Electric Field in Sheet Frame

and $$\eta = 1 - \xi \tag{45}$$

as coordinates (but $\delta = \delta(t)$). We will also omit the ranges of applicability in equations of the type of (43) for instance.

The pressure profile follows from equation (28):

$$P = \begin{cases} P_1 - \dfrac{B_2^2}{2\mu_o} \\ P_1 - \dfrac{B_2^2}{2\mu_o}\ \dfrac{1-\xi^2}{4} \\ P_1 \end{cases} \tag{46}$$

Incidentally, from Figure C-6 it can be appreciated how, when δ grows, the local pressure increases near $x = -\delta$ are far more important than the corresponding decreases near $x = \delta$. This net "compression" effect is what was discussed before, in connection with equation (39).

If the evolution of $\delta(t)$ and $T_m(t)$ are known, the continuity equation can be used to calculate the gas velocity profile $u(x,t)$ (relative to the current sheet):

$$u = \frac{1}{\rho}\left[\rho_1 u_1 + \int_x^\infty \frac{\partial \rho}{\partial t}\, dx\right] \tag{47}$$

where $\rho = \dfrac{P}{RT}$. In calculating $\dfrac{\partial \rho}{\partial t}$ care must be taken to include Dirac delta function contributions from the motion of the density discontinuity at each edge of the current sheet. We have

$$\rho = \frac{1}{R} \begin{cases} (P_1 - B_2^2/(2\mu_o))/T_2 \\ \left[P_1 - \dfrac{B_2^2}{2\mu_o}\ \dfrac{(1-\xi)^2}{4}\right]/T_m \\ 1/T_1 \end{cases} \tag{48}$$

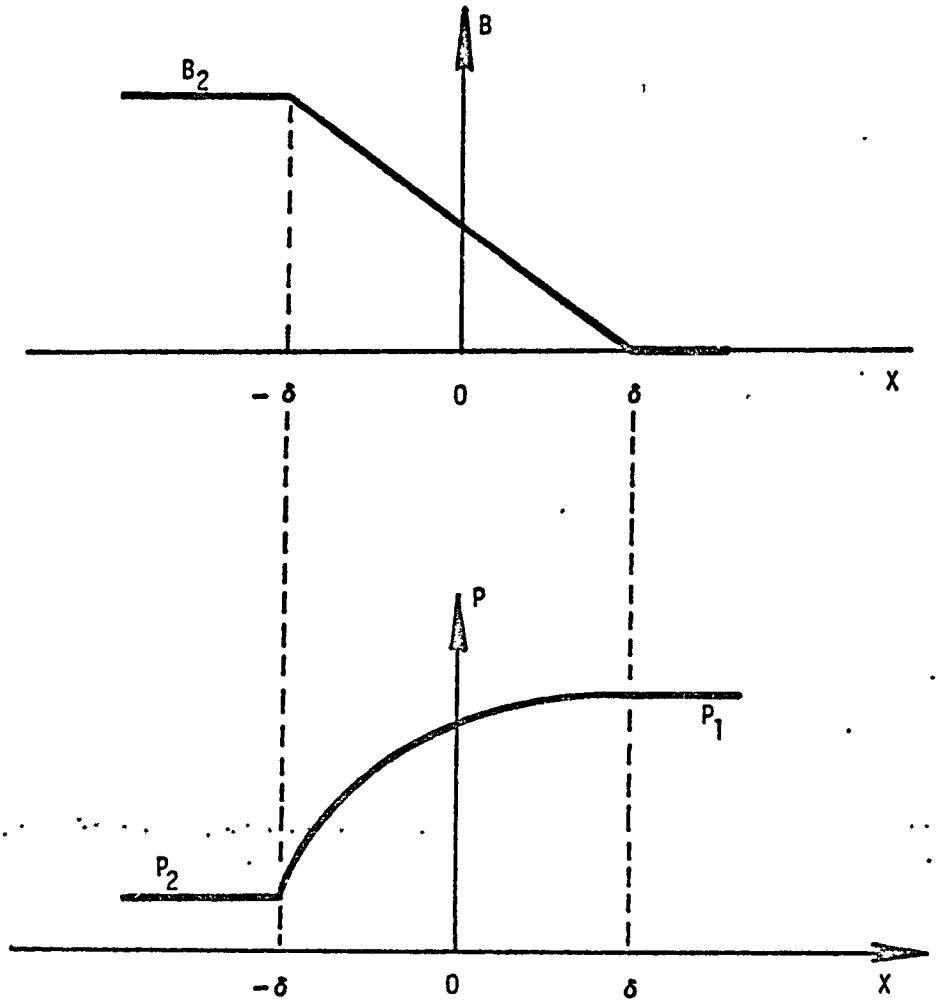

Figure C-6. Pressure Profile (Notice the Asymmetry)

and if we arbitratily assign the δ_D - functions to the outside ranges,

$$\frac{\partial \rho}{\partial t} = \frac{1}{R} \begin{cases} \left(\frac{1}{T_m} - \frac{1}{T_1}\right)\left(P_1 - \frac{B_2^2}{2\mu_o}\right)\delta_D \ (\xi + 1)\ \frac{d\delta}{dt} \\ - \frac{1}{2T_m}\left(\frac{B_2^2}{2\mu_o}\right)\frac{x}{\delta^2}\ (1 - \xi)\ \frac{d\delta}{dt} - \frac{1}{T_m^2}\left[P_1 - \frac{B_2^2}{2\mu_o}\frac{(1 - \xi)^2}{4}\right]\frac{dT_m}{dt} \\ P_1\left(\frac{1}{T_m} - \frac{1}{T_1}\right)\delta_D\ (\xi - 1)\ \frac{d\delta}{dt} \end{cases} \quad (49)$$

Performing the x integration indicated in (47) we obtain the result

$$\frac{u}{u_1} = \begin{cases} \frac{\Theta_{12}/\Theta}{1 - \pi}\left[\frac{\pi}{3}\nu - \left(2 - \frac{2\pi}{3}\right)\tau + (1 - \Theta)\nu + (1 - \pi)\left(1 - \frac{\Theta}{\Theta_{12}}\right)\nu\right] \\ \frac{\Theta - \frac{\pi}{12}\eta^2\ (3 - 2\eta)\ \nu - \left(\eta - \frac{\pi}{12}\eta^3\right)\tau + (1 - \Theta)\nu}{1\ \frac{\pi}{4}\eta^2} \\ 1 \end{cases} \quad (50)$$

where we have introduced several nondimensional quantities:

$$\pi = \frac{B_2^2}{2\mu_o\ P_1}\ ;\ \Theta = \frac{T_m}{T_1}\ ;\ \Theta_{12} = \frac{T_2}{T_1}\ ;\ \nu = \frac{1}{u_1}\frac{d\delta}{dt}\ ;$$

$$\tau = \frac{\delta}{u_1\ T_m}\frac{dT_m}{dt} \quad (51)$$

and as before, $\eta \equiv 1 - \frac{x}{\delta}$.

It is now possible to construct expressions for the plasma-frame field E - uB. For the layer range ($-\delta < X < \delta$), we obtain, from (40), (43) and (50), and after some algebra,

$$\frac{E - u\ B}{u_1\ B_2} = \left(\frac{\nu + 2\tau}{12}\right)\eta^2 + \frac{4}{\pi}\left(\frac{\nu - \tau}{3}\right) - \frac{\Theta(1 - \nu)\ \eta + \frac{8}{\pi}\left(\frac{\nu - \tau}{3}\right)}{2\ (1 - \frac{\pi}{4}\ \eta^2)} \quad (52)$$

In consistency with our assumed profile of temperature, we now assume the conductivity σ to be constant ($\sigma = \sigma_m$) within the current sheet, and zero outside it. This latter assumption is justified by the negligible conductivity of most gases below some 6000 K. We can then integrate Ohm's law (with $j = -\frac{1}{\mu_o}\frac{\partial B}{\partial x}$) to obtain

$$B_2 = \mu_o \int_{-\infty}^{\infty} \sigma (E - u\,B)\cdot dx \simeq \mu_o \sigma_m \; u_1 \; B_2 \int_{-\delta}^{\delta} \frac{E - u\,B}{u_1\,B_2} \; dx \qquad (53)$$

and, using (52)

$$\left[\frac{2}{9} + \frac{8}{3\pi} - \frac{4}{3\pi^{3/2}} \ln\left(\frac{1+\sqrt{\pi}}{1-\sqrt{\pi}}\right) - \frac{\Theta}{\pi} \ln\,(1-\pi)\right]\nu \quad + \left[4 - \frac{8}{3\pi} + \frac{4}{3\pi^{3/2}} \ln\left(\frac{1+\sqrt{\pi}}{1-\sqrt{\pi}}\right)\right]\tau$$

$$= \frac{1}{\mu_o \sigma_m u_1 \delta} - \frac{\Theta}{\pi} \ln\,(1-\pi) \qquad (54)$$

From the definitions of ν and τ (equation 51), this can be seen to be a linear equation between $\frac{d\delta}{dt}$, $\frac{dm}{dt}$ and u_1. We can obtain two additional equations of the same sort as follows: first, u_2 can be eliminated between (39) (overall energy balance) and the upper line of (50) (continuity). Secondly, an additional partial integration of equation (38) can provide an extra equation highlighting the local role of thermal diffusion.

Firstly, equation (39) can be made explicit using the assumed profiles; that of pu follows from (46) and (50), while that of $E\frac{\partial B}{\partial x}$ follows from (40) and (43).

The calculations are straightforward and the result takes the form

$$(1-\pi)\frac{u_2}{u_1} = 1 + \left(\frac{2-\gamma}{\gamma}\right)\frac{\pi}{3}\;\nu \qquad (55)$$

Now, the first line of (50) gives $\frac{u_2}{u_1}$; eliminating this quantity between the two equations gives

$$\left[\Theta + \frac{\Theta}{\Theta_{12}}\left(1 - \left(\frac{2\gamma-1}{\gamma}\right)\frac{2\pi}{3}\right) + \frac{2\pi}{3} - 2\right]\nu + \left(2 - \frac{2\pi}{3}\right)\tau = \Theta - \frac{\Theta}{\Theta_{12}} \qquad (56)$$

For our third linear equation ($\frac{d\delta}{dt}$, $\frac{dT_m}{dt}$, u_1) we return to the form (38) of the energy equation, which as it stands is an energy flux equation. Using the assumed profiles, we can obtain an explicit form of this flux equation, namely,

$$\left\{ \begin{array}{c} 0 \\ \left[1 - \Theta + \frac{\pi}{12}\eta^2(3-2\eta)\ \nu + (\eta - \frac{\pi}{12}\eta^3)\,\tau + \right] \\ \left[(\Theta-1)\,\nu - \frac{\pi}{4\gamma}\nu\left[\eta^2(2-\eta) - (2-\gamma)(\eta^2 - \frac{\eta^3}{3})\right]\right] \\ 0 \end{array} \right\} + \frac{\gamma-1}{\gamma}\frac{\frac{d}{dx}\left(\int_{T_1}^{T} k\,dT\right)}{p_1\ u_1} = 0 \quad (57)$$

where we have used $k\frac{\partial T}{\partial x} = \frac{\partial}{\partial x}\left(\int^{T} k\,dT\right)$, since the thermal conductivity k is mostly a function of temperature itself. The quantity $\int^{T} k\,dT$ is sometimes called the heat flux potential. A useful integral relation can be obtained by integrating equation (57) first between $-\infty$ and 0, then between 0 and $+\infty$, and taking the difference of the two results. This process has the virtue of cancelling from the bracketed part of (57) any terms not multiplying either ν or τ; since both ν and τ contain $1/u_1$ in their definition, and so does the last term of (57), the resulting equation does not contain u_1, and is a linear relationship between $\frac{d\delta}{dt}$ and $\frac{dTm}{dt}$, in which the heat conduction terms appear prominently. The result after some algebra is

$$\frac{\gamma - 1}{\gamma}\frac{7\pi}{24}\nu - (1 - \frac{7\pi}{24})\,\tau = -(2\,K_{1m} - K_{12}) \quad (58)$$

where

$$K_{1m} = \frac{\gamma - 1}{\gamma}\frac{\int_{T_1}^{T_m} k\,dT}{p_1\ u_1\ \delta}\ , \quad K_{12} = \frac{\gamma - 1}{\gamma}\frac{\int_{T_1}^{T_2} k\,dT}{p_1\ u_1\ \delta} \quad (59)$$

6. Solution of the Equations. We have now a set of three linear equations involving ν, τ and independent terms. These are equations (54), (56), and (58). We could revert to dimensional quantities to expose the fact that some of the independent (right hand side) terms of these equations

are proportional to u_1, and solve the three equations for u_1, $\frac{d}{dt}$, $\frac{dT_m}{dt}$. An alternative procedure is to eliminate first ν and τ among the three equations and then solve the resulting relation for u_1. For algebraic ease, we rewrite the three quations in the form

$$a_{11}\nu + a_{12}\tau = \frac{1}{\mu_o \sigma_m u_1 \delta} - \frac{\Theta}{\pi} \ln (1 - \pi) \qquad (54a)$$

$$a_{21}\nu + a_{22}\tau = \Theta - \frac{\Theta}{\Theta_{12}} \qquad (56a)$$

$$a_{31}\nu + a_{32}\tau = - \frac{2 K'_{1m} - K'_{12}}{u_1 \delta} \qquad (58a)$$

where

$$K'_{1m} \equiv K_{1m} x (u_1 \delta) = \frac{\gamma - 1}{\gamma} \frac{\int_{T_1}^{T_m} k dT}{p_1} \qquad (59)$$

with a similar definition for K'_{12}. The definitions of a_{11}, a_{12}, a_{21}, a_{22}, a_{31} and a_{32} are obvious from the original equations. The eliminant relationship is the vanishing of the determinant

$$\begin{vmatrix} a_{11} & a_{12} & - \frac{1}{\mu_o \sigma_m u_1 \delta} + \frac{\Theta}{\pi} \ln (1 - \pi) \\ a_{21} & a_{22} & - \Theta + \frac{\Theta}{\Theta_{12}} \\ a_{31} & a_{32} & \frac{2 K'_{1m} - K'_{12}}{u_1 \delta} \end{vmatrix} = 0 \qquad (60)$$

which can be solved for $u_1 \delta$:

$$u_1 \delta = \frac{\frac{A_1}{\mu_o J_m} - (2K'_{1m} - K'_{12}) A_3}{\frac{\Theta}{\pi} \ln (1 - \pi) A_1 + (-\Theta + \frac{\Theta}{\Theta_{12}}) A_2} \qquad (60)$$

where A_1, A_2, A_3 are the adjoint determinants

$$A_1 = a_{21}\, a_{32} - a_{31}\, a_{22}$$

$$A_2 = a_{31}\, a_{12} - a_{32}\, a_{11} \qquad (61\ a, b, c)$$

$$A_3 = a_{11}\, a_{22} - a_{21}\, a_{12}$$

Once $u_1\delta$ has been calculated, any pair of (54), (56), (58) can be solved for ν, τ. Using for instance (56a) and (56a)

$$\nu = \frac{a_{32}\left(\Theta - \frac{\Theta}{\Theta_{12}}\right) + a_{22}\left(\frac{2K'_{1m} - K'_{12}}{u_1\delta}\right)}{A_1} \qquad (62)$$

$$\tau = -\frac{a_{21}\left(\frac{2K'_{1m} - K'_{12}}{u_1\delta}\right) + a_{31}\left(\Theta - \frac{\Theta}{\Theta_{12}}\right)}{A_1} \qquad (63)$$

The velocity u_2 could now be calculated from, say, equation (55). We notice at this point that the right hand sides of (60), (52) and (63) are functions of the single unknown T_m (plus given quantities). In other words, using the definitions of ν and τ (equations (51),

$$\frac{1}{u_1}\frac{d\delta}{dt} = \nu\,(T_m) \qquad (64)$$

$$\frac{\delta}{u_1 T_m}\frac{dT_m}{dt} = \tau\,(T_m) \qquad (65)$$

$$u_1\delta = F\,(T_m) \qquad (66)$$

From these we can obtain easily

$$\frac{d(\delta^2)}{dt} = 2\,(u_1\delta)\,\nu \tag{67}$$

$$\delta^2 \frac{dT_m}{dt} = (u_1\delta)\,T_m\,\tau \tag{68}$$

and by division, time is eliminated:

$$\frac{d\ \ln \delta^2}{d\ T_m} = \frac{2\nu}{T_m \tau} \tag{69}$$

or

$$\delta^2 = \delta^2(0)\ \exp\left(\int_{T_m(0)}^{T_m} \frac{2\nu}{T_m \tau}\ d\ T_m\right) \tag{70}$$

since the right hand side of (69) (as well as of (67) and (68)) depends on T_m alone. Once δ has been thus obtained as a function of T_m, a second integration gives time; from (68),

$$t = \int_{T_m(0)}^{T_m} \left(\frac{\delta^2}{u_1 \delta\ T_m^2}\right) d\ T_m \tag{71}$$

which completes the calculation.

7. Application to the Electro-magnetic Fanjet. For discharges in air, we will use some rough apporixmations to the electrical and thermal conductivity, from the original data of Yos (Reference 2). Since there is a weak pressure dependence in both cases, we adopt values corresponding to approximately 0.1 - 1 atm. The fits are

$$\underset{(\text{mho/m})}{\sigma} = \begin{cases} 0 & \text{for } T < 6000\ \text{K} \\ \dfrac{T - 6000}{1.5} & 6000 \le T \le 18{,}000\ \text{K} \\ 8000 & T > 18{,}000\ \text{K} \end{cases} \tag{72}$$

and

$$k = 3\left(\frac{T}{26000}\right) + 4.5 \exp\left[-\left(\frac{T - 5000}{1000}\right)^2\right] \quad (73)$$

(watt/m-K)

The last term here accounts for the sharp peak in thermal conductivity associated with transport of dissociation energy at about 5000 K. From (73) the heat flux potential is

$$\int_{T_1}^{T} k\,dT = 1000\left\{\frac{3}{52}\,(y^2 - y_1^2) + 4.5\sqrt{\frac{\pi}{2}}\left[\operatorname{erf}(y-5) - \operatorname{erf}(y_1-5)\right]\right\} \quad (74)$$

where $y \equiv T/1000$. For $T = T_m \gtrsim 7000$ K and $T_1 \lesssim 3000$ K, the error functions (erf) approach ± 1, and we can use

$$\int_{T_1}^{T_m} k\,dT \simeq 1000\left[\frac{3}{52}\,(y_m^2 - y_1^2) + 4.5\sqrt{\pi}\right] \quad (75)$$

while for $T = T_2 \lesssim 3000$ K as well,

$$\int_{T_1}^{T_2} k\,dT \simeq 1000\,\frac{3}{52}\,(y_2^2 - y_1^2) \quad (76)$$

Calculations were performed for two sets of conditions, corresponding to Cases 1 and 4 of Chapter VII . Starting from the given altitude and flight speed, and assuming 90% propulsion efficiency, a "piston" velocity u_p (relative to the undisturbed flow) was calculated for each case using $u_p = 2\,v\left(\frac{1 - \eta_p}{\eta_p}\right)$. After converting this to a piston Mach number, M_p, the equations of Section 2 were used to compute P_1, T_1, P_2, T_2 and the nondimensional magnetic pressure

$$\pi = \frac{B_2^2}{2\mu_o} = 1 - \frac{P_2}{P_1} \quad (77)$$

Then, a range of a sheet temperatures from 7000 K to about 34,000 K was assumed in each case, and the equations of Section 5 were used to calculate corresponding values of ν, τ, u_2/u_1 and, consequently, $\frac{d\ln\delta^2}{d\bar{T}_m}$ and $\frac{1}{\delta^2}\frac{dt}{d\bar{T}_m}$ (equations (69) and (68) respectively). These give at a glance the rates of change of thickness and temperature as well as the magnitudes and directions of the relative velocities u_1, u_2. For further detail, integrations versus T_m could be made easily, but only after initial values $T_m(0)$, $\delta(0)$ are specified. Sample calculations of this sort are also reported for completeness (Figure C-7 and C-8).

The results are tabulated in Table C-4 (Case 1) and Table C-5 (Case 4). These tables include also the quantity $d\delta^2/dt = \left(\frac{d\ln\delta^2}{d\bar{T}_m}\right)\Big/\left(\frac{1}{\delta^2}\frac{dt}{d\bar{T}_m}\right)$, which, although it is not directly useable for integration (until t itself is determined), can give a direct indication of the rate of expansion of the sheet.

Figure C-7 shows the time development of the sheet temperature and thickness and the relative flow velocities u_1 (ahead of the sheet) and u_2 (behind), for the conditions of Case 1, with the initial layer thickness taken to be 0.40m (δ = 0.2m). The sheet Mach number M_p in this case is only 0.595 (relative velocity, 178 m/sec), and the pressure p_o is 0.01 atm.

If the initial sheet temperature (provided by the preionizing mechanism, whatever it is) is 7000 K, which is about the minimum temperature for which there is significant conductivity in equilibrium air, it takes about 2 msec for the layer thickness to grow by 5% during which time the layer temperature changes by 4000 K. If the initial temperature is 10,000 K, on the other hand, the thickness variation becomes neglible, while the temperature increases somewhat faster (by 10,000 K in 2 msec).

The most striking difference between the two initial temperatures is in the relative flow speeds. For $T_m(0)$ = 7000 K, u_1 starts out at -80 m/sec (flow into the sheet), and u_2 at -412 m/sec (flow out of the

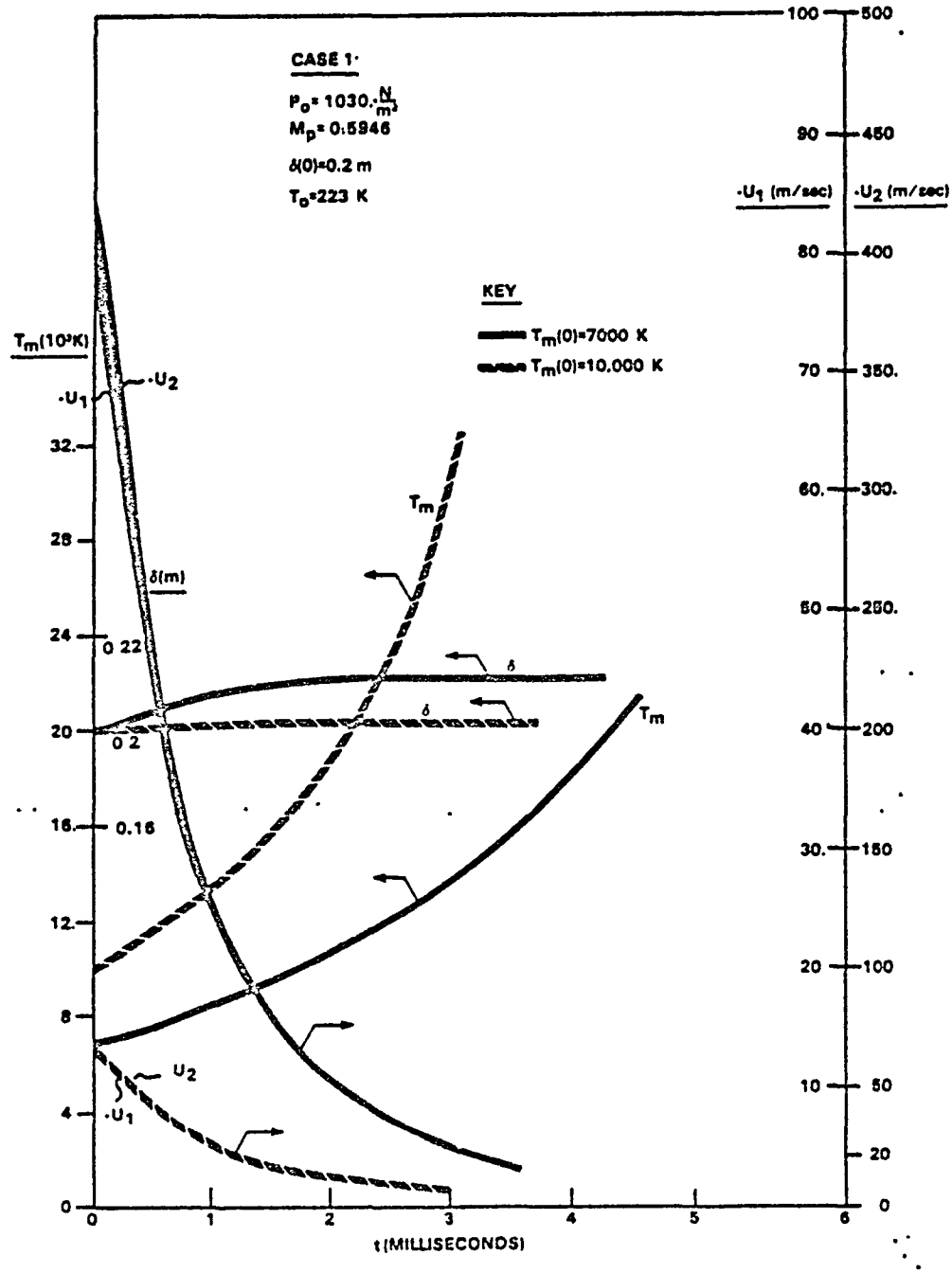

Figure C-7. Results for Case I

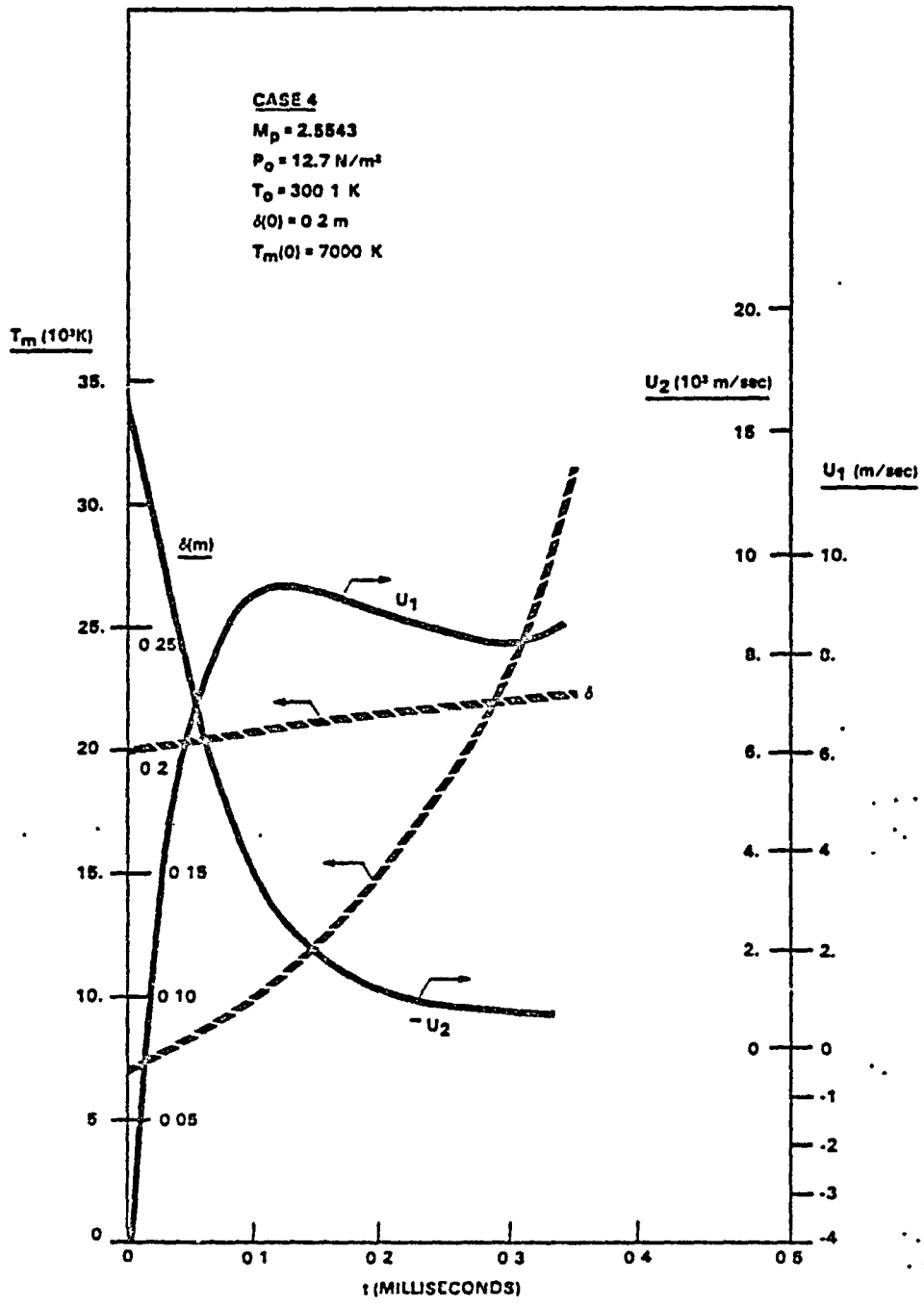

Figure C-8. Results for Case IV

TABLE C-4. RESULTS FOR CASE I

(y = 31 km, v = 800 m/s)

P_0 = 1030 $\frac{N}{m^2}$, T_0 = 223.1 K, M_p = 0.5946, M_s = 1.4185, π = 0.81097, B_2 = 0.06764 Tesla, P_1 = 2246. $\frac{N}{m^2}$, T_1 = 282.6 K, P_2 = 424.5 $\frac{N}{m^2}$, T_2 = 173.2 K

T_m (K)	7000	8000	10,000	13,000	16,000	19,000	22,000	25,000	28,000	31,000
$\sigma_m \left(\frac{mho}{cm}\right)$	6.67	16.07	26.67	46.67	66.67	80.0	80.0	80.0	80.0	80.0
$u_1 \delta \left(\frac{m^2}{sec}\right)$	-16.414	-5.368	-2.828	-2.2188	-0.6755	-0.4619	-0.3933	-0.3404	-0.2982	-0.2635
ν	-0.4120	-0.3681	-0.3204	-0.2071	-0.05911	+0.0914	0.1753	0.2746	0.3906	0.5250
η	-0.6610	-2.027	-4.0032	-10.341	-21.13	-35.30	-47.53	-62.95	-82.21	-106.05
$\frac{d \ln \delta^2}{dT_m}$ (K^{-1})	1.7808×10^{-4}	4.274×10^{-5}	1.601×10^{-5}	3.081×10^{-6}	3.496×10^{-7}	-2.718×10^{-7}	-3.353×10^{-7}	-3.490×10^{-7}	-3.394×10^{-7}	-3.194×10^{-7}
$\frac{1}{\delta^2} \frac{d\delta^2}{dT_m} \left(\frac{sec}{m^2 \cdot K}\right)$	1.316×10^{-5}	1.081×10^{-5}	8.932×10^{-6}	6.103×10^{-6}	4.378×10^{-6}	3.228×10^{-6}	2.432×10^{-6}	1.867×10^{-6}	1.457×10^{-6}	1.154×10^{-6}
u_2/u_1	5.038	5.065	5.094	5.1637	5.254	5.346	5.399	5.459	5.530	5.612
$\frac{d\delta^2}{dt} \left(\frac{m^2}{sec}\right)$	13.5	3.954	1.812	0.5042	0.0799	-0.0842	-0.1379	-0.1869	-0.2329	-0.303

TABLE C-5. RESULTS FOR CASE IV

(y = 65km, v = 4000 m/s)

P_2 = 0.085 N/m$_2$, T_2 = 71.8 K, P_0 = 12.7 N/m^2, T_0 = 300.1 K, M_p = 2.5543, M_s = 3.3625, w = 0.99486, B_2 = 0.02038 Tesla, P_1 = 165.N/m^2, T_1 = 939.5 K

T_m (K)	7000	7100	7200	7210	7220	7230	7300	7500	8000	9000
$\sigma_m(\frac{mho}{cm})$	7.67	7.33	8.	8.067	8.133	8.2	8.67	10	13.33	20.
$u_1\delta\left(\frac{m^2}{sec}\right)$	-0.7889	-0.3773	-0.0424	-0.0124	+0.01706	0.0460	0.2339	0.6590	1.284	1.765
v	8.071	21.417	222.7	771.7	-568.1	-213.4	-45.15	-18.56	-11.29	-8.950
τ	-189.1	-395.8	-352.6	-12065.	+8774.	3257	640.7	228.4	118.7	89.06
$\frac{d\ln\delta^2}{dT_m}$ (K^{-1})	-1.2196×10^{-5}	-1.523×10^{-5}	-1.755×10^{-5}	-1.774×10^{-5}	-1.794×10^{-5}	-1.821×10^{-5}	-1.931×10^{-5}	-2.166×10^{-5}	-2.376×10^{-5}	-2.233×10^{-5}
$\frac{1}{\delta^2}\frac{d\tau}{dT_m}\left(\frac{sec}{m^2\cdot K}\right)$	9.577×10^{-7}	9.429×10^{-7}	9.283×10^{-7}	9.269×10^{-7}	9.254×10^{-7}	9.240×10^{-7}	9.140×10^{-7}	8.857×10^{-7}	8.198×10^{-7}	7.070×10^{-7}
u_2/u_1	4184	7866	63770	216200	-155770.	-57263.	-10590	-3207	-1189	-540.2
$\frac{d\delta^2}{dt}\left(\frac{m^2}{sec}\right)$	-12.735	-16.15	-18.90	-19.13	-19.38	-19.61	-21.13	-24.45	-28.98	-31.58

TABLE C-5. RESULTS FOR CASE IV (CONTINUED)

T_m (K)	10,000	12,000	14,000	16,000	18,000	20,000	22,000	24,000	26,000	30,000
$\sigma_m\left(\frac{\text{mho}}{\text{cm}}\right)$	26.67	40	53.33	66 67	80 0	80 0	80 0	80 0	80 0	80 0
$u_1\,\delta\left(\frac{m^2}{sec}\right)$	1.905	1 9320	1.8914	1 8537	1 8312	1.8067	1 8029	1 8142	1.8372	1.9033
ν	-8 283	-7.778	-7 566	-7 450	-7 376	-7.356	-7 337	-7.320	-7.305	-7 279
η	85.32	90.64	100.45	111.7	123 7	137,3	150.8	164 3	177.7	204.4
$\frac{d\ln\delta^2}{dT_m}$ (K^{-1})	-1.941×10^{-5}	-1.430×10^{-5}	-1.076×10^{-5}	$-8\ 335\times10^{-6}$	$-6\ 627\times10^{-6}$	-5.357×10^{-6}	$-4\ 422\times10^{-6}$	-3.713×10^{-6}	-3.162×10^{-6}	-2.374×10^{-6}
$\frac{1}{\delta^2}\frac{d\xi}{dT_m}\left(\frac{sec}{m^2-K}\right)$	$6\ 152\times10^{-7}$	4.758×10^{-7}	$3\ 759\times10^{-7}$	$3\ 218\times10^{-7}$	2.453×10^{-7}	$2\ 015\times10^{-7}$	$1\ 671\times10^{-7}$	$1\ 398\times10^{-7}$	1.178×10^{-7}	8.543×10^{-7}
u_2/u_1	-355 2	-214 8	-156 1	-123 8	-103 5	-97.76	-92 55	-87 83	-83 58	-76.37
$\frac{d\xi^2}{dt}\left(\frac{m^2}{sec}\right)$	-31 55	-30 05	-28.62	-27.62	-27.01	-26.59	-26.46	-26.56	-26 84	-27.78

sheet). These high velocities then decay with time, but remain significant for the first 1 - 2 msec. Their significance is that the current sheet is quite permeable to the flow, contrary to the initial assumption of a "perfect piston" as a first approximation. Although u_1 falls rapidly from -80 m/sec to -30 m/sec after 1 ms, the sheet is itself advancing at only 178 m/sec relative to the undisturbed air; this implies relative "permeabilities" of between 0.44 and 0.17. On the other hand, for $T_m(0) = 10{,}000$ K, the relative velocities are low: u_1 from -14 m/sec to -5 m/sec after 1 m/sec, or relative permeability from 0.08 to 0.03.

Figure C-8 shows results for a very low pressure case ($p_o \simeq 10^{-4}$ atm) with high sheet Mach number ($M_p = 2.55$). Here the pressure ahead of the sheet is significantly greater than ambient ($p_1 = 165$ N/m^2 vs. $p_o = 12.7$ N/m^2), and the time scale is seen to follow in proportion to this pressure p_1, which prevails throughout most of the sheet (see Figure C-8). Thus, it only takes 0.3 msec for T_m to raise from 7000 K to 30,000 K (although the thickness remains nearly constant). Regarding the relative flow velocities, we see here a reversal of u_1; at the initial time ($T_m(0) = 7000$ K), u_1 starts at -4 m/sec in the usual sense (flow crossing the sheet backwards). Later, however, u_1 becomes positive and settles to about 8 m/sec, while u_2 remains negative and continues to decrease with time. This corresponds to net "blowing" of gas out of the sheet region, and, as seen from the air entrained ahead of it, to a retrograde motion of the sheet. The magnitude of u_1 remains, however, small compared to the sheet velocity of 889 m/sec.

8. Discussion of Results

Figure C-7 and C-8 give us some understanding of how the current sheet temperature, thickness and permeability evolve throughout a single thrust pulse of an electromagnetic "piston". For good "gas sweeping" performance, permeability of the current sheet (proportional to u_1/u_p) must quickly be reduced to the level of a few percent, and the gas temperature within the sheet quickly driven above 18,000 K (in order to

reach the maximum gas conductivity)shortly after initiation of the discharge. Since the "point design" for a laser driven MHD generator output calls for a 0.5 to 1.0 msec duration pulse, peak current sheet sweeping performance should really occur within 0.1 msec or earlier.

As shown in Figure 7 for the 31km altitude case ($T_m(0)$ = 7000 K) acceptable levels of current sheet temperature and permeability are not reached until 9 msec into the pulse. This condition demands a pulse duration of 40 to 400 msec--quite outside the range of interest. Increasing the initial current sheet temperature to 10,000 K permits the attainment of a reasonable current sheet efficiency by 2 msec, which is only a factor of two better. The necessary levels of improvement can be accomplished only by raising the voltage of the MHD generators--by switching them into various parallel/series combinations.

The 68km case shown in Figure C-8 presents an altogether different picture. Sufficiently low levels of current sheet permeability are attained at the moment of discharge initiation, even at $T_m(0)$ = 7000 K. Peak conductivity of the current sheet (i.e., 18,000 K) is reached in the first 0.22 msec of the 1 ms long pulse, which is probably adequate: Hence we conclude that the MHD generator load line pictured in Figure C-3 (i.e., all 24 generators wired in parallel) of Appendix D should be suitable for the 4 km/s, 70 KM altitude regime at the upper end of the MHD-fanjet performance envelope. At lower altitudes and velocities, substantially higher voltage discharges will be required for rapid escalation of the plasma sheet temperature to 18,000 K.

Finally, we suggest that any current sheet driven hard enough to reach 18,000 K (and very low permeability) in the first 10μseconds will probably have a piston velocity, (u_p), of at least 330 m/s--anywhere along the nominal MHD fanjet flight trajectory.

Nomenclature For Appendix C

a_o	=	the undisturbed speed of sound ($\sqrt{\gamma RT_o}$)
A_1, A_2, A_3	=	adjoint determinants
B	=	magnetic induction
C_f	=	piston thrust coefficient = $F/\rho_o u_p^2$
E	=	electric field
F	=	thrust
h	=	enthalpy
j	=	current per unit area
J	=	electric current per unit depth (of current sheet)
K	=	gas thermal conductivity
M_p	=	piston Mach number = u_p/a_o
M_s	=	shock Mach number = V_s/a_o
P	=	gas pressure
R	=	gas constant
T	=	gas temperature
T_m	=	gas temperature within the actuator current sheet
U	=	forward local gas velocity
u_p	=	actuator sheet speed; "piston" speed
u(x,t)	=	gas velocity relative to the actuator current sheet
u_1	=	relative gas flow velocity ahead of the actuator sheet
u_2	=	relative gas flow velocity behind the actuator sheet
V_s, V_{shock}	=	leading edge shock wave velocity (ahead of advancing actuator sheet)
X	=	positive distance in the direction of "piston" advance
γ	=	ratio of specific heats = C_p/C_v
δ	=	actuator current sheet "half" width
δ_D	=	Dirac delta function
η	=	nondimensionalized variable = $1 - \xi = 1 - x/\delta$
Θ	=	nondimensional quantity = T_m/T_1
Θ_{12}	=	nondimensional quantity = T_2/T_1
μ_o	=	permeability constant = $4\pi \times 10^{-7}$ Henry/meter

ν	=	nondimensional quantity = $\frac{1}{u_1}\frac{d\delta}{dt}$
ξ	=	nondimensionalized variable = x/δ
π	=	nondimensional magnetic pressure = $B_2^2/2\mu_0 P_1$
ρ	=	gas density
σ	=	gas conductivity
τ	=	nondimensional quantity = $\frac{\delta}{U_1 T_m}\frac{dTm}{dt}$
φ_a	=	work function of anode material

Subscripts

"0"	-	undisturbed or ambient gas conditions
1	-	far behind piston
2	-	expansion fan
3	-	behind piston
4	-	shocked gas
5	-	undisturbed gas

REFERENCES FOR APPENDIX C

1. Thompson, Phillip A., Compressible Fluid Mechanics, Chapter 8, McGraw-Hill, 1972.

2. Yos, J., "Transport Properties of Nitrogen, Hydrogen, Oxygen and Air to 30,000°K, AVCO TM RAD-TM-63-7, 1963. Reprint 1966.

APPENDIX D

MHD FANJET "SNOW PLOW" CALCULATIONS

AUTHOR:

D. Heimerdinger
Graduate Student
Department of Aeronautics and Astronautics
Massachusette Institute of Technology
Cambridge, MA

This study was performed for the Defense Advanced Research Projects Agency under contract No. 555713-S to The Brookhaven National Laboratory.

APPENDIX D
MHD FANJET "SNOW PLOW" CALCULATIONS

In this appendix, performance calculations are reported for a nominal 10 m diameter MHD fanjet flying along an exemplary trajectory to space. The calculations were performed with a radially-symetric two-dimensional "snow plow" model, for which derivations of the equations are provided. Due to the 2-D non-steady nature of the problem, the equations are solved numerically.

1. Two-Dimensional Snow Plow Model

For an accurate representation of the MHD fan actuator disk, two dimensionality is unavoidable due to the nature of the Lorentz force in the discharge. As current flows radially from the cathode to the anode through the actuator disk, a pseudo-toroidal self-magnetic field is created which varies as $\frac{1}{r}$ from the vehicle central axis. Coincidentally, due to current conservation, the electric current density must also follow a $\frac{1}{r}$ rule. The resultant $\bar{j} \times \bar{B}$ force provides for a decrease in force per unit area as the radial distance increases. Thus significant deformation of the initially planar current sheet will occur as the discharge progresses in time. One viable approach to the problem is to follow discrete material points along the accelerating current disk. This approach will form the basis for the derivation.

Let us assume that the shape of the current sheet can be parameterized by the equation $x = X(r,t)$, that material points on it move with change of velocity $\bar{u} = (u_r, u_x)$, and that a material point has position (r,x) at time t. At any time $t + dt$, that point has shifted to $(r + u_r dt, x + (u_x + U_o)dt)$, where U_o is the flight speed, which must still satisfy $x = X(r,t)$, so:

$$x + (u_x + U_o)dt = X(r + u_r dt, t - dt)$$

$$= X(r,t) + \frac{\partial X}{\partial r} u_r \, dt - \frac{\partial X}{\partial t} \, dt \qquad (1)$$

Therefore X(r, t) satisfies

$$\frac{\partial X}{\partial t} + u_r \frac{\partial X}{\partial r} = u_x + U_o \tag{2}$$

Figure D-1 portrays the analytical approach used to model a differential element as it deforms from initial time t to time t+ dt. As indicated in Figure D-1, ds is the differential arc-length, and $\mu(r,t)$ is the mass per unit area carried on the current sheet. For a given δs, the total mass around the ring can be found by integrating over the entire current sheet as follows:

$$dm = 2\pi r \, ds \, \mu \tag{3}$$

The material rate of change of that δs equals the amount of mass scooped up as the sheet progresses in time.

$$\frac{d}{dt}(2\pi r \delta s \mu) = 2\pi r \delta s \rho_o u_N \tag{4}$$

where ρ_o is the air density and u_n is the velocity normal to the current sheet. From Figure D-1, it is readily seen that

$$\frac{\delta x}{\partial r} = -\tan x; \quad \delta r = \delta s \cos x; \quad \delta x = -\delta s \sin x \tag{5}$$

Also using the relations

$$\frac{d(\delta \vec{s})}{dt} = (\delta \vec{s} \nabla)\vec{u} \tag{6}$$

and

$$\frac{dr}{dt} = u_r \tag{7}$$

the result comes directly through the application of fluid mechanics:

$$\mu\left[\frac{u_r}{r} + \cos\alpha\left(\cos\alpha\ \frac{\partial u_r}{\partial r} - \sin\alpha\ \frac{\partial u_x}{\partial r}\right)\right] + \frac{\partial u}{\partial t} + u_r\ \frac{\partial u}{\partial r}$$
$$= \rho_o(u_r \sin\alpha + u_x \cos\alpha) \qquad (8)$$

In deriving the force equations, additional complexity results from coupling between fluid dynamics and electrodynamics within the system. As current moves through the actuator disk, a magnetic field (and an associated magnetic pressure) is established. The magnetic pressure is defined as $P_m = B^2/2\mu_o$. The rate of change of momentum is therefore equated with the magnetic pressure integrated over the current sheet:

$$\frac{d}{dt}\ (2\pi r\delta s\mu\vec{u}) = \frac{B^2}{2\mu_o}\ 2\pi r\delta\vec{s}n \qquad (9)$$

Taking this derivative

$$\ldots\ \mu\frac{d\vec{u}}{dt} = \frac{B^2}{2\mu_o}\ \vec{n} - \rho_o\, u_n\ \vec{u} \qquad (10)$$

or in component form.

$$\mu\left(\frac{\partial u_r}{\partial t} + u_r\ \frac{\partial u_r}{\partial r}\right) = \frac{B^2}{2\mu_o}\ \sin\alpha - \rho_o\ (u_r\sin\alpha + u_x\cos\alpha)\ u_r \qquad (11)$$

$$\mu\left(\frac{\partial u_x}{\partial t} + u_r\ \frac{\partial u_x}{\partial r}\right) = \frac{B^2}{2\mu_o}\ \cos\alpha - \rho_o\ (u_r\sin\alpha + u_x\cos\alpha)\ u_x \qquad (12)$$

From Gauss' Law the magnetic field is related to the total current by

$$B = \frac{\mu o}{2\pi} \left(\frac{I_{tot}}{r}\right) \tag{13}$$

As the current sheet develops in time, the electrodynamics change. An induced voltage occurs--which changes with the inductance of the actuator disk. This resultant change in induced voltage alters the circuit dynamics in accordance with the following expression

$$V_{Gen} = V_{ind} - I_{tot}R \tag{14}$$

Depending on the generator's characteristics and the load resistance of the plasma sheet, the effects of V_{ind} on I_{to} can be dominant. From electrodynamics

$$V_{ind} = \frac{d\Phi}{dt} \tag{15}$$

where

$$\Phi = \iint B\, dxdr = \frac{\mu_o I_{tot}}{2\pi} \int_{x_o}^{x} \int_{r_{min}}^{r_{max}} \frac{dx(r, t)}{r}\, dr$$

$$\Phi = \frac{\mu_o I_{tot}}{2\pi} \int_{r_{min}}^{r_{max}} (x - x_o) \frac{dr}{r} \tag{16}$$

Differentiating Φ with respect to time, we have

$$V_{ind} = \frac{\mu_o}{2\pi}\left[\frac{dI_{tot}}{dt}\int_{r_{min}}^{r_{max}}(x - x_o)\frac{dr}{r} + I_{tot}\int_{r_{min}}^{r_{max}}\left(\frac{\partial x}{\partial t} - \frac{\partial x_o}{\partial t}\right)\frac{dr}{r}\right] + I_{tot}\left[\left(\frac{x-x_o}{r}\ \frac{dr}{dt}\right)_{r_{max}} - \left(\frac{x-x_o}{r}\ \frac{dr}{dt}\right)_{r_{min}}\right] \quad (17)$$

But at r_{max}, $dr/dt = 0$; and at r_{min}, $X = X_o$. Thus the derivative terms at the end points are identically 0, leaving

$$V_{ind} = L(t)\frac{dI_{tot}}{dt} + I_{tot}\dot{L} \quad (18)$$

A generator that has a characteristic internal resistance and follows a standard load line graph has the following equation of operation

$$V_{gen} = V_{gen}^{oc}(t) - R_{int}\,I_{tot} \quad (19)$$

where V_{gen}^{oc} is the open circuit voltage, and R_{int} is the MHD generator internal resistance.

Combining terms

$$V_{gen} = V_{ind} - RI_{tot} \quad (20)$$

$$V_{gen}^{oc} - R_{int}\, I_{tot} = \frac{dI_{tot}}{dt} + \dot{L}\, I_{tot} + R I_{tot}$$

$$\frac{dI_{tot}}{dt} = \frac{1}{L}\left[V_{gen}^{oc} - I_{tot}\,(\dot{L} + R_{int} + R)\right] \qquad (21)$$

If it is assumed that the MHD generators are rectangular prismatic shapes as in Figure D-2, the behavior of the generator is seen in the equations below.

$$R_{int} = \frac{1}{N_{gen}} \quad \frac{1}{\sigma_{gen}} \quad \frac{H}{LD} \qquad (22)$$

$$V_{gen}^{oc}\,(t) = u_{gen}\,(t)\, B_{gen}\, H \qquad (23)$$

The load resistance of the actuator disk is calculated by the following equation.

$$R_{load} = \frac{1}{2\pi\sigma\ell} \ln \frac{R_o}{R_i} \qquad (24)$$

where

σ = 200 mho/cm

ℓ = 0.5 (sheet thickness)

R_o = cathode radius

R_i = 5 m (anode radius)

From nominal performance data estimated in Appendix B for the XMHD generators, a mock load line plot was constructed. From it an open circuit voltage of 12957 V was determined, and the slope provided for a total MHD resistance of $5.7 \times 10^{-4}\ \Omega$, as shown in Figure D-3. This represents the combined output of 24 MHD generators, electrically connected in parallel.

A value for the initial plasma inductance was computed on the basis of a toroid measuring 1.0 meter in height. As the radius increases so does the inductance, in accordance with the equation

$$L_o = \mu_o \, h \ln \frac{R_o}{R_i} \tag{25}$$

where h is the toroid height.

The major output parameters calculated by the computer are the time-stepped position of the current sheet, routine the total momentum change ($\int F dt$) and the total electric energy consumed within one pulse. These quantities are defined as

$$\int F dt = U_o \Sigma \mu_i A_i \mu_{x_i} \tag{26}$$

$$\Delta Ke = \tfrac{1}{2} \Sigma \mu_i A_i u_N^2 - \mu_i A_{o_i} U_o^2 \tag{27}$$

2. Numerical Calculation Procedure

This section provides a brief discussion of the conversion from continuous time equations to discrete time equations used in the computer routine.

As mentioned earlier, the approach is to select a number of material points that will be followed throughout the numerical computation. The parameters in the problem are calculated at each material point and these values are considered to act over an area determined by the method of centered difference. Over a given area sector, the parameters are assumed constant. In Figure D-4, point "i" has parameters which act on area δs_i, which is shown as a dashed line.

Once a number of discrete material points has been selected, their up-dates are constructed in a linear manner. The subscripts and superscripts that are used signify the following

Subscripts	Superscripts
x - x direction	n "n"th integer time step
r - r direction	
n - normal direction	
o - ambient conditions	
i - i^d particle	

The x and r directions are indicated in Figure D-5 for five sample material points. In the numerical approach a stepwise procedure is followed, as outlined below.

a. Position Update

Since the particles are convected to a new location, spacial updates are derived from the following equations.

$$\frac{dx_i}{dt} = u_{x_i} - U_o \,, \quad \frac{dr_i}{dt} = U_{r_i} \qquad (27a,b)$$

To first order, expressions can be written for x_i^{n+1} and r_i^{n+1} given their previous values.

$$x_i^{(n+1)} = x_i^{(n)} + (u_{xi}^{(n)} + U_o)\,\Delta t \qquad (28)$$

$$r_i^{(n+1)} = r_i^{(n)} + u_{ri}^{(n)}\,\Delta t \qquad (29)$$

b. Area Element Update

In the two dimensional plane it can be seen from previous Figures 4 and 5 that

$$\tan \alpha_i^{(n+1)} = \left(\frac{x_{i+1} + x_i}{2} - \frac{x_i + x_{i-1}}{2}\right) \left(\frac{r_{i+1} + r_i}{2} - \frac{r_i + r_{i-1}}{2}\right)^{-1}$$

$$= \frac{x_{i+1} - x_{i-1}}{r_{i+1} - r_{i-1}} \tag{30}$$

The line length is simply

$$\delta s_i^{(n+1)} = \left[\left(\frac{x_{i+1} + x_i}{2} - \frac{x_i + x_{i-1}}{2}\right)^2 + \left(\frac{r_{i+1} + r_i}{2} - \frac{r_i + r_{i-1}}{2}\right)^2\right]^{\frac{1}{2}} \tag{31}$$

$$\delta s_i^{(n+1)} = \tfrac{1}{2} \left[(x_{i+1} - x_{i-1})^2 + (r_{i+1} - r_{i-1})^2\right]^{\frac{1}{2}}$$

c. Update r (mass/area)

From

$$\frac{d(r\delta su)}{dt} = r\delta s \rho_o u_n$$

where

$$u_n = u_r \sin \alpha + u_x \cos \alpha$$

Again using a first order update for this

$$r_i(n+1)\ \delta s_i(n+1)\ \mu_i(n+1) = r_i(n)\ \delta s_i(n)\ \mu_i(n) + \Delta t\ r_i(n)\ \delta s_i(n)\ \rho_o(n)\ u_n(n)$$

$$= r_i(n)\ \delta s_i(n)\left(\mu_i(n) + \Delta t\ \rho_o\ u_n(n)\right)$$

$$\mu_i(n+1) = \frac{(r_i \delta s_i)^n}{(r_i \delta s_i)^{n+1}} \left(\mu_i(n) + \Delta t\ \rho_o\ u_n(n)\right) \qquad (32)$$

d. Update Velocities Using the Vector Equation

where

$$\mu \frac{d\vec{u}}{dt} = \frac{B^2}{2\mu_o} \vec{n} - \rho_o u_n \vec{u}$$

$$B = \frac{\mu_o}{2\pi} \frac{I_{tot}^{(n)}}{r_i}$$

Rearranging and using a first order update.

$$u_{r_i}^{(n+1)} = u_r^{(n)} + \Delta t \left[\frac{\left(B_i^{(n)}\right)^2}{2\mu_o} \sin \alpha^{(n)} - \rho_o u_{n_i}^{(n)} u_{r_i}^{(n)}\right] \left(\mu_i^{(n)}\right)^{-1} \qquad (33)$$

$$u_{x_i}^{(n+1)} = u_x^{(n)} + \Delta t \left[\frac{\left(B_i^{(n)}\right)^2}{2\mu_o} \cos \alpha^{(n)} - \rho_o u_{n_i}^{(n)} u_{x_i}^{(n)}\right] \left(\mu_i^{(n)}\right)^{-1} \qquad (34)$$

e. Inductance Update

By definition the inductance is

$$L = \frac{\mu_o}{2\pi} \int \frac{x}{r}\, dr$$

For a given segment i to i+1

$$L_{i+1} = \frac{\mu_o}{2\pi} \int_{r_i}^{r_{i+1}} \frac{x}{r} \, dr \tag{35}$$

and for this given segment, any value for x can be determined from the equation of a line

$$x = x_i + \frac{x_{i+1} - x_i}{r_{i+1} - r_i} (r - r_i) \tag{36}$$

Integrating

$$L_{i+1} = \frac{\mu_o}{2\pi} \int_{r_i}^{r_{i+1}} \left(x_i + \frac{x_{i+1} - x_i}{r_{i+1} - r_i} (r - r_i) \right) \frac{dr}{r}$$

$$= \frac{\mu_o}{2\pi} \left[\left(x_i - r_i \frac{x_{i+1} - x_i}{r_{i+1} - r_i} \right) \ln \left(\frac{r_{i+1}}{r_i} \right) + \left(x_{i+1} - x_i \right) \right]$$

$$L_{i+1} = \frac{\mu_o}{2\pi} \left[\left(\frac{r_{i+1} x_i - r_i x_{i+1}}{r_{i+1} - r_i} \right) \ln \left(\frac{r_{i+1}}{r_i} \right) + \left(x_{i+1} - x_i \right) \right] \tag{37}$$

For a total inductance it is necessary to sum over all i

$$L = L_o + \frac{\mu}{2\pi} \sum_{i=1}^{N} L_{i+1} \tag{38}$$

The derivation for $\dot{L}$ is very similar. Starting from an earlier equation in this chapter, it is seen that

$$\dot{L} = 2\frac{\mu}{\pi}\int_{r_{min}}^{r_{max}} \left(\frac{\partial x}{\partial t} - \frac{\partial x_o}{\partial t}\right) \frac{dr}{r}$$

This leads directly to the equation for $\dot{L}_{i+1}$ which is the same for L_i except $\partial x_i/\partial t$ replaces x_i and $\partial x_{i+1}/\partial t$ replaces x_{i+1}. In the beginning of the system derivation above, it was found that

$$\frac{\partial x}{\partial t} r\, u_r \frac{\partial x}{\partial r} = u_x + U_o$$

$$\frac{\partial x}{\partial t} = u_x + U_o - u_{r_i} \tan \alpha$$

Discretizing this

$$\frac{\partial_{x_i}}{\partial t} = u_{x_i} + U_o - u_{r_i} \tan \alpha \qquad (39)$$

f. Current Update

Again using a linear approximation for the update

$$I_{tot}^{n+1} = I_{tot}^{n} + \Delta t \left(\frac{dI_{tot}}{dt}\right)^n$$

$$= I_{tot}^{N} + \frac{\Delta t}{\dot{L}^n} \left[V_{gen}^{cc} - I_{tot}^{N} \left(\dot{L}^n + R_{int} + R\right)\right]$$

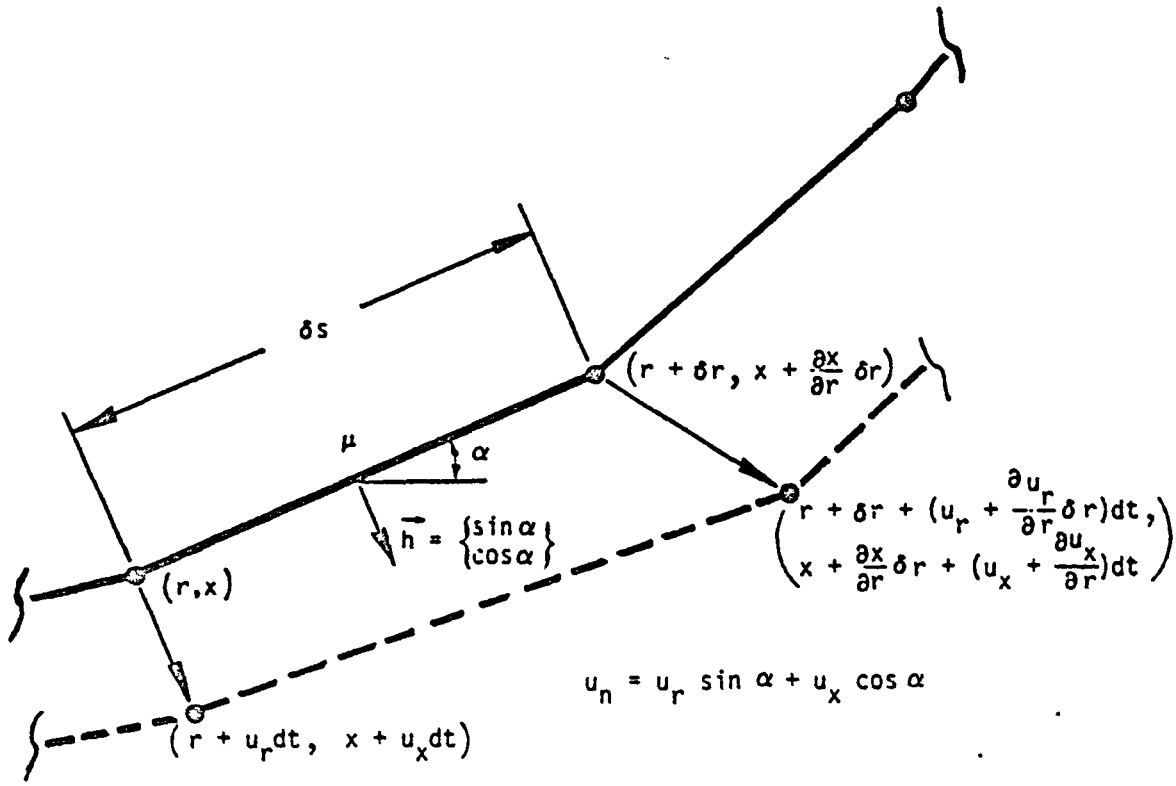

Figure D-1. Analytical Approach

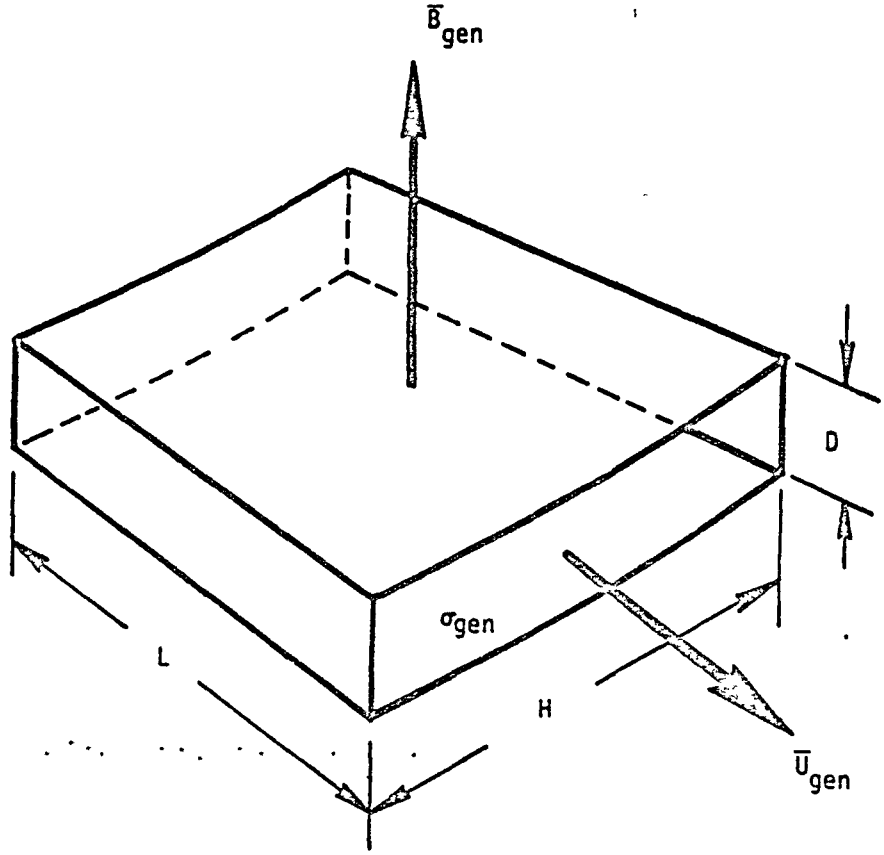

Figure D-2. XMHD Generator

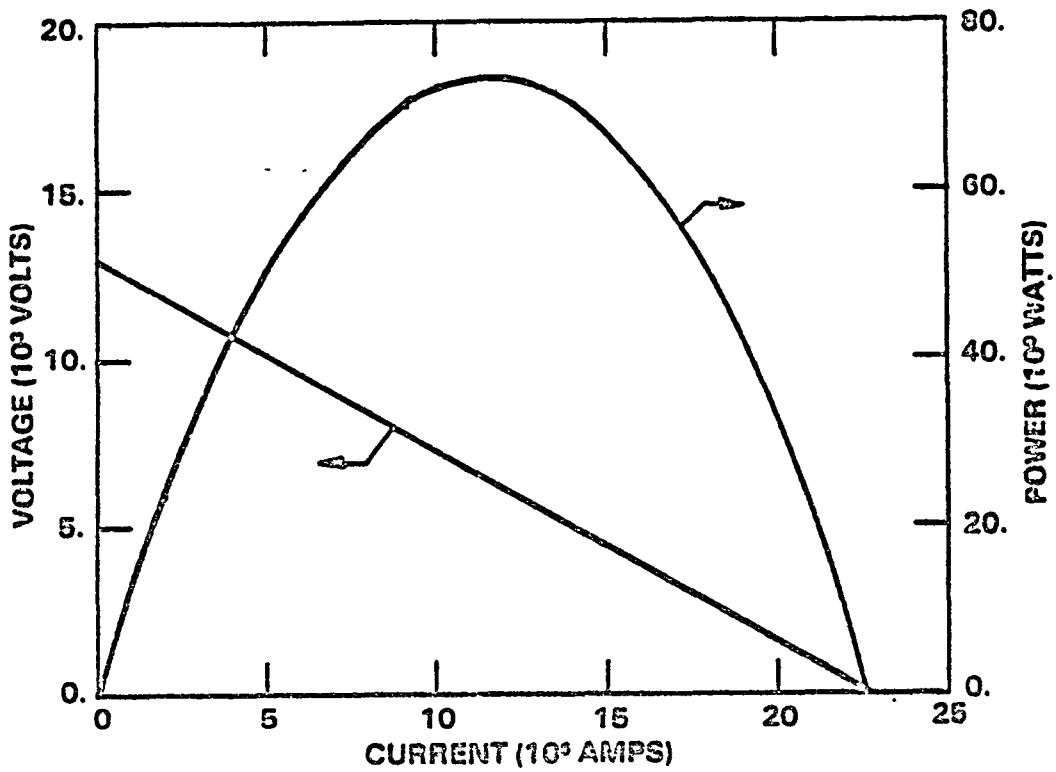

Figure D-3. Voltage and Power Output of XMHD Generators (All 24 are Wired in Parallel)

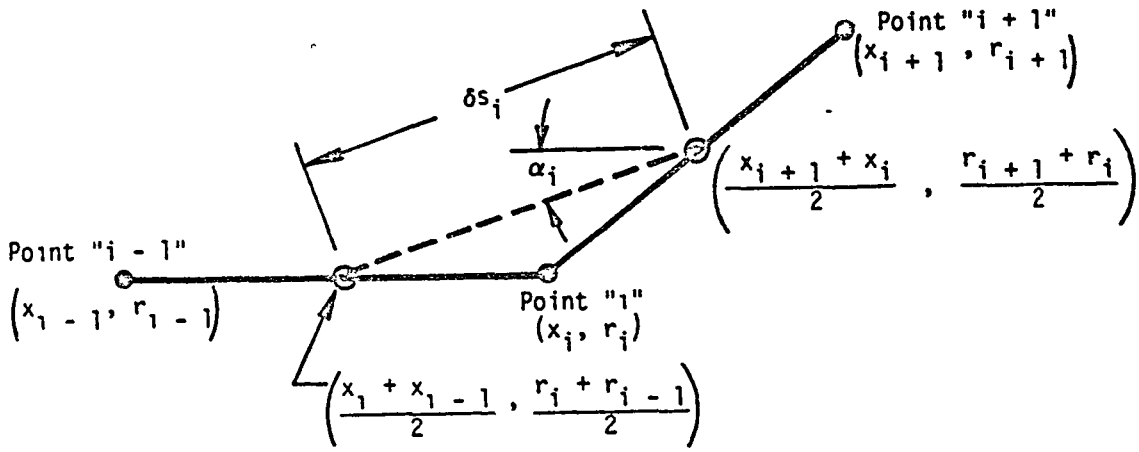

Figure D-4. Nomenclature for Discrete Material Points

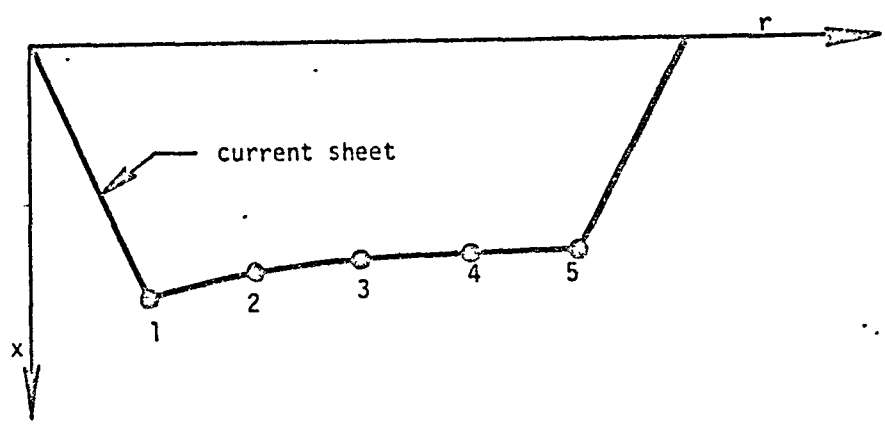

Figure D-5. Coordinates for Stepwise Procedure

END

DATE

FILMED

OCT 22 1986

End of Document